HIGH TEMPERATURE PROPERTIES OF MOLTEN NITRATE SALT FOR SOLAR THERMAL ENERGY STORAGE APPLICATION

By:

MEHEDI BIN MOHAMMAD

A Thesis Presented for the Degree of Doctor of Philosophy,
Submitted to
FSET, Mechanical Engineering Department,
Swinburne University of Technology.

Supervisors
Professor Geoffrey Alan Brooks
A/Professor Muhammad Akbar Rhamdhani

June, 2016

DECLARATION

The author declares that:

- This thesis is a presentation of my original research work to obtain a doctor of philosophy degree at the Swinburne University of Technology.
- This Thesis has no material which has been accepted for other degree or diploma except proper referencing and acknowledgment is made in the thesis where due.

ARTICLES SUBMITTED

1) –*Thermal analysis of molten ternary lithium-sodium-potassium nitrates*" under review in Renewable Energy.
2) –*High temperature study of single alkali nitrate salts:* $NaNO_3$, KNO_3, $LiNO_3$; *and binary alkali nitrate salt:* $NaNO_3$-KNO_3" under review in Thermochimica Acta.
3) –*Alkali nitrates as heat storage and transfer media in thermal energy storage system: A review*" under review in Renewable & Sustainable Energy Reviews.
4) –*The binary alkali nitrate and chloride phase diagrams:* $NaNO_3$-KNO_3, $LiNO_3$-$NaNO_3$, $LiNO_3$-KNO_3, *and NaCl-KCl*" under review in The Journal of Chemical Thermodynamics.

Author: **Mehedi Bin Mohammad**
B.Sc. Engg. (IUT, Bangladesh)
M.Sc. Engg. (POLIMI, Italy)
Date: June, 2016

ABSTRACT

The use of molten alkali nitrate/nitrite and alkaline nitrate salts as a heat transfer fluid (HTF) is promising in concentrated solar power (CSP) plants because of their negligible vapor pressure and optimum fluid velocity. The well-established HTF, a binary $NaNO_3$-KNO_3 (60-40 weight ratio) solar salt, has a melting point 220°C and decomposition point at 565°C. The ternary $NaNO_3$-KNO_3-$LiNO_3$ salt (13.23-57.14-29.63 weight ratio) has a melting point of 120.8°C, offering 100°C less fusion temperature compared to the binary nitrate. The purpose of this study is to increase the degradation limit of proposed ternary nitrate salt system using oxygen as a cover gas to obtain broader operating temperature range (to increase the steam-Rankine cycle efficiency) and for potential use in thermal energy storage (TES) systems as a HTF.

Recent studies showed that in alkali nitrate/nitrite (Hitec salt) system pure oxygen as a blanket gas (partial pressure of oxygen, P_{O_2}=1) alters the nitrite back to nitrate at higher temperatures by exothermic oxidation and delays the thermal degradation point. The decomposition limits of many alkali nitrate systems reported were based on thermo gravimetric analysis (TGA) or TGA and differential thermal analysis (DTA) only and the fundamental decomposition reactions have not been reported in detail. To address these issues, the proposed ternary nitrate salt were studied using simultaneous thermal analysis techniques (STA) which includes simultaneous DTA/DSC-TGA and MS under three purge gases (argon, air and O_2) and scanning rates (2.5, 5 and 10°C/min) to observe decomposition behavior and identify thermal events accurately. To aid this evaluation the single $LiNO_3$, $NaNO_3$ and KNO_3 and binary solar salts were also subjected to STA.

The STA study showed that the oxygen blanket gas delayed the degradation temperature of ternary molten nitrate by 55°C at 10°C/min heating rate compared to an inert argon atmosphere. Similar effects of oxygen atmosphere are seen in the case of binary and single constituent nitrates. Also higher heating rate of 10°C/min resulted in a delayed degradation point compared to the lower heating rate of 2.5°C/min as observed in argon for the ternary nitrate system. The liquidus and solidus temperature gap was higher in ternary and binary nitrates compared to single nitrates perhaps due to supercooling. Also, the solid-solid transition did not appear during cooling for the binary and ternary nitrates. There was little effect of heating rates on transition, fusion, and crystallization temperatures compared to decomposition temperature for nitrates. N_2, O_2, NO, N_2O, and NO_2 were the main gasses evolved during decomposition of nitrates suggesting primary and secondary reversible reactions are concurrent and overlapping. A transpiration test method was used to measure the reaction mass loss and onset vapor pressure of single and binary nitrate salts. This study suggests that due to numerous sensitive experimental parameters and subsequent inconsistent weight loss results, the transpiration method is not suitable for measuring the vapor pressure of alkali nitrate systems.

To avoid time-consuming and costly experimentation, the thermodynamic modeling was performed to obtain a eutectic composition of ternary nitrate system and verified experimentally by STA. The mathematical models of three binary systems $NaNO_3$-KNO_3, $NaNO_3$-$LiNO_3$, and KNO_3-$LiNO_3$, were formulated based on the regular solution assumption and Gibbs energy minimization method of Kramer and Elliott; were solved numerically using a contour plot technique. An algorithm was developed to find the convergence of real roots of the coupled nonlinear equations. The liquidus and solidus curves of mathematical modeling were fitted well against values obtained from the quasi-chemical model used in FactSage and experimental value from literature. Temperature dependent heat capacities have some effect on liquidus and solidus curves. This study showed that the regular solution model described alkali binary nitrates system well and could be a useful method for predicting the phase diagrams for higher order alkali nitrates and alkali halide systems.

In summary, oxygen as a blanket gas delayed the decomposition point of ternary nitrate by 55°C. Higher heating rates increased the decomposition point. As observed in an argon atmosphere, NO, and O_2 evolution after melting and onward indicates concurrent overlapping reversible decomposition reactions. Similar phenomena were observed for single and binary nitrates. The ternary nitrate offered 65°C more operating temperature compared to binary solar salt. This study demonstrated that the transpiration technique is not suitable for vapor pressure study of alkali nitrates. The eutectic melting point of ternary nitrate obtained from STA agreed well with FactSage eutectic composition formulation. A regular solution model predicted experimental literature values well. The overall conclusion is that the use of oxygen as an ullage gas for alkali molten nitrates is likely to increase the thermal degradation point and hence the Rankine cycle efficiency of a solar thermal power plant.

Keywords: heat transfer fluids, molten nitrate salt, thermal energy storage system, concentrated solar power, thermal analysis, off-gas analysis, thermodynamic, transpiration, mathematical modeling, numerical solution, FactSage, Matlab, phase diagrams.

“All truths are easy to understand once they are discovered; the point is to discover them.”

- *Galileo Galilei*

ACKNOWLEDGEMENTS

Bismillahir Rahmanir Rahim, all praise to Allah. I wish to express my wholehearted thanks to my supervisor *Professor Geoffrey Brooks* for the interest, help, advice, patience, guidance and settled me throughout the course of this work. I joined Geoff's High temperature processing (HTP) group as a Mechanical Engineering graduate, with only the most basic comprehension of metallurgy and chemical thermodynamics. Therefore, I had a puzzle and obtuse start in the first year. However, Geoff was kind and supportive. Geoff‘s approach towards guiding a student based research team is inspirational. He trained me to think critically and always expressed optimism towards research challenges while maintaining an encouraging attitude. I am thankful to Geoff for patiently reading and correcting my numbers of thesis drafts! Thanks go to my co-supervisor *A/Prof. M. Akbar Rhamdhani*, who was always patience for teaching me the DSC/DTA/TGA-MS apparatus test procedure.

I am very thankful to *Professor Peter Cadusch* for his valuable time on numerous occasions to correct and finalize the binary algorithms. Without his guidance and correction, it was difficult for me to solve the coupled nonlinear equations.

I also thank T. Bauer of German Aerospace Center (DLR); Rene I. Olivares of CSIRO for technical information. I am thankful to all the HTP group members and Ph.D. students notably: Winny Wulandari, Saiful, Nazmul, Sazzad, Abdul Khaliq, Francesco, Ben, Reiza, Kamrul Rakib and Bapin. They have helped me on various occasions till now to this project.

I wish to thank the workshop Warriors David Vass, Meredith Jewson, Alec Papanicolaou and others for helping me to build experimental apparatus. I am thankful to faculty officers Walter Chetcuti, Ralph Timpano, Warren Gooch, Andrew Moore, Brian Dempster and others for their technical help. I am thanking for academic help and support from Madeline, Kim Hodgman, Mez Wilkinson, Rani and Dr. Sylvia Anne Mackie. I wish to show my gratitude to Adriana Mare, Sudip Sam, Sophia Haccou, Mr. Chris Key, Ms. Angela

McKellar, Ms. Kirsty McKinnon, Mrs. Merryl McHugh, Melissa Cogdon, Justin Raymond, Andrew Zammit, Rob Anderson, Fon, Deivom, Michael Haughton and other ITS and FSET officers.

I wish to thank all the staffs, investor, and well-wishers of HTP group, MEPD, FSET (formerly FEIS) and the Swinburne University of Technology for their help and funding of this project. Without full tuition fee waiver, SUPRA scholarship and funding from Geoff, it was difficult for me to carry out this research project.

I, genuinely thank all my School friends; college; university friends; friends in Bangladesh; friends in Italy and friends in Australia for their moral support.

I want to thank all my previous teachers/Professors; especially Prof. Paolo Silva, Prof. Barbara Rivolta, and Prof. Rahat.

Thank my family members and my relatives for their love and affection!

Lastly, I am grateful to my beloved parents for continuous financial and moral support; and encouragement for me, for my education, and for keeping me sane!!

This thesis is dedicated to some greatest scientists of the world!!!

Dedicated to

Archimedes, Aristotle, Galileo Galilei, Leonardo da Vinci, Pythagoras, Ibn Hayyan, Bernoulli, Avicenna, al-Khwarizmi, Al-Battani, René Descartes, Fibonacci, Pascal, Carl Gauss, Euler, Kepler, Ptolemy, Wilhelm Leibniz, Copernicus, Lagrange, Newton, Dalton, Dmitri Mendeleev, Le Châtelier, Napier, Raoult, Henry, van 't Hoff, Arrhenius, Hertz, Babbage, George Boole, Nikola Tesla, Thomas Edison, Faraday, Max Planck, Maxwell, Boltzmann, Venturi, Clausius, Carnot, Volta, Galvani, Kelvin, Niels Bohr, Pauli, Rutherford, William Bragg, Einstein and *Josiah Willard Gibbs.*

Table of Contents

DECLARATION iii

ABSTRACT v

ACKNOWLEDGEMENTS xi

LIST OF FIGURES xix

LIST OF TABLES xxvii

CHAPTER 1 INTRODUCTION 1

1.1 BACKGROUND 1

1.2 RESEARCH OBJECTIVES 3

1.3 OVERVIEW OF CHAPTERS 3

CHAPTER 2 CONCENTRATED SOLAR POWER GENERATION 5

2.1 OVERVIEW OF CSP SYSTEMS 11

2.1.1 CENTRAL RECEIVER SOLAR TOWER 11

2.1.2 PARABOLIC TROUGH 13

2.1.3 SOLAR DISH ENGINE 14

2.1.4 COMPACT LINEAR FRESNEL REFLECTOR (CLFR) 16

2.2 ANALYSIS OF THERMAL ENERGY OF CSP PLANTS 17

2.3 STORAGE SYSTEM AND LOAD 21

CHAPTER 3 HEAT TRANSFER AND STORAGE FLUIDS 27

3.1 OTHER POTENTIAL HTFS 28

3.2 MOLTEN ALKALI NITRATE AND NITRITE SALTS 29

3.2.1 COMMERCIAL HEAT TRANSFER FLUIDS 36

3.2.1.1 SOLAR SALT 36

3.2.1.2 DRAW SALT 36

3.2.1.3 HITEC 37

3.2.1.4 HITEC XL 39

3.2.1.5 DOWTHERM A AND THERMINOL VP-1 39

3.2.2 APPLICATION OF MOLTEN SALT 40

3.3 CHEMISTRY OF ALKALI NITRATES AND NITRITES 41

3.3.1 NITRITES AND NITRATES IONS 41

3.3.1.1 NITRITE ION, NO_2^- 41

3.3.1.2 NITRATE ION, NO_3^- 43

3.3.2 GENERAL PROPERTIES OF ALKALI NITRATES AND NITRITES 45
3.3.2.1 ALKALI NITRITES 45
3.3.2.2 ALKALI NITRATES 47
3.3.3 THE HIGH TEMPERATURE CHEMISTRY OF ALKALI NITRATES AND NITRITES 53
3.3.4 VAPOR, LIQUID AND SOLID STATES OF ALKALI NITRATES 58
3.3.5 PREVIOUS STUDIES 61
3.3.5.1 OVERVIEW 62
3.4 THERMAL ANALYSIS TECHNIQUES 64
3.5 VAPORIZATION CHEMISTRY 65
3.6 THERMODYNAMIC MODELING OF BINARY ALKALI NITRATES 65
3.6.1 PREVIOUS STUDIES 66
CHAPTER 4 RESEARCH ISSUES 69
CHAPTER 5 THERMODYNAMIC MODELING, PHASE DIAGRAMS 73
5.1 THERMODYNAMIC MODELING OF BINARY NITRATES 73
5.2 BINARY NITRATES MATHEMATICAL EXPRESSIONS 74
5.3 BINARY SYSTEM'S EQUATIONS 74
5.4 TERNARY NITRATE MATHEMATICAL EXPRESSIONS 76
5.5 NUMERICAL SOLUTIONS OF BINARY NITRATE SYSTEMS 78
5.5.1 CONCLUSIONS: NUMERICAL FORMULATION 92
5.6 FACTSAGE, LITERATURE EXPERIMENTAL DATA AND CALCULATED PHASE DIAGRAMS COMPARISON 93
5.7 CONCLUSIONS 107
CHAPTER 6 EXPERIMENTAL PROCEDURES 109
6.1 REAGENTS AND LAB EQUIPMENT 109
6.2 TEST APPARATUS 110
6.3 SAFETY EQUIPMENT 114
6.4 SAMPLE PREPARATION 115
6.5 THERMAL ANALYSIS APPARATUS CALIBRATION 117
6.6 THERMAL AND OFF GAS ANALYSIS TEST PROCEDURE 117
6.7 THE TRANSPIRATION METHOD TEST PROCEDURE 124
6.8 THE PHASE AND MORPHOLOGY STUDY: TEST PROCEDURE 128
CHAPTER 7 RESULTS: SINGLE & BINARY NITRATE SALTS 131

7.1 THERMAL ANALYSIS OF SINGLE AND BINARY NITRATE SALTS 131

7.2 RESULTS 132

7.2.1 RESULTS: TRANSITION, MELTING, AND FREEZING TEMPERATURES AT VARIOUS HEATING-COOLING RATES 132

7.2.2 RESULTS: DECOMPOSITION BEHAVIOR 134

7.3 SINGLE AND BINARY SALT THERMAL ANALYSIS: DISCUSSION 162

7.3.1 LITHIUM NITRATE 163

7.3.2 SODIUM NITRATE 164

7.3.3 POTASSIUM NITRATE 165

7.3.4 BINARY SODIUM-POTASSIUM NITRATE 165

7.4 SINGLE AND BINARY NITRATES THERMAL ANALYSIS TEST: CONCLUSION 172

7.4.1 MAJOR CONCLUSIONS ON SINGLE AND BINARY NITRATES 177

7.5 COMPOSITION ANALYSIS OF BINARY SOLAR SALT 178

XRD, SEM, EDS AND CHEMICAL ANALYSIS RESULTS 178

7.6 TRANSPIRATION TEST RESULTS 183

7.6.1 DISCUSSION ON TRANSPIRATION TEST RESULTS 188

7.6.2 CONCLUSIONS 189

CHAPTER 8 STA RESULTS FOR TERNARY NITRATE SALT 191

8.1 RESULTS 191

8.2 TERNARY SALT THERMAL ANALYSIS: DISCUSSION 207

8.2.1 IN ARGON (PARTIAL PRESSURE OF O_2= 0) 210

8.2.2 IN AIR (PARTIAL PRESSURE OF O_2= 0.21) 210

8.2.3 IN OXYGEN (PARTIAL PRESSURE OF O_2=1.0) 210

8.3 TERNARY NITRATE THERMAL ANALYSIS TEST: CONCLUSION 213

8.4 MAJOR CONCLUSIONS ON TERNARY NITRATE 214

CHAPTER 9 DISCUSSION 217

CHAPTER 10 CONCLUSIONS AND RECOMMENDATIONS 225

APPENDIX A: SELECTIVE STUDIES TABLE 229

APPENDIX B: THERMAL ANALYSIS TECHNIQUES AND DTA/DSC CURVES EVALUATION 239

B.1 THERMAL ANALYSIS TECHNIQUES 239

B.1.1 THERMAL ANALYSIS TECHNIQUES BACKGROUND 239

B.1.2 VARIOUS THERMAL ANALYSIS TECHNIQUES 240

B.1.2.1 THERMOGRAVIMETRIC ANALYSIS 240
B.1.2.2 DIFFERENTIAL THERMAL ANALYSIS 243
B.1.2.3 DIFFERENTIAL SCANNING CALORIMETRY 245
B.1.2.4 SIMULTANEOUS DSC/DTA, TGA, AND EGA 246
B.1.3 EVOLVED GAS ANALYSIS, MASS SPECTROMETRY 247
B.2 THERMAL CURVES ANALYSIS 249
APPENDIX C: VAPORIZATION CHEMISTRY 261
C.1 BACKGROUND 261
C.2 TRANSPIRATION METHOD 261
APPENDIX D: BINARY PHASE DIAGRAMS THERMODYNAMIC CALCULATION 271
D.1 INTRODUCTION 271
D.2 FORMULATION OF BINARY NITRATE SYSTEMS: BACKGROUND 273
D 3: BINARY NITRATE THERMODYNAMIC MODELING 277
D 3: TERNARY NITRATE SALT THERMODYNAMIC MODELING 287
APPENDIX E: MATLAB ALGORITHMS AND HEAT CAPACITY VALUES 289
APPENDIX F: FACT SAGE6.4 CALCULATIONS 299
APPENDIX G: SAMPLE MIXING CALCULATION 303
APPENDIX H: STA CALIBRATION PROCEDURE 307
H 2: TEMPERATURE COEFFICIENT CORRECTION AT 3 SCANNING RATES 308
H 3: HEAT FLOW SENSITIVITY COEFFICIENT CORRECTION AT 3 SCANNING RATES 311
APPENDIX I: MS CURVES 315
APPENDIX J: ERROR ANALYSIS IN DSC/DTA-TGA-MS 319
APPENDIX K: ERROR ANALYSIS IN TRANSPIRATION RIG 321
BIBLIOGRAPHY 325

LIST OF FIGURES

Figure 2.1 (a): Four major types of CSP systems 5

Figure 2.1 (b): The major components and accessories of CSP plants 6

Figure 2.1 (c): Simple schematic diagram of a CSP plant 6

Figure 2.2: Schematic of a CSP system with parabolic trough power plant 7

Figure 2.3: Schematic diagram of Gemasolar power tower (central receiver tower) plant 8

Figure 2.4: The parabolic trough (a) and Linear Fresnel (b), both works on focal line and has one axis/single axis tracking system 9

Figure 2.5: The dish system (a) and central receiver solar tower or power tower or heliostat power plants (b), both works on focal points and has two axis tracking system 10

Figure 2.1.1.1: (a) A central receiver solar tower system with molten salt TES system and (b) PS-10 and PS-20 central receiver power tower plants in Sanlúcar la Mayor, Seville, Andalusia, Spain 11

Figure 2.1.2.1: (a) A simple schematic diagram of a parabolic trough and (b) SEGS III (Solar Energy Generating Systems) trough solar thermal power plants in Kramer Junction, Mojave Desert, CA, U.S.A 13

Figure 2.1.3.1: (a) A simple schematic diagram of a solar dish system and (b) SANDIA (US department of energy laboratory) single dish unit 15

Figure 2.1.4.1: (a) A schematic diagram of a compact linear Fresnel reflector system, using water as working fluid and (b) DLR (German Aerospace Center) linear Fresnel power plant 16

Figure 2.2.1: A simple schematic diagram of a typical steam-Rankine cycle and corresponding Mollier T-S (Temperature – Entropy) diagram 18

Figure 2.2.2: A schematic diagram of a parabolic trough power plant with indirect two-tank thermal energy storage system 21

Figure 2.3.1: A simplified diagram of solar thermal storage system 22

Figure 2.3.2: Solar two power tower CSP plant‘s TES system consist of cold and hot tanks from left hand side of the image respectively. Solar two TES tanks operate on binary solar salt. The power tower is seen in between the two tanks 24

Figure 3.1: Storage system subdivisions 27

Figure 3.2.1: A phase diagram of 1:1 molar or Na:K//NO_3- 46:54 wt%, binary $NaNO_3$-KNO_3 molten salt system 31

Figure 3.2.2: A phase diagram of a five compound‘s salt mixture consisting of $LiNO_3$-$NaNO_3$-KNO_3-$CsNO_3$-$Ca(NO_3)_2$ (15-10-30-30-15 mole % respectively) with fixed Cesium (0.3) and Calcium (0.15) mole fraction 32

Figure 3.2.3: A phase diagram of three compounds salt mixture consisting of 33

$LiNO_3$-$NaNO_3$-KNO_3 (30-18-52 wt % respectively)

Figure 3.2.1.2: The commercial grade $NaNO_3$ and KNO_3 of Chilean origin (Multi-K, Haifa Company) gathered prior to melting 37

Figure 3.3.1.1.1: Two possible canonical resonance structures of nitrite ion 42

Figure 3.3.1.1.2: Common electronic structure of nitrite ion 43

Figure 3.3.1.2.1: Three possible molecular resonance structures of nitrate ion 44

Figure 3.3.1.2.2: Common electronic structure of nitrate ion 44

Figure 3.3.2.1.1: Results of decomposition of alkali nitrates by two methods studied by Bordyushkova et al.. ―A” indicates nitrites content in %; ―t” indicates temperature in ºC. Curve 1= $LiNO_2$, 2=$NaNO_2$, 3=KNO_2, 4=$RbNO_2$ and 5=$CsNO_2$. Curves in a) graph were studied by 291-540 colorimetric method; curves in b) graph were studied by 430-640 permanganate method. 46

Figure 3.3.4.1: Mutual orientation of polyatomic NO_3^- anions and Na^+ cations 59

Figure 3.3.4.2: Decomposition temperature variation with respect to the metallic radius of cations of alkali nitrates and alkaline earth nitrates. Here, $K_1 = 1x10^{-20}$, equilibrium constant described by Stern 60

Figure 3.3.5.1.1: A simple illustration of fusion point depression by adding another component 63

Figure 5.5.1.a: Contour plot of binary $NaNO_3$-KNO_3 at 490K or 217°C 80

Figure 5.5.1.b: Contour plot of binary $NaNO_3$-KNO_3 at 495K or 222°C 81

Figure 5.5.1.c: Contour plot of binary $NaNO_3$-KNO_3 at 500K or 227°C 82

Figure 5.5.2.a: Locus of solutions of binary $NaNO_3$-KNO_3 system in X or (x_A^S), Y or (x_A^l) and Z or (T) plane 83

Figure 5.5.2.b: Locus of solutions of binary $LiNO_3$-$NaNO_3$ system in X or (x_A^S), Y or (x_A^l) and Z or (T) plane 83

Figure 5.5.2.c: Locus of solutions of binary $LiNO_3$-KNO_3 system in X or (x_A^S), Y or (x_A^l) and Z or (T) plane 84

Figure 5.5.3: Calculated phase diagram of binary $NaNO_3$-KNO_3 system using the regular solution model 87

Figure 5.5.4: Calculated phase diagram of binary $LiNO_3$-$NaNO_3$ system using the regular solution model 88

Figure 5.5.5: Calculated phase diagram of binary $LiNO_3$-KNO_3 system using the regular solution model 89

Figure 5.5.6: Binary $NaNO_3$-KNO_3 phase diagram obtained by calculation using the regular solution model 91

Figure 5.5.7: Binary $LiNO_3$-KNO_3 phase diagram obtained by calculation using the regular solution model 91

Figure 5.5.8: Binary $LiNO_3$-$NaNO_3$ phase diagram obtained by calculation using regular solution model 92

Figure 5.6.1: Calculated eutectic composition phase diagram of binary Li-Na//NO_3 salt obtained from FactSage 94

Figure 5.6.2: Calculated eutectic composition phase diagram of binary K-Li//NO_3 salt obtained from FactSage 95

Figure 5.6.3: Calculated eutectic composition phase diagram of binary K-Na//NO_3 salt obtained from FactSage 96

Figure 5.6.4: Calculated eutectic composition phase diagram (Gibbs Triangle) of ternary nitrate obtained from FactSage. Isotherms are shown at 0.1°C intervals 97

Figure 5.6.5: $NaNO_3$-KNO_3 phase diagram comparison with FactSage, DSC literature, and calculated values 98

Figure 5.6.5.a: Binary $NaNO_3$-KNO_3 calculated phase diagram using ABθ model 99

Figure 5.6.5.b: Comparison of liquidus and solidus curves of sodium-potassium nitrate (zoomed view) 101

Figure 5.6.6: $LiNO_3$-KNO_3 phase diagram comparison with FactSage, DSC literature, and calculated values 102

Figure 5.6.7: $LiNO_3$-$NaNO_3$ phase diagram comparison with FactSage, DSC literature, and calculated values 103

Figure 5.6.6.a: Comparison of liquidus and solidus curves of lithium-potassium nitrate (zoomed view) 105

Figure 5.6.7.a: Comparison of liquidus and solidus curves of lithium-sodium nitrate (zoomed view) 106

Figure 6.2.1 (a): SETSYS Evol simultaneous DSC/DTA-TGA and coupled MS Pfeiffer Units 111

Figure 6.2.1 (b): A simple schematic diagram of STA (DSC/DTA-TGA) furnace 112

Figure 6.2.2: Nabertherm TR60/B180 oven furnace 113

Figure 6.2.3: Full view of transpiration rig. A de-oxidation vertical tube furnace connected to the gas cylinders, air supply port, and flow meter; horizontal tube furnace; gas trap and exhaust system from left hand side of the image 113

Figure 6.2.4: (a) BRUKER D8 Advanced X-ray diffractometer. (b) *Carl Zeiss supra 40vp* Scanning electron microscopy and *Gemini Oxford INCA energy 250* Energy-dispersive X-ray spectroscopy 114

Figure 6.4.1 (a): Ternary nitrate salt after weighing and before storing in container 116

Figure 6.4.1: (b) Freshly prepared binary (left hand side) and ternary salt containers before storing into the desiccator. (c) Vacuum Duran stop cock 116

desiccator for salt mixtures storage

Figure 6.6.1: (a) DSC/TGA thermocouple transducer sample plate holder. (b) DSC/TGA with 100µL sample and reference crucibles mounted on metal plate from left hand side of the image 120

Figure 6.6.2: (a) protected DTA/TGA thermocouple rod with the protected ceramic jacket. (b) DSC/TGA with 80µL reference and sample crucibles mounted on holder tips from left hand side of the image 121

Figure 6.6.3: High purity 100µL alumina DSC/TGA crucibles and 80µL alumina DTA/TGA crucibles from left to right respectively 121

Figure 6.6.4: (a) A chemically strained DSC/TGA rod. (b) A wire damaged DSC/TGA transducer marked in red circle. (c) Distorted and broken sample holder of the protected DTA/TGA rod 123

Figure 6.7.1: Full transpiration rig setup with piping and valve assembly 125

Figure 6.7.2: A simple schematic diagram of transpiration test rig 126

Figure 6.7.3: The binary salt two minutes after brought out from HT furnace. Within a short period, the salt surface started to crystallize 128

Figure 7.1.1: $LiNO_3$ melting peaks at various heating rates 142

Figure 7.1.2: $LiNO_3$ freezing peaks at various cooling rates 143

Figure 7.1.3: $NaNO_3$ melting peaks at various heating rates 144

Figure 7.1.4: $NaNO_3$ freezing peaks at various cooling rates 145

Figure 7.1.5: KNO_3 melting peaks at various heating rates 146

Figure 7.1.6: KNO_3 freezing peaks at various cooling rates 147

Figure 7.1.7: Binary $NaNO_3$- KNO_3 melting peaks at various heating rates 148

Figure 7.1.8: Binary $NaNO_3$- KNO_3 freezing peaks at various cooling rates 149

Figure 7.2.1: $LiNO_3$ in an argon atmosphere at 10°C/min heating rate. The black circles are indicating corresponding temperatures 150

Figure 7.2.2: $LiNO_3$ in an air atmosphere at 10°C/min heating rate. The black circles are indicating corresponding temperatures 151

Figure 7.2.3: $LiNO_3$ in an oxygen atmosphere at 10°C/min heating rate. The black circles are indicating corresponding temperatures 152

Figure 7.2.4: $NaNO_3$ in an argon atmosphere at 10°C/min heating rate. The black circles are indicating corresponding temperatures 153

Figure 7.2.5: $NaNO_3$ in an air atmosphere at 10°C/min heating rate. The black circles are indicating corresponding temperatures 154

Figure 7.2.6: $NaNO_3$ in O_2 atmosphere at 10°C/min heating rate. The black circles are indicating corresponding temperatures 155

Figure 7.2.7: KNO_3 in an argon atmosphere at 10°C/min heating rate. The black circles are indicating corresponding temperatures 156

Figure 7.2.8: KNO_3 in an air atmosphere at 10°C/min heating rate. The black circles are indicating corresponding temperatures 157

Figure 7.2.9: KNO_3 in an oxygen atmosphere at 10°C/min heating rate. The black circles are indicating corresponding temperatures 158

Figure 7.2.10: Binary in an argon atmosphere at 10°C/min heating rate. The black circles are indicating corresponding temperatures 159

Figure 7.2.11: Binary in an air atmosphere at 10°C/min heating rate. The black circles are indicating corresponding temperatures 160

Figure 7.2.12: Binary in O_2 atmosphere at 10°C/min heating rate. The black circles are indicating corresponding temperatures 161

Figure 7.3.1: Influence of heating rates on DSC peaks of rubidium nitrate 167

Figure 7.3.2: A typical thermal lag in DSC furnace during sodium nitrate melting-freezing cycles at low set point temperatures. Black line is indicating set temperature, and red line is indicating actual sample temperature 170

Figure 7.3.3: Thermal lag at the dynamic heating condition at higher set point temperature (900°C) during decomposition of binary salt in single heating-cooling step using DSC/TGA transducer. Sample temperature (red line) is compared with set point temperature (black line) in the inset. Inset picture indicating 5°C temperature lag and approximately 30 seconds Tau lag 171

Figure 7.4.1: Identical melting and solidification peaks of binary nitrate salt heated up to 250°C in argon sweep gas 174

Figure 7.4.2: Cyclic short term DSC heat flow curve (5 heating and cooling) for binary salt heated up to 600°C 175

Figure 7.5.1: X-Ray diffraction patterns of 60:40 weight ratio $NaNO_3$-KNO_3 binary salt with Cu K_α emission 179

Figure 7.5.2: (i) (ii) SEM image of 60:40 wt% binary Na-K//NO_3. Salts were mixed, homogenized and equilibrated in Air 180

Figure 7.5.2: (iii) (iv) SEM image of 60:40 wt% binary Na-K//NO_3. Salts were mixed, homogenized and equilibrated in Air 181

Figure 7.5.3: (a) Gold-sputtered sample substrate image of EDS spectrum area; (b) N, O, Na and K showed from surface EDS spectrum; (c) elemental composition percentage of N, O, Na and K 182

Figure 7.6.1: Weight change curves of $NaNO_3$ at 530°C in argon gas flow rate of 0.9l/min 184

Figure 7.6.2: Weight change curves of KNO_3 at 450°C in various argon gas flow rate 185

Figure 7.6.3: Weight change curves of $LiNO_3$ at 450°C in various argon gas flow rate 185

Figure 7.6.4: Weight change curves of Na-K//NO_3 in air flow rate of 0.9l/min 186

Figure 7.6.5: Weight change curves of Na-K//NO_3 in air and argon flow rate of 187

0.9l/min

Figure 8.1.1: Ternary melting peaks at various heating rates 196

Figure 8.1.2: Ternary freezing peaks at various cooling rates 197

Figure 8.2.1: Ternary salt in an argon atmosphere at 10°C/min heating rate. The black circles are indicating corresponding temperatures 198

Figure 8.2.2: Ternary salt in an air atmosphere at 10°C/min heating rate. The black circles are indicating corresponding temperatures 199

Figure 8.2.3: Ternary salt in an oxygen atmosphere at 10°C/min heating rate. The black circles are indicating corresponding temperatures 200

Figure 8.2.4: Ternary salt in an argon atmosphere at 5°C/min heating rate. The black circles are indicating corresponding temperatures 201

Figure 8.2.5: Ternary salt in an air atmosphere at 5°C/min heating rate. The black circles are indicating corresponding temperatures 202

Figure 8.2.6: Ternary salt in an oxygen atmosphere at 5°C/min heating rate. The black circles are indicating corresponding temperatures 203

Figure 8.2.7: Ternary salt in an argon atmosphere at 2.5°C/min heating rate. The black circles are indicating corresponding temperatures 204

Figure 8.2.8: Ternary salt in an air atmosphere at 2.5°C/min heating rate. The black circles are indicating corresponding temperatures 205

Figure 8.2.9: Ternary salt in an oxygen atmosphere at 2.5°C/min heating rate. The black circles are indicating corresponding temperatures 206

Figure B.1.2.1.1: (a) Schematic diagram of thermogravimetric analyzer and (b) simple workflow diagram of a thermobalance 241

Figure B.1.2.1.2: A TG weight change curve for $CuSO_4 \cdot 5H_2O$ 242

Figure B.1.2.2.1: (a) the sample and reference temperature as a function of time showing endothermic effect during melting. (b) An ideal ΔT vs. T, DTA curve showing an exothermic peak upward and an endothermic peak downward 244

Figure B.1.3.1: Mass spectrometry working basics 247

Figure B.1.3.2: Mass Spectrometer block diagram 248

Figure B.2.1: DSC curves indicating baseline, peak, zero line, and their corresponding temperatures 250

Figure B.2.2: Different procedures for baseline construction suggested by Brown 252

Figure B.2.3: DSC curve showing different parts or region 255

Figure B.2.4: The construction of the baseline with degree of reaction α(t) 257

Figure B.2.5: The Possible baseline construction in case of unknown T_i (initial) and T_f (final) temperatures 258

Figure C.2.1 (a): Schematic of transpiration apparatus used by Dharwadkar et al. and Merten 262

Figure C.2.1 (b): Schematic portion of transpiration apparatus (reaction zone) used by Alexander 263

Figure C.2.1 (c): Schematic of transpiration apparatus used by Son et al. 264

Figure C.2.2: Vapor pressure dependency of a given sample as a function of flow rate at fixed temperature (404K) 268

Figure C.2.3: Equilibrium vapor pressure variation as a function of temperature of $CdCl_2$ 268

Figure C.2.4 (a): A cross-sectional view of horizontal beam balance simultaneous DSC/TGA with off-gas analyzer coupling option 269

Figure C.2.4 (b): Horizontal DSC/TGA ceramic transducer for sample temperature and heat flow measurement 270

Figure F1: A screen shot of FactSage 6.4 various modules operation window 299

Figure F2: A screen shot of variable sub window 300

Figure F3: A screen shot of ―phase module” ready for calculation 300

Figure H.2.1: Temperature correction module in Calisto data processing software 309

Figure H.3.1: Heat flow sensitivity correction module in Calisto data processing software 312

Figure I1: Spectra AMU bar of air and common air impurities. 315

Figure I2: Spectra AMU bar of N_2 and O_2 316

Figure I3: Spectra AMU bar of nitrous oxide 316

Figure I4: Spectra AMU bar of nitric oxide 317

Figure I5: Spectra AMU bar of nitrogen dioxide 317

Figure I6: Spectra AMU bar of argon and other noble gasses 318

Figure K1: Temperature profile measurements of Labec horizontal tube furnace using K-type (chromel - alumel) thermocouple ceramic sheath/probe and multimeter 322

LIST OF TABLES

Table 3.2.1: A comparison of thermo physical properties and cost of different HTF used in TES plants and other sectors 34

Table 3.3.2.1: Physical properties of common alkali nitrates and alkali nitrites 51

Table 3.3.2.2: Physical properties of common cations, anions, alkali nitrates and alkali nitrites obtained from references of FactSage™ 52

Table 3.3.5.2: Summary of effect of atmospheric gases on Hitec salt ($NaNO_3$–KNO_3–$NaNO_2$= 7:53:40 wt.%) of NO_2/NO_3 wt. ratio= 0.72; and ternary ($NaNO_3$–KNO_3–$NaNO_3$= 30:18:52 wt.%) conducted by Rene using simultaneous DSC/TGA-MS apparatus 79

Table 5.5.1: Thermo physical properties of single alkali nitrate salt obtained from references 85

Table 5.5.2: Empirical coefficients of binary alkali nitrate salts obtained from references 85

Table 5.7.1: Binary phase diagrams comparison 107

Table 6.4.1: Binary and ternary salt samples composition 115

Table 7.2.2.1: Thermal events of single $NaNO_3$, KNO_3, $LiNO_3$ and binary $NaNO_3$-KNO_3 salt (*60-40 weight ratio*) heated at argon atmosphere (flow rate 40ml/min) and at various heating and cooling rates using a Setaram STA DSC/TGA-MS 136

Table 7.2.2.2: Thermal events comparison of single and binary nitrates heated at 10°C/min heating rate in argon atmosphere (40ml/min) 139

Table 7.2.2.3: Thermal events of single $NaNO_3$, KNO_3, $LiNO_3$ and binary $NaNO_3$-KNO_3 salt (*60-40 weight ratio*) heated from 50 to 800°C at three atmosphere (*sweep gas velocity of 40ml/min*) at 10°C/min heating and cooling rates using a simultaneous STA Setaram setsys DTA/TGA- Pfeiffer MS(off-gas analyzer) 141

Table 7.5.1: ICPOES and Ion chromatography results of binary nitrate salt 183

Table 8.1.1: Thermal events of ternary $LiNO_3$-$NaNO_3$-KNO_3 salt heated at argon atmosphere (flow rate 40ml/min) and at various heating and cooling rates using a simultaneous STA (Setaram setsys DSC/TGA-MS) 194

Table 8.1.2: Thermal events of ternary $NaNO_3$-KNO_3-$LiNO_3$ salt (*13.23-57.14-29.63 weight or 13.53-49.12-37.35 mol ratio*) heated from 50 to 800°C at three atmospheres (*sweep gas velocity of 40ml/min*) and scanning rates using a simultaneous Setaram setsys DTA-TGA- Pfeiffer MS thermal and off-gas analyzer 195

Table 8.1.3: Ternary nitrate salt samples (heated from 50 to 800°C) average weight change at three atmospheres (gas velocity: 40ml/min) and scanning rates 208

Table 9.1: Comparative thermal events of single, binary and ternary nitrates at 10°C/min heating rate and 40ml/min sweep gas velocity (argon, air, and O_2), using a simultaneous thermal analyzer (DTA-DSC/TGA and MS) 220
Table A.1: Selected studies on various molten nitrate/nitrite salt systems 229
Table E1: Heat capacities (C_p) from work of Takahashi et al. 296
Table F1: Eutectic point equilibrium calculation 301
Table H1: Certified reference materials used for Temperature and energy calibration 308

CHAPTER 1 INTRODUCTION

1.1 BACKGROUND

Solar thermal power (STP) or concentrated solar power (CSP) is a form of renewable energy which is environmental friendly [1] compared to non-renewable energy sources (fossil, coal) [2]. CSP plant‘s electricity generation is similar to conventional power plant [3] using conventional cycles [4], but instead of fossil fuel to supply heat to the boiler or heat exchanger, it uses concentrated solar radiation from solar field which is stored in thermal energy storage (TES) system [3, 5]. Electricity can also be produced by solar photovoltaic (PV) systems, where PV cells convert sun radiation directly to electricity via semiconductors (photovoltaic effect) [6, 7]. STP has the advantage over PV for large-scale solar energy power generation because it has much higher operating temperatures resulting in higher net efficiencies compared to PV [8]. Moreover, PV a stand-alone system cannot operate 24 hours a day, as it depends on solar incident directly [9, 10]. STP plant can store the solar thermal energy via storage fluids or heat transfer fluids (HTF) [11] for up to 15 hours [12-15] to provide backup power and thus maintain peak load and base load power in the absence of sunlight [16].

The various types of CSP systems, central receiver solar tower, parabolic trough, dish engine, and Fresnel system, are globally available technologies. Commercially the central receiver solar tower system, and the parabolic trough system use TES with HTF [17, 18]. A TES system consists of two tanks: a cold and hot storage tanks. A cold tank dispatch HTF and hot tank collect HTF from the solar field via pipe and pump accessories. Several STP plants use synthetic oil or steam, or alkali/alkaline nitrate/nitrite molten salt or salt mixtures, or paraffin, or organic mixture (hydrocarbon), such as biphenyl and diphenyl oxides mixture [17], as heat transfer media and HTF. Molten nitrate and/or nitrite salt mixtures are the commonly utilized for both heat transfer media and HTFs. Most of the nitrate molten salt mixtures possess higher melting point and higher thermal decomposition or degradation temperature compared to oil and steam [19]. One of the major scientific challenges for STP technologies is to increase the steam-Rankine cycle efficiency by extending operating temperature range of HTF. The crystallization temperature should be ideally below 100°C to reduce the heat tracing components (e.g: an auxiliary heater [20]) in the field piping accessories; to reduce the required energy of melting [21, 22]; and at higher temperature for given amount of salt more energy can be stored [23] inside a TES system. The thermal degradation temperature should ideally be near or above 600°C without vapor formation, to have a broader operating temperature range [24].

Recent studies showed that, the degradation of a nitrate melt at a higher temperature usually takes place by changing the nitrite/nitrate ratio depending upon temperature and partial pressure of oxygen [25]. Where nitrate converts to nitrite and oxygen in slow and reversible manner initially [24, 26-29]. Then, the nitrite decomposes to metal oxides, nitrogen oxide, nitrogen and several other stable/unstable gas species [26, 29, 30] resulting in thermal decomposition or thermal breakdown [24, 26]. The high temperature product gasses in contact with the salt reservoir inside the closed system, alter the chemistry of the salt melt, affecting the equilibrium reaction and the thermal degradation behavior [26]. Recent research has shown, using an oxygen rich atmosphere such as air or pure O_2 can increase the thermal stability range of the nitrite/nitrate based salt system [26]. At higher temperature the oxygen suppresses the nitrite formation [26, 30, 31] by nitrite oxidation. Thus, to understand these phenomena at higher temperatures, the mass loss studies, the effect of ullage gasses and heating rates on thermal stability of nitrates are important issues.

In this study, a novel HTF with a low melting point and boarder operating temperature range with minimum production cost compared to binary solar salt will be examined. Binary nitrate salt has a melting point around 220°C and the decomposition temperature lies between 500°C to 600°C [23, 32-38]. In this aspect lithium nitrate was selected with sodium and potassium nitrates to lower the eutectic point. A ternary $NaNO_3$-KNO_3-$LiNO_3$ (13.23-57.14-29.63 wt%) has been proposed from thermodynamic analysis offering 120.8°C melting point. This study aims to enhance the decomposition limit of the proposed ternary nitrates and observe the decomposition behavior in reactive (air and oxygen) and inert atmosphere (argon) using STA. The reported decomposition limits of many alkali nitrates were based on either rapid weight loss point detection by thermogravimetric analysis (TGA) alone or TGA and heat flow variation by DTA/DSC (differential thermal analysis/differential scanning calorimetry), ignoring evolved gaseous species by evolved gas analyzer (EGA). Hence, STA will be used to identify potential operating temperature ranges samples by observing various thermal events concurrently.

1.2 RESEARCH OBJECTIVES

Thus, the main focus of this thesis is to study the effect of heating rates and blanket atmosphere on decomposition limit of proposed ternary $NaNO_3$-KNO_3-$LiNO_3$ (13.23-57.14-29.63 weight%) molten nitrate salt. The binary molten $NaNO_3$-KNO_3; and single $NaNO_3$, KNO_3 and $LiNO_3$ molten nitrate systems will be subjected to atmospheric gasses effect study only. The transpiration test method will be used to measure the reaction mass loss and onset vapor pressure of single and binary nitrate salts. To obtain a eutectic composition of ternary salt thermodynamic modeling will be performed using FactSage [39]. A mathematical formulation based on the regular solution hypothesis will be performed accounting C_P as dependent of temperature to observe variation of liquidus and solidus curves compared with FactSage quasi chemical model and literature experimental values.

1.3 OVERVIEW OF CHAPTERS

In chapter two the basic of CSP systems are described. Chapter three describes heat transfer and storage fluids; literature review; thermal analysis; vaporization chemistry; and thermodynamics. Chapter four describes research issues. Chapter five describes thermodynamic and mathematical formulation results. Chapter six describes sample preparation and experimental procedures. Chapter seven presents experimental results of single and binary nitrate salt systems. Chapter eight presents thermal analysis results of ternary alkali nitrate salt. Chapter nine describes discussion. Chapter ten presents conclusion and recommendations. Appendices and references are produced at the end of this thesis.

CHAPTER 2 CONCENTRATED SOLAR POWER GENERATION

The major commercial available CSP technologies are: central receiver solar tower commonly known as power tower system, parabolic trough system, linear Fresnel system, and dish Stirling system, are shown schematically in Figure 2.1 (a). All these CSP power plants have two common divisions, such as solar block (including thermal energy storage system), and the power block [40], as shown schematically in Figure 2.1 (b). A solar block usually consists of reflectors, receivers, storage tanks, HTF, heat exchanger, pumps, pipe and other accessories. The power conversion unit consists of a heat exchanger, boiler, condenser, turbine, generator and associate accessories [3, 41]. A simple schematic diagram of CSP plant and parabolic trough power plants are shown in Figure 2.1 (c) [42] and 2.2 [41] respectively.

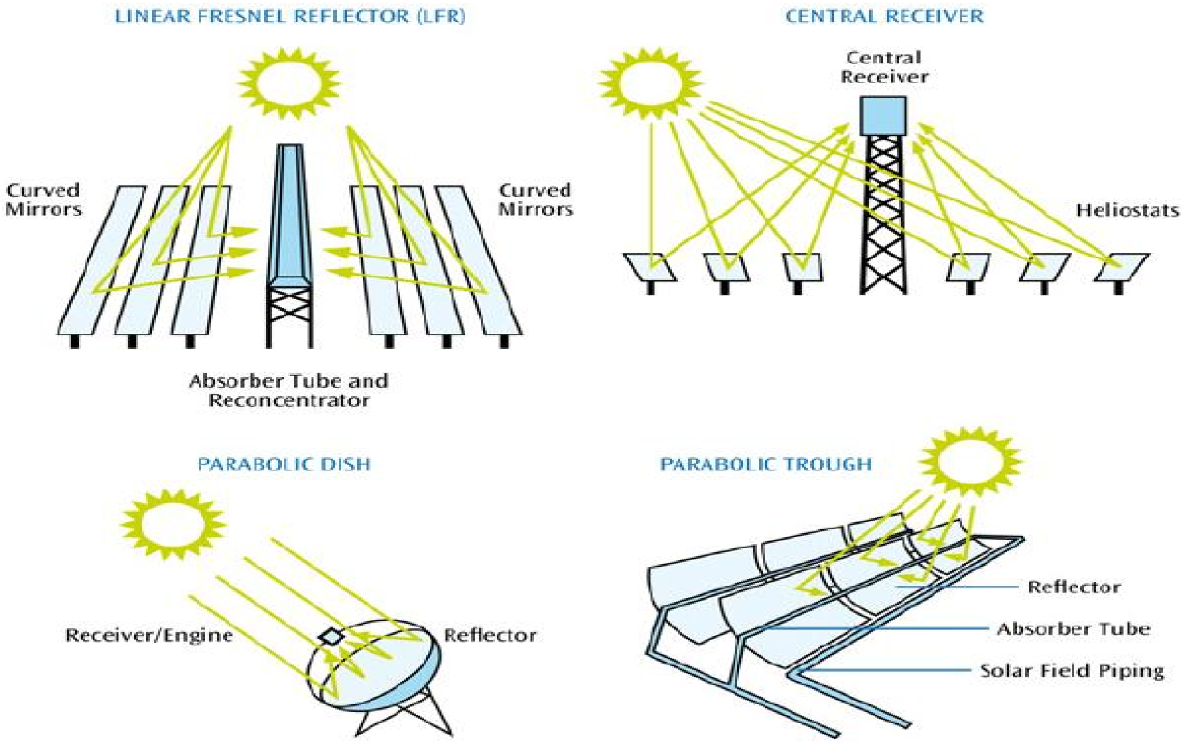

Figure 2.1 (a): Four major types of CSP systems [43]. Kind permission obtained from: © *OECD/IEA, 2010 Technology Roadmap: Concentrating Solar Power, IEA Publishing. License:* www.iea.org/t&c/termsandconditions.

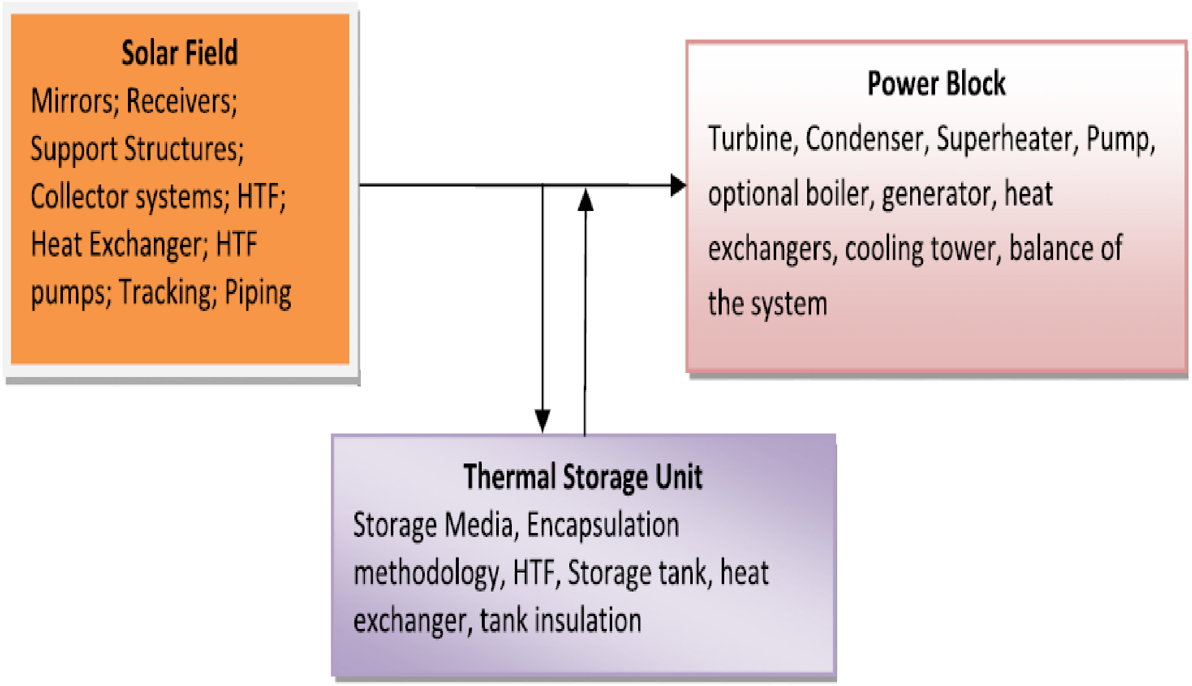

Figure 2.1 (b): The major components and accessories of CSP plants [15].

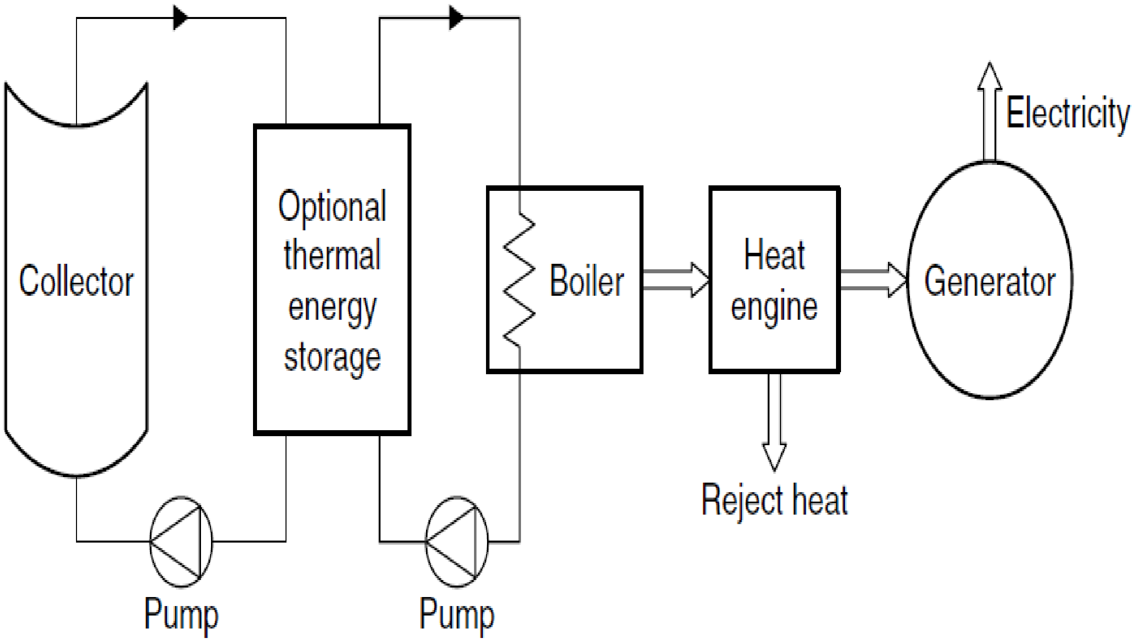

Figure 2.1 (c): Simple schematic diagram of a CSP plant [42].

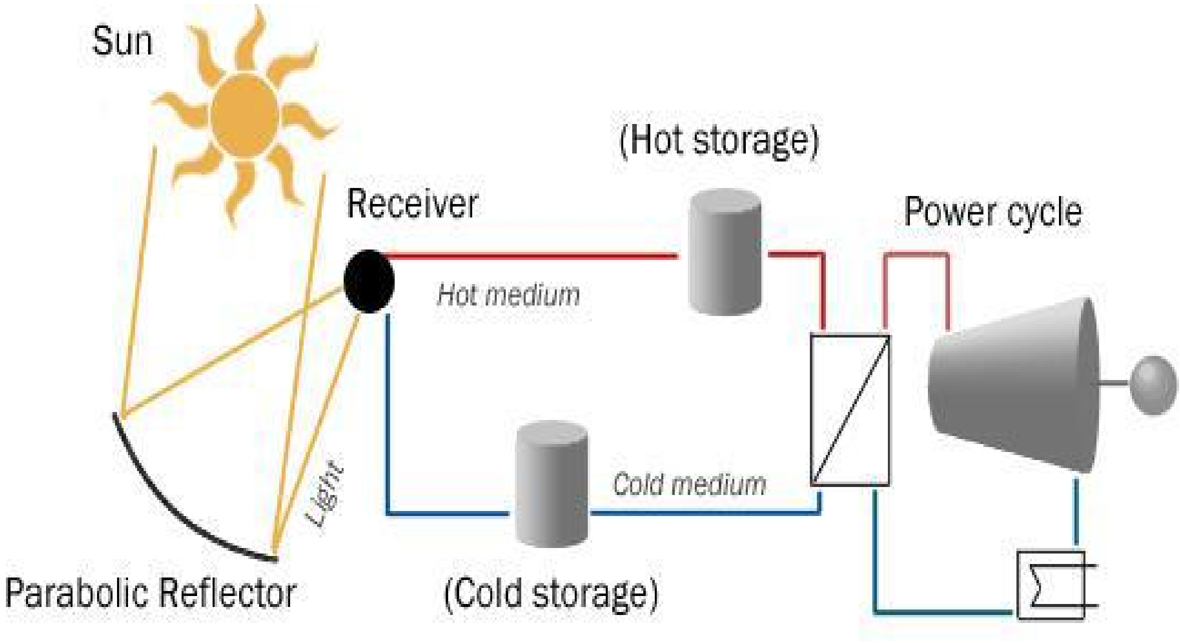

Figure 2.2: Schematic of a CSP system with parabolic trough power plant [41].

The Sun‘s rays are collected by the reflector and focused into the collector or the receiver as shown schematically in Figure 2.2. In the collectors or receiver, the HTF flows from the cold thermal storage tank and goes back to hot storage tank via closed loop piping and pumping systems, as shown schematically in Figure 2.1 (c) and Figure 2.2.

Inside the receiver or collector tubes, the HTF gains heat by receiving focused sunlight and thus sunlight converted to thermal energy [44]. HTF can work directly in a turbine to produce electricity (such as steam) or dissipate heat into the heat exchanger to produce steam (such as molten salt). From the hot storage system, the higher temperature HTF is pumped to a heat exchanger to generate steam from feed water in the boiler. Thus, the solar thermal energy is converted to mechanical energy, which generates work via a turbine. With the help of generator coupled to the turbine, mechanical energy is converted to electricity as a final product of solar thermal power plants [42] and supply to the grid, as shown schematically in Figure 2.3. The HTF then returns to a cold storage tank system and goes to the collector or receiver via a pumping system, as shown schematically in Figure 2.2. The system described can be classified as a Rankine cycle.

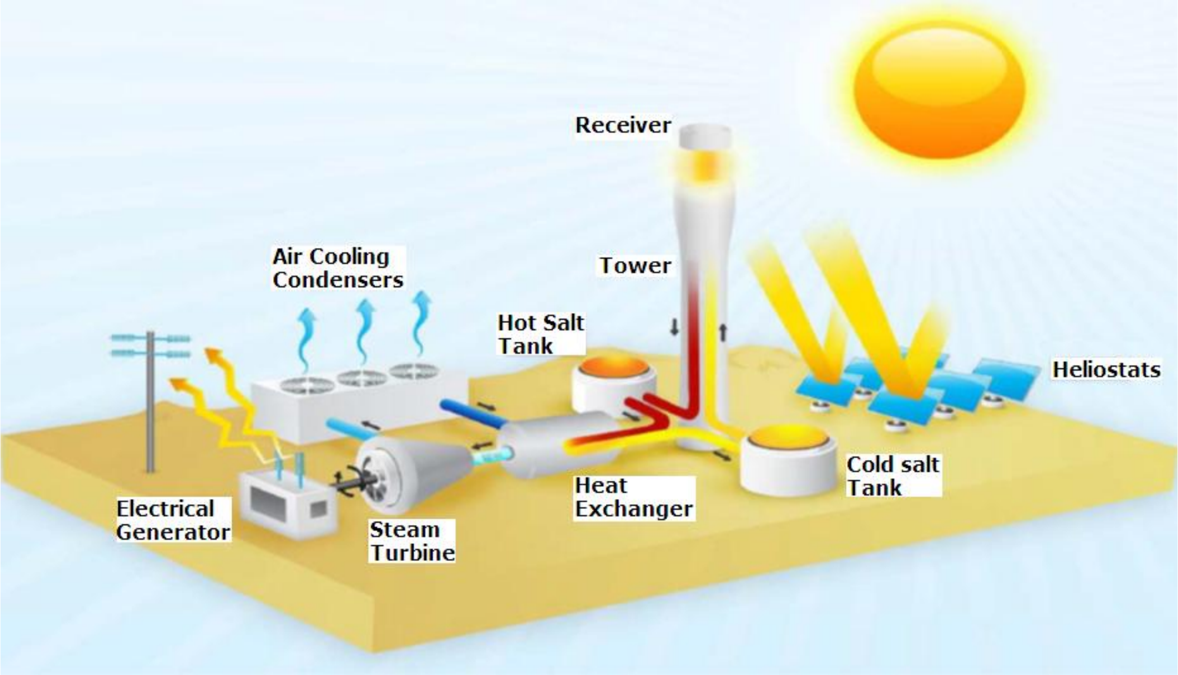

Figure 2.3: Schematic diagram of Gemasolar power tower (central receiver tower) plant [23]. Reprinted with kind permission from copyright line © 2011 IEEE.

Depending on the CSP system, the solar radiation is concentrated from the reflector and focused to receiver/collector tubes by either on a focal point or a focal line [45-47]. On the focal line a collector tube and the focal points a receiver is placed respectively to harness solar radiation [47], as shown schematically in Figures 2.4 and 2.5 respectively. Thus, CSP system can be classified as one axis/single axis tracking and two axis tracking depends on the reflectors/mirrors movement to harness or track the sun radiation [45]. Parabolic trough and linear Fresnel systems have single axis tracking, as they track the sun by changing its reflectors axis vertically [48]. Central receiver or heliostat power tower and dish engine systems have two axes tracking, as the reflectors track the sun by changing the reflector axis both horizontally and vertically [48], as shown schematically in Figures 2.5 (a) and 2.5 (b) respectively.

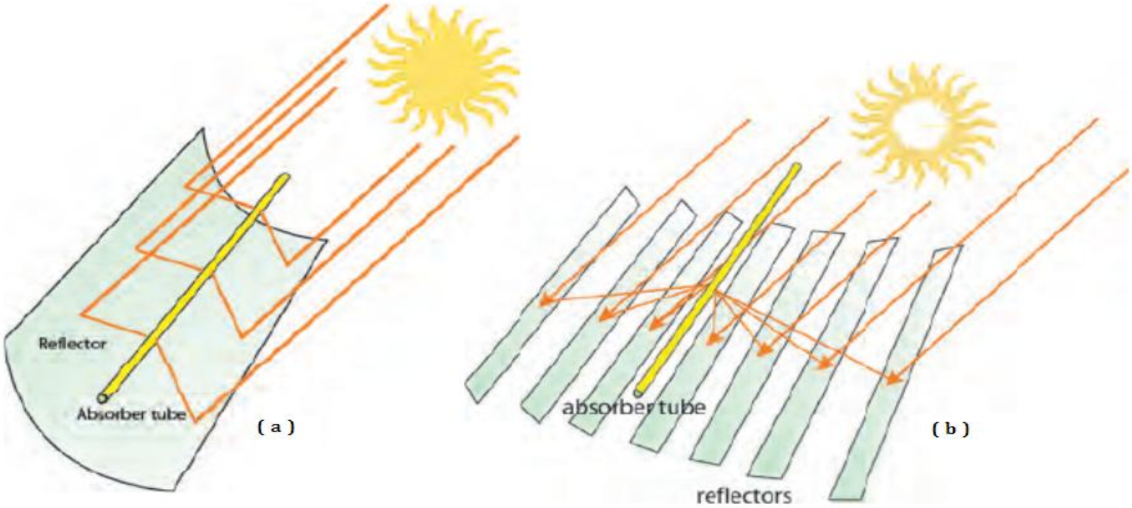

Figure 2.4: The parabolic trough (a) and Linear Fresnel (b), both works on focal line and has one axis/single axis tracking system [45]. Reprinted with kind permission from copyright line © Earthscan, Deutsche Gesellshaft Fur Sonnenergie, 2010 in conjunction to www.volker-quaschning.de.

A parabolic trough with parabolic shaped reflector and linear Fresnel with flat shape reflector has collector tube in the center of the trough and in the center of the reflector arrays respectively, where the solar radiation focuses sunlight on the tube on a focal line, as shown schematically in Figure 2.4 (a) and Figure 2.4 (b). In the focal line, the collector tube is placed horizontally above from the reflectors for both systems [45]. The geometry of the reflectors are made or arrange in a way, that the sun rays always concentrate on the focal line from each given point of the reflector [45]. For both systems, the cold HTF enters from one side of the collector tubes and exits from another and circulate through the solar field. The reflector and collector assembly systems (typically hundreds) are placed side by side and are connect via parallel piping systems in between cold and hot storage tanks [45].

The power tower and the dish stirling system focus sunlight on the focal point of the receivers. The dish receiver (usually stirling engine) is mounted on the focal center of the dish-shaped reflectors, as shown schematically in Figure 2.5 (a). The geometry of the dish is made in a way that the sun rays always concentrate on the focal point of the receiver. The reflector receiver structure supports the receiver. In the central receiver solar tower, the receiver is placed at the top of the tower, where the reflectors called heliostats are faced the sun and the towers. The heliostats, typically hundreds, are placed in a field of an oval shape arrays to concentrate the sun lights from individual reflectors to the focal points of the receiver, as shown schematically in Figure 2.5 (b).

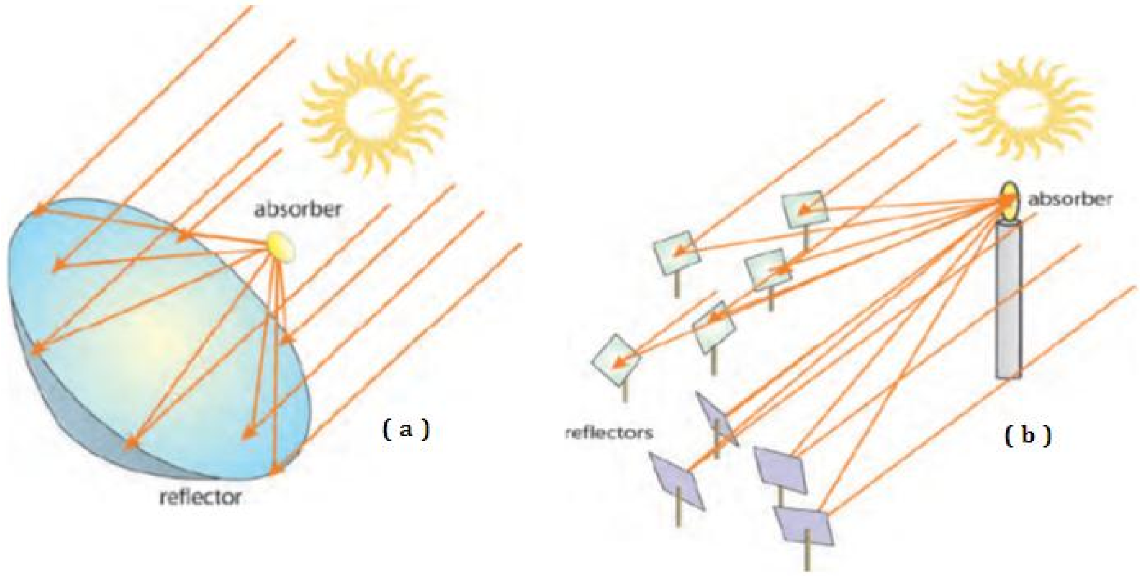

Figure 2.5: The dish system (a) and central receiver solar tower or power tower or heliostat power plants (b), both works on focal points and has two axis tracking system [45]. Reprinted with kind permission from copyright line © Earthscan, Deutsche Gesellshaft Fur Sonnenergie, 2010 in conjunction to www.volker-quaschning.de.

Other notable CSP systems include solar sea water desalination system, solar pond, and fossil solar hybrid power plant. These are well described by Kalogirou [42]. The list of existing solar thermal power plants and the list of thermal power stations under construction has been described by Tian et al., Chen et al., Behar et al. and Baharoon et al. [47, 49-51]. The details cost comparison, and levelized cost of electricity for each CSP systems has been described by Hinkley et al. [52]. The available HTF and cost comparison has been described by Hoshi et al. [53].

2.1 OVERVIEW OF CSP SYSTEMS

2.1.1 CENTRAL RECEIVER SOLAR TOWER

In a central receiver or power tower system, the solar field consists of many planar mirrors known as heliostats which track the sun [42, 46]. Typical heliostat size is usually from 100 to 200 m^2 [46]. The mirror is held by a mechanical structure, capable of moving or rotating in two axes [46]. The sun ray is reflected from a mirror onto absorber or receiver mounted at the top of a tower. The tower is located in the center of the solar field. A heat transfer fluid flows through the receiver, collects the concentrated heat from the sun and store into a storage system with the help of a pump [41]. There are three types of receivers commercially available; they are [46]: direct steam generator (DSG) receiver, volumetric air receiver (both open and pressurized [54]), molten salt receiver.

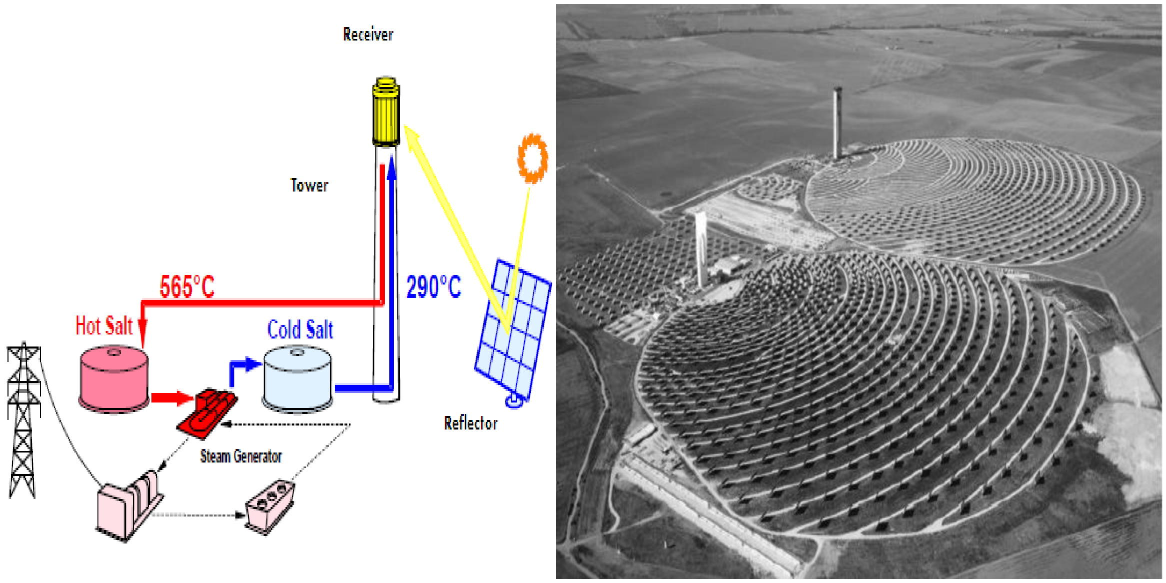

(a) (b)

Figure 2.1.1.1: (a) A central receiver solar tower system with molten salt TES system [55, 56] and (b) Bird‘s eye view of PS-10 and PS-20 central receiver power tower plants in Sanlúcar la Mayor, Seville, Andalusia, Spain [46], Copyright Wiley-VCH Verlag GmbH & Co. KGaA., Reproduced with permission.

The central receiver system has five main components [42, 46], they are: heliostats (planar mirror, membrane) include tracking systems (motor, controller); tower; receiver; heat transfer fluid and TES system (oil, steam, molten salt, and storage tanks); power generating system and auxiliary subsystems, as shown schematically in Figure 2.1.1.1 (a) and (b). A typical heliostat power tower power plant has arrays of heliostat mirrors concentrate sun lights into the receiver to supply heat to the molten salt pumped from the cold salt tank. The heat gained via the molten salt HTF inside the receiver is then pumped back to the hot salt tank. From the hot reservoir, the salt pumped to the steam generator via a heat exchanger to produce steam, and subsequently electricity. The steam condensate pumped to the condenser to feed the steam generator, as shown schematically in Figure 2.1.1.1 (a).

The working temperature of a power tower system ranges from 500°C to 800°C [57] depending upon the working fluid‘s operating temperature stability range, cooling medium, and receiver type used [46]. The concentration ratio of a typical heliostat mirror varies from 600 to 1000 [57]. The concentration ratio is the aperture area of the reflector divided by the absorber or receiver area of the collector [42, 58]. The maximum conversion efficiency or Carnot efficiency is 73% [57]. The Carnot efficiency is described in subsection 2.2. Depending upon on the plant size the power output range varies from 10 to 400 MW [57].

The advantages of a heliostat power tower are highest solar to electric conversion efficiency compared to other large-scale CSP plants (except small scale dish engine), high operating temperature, hybridization option present with current power tower technology, cogeneration possible, and grid connection available [18, 42]. The disadvantages of a heliostat power tower are: high heliostat maintenance requires because of the wind load and axes control, water consumption is high for cooling and cleaning of heliostat and investment, and operating costs are high compared to other CSP technologies [18, 42]. A review on central receiver solar tower power plants is well described by Behar et al. [51].

2.1.2 PARABOLIC TROUGH

A parabolic trough has a parabolic or concave shaped long mirror where a collector tube is situated in the center of the focal line, as shown schematically in Figure 2.1.2.1 (a) and (b). The trough mirror working procedure is similar as power tower, but reflectors and receivers are different [41]. Here, the receiver is the long tube, inside the HTF flows from one side to another side. The reflector is the parabolic mirror typically 150 meters long and 6 meters in aperture width, which is mounted on a mechanical structure, capable of one axes rotation [46]. The motor driven controller controls the rotation. A parabolic trough power system has five main components [42, 46], they are the parabolic trough-shaped reflector; collector tube or receiver; field piping; heat transfer fluid and storage system; power generating system and auxiliary subsystems.

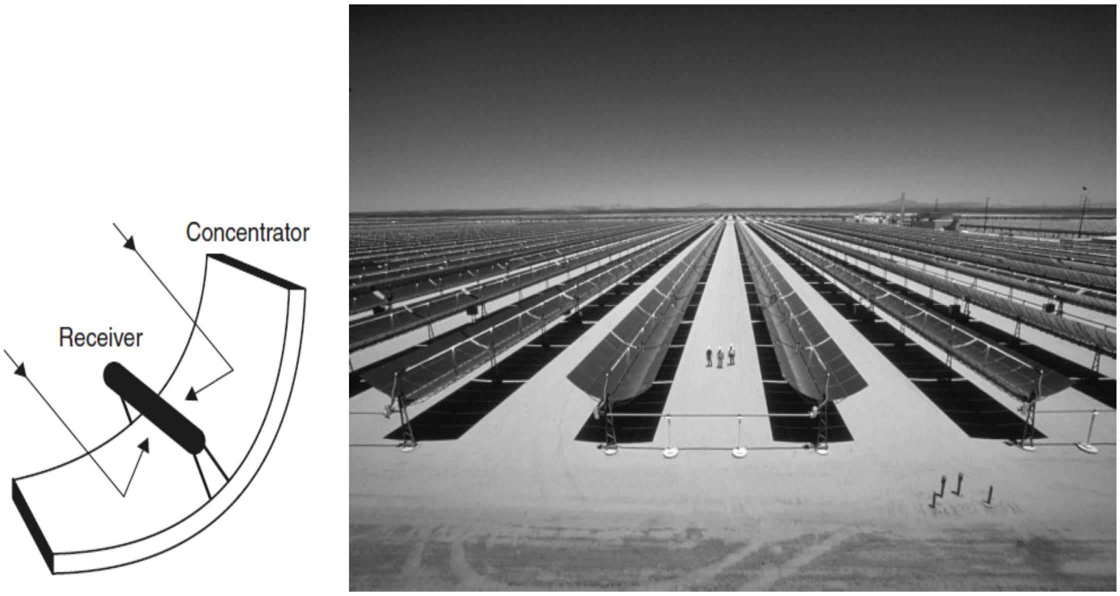

(a) (b)

Figure 2.1.2.1: (a) A simple schematic diagram of a parabolic trough [59] and (b) SEGS III (Solar Energy Generating Systems) trough solar thermal power plants in Kramer Junction, Mojave Desert, CA, U.S.A [46, 60], Copyright Wiley-VCH Verlag GmbH & Co. KGaA., Reproduced with permission.

The working temperature of a parabolic trough system ranges from 260°C to 400°C [57]. The concentration ratio of the parabolic trough mirror is 8 to 80 [57]. The maximum conversion efficiency or Carnot efficiency is 56% [57]. Depending upon on the plant size the power output range is 10 to 400 MW [57].

The advantages of a parabolic trough system are a well-established system, high maturity, and plant experience level, hybridization option present within the system, cogeneration possible and available for grid connection [18, 42]. The disadvantages of a parabolic trough system are: high reflector maintenance requires, high water consumption for cooling and cleaning, oil-based heat transfer fluid has low solar electric conversion efficiency compared to salt based HTF, oil to salt heat exchanger also reduces the efficiency [46], pumping costs are higher, large scale freezing protection are needed, pipe expansion damage usually occurs, and the operating temperature is not high compared to a power tower system [18, 42].

2.1.3 SOLAR DISH ENGINE

A solar dish with the receiver engine has the highest concentration factor [57] among CSP systems. A parabolic shape dish concentrates the solar radiation into a focal point of Stirling dish engine receiver mounted on top, as shown schematically in Figure 2.1.3.1 (a) and (b). The Stirling motor is coupled to an electric generator, where the motor uses the external heat radiation to convert and generate electricity [46]. The engine has a control system, operates according to available sunlight [42]. The extra heat or the waste heat is released to the atmosphere.

The dish Stirling system components are [42, 46]: dish concentrator, receiver engine, control system and auxiliary subsystems. The dish mirror or reflector can be three types; they are a continuous mirror surface, facets or closely spaced individual mirrors, and separate concentrator having common focal points [46].

The dish surface area is typically 50 to 100 m^2 [46]. The working temperature of a dish engine system ranges from 500°C to 1200°C [57]. The concentration ratio of the dish reflector varies from 800 to 8000 [57]. The maximum conversion efficiency or Carnot efficiency is 80% [57]. Depending upon on the dish engine system size the power output range is 3 to 50 kW [57].

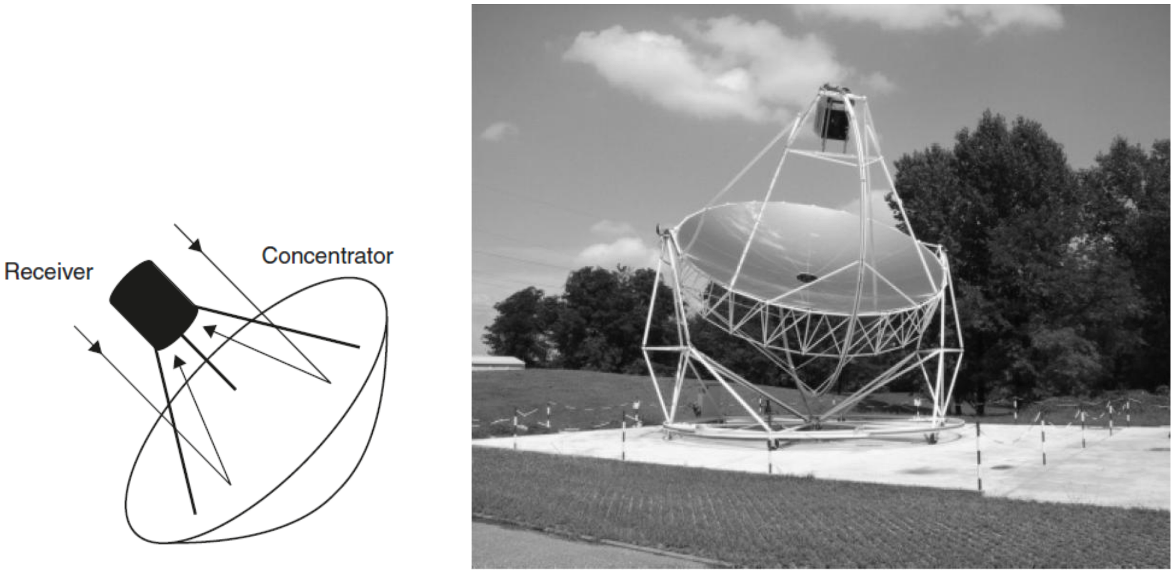

(a) (b)

Figure 2.1.3.1: (a) A simple schematic diagram of a solar dish system [59] and (b) SANDIA (US department of energy laboratory) single dish unit [46], Copyright Wiley-VCH Verlag GmbH & Co. KGaA., Reproduced with permission.

The advantages of a dish Stirling system are: no water cooling required, simple operation, modular unit [46], the stand-alone option is available and the highest solar to electric conversion efficiency among the other CSP system [18, 42]. The disadvantages of a dish system are: prototype stage technology, storage is limited by battery storage, hybridization is not implemented yet, accurate sun tracking required and very small scale operation compared to other CSP systems [18, 42, 46].

2.1.4 COMPACT LINEAR FRESNEL REFLECTOR (CLFR)

A linear Fresnel reflector has a number of flat mirrors are used to concentrate the sunlight [59]. The flat mirror is placed side by side and mounted near the ground (10 to 15 meter from ground), focusing sunlight on the focal line of the absorber or receiver tube [46], as shown schematically in Figure 2.1.4.1 (a).

The linear Fresnel reflector components are flat planner mirrors, collector tube, heat transfer fluid and thermal storage, power generating system, as shown schematically in Figure 2.1.4.1 (a) and (b). The working temperature of a linear Fresnel reflector system ranges from 260°C to 400°C [57]. The concentration ratio of the linear Fresnel reflector vary from 8 to 80 [57]. The maximum conversion efficiency or Carnot efficiency is 56% [57]. Depending upon on the plant size the power output range is 5 to 50 MW [57].

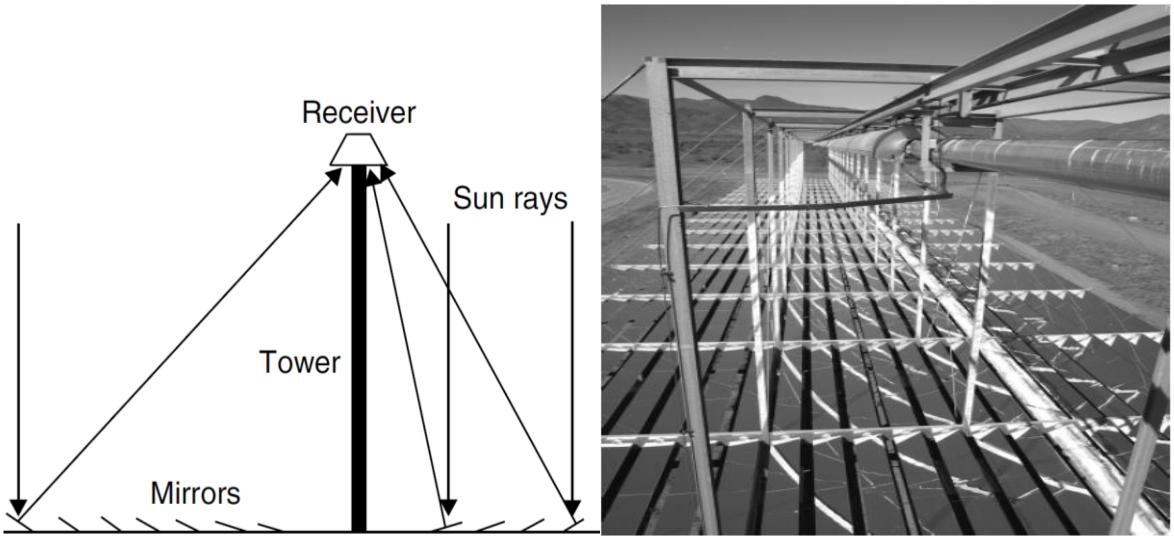

(a) (b)

Figure 2.1.4.1: (a) A schematic diagram of a compact linear Fresnel reflector system, using water as working fluid [42] and (b) DLR (German Aerospace Center) linear Fresnel power plant [46], Copyright Wiley-VCH Verlag GmbH & Co. KGaA., Reproduced with permission.

The advantages of a linear Fresnel system are [42, 46]: low transport cost for the reflector, modular unit, hybridization option present, simpler installation and production, less water consumption compared to parabolic trough, less land requires compare to the parabolic trough and possible grid connection [18, 42]. The disadvantages of a linear Fresnel system are low efficiency (lower solar to electricity conversion rate) technology compared to other CSP systems and low operating temperature [18, 42, 49]. Zhu et al. [61] have described a review of LFR system.

2.2 ANALYSIS OF THERMAL ENERGY OF CSP PLANTS

CSP plants are similar to conventional fossil power plants, except the solar field is used to provide solar thermal heat energy instead of fossil fuels in a boiler [42]. The thermodynamics of the system can be described using the steam-Rankine cycle similar to fossil-fueled power plants. Below is the explanation of thermal analysis of CSP plants.

The Rankine cycle is the most commonly used thermodynamic cycle model to describe a heat engine or steam engine, as shown schematically in Figure 2.2.1. A turbine is a heat engine, which converts the steam into the rotational mechanical work [62]. The heat of a HTF (e.g., molten salt), transfers the concentrated solar heat energy to the heat exchanger or boiler. The constant high pressure heated steam from the boiler or heat exchanger enters into the turbine at T_3 temperature, which is denoted as operating temperature of the power plant. Steam then expands adiabatically into the turbine converts heat energy into the mechanical energy and hence produce electricity via coupled generator. After expansion work in the turbine, the steam condensate is stored in the condenser at lower pressure. The pump feeds the condensate adiabatically to the boiler in a closed loop heat cycle, as shown schematically in Figure 2.2.1.

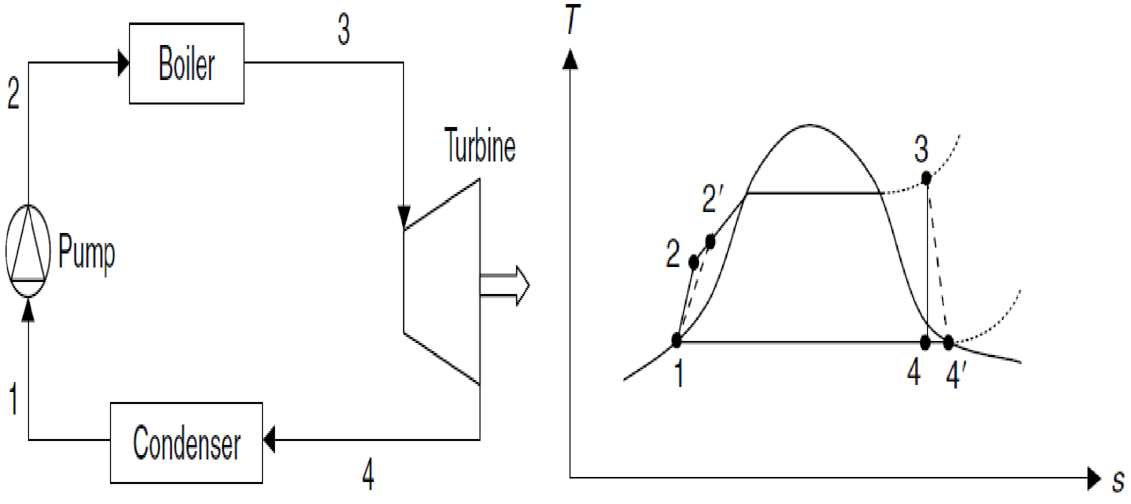

Figure 2.2.1: A simple schematic diagram of a typical steam-Rankine cycle and corresponding Mollier T-S (Temperature – Entropy) diagram [42].

The maximum conversion efficiency or Carnot efficiency or theoretical thermodynamic efficiency is generally described for the heat engine of hot and cold reservoirs according to the second law of thermodynamics [63]. The maximum amount of work that can be done using a heat engine is Carnot efficiency. The maximum steam temperature extracted from the solar thermal heat of TES system is the theoretical power or Carnot efficiency of a given CSP plant‘s heat engine power cycle. The Carnot efficiency is the ratio of total work done W, in one full cycle divided by the amount of heat required Q, during that cycle is given in equation 2.2.1.

Carnot efficiency, $\eta = \frac{W}{Q} \leq \frac{T_h - T_c}{T_h} \leq 1 - \frac{T_c}{T_h}$ eqn 2.2.1

Here,

T_h =hot reservoir (hot storage tank) absolute temperature (°C),
T_c= cold reservoir (cold storage tank) absolute temperature (°C), $T_c \leq T_h$ [64].

Although the real steam cycle or Rankine cycle efficiency is much lower than the thermodynamic efficiency or Carnot efficiency of a given heat engine system, due to various radiative and convective heat losses. The operating temperature of a heat engine, T_3 directly depends on upon solar receiver and TES system‘s temperatures [63]. The efficiency of the Rankine cycle is the ratio of net-work output by work input or heat input. Here, the heat input is from the heat exchanger or boiler. To calculate the net-work output of the cycle, the turbine work, and pump work needs to be known. The turbine work is given in equation 2.2.2. Turbine efficiency is the ratio of actual turbine expansion by the ideal turbine expansion, given in equation 2.2.3.

Turbine work = $h_3 - h_{4'}$ [42] eqn 2.2.2

Turbine efficiency, $\eta_{\text{turbine}} = \frac{h_3 - h_{4'}}{h_3 - h_4}$ [here actual turbine expansion is 3-4′] eqn 2.2.3

The pump work is to acquire and compress the condensate in higher pressure from P_1 to P_2, given in equation 2.2.4. Here the pump efficiency is the ratio of ideal pumping compression by actual pumping compression, given in equation 2.2.5.

Pump work, ${}_1W_{2'} = h_{2'} - h_1 = \frac{v(P_2 - P_1)}{\eta_{pump}}$ [42] eqn 2.2.4

Pump efficiency, $\eta_{pump} = \frac{h_2 - h_1}{h_{2'} - h_1}$ [here actual pumping compression is$1 - 2'$] eqn 2.2.5

Thus, the net-work output of the system is the difference between, the work done by the turbine and work done by the pump, given in equation 2.2.6. The heat input from the boiler is given in equation 2.2.7.

Net-work output,

W= turbine work – pump work = $(h_3 - h_{4'})$ - $(h_{2'} - h_1)$ [42] eqn 2.2.6

Heat input from boiler or heat exchanger,

$Q_{32'} = Q = h_3 - h_{2'}$ [here heat rejection is Q_{41}] [42] eqn 2.2.7

Finally, the power plant cycle efficiency can be derived as the ratio of W to Q expressed in equation 2.2.8.

$\eta = \frac{Net\ work\ output\ ,W}{Heat\ input\ ,Q} = \frac{(h_3 - h_{4'}) - (h_{2'} - h_1)}{h_3 - h_{2'}}$ [42] eqn 2.2.8

Here,

h = specific enthalpy ($\frac{kJ}{kg}$).

ν = specific volume ($\frac{m^3}{kg}$).

P = pressure (bar) 10^5 ($\frac{N}{m^2}$) [42].

The heat input in the heat exchanger is accumulated from the molten salt HTF via a salt-steam heat exchanger. The higher the molten salt‘s temperature, the higher will be the conversion of steam thus; higher steam heat enthalpy will enter into the turbine. It means that the power cycle will operate at higher T_3 or higher enthalpy h_3, as shown schematically in Figures 2.2.1 and 2.2.2. Hence, the higher operating temperature T_3, will raise the net-work output and will increase the Rankine cycle efficiency of CSP plants [42] as described earlier in section 2.2.

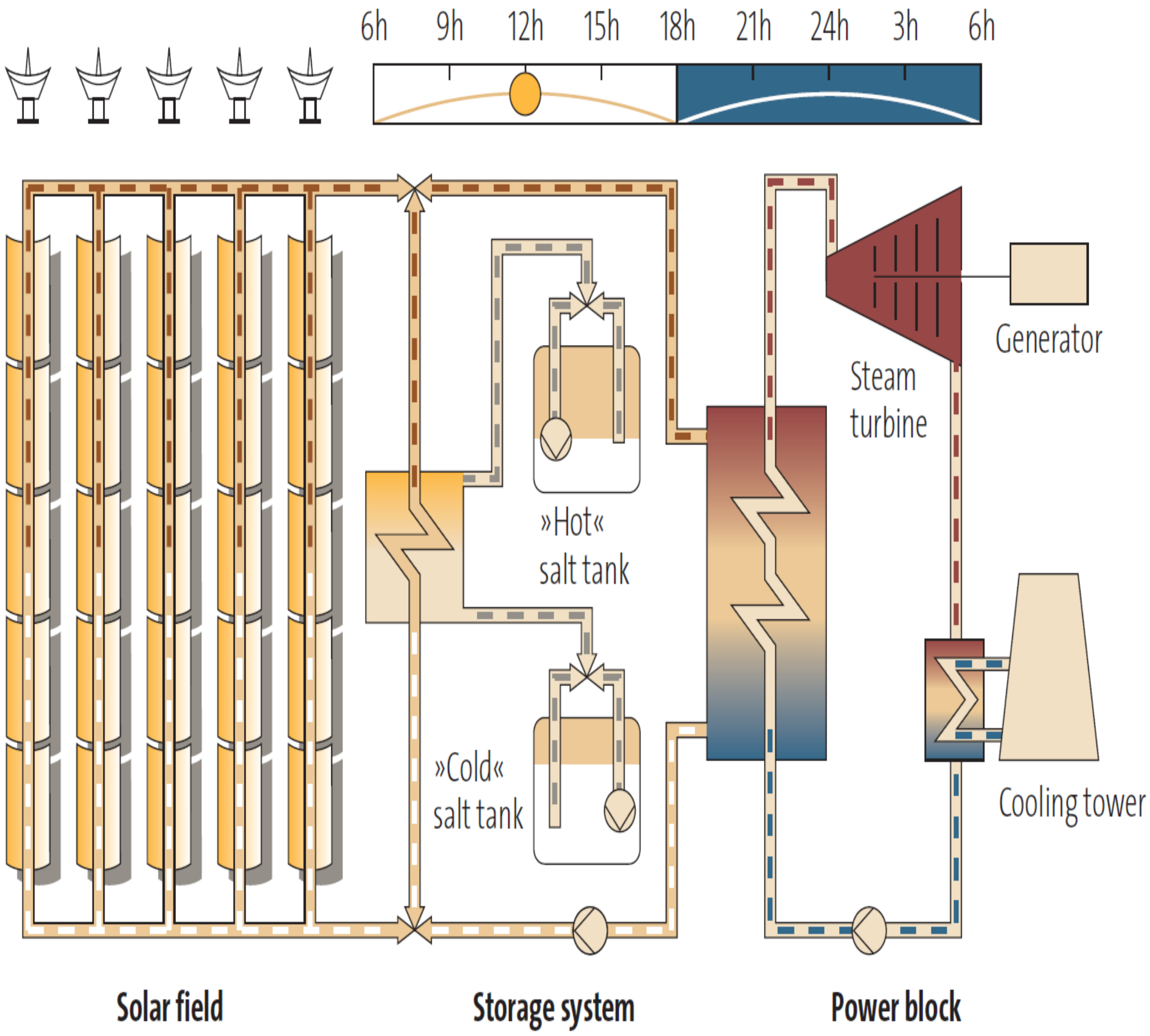

Figure 2.2.2: A schematic diagram of a parabolic trough power plant with indirect two-tank thermal energy storage system [65, 66].

2.3 STORAGE SYSTEM AND LOAD

Usually, the collectors and receivers are connected to the storage system via pipes and accessories. The cold HTF from storage system pumps into the solar field. Where solar collectors, accumulates concentrated solar radiation from reflectors and provides thermal energy to the storage system. Solar collection array dispatches the hot HTF to the thermal storage system at T_{out} temperature. The hot HTF flows via pipe to the heat exchanger at $\dot{m}_L$ mass flow rate to produce steam. In heat exchanger the hot HTF rejects the heat at $T_{L,in}$

temperature to provide useful heat energy to the turbine-generator system at $\dot{Q}_L$ Joule [67]. Then, the HTF returns to storage system via pumping system for gathering solar thermal heat again, as shown schematically in Figure 2.3.1.

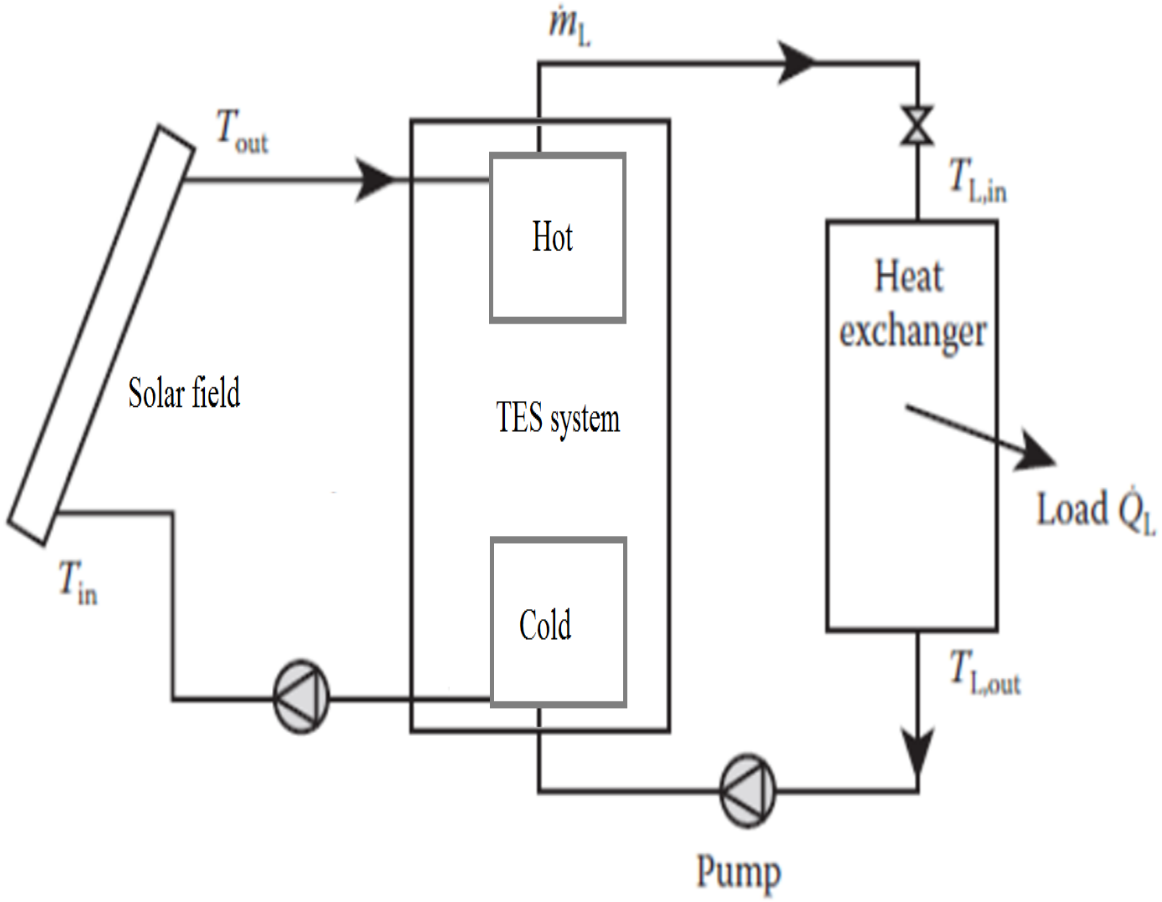

Figure 2.3.1: A simplified diagram of solar thermal storage system [67].

The energy is taken from the solar thermal storage to provide the heat load on the heat exchange on the power generating system side [67], is given by,

$$\dot{Q}_L = \dot{\delta}_L \, \dot{m}_L C \, (T_{L,in} - T_{L,out}) \quad \text{eqn 2.3.1}$$

Here,

$\dot{\delta}_L$= variable control, either 0 or 1. This depends on the supply condition of the load.
C = specific heat capacity of heat transfer fluid.
T_{in}= temperature of the fluid leaving the cold storage system, (°C).
T_{out}=useful collector temperature entering into the hot storage system, (°C).
$\dot{m}_L$= mass flow rate of heat transfer fluid, ($\frac{Kg}{sec}$).
$T_{L,in}$= storage temperature of the HTF entering heat exchanger, (°C).
$T_{L,out}$= temperature of the HTF leaving the heat exchanger, (°C).
$\dot{Q}_L$= heat load, useful heat taken from the heat exchanger, (J).

The rate of change of amount of energy stored in a storage tank is given by,

$$\dot{Q}_{st} = \dot{Q}_u - \dot{Q}_L - \dot{Q}_{pipe} - \dot{Q}_{st,loss} \quad [67] \qquad \text{eqn 2.3.2}$$

Here,

$\dot{Q}_u$= useful energy extracted from the collector, (J).
$\dot{Q}_L$= useful energy load taken from the heat exchanger, (J).
$\dot{Q}_{pipe}$ = total energy losses from the pipes, (J).
$\dot{Q}_{st,loss}$= heat losses from energy tank, (J) [67].

Molten salts are used as HTFs and storage fluids are discussed in Chapter three of this thesis. Sometimes the molten salts are used directly in both solar fields and storage tanks for thermal energy accumulation and storage purpose known as a direct storage system, as shown in Figures 2.3 and 2.3.2. In some power plants, separate fluids are used in solar fields, such as synthetic oil for solar energy accumulation; and molten salt for solar energy storage known as an indirect storage system, as shown in Figure 2.2.2. An image of a TES system of the Solar two power tower (10MW$_e$ capacity) of Sandia, DOE (U.S. Department of Energy) located in Barstow, California, U.S.A [55], is shown in Figure 2.3.2.

Figure 2.3.2: Solar two central receiver tower plant‘s TES system consist of cold and hot tanks from left hand side of the image respectively. Solar two TES tanks operate on binary solar salt. The power tower is seen in between the two tanks [55].

Various practical aspects of TES systems with molten salt as HTF have been described by Rodríguez-García et al. [68] and Kuravi et al. [15]; and the molten salt database are well formulated by Serrano-López et al. [69]. For a simple overview of CSP systems, only basic contents have been described in this chapter. Mainly parabolic trough and power tower are commercially deployed in several countries for electricity production due it's higher solar to electric conversion efficiency and large operating temperature range. Most of the CSP power plants have TES (thermal energy storage) tanks, reflectors, receivers/collectors (collectively known as a solar block). Most of the existing CSP plants work in Rankine cycle, few of them work in Brayton cycle (with compressed air/natural gas) and hybrid (coal/gas with solar: both Rankine and Brayton) dual cycles. The parabolic dish system works in Stirling cycle. Therefore, only the working principals of the steam-Rankine cycle have been described in this chapter. The steam-Rankine cycle with superheat, reheat, and regeneration [70] are not described here.

CHAPTER 3 HEAT TRANSFER AND STORAGE FLUIDS

Liquid phase heat transfer fluids (HTFs) and/or storage fluids are used to store solar radiation as thermal energy in a hot tank for thermal energy storage (TES) system in CSP plant. Most of the CSP plants use molten nitrate salt or nitrate/nitrite salt mixtures, steam, organic fluids, inorganic fluids and synthetic oil as HTF and/or heat storage fluids. These chapter aims to describe first energy storage system and then, some of the features and properties of the HTFs. Then, the inorganic fused alkali nitrate/nitrite salt chemistry and research backgrounds have been described. Then finally the thermal analysis techniques, reaction kinetics and thermodynamic modeling of alkali nitrates have been described.

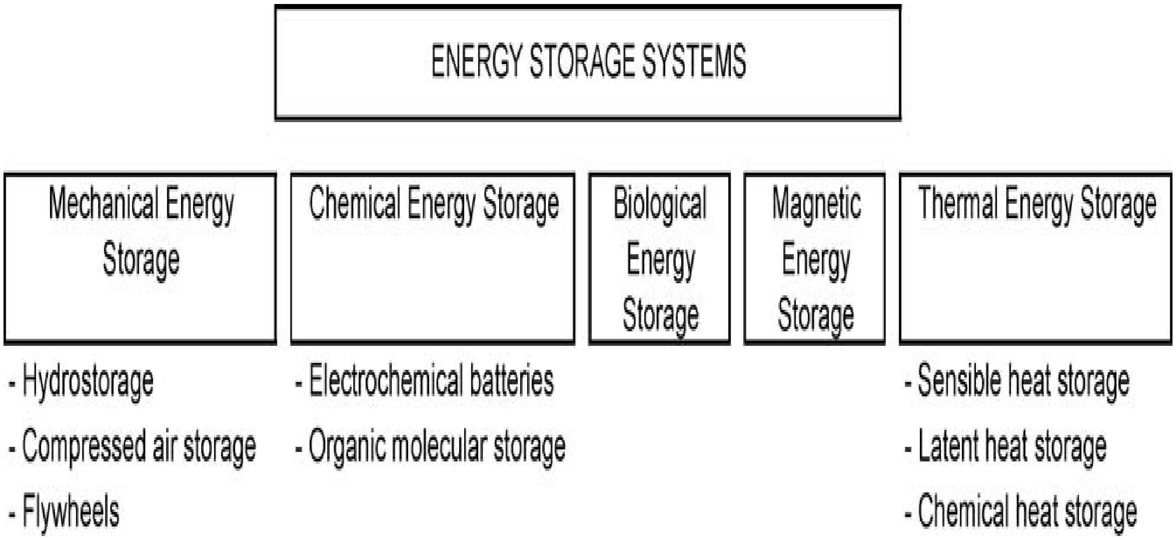

Figure 3.1: Storage system subdivisions [3, 71].

A classification of energy storage systems is shown schematically in Figure 3.1. Five major classifications of energy storage systems are mechanical energy storage, chemical energy storage, biological energy storage, magnetic energy storage, and thermal energy storage [72-74]. This thesis is studying molten salts as a sensible heat transfer medium and storage fluid for the thermal energy storage system. Thermal energy storage system mainly three types, sensible heat storage, latent heat storage, and chemical heat storage system [72], as shown schematically in Figure 3.1. Sensible heat media usually uses solids such as rock, metals, and sand, or liquids such as water, molten salts, synthetic oils, and mineral oils [3, 75]. The latent heat is associated with the change of phases of the materials, such as heat of melting and heat of vaporization [74]. Phase change materials (PCM) can change their phase from liquid to gas, or solid to liquid, and vice versa [74] to store and release energy. PCMs can be paraffins (C_nH_{2n+2}), inorganic salt hydrates, fatty acids (capric acid, $C_{10}H_{20}O_2$), and encapsulated PCM materials [76-87]. To increase thermal conductivity and heat capacity of HTFs, small mass fraction nanoparticles such as silica are doped with a base fluid such as oil. Such dispersion and colloidal suspension of nano solid particles are generally termed as —nanofluids” [88-90]. Metallic and nonmetallic solid nanoparticles such as Al_2O_3, MgO, CuO, ZnO, TiO_2, Fe_3O_4, ZrO_2, WO_3, Fe, Cu, Au, Ag, SiC, carbon nanofibers, carbon nanotubes, SiO_2, and graphite diamond have been studied [91]. As a base fluid usually water, ethanol, engine oil, ethylene glycol, glycerol, oil, toluene, and anti-freeze are used [92-95]. The chemical energy storage is involved with two methods, endothermic reaction or absorbs energy mode and exothermic reaction or energy release mode [3, 74, 96]. The heat of both reactions usually stored either at ambient temperature or working temperature in a TES system.

3.1 Other potential HTFs

Beside commercially existing molten salts and synthetic oils; liquid metals such as Na, Na-K eutectic alloy, Pb-Bi molten alloys and liquid glasses have been investigated as potential HTFs [97]. Most of these liquid metals have low melting point, higher maximum temperature but high cost compared to nitrate salts [98]. Pressurized air, supercritical fluids (steam, CO_2) have been used as HTFs in some CSP plants as operated in Brayton and Rankine cycles [99]. Alongside air and steam; helium and nitrogen can be used as HTFs [97]. Carbonates have advantages over nitrates regarding higher maximum temperature but have high solid-liquid equilibrium temperatures. Most of these HTFs have some thermophysical limitations compared to molten nitrate salt, as described in detail by Heller [97] and Ushak et al. [100] and shown in Table 3.2.1. Various practical aspects of TES systems have been described by Rodríguez-García et al. [68], Kuravi et al. [15] and Kousksou et al. [101]. A HTF database is represented by Serrano-López et al. [69] and

Bauer et al. [102]. This section describes some of the existing and potential HTF and storage fluids.

3.2 MOLTEN ALKALI NITRATE AND NITRITE SALTS

The alkali and alkaline nitrates/nitrites are solid granular (dehydrated) at standard temperature and pressure and at the elevated temperature they form liquid (usually light yellow or pale yellow color) and remain liquid up to several hundred degrees Celsius with negligible vapor formation. Their mixtures are used as HTFs in liquid state hence commonly known as molten salts [103]. Molten alkali nitrates are more stable than alkali nitrites, and most alkaline earth nitrates [102] discussed in subsection 3.3.4. Most of the molten salt HTF's constitute compounds are cheaper and naturally abundant compared to other HTFs used [104]. Cordaro et al. [24] examined the market price of nitrates and stated that the lithium nitrate is more expensive than other commercial nitrates, and the costs order is: $Ca(NO_3)_2 < NaNO_3 < KNO_3 < LiNO_3$.

These molten salt HTFs can be various combination and composition of fused alkali/alkaline earth nitrate/nitrite, such as: $NaNO_3$, KNO_3, $LiNO_3$, $CsNO_3$, $NaNO_2$, KNO_2, $Ca(NO_3)_2$, $Mg(NO_3)_2$. The combinations of the salts can be binary, ternary, quaternary, or higher order compound systems. The salt solution mixture can be common anion solution or reciprocal anion solution. Such as, $NaNO_3$-KNO_3-$LiNO_3$, is a common anion ternary system, and $NaNO_3$-KNO_3-$NaNO_2$ is a reciprocal anion ternary system. Similarly, $NaNO_3$-KNO_3-$LiNO_3$-$Ca(NO_3)_2$, is a common anion additive type quaternary system, and $NaNO_3$-KNO_3-$NaNO_2$-$LiNO_3$ is a reciprocal anion quaternary system.

Molten nitrate salts are used in high temperature solar thermal application because of they have good heat transfer properties [105, 106], high heat capacity, high thermal stability, high density [72, 106-109], lower vapor pressure [72], lower unit cost [109], are non-flammable [110] and have higher operating temperature than other HTFs [111]. However, molten nitrate salt have lower heat capacity and lower melting point compared to chlorides, carbonates and fluorides salts [69, 112]. Some of the common properties are compared in

Table 3.2.1. Using molten nitrate salt HTFs in solar thermal power plants gives, some advantages and disadvantages over synthetic oil, organic (mainly hydrocarbon) and other HTFs they are:

i) Wider operating temperature range compared to other types of HTF as shown in Table 3.2.1.
ii) Can be used as both HTF and heat storage fluid in a direct type TES system and eliminating the need for an expensive oil to salt heat exchanger [17, 22], reduces thermal losses [113]. Which also offer simplified CSP plant design [114].
iii) Reduces the collector area and storage tank size, thus reducing cost [17]. For example for a given parabolic trough power plant using molten nitrate salt will reduce the size of TES tanks by two third compared to oil as HTF and also it will reduce 30% built cost [114].
iv) Standard turbines can be used without modification as molten salt has higher operating temperature compared to oil [114], as shown in Table 3.2.1.
v) Higher melting temperature of molten nitrate salt increases the cost of freeze protection and decrease the solar field efficiency due to heat losses [115].
vi) Due to the high melting point compared to oil and steam, the energy require to melt is higher for molten nitrate salts.

To understand the actual performance of heat transfer fluids in a solar thermal power plant; the heat transfer properties, solvent properties, latent heat, thermal stability, melting temperature range, fluid velocity, vapor pressure, thermal conductivity and liquidus temperature, are essential criteria [3, 105]. For potential HTF selection, these thermophysical properties and cost are important factors. For an example, a ternary $Ca(NO_3)_2$-KNO_3-$NaNO_3$ (44-44-12wt%) nitrate mixture patented by Michel [116] was not selected for use because of high viscosity. However, ‗HitecXL®solar‘ salt a ternary mixture of similar compounds of Ca: K: Na nitrate but different composition (of 48-45-7 weight ratio) offers optimum transport properties as shown in Table 3.2.1.

Nitrate salt compound mixtures have lowest melting or freezing points than the single constituent nitrate itself in that particular solutions mixture [108, 117]. Usually for a given solutions mixture of specific composition, the solidus and liquidus temperature are identical, where mixture melts or solidifies completely at one temperature, commonly expressed as eutectic melting temperature or simply eutectic point [118]. The liquidus temperature of a particular composition is at which liquid phase observed and the solidus temperature at which solid state observed [17]. The liquidus and solidus in phase diagrams are described as follow: liquidus locus or line in phase diagram indicates that the system at this temperature with various compositions started to freeze during cooling or finished melting during heating; solidus locus or line in phase diagram indicates that the system at this temperature with various compositions finished freezing during cooling or started melting during heating [119].

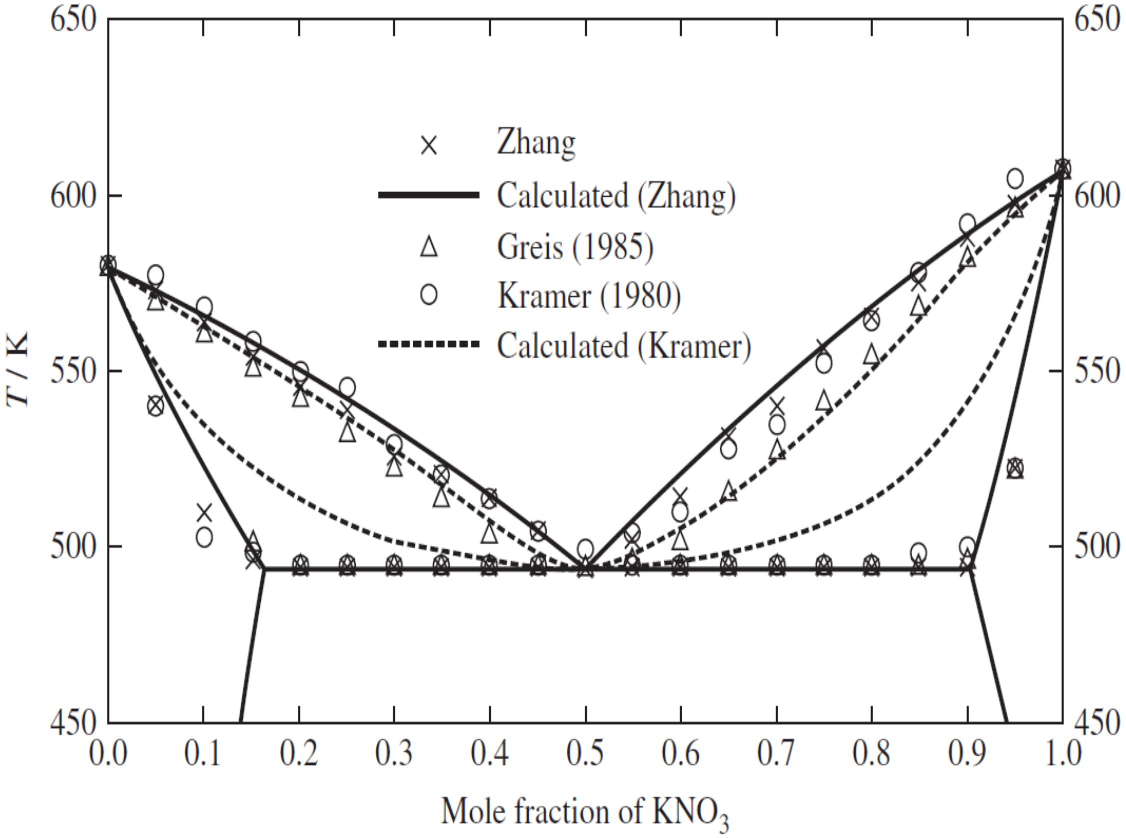

Figure 3.2.1: A phase diagram of 1:1 molar or Na:K//NO_3- 46:54 wt%, binary $NaNO_3$-KNO_3 molten salt system [35, 37].

A phase diagram of a binary common anion salt system is shown schematically in Figure 3.2.1. The eutectic point is seen where around 490K and at 0.5 mole KNO_3 (or 0.5 mole $NaNO_3$) in the intersection of solidus and liquidus line [31]. The boiling point of sodium nitrate is 580K, and potassium nitrate is 608K, as shown schematically in Figure 3.2.1. The binary phase diagram shows two phase regions in between solidus and liquidus lines. Various studies have generated different liquidus lines, as shown in Figure 3.2.1 [35, 37, 108]. Usually, complex or higher order solution mixture has more complex phase diagrams than the simple binary eutectic system [120]. A phase diagram of five compounds $LiNO_3$-$NaNO_3$-KNO_3-$CsNO_3$-$Ca(NO_3)_2$ salt system of 8-6-23-44-19 weight % or 15-10-30-30-15 mole %, is shown schematically in Figure 3.2.2. The poly-thermal projection of quinary eutectic salt systems is showing the melting point as 65°C with fixed Cesium mole fraction 0.3 and Calcium mole fraction 0.15 [108].

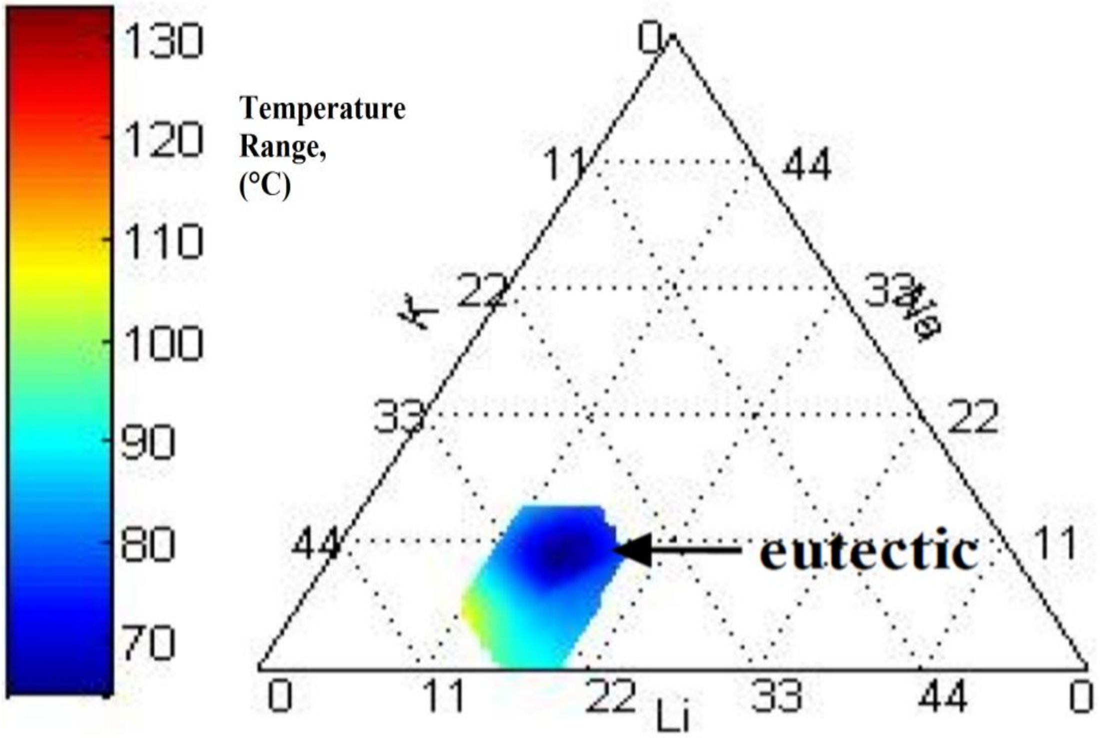

Figure 3.2.2: A phase diagram of a five compound‘s salt mixture consisting of $LiNO_3$-$NaNO_3$-KNO_3-$CsNO_3$-$Ca(NO_3)_2$ (15-10-30-30-15 mole % respectively) with fixed Cesium (0.3) and Calcium (0.15) mole fraction [108].

The ternary Gibbs triangle consist of sodium, potassium and lithium nitrates, is shown schematically in Figure 3.2.3. Here $LiNO_3$ has a melting point at 253°C, but the ternary system itself shows lower melting points at 120 to 121°C [108, 121]. Similarly, quaternary mixtures of lithium nitrate, sodium nitrate, potassium nitrate, calcium nitrate have eutectic points below 100°C [17]. The details thermodynamics of phase diagrams are described in subsection 3.6.

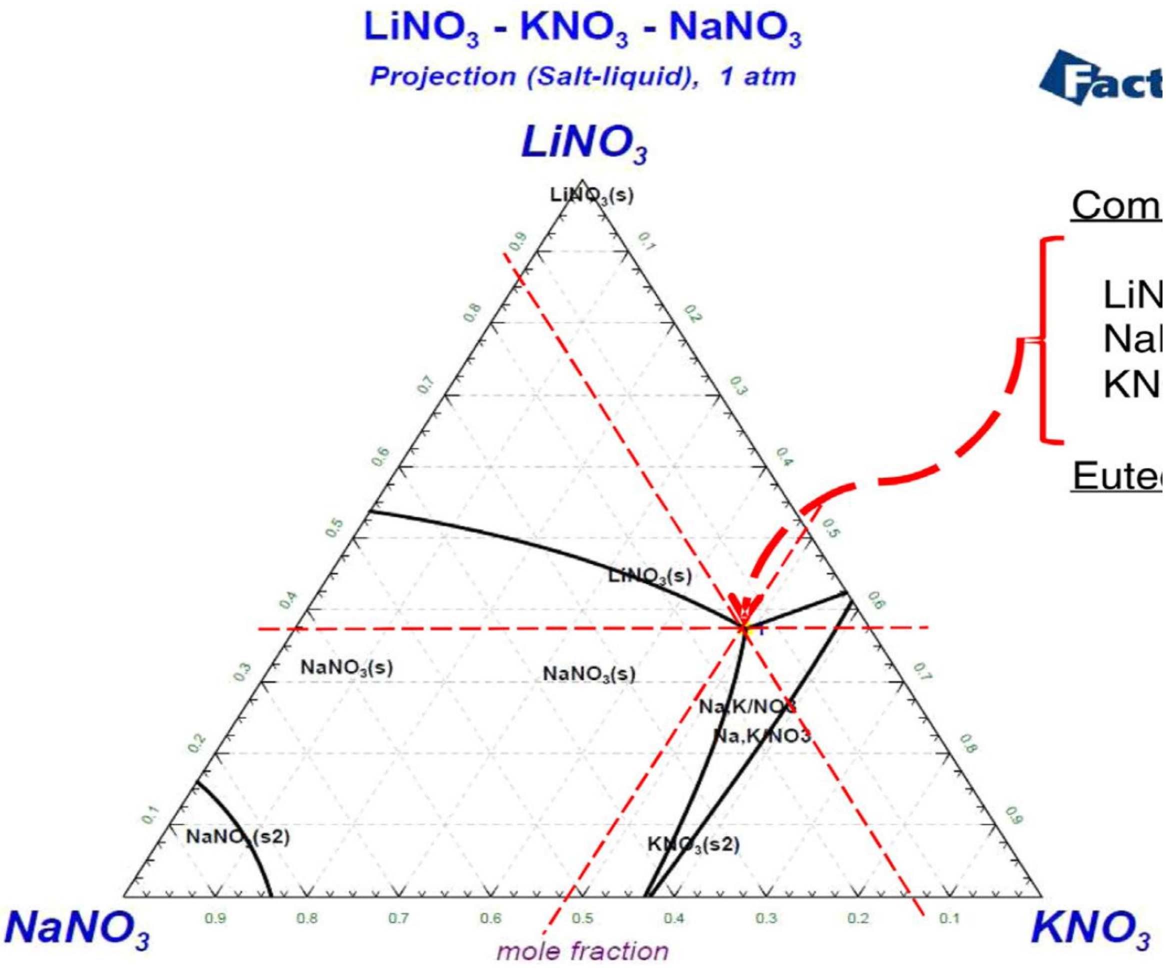

Figure 3.2.3: A phase diagram of three compounds salt mixture consisting of $LiNO_3$-$NaNO_3$-KNO_3 (30-18-52 wt % respectively) [121].

Some of the commercially used molten nitrates compounds are compared with other HTFs, are shown in Table 3.2.1. Hitec and Hitec XL both have a lower melting point and stability limit compared to solar salt, as discussed in Section 3.2.1 in this Chapter.

Table 3.2.1: A comparison of thermophysical properties and cost of various HTF and heat storage media for use and application in TES plants and other sectors [3, 23, 47, 49, 102, 122-134].

HTF/storage materials (*weight ratio*)	**Operating Temperature range** °C (melting point-upper limit)	**Average Density** kg/m^3	**Viscosity** Pa.s	**Average Thermal conductivity** W/m.K	**Average heat capacity** kJ/kg°C	**Volume specific heat capacity** $kWh_t/m^3°C$	**Costs per kg** US$ per kg	**Cost per kWh_t** US$ per kWh_t
Hitec®solar salt (*60:40 Na:K nitrate*)	220–565/600	1899 [a]	0.00326 [a]	0.55 [b]	1.5 [b]	0.79	0.49	10.7
Hitec®salt (*7:53:40 Na:K:Na///*NO_3-NO_2)	142–535/540	1790 [b]	0.00316 [c]	0.61 [a]	1.56 [b]	Nil	0.93	Nil
HitecXL®solar salt (*7:45:48 Na:K:Ca///*NO_3)	120/130–500/554	1992 [a]	0.00637 [a]	0.52	1.45 [a]	0.77	1.19	13.1
Draw salt (*46:54 Na:K nitrate*)	220–550	1733 [c]	0.0011 [c]	0.57 [c]	Nil	Nil	Nil	Nil
Biphenyl/Diphenyl oxide; Dowtherm A/ Therminol VP-1 (*26.5-73.5*)	12–393	805 [a]	0.00059 [a]	~0.117	1.93 [a]	Nil	2.2 to 3.96	Nil
Sandia mix QA (*18:56:8:18 Na:K:Li:Ca nitrate*)	<95–500	2018 [d]	0.005-0.007 [a]	0.522 [e]	1.44 [f]	Nil	Nil	Nil
Sandia mix QB (*13:66:7:14 Na:K:Li:Ca nitrate*)	<95–500	2015 [d]	0.005-0.007 [a]	0.654 [e]	1.16 [f]	Nil	Nil	Nil
Halotechnics HTF (*6:23:8:19:44 Na:K:Li:Ca:Cs nitrate*)	65–561	Nil	Nil	Nil	Nil	Nil	Nil	Nil

Continuation of Table 3.2.1

HTF/storage materials	**Operating Temperature range** °C (melting point-upper limit)	**Average Density** kg/m^3	**Viscosity** Pa.s	**Average Thermal conductivity** W/m.K	**Average heat capacity** kJ/kg°C	**Volume specific heat capacity** $kWh_t/m^3°C$	**Costs per kg** US$ per kg	**Cost per kWh_t** US$ per kWh_t
Mineral oil	200–300	770	N/A	0.12	2.6	0.56	0.30	4.2
Synthetic oil	250–350	900	N/A	0.11	2.3	0.58	3.00	43.0
Silicone oil	300–400	900	N/A	0.10	2.1	0.53	5.00	80.0
Nitrite salts	250–450	1825	Nil	0.57	1.5	0.76	1.00	12.0
Liquid Na	89–883	850	0.00021[g]	71.0	1.3	0.31	2.00	21.0
Liquid Na-K (*22.2–77.8*)	-12–785	Nil	0.00018[g]	26.2[g]	0.9 [g]	Nil	2.00	Nil
Liquid Pb-Bi (*44.5–55.5*)	125–1533	Nil	0.00108[g]	12.8[g]	0.2 [g]	Nil	13.00	Nil
Nitrate salts	265–565	1870	Nil	0.52	1.6	0.83	0.50	3.7
Carbonate salts	Nil	2100	Nil	2.0	1.8	1.05	2.40	11.0
Sand- rock-mineral oil	200–300	1700	Nil	1.0	1.30	.60	0.15	4.2
NaCl (solid)	200–500	2160	Nil	7.0	0.85	0.51	0.15	1.5
Na-K-Zn//Cl (*7.5–23.9–68.6*)	204–850	Nil	0.004[g]	0.33[a]	0.81[a]	<1	Nil	Nil
Cast iron	200–400	7800	Nil	40	0.60	1.30	5.0	60.0
Air	N/A–	Nil	0.00003[g]	.06[g]	1.12[g]	Nil	0	0
Water/steam	N/A–	Nil	0.00133[g]	.08[g]	2.42[g]	Nil	~0	~0

a = at 300°C , b = at 400°C , c = at 540°C, d = at 150°C, e = at 250°C, f = at 247°C, g = at 600°C
N/A: Not applicable. Nil: indicating no data available.

3.2.1 COMMERCIAL HEAT TRANSFER FLUIDS

The most common commercially used molten salts are: Hitec, Hitec XL, solar salt and Therminol VP-1 or Dowtherm A [12, 47]. The properties of these HTFs are described in the following section.

3.2.1.1 SOLAR SALT

Solar salt® is a binary salt mixture of 60 weight % (64 mole %) $NaNO_3$ and 40 weight % (36 mole %) KNO_3 [35]. Binary salt with a high content of sodium nitrate will reduce the inventory cost since $NaNO_3$ is cheaper compared to KNO_3 and economically favorable than draw salt. Park Chemical company marketed the salt as Partherm 430 [135] and Coastal Chemical Co., llc marketed as Hitec solar salt [136]. The eutectic point varies from 220°C to 240°C [108, 110, 137], although in CSP plant in actual practice the lower operating point is 290°C to ensure freeze protection. The highest operating temperature is 565°C [138] (to limit corrosion [139]) and can work up to 600°C [17, 23, 55, 56, 108, 139, 140]. This binary solar salt is proven HTFs [141] and used at several CSP plants [15], such as: at solar two central receiver power plants in Barstow, California, USA [55, 56, 142, 143], at the ANDASOL plant in Spain [17, 144], the ARCHIMEDE power plant [145, 146] in Italy and the GEMASOLAR power plant [147] in Spain [40, 111, 148]. It has the higher thermal stability and melting point and lower cost [17] compared to Hitec XL salt. Similar to other nitrate salt mixtures, solar salt is corrosive when reacting with carbon steel [30, 105, 149]. Various authors have reported the phase diagrams for the binary Na-K//NO_3 system [37, 150-155].

3.2.1.2 DRAW SALT

Draw salt® is a binary salt mixture of 1:1 molar [30, 156] or 54 weight% KNO_3 and 46 weight% $NaNO_3$ with melting point 220ºC [128]. Draw salt has been used in intenco carbon black metal treating industries in Houston, Texas, U.S.A for 30 years [30] and many other industrial sectors. It has density 1733 kg/m^3, thermal conductivity 0.57 W/m.K and viscosity 0.0011 Pa/s [128]. Unlike other molten nitrate/nitrite salt mixture, the draw salt needs freezing point protection and heat tracing elements in piping and accessories [128]. A commercial grade sodium nitrate and potassium nitrate, are shown in Figure 3.2.1.2.

Figure 3.2.1.2: The commercial grade $NaNO_3$ and KNO_3 of Chilean origin (Multi-K, Haifa Company) gathered prior to melting [23].

3.2.1.3 HITEC

Hitec® is a ternary nitrate/nitrite mixture of $NaNO_3$, KNO_3 and $NaNO_2$ (with a NO_2^-/NO_3^- ratio of 0.7 [26]) with 7-44-49 mole% [17, 35] or 7-53-40 weight% [36, 128] respectively and its freezing temperature is 141°C to 142°C [17, 36, 108, 128, 129, 136, 137] and highest operating temperature is 538°C [17, 108, 136], as shown in Table 3.2.1. According to Peng et al. [157] the reciprocal anion salt mixture possesses stability up to 500°C without decomposition. Due to its lower melting point, the salt can be melted with the help of a steam heat exchanger at 446kPa [136]. Hitec has a density 1990 kg/m^3 [129], thermal conductivity 0.5 to 0.6 W/mK [129, 158], specific heat 1.5 kJ/kgK [47] and viscosity is similar to water at high temperatures [17, 105]. This molten salt has been used since 1937 [35, 159] and used in 2 MW Themis pilot power tower plant in 80's in France [111, 160]. Also, it has been used in many heat treating industries in the USA [30]. According to Coastal Chemical Company (a Dupont subsidiary) [136] in a closed system the Hitec shows slow thermal breakdown can be expressed as:

$5NaNO_2 \rightarrow 3NaNO_3 + Na_2O + N_2 \uparrow$ [128, 136] eqn 3.2.1.3.1

The nitrogen gas also evolves slowly and raises the melting point of the mixture and equation 3.2.1.3.1 thermodynamically favorable at any temperature. At temperatures above 816^{o}C nitrogen evolves rapidly and salt starts to boil. Once the heat is removed, the salt decomposition reaction ceases, which indicate endothermic reaction [136]. However, in open system, the nitrite slowly oxidized in presence of O_2 in atmosphere,

$2NaNO_2 + O_2 \rightarrow 2NaNO_3$ [136] eqn 3.2.1.3.2

In nitrate-nitrite melt the time required to reach equilibrium depends on several factors [102, 161], such as:

- reaction direction: either oxidation or decomposition (interdependent reactions)
- the atmosphere over melt sample
- experimental setup

The Coastal Chemical Company report stated that some other reactions happen such as, carbonate and hydroxide formation in the presence of CO_2 and H_2O in the atmosphere, which tends to precipitate and raise the freezing point [136]. These problems can be eliminated by using N_2 as cover blanket gas [136]. Moreover, when operated at high temperature (520^{o}C) nitrite salt needed to add periodically (e.g. annually) to minimize nitrite degradation loss [30, 128]. This salt is also manufactured by Park Chemical

Company as Patherm 290 [135]. Various authors have reported the phase diagrams for this constituent reciprocal anion ternary system [162-166].

3.2.1.4 HITEC XL

Hitec XL® is a ternary mixture of $Ca(NO_3)_2$, $NaNO_3$ and KNO_3, of Ca:Na:K// NO_3-48:7:45 weight% and its eutectic point is 120°C [23, 167, 168]. A different composition of Ca:Na:K//NO_3-30:24:46 weight% [169] has a melting point at 160°C. The highest operating temperature is 500°C [108, 167], as shown in Table 3.2.1. HitecXL has working temperature range from 120°C to 500°C, density 1992 kg/m^3, thermal conductivity 0.519 W/mK [47, 129], specific heat 1.4 kJ/kgK [47]. When used in CSP plants the commercial grade Hitec XL contains water as calcium nitrate is only available in tetrahydrate form [167]. The dissolved salt is heated to flash off water to obtain dehydrated salt mixture [167]. Due to residual water presence in calcium nitrate the melting point varied among the authors. Calcium-potassium-sodium nitrate system has glass forming tendency (metastable solid amorphous) during solidification [170]. Various authors have reported the phase diagrams for this ternary additive common anion system [35, 169, 171-174].

3.2.1.5 DOWTHERM A AND THERMINOL VP-1

Dowtherm A is a synthetic organic fluid mixture of biphenyl: $(C_6H_5)_2$ and diphenyl oxide: $(C_6H_5)_2O$ commonly denoted as DPO synthetic oil. Biphenyl oxide and diphenyl oxide have similar vapor pressures. Thus, the mixture can be used as the single compound. DPO has operating temperature ranging between 15°C to 400°C with flash point 110 to 113°C [130, 131] and density 1056 kg/m^3 at 25°C [130]. Dowtherm A is being used in U.S industries as a heat transfer medium in both vapor phase and liquid phase heating for 60 years [130]. DPO hydrocarbon mixture is being used in Palma del rio parabolic trough power plants (Spain), in Manchasol parabolic trough power plants (Spain), Andasol parabolic trough power plants (Spain) and other CSP plants [47, 175-181]. This eutectic mixture has been used at the Nevada Solar One parabolic trough power plant in the USA as Dowtherm A [130] of Dow Chemical Company [182] and in Genesis Solar Energy Project parabolic trough power plants in the USA as Therminol VP-1 [131] of Solutia Company [183]. Most of the parabolic trough power plants use Therminol VP-1 or Dowtherm A synthetic oil [97]. Silverman and Engel [128] suggested that Dowtherm A has poor heat transfer rate, and decomposition causes fouling. Usually, H_2 is produced as decomposition product [184].

3.2.2 APPLICATION OF MOLTEN SALT

Lai [185] described the use of molten salts in various sectors, including materials processing, minerals extraction, nitriding of steel, quenchant baths, nuclear energy power plants [32, 34], solar ponds and seawater desalination [185]. Nitrate and nitrite are also used in the meat industry for curing raw red meats [186, 187], in the fish industry [188], high temperature electrochemistry [31, 189], electrolytes for thermal battery [31, 189], in gunpowder [190], as an explosive compound [191], and as high temperature heat transfer medium in the chemical and metal industries [30, 34, 192]. Molten salt also used in melamine industries, production of aluminum oxide and aluminum, caustic soda or sodium hydroxide production, natural fertilizer production. In most industries the nitrate and nitrite salts used as isothermal temperature operation such as in chemical reactors, while in STP plants they used as cyclic operation (cyclic heating-cooling) [30] in TES systems.

Raade and Padowitz [108] described some limitations of both organic and inorganic heat transfer fluids. For an example, VP-1 or Dowtherm A is expensive compared to binary solar salt, as shown in Table 1. It has a limited upper temperature of 390°C, above this temperature thermal degradation occurs. Narrower operating temperature range limits the efficiency of Rankine cycle using VP-1 and Dowtherm [17]. Also, it possesses high vapor pressure at an elevated temperature of 10 bars at 390°C [130]. Inorganic fluids such as molten nitrate and nitrite have some drawbacks too. They possess relatively high melting points ranging from 140°C to 240°C compared to 12°C of VP-1 and Dowtherm A. [17, 115]. Thus, these inorganic fluids require higher energy to melt compared to organic liquids [17]; higher cost of construction materials; and added the cost of an effective heating system to avoid clotting and blocking of the pipes. Due to higher melting temperature (typically 140ºC to 240ºC) a routine freeze protection is required in the solar field. Usually heat tracing element, heat insulator, and emergency water dilution system are used against salt freezing [127]. At higher temperature due to salt degradation insoluble and soluble corrosive oxide, products may form, and the viscosity and melting point increased as reported by Kramer [192]. At elevated temperature mainly soluble oxide ion may promote corrosion with storage materials especially, with stainless steel [26, 193]. The corrosion properties of nitrate salts studied by Guillot et al. [194] and well-reviewed by Vignarooban et al. [195]. Inorganic fused nitrates and nitrites salt have good wettability and hence due to creeping physical loss of salt occurs (leaking) through valve stem packing, relief valves, cracks and flanges very often in industries and CSP plants [30, 55]. Main advantage of Nitrates are, they can be used as both HTF and heat storage fluid in a direct type TES system and eliminate the need for an expensive oil to salt heat exchanger (HE) [17, 22], reduces thermal losses in HE [113], offer simplified CSP plant design and allow usage of standard turbines without modification [72]. It also reduces the collector area and storage tank size, thus reducing cost [17].

3.3 CHEMISTRY OF ALKALI NITRATES AND NITRITES

High temperature chemistry is a fundamental aspect to understand the thermal breakdown reaction, nitrate/nitrite equilibrium chemistry of the salt melt, and vaporization chemistry. The atomic bond structure of polyatomic anions and their formation with alkaline/alkali cations are important issues to understand the reactions [196] and vapor species of the molten salt.

3.3.1 NITRITES AND NITRATES IONS

3.3.1.1 NITRITE ION, NO_2^-

In the periodic table Nitrogen belongs to group 15 elements also called group five elements (denoted as Roman numeric V). The Nitrogen has five valence electrons. Oxygen is group 16 elements in the periodic table also called group six elements (denoted as Roman numeric

VI). Nitrogen and oxygen atoms form covalent bonds between each other to complete octet orbital states for all three atoms. In the octet forming process, the extra electron of the negative charge has a tendency to make a pair with either side of the oxygen atom. The ion has two canonical structures with a resonant hybrid [197]. Because of the oxygen atom have a higher electronegativity than the nitrogen atom. These structures are shown schematically in Figure 3.3.1.1.1. The straight arrow indicates a pair of electrons. As from Figure 3.3.1.1.1, it is seen that all the atoms complete their octet using four pairs of electrons. The nitrite ion electronic structure is commonly represented as Figure 3.3.1.1.2 [198].

The Nitrite ion is a polyatomic anion with a negative charge and has 18 valence electrons [199]. Five electrons of a central nitrogen atom, six electrons for each of the oxygen atoms, and one electron of the negative charge ion, total eighteen electrons. The ion is V-shaped planar triangular [199, 200] or bent symmetrical [25, 123] as shown schematically in Figure 3.3.1.1.2. This form of the molecule is due to a lone pair of electrons in central nitrogen atom [200]. The bond angle is 115° [25, 197, 200]. In nitrite ion, the electron in the nitrogen atom has Sp^2 hybridization [25, 197, 199]. The nitrogen oxygen bond length 1.24 x 10^{-12} meter [197, 200].

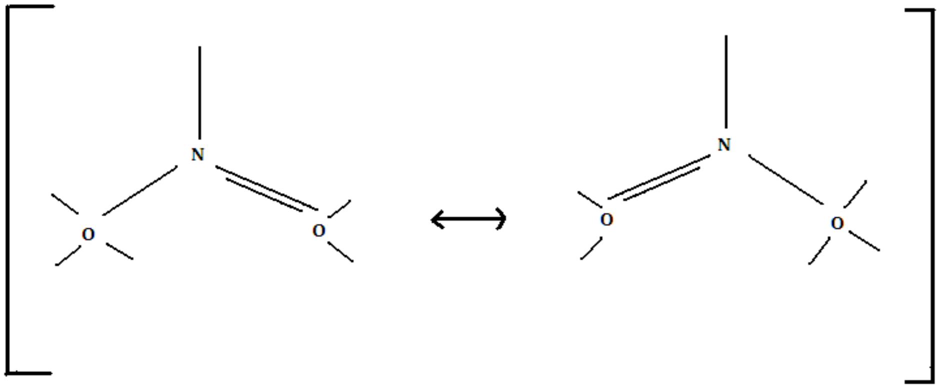

Figure 3.3.1.1.1: Two possible canonical resonance structures of nitrite ion [197].

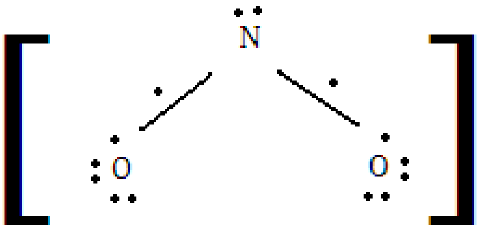

Figure 3.3.1.1.2: Common electronic structure of nitrite ion [198].

Nitrite oxyanions all the atoms have four pairs of electrons, shown schematically in Figure 3.3.1.1.2. The arrow indicates electron sharing pairs between nitrogen and oxygen atom. The nitrite ion is a nonlinear triatomic structure, having π and σ bonds [201]. In the nitrite ion, nitrogen atom forms σ bond with each oxygen atoms. Three atomic orbitals are involved in π bonding. The $2P_z$ orbital is present on the nitrogen atom and both oxygen atoms [199]. Nitrite ion is weak oxidizing agent [200]. As an example, nitrite will oxidize iron (II) ion to iron (III) ion and eventually reduced to lower oxides of nitrogen [200].

3.3.1.2 NITRATE ION, NO_3^-

The nitrate ion is an isoelectronic polyatomic anion consisting of one nitrogen atom and three oxygen atoms. It has 24 electrons in its valence shell [199]. Five electrons for the central nitrogen atom, six electrons for each of the oxygen atoms, and one electron for the negative charge ion total twenty-four electrons. The ion is a symmetrical planner triangle and similar to the CO_3^{2-} ion [123, 199, 202]. In the nitrate ion, the nitrogen atom also has Sp^2 hybridization [197] in its orbital system. The nitrogen and oxygen bond length is shorter in nitrate ion (1.22 x 10^{-12} meter) [197, 198, 200]. The nitrogen and oxygen bond length is shorter in nitrate ion [200]. Here the coordination take place from oxygen atom, because nitrogen atom has no available orbital [197]. Nitrogen atom and three oxygen atoms make covalent bonds with each other, to complete an octet orbital state in all four atoms. The extra electron has the tendency to make pair with either three of the oxygen atom. Thus nitrate ion gives three resonance structures. This is shown schematically in Figure 3.3.1.2.1. The nitrite ion is also commonly represented by the structure shown in Figure 3.3.1.2.2.

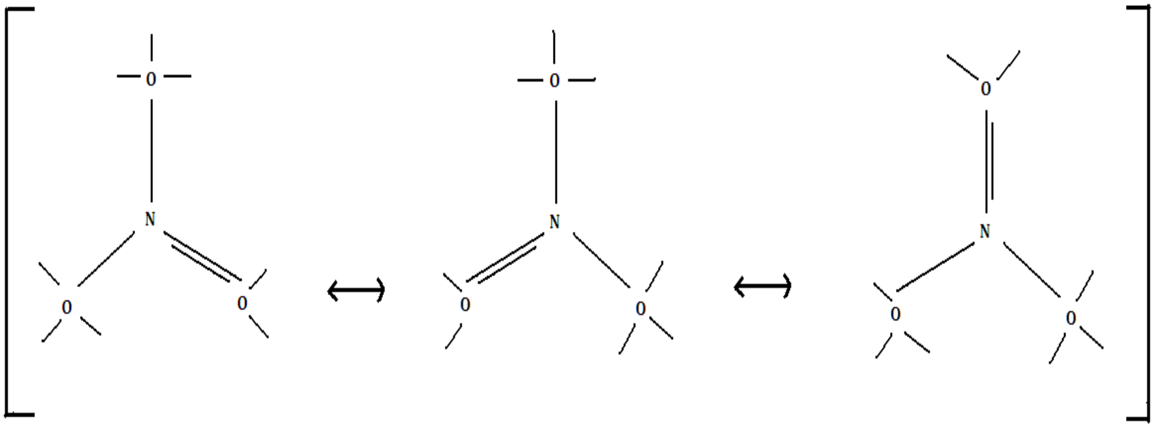

Figure 3.3.1.2.1: Three possible molecular resonance structures of nitrate ion [197, 203].

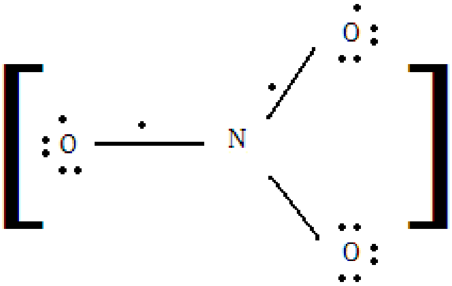

Figure 3.3.1.2.2: Common electronic structure of nitrate ion [198].

Nitrate polyatomic anions all the atoms have four pairs of electrons, shown in Figure 3.3.1.2.2. In nitrate ion, six electrons are used to form sigma (σ) bonding between nitrogen and three oxygen atoms [199]. These three σ bonds using the Sp^2 hybrid orbital [198]. Each oxygen atom has four nonbonding electrons. This gives six electrons availability to form pie (π) bonding. π bonding gives $2P_z$ atomic orbital for nitrogen and three oxygen atoms. Combining these four atomic orbital gives four, 4 center π molecular orbital [199]. The partial π bonding gives it a bond order of $1\frac{1}{3}$ [197, 200]. The nitrite ion is easily soluble in to nitrate ion. Similarly, the alkali nitrite is soluble in to alkali nitrate [31].

3.3.2 GENERAL PROPERTIES OF ALKALI NITRATES AND NITRITES

Alkali nitrates, alkali nitrites, are oxyanion polyatomic inorganic compounds. They are commonly called alkali salts. Normally, these ionic salts formed by the reaction of acid and base. Such compounds are consists of cation and anion. Alkalis metals are from group one of the periodic tables, and all have positive charge (1^+). These cations are denoted as : Li^+, Na^+, K^+, Rb^+, Cs^+ and Fr^+ [204].

3.3.2.1 ALKALI NITRITES

Alkali nitrites can generally be denoted as MNO_2 (here M= Li, Na, K, Rb, Cs [205]). Alkali nitrites formed by absorbing a mixture of nitric oxide and nitrogen dioxide in alkali hydroxide solution. Nitrites can be obtained by mild reduction of nitrates. As an example, the reaction between sodium nitrate and lead give a product of sodium nitrite and lead oxide. The reaction is given in equation 3.3.2.1.1

$NaNO_3 + Pb \xrightarrow{heat} NaNO_2 + PbO$ [206, 207] eqn 3.3.2.1.1

The general preparation of alkali nitrites are given in equation 3.3.2.1.2:

$4NO + 2MOH \rightarrow 2MNO_2 + N_2O + H_2O$ [205] eqn 3.3.2.1.2

Here, M = Li, Na, K, Rb, Cs [205]

Equation 3.3.2.1.2 states that the reaction between nitric oxide and alkali hydroxide gives the alkali nitrites, nitrogen dioxide, and H_2O [205]. As an example of the reaction 3.3.2.1.2, the potassium hydroxide and nitric oxide, provide the potassium nitrite, nitrogen dioxide, water. The reaction is given in equation 3.3.2.1.3. Alternatively, thermal decomposition of alkali nitrate also gives nitrite and liberated oxygen [205]. The reaction is given in equation 3.3.2.1.4.

$4NO + 2KOH \rightarrow 2KNO_2 + N_2O + H_2O$ [205] eqn 3.3.2.1.3

$2MNO_3 \overset{\Delta}{\leftrightarrow} 2MNO_2 + O_2$ [198, 204, 205] eqn 3.3.2.1.4

Here, M = Li, Na, K, Rb, Cs [205]

Although Bordyushkova et al. [208] disputed equation 3.3.2.1.4. They stated that preparation of pure nitrites from the thermal decomposition of nitrates is difficult because of the concurrent reversible nature of reaction (equation 3.3.2.1.4) and the presence of unstable oxides [208]. They conducted experiments on alkali nitrates and determined nitrites quantitatively from their respective nitrates using 291-540 colorimetric and 430-640 permanganate methods. The details apparatus setup and methods were not described by the authors [208]. The results indicated that the melts possessed stability until the formation of 1% nitrites [208], as shown schematically in Figure 3.3.2.1.1.

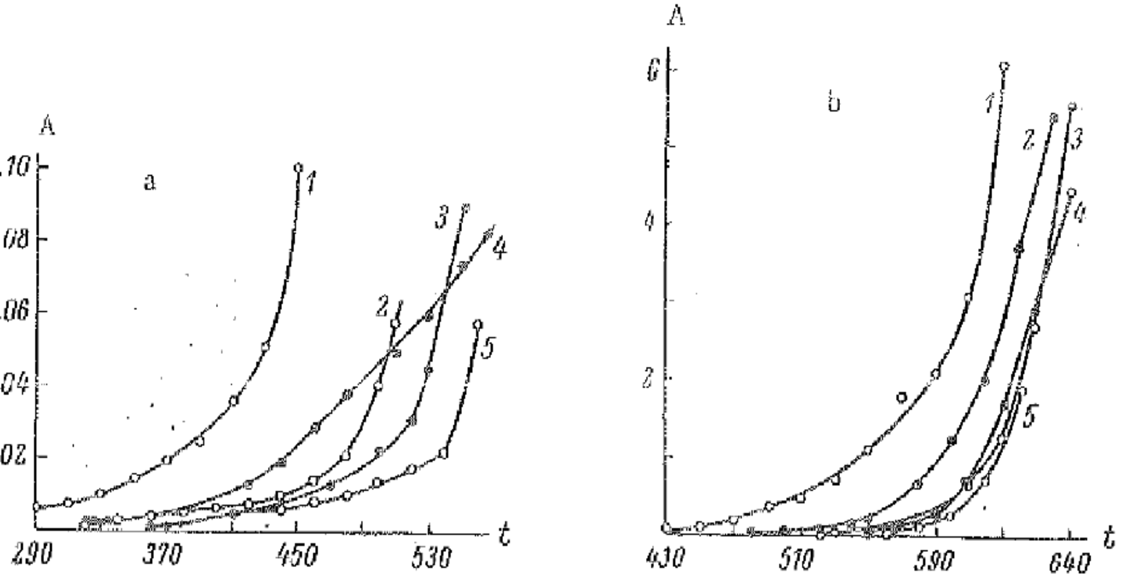

Figure 3.3.2.1.1: Results of decomposition of alkali nitrates by two methods studied by Bordyushkova et al. [208]. –**A**” indicates nitrites content in %; –**t**’ indicates temperature in ºC. Curve 1= $LiNO_2$, 2=$NaNO_2$, 3=KNO_2, 4=$RbNO_2$ and 5=$CsNO_2$. Curves in a) graph were studied by 291-540 colorimetric method; curves in b) graph were studied by 430-640 permanganate method.

General properties of nitrites:

All nitrites are produced artificially from their corresponding nitrates, given in equations 3.3.2.1.1 and 3.3.2.1.4. Alkali nitrites tend to form small solid crystals and have white color [205]. They can be fused without decomposition. They also used as reducing agents. When they are heated in air, they oxidize to nitrogen oxide compounds [205]. They are water soluble and hygroscopic in nature [206]. As an example, at 25 °C, 85.5 g of $NaNO_2$ dissolves in a 100 g of water. Sodium nitrites in the laboratory are found in pale yellow sticks [206]. Nitrites are less soluble in alcohol [206]. By comparison, at 25 °C, 314 g of KNO_2 dissolves in 100 g of water. Potassium nitrite is more water soluble than sodium nitrite [206]. Nitrites can be determined chemically by sulfanilic acid coupling with α-napthylamine test suggested by Kust and Burke [209] and Brough et al. [210]. Also, nitrites can be detected by the naphthyl ethylenediamine hydrochloride spectrophotometric method described by Wei et al. [211]. Nitrites are not flammable, but can cause fire or explosion in contact with reducing agent. Contact with eye and skin cause irritation; and inhalation and digestion cause pain, dizziness, headache, and nausea. Safety gear and self-protective equipment are needed for handling nitrites.

3.3.2.2 ALKALI NITRATES

Alkali nitrates are commonly denoted as MNO_3 (here M= Li, Na, K, Rb, Cs [205]). Nitrates can be derived from simple inorganic bases. The evaporation reaction of a Nitric acid and corresponding alkali metal hydroxide or alkali carbonate produces nitrates [205, 206, 212]. Equation 3.3.2.2.1 is the example of producing nitrates from corresponding metal carbonate.

$$2HNO_3 + M_2CO_3 \rightarrow 2MNO_3 + H_2O + CO_2 \qquad [205] \qquad \text{eqn 3.3.2.2.1}$$

Here, M= Li, Na, K, Rb, Cs

Alternatively, alkali nitrates (MNO_3) can be obtained from ammonia nitrate and metal hydroxide reaction:

$NH_4NO_3 + MOH \rightarrow MNO_3 + NH_4OH$ [205] eqn 3.3.2.2.2

Here, M = Li, Na, K, Rb, Cs

Initially, when heated all pure alkali nitrates decompose to nitrites and oxygen. They lose oxygen and convert to nitrites [30]. For example during the heating of potassium nitrate, potassium nitrite (pale yellow solid) [213] and oxygen are the products [206, 213].

$2KNO_3 \overset{heat}{\longleftrightarrow} 2KNO_2 + ½ O_2$ [29, 30, 156, 189, 206, 207, 214] eqn 3.3.2.2.3

Another example of heating the sodium nitrate gives sodium nitrite and oxygen

$2NaNO_3 \overset{heat}{\longleftrightarrow} 2NaNO_2 + ½ O_2$ [29, 30, 156, 189, 200, 214] eqn 3.3.2.2.4

However, the nitrates of the heavy metals decompose completely. As an example, of mercury nitrate decomposition gives mercury oxide, nitrogen dioxide, and oxygen gas.

$Hg(NO_3)_2 = HgO + 2NO_2 + \frac{1}{2} O_2$ [206] eqn 3.3.2.2.5

General properties of nitrates:

Sodium nitrate commonly known as, Chile saltpeter or Peru saltpeter, and potassium nitrate is commonly known as saltpeter are extracted from the Atacama Desert in northern Chile [215]. The Atacama Desert in the north of Chile is the natural resource of the nitrates in the early 1950s. Usually, the nitrates are produced artificially in recent days, as given in equations 3.3.2.2.1 and 3.3.2.2.2. Lithium nitrate is generally prepared from lithium carbonate [216]. The history of the nitrate mining industry has been briefly described by Penrose [217] and Diaz [218].

At standard temperature and pressure, the alkali nitrates are freely soluble in water without chemical interaction (molecular identity preserved without any dissociation or association in aqueous melt) and the dissolution is reversible [102, 206, 213, 219]. According to Henry‘s Law, the concentration of water in the alkali metal nitrate melt is directly proportional to the partial pressure of water vapor [102]. Adding water to alkali nitrate decreases the melting temperature of water salt mixture (slurries) which don‘t solidify at room temperature [102]. Nitrates are good oxidizing agents at high temperature. At high temperature nitrates loses oxygen [213]. However, the aqueous solution of nitrate have no oxidizing properties [206]. The nitrate salts are usually hygroscopic in the molten and solid state [31]. Except lithium nitrate, all alkali nitrates show crystalline transition [220]. Similar to lithium nitrate, all alkaline earth nitrates also don‘t possess crystalline transformation [220]. Two common alkali nitrate salts heavily use in the market are sodium nitrate and potassium nitrate. KNO_3 and $NaNO_3$ have melting points 339°C and 311°C (approximately) respectively [206]. Sodium nitrate is colorless, odorless [156] rhombohedral crystalline salt. It has cold, bitter taste, readily soluble in water. Its solubility in water increases with increasing temperature [206]. As an example, at 0°C, 73 g of $NaNO_3$ dissolves in 100 g of H_2O. Moreover, at 100°C, 175.5 g of $NaNO_3$ dissolve in 100 g of H_2O [206]. The potassium nitrate has a higher solubility than $NaNO_3$ in higher temperature. By comparison, at 0°C, 13.27 g of KNO_3 dissolves in 100 g of H_2O. At 100°C, 246 g of KNO_3 dissolves in 100 g of H_2O [206]. KNO_3 is also colorless and odorless salt [156], has a cold and bitter taste. This dimorphous salt has three different crystalize forms, α-KNO_3 (stable above 128°C) and β-KNO_3 (stable at room temperature) [221] and metastable γ-KNO_3 [222]. KNO_3 shows aragonite structure II below 128°C and transform to calcite structure I above 128°C and crystallizes in rhombohedral, $R3m$ space group [223-225]. $LiNO_3$ and $NaNO_3$ are usually regarded as isostructural to calcite and crystallize in rhombohedral, $R\bar{3}c$ spatial group [226]. The details crystal structure and growth; polymorphism; and phase transitions of alkali nitrates are well described by Benages-Vilau et al. [226] and Rao et al. [224]. Monovalent nitrates such as $NaNO_3$ and KNO_3 are considered as D_{3h} symmetry group based on the ionic potential of the cations [227]. Some of the common properties of alkali nitrate and alkali nitrite salts are given in Tables 3.3.2.1 and 3.3.2.2 [205].

Nitrates are detected by the brown ring test [213] and also by Brucine ($C_{23}H_{26}N_2O_4$) [228]. Most metal nitrates give the metal oxide when heated [200]. As an example, heating of copper nitrate heptahydrate gives nitrogen dioxide, oxygen, and copper oxide.

$$2Cu\,(NO_3)_2\,(s) \xrightarrow{heat} 2CuO(s) + 4NO_2\,(g) + O_2\,(g) \qquad [200] \qquad \text{eqn 3.3.2.2.6}$$

Calcium metal is most reactive in nitrate melt compared to other alkali and alkaline metals [229]. Nitrates are not flammable, but cause fire or explosion in contact with reducing agent and combustible materials [156]. Contact with eye and skin cause irritation; and inhalation and digestion cause pain, dizziness, headache, and nausea. Safety gear and self-protective equipment are needed for handling nitrates. The nitrates can be stored for a long time [156] in sealed containers and dry atmospheres [31].

Common salt properties of some alkali nitrates/nitrites are shown in Tables 3.3.2.1 and 3.3.2.2. The melting point is lower in lithium nitrite at 254°C [208]. The sodium nitrate has the melting point ranging from 308 to 311°C [205]. Lower melting point and viscosity are essential criteria for efficient pumping of the salts. Cesium nitrate has the highest decomposition, as shown in Table 3.3.2.1. The single alkali and alkaline nitrates and nitrites; the binary and ternary nitrates salt‘s density vary linearly with temperature [24, 123, 230]. The viscosity of the alkali nitrate and nitrite salts decrease with increasing temperature [24, 123, 230]. The thermal conductivity according to White and Davis [231]; and McDonald and Davis [232] has linear temperature dependency in molten alkali nitrates. Cordaro [123] stated that for alkali nitrates the heat of fusion depends on upon cation size. The decomposition rates of alkali nitrates increase rapidly with increasing temperature and at the same time, the reversibility of decomposition reactions decrease [233].

Table 3.3.2.1: Physical properties of common alkali nitrates and alkali nitrites [102, 205, 208, 234, 235].

Property	**$NaNO_2$**	**KNO_2**	**$NaNO_3$**	**KNO_3**	**$RbNO_3$**	**$CsNO_3$**	**$LiNO_3$**
Formula weight	69.00	85.11	84.9947	101.10	147.49	194.92	68.95
Enthalpy of fusion ΔH_f (kJ/mol)	-359.40	-370.28	-467.60	-492.70	Nil	494.17	Nil
Melting point (°C)	271	440	306 [102] –308	334-335 [102, 236]	316 [234]	414	254 [216, 234]
Decomposition temperature (°C)	320	Nil	510 [208] – 520 [102]	533	512 [208]	584	430 [208]
Density (kg/m^3)	2168	Nil	2260 [206] – (1850 [102] at 400°C)	2315 [234]	3049 [234]	3620.6 [234]	2068 [234]
Viscosity (Pa.s)	0.0000209	0.00000767	0.0000282	0.0000278	Nil	Nil	0.0002283
Surface tension (N/m)	0.1202	0.1067	0.1166	0.1108	0.14964 [234]	0.0925	0.14339 [234]
Nil indicates no data available.							

Table 3.3.2.2: Physical properties of common cations, anions, alkali nitrates and alkali nitrites obtained from references [237-244] of FactSage™ [39].

	Property			
Species:	Standard Molar Enthalpy of formation **$\Delta_f H°$** (kJ/mol) at 25°C	Standard Gibbs Free Energy of Formation, Δ_f**G°** at 25°C (kJ/mol)	Standard molar entropy **S°**, (J/mol.K) at 25°C	Molar heat capacity at constant pressure **C_p**, (J/mol.K) at 25°C
K^+	-252.4	-283.3	102.5	21.8
Li^+	-278.5	-293.3	13.4	68.6
Na^+	-240.1	-261.9	59.0	46.4
NO_2^-	-104.6	-32.2	123.0	-97.5
NO_3^-	-207.4	-111.3	146.4	-86.6
KNO_2	-369.8	-306.6	152.1	107.4
$LiNO_2$	-372.4	-302.0	96	Nil
$NaNO_2$	-358.7	-284.6	103.8	Nil
KNO_3	-459.7	-394.5	248.9	-64.9
$LiNO_3$	-485.9	-404.5	160.2	-18.0
$NaNO_3$	-447.5	-373.2	205.4	-40.2
Nil indicates no data available.				

3.3.3 THE HIGH TEMPERATURE CHEMISTRY OF ALKALI NITRATES AND NITRITES

According to Emeléus and Sharpe [202] the initial decomposition of the alkali nitrate is difficult to detect, so the approximate temperature value is taken at which the oxygen is first detected. As every alkali nitrate gives oxygen and nitrite at initial decomposition [202]. Gordon [220] studied single nitrates by DTA and stated that the decomposition temperature is ascertain when oxygen gas evolving was visually observed (endothermic reaction). According to Bordyushkova and coworkers [208], the definition of decomposition temperature is as follow: ―the temperature at which 0.05 percent of the corresponding nitrite can be detected after ten minutes of heating of nitrate is denoted as decomposition temperature" [208]. According to Bauer et al. [102, 245], decomposition temperature is described as, ―when nitrate salt sample lost 3 weight percent of its total mass". The thermal decomposition process of polyatomic oxyanions alkali nitrates is complex process [161, 246, 247] compared to monoatomic anions compound salts, such as alkali chlorides/fluorides [102]. In decomposition of covalent metal nitrates the metal nitrites appear as unstable intermediates. But in case of iconic alkali nitrates during decomposition, both nitrates and nitrites are equally unstable more or less in reversible manner over some temperature range. This means that they are either oxidized or reduced by evolved gaseous products (concurrent reversible nature) which make the decomposition reaction more complex [25]. The reversibility and overlapping nature of reactions, type of cations presence in melt, surface area, purity, sample size, surrounding atmosphere and heating temperature are governing criteria for ambiguous reaction paths [25, 102, 161, 192, 246-250]. Thus decomposition kinetic studies during calculation of rate constant and activation energies, reported by various authors didn‘t clarify which particular reaction/s they are studying [25]. The melting point temperatures are reported by various authors are somewhat consistent, the decomposition temperatures of various alkali nitrate salt systems reported vary significantly between the authors [34, 102, 192, 248-251]. The thermal stability is measured experimentally mainly by thermal analysis method described in subsection 3.4. Based on recent studies it can be concluded that, the nature and results of alkali nitrates decomposition are depending upon following phenomena [25, 34, 102, 192, 248-252]: experimental technique and parameters; apparatus type used; sample composition and preparation; sample size and crucible types; crucible sample arrangement; calibration procedures; and decomposition temperature identification methods.

Kust and Bruke [209] studied the thermal decomposition of binary equimolar sodium nitrate and potassium nitrate by chemical sensitive test and oxygen gas electrode potentiometer. The result found that the binary nitrate undergoes thermal decomposition into their corresponding nitrites and oxygen at 300°C [209]. Nissen et al. [27] in their study of equimolar Na-K//NO_3 by chemical analysis found that the nitrite ion concentration in air atmosphere increased from 1.1mol% at 500°C to 5.7mol% at 600°C. Cordaro et al. [24] observed the molal concentration of Na-K-Li///NO_3-Na-K//NO_2 a quinary nitrate/nitrite mixer using chemical analysis. They observed that the nitrate to nitrite ratio increased to 20:1 after 120 days keeping the salt at 450°C temperature in the presence of air. Wei et al. [211] performed chemical analysis on binary solar salt and observed that around 450ºC temperature the nitrite formation is slow and small in quantity because of high activation barrier of NO_3^- ion. However, nitrite concentration increases with increasing temperature (>450ºC). In sodium nitrate and potassium nitrate, the primary decomposition reaction is the partial dissociation of nitrate ion to nitrite ion and oxygen [26-31, 36, 102, 123, 156, 163, 189, 209, 253-255], is given by equation 3.3.3.1. The equation 3.3.3.1 is an endothermic and reversible reaction for both $NaNO_3$ and KNO_3 [156].

$$NO_3^- \rightleftharpoons NO_2^- + \frac{1}{2}\, O_2 \qquad \text{(reversible and slow initially)} \qquad \text{equation 3.3.3.1}$$

$$K_{eq} = \frac{[NO_2^-]}{[NO_3^-]} X \left(P_{O_2}\right)^{\frac{1}{2}} \quad \left(\frac{\text{molal concentration of anions and } P_{O_2} \text{ are substituted}}{\text{for thermodynamic activities of compounds}}\right) \qquad \text{equation 3.3.3.2}$$

The alteration of nitrate to nitrite usually depend on the atmosphere surrounding the molten salt, temperature, experimental setup and the partial pressure of oxygen [26, 28, 31, 233, 256]. The equilibrium constant of Equation 3.3.3.1 in the absence of H_2O and CO_2 can be calculated from the partial pressure of oxygen [27, 28, 31, 102, 123, 250, 253, 257] is given by equation 3.3.3.2. The nitrate/nitrite equilibrium constant shown in equation 3.3.3.2

depend primarily on temperature according to Arrhenius principle [256]. Upon increasing temperature the relative concentration of nitrite will increase. Carling et al. [30] studied the Hitec salts by special purpose-built chemical analysis reactor stated that the nitrate/nitrite ratio depends on two parameters, they are: the pressure and the composition of the cover or atmospheric gas; and the heating temperature. At higher temperature nitrite ion decomposition results in partial dissociation into nitrous oxide, nitrogen dioxide and oxygen ions [25], regarded the reaction described by equation 3.3.3.3. Carling et al. [30], suggested the equation 3.3.3.3 as a secondary decomposition reaction in case of Hitec salt. According to their study, the equation 3.3.3.3 is associated with high temperature corrosion between salt and reservoir materials.

$NO_2^- \rightleftharpoons O_2^- + NO_2 + NO$ [26, 123, 209] equation 3.3.3.3

(Here, $2NO_2 \rightleftharpoons 2\mathrm{NO} + O_2$) [25] equation 3.3.3.4

Nitrite ion partial dissociation, shown in equation 3.3.3.3 also disputed by certain authors as per following equation.

$NO_2^- \rightleftharpoons O_2^- + \frac{3}{2}O_2 + N_2$ [17, 26] equation 3.3.3.5

Again nitrite anion can be oxidized to nitrate ion as per equations 3.3.3.6 and 3.3.3.7. Moreover, oxide ions can react with NO_2 and produce nitrite as per equation 3.3.3.8. According to Stern [25] equations 3.3.3.1 to 3.3.3.8 depend on experimental parameters (pressure, temperature, heating rate, vessel size, and volume to surface ratio) and type of cations in the melt.

$NO_2^- + NO_2 \rightleftharpoons NO_3^- + NO$ [25] equation 3.3.3.6

$NO_2^- + NO \rightleftharpoons NO_3^- + \frac{1}{2}N_2$ [25] equation 3.3.3.7

$O_2^- + 2NO_2 \rightleftharpoons NO_3^- + NO_2^-$ [25, 258, 259] equation 3.3.3.8

Corrosion studies of molten salt have been mainly focused on container and pipe materials compatibility. McConohy [256] studied corrosion of binary solar salt in corrosion test vessel [260], stated that at 680ºC container materials (Ni-based alloys) loss metals due to corrosion because of high nitrite concentration. At 680ºC nitrite concentration increased which resulted in decreasing melting points (as much as 60ºC) of the binary solar salt. McConohy concluded that severe corrosion condition and dissolved impurities (such as metals from container and carbonate) have a negligible effect on salt specific heat [256]. Bradshaw [17] studied quaternary Li-Na-K-Ca////NO_3 molten salt by chemical analysis also stated that the change in salt melts physical properties due to the result of decomposition byproduct oxide ions is less important compared to nitrite breakdown. Kruizenga and Gill [261] studied the corrosion of binary solar salt and found that oxidation mechanism of 347SS alloy in binary nitrate melt varied with temperature where the steel corrosion rate increased exponentially with temperature. Wei et al. [211] conducted corrosion studies on binary solar salt in contact with 45 carbon steel and found increased NO_x emission and NO_2^- ion concentration, perhaps due to the reactivity of ferrous elements with the salt melt. Fernández [262] observed similar phenomena in binary solar salt's in his corrosion studies, as ferrous elements oxidized to form ferrous oxides and exhibit corrosion. Fernández [262] suggested that low Chromium steel can minimize corrosion when container materials heat treated (removing moisture) prior to salt contact. Fernández et al. [263] stated that impurities present in the solar salt reacted with chromium alloys and produce a protected spinel layer of $MgCr_2O_4$ and stable compounds was formed such as magnesium ferrite ($MgFe_2O_4$), MgO and FeO. They found that Fe_2O_3 and Fe_3O_4 were the main corrosion products observed in corrosion study of solar salt.

Atmospheric and container gasses can react with salt melt and alter the chemistry. Olivares et al. [26, 121, 264] studied the effect of blanket gasses on nitrate and nitrate/nitrite melt using simultaneous differential scanning calorimetry /thermogravimetry-mass spectrometry (DSC/TGA-MS). They observed a delay in degradation temperature in Hitec salt in O_2 as blanket gas, due to exothermic nitrite oxidation and subsequent alteration of nitrite [102]. Bradshaw [17] studied the stability of Li-Na-K///NO_3 and Na-K-Ca///NO_3 ternary nitrates by chemical analysis and found that nitrate melts react with ullage gasses namely H_2O and

CO_2 and form carbonates and hydroxides [17, 30, 128]. Water vapor and CO_2 impurities behave as Lux-Flood acids in nitrate melts and have an effect on the concentration of oxide ion species. For an example CO_2 in the air reacts with oxide ions in nitrate melt to form carbonate ion in a reversible manner, as per equation 3.3.3.9.

$$CO_2 + O_2^- = CO_3^- \quad [36] \quad \text{equation 3.3.3.9}$$

Dissolved carbonate ions concentration increases with increasing temperature and increasing melt and CO_2 gas contact area [17, 192]. Although saturation levels have not determined by Bradshaw and solubility limit is not defined [17]. Bradshaw [36] indicated that ternary Na-K-Li///NO_3 salt at higher temperature produced a larger concentration of oxide ions compared to the binary Na-K//NO_3 mixture, perhaps because of the presence of $LiNO_3$. In the ternary Na-K-Li///NO_3 salt system, $LiNO_3$ is less stable and decomposes earlier than KNO_3 and $NaNO_3$ might produce lithium nitrites. At higher temperatures, around 500ºC to 550ºC the oxide ion concentration increased but at 600ºC, the concentration fell because the nitrite might participate to react reversibly with oxide ions and retard oxide ion concentration in nitrate melt. The cation also has a tendency to react with nitrite and oxide ions besides nitrate ions. Sometimes these oxide ions products in melt tend to interact with container materials at high temperature. The insoluble products in nitrate melt tend to block pipe, valves, and soluble oxide ion products aggravate corrosion at high temperatures. Also, carbonate elevated viscosity and precipitate in TES system [192]. Alexander and Hindin [163] and Silverman and Engel [128] performed chemical analysis on ternary Na-K//NO_3-Na/NO_2 nitrate-nitrite salt and Hitec salt. They stated that the formation of hydroxide and carbonate lowers the freezing point initially but when their concentration increases (with increasing temperature) resulted in precipitation and hence elevation in the freezing point.

Impurities have some effect on thermal events in nitrate melts. Gimenez and Fereres [251] studied binary solar salt and Hitec salt by thermal analysis (TGA-DSC) found that, impurities such as NaCl in binary solar salt and Na_2CO_3 in Hitec solar salt enhanced the thermal stabilities. Kramer et al. [192] indicated that weak base compound such as carbonate (compared to metal hydroxide and metal oxides [265]) formation in nitrate melt, can be neglected compared to other variables (e.g., effect of temperature and atmosphere) because of low increment in pH level (High level of pH exhibits high corrosion). Kramer et al. [192] concluded that in the presence of CO_2 the nitrite formation was suppressed perhaps due to nitrite reacting with CO_2. Alexander and Hindin [163] suggested some methods to remove these impurities from the nitrate melt; one method is: the nitrate melt should be treated with nitric acid which will convert hydroxide and carbonate to nitrate and in turn the nitrate will partially reduce to nitrite. A second method is to cool the salt to allow precipitate carbonate to settle down (separable distinctive solid) and be removed. The third method involves, adding nitrate to precipitate the corresponding carbonate and remove by filtering the insoluble carbonate [128, 163].

3.3.4 VAPOR, LIQUID AND SOLID STATES OF ALKALI NITRATES

Stern [25] reviewed various studies of alkali nitrates and nitrites mainly by chemical and thermal analysis (e.g. TGA, reaction calorimeter, evolved gas analyzer) and summarized what gaseous decomposition products had been observed. He stated that depending upon the salt type, temperature and test environment usually the common gaseous products of nitrate decomposition are: O_2, N_2, NO, NO_2, N_2O_3, N_2O_4, N_2O_5 [25, 266, 267]. According to Stern [25] if all the gaseous product reached equilibrium quickly during decomposition of salt melt, N_2 and O_2 will be only gaseous species.

According to Stern [25] the hydrated, anhydrous and aqueous nitrate solution can be of ionic or covalent bond depending on their respective infrared spectra. Generally, during heating the covalent nitrates are not stable in liquid phase because they first sublime, produce stable molecular vapor and finally decomposes [25]. The ionic nitrates formed liquid upon heating without decomposing and are stable in liquid phase usually 200°C above their melting point. The melting points of the alkali metal nitrates are lower than corresponding chlorides [112]. Because based on Raman spectrum [268], there are more unoccupied space in the solid alkali nitrates (non-spherical shape ions) than in solid alkali chlorides (spherical ions in chlorides allow close packing) [202].

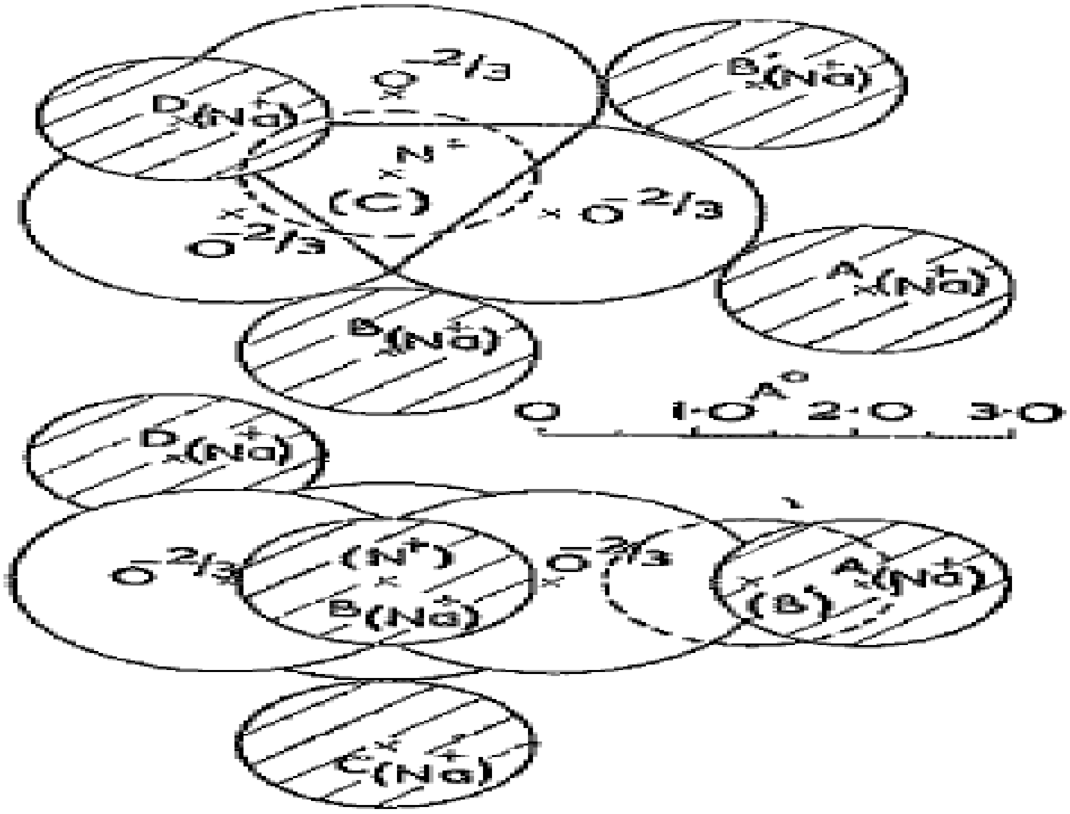

Figure 3.3.4.1: Mutual orientation of polyatomic NO_3^- anions and Na^+ cations [203].

Based on Raman and infrared spectrum [268, 269], the polyatomic nitrate ion in the melt assumed to behave as kinetically free species due to the tendency of not departing greatly from the D_{3h} symmetry of the free ion [202, 270]. Ubbelohde [270] used X-rays analysis and found that, near the melting point of $NaNO_3$, in the crystal, the Na^+ cation is surrounded by 6 polyatomic NO_3^- anions at equivalent distances [270]. Furukawa [203] have studied the structure of molten sodium nitrate salts using X-ray and neutron diffraction found from radial distribution curves that in sodium nitrate the sodium (Na^+) cation and nitrate (NO_3^-) anion have a linear shape due to electrostatic repulsion [271, 272], shown schematically in Figure 3.3.4.1. Based on measured inter atomic distances of alkali chlorides using electron diffraction [271], Hardy and Field [272] claimed that, the alkali nitrates might be present as ion-pair in vapor state. The coordination of anions and cations have not been extensively studied and there is a lack of data on the vapor species of the alkali nitrate salts [25].

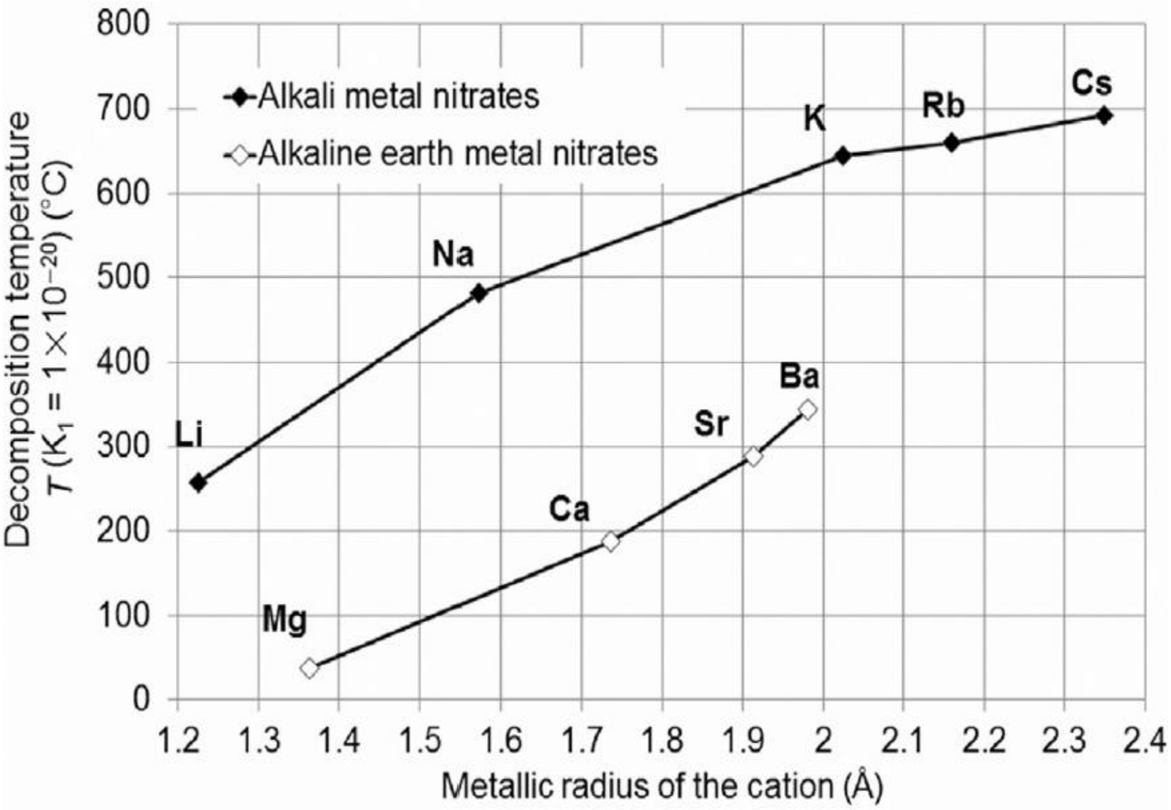

Figure 3.3.4.2: Decomposition temperature variation on the metallic radius of cations of alkali nitrates and alkaline earth nitrates [102, 233, 273, 274]. Here, $K_1 = 1 \times 10^{-20}$, equilibrium constant described by Stern [25, 102, 274].

Alkali nitrates are more stable than the alkali nitrites and alkaline nitrates and have higher decomposition temperatures [25, 34], as shown schematically in Figure 3.3.4.2. The stability of alkali and alkaline nitrates have been summarized by Stern [25] from various works based on chemical analysis and thermal analysis, where he proposed an order of stability by decomposition pressure or equilibrium constant as follow: $KNO_3 > NaNO_3 > LiNO_3 > Ca(NO_3)_2$ [102]. The alkali nitrate salt with greater ionic bond possesses higher thermal stability [208, 275].

There are several influencing and intrinsic factors for thermal stability of nitrates, such as: state of nitrate (solid, gas or liquid), lattice energy, polarizing power of cations, covalency and valence states of metals, volatility, vibration spectrum, type of metal-nitrate bond, and activation energy [202]. Among these, the polarization power is the most important. When the polarizing power is stronger, then the electron distribution of free nitrate ion is distorted [25, 102, 276]. Which leads to lower thermal decomposition temperatures for group IA-nitrate salts compared to IIA-carbonates and IIIB-borates [202, 275]. Cation polarization generally weakens the intra ionic bond by distorting electron distribution in polyatomic anion structure [25]. Stern [274], Addison and Logan [276] and Yuvaraj et al. [277], studied alkali and alkaline nitrate salt systems by infrared, X-ray studies and stated that the polarization power induced by cation on polyatomic anion has an impact on decomposition behavior of the salt systems [102]. The thermal instability of polyatomic anion depends on the electronic configuration of the variable cation. The cation acts as an elemental catalyst which accelerates the decomposition of unstable polyatomic anion [208]. The cation‘s catalytic influence on nitrate ion decomposition rate is proportional to its electrostatic field, is expressed as cation formal charge to cation radius, e/r. When the radius r, of a given cation increases (such as in IA group: from Li to Cs), the electrostatic field potential decreases (or e/r decreases), which leads to increase in thermal stability of nitrate melt [202, 208]. The specific charge of cation plays a role for instability of some IA and IIA nitrites. The specific charge of a cation is the ratio of charge to mass is expressed as, e/m [208]. The smaller sized highly charged cations forming alkali nitrites are highly unstable, such as magnesium and beryllium nitrites [25].

3.3.5 PREVIOUS STUDIES

Numerous studies have been conducted on several molten nitrate and/or nitrite eutectic systems. This subsection is highlighted the survey outcomes. Selective studies have been summarized in a Table A.1 and shown in Appendix A. Surveying the literature; it has been found out that, commercial thermal analyzers have conducted most of the thermophysical studies of molten salts, followed by calorimeters, chemical analyses and some laboratory built special purpose apparatus. Most of the studies involved the use of a TGA apparatus. The simultaneous thermal analyzer also used, such as: DSC/TGA apparatus, or DTA/TGA apparatus, melting point apparatus. Very few used gas analyzers with TGA/DTA/DSC, such as: mass spectrometry, FTIR, ion chromatography with DTA/DSC. For phase study

XRD, SEM/EDS were used. Sample preparation, sample loading, crucible arrangement, test parameters and apparatus varied among the authors.

The decomposition reaction pathway of alkali nitrate salts can be described as follow. Upon heating solid alkali nitrate salt forms a liquid and the fused melt remain stable up to several hundred degrees centigrade (varies among the salts) above the melting point. However, partial decomposition of nitrates to their respective nitrites and liberating oxygen may happen just after melting in the slow, and reversible manner reported as primary decomposition reaction. Rapid decomposition in alkali nitrate melts occurs at higher temperatures far above their melting point. Where with increasing temperature the alkali nitrate-nitrite equilibrium observed as per equation 3.3.3.1. Both nitrate and nitrite in the melt partially dissociate to metal oxide (oxide ions concentration increases with increasing temperature), NO and NO_2 as per equation 3.3.3.3 (reversible concurrent reaction) denoted as secondary and tertiary reactions. Secondary and tertiary reactions occurring temperature also involve rapid vaporization of the melt is denoted as decomposition temperature. The nitrate–nitrite equilibrium in equation 3.3.3.1 is endothermic reversible and slow initially but at higher temperature the extent increases with increasing nitrite concentration depending upon many experimental factors. The equilibrium constant depends on upon several factors such as: reaction temperature, composition and pressure of the blanket gas, the partial pressure of oxygen and experimental condition.

3.3.5.1 OVERVIEW

Based on availability, market price, minimum melting point and thermal stability of single alkali and alkaline earth nitrates, forming of the potential mixture for this study were limited to six salts: $LiNO_3$, $NaNO_3$, KNO_3, $CsNO_3$, $Mg(NO_3)_2$ and $Ca(NO_3)_2$. Among the six potential salts, an additive compound required to team up with binary sodium and potassium nitrates. Calcium nitrate is the cheapest and is already in used as Hitec XL with sodium and potassium nitrates offers limited stability below 500°C. Moreover, magnesium nitrate possesses lower decomposition temperature compared to lithium nitrate. Sodium nitrite is already in used with sodium and potassium nitrate as Hitec salt, and the HTF‘s use is restricted to inert atmospheres (N_2) only. Because, in air or oxygen atmosphere at a higher temperature, the sodium nitrite converts to nitrate and change salt's melt composition. Hence, lithium and cesium nitrates were only alternative remain to choose as an additive with binary nitrates for potential novel HTF mixture. A quaternary or quinary system was not considered because of complex eutectic phase diagram and have higher salt production cost compared to binary solar salt. Although higher order compound will decrease the solid-liquid equilibrium point also, it might decrease the decomposition limit. Lithium nitrate is expensive compared to potassium and sodium nitrate but has a lower melting point compared to cesium nitrate.

According to Stølen et al.'s [278] thermodynamic criteria for low melting point formulation of a given multicomponent mixture, the lowest solid-liquid equilibrium point can be achieved with an additive of another component/s due to its miscibility in the eutectic mixture [17]. Usually by adding an extra element, the chemical potential of the mixture decreased and subsequently the temperature which depends on chemical potential will also decrease [279], as shown schematically in Figure 3.3.5.1.1.

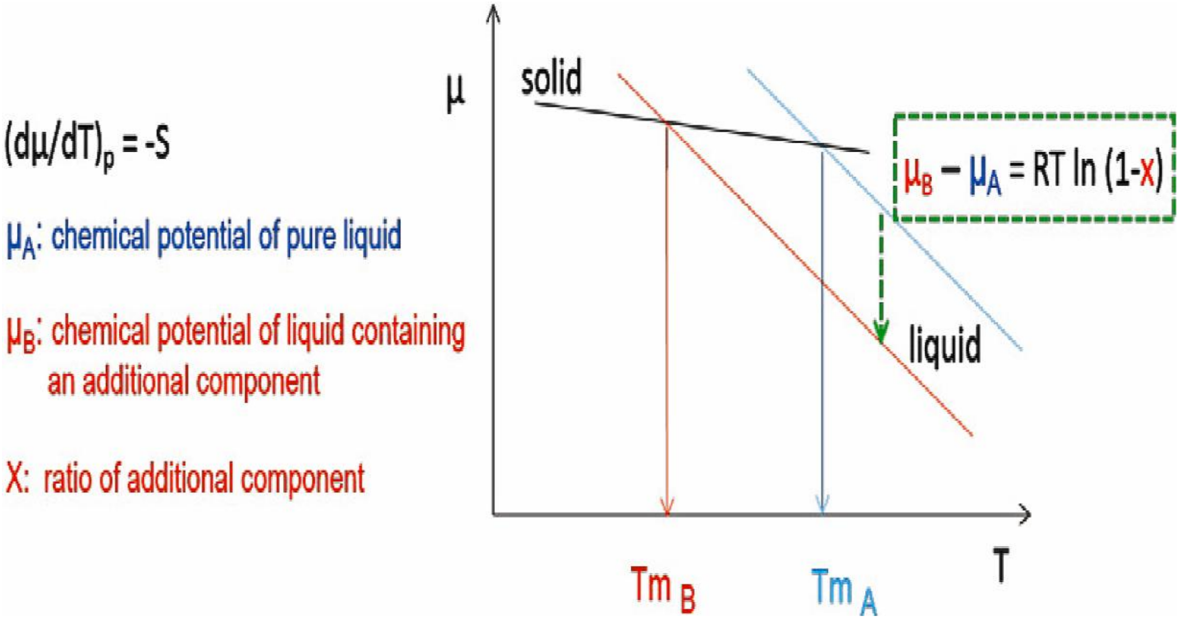

Figure 3.3.5.1.1: A simple illustration of fusion point depression by adding another component [279].

In this aspect lithium nitrate was selected with sodium and potassium nitrates. Because $LiNO_3$ has a lower melting point compared to $NaNO_3$ and KNO_3; and this three nitrate‘s mutual binary systems ($LiNO_3$-$NaNO_3$, $NaNO_3$-KNO_3, and $LiNO_3$-KNO_3), possess simple eutectic with melting point depression [169]. A ternary $NaNO_3$-KNO_3-$LiNO_3$ (13.23-57.14-29.63 wt%) salt is formulated from FactSage [39] thermodynamic software offering 120.8°C melting point which is approximately 100°C less compared to the solar binary $NaNO_3$-KNO_3 salt.

There are five papers available that have studied the lithium nitrate-sodium nitrate-potassium nitrate ternary eutectic salts of different compositions. They are by Wang et al. [106], by Bradshaw et al. [36], Fernandez et al. [124], Roget et al. [280] and Olivares et al. [121]. These papers are summarized in Table A.1 in Appendix A and correctly evaluated in section 3.3.5. In summary, the studied issues of these five papers are:

- the high temperature stability and chemical composition,
- phase equilibrium and effect of composition on the stability,
- sweep gas effects on stability,
- phase composition and morphology analysis.

Till date, the ternary system of $NaNO_3$-KNO_3-$LiNO_3$ of 13.23-57.14-29.63 weight ratio has not subjected to evolved gas analysis in conjunction with other decomposition parameter to understand degradation process at different heating rates. This research aims to study the decomposition behavior of molten nitrates at high temperature and observe thermal stability under various atmospheric gasses and scanning rates for potential use as a HTF in TES system.

3.4 THERMAL ANALYSIS TECHNIQUES

This subchapter describes the thermal analysis methods for the high temperature properties study of molten nitrate salt systems. The alkali nitrate salts were subjected to control heating-cooling inside automated furnace to certain set point temperatures to observe various thermal events simultaneously. The STA test methods are described in Chapter 6 of this Thesis. The common thermal analysis techniques and curves interpretation are described in Appendix B.

3.5 VAPORIZATION CHEMISTRY

Chemical kinetics deals with the chemical reactions of the sample, chemical processes, reaction types, reaction rate and variables such as: concentration, pressure, rate of heat transfer, the rate of mass transfer and temperature which affect the reaction rate of the sample [281-283]. This subsection describes the effective onset vapor pressure measurement. The transpiration test method is described in Chapter 6 of this Thesis. The technique involved in mass loss studies in transpiration methods are described in Appendix C.

3.6 THERMODYNAMIC MODELING OF BINARY ALKALI NITRATES

To understand the principle of thermochemistry, thermodynamic properties, design and development of nitrate salt the phase equilibria study is necessary. For an example temperature at which the solid and liquid phase form or excess Gibbs energy for certain composition can be obtained from phase diagrams [284]. For practical use of the salt system, the compound with a lower melting point or eutectic composition is an important aspect which can be obtained from phase diagrams. Mathematical formulation or software simulation can limit the need for costly and difficult experimentation such as: high numbers of tests, the requirement of long annealing times at low temperatures, contamination problem, and composition controls [285, 286]. Higher order systems can be computed using constituent simple binary phase systems [241, 287-289]. Similarly, experimental data served basis on validation of simulation and mathematical model data. The literature survey of thermodynamic modeling is described here. The theoretical background of thermodynamic modeling and phase diagrams are described in Appendix D.

3.6.1 PREVIOUS STUDIES

Mathematical modeling of binary ionic liquid is mainly based on numerical approaches involving various non-ideal mixing models. Such as: the Margules equation, excess Gibbs energy methods including nonrandom two liquid equation (NRTL), modified Van Laar equations, the Wilson equation, universal quasi-chemical equation (UNIQUAC), and lattice theory or quasi-chemical equation [290-298]. Binary nitrate‘s solid-liquid phase equilibrium calculation are usually modeled as a neutral, non-interacting and non-aqueous mixtures [295].

Most recent modeling of various nitrate systems is based on the regular solution model [32, 33, 37, 38, 153, 164, 299-310]. The $NaNO_3$-KNO_3 system has been studied heavily compared to other binary alkali nitrate systems [38, 153, 164, 306-310]. Zhang et al. [37] studied the binary sodium-potassium nitrate using two models, the Henrian and the regular solution models, and determined the binary system as a limited solid solution model rather than a continuous solid solution. Benages-Vilau R. et al. [311] studied the binary sodium-potassium nitrate by chemical analysis and found that the binary system‘s mixing properties are well describable using an ABθ model [312] as a mixed crystal formation. Benages-Vilau R. et al. [311] concluded that the binary Na-K//NO_3 system possesses very limited solid solution, have an invariant eutectoid minimum and immiscibility gap in the solid state. Abe et al. [33] and Kramer and Wilson [153] studied the binary Na-K//NO_3 system using the regular solution assumption and found their liquidus and solidus curves were in good agreement with experimental values. Maeso and Largo [32] studied binary lithium-sodium and lithium-potassium nitrates based on the regular solution assumption and stated that they fitted well with their DSC experimental values. Mantha et al. [304] modeled the ternary lithium-sodium-potassium nitrate mixture‘s eutectic point using the regular solution approximation and ideal solution behavior. They formulated Gibbs energy of fusion of ternary nitrate by accounting the constituent single and binary alkali nitrates. They ignored the ternary excess Gibbs energy (equal to zero). Using Newton-Raphson iteration method Mantha et al. [304] solved both model‘s simultaneous equations and found eutectic point 116°C by the regular solution and 154.7°C by the ideal solution assumption.

To verify thermodynamically calculated composition, Mantha et al. [304] used DSC apparatus and obtained eutectic composition‘s melting point at 118.4°C and stated that the ternary alkali nitrate is best describable by regular solution model. Elliott [313] also formulated three binary systems of sodium-potassium, lithium-sodium and lithium-potassium nitrates and ternary lithium-sodium-potassium nitrate using regular solution theory and validated experimentally using DSC. This study aims to formulate three binary alkali nitrate systems using the regular solution assumption and solve the nonlinear simultaneous equations by taking temperature dependent heat capacities to observe variations in liquidus and solidus curves.

CHAPTER 4 RESEARCH ISSUES

The heat transfer fluids (HTFs) are an important parameter in CSP plants for the Rankine cycle efficiency improvement. The low melting point and higher operating temperature of HTF are necessary for higher thermal conversion efficiency of the CSP plant. The low melting point of HTF will reduce the cost of heating of the pipes and accessories. The heating of pipes is needed to avoid the pipe freezing. Also, less energy will require for melting. Higher decomposition temperature or T_3 will ensure broader working temperature range; higher energy can be stored in given size of TES system and higher Rankine cycle efficiency. Thus, the primary objective is to propose a novel HTF with low melting point and boarder operating temperature range with minimum production cost compared to binary solar salt. By adding an additive compound in existing binary sodium and potassium nitrate mixture, the melting point will be assessed by thermal analysis. Then the extending decomposition temperature study of selected salt mixture will be performed by STA. In this regard, a Li-Na-K//NO_3 ternary salt was chosen from FactSage formulation which offers 100°C less liquidus temperature compared to binary solar salt.

Using oxygen as sweep gas will increase the decomposition temperature. Thus, the objectives are to study the effect of heating rates and blanket atmosphere on thermal stability of molten nitrate salts. Except the studies of Wang et al. [314] of quaternary Li-K-Na//NO_3//NO_2 salts, Mar et al. [30] of binary Na-K//NO_3 salts, and Kramer et al. [189] of ternary Na-K//NO_3//NO_2 salt systems, no studies have been performed to understand the vaporization equilibrium chemistry of these molten nitrate salt systems. Olivares et al. [121] studied the effect of atmospheric gasses on ternary Na-K-Li///NO_3 salts of different composition, but in their study no degradation delay was observed in a pure oxygen environment and no explanations for ambiguous results was provided. This study investigates decomposition behavior carefully considering evolved gaseous species.

From the review of the literature, two possibilities arise to conduct an experiment on Ternary Li-Na-K///NO_3 salt mixture to identify various thermal events for potential application as a HTF. The first possibility is to study reaction mass loss using the transpiration test method. And, the second option is to study the thermal stability in inert and oxidative environment using the simultaneous thermal analysis method.

Below are important research questions related to ternary molten nitrate salt:

1. At which temperature does the thermal degradation occur and which type of gas evolved?

2. What is the decomposition pathway at elevated temperatures?

3. What are the effect of different sweep gasses (O_2, ar, and air) on decomposition temperature and the thermal stability of single, binary and ternary molten salt systems?

4. What are the effects of heating rates (2.5, 5 and 10°C/min) on decomposition temperature and on the thermal events (melting and freezing) of the ternary system?

5. Taking temperature dependent heat capacity instead as constant; can Kramer‘s and Elliott‘s binary formulations (based on Kleppa‘s assumption and Gibbs energy minimization) correctly represent the literature experimental values and quasi-chemical models from FactSage?

6. What are the mass loss behaviors of nitrates at various flow rates?

Question one to four will be resolved by using the simultaneous thermal analyzer (DSC/TGA/DTA-MS apparatus) at various temperatures ranges (50°C to 800°C), heating-cooling rates and gas flow rates [31, 250, 253]. Question five will be studied using software to obtain numerical results. Question six will be explored using a transpiration rig.

In simultaneous DSC/TGA/DTA-MS test, some observations will be carried out, they are:

a) Decomposition temperature detection.

b) Evolved gaseous products detection.
c) Observe the effect of the various atmosphere (oxygen/air/argon) gas blankets on thermal decomposition of nitrates.
d) Observe the effect of heating and cooling rates on melting, transition and decomposition temperature of ternary nitrate.

Transpiration tests will be carried out by observing followings:

a) The weight loss vs. time;
b) The weight loss vs. temperature/flow rate curves; will be obtained.

The thermodynamic equilibrium modeling, phase diagram construction and comparison with experimental literature values will be performed for the three binary salt mixtures, using thermodynamic software package FACTSAGE 6.4 [315] and the mathematical package MATLAB [316].

CHAPTER 5 THERMODYNAMIC MODELING, PHASE DIAGRAMS

The theoretical background and literature survey is presented in section 3.6 in Chapter 3 of this thesis. In this chapter phase diagrams for three binary ($LiNO_3$-$NaNO_3$, $NaNO_3$-KNO_3, $LiNO_3$-KNO_3) and ternary nitrate ($LiNO_3$-$NaNO_3$-KNO_3) systems are obtained using the quasi-chemical formulation in FactSage. Also by Regular solution assumption and using Gibbs energy minimization mathematical formulation for three binary nitrate systems were presented with the help of already established model by Elliott [313] and Kramer [153].

This study aims to observe the effect of varying heat capacities on solidus and liquidus curves of binary nitrate systems by regular solution model. The numerical solutions of coupled nonlinear equations were obtained using contour plot technique and were compared with FactSage and literature experimental values.

5.1 THERMODYNAMIC MODELING OF BINARY NITRATES

The Regular solution assumption from Kleppa [301] and his empirical coefficients; and Gibbs energy minimization by Kramer [153] were used by Elliott [313] to formulate one equation (for $NaNO_3$) of binary sodium-potassium nitrate system (Na-K//NO_3). In this study, a similar approach of Elliott [313] and Kramer [153] has been used to obtain second equation (for KNO_3) of binary Na-K//NO_3 and to formulate other two binary systems of Li-Na//NO_3 and Li-K//NO_3. Gibbs-Duhem equation was used to obtain partial enthalpy of mixing of each component of liquid and solid phase.

Elliott [313] took the same approach as Kramer [153] and used Kleppa and Hersh‘s [302] empirical coefficient values for numerical solution. Kramer calculated free energies of each component with three terms: fusion term, free energy of mixing of liquid solution and free energy of mixing of the solid solution. Kramer assumed solid and liquid solutions of each component in thermodynamic equilibrium according to Gibbs energy minimization method. Elliott [313] in his work took heat capacity and latent heat as a constant value. This work aims to reproduce the Gibbs energy modeling for binary systems similar to Elliott and

Kramer but with the input of varying heat capacities and compare the results with FactSage [39] and literature data.

5.2 BINARY NITRATES MATHEMATICAL EXPRESSIONS

Elliott [313] has calculated ternary system and elaborately described system's equations. Thus, only binary formulations are explained in this thesis, and final equations are shown in subsections 5.3 and 5.4. Detailed mathematical calculations for binary systems are shown in Appendix D. Kleppa and Hersh‘s [302] took the nitrate with smaller sized alkali cation as the first compound in his binary salt‘s enthalpy of mixing formulation. The cation size in alkali metal is increased periodically from Lithium to Francium.

5.3 BINARY SYSTEM’S EQUATIONS

Equations for A-B binary salt system (A=NaNO$_3$, B=KNO$_3$)

Components composition at liquid phase: $x_A^l + x_B^l = 1$ eqn 5.3.1

Components composition at solid phase: $x_A^S + x_B^S = 1$ eqn 5.3.2

$$\Delta G^{A/NaNO_3} = \left(1 - \frac{T}{T_{mp}^A}\right) \Delta H_{fus}^A + \Delta C_{PA} \left[T - T_{mp}^A - T \ln\frac{T}{T_{mp}^A}\right] + RT\left(\ln x_A^l - \ln x_A^s\right) + ({a_l x_B^l}^2 + 2b_l x_A^l {x_B^l}^2 + 2c_l x_A^l {x_B^l}^3 - c_l {x_A^l}^2 {x_B^l}^2) - ({a_s x_B^s}^2 + 2b_s x_A^s {x_B^s}^2 + 2c_s x_A^s {x_B^s}^3 - c_s {x_A^s}^2 {x_B^s}^2)$$

eqn 5.3.3

$$\Delta G^{B/KNO_3} = \left(1 - \frac{T}{T_{mp}^B}\right) \Delta H_{fus}^B + \Delta C_{PB} \left[T - T_{mp}^B - T \ln\frac{T}{T_{mp}^B}\right] + RT\left(\ln x_B^l - \ln x_B^s\right) + (a_l {x_A^l}^2 + b_l {x_A^l}^3 - b_l {x_A^l}^2 x_B^l - c_l {x_A^l}^2 {x_B^l}^2 + 2c_l {x_A^l}^3 x_B^l) - (a_s {x_A^s}^2 + b_s {x_A^s}^3 - b_s {x_A^s}^2 x_B^s - c_s {x_A^s}^2 {x_B^s}^2 + 2c_s {x_A^s}^3 x_B^s)$$

eqn 5.3.4

Equations for C-B binary salt system (C=LiNO$_3$, B=KNO$_3$)

For Li-K//NO$_3$ salt, the derivation has been shown with similar calculation as previously obtained for A-B or Na-K//NO$_3$ system.

$$\Delta G^{C/LiNO_3} = \left(1 - \frac{T}{T_{mp}^{C}}\right) \Delta H_{fus}^{C} + \Delta C_{PC} \left[T - T_{mp}^{C} - T \ln \frac{T}{T_{mp}^{C}}\right] + RT \left(\ln x_C^{l} - \ln x_C^{s}\right) + (a_l x_B^2 + 2b_l\, x_C x_B^2 + 2c_l x_C x_B^3 - c_l x_C^2 x_B^2) - (a_s x_B^2 + 2b_s\, x_C x_B^2 + 2c_s x_C x_B^3 - c_s x_C^2 x_B^2)$$

eqn 5.3.5

$$\Delta G^{B/KNO_3} = \left(1 - \frac{T}{T_{mp}^{B}}\right) \Delta H_{fus}^{B} + \Delta C_{PB} \left[T - T_{mp}^{B} - T \ln \frac{T}{T_{mp}^{B}}\right] + RT \left(\ln x_B^{l} - \ln x_B^{s}\right) + (a_l x_C^2 + b_l x_C^3 - b_l x_C^2 x_B - c_l x_C^2 x_B^2 + 2c_l x_C^3 x_B) - (a_s x_C^2 + b_s x_C^3 - b_s x_C^2 x_B - c_s x_C^2 x_B^2 + 2c_s x_C^3 x_B)$$

eqn 5.3.6

Liquid phase: $x_C^{l} + x_B^{l} = 1$ eqn 5.3.7

Solid phase: $x_C^{S} + x_B^{S} = 1$ eqn 5.3.8

Equations for C-A binary salt system (C=LiNO$_3$, A=NaNO$_3$)

For Li-Na//NO$_3$ salt, the derivation has been shown with similar calculation as previously obtained for A-B or Na-K//NO$_3$ system except the expression of enthalpy of mixing is shown in Equation 5.3.9.a.

$$\Delta Hmix = x_A\, x_B\, (a + b x_A) = a x_A\, x_B + b x_A^2 x_B$$ [301] eqn 5.3.9.a

$$\Delta G^{C/LiNO_3} = \left(1 - \frac{T}{T_{mp}^{C}}\right) \Delta H_{fus}^{C} + \Delta C_{PC} \left[T - T_{mp}^{C} - T \ln \frac{T}{T_{mp}^{C}}\right] + RT \left(\ln x_C^{l} - \ln x_C^{s}\right) + (a_l x_A^2 + 2b_l\, x_C x_A^2) - (a_s x_A^2 + 2b_s\, x_C x_A^2)$$

eqn 5.3.9

$$\Delta G^{A/NaNO_3} = \left(1 - \frac{T}{T^A_{mp}}\right) \Delta H^A_{fus} + \Delta C_{PA}\left[T - T^A_{mp} - T\ \ln\frac{T}{T^A_{mp}}\right] + RT\left(\ln x^l_A - \ln x^s_A\right) + (a_l x_C^2 + b_l x_C^3 - b_l x_C^2 x_A) - (a_s x_C^2 + b_s x_C^3 - b_s x_C^2 x_A)$$

eqn 5.3.10

Liquid phase: $x^l_C + x^l_A = 1$ eqn 5.3.11

Solid phase: $x^S_C + x^S_A = 1$ eqn 5.3.12

Here,

$T^{A/B/C}_{mp}$= melting temperature of component A or B or C,

$\Delta H^{A/B/C}_{fus}$= heat of fusion of component A or B or C,

$\Delta S^{A/B/C}_{fus} = \frac{\Delta H^{A/B}_{fus}}{T^{A/B}_{mp}}$, entropy of fusion of component A or B or C,

$\Delta C_{P\ A/B/C}$= difference between C_{PL} and C_{PS}, heat capacity of component A or B or C.

T = temperature at which the equation is being solved.

$x^l_{A/B/C}$ = mole fraction of component A or B on the liquidus curve for liquid phase,

$x^s_{A/B/C}$= mole fraction of component A or B on the solidus curve for solid phase,

R= universal gas constant.

$a_s/b_s/c_s$= Empirical coefficients at solid.

$a_l/b_l/c_l$= Empirical coefficients at liquid.

5.4 TERNARY NITRATE MATHEMATICAL EXPRESSIONS

The similar approach of Kramer [153] was used to formulate a ternary salt system by Elliott. The Gibbs free energy of component A, B and C is assumed zero considering that both phases (liquid and solid) of each component are in thermodynamic equilibrium [305] with each other. Kevin et. al [305] and Elliott [313] neglected the ternary interaction during formulation [305]. Similar to the binary system in this section, the ternary formulation is presented. Only final equations are shown here; the details can be found in Elliott‘s work [313].

For component A,

$$\Delta G^{A/NaNO_3} = \left(1-\frac{T}{T_{mp}^{A}}\right)\Delta H_{fus}^{A} + \Delta C_{PA}\left[T - T_{mp}^{A} - T\,\ln\frac{T}{T_{mp}^{A}}\right] + RT\left(\ln x_A^l - \ln x_A^s\right) + [(1 - x_a)(a_1x_b + 2b_1x_ax_b + a_3x_c + b_3x_c^2) - a_2x_bx_c - 2b_2x_bx_c^2 - b_3x_ax_c^2 - 3c_2x_b^2x_c^2] + [(1 - x_a)(a_1x_b + a_3x_c + b_3x_c^2) - a_2x_bx_c - 2b_2x_bx_c^2 - b_3x_ax_c^2] \qquad \text{eqn 5.4.1}$$

For component B,

$$\Delta G^{B/KNO_3} = \left(1-\frac{T}{T_{mp}^{B}}\right)\Delta H_{fus}^{B} + \Delta C_{PB}\left[T - T_{mp}^{B} - T\,\ln\frac{T}{T_{mp}^{B}}\right] + RT\left(\ln x_B^l - \ln x_B^s\right) + [(1 - x_b)(a_1x_a + b_1x_a^2 + a_2x_c + b_2x_c^2 + 2c_2x_bx_c^2) - b_1x_a^2x_b - b_2x_bx_c^2 - c_2x_b^2x_c^2 - 2b_3x_a\,x_c^2 - a_3x_ax_c] + [(1 - x_b)(a_1x_a + a_2x_c + b_2x_c^2) - b_2x_bx_c^2 - 2b_3x_a\,x_c^2 - a_3x_ax_c] \qquad \text{eqn 5.4.2}$$

For component C,

$$\Delta G^{C/LiNO_3} = \left(1-\frac{T}{T_{mp}^{C}}\right)\Delta H_{fus}^{C} + \Delta C_{PC}\left[T - T_{mp}^{C} - T\,\ln\frac{T}{T_{mp}^{C}}\right] + RT\left(\ln x_C^l - \ln x_C^s\right) + [(1 - x_c)(a_2x_b + 2b_2x_bx_c + 2c_2x_b^2x_c + a_3x_a + 2b_3x_ax_c) - a_1x_ax_b - 2b_1x_a^2x_b - c_2x_b^2x_c^2] + [(1 - x_c)(a_2x_b + 2b_2x_bx_c + a_3x_a + 2b_3x_ax_c) - a_1x_ax_b] \qquad \text{eqn 5.4.3}$$

The coefficients in first parentheses are related to the liquid enthalpy of mixing empirical coefficients; the last parentheses are for solid enthalpy of mixing empirical coefficients.

Now the concentration related equations for two phases are:

Liquid phase: $x_A^l + x_B^l + x_C^l = 1$ eqn 5.4.4

Solid phase: $x_A^S + x_B^S + x_C^S = 1$ eqn 5.4.5

5.5 NUMERICAL SOLUTIONS OF BINARY NITRATE SYSTEMS

Nonlinear equations are generally solved using numerical methods [317]. To obtain the numerical solution of unknown variables of simultaneous equations, a visualization (intersection of the zero curves) are performed [318]. Usually, Newton‘s iterative method and bisection method are used to obtain numerical solutions of multi-dimensional nonlinear equations [319]. At the beginning of this study an algorithm was written for the binary Na-K//NO_3 system consist of four coupled nonlinear equations (Equations 5.3.1 to 5.3.4) and five unknowns $(x_A^l, x_B^l, x_A^S, x_B^S$ and $T)$ using built in Matlab solver ‗*fsolve*‘. The ‗*fsolve*‘ optimization toolbox has three algorithms, only the default routine ‗*trust region dogleg*‘ was used. The ‗*trust region dogleg*‘ [320] optimization is based on Newton- Raphson iteration method [321, 322]. One of the difficulties associate with ‗*fsolve*‘ solver for optimization of multi-dimensional nonlinear equations was to guess accurate first initial value. The first initial guess approximation needed to be accurate in order to converge the real roots (avoid complex plain of the polynomial). This phenomena is common in finding roots of coupled nonlinear equations using Newton-Raphson method [323]. Failing to obtain reasonable results using ‗*fsolve*‘ a different approach was sought. However, Elliott [313] used ‗*fsolve*‘ successfully in his work to solve nonlinear coupled equations for both binary and ternary systems. The primary reason that the ‗*fsolve*‘ failed to solve, was because of poorly written algorithms.

An alternative algorithm was developed to solve the binary system's equations. In A-B binary alkali nitrate system the four coupled nonlinear equation‘s roots were opt out by visualizing convergence of Gibbs free energies at equilibrium of compound A and B (A is alkali nitrate with smaller sized cation). A contour plot was obtained for the equations at 5K interval temperatures in Matlab. Algorithms were developed to get intersection point of the converging roots of the coupled equations, and subsequently, the phase diagrams were plotted. At first, the equations were solved using heat capacity as a constant. And, in the second stage, the heat capacities were varied as temperatures varied and phase diagrams were plotted. In subsection 5.6, these calculated phase diagrams were compared with FactSage and literature experimental values. The algorithms are shown in Appendix E.

The Gibbs free energy at equilibrium of component A ($NaNO_3$) and B (KNO_3) in binary A-B system was graphically observed using contour plot technique. The mole fraction of A, at solid phase (x_A^S) and liquid phase (x_A^l) were plotted in X and Y axes respectively at 5K temperature (T) intervals. Then from the zero contour lines of $\Delta G^{A/NaNO_3}$ and $\Delta G^{B/KNO_3}$ the converging intersections values were plotted to obtain liquidus and solidus curves of corresponding temperature of the respective binary systems. As an example, such converging points in case of the binary Na-K//NO_3 are shown in Figures 5.5.1.a, 5.5.1.b and 5.5.1.c. And the locus of a solution of this system is shown in Figure 5.5.2.a. Similarly for Li-Na//NO_3 and Li-K//NO_3 systems the locus are shown in Figures 5.5.2.b and 5.5.2.c. Figures 5.5.1.a to 5.5.1.c are showing converging behavior of the ΔG^A and ΔG^B from 490K to 500K. For plotting the intersection point values (x_A^l and x_A^S) a separate function was wrote for each three binary system and phase plots were obtained subsequently. Such calculated binary phase diagrams are shown in Figures 5.5.3, 5.5.4 and 5.5.5. And finally, the phase diagrams accounting varying C_p were obtained and shown in Figures 5.5.6, 5.5.7 and 5.5.8.

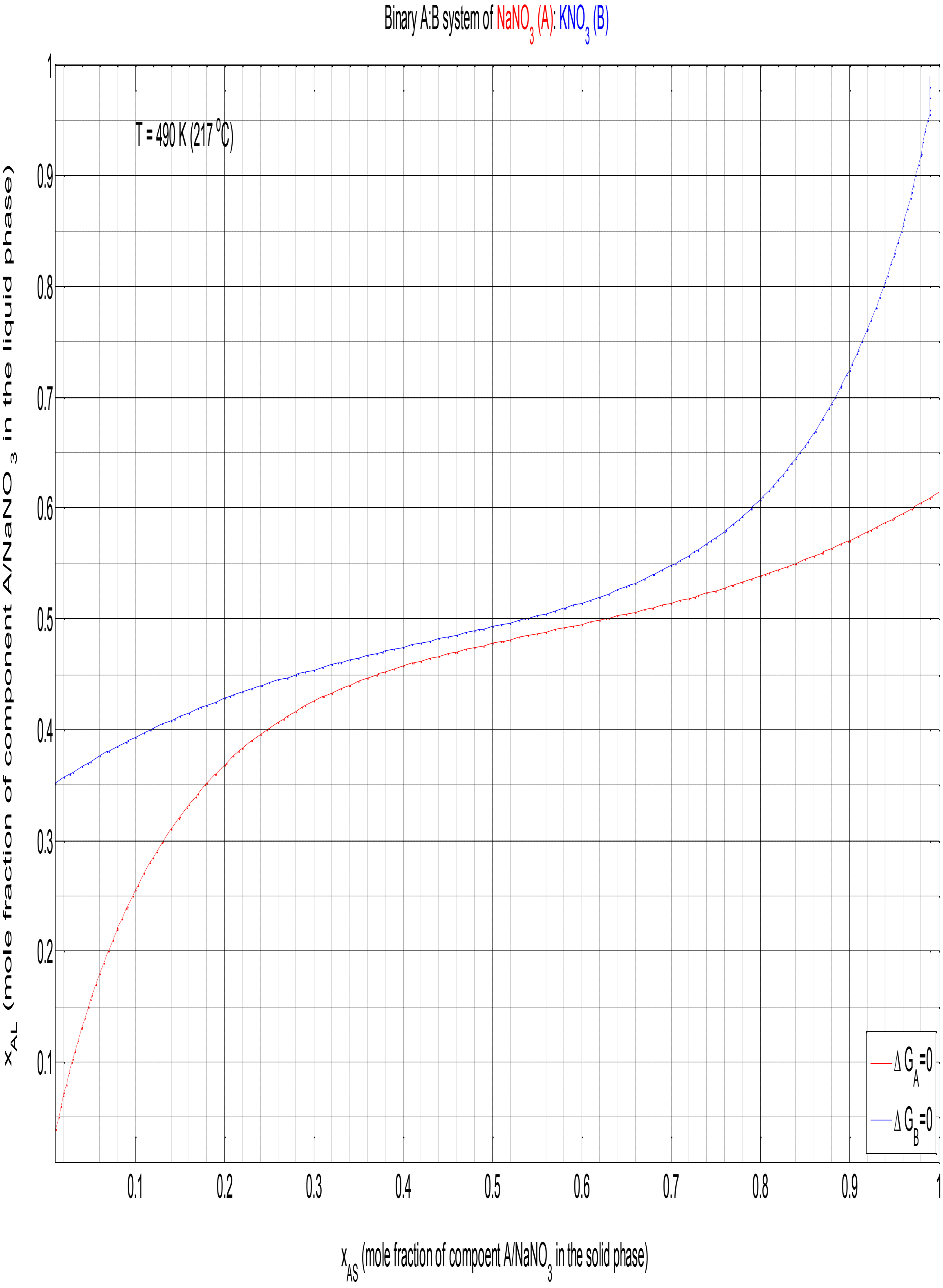

Figure 5.5.1.a: Contour plot of binary $NaNO_3$-KNO_3 at 490K or 217°C.

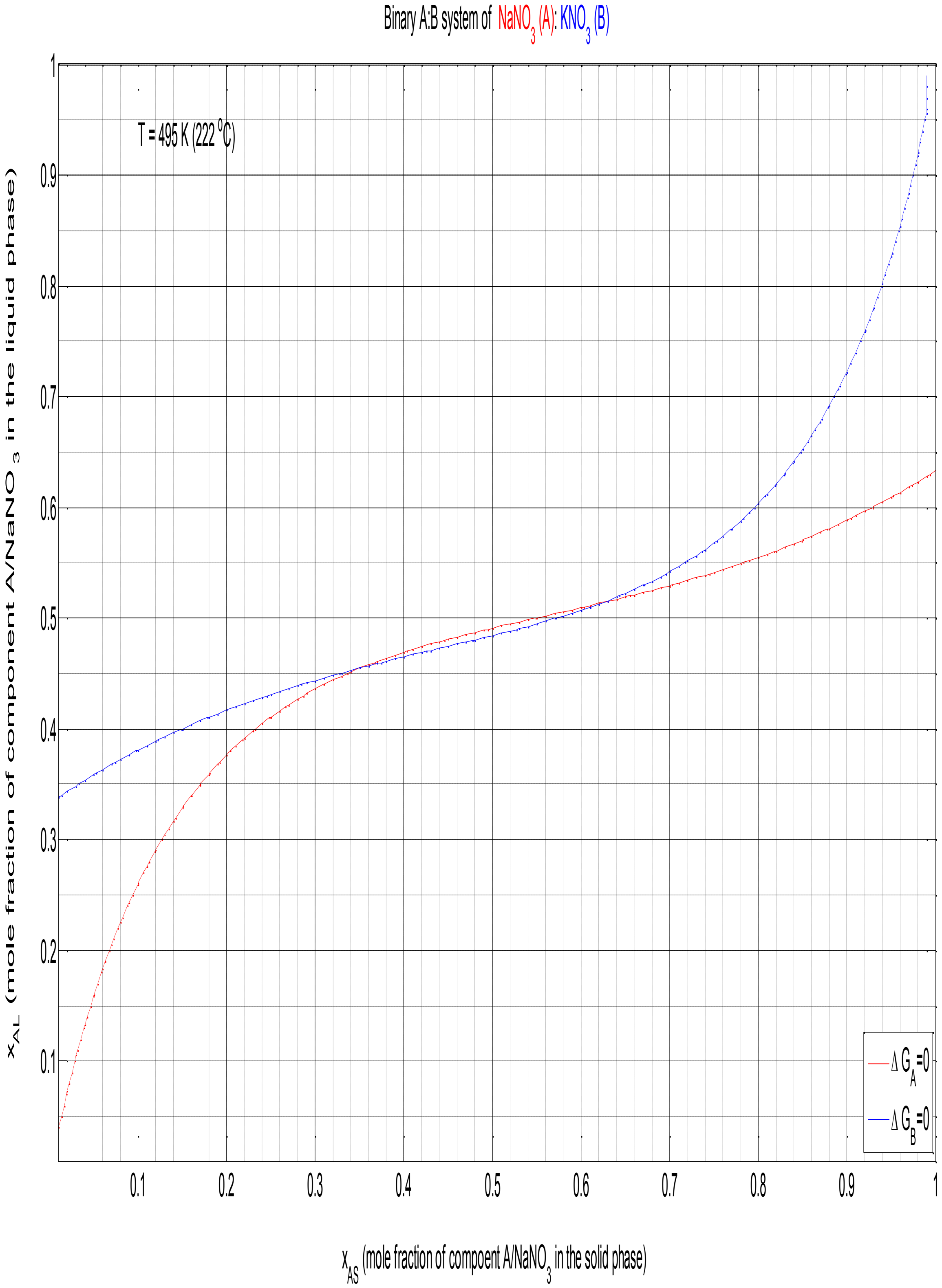

Figure 5.5.1.b: Contour plot of binary NaNO$_3$-KNO$_3$ at 495K or 222°C.

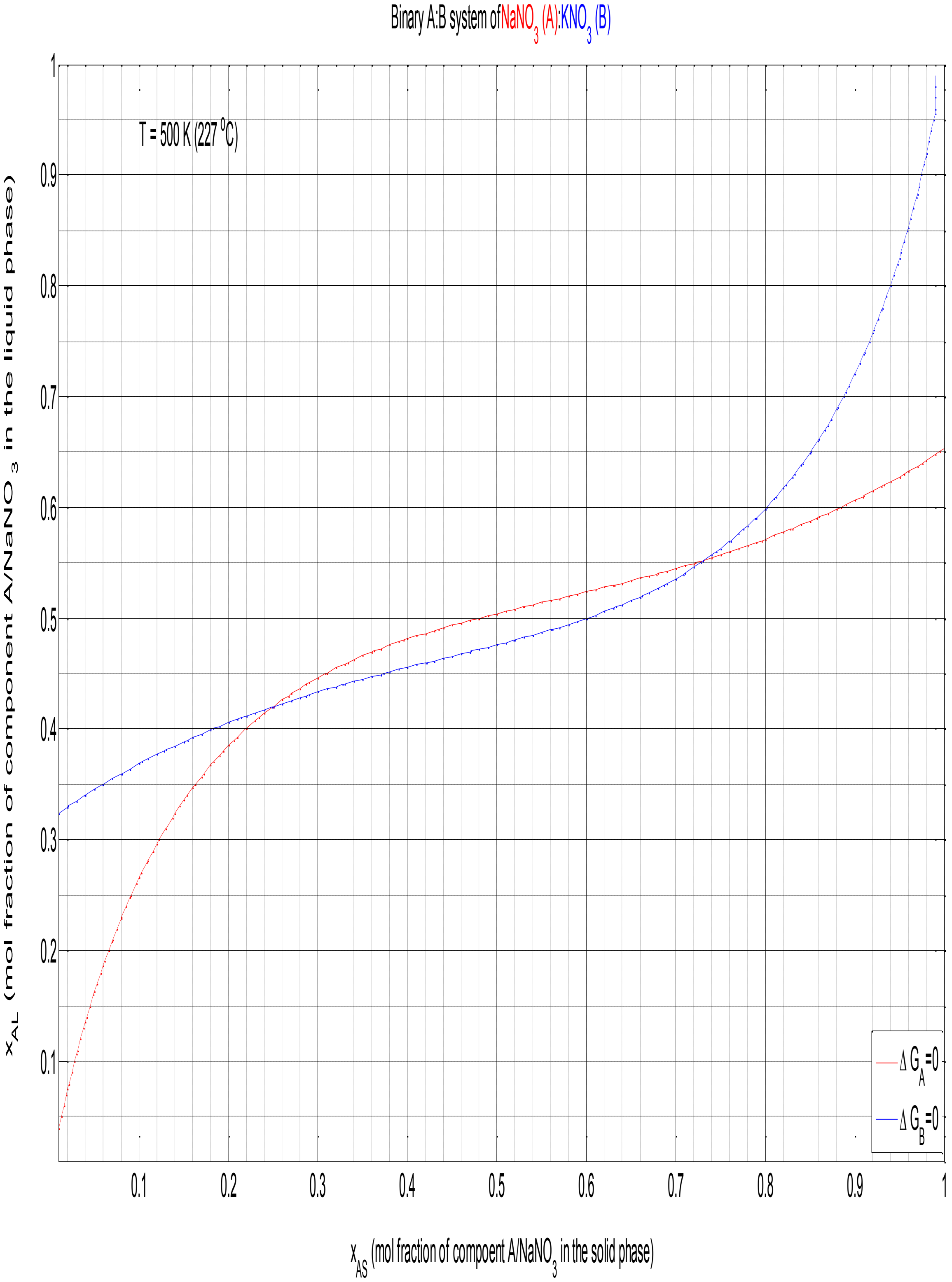

Figure 5.5.1.c: Contour plot of binary NaNO$_3$-KNO$_3$ at 500K or 227°C.

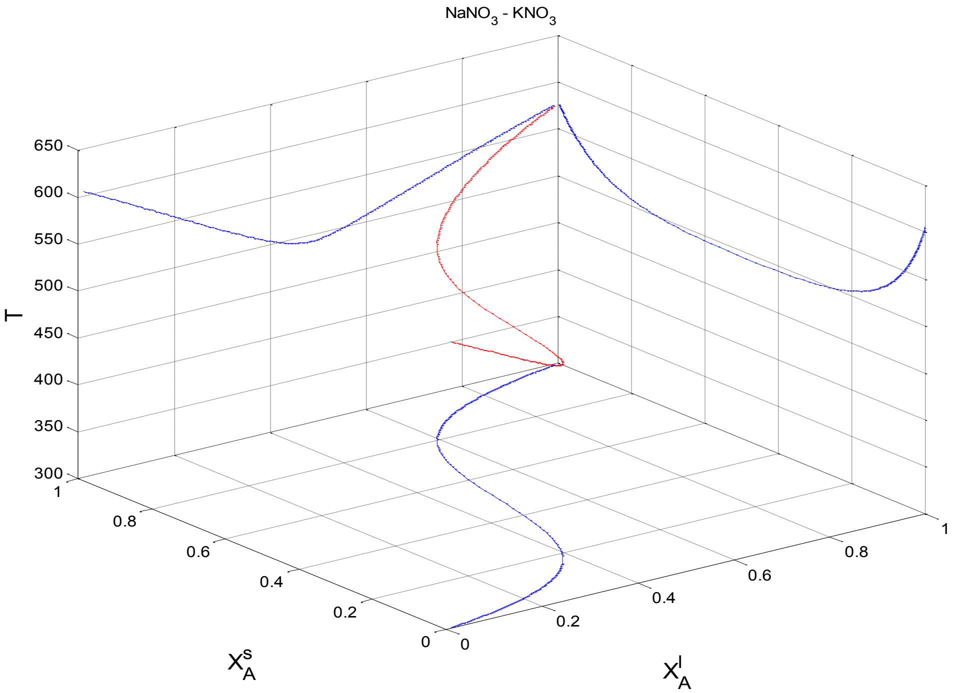

Figure 5.5.2.a: Locus of solutions of binary NaNO$_3$-KNO$_3$ system in X or (x_A^S), Y or (x_A^l) and Z or (T) plane.

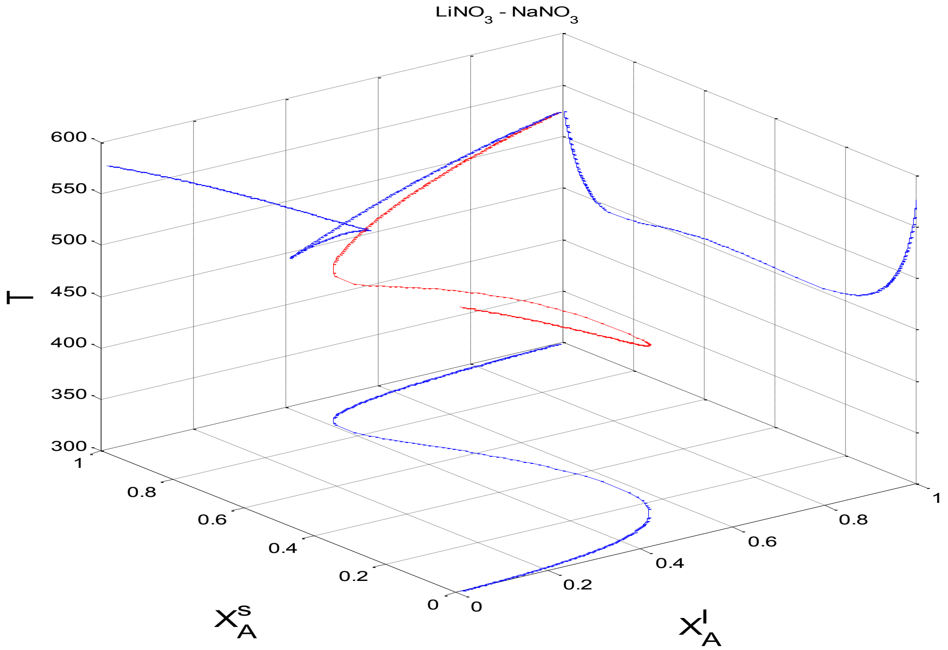

Figure 5.5.2.b: Locus of solutions of binary LiNO$_3$-NaNO$_3$ system in X or (x_A^S), Y or (x_A^l) and Z or (T) plane.

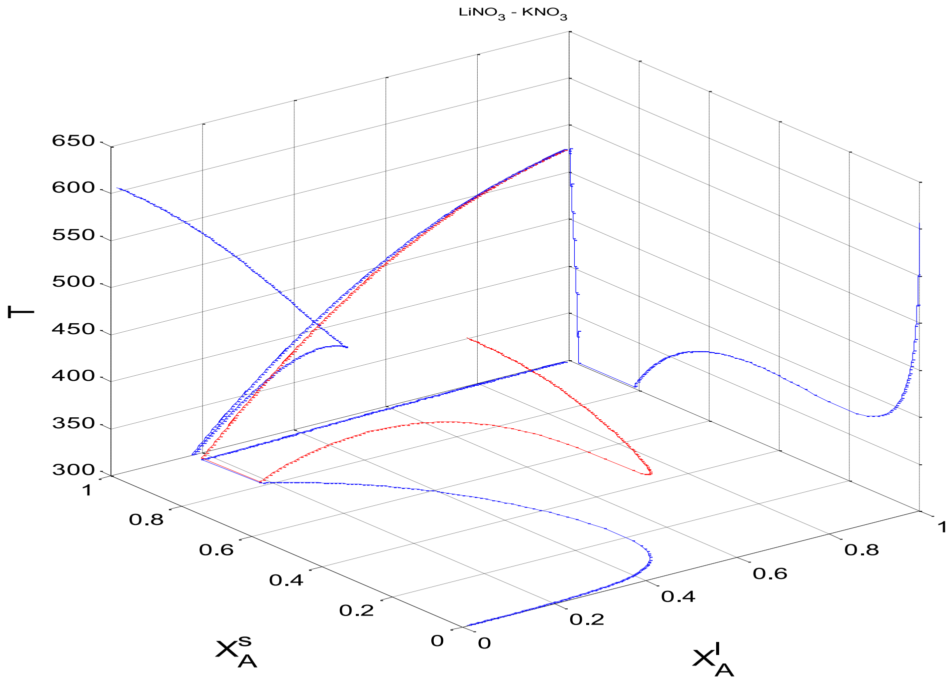

Figure 5.5.2.c: Locus of solutions of binary $LiNO_3$-KNO_3 system in X or (x_A^S), Y or (x_A^l) and Z or (T) plane.

The thermophysical properties of single salts were obtained from Takahashi et al. [324], Kramer et. al [153], Kevin et. al [305] and Elliott‘s [313] work, as shown in Table 5.5.1. The empirical coefficients were obtained from Kleppa and Hersh [302], Kramer et. al [153] and Elliott‘s [313] work, as shown in Table 5.5.2. Molar mass of lithium, sodium and potassium nitrates were taken as 68.9460 g/mol, 84.9947 g/mol, and 101.1030 g/mol respectively. The empirical coefficients of partial molar enthalpy of mixing of liquid phase for three binary systems were obtained from Kleppa and Hersh‘s [302] least square polynomial fitting expressions from their experimental heat of mixing values of the binary alkali nitrates. Empirical coefficients for the solid phase of binary sodium-potassium nitrate were modeled by Kramer [153] and in similar manner Elliott [313] and Coscia [305] obtained the solid coefficient values for other two binary systems. As discussed by Kramer [153], the change in empirical coefficient _a‘ magnitude shifts the eutectic point up or down. Change in _b‘ magnitude shifts the eutectic point left or right in a phase diagram. And, _c‘ coefficient was used in case of lithium-potassium nitrate system because the eutectic point and melting temperatures of each nitrate have bigger differences compared to other two binary systems (Na-K//NO_3 and Na-Li//NO_3) [153, 313]. The values that had been used in this study are shown in Tables 5.5.1 and 5.5.2.

Table 5.5.1: Thermophysical properties of single alkali nitrate salt obtained from references [153, 302, 305, 313, 324].

Salt	Fusion temperature		Heat of fusion (J/mol)	Heat capacity as constant (J/mol.K) $\Delta\ C_P = C_{P_{Liquid}} - C_{P_{Solid}}$	Temperature dependent heat capacity (J/mol.K) [*]
	(K)	(°C)			
$LiNO_3$	525.9	252.75	25027.398	17.2365	From [324]
$NaNO_3$	577.5	304.35	14704.0831	-9.349417	From [324]
KNO_3	607.4	334.25	9766.5498	-3.03309	From [324]
[*] Obtain series of Cp values against series of temperatures from Takahashi et al. work. The values are shown in Table E1 in Appendix E.					

Table 5.5.2: Empirical coefficients of binary alkali nitrate salts obtained from references [153, 302, 313].

Salt system	Empirical coefficients for heat of mixing of binary alkali nitrates					
	at liquid (J/mol)			at solid (J/mol)		
	a_l	b_l	c_l	a_s	b_s	c_s
$LiNO_3$-$NaNO_3$	-1941.4	-48.2	0	9204.8	3347.2	0
$LiNO_3$-KNO_3	-7359.66	-364.01	-1937.2	10460.0	4184.0	0
$NaNO_3$-KNO_3	-1709.2	-284.52	0	6276.0	0	0

In coupled nonlinear equations of binary A-B system, the ΔG^A and ΔG^Bassumed zero and three variables, mole fraction of component A at liquid phase (x_A^l), mole fraction of component A at solid phase x_A^S and temperature (T) were considered to obtain the locus of the solution. Other variables mole fraction of component B at liquid phase x_B^l and mole fraction of component B at solid phase x_B^S are correlated to their counterpart x_A^l and x_A^S respectively, as shown in Equations 5.3.1 and 5.3.2. Initially at fixed temperature, T and varying the x_A^l and x_A^S has showed some difficulties near the eutectic points. Hence, later the x_A^l was fixed and the x_A^S and T were scanned in the plane. At each given mole fraction of component A at liquid phase the other two variables were scanned and ΔG^A was calculated on a 500 x 500 points plane (for better resolution). Using the ‗*contour*' command in Matlab the locus of the solution of $\Delta G^A = 0$ was searched in the scanned plane (x_A^S *and* T) and subsequently along this contour, the locations of the zeros of ΔG^B was tracked. The results were obtained at 5K temperature interval separately. The intersection points of ΔG^A and ΔG^B provided x_A^l and x_A^S mole fractions, as shown in Figures 5.5.1 and 5.5.2. In similar approach other two binary systems were solved and plotted, as shown in Figures 5.5.3 to 5.5.5.

This method was quick and effective compared to ‗*fsolve*' method but was limited to binary systems only. The ternary system has five equations and seven unknown variables which makes the task difficult to build an efficient algorithm routine while using a contour plot. After several modifications, the contour plot technique was not successful to obtain the roots. Hence, only the binary algorithms are presented and showed in Appendix E. For lithium-potassium and lithium-sodium nitrate binary systems the solidus curves of Elliott were very linear which suggests they were fixed in some ad-hoc way. In this study, the similar phenomena observed where below the eutectic points a loop of liquidus curve appeared that had no physical meaning and were discarded. By artificial line fitted parallel to X-axis through the eutectic point were imposed to obtain corrected solidus curves, as shown in Figures 5.5.4 and 5.5.5.

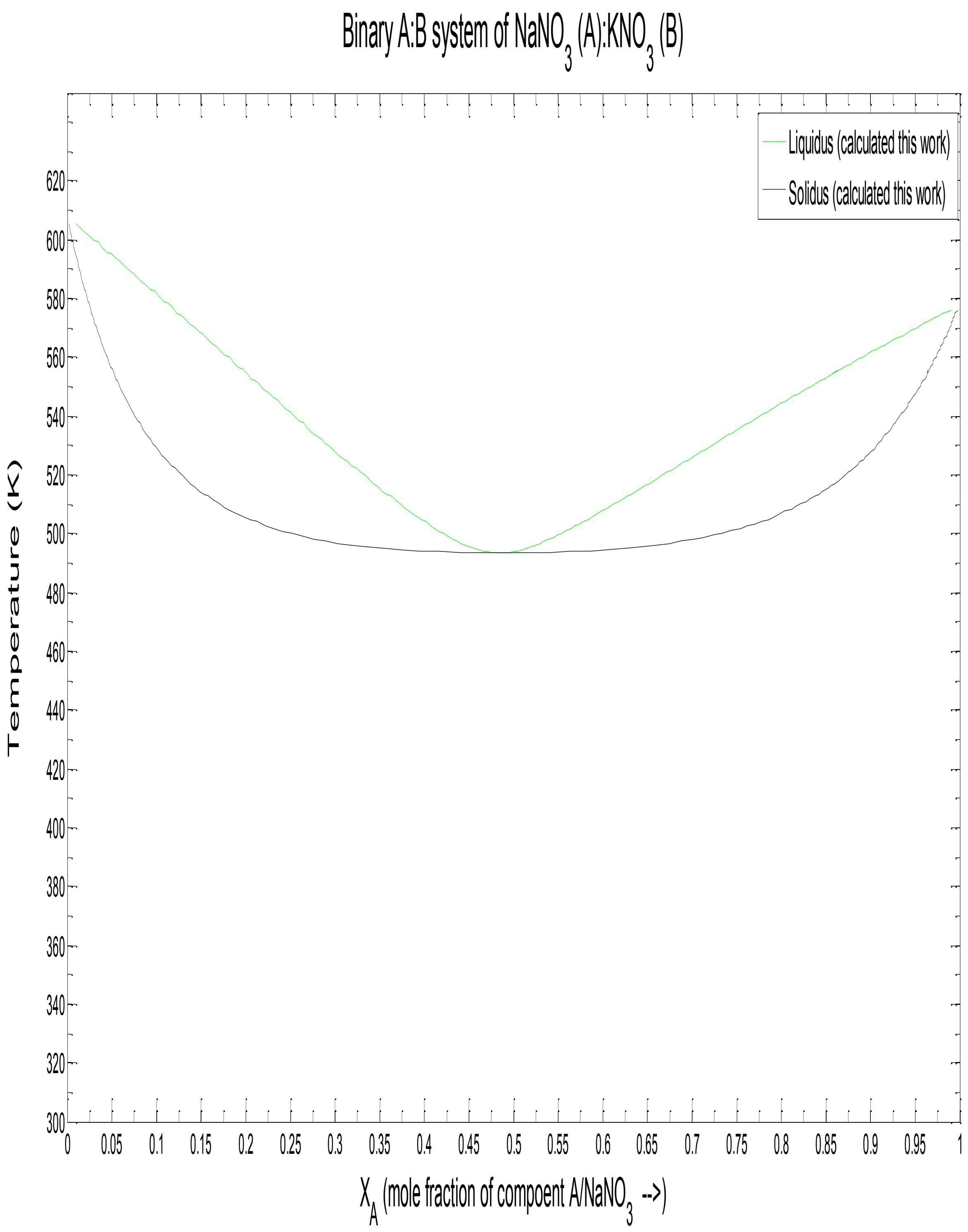

Figure 5.5.3: Calculated phase diagram of a binary $NaNO_3$-KNO_3 system using the regular solution model.

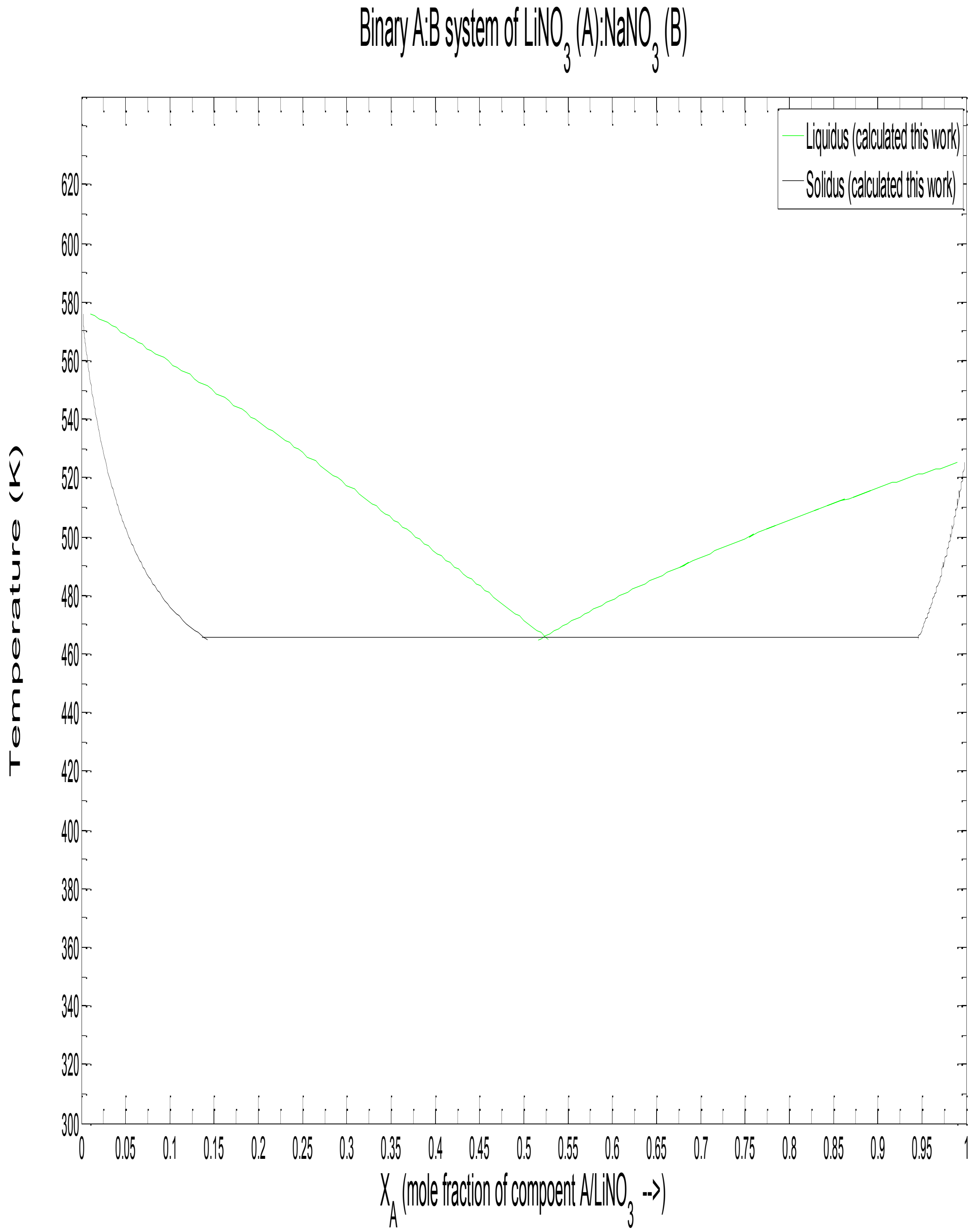

Figure 5.5.4: Calculated phase diagram of a binary $LiNO_3$-$NaNO_3$ system using the regular solution model.

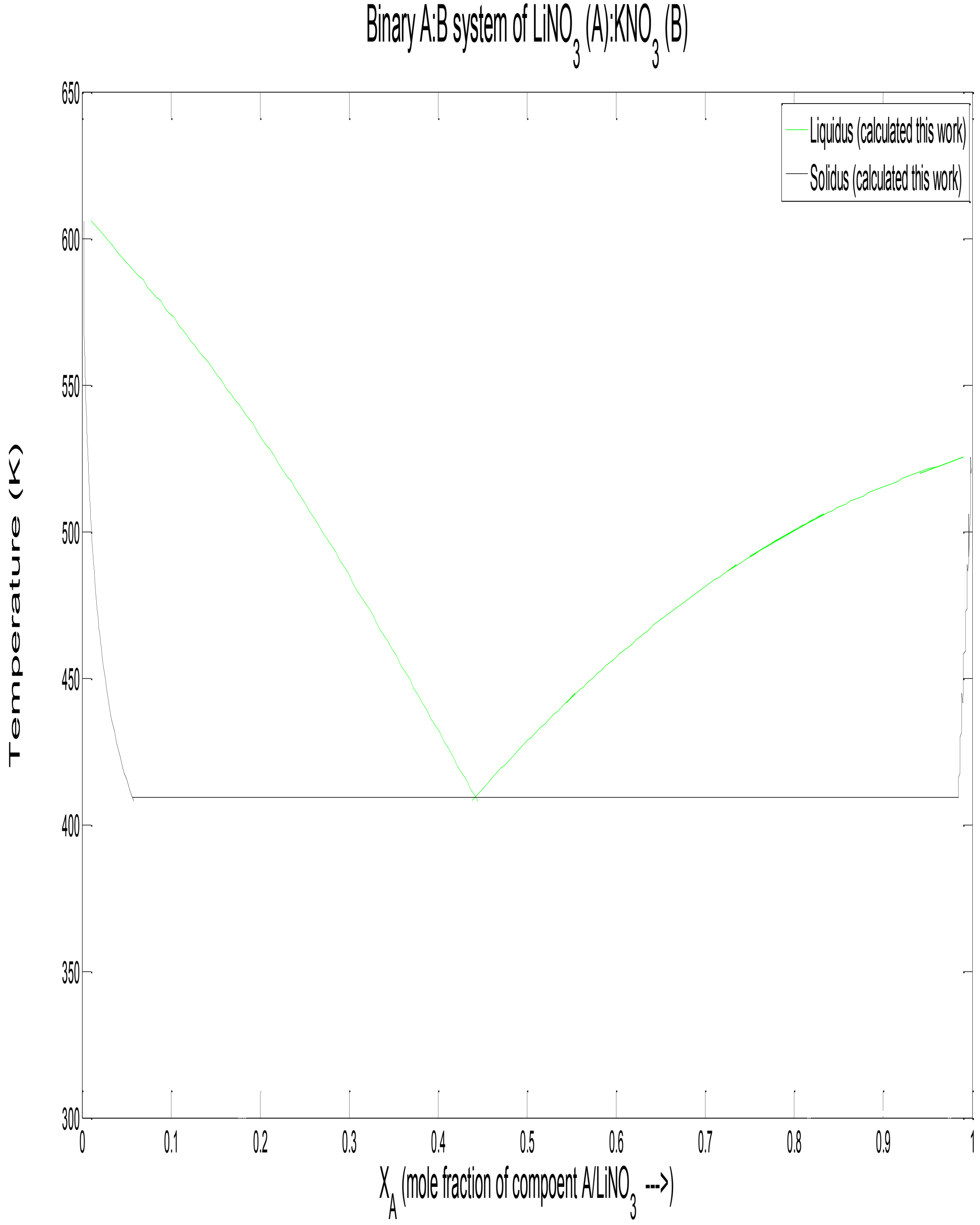

Figure 5.5.5: Calculated phase diagram of a binary $LiNO_3$-KNO_3 system using the regular solution model.

In the case of varying heat capacities (temperature dependent), the values were fitted in conjunction with the specified calculated temperature range (335 to 650K) by linear interpolation. Using one-dimensional linear interpolation (Matlab function: ‗interp1') method, the corresponding heat capacity (C_p) values were utilized to obtain contour plot of each system at each temperature intervals. Then the phase diagrams were plotted for three binary systems and are shown in Figures 5.5.6, 5.5.7 and 5.5.8. These phase diagrams are compared with previously calculated diagrams (where C_p was taken as constant). No smoothing operation was performed during calculation. In the case of Li-K and Li-Na nitrates similar to previous calculations, the solidus lines were artificially fitted through the eutectic temperature parallel to X-axis to obtain corrected solidus curves.

The calculated binary $NaNO_3$-KNO_3 had eutectic at 0.5 mole KNO_3 (temperature 220.85°C) in the case of constant heat capacity value and 0.52 mole KNO_3 (temperature 221.85°C) in the case of varying heat capacities. Slight flat solidus was observed in the second calculation, as shown in Figure 5.5.6. The calculated binary $LiNO_3$-KNO_3 had eutectic at 0.44 mole $LiNO_3$ (temperature 137°C) in the case of constant heat capacity value and 0.424 mole $LiNO_3$ (temperature 135°C) in the case of varying heat capacities, as shown in Figure 5.5.7. The calculated binary $LiNO_3$-$NaNO_3$ had eutectic at 0.524 mole $LiNO_3$ (temperature 192.8°C) in the case of constant heat capacity value and 0.524 mole $LiNO_3$ (temperature 190°C) in the case of varying heat capacities, as shown in Figure 5.5.8. Despite the irregular pattern of liquidus and solidus curves in the event of temperature dependent C_p the eutectic points were close to predicted phase diagrams when C_p was taken as a constant value.

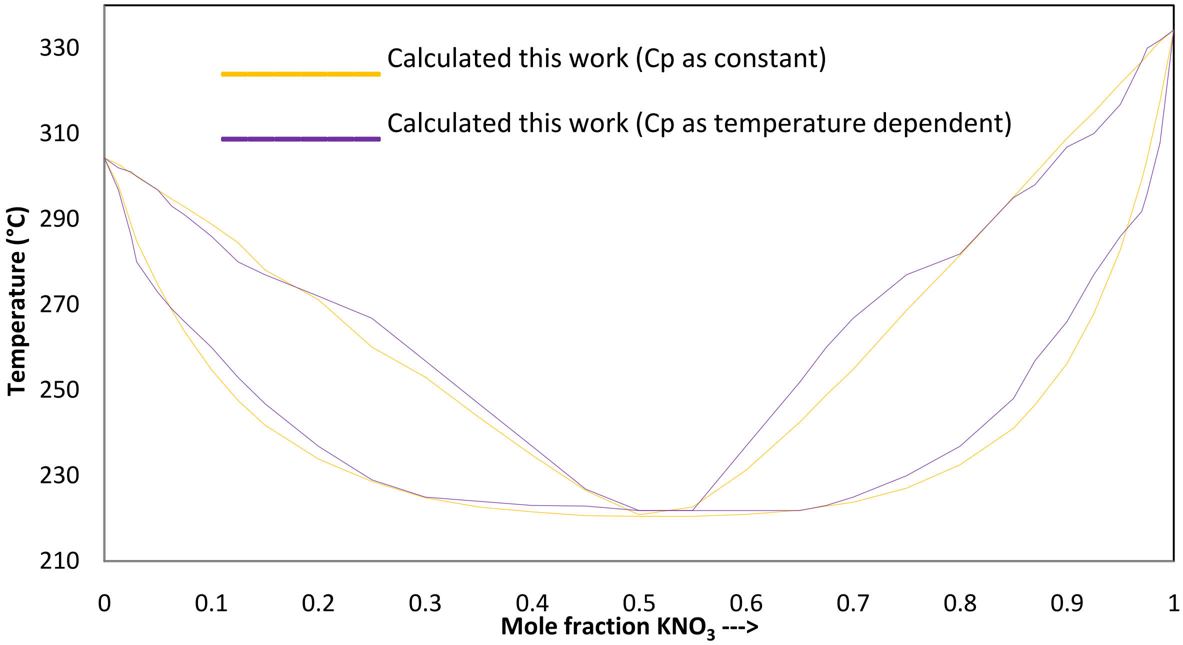

Figure 5.5.6: Binary $NaNO_3$-KNO_3 phase diagram obtained by calculation using the regular solution model.

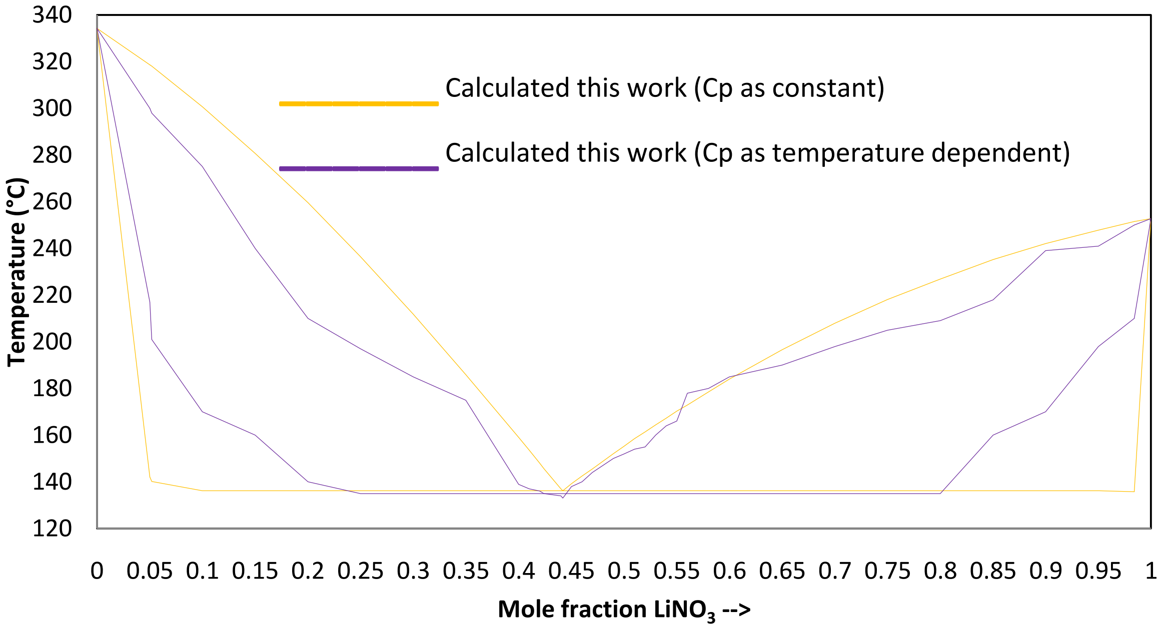

Figure 5.5.7: Binary $LiNO_3$-KNO_3 phase diagram obtained by calculation using the regular solution model.

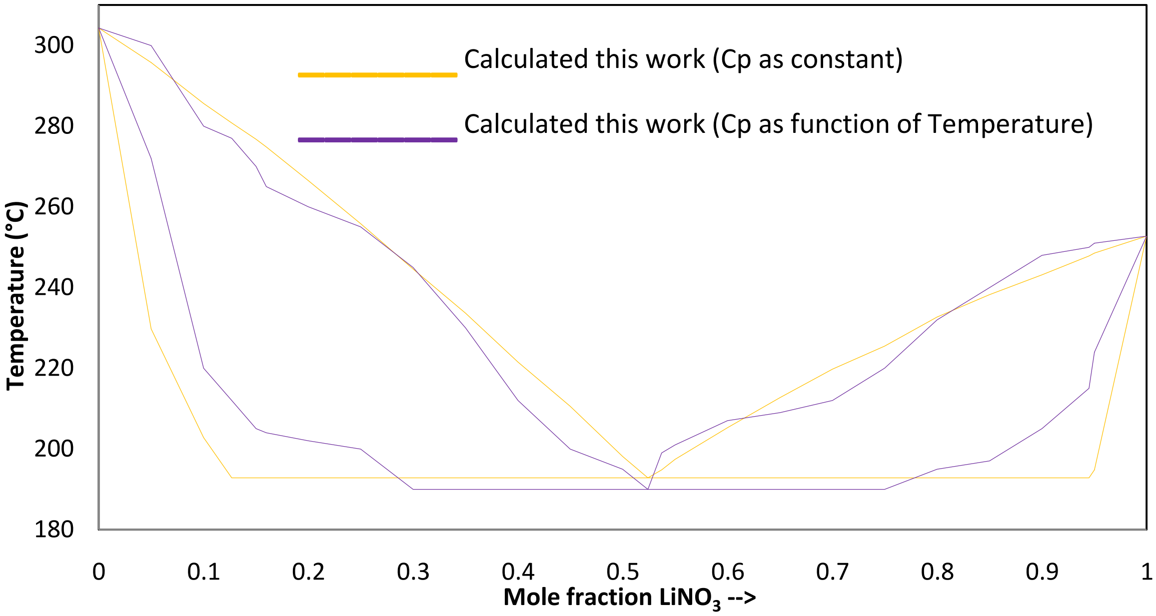

Figure 5.5.8: Binary $LiNO_3$-$NaNO_3$ phase diagram obtained by calculation using the regular solution model.

5.5.1 CONCLUSIONS: NUMERICAL FORMULATION

The ‗*contour plot*' technique was effective for a binary system. However, due to the poorly written algorithm, this technique did not work for the ternary system. Temperature dependent heat capacities (C_p) provided dispersed liquidus and solidus curves compared to the C_p as constant value over the full temperature range for each binary systems. The eutectic points for both calculations were closed to literature experimental values were discussed in subsection 5.6.

5.6 FACTSAGE, LITERATURE EXPERIMENTAL DATA AND CALCULATED PHASE DIAGRAMS COMPARISON

FACTSAGE [39] is a combination of two computational thermochemistry software F*A*C*T/FACT-Win and ChemSage and renamed as FACTSAGE in 2001. FactSage can be used to calculate phase diagrams, complex-phase equilibria, predominant diagrams, and reactions [315]. The ―Reaction”, ―Equilib” and ―Phase Diagram” and module were frequently used in this study. These modules include H, S, C_p and G of the salt systems. The ―Reaction” module calculates the changes in extensive thermochemical properties (H, G, V, S, C_p, A) for a given mixture. The ―Equilib” module was used to calculate the concentrations of chemical species which worked on Gibbs energy minimization method. The ―Phase Diagram” module was used to generate binary and ternary diagrams using quasi-chemical model [315].

The solution databases such as FTsalt-ALKN, FTsalt-NKNA, FTsalt- SALTA and FTsalt-SALTE [39] have been used to produce plots for three binary and one ternary phase diagrams, as shown in Figures 5.6.1, 5.6.2, 5.6.3 and 5.6.4. The phase diagrams obtained from FactSage are in good agreement with literature experimental data for liquidus and solidus curves, except some intermediate values, as shown schematically in Figures 5.6.5, 5.6.6 and 5.6.7. The ternary phase diagram obtained by FactSage showed the eutectic point at 120.84°C. The mole fraction of the sodium nitrate was 0.13529, potassium nitrate was 0.49118, and lithium nitrate was 0.37352, which was about 13.23 weight% Na -57.14 weight% K-29.63 weight% Li///NO_3. The binary Li-Na//NO_3 phase diagram obtained from FactSage has a eutectic point at 0.463 mole $NaNO_3$ and temperature at 195°C, as shown in Figure 5.6.1. The binary Li-K//NO_3 phase diagram obtained from FactSage has a eutectic point at 0.424 mole $LiNO_3$ and temperature at 125°C, as illustrated in Figure 5.6.2. The binary Na-K//NO_3 phase diagram obtained from FactSage has a eutectic point at 0.49 mole $NaNO_3$ and temperature at 223°C, as shown in figure 5.6.3.

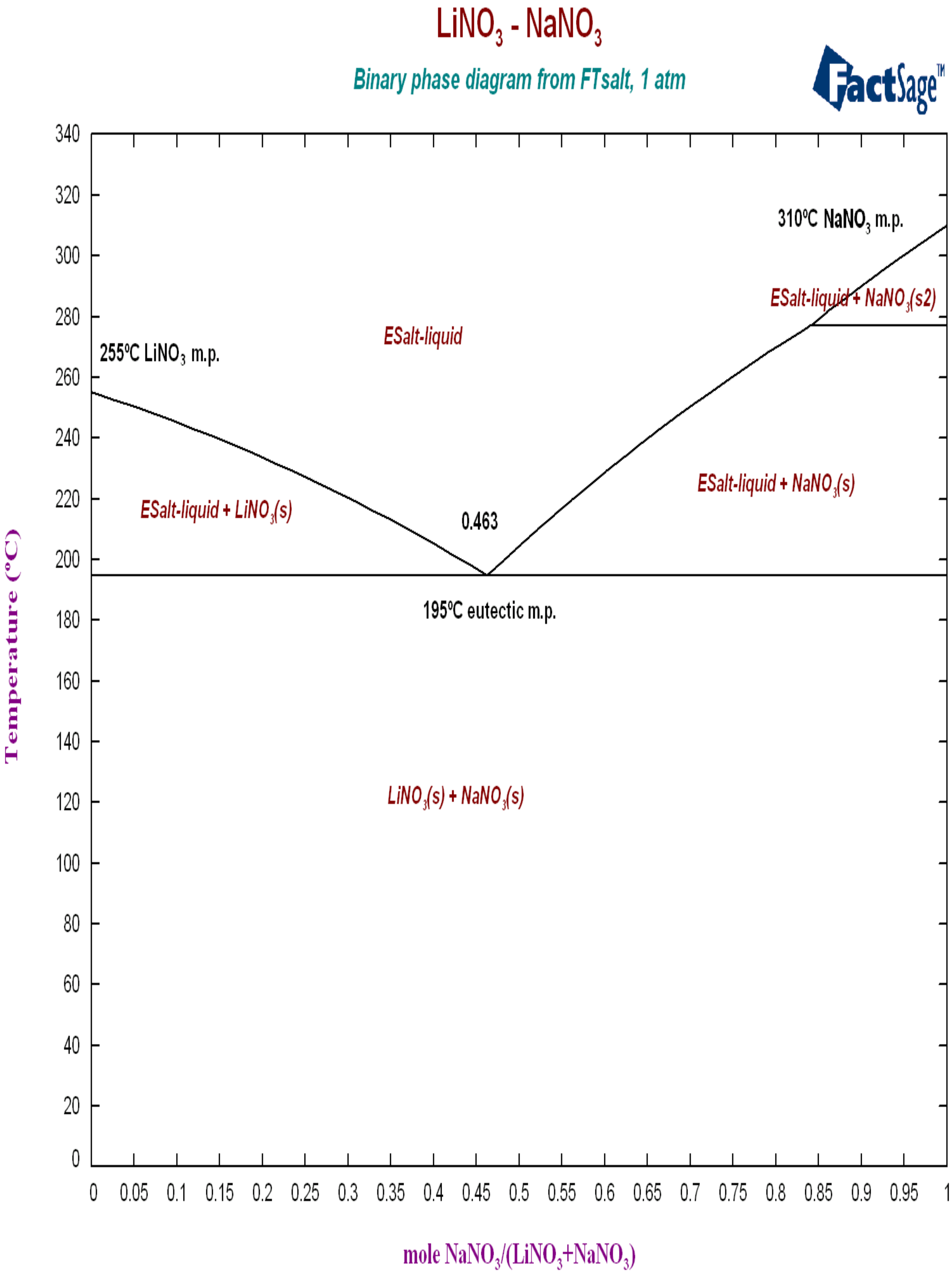

Figure 5.6.1: Calculated eutectic composition phase diagram of binary Li-Na//NO$_3$ salt obtained from FactSage.

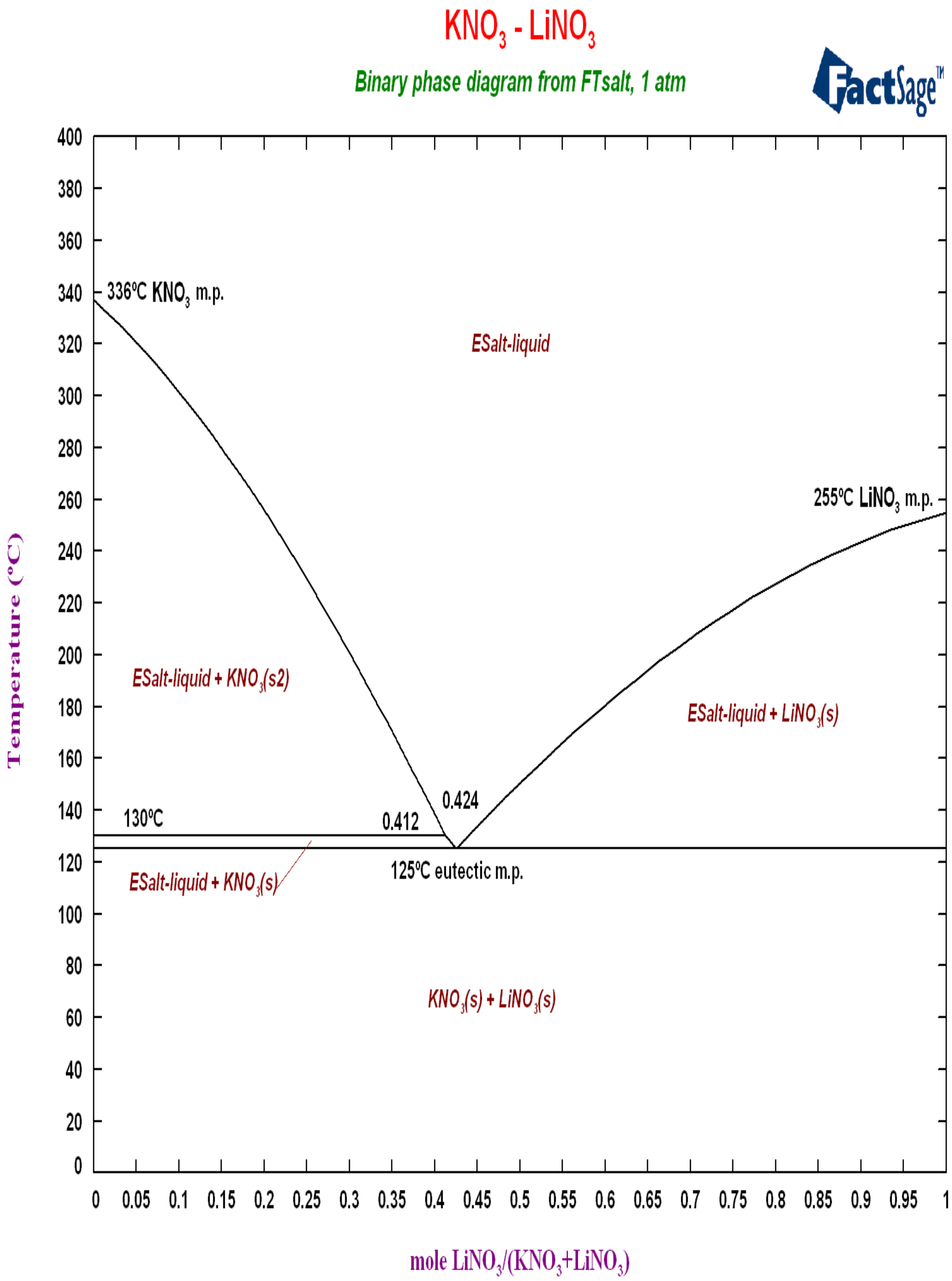

Figure 5.6.2: Calculated eutectic composition phase diagram of binary K-Li//NO$_3$ salt obtained from FactSage.

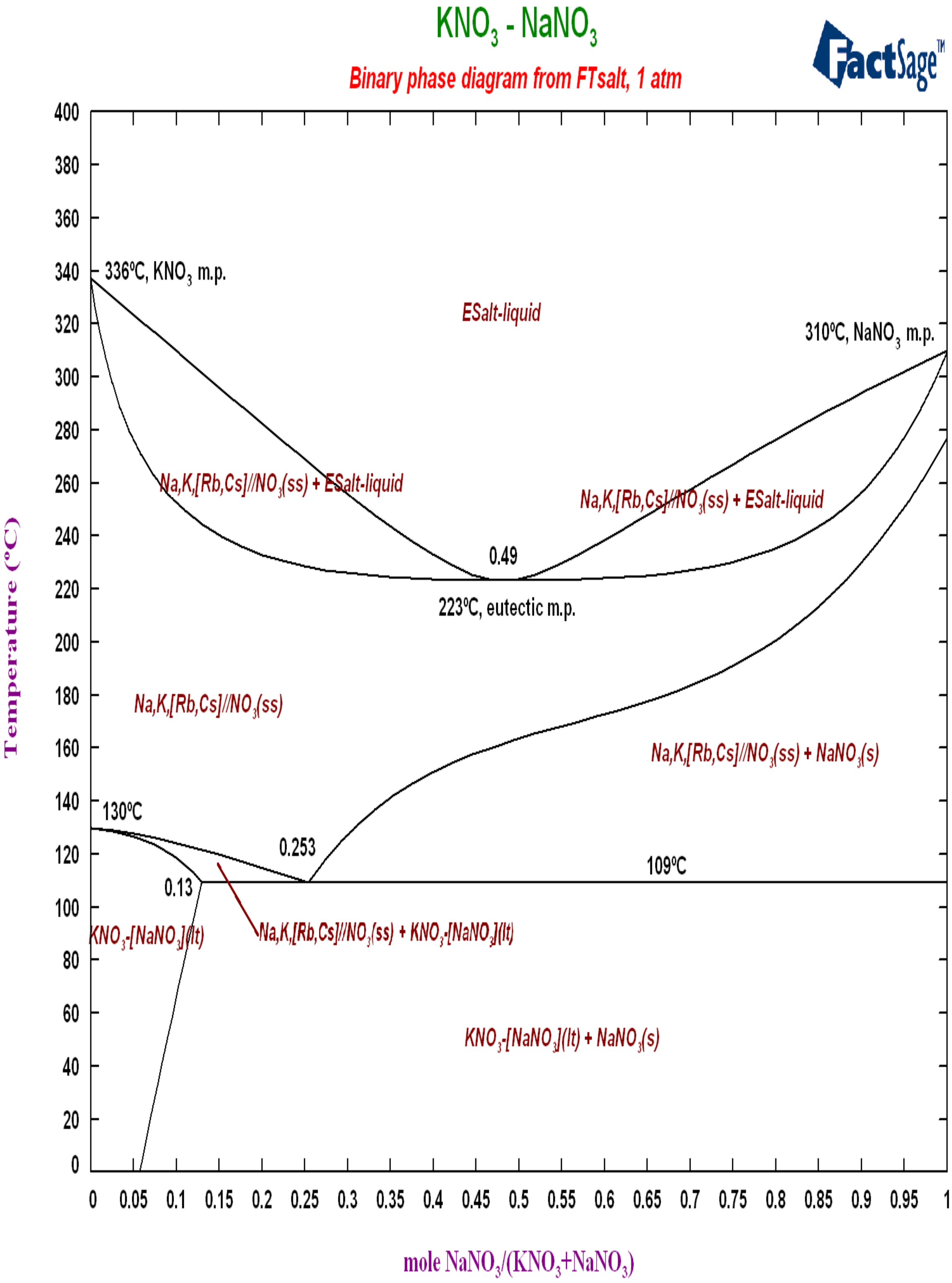

Figure 5.6.3: Calculated eutectic composition phase diagram of binary K-Na//NO_3 salt obtained from FactSage.

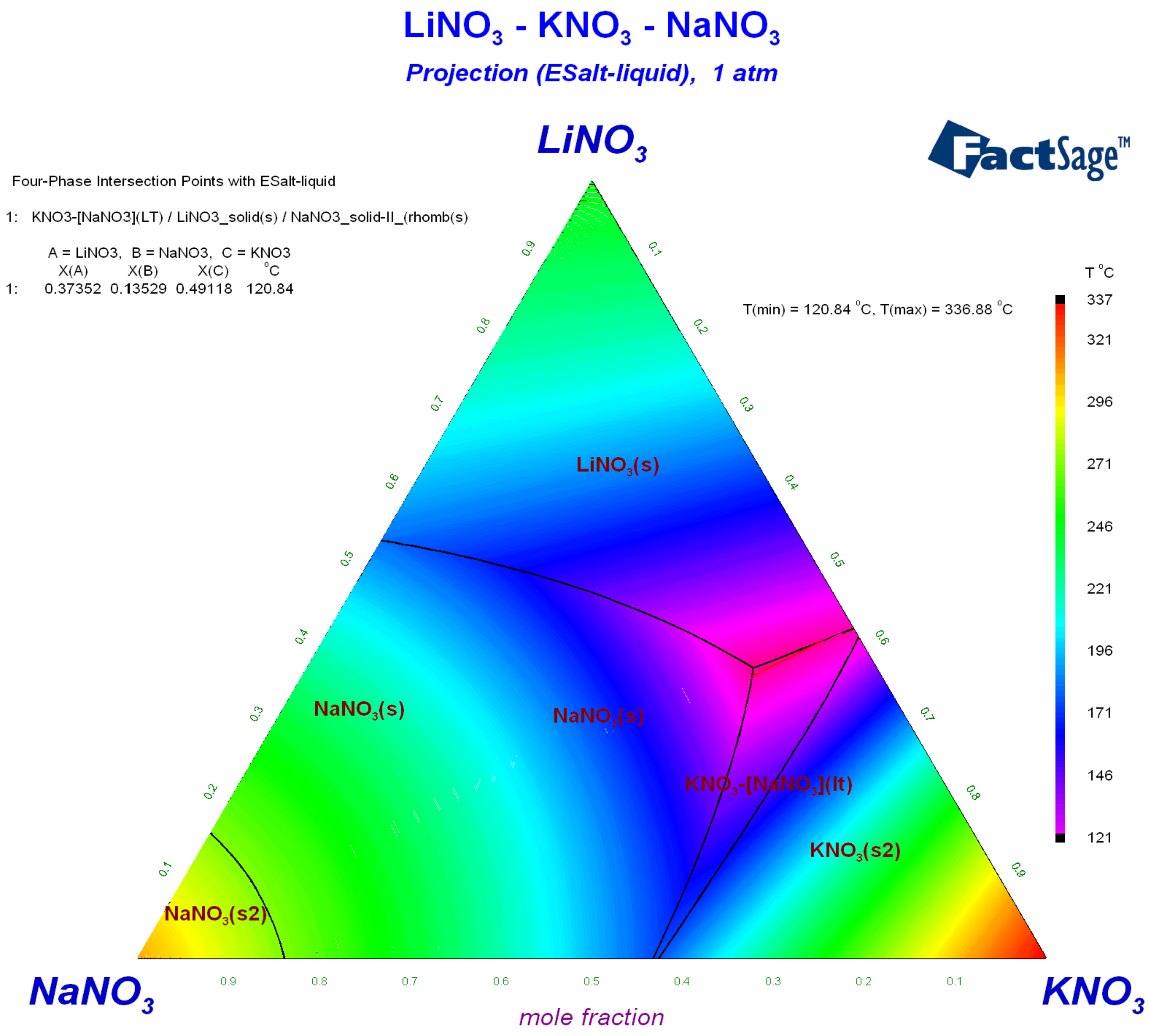

Figure 5.6.4: Calculated eutectic composition phase diagram (Gibbs Triangle) of ternary nitrate obtained from FactSage. Isotherms are shown at 0.1°C intervals.

The experimental phase diagram‘s published values in literature which are presented as numbers in tabulated form are only considered for comparison with FactSage and calculated thermodynamic data. Except few discrepancies for some intermediates, all the solidus and liquidus points of all three binary systems from the literature are almost overlaid with FactSage values indicating good agreement. The differences from author to author mainly because different apparatus used, sample pretreatment and preparation, sample pan type, calibration materials, super-cooling phenomena and finally difficulties achieving equilibrium in the sub-solidous region during cooling and heating [38].

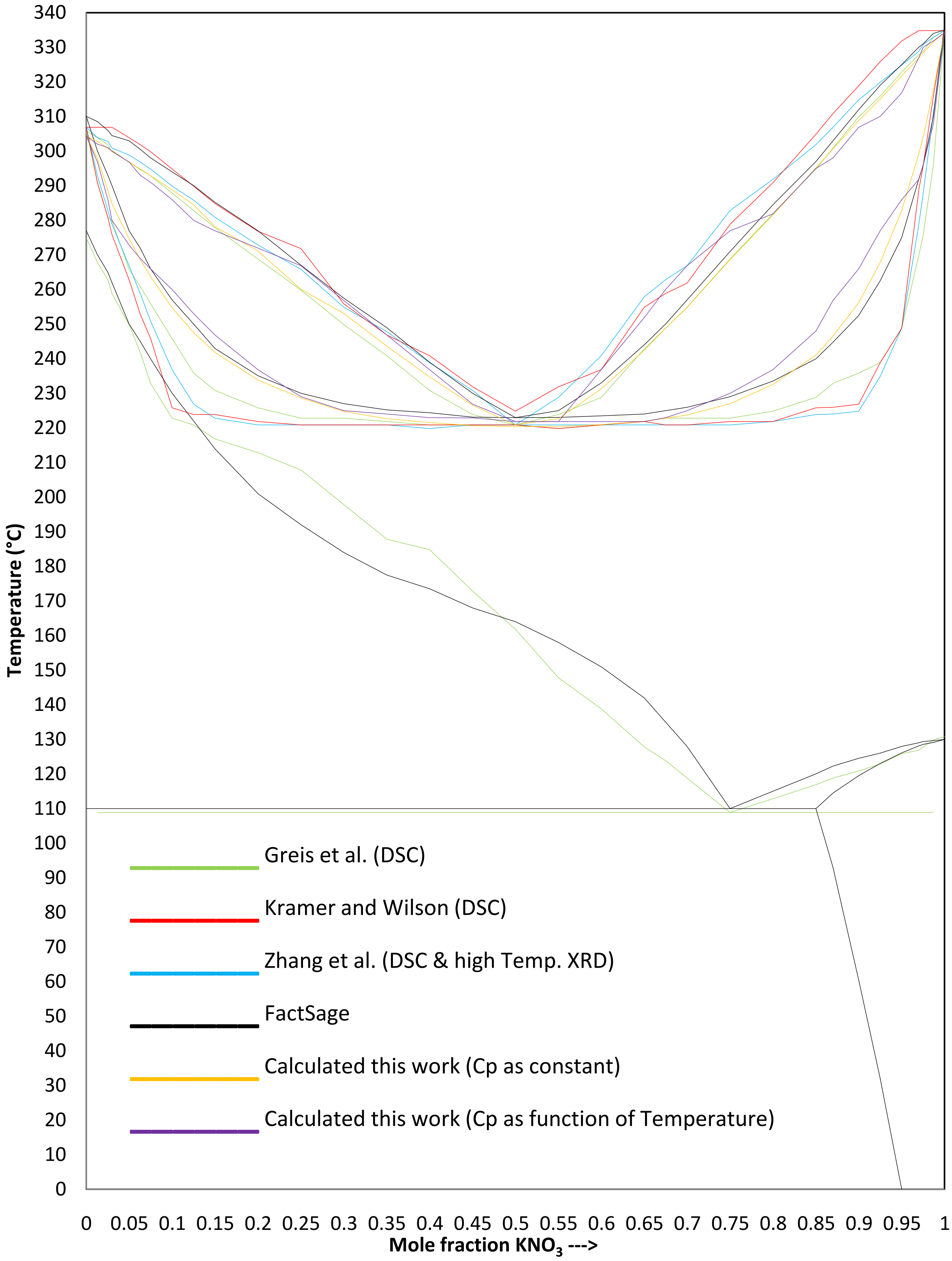

Figure 5.6.5: $NaNO_3$-KNO_3 phase diagram comparison with FactSage, DSC literature, and calculated values.

The sodium-potassium nitrate phase diagram is disputed in literature as either invariant eutectic or solid-liquid equilibrium with minimum melting behavior. Many researchers did not report subsolidus curves. Benages-Vilau, R., et al. [311] studied the binary system using XRD, DSC, Raman spectroscopy and hot stage microscopy and stated that their experimental phase diagram is best describable by ABθ model [312, 325, 326] as mixed crystal system. Benages-Vilau et al. [311] calculated angles of the subsolidus curve at right hand side of phase diagram using Van't Hoff's law [325], as shown in Figure 5.6.5.a. Benages-Vilau et al.'s simulated values were closely fitted to the subsolidus region obtained by FactSage simulation, as shown in Figures 5.6.3 and 5.6.5.a. Their calculation was not compared here due to unavailability of tabulated data. They stated that the binary phase diagram possess very limited solid solution, immiscibility gap in the solid state with invariant eutectoid.

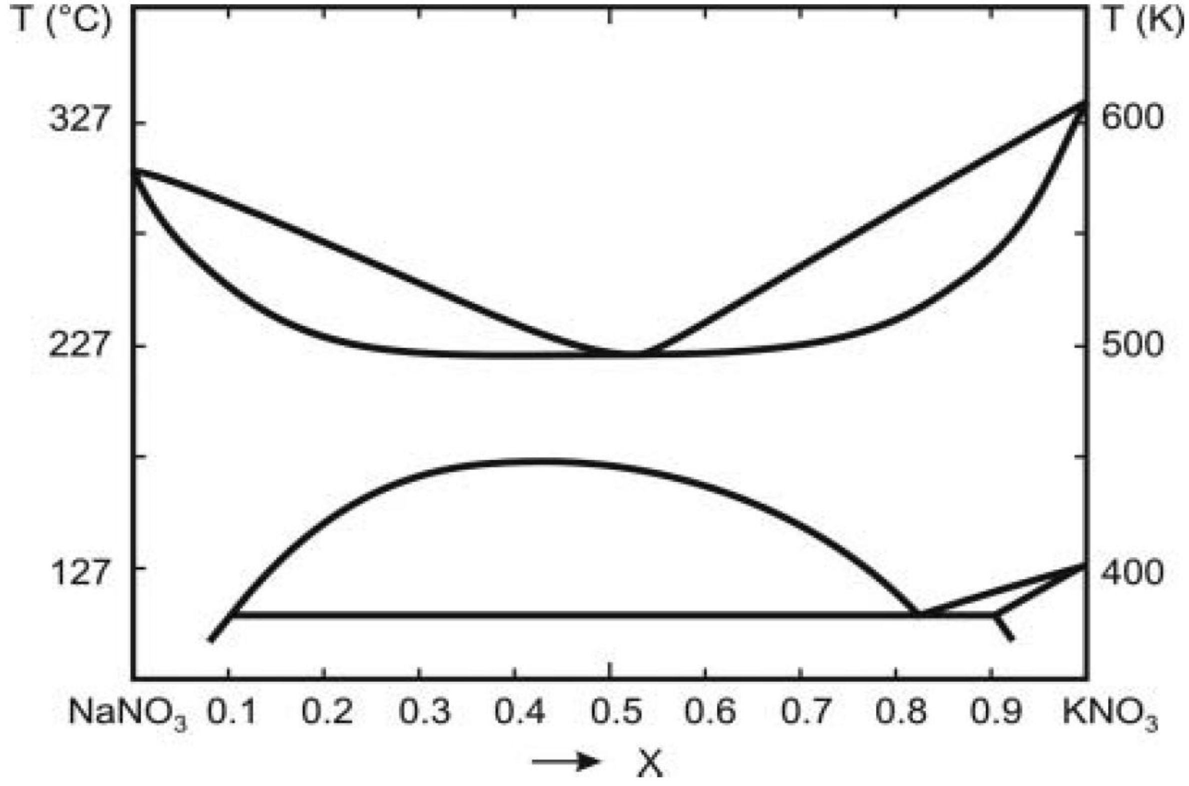

Figure 5.6.5.a: Binary $NaNO_3$-KNO_3 calculated phase diagram using ABθ [312] model [311].

Dessurreault et al. [240] calculated binary system and stated it as a complete solid solution. Kramer [153] studied that isomorphous binary Na-K//NO_3 using Perkin Elmer Differential Scanning Calorimetry (DSC) calibrated against Indium and K_2CrO_4. Kramer's solidus is flatter in the intermediate range (0.1 to 0.9 mol KNO_3) compared to FactSage curved shape which usually indicates the possibility of a eutectic with limited or two phase solid solution [37, 153], as shown in Figure 5.6.5. Zhang [37] used Perkin Elmer DSC to study binary Na-K//NO_3 system also suggested the behavior just below the solidus indicate the binary system might possess limited solid solubility rather than continuous series of a solid solution. Irrespective of flat or curve solidus many published phase diagrams [38, 150, 153, 164, 306-308, 327] of this binary system portrayed it as a continuous solid solution. The nearly horizontal solidus is representing the free energy at a minimum melting temperature which is a function of composition [328]. Usually, a flat solidus is appeared due to contamination of samples mainly humidity/moisture which lowers the liquidus point compared to the dried samples. Greis's [38] solidus also appeared flat and closer to FactSage and Kramer's value. At 275.35°C $NaNO_3$ undergoes a transformation from an ordered rhombohedral phase to disordered rhombohedral phase structure [153]. KNO_3 transforms from orthorhombic to the rhombohedral structure at 129.85°C to become isostructural with $NaNO_3$. For Na-K//NO_3, all of the solidus values from the literature are lower than the FactSage values. All the liquidus curves have some degrees of curvature and do not show a sharp kink at the eutectic point. Calculated liquidus and solidus curves (both C_p as constant and temperature dependent) were relatively close to the FactSage value, as shown in Figure 5.6.5.b.

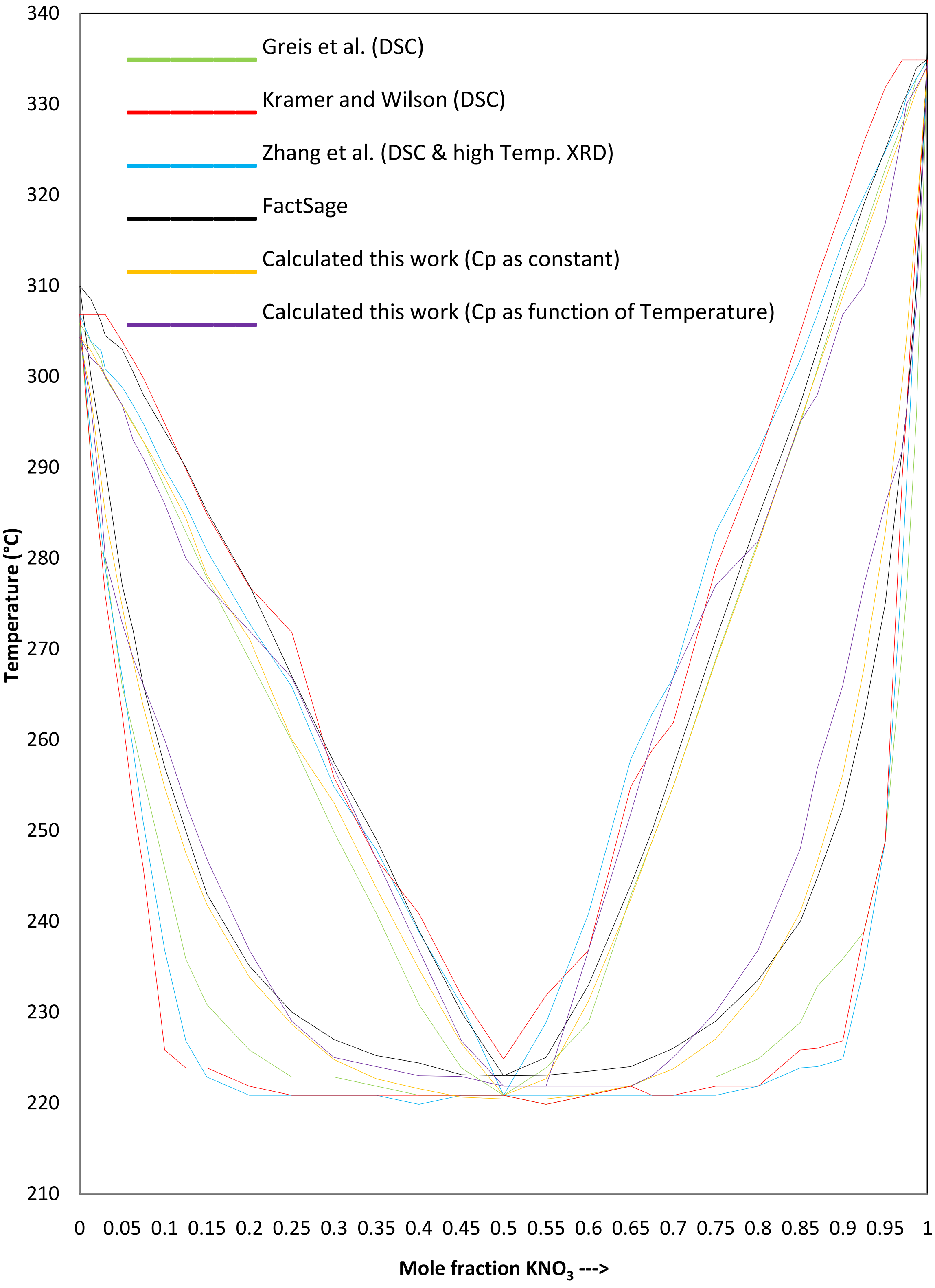

Figure 5.6.5.b: Comparison of liquidus and solidus curves of sodium-potassium nitrate (zoomed view).

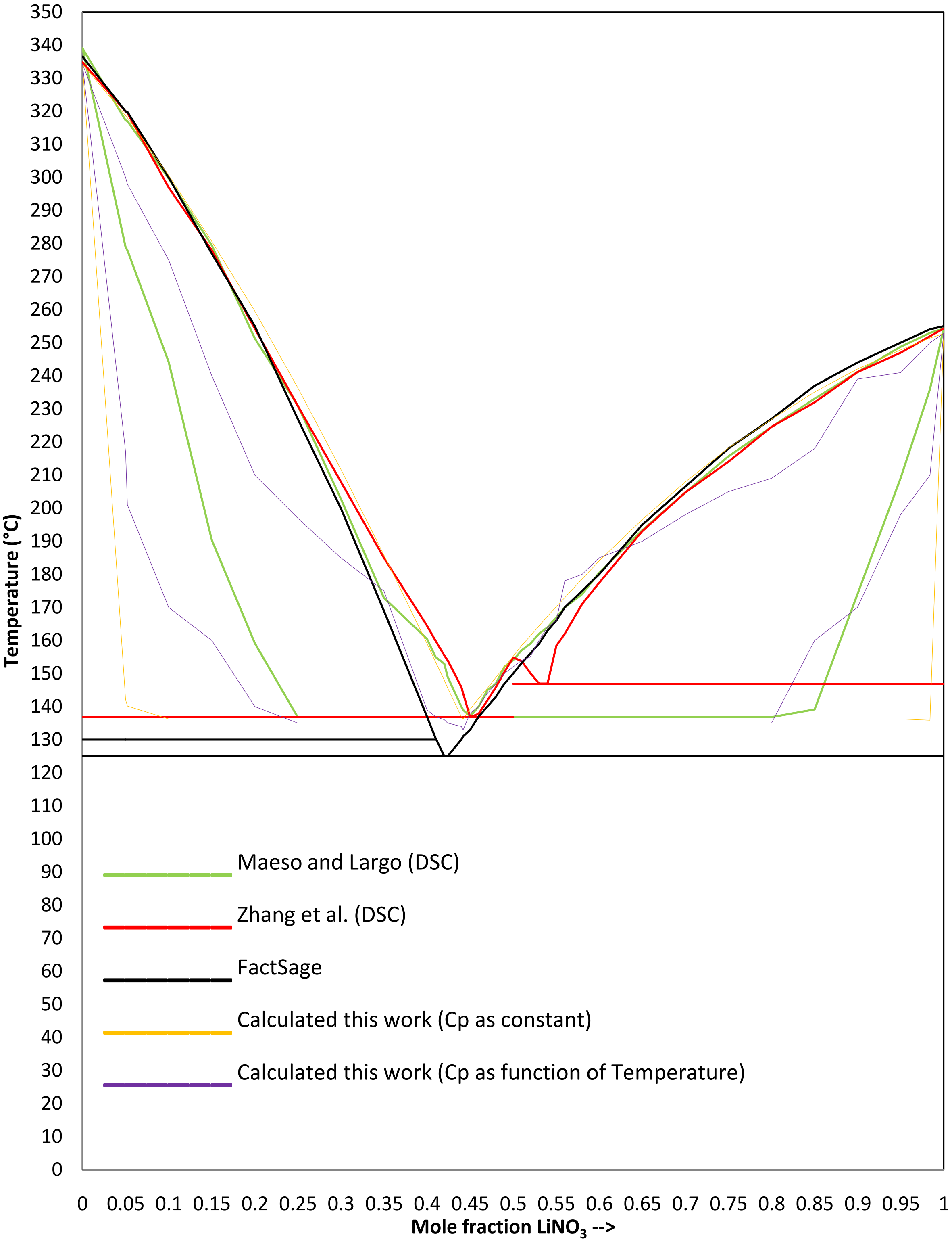

Figure 5.6.6: $LiNO_3$-KNO_3 phase diagram comparison with FactSage, DSC literature, and calculated values.

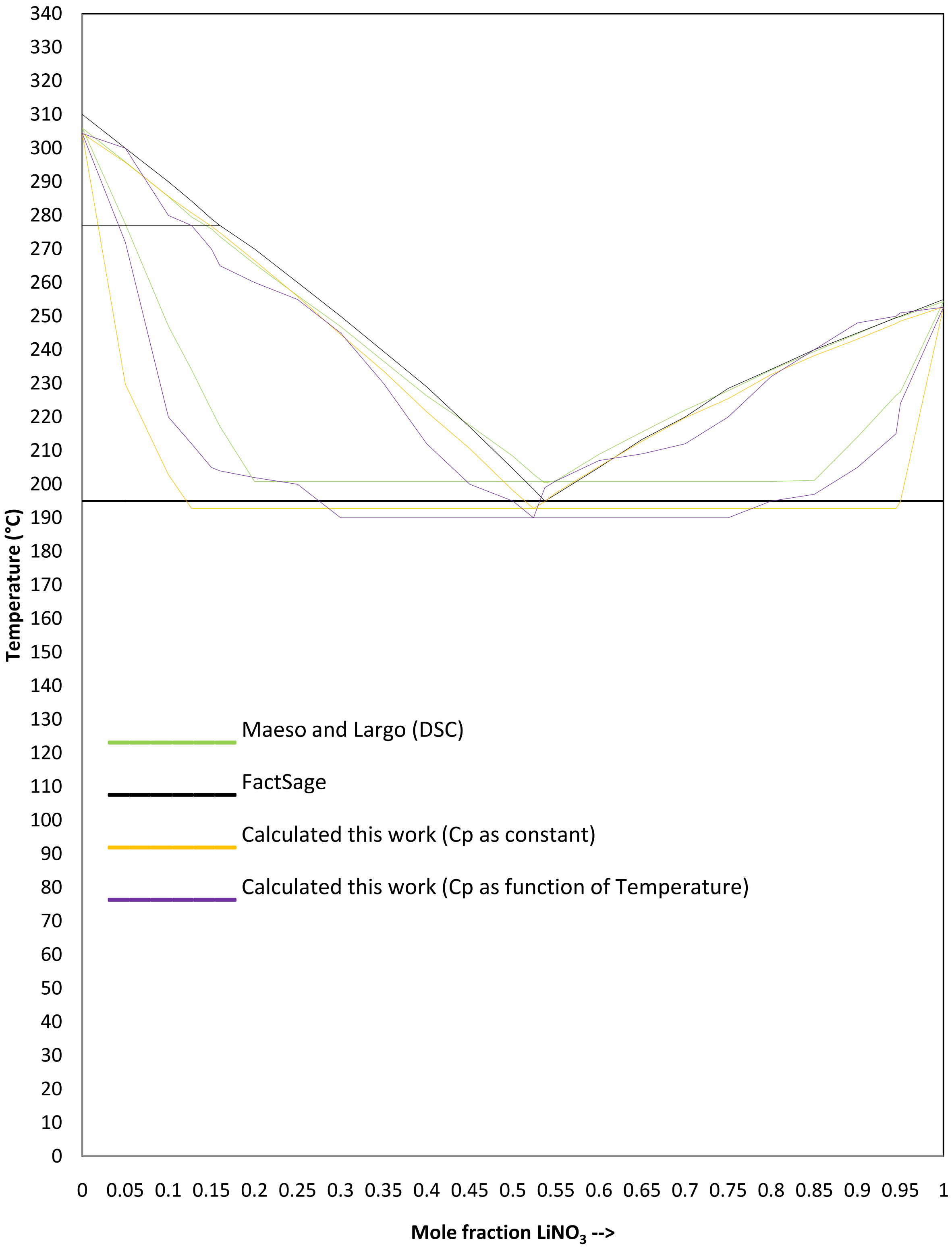

Figure 5.6.7: $LiNO_3$-$NaNO_3$ phase diagram comparison with FactSage, DSC literature, and calculated values.

For lithium-potassium and lithium-sodium nitrates thermodynamic formulation indicates that the liquidus and solidus lines are in good agreement except for some intermediate values with a study from Maeso [32] and Zhang et al. [329], as shown schematically in Figures 5.6.6 and 5.6.7 respectively. Maeso performed heating, and cooling curves experiment of various compositions on high purity reagent grade nitrates mixture in Perkin Elmer DSC accordance with temperature and heat calibration of Indium, K_2CrO_4, and sapphire for heat capacity. The solidus lines are flatter as FactSage lines as shown in Figures 5.6.6 and 5.6.7. Perhaps due to contamination (moisture absorptivity due to hygroscopic nature of alkali nitrates) and limited solid solution behavior may possess flatter solidus lines. However according to Dessurreault et al. [240] calculated the lithium-sodium nitrate stated that it possesses eutectic and lithium-potassium nitrate possess eutectic invariant behavior without a solid-solution. The experimental results were good agreement with his calculated values for the points outside of the eutectic, and Maeso [32] stated that both binary Li-K and Li-Na nitrate mixtures exhibit the regular solution behavior. Zhang and coworkers [329] used Raman spectroscopy and Perkin Elmer DSC (calibrated against In and Zn), observed a discontinuity in lithium-potassium nitrate mixture at Lithium= 0.41 and 0.45 mole fraction, as shown in Figure 5.6.6. Xu et al. [330] studied the system using Raman spectroscopy and agreed with Zhang et al. [329]. They indicated the discontinuity as intermediate incongruently melting compound $KLi(NO_3)_2$ and proposed the system with two eutectics. They suggested that compound $KLi(NO_3)_2$ could exist in narrow composition and temperature range at an equimolar point just below the solidus and appeared during fast cooling [329, 330]. At room temperature compound $KLi(NO_3)_2$ subsequently decomposed to $LiNO_3$ and α-KNO_3 [329]. For Li-K//NO_3 and Li-Na//NO_3 all of the solidus values from the literature are higher than the FactSage values, and liquidus values have a sharp kink at the eutectic point. Calculated liquidus and solidus curves (both C_p as constant and temperature dependent) were relatively close to the FactSage value, as shown in Figures 5.6.6.a and 5.6.7.a.

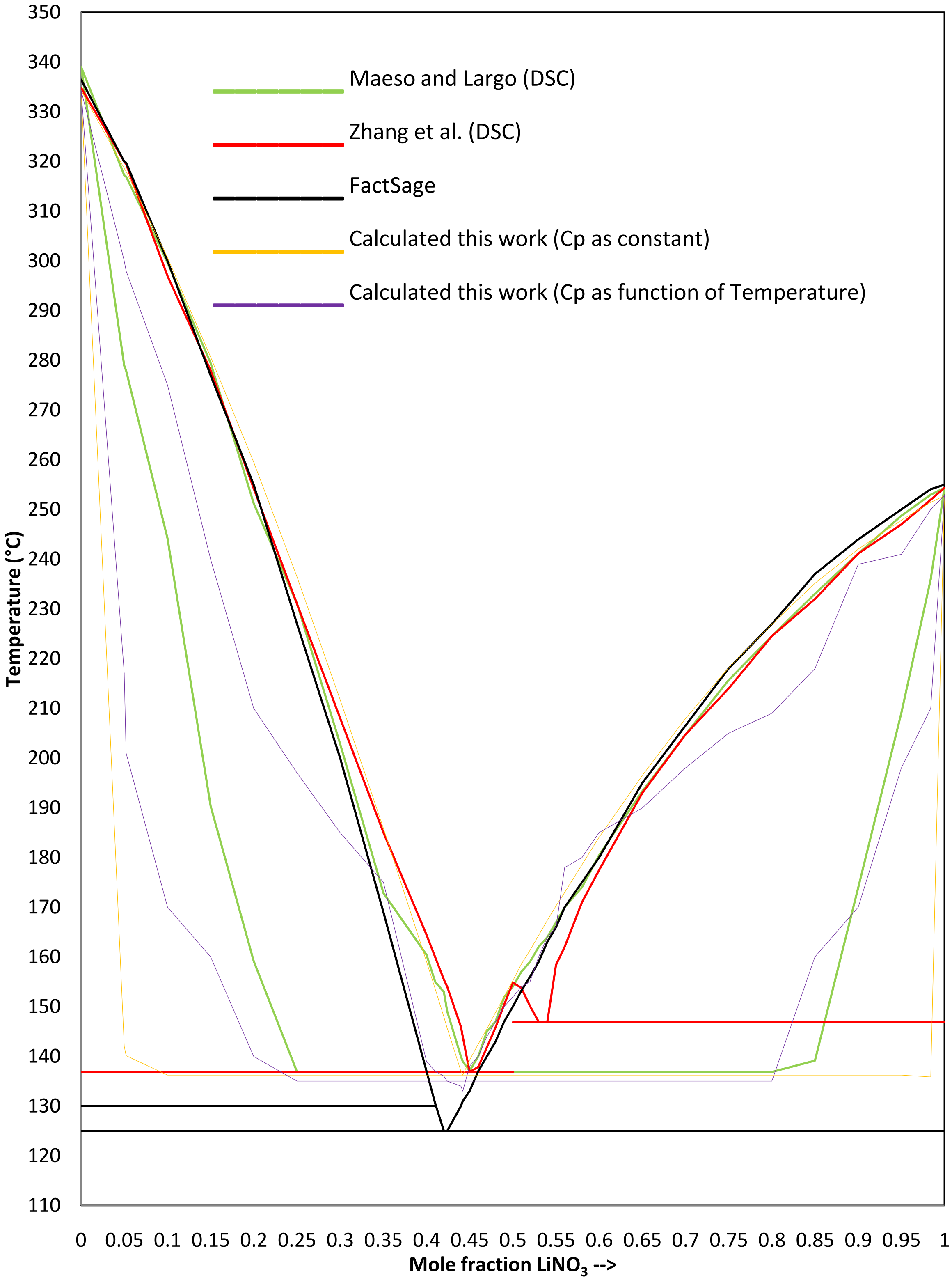

Figure 5.6.6.a: Comparison of liquidus and solidus curves of lithium-potassium nitrate (zoomed view).

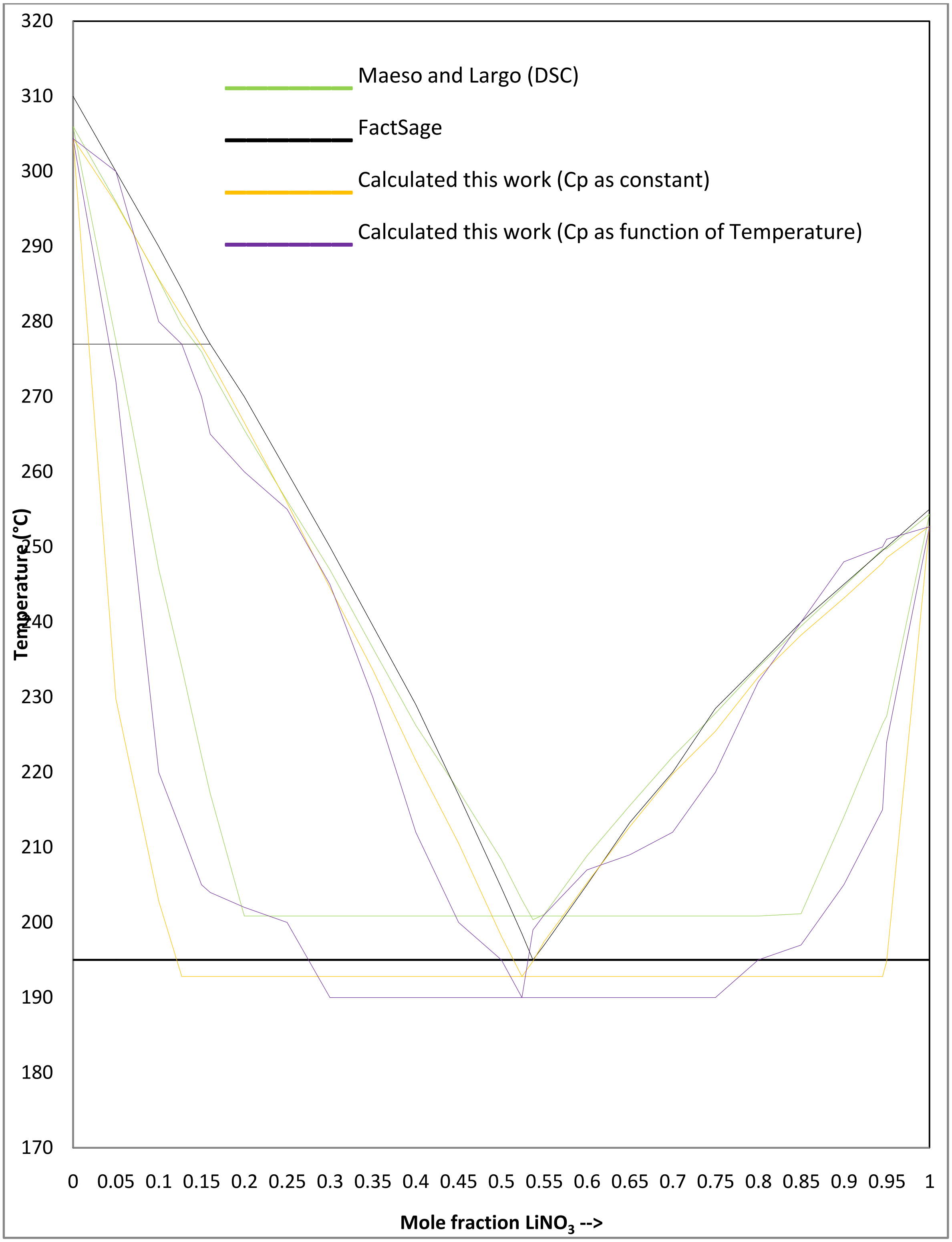

Figure 5.6.7.a: Comparison of liquidus and solidus curves of lithium-sodium nitrate (zoomed view).

5.7 CONCLUSIONS

FactSage quasi-chemical and calculated values are close to experimental phase diagrams values, as shown in Table 5.7.1. Flat solidus lines were common for three alkali nitrate binary systems in mid span of the eutectic points. The regular solution model predicted three binary phase diagrams well except some subsolidus region. ABθ theory based on mixed crystal assumption can illustrate a subsolidus region of binary $NaNO_3$-KNO_3 closely compared to the FactSage values. Observation from Kleppa‘s [300-303] heat of mixing studies it is reasonable to assume that the regular solution can also be useful to describe higher order alkali nitrates and alkali halides. Single alkali nitrates have polymorphism behavior discussed in Chapter 3 of this thesis. Which showed some degrees of disorder at high temperature, perhaps is one of the reasons of dispersed phase boundaries in binary alkali nitrate systems as observe in Figures 5.6.5, 5.6.6 and 5.6.7. Varying heat capacities have an effect on predicted liquidus and solidus curves. Calculation involved of C_p as a constant was fairly close to the literature experimental and FactSage values.

Table 5.7.1: Binary phase diagrams comparison.

Salt systems	Eutectic composition (mole %)	Eutectic temperature (ºC)	Method [reference]
$NaNO_3$-KNO_3	0.5 KNO_3	224.85	DSC [153]
	0.5 KNO_3	220.85	DSC [38]
	0.5KNO_3	220.85	DSC & high temperature XRD [37]
	0.51 KNO_3	223	FactSage [39]
	0.5 KNO_3	220.85	This work calculated C_p as constant
	0.52 KNO_3	221.85	This work calculated varying C_p
$LiNO_3$-$NaNO_3$	0.537 $LiNO_3$	200.35	DSC [32]
	0.537 $LiNO_3$	195	FactSage [39]
	0.524 $LiNO_3$	192.8	This work calculated C_p as constant
	0.524 $LiNO_3$	190	This work calculated varying C_p
$LiNO_3$-KNO_3	0.45 $LiNO_3$	137.05	DSC [32]
	0.46 and 0.53 $LiNO_3$	136.85 and 146.85	DSC [329]
	0.424 $LiNO_3$	125	FactSage[39]
	0.44 $LiNO_3$	137	This work calculated C_p as constant
	0.424 $LiNO_3$	135	This work calculated varying C_p

CHAPTER 6 EXPERIMENTAL PROCEDURES

After completing the literature review and identifying the key research issues, the thermal analysis and transpiration test method have been selected for studying thermal stability and mass loss chemistry. To understand the sample preparation and to familiarize with the experimental procedure, single salts and 60:40 weight ratio binary Na-K//NO_3 salt have been chosen for thermal and transpiration test analysis as discussed in Chapter 7. Moreover, then the ternary Na-K-Li///NO_3 salt system was thermally analyzed, and results are provided in Chapter 8.

In this chapter the materials preparation, apparatus setup, the experimental procedure has been described. The basic technique for both thermal analyzer and transpiration rig are to observe the weight loss and record thermal events of the sample that is subjected to heat treatment in a controlled environment. The salt systems were prepared in certain weight ratios and stored in a desiccator. From these, a sub-sample was taken and loaded into a crucible (for thermal analyzer) or combustion boat (for transpiration rig) for heat treatment.

6.1 REAGENTS AND LAB EQUIPMENT

Anhydrous reagent grade sodium nitrate (Sigma 99.999% puratonic metals basis), potassium nitrate (Sigma 99.997% puratonic metals basis), and lithium nitrate (Sigma 99.99% reagent grade) were used for DSC/DTA-TGA-MS and transpiration tests. Pure argon (99.99%) and oxygen (99.99%) supplied from Coregas, and compressed air was used as sweep gasses. Alumina micro crucibles (Al_2O_3 100/80 µL) were used for simultaneous thermal analysis (STA). A Metller Toledo digital balance of ±0.0001 g (±0.01mg) was used for sample weighing. A combustion boat (Porcelain glazed Al_2O_3) was used in transpiration tests. Borosilicate glass tubes and high purity alumina crucibles were used for salt dehydration, melting and homogenization. Silica gel/drying agents SiO_2 [331] was used for moisture absorbance inside a Duran vacuum desiccator.

6.2 TEST APPARATUS

A SETARAM DSC/TGA/DTA-SETSYS Evolution 18 analyzer unit (heat flux DSC/DTA-TGA) coupled with Pfeiffer QUADSTAR-422 mass spectrometer was used for thermal and evolved gas analysis, as shown in Figure 6.2.1(a). The simultaneous thermal analyzer (STA) equipped with alumina reaction tube which is placed inside a cylindrical shape graphite furnace‘s heating element and enclosed with insulation of graphite felt. The graphite felt is surrounded by cooling water circuit, as shown in Figure 6.2.1 (b). The STA furnace consists of digital hang down microbalance; digital mass flow controller (MFC precision 0.2% full scale) equipped with carrier and auxiliary gas mixture circuits; sample and furnace thermocouple transducers; pressure transducers; primary and secondary vacuum; and command module unit. The MS unit was connected to the outlet port of the DTA/DSC furnace and was used to detect multiple ions of evolved gasses. A platinum/platinum-rhodium10% S-type thermocouple (-50ºC to 1600ºC) was used in DSC/TGA quantitative measurements. And platinum-rhodium6%/platinum-rhodium30% protected B-type thermocouple (150ºC to 1700ºC) was used for DTA/TGA qualitative measurements. Water, air, gas cylinders (argon, oxygen) and vacuum pump were connected to the simultaneous DSC/TGA- MS analyzer. The mass spectrometer‘s inlet was connected to the outlet of STA. A computer was connected with the simultaneous DSC/TGA and Mass spectrometry via Ethernet links to control the apparatus via CPU and machine command module unit. Pre-installed data acquisition and processing software were used for tested thermal curves gathering and analysis.

A Nabertherm TR60/B180 oven furnace with resistance heating was used for dehydration, as shown in Figure 6.2.2. A Labec VTF 50/12 Vertical Tube Furnace and a Labec HTF 50/12 Horizontal Tube Furnace were used for transpiration test purpose, as illustrated in Figure 6.2.3. An XRD, SEM/EDS apparatus were used for sample phase and morphology study, are shown in Figure 6.2.a (a) and Figure 6.2.4 (b) respectively. Both the horizontal and vertical tube furnaces are 0.6 meters in length and have an internal diameter of 0.05 meter with stainless steel exterior. Maximum heating lengths are 0.540 meter for each furnace. The heating elements equipped with a euro-therm digital microprocessor based

PID (Proportional-Integrative-derivative) temperature controllers. The electrical heating element, ‗Kanthal wire‘ winding spaced inside light weighted ceramic fiber board equipped with an N-type temperature sensor which can operate up to 1200ºC, maximum ramp rate of 30ºC/min and with power consumption of 2000W. A gas cylinder was connected to de-oxidation vertical tube furnace via polyvinyl chloride clear gas tubes and high-pressure gas tubes. De-oxidation furnace was used to remove ppm content oxygen from argon gas. An MPB 1200 series variable area gas flow meter of 1 liter/minute capacity was connected to VT furnace, and then gas outlet tube from the VT furnace is then connected to transpiration rig a HT furnace‘s inlet portion. A gas trap was fitted at the outlet of the HT furnace. The system was sealed using high temperature silica adhesive gel.

Figure 6.2.1 (a): SETSYS Evol simultaneous DSC/DTA-TGA and coupled MS Pfeiffer Units.

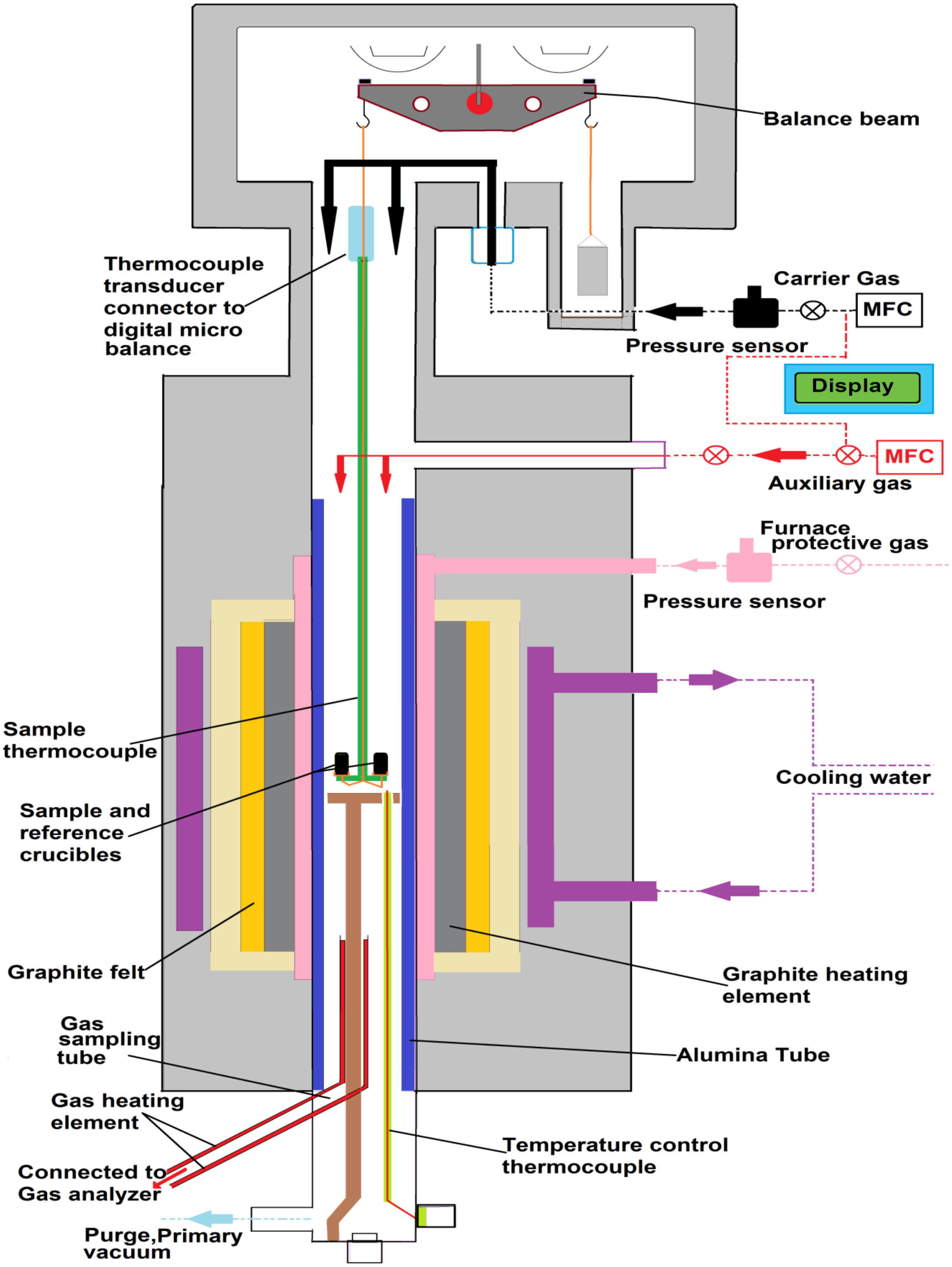

Figure 6.2.1 (b): A simple schematic diagram of STA (DSC/DTA-TGA) furnace [332].

Figure 6.2.2: Nabertherm TR60/B180 oven furnace.

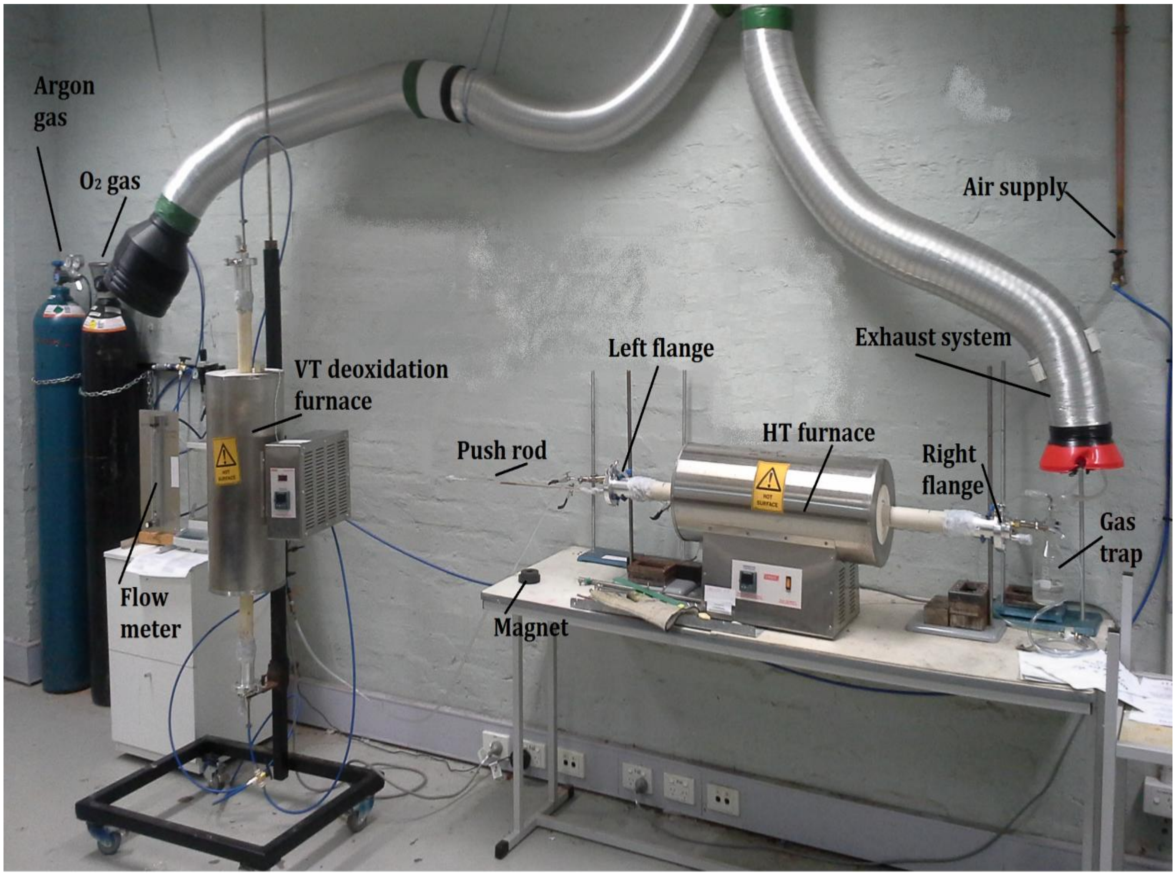

Figure 6.2.3: Full view of the transpiration rig. A de-oxidation vertical tube furnace connected to the gas cylinders, air supply port, and flow meter; horizontal tube furnace; gas trap and exhaust system from left hand side of the image.

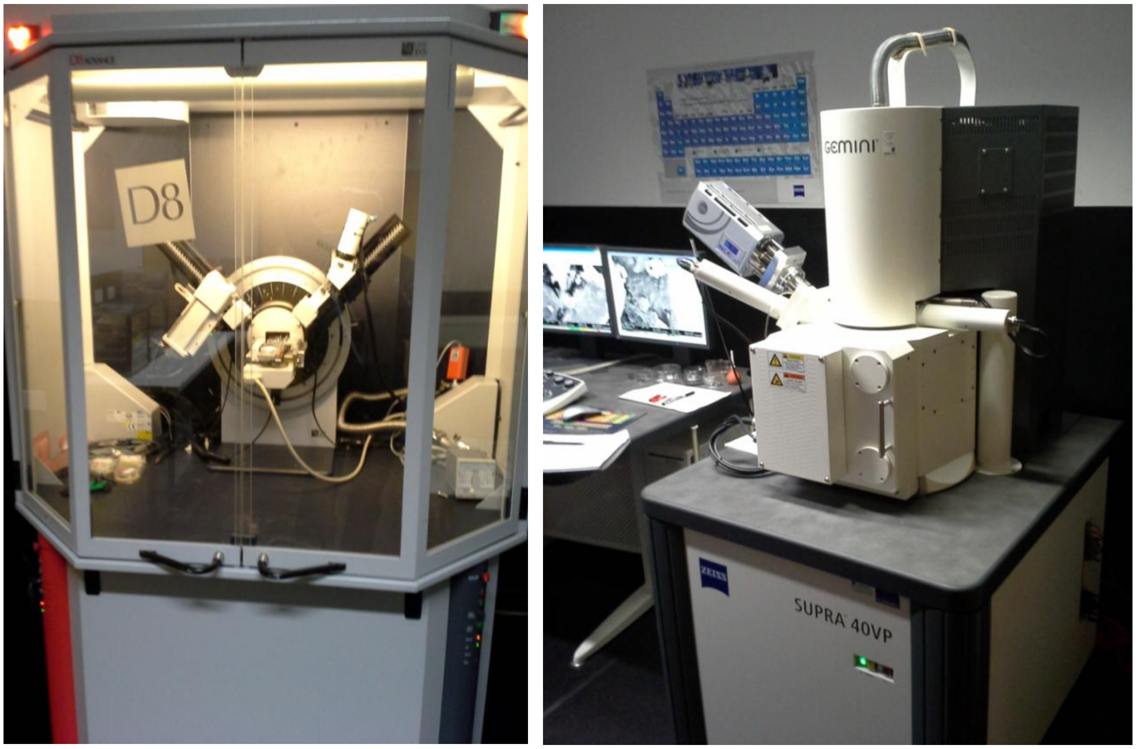

(a) (b)

Figure 6.2.4: (a) BRUKER D8 Advanced X-ray diffractometer. (b) *Carl Zeiss supra 40vp* Scanning electron microscopy and *Gemini Oxford INCA energy 250* Energy-dispersive X-ray spectroscopy.

6.3 Safety equipment

Safety goggle was used to protect the eye, disposable nitrile gloves were used for salt handling, heat resistance gloves were used to handle salt melt, 3m respirator toxic gas purifier mask was used during the experiment. Lab coat and protective shoes were worn all the time [333, 334]. Sample handling, risk assessment sheet, materials safety data sheet (MSDS) and standard operation procedure (SOP) were prepared for this experimental study.

6.4 SAMPLE PREPARATION

The ternary salt composition was used from FACTSAGE [39] formulation using "Phase diagram" module; details are shown in Appendix F. And binary Na-K//NO_3 salt composition is similar to that Hitec solar salt. As consistent with earlier studies by Reddy et al., Abe et al., and Skoog et al. [33, 109, 335, 336], the dehydration of salts were carried out separately at 110°C for 24 hours in air in ceramic crucibles in a drying oven furnace [33, 109, 335, 336]. Then using a stainless steel spatula the dried salts were weighed separately as 3 g each in a microbalance with ±0.001 g accuracy. The salts were mixed and weighed using a microbalance at composition described in Table 6.4.1 to obtain 5 g samples each (for binary and ternary). The stoichiometric calculation of each sample‘s composition is described in Appendix G.

Table 6.4.1: Binary and ternary salt samples composition.

Salt system name	Salt compound	Supplier	Purity (%)	Form	Weight percentage	Mole percentage
Binary solar [35]	$NaNO_3$	Sigma Aldrich	99.995	Anhydrous white powders, Reagent grade	60	64
	KNO_3		99.997		40	36
Ternary [39]	$NaNO_3$		99.995		13.23	13.53
	KNO_3		99.997		57.14	49.12
	$LiNO_3$		99.99		29.63	37.35

Then the 5gm salt mixture for both salts was placed in pyrex crucible and melted in an oven furnace. Binary salt was heated at 250°C, and the ternary salt mixture was heated at 150°C. The mixture was kept in molten state for 2 hours to achieve homogenization at their respective heating temperatures. Then the salts were cooled by slow cooling for overnight by keeping the salts insulated and turning off the furnace. Then the quenched mixture was crushed and ground into fine powder using mortar and pestle and the heating process repeated for three times to ensure proper mixing. Finally, they were stored in a master container and placed in the desiccator before subsequent testing, as shown in Figures 6.4.1 (a), (b) and (c).

Figure 6.4.1 (a): Ternary nitrate salt after weighing and before storing in a container.

(b) (c)

Figure 6.4.1: (b) Freshly prepared binary (left hand side) and ternary salt containers before storing into desiccator. (c) Vacuum Duran stop cock desiccator for salt mixtures storage.

6.5 THERMAL ANALYSIS APPARATUS CALIBRATION

The simultaneous DSC/DTA-TGA Setsys evolution apparatus (STA) has DSC heat-flow sensor resolution of 1μW, DTA heat-flow sensor resolution 0.4μW; root mean square (RMS) noise of 20μW. The TGA works with hanging digital microbalance which has a measuring range of ±200mg and of 0.002 μg resolution (RMS noise 0.03μg). The graphite furnace operated with digital mass flow controller (range from 4 to 200ml/min) has scanning range from 0.01 to 100°C/min and can work up to 2400°C depending upon thermocouple transducer type used. The STA were calibrated for temperature correction coefficient and heat sensitivity coefficient using standard certified reference materials (CRM) according to ASTM, NIST and ISO guide [337-343]. The CRMs, namely pure (purity of 4N or 99.99%) Indium, Lead, Aluminium and Aurum were placed in alumina crucibles and heated in DTA/DSC furnace by which temperature range from 150 to 1100°C was covered. The calibration tests for each standard CRM were performed in argon (20ml/min) in three scanning rates 5, 10 and 15°C/min. A built-in least square optimization routine was used to calculate these coefficients are discussed in Appendix H. The error associated with temperature uncertainty was ±4.9°C, heat sensitivity variation was ±3.02J/g, and the noise level was ±6.7 mK, which are discussed in Appendix H.

The heating action parameters P, I, D and U were pre-set for S-type Platinum/Platinum-Rhodium 10% DSC/TGA transducer thermocouple (proportional: 200°C, Integral: 15s, derivative: 1000s and rate action: 0) and B-type Pt-Rh6%/Pt-Rh30% DTA/TGA transducer thermocouple (proportional: 455°C, Integral: 950s, derivative: 4s and rate action: 1). A water line and three gas lines (for argon, air, and oxygen) were connected behind thermal analyzer gas inlet port which was controlled automatically using command module. A vacuum pump was connected to the simultaneous DSC/TGA-MS analyzer unit.

6.6 THERMAL AND OFF GAS ANALYSIS TEST PROCEDURE

A laboratory desktop computer was connected with the simultaneous DSC/DTA-TGA and MS apparatus via Ethernet links to control the simultaneous thermal analyzer and MS unit via CPU and machine command module controller. Two pre-installed software, Calisto data acquisition, and processing were used for tested thermogram data gathering (DSC/DTA-TGA) and analysis. In the case of evolved gasses detection in MS unit, the curves were recorded in Quadera software and imported in ASCII file format into Calisto software to process data with other simultaneous curves. The detailed working procedures of DSC/TGA and MS unit are described in subsection 3.4 in Chapter 3 of this thesis.

After weighing the sample was loaded in an alumina crucible and placed in thermocouple sample holder pan along with an empty reference crucible, shown in Figures 6.6.1 and 6.6.2. Then the balance head was adjusted manually to null position and with automated switch the sample holder thermocouple was entered vertically inside DSC/DTA-TGA furnace and finally the head was closed provided sealing. After loading samples in the furnace, the chamber was placed under a vacuum using Pfeiffer vacuum pump and then purged with test gas (either inert or oxidative) of desired flow rate. Once the pressure inside chamber attains atmospheric pressure (around 1040mbar), then the sample was adjusted to 0 mg, and finally, protective gas and water flow were turned on before starting heat treatment run. A protective gas and cold water were circulated adjacent to the furnace wall for cooling purpose and to prevent any thermal crack. For the entire period of the experiment the DSC/DTA-TGA furnace chamber was purged with desired carrier gas to carry away the evolved mass to either exhaust system or inside mass spectrometry vacuum chamber. A digital thermobalance connected to thermocouple transducer sample holder recorded fractional weight change, heat flow variation of sample crucible compared to an empty reference crucible as a function of time and temperature. In the case of mass spectrometry test the tungsten filament and inlet capillary tube which were connected to the gas outlet port of DTA/DSC-TGA furnace were heated prior to vacuum. After heating (150°C), the spectrometry ionization chamber of MS unit was subjected to high vacuum (from atmospheric pressure to 10^{-7} mbar) for evolved gas analysis.

To avoid buoyancy in TG and DSC/DTA curves, all test results were subtracted from blank run [344]. When sample mass was greater than 40mg during higher heating temperature the sample started creeping out from crucible (may be bubbling) caused the baseline drift in curves [34]. Also, the crept salt and vapor chemically attacked the DSC sensor and cause straining in protected DTA sensor. A typical brown staining observed in the DSC/TGA rod and sensor surface. Thus, the protected DTA/TGA rod was used to prevent high temperature stress corrosion cracking of thermocouple wire. After every run, a through chemical cleaning was performed, followed by heating the rod up to 1000°C in argon to remove any further residue. This procedure will eliminate any deposition on the rod before running next test.

The thermal analyses that are presented in Chapters 7 and 8 consist of 4 curves. The red line indicates sample heating and cooling temperature steps in degree Celsius with certain data acquisition periods (typical ranges 0.2seconds to 1.2 seconds) which follows the set point temperature. The green curve named as TGA indicates the weight change of the salt sample in milligram with respect to time and temperature. Usually, when there is no weight change the TGA curve remains flat/horizontal (except in the case of buoyancy and smearing). The blue curve is the heat flow curve in either milli-watt (in the case of DSC/TGA transducer) or micro-volt (in the case of DTA/TGA transducer). When the HF curve is horizontal (no discontinuity), usually it indicates no transformation or reaction; and no change in measured signal. In this study, a blank run was performed before each test, and blank HF curve was subtracted from sample HF curve to obtain a constant horizontal baseline. Deviation from horizontal baseline was indicating a change in heat flow, either endothermic or exothermic reactions of the tested sample. In this study, by convention, the upward heat flow peak is taken as an exothermic reaction (heat released by the sample crucible) and downward directed of heat flow peak taken as an endothermic reaction (heat absorbed by the sample crucible). As standard usually a baseline integration (in this study mainly tangential sigmoidal and linear baseline integration methods were used) was constructed to observe the heat flow curve deviation in mW or μV, which has been described in Appendix B. The MS curves were of several colors with name labels indicate various gaseous product evolution.

Single salts: $NaNO_3$, KNO_3 and $LiNO_3$; binary: $NaNO_3$-KNO_3 salt; and ternary $NaNO_3$-KNO_3-$LiNO_3$ salt systems were subjected to programmed heating and cooling (at different scanning rates) in DSC/DTA-TGA-MS apparatus. Samples were heated from room temperature to certain higher temperature in three atmospheres, argon, air and in oxygen. The salt sample was mounted in high purity (DSC 100μL and DTA 80μL capacity) alumina micro crucible without lid together with an identical empty crucible without lid, as shown in Figures 6.6.1 and 6.6.2. The sample and reference crucibles situated side by side in either S-type DSC/TGA metallic sample holder or B-type DTA/TGA alumina-metallic sample holder and suspended from digital balance head, as shown in Figures 6.6.1 and 6.6.2 respectively. Since the DSC/TGA simultaneous balance transducer has higher sensitivity (heat flow and temperature coefficients) thus used for transition and melting points detection. The DTA/TGA transducer rod has a protective ceramic jacket to prevent thermocouple metallic part exposure from salt vapor was used for high temperature thermal stability test. Before each test, a duplicate blank run test was performed using two identical empty crucibles, as shown in Figure 6.6.3. A blank run was carried out at high sweep gas velocities and desired set point parameters (heating and cooling rates, temperatures) and subtracted from original test to reduce the effect of buoyancy in measured curves.

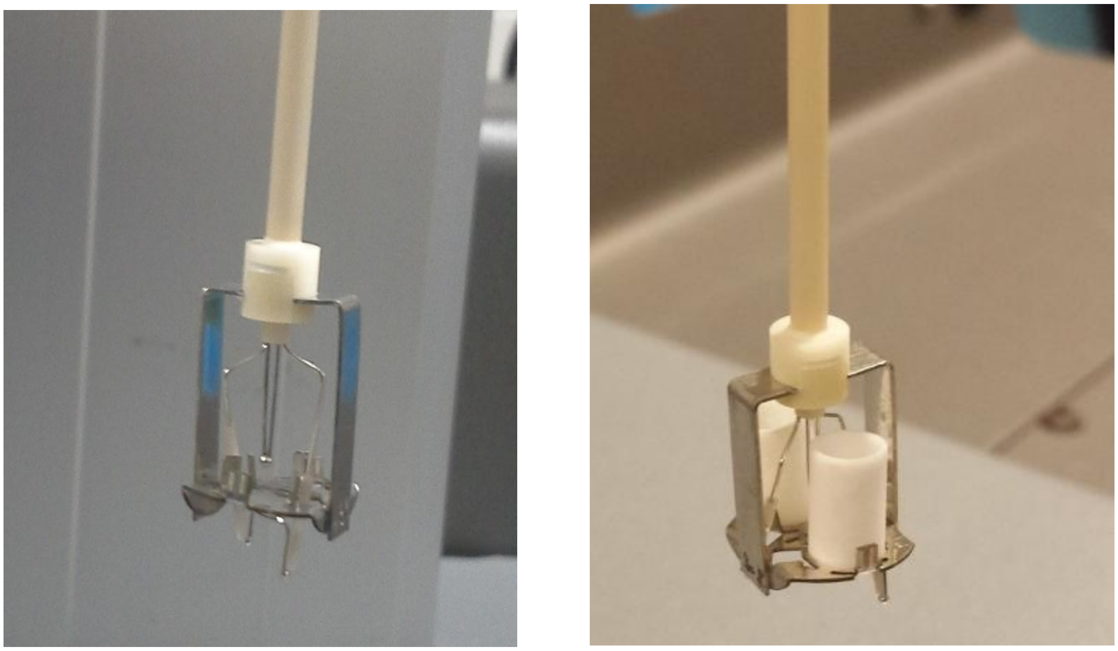

(a) (b)

Figure 6.6.1: (a) DSC/TGA thermocouple transducer sample plate holder. (b) DSC/TGA with 100μL sample and reference crucibles mounted on a metal plate from left hand side of the image.

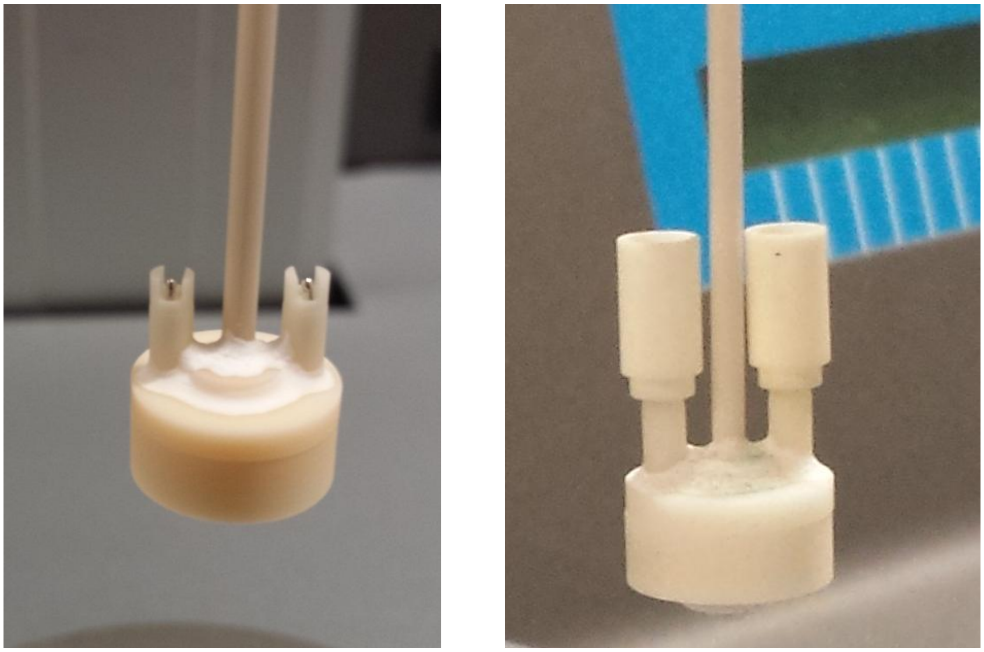

(a) (b)

Figure 6.6.2: (a) Protected DTA/TGA thermocouple rod with the protected ceramic jacket. (b) DTA/TGA with 80μL reference and sample crucibles mounted on holder tips from left hand side of the image.

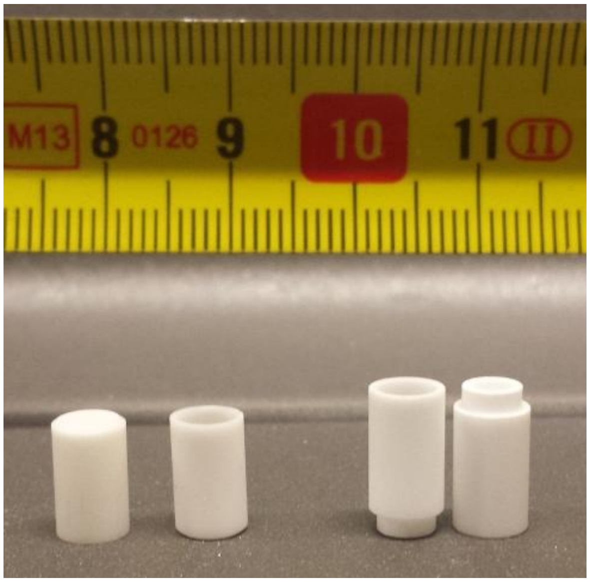

Figure 6.6.3: High purity 100μL alumina DSC/TGA crucibles and 80μL alumina DTA/TGA crucibles from left to right respectively.

During thermal events detection, 5 successive heating and cooling runs were carried out for a single sample with same temperature increment and decrement rates. The reason was to observe any weight change or change in heat flow peaks. The first cycle test was done to ensure the solid salt melted completely, has full contact with crucible base and to remove moisture. During this five heating cooling cycles, the only first cycle was shown some weight loss which attributes to sample dehydration also showed by H_2O evolution in MS curves. The salt absorbed moisture easily during weighing and loading. Thus, first cycle peak always varied from sample to sample because of moisture pickup and improper contact between salt and crucible base. The last four runs were compared with each other to observe at least three consecutive repeatable curves. If after first cycle, there were consequent weights loss occurs in successive cycles; total weight change was greater than 2wt% of the original sample mass, and the melting and solidification peaks were dissimilar then the data were discarded, and a new set of samples were tested with modified set point temperature. The change in weight and HF peaks below decomposition temperature usually happened for binary and ternary mixtures because of the heating temperature is much higher and close to decomposition temperature to cause little vaporization of sample and subsequently change in heat of melting and solidification peak values. Or, the salt mixture was not homogeneous and oxide ions might form during sample preparation in contact with air. Although an investigation by ICPOES (Inductively coupled plasma atomic emission spectroscopy) and ion chromatography confirmed that the possibility of the presence of oxides, nitrites and other elements during sample preparation was less, as discussed in section 7.5 in Chapter 7 of this thesis. Usually, common air impurities such as CO_2 or H_2O tend to react with salt melt and may produce carbonate and hydroxide species.

For decomposition test, the sample was heated from room temperature to final high temperature and cooled off to room temperature. Based on TGA, DSC/DTA, and MS curve the rapid weight loss point; the irreversible endothermic event was detected; along the evolution of gasses from MS curves.

Nitrates are corrosive salts according to the Ellingham diagrams for oxyanions, emitting NO_x including NO_2, which chemically attack the platinum [345]. A typical brown staining observed in the DSC/TGA rod and sensor surface after the test, as shown in Figure 6.6.4 a. Thus after each test, DSC/DTA rod was taken out for thorough cleaning to remove any contamination, stain or residue (typically brown stain observed around the sensor [26]). At first, the sensor was put in hot distilled water (120°C) for half an hour and rinsed thoroughly. Then the DSC/TGA rod was heated in argon in DSC/DTA-TGA furnace at 20°C/min up to 1000°C to remove remaining residue. The DTA/TGA supplied by Setaram had protected sensor wire opening, was not enough to prevent high temperature corrosion damage. A damaged DTA and DSC transducers are shown in Figures 6.6.4 a, 6.6.4 b and 6.6.4 c. Lower gas flow rates were avoided to inhibit thermocouple-sample vapor contact.

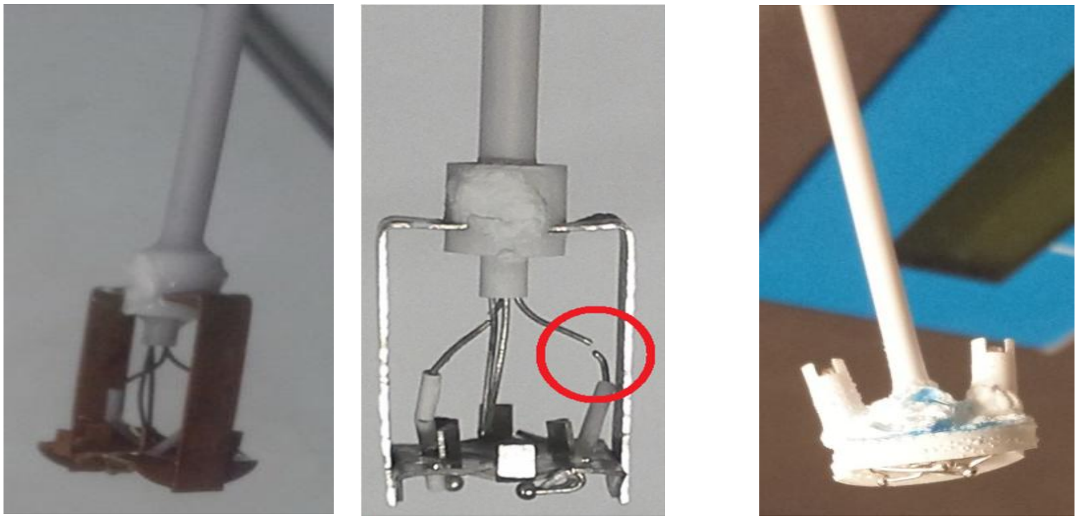

(a) (b) (c)

Figure 6.6.4: (a) A chemically strained DSC/TGA rod. (b) A wire damaged DSC/TGA transducer marked in red circle. (c) Distorted and broken sample holder of the protected DTA/TGA rod.

Before the final test, a ternary salt of same mass was heated in identical experimental condition with AMU scanning range from 0 to 200 (Faraday MID: for all gas detection) to detect evolved gasses. The dwell time was 500 milliseconds (tracking speed: 500ms/amu). 500ms was chosen to avoid larger file size. At or during decomposition only a few gaseous product showed significant peaks and were consistent for longer periods, thus during final tests only O_2 , N_2 , NO , NO_2 , N_2O gaseous products with distinguishable AMU were considered for ion current intensity measurement (selecting Faraday Scan stair: for individual gases detection). Other ionic species such as pyronitrate ($N_2O_7{}^{-4}$), ortho nitrate ($NO_4{}^{-3}$) and nitryl ($NO_2{}^{+}$) [346] might be non-existent or insignificant and have no supporting evidence in literature. Also the preliminary test didn't show any peaks in support of this species. Hence they were not considered for measurement. The condensed phases such as nitrates, nitrites, metal oxides, peroxides and super oxides were not possible to measure in this study because of micro size sample.

In an air atmosphere, the O_2 and N_2 were unable to detect wherein oxygen atmosphere the O_2 evolution was not detected. The spectra library from Quadera software has all possible products AMU (atomic mass unit) chart [347], as shown in Appendix I. Taking reference from this library it can be concluded that argon was occupying 20 (an isotope of argon) and 40 AMU bar. AMU bar of 28 was indicating either N_2 or air. In the case of the argon atmosphere, 28 AMU was considered as N_2 gas. AMU bar 17 and 18 were indicating H_2O, which was moisture in sample evolved during the holding stage for dehydration. The 30 AMU bar was indicating nitrous/NO gas evolution which is very common gas formation during decomposition as discussed in Chapter 3. The AMU bar 32 was indicating O_2 is another primary decomposition product of alkali nitrates. AMU 46 indicated NO_2 and AMU 44 indicated N_2O gas. Other smaller intensity peaks and randomly appeared peaks were ignored such as AMU 14 indicating nitrogen ion and 16 indicating oxygen ion.

6.7 THE TRANSPIRATION METHOD TEST PROCEDURE

In this study, a horizontal tube (HT) furnace was used for heating the pre-weighed samples in combustion boat as shown schematically in Figures 6.7.1 and 6.7.2. A vertical tube (VT) furnace was used as de-oxidation furnace for removing trace amount of oxygen from high purity argon. The gas cylinder, de-oxidation VT furnace, flow meter, HT furnace, and gas trap were connected in series via polyvinyl clear gas tube and the whole system was sealed using silica adhesive to prevent any gas leak.

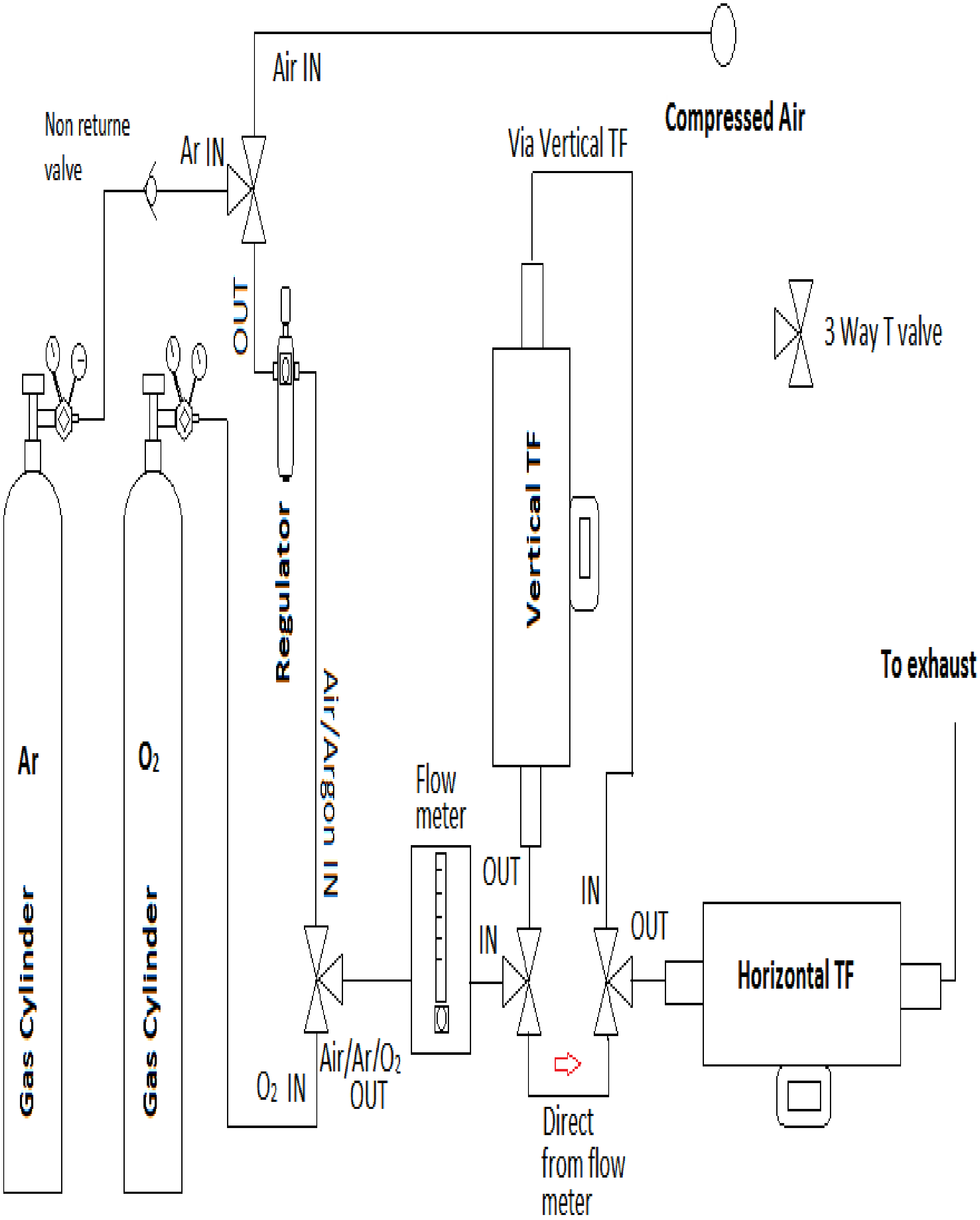

Figure 6.7.1: Full transpiration rig setup with piping and valve assembly.

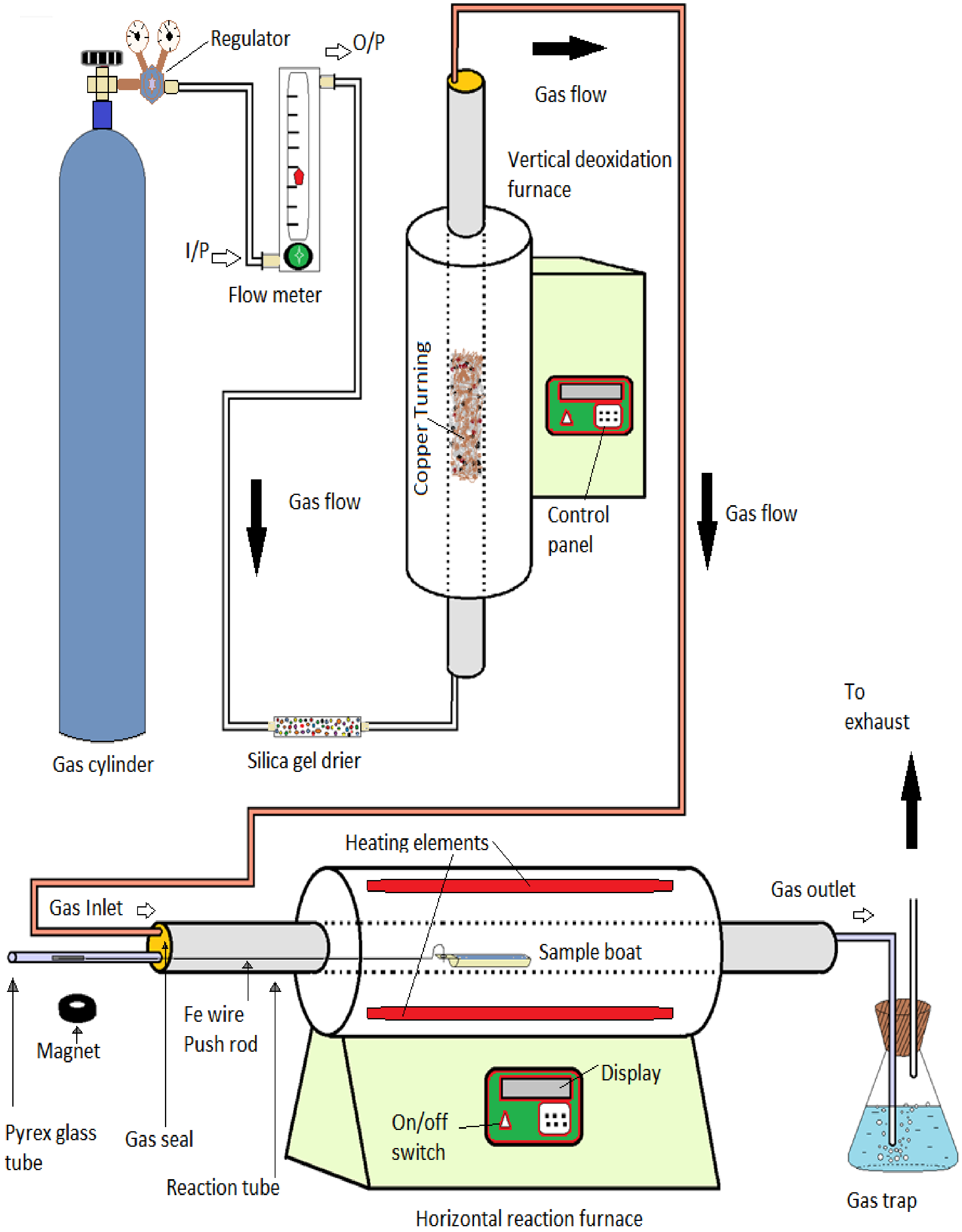

Figure 6.7.2: A simple schematic diagram of transpiration test rig.

At first, the electrical connections, gas connections were inspected for any visible damage. The sample and ceramic boat were weighed separately, and the actual sample weight was calculated. The mullite tube was inserted into the horizontal tube furnace from left hand side, and flange cap arrangement was adjusted using high temperature silica gel adhesive. The ceramic boat was inserted to the left end of mullite tube, and the flanges were tightened to provide sealed atmosphere. The test rig was closed from both ends using flange-clamp arrangement. The gas flow was checked from the exit side of the horizontal tube furnace using a gas trap bottle, as shown schematically in Figure 6.7.2. Argon gas cylinder valve (or air valve) was opened slowly, and the furnace was turned on. After a set period, the tube was opened, and the sample boat was inserted and sealed.

Argon gas from the cylinder was passed via a flow meter and deoxidized in preheated VT furnace. O_2 and air were passed through HT furnace directly using three-way valves, as shown in Figure 6.7.1. The argon was passed via inside VT furnace which was preheated to 700°C. At isothermal zone section (an approximately middle portion of the reaction furnace) of VT furnace, copper chips were placed to oxidize any ppm content of O_2 that might present in argon. Ellingham diagram indicates that the copper-copper oxide showed an equilibrium at 700°C when partial pressure of oxygen (P_{O_2}) is 10^{-10} (parts per million) atmosphere.

Gas from a flow meter or VT furnace was entered in HT furnace saturating the sample and carrying the vapor toward the right end of the HT furnace, as shown in Figures 6.7.1 and 6.7.2. In the gas exit outlet, a gas trap beaker was connected via a tube to ensure gas was passing through the system and finally the sweep gas escaped to atmosphere via the industrial exhaust system. A push rod made of ferrous; an o-ring magnet and glass tube assembly was placed below the gas inlet mounting on the left side of HT furnace to facilitate movement of sample boat toward the isothermal zone without breaking seals during the running of the experiment.

Before actual test the temperature profiles measurement was carried out at various heating temperature. A K-type thermocouple was used to determine temperature profiles of HT furnace at various positions of the tube to find out isothermal zone for a given set point temperature. The details procedure are described in Appendix K. Before each experiment the system was checked for a potential gas leak with classic ‗soap water leak' test. Electrical connections were inspected for any visible damage or loose connections. The measurement errors (flow rate, temperature, and weight) are outlined in Appendix K.

After each run the combustion boat was taken out breaking the seal (by removing flange cap) and weighed in digital balance very quickly to avoid moisture absorbance. Figure 6.7.3 showing a combustion boat carrying binary solar nitrate salt caked or solidified rapidly. After weighing, the sample boat was put back inside the tube, and the seal was activated again (flanged was closed by aluminum swing clamp-screw arrangement), then with the help of magnet the steel rod inside glass tube was pushed horizontally towards the center of the furnace to guide the boat in the isothermal zone.

Figure 6.7.3: The binary salt two minutes after brought out from HT furnace. Within a short period, the salt surface started to crystallize.

6.8 THE PHASE AND MORPHOLOGY STUDY: TEST PROCEDURE

XRD

X-ray diffraction analyses were performed to identify the phase of the salt sample using an ―Advanced Bruker D8" X-ray diffractometer. XRD equipped with a graphite monochromator emitting Cu K_α radiation (*with θ ranging from 2.5° to 45°; step size was*

0.02°; with scan rate 0.02°/min; and $\lambda = 1.5406\text{Å}$). Grains size of tested sample was calculated using Scherrer‘s equation:

$$B = \frac{k\lambda}{D \cos\theta} \qquad \text{eqn 6.8.1}$$

Here,
B = width of XRD peaks (full width at half maximum peaks) rad,
k =Scherrer constant,
λ = CuKα incident radiation‘s wave length (0.15406 nm),
D=average crystallite/grain size (nm),
θ =half diffraction angle.

The sample was placed in a standard ray targeted area of (25mm diameter) a sample holder for diffraction pattern measurement. The powder salt sample was deposited on the shallow portion of the sample holder and was pushed with a flat plate from top to make a compact, smooth and flat sample surface for effective absorption of X-ray. The data were collected from 0° to 90° of 2θ angle and recorded via software. From software reference files of inorganic compound‘s structure, the unknown peaks were identified.

SEM and EDS

The morphology and texture of the salt substrate recorded with field emission scanning using a ―Carl Zeiss Supra 40 VP" scanning electron microscope. An ―Oxford INCA energy 250" energy dispersive X-ray spectroscope (EDX or EDS) was used to identify the elemental compositions of the sample. As the salt samples were nonconductive thus before SEM/EDS, test a gold sputtering was performed at 10 Nano gram scale on the salt substrate.

Chapter 7 Results: Single & binary nitrate salts

7.1 Thermal analysis of single and binary nitrate salts

In this chapter, three single nitrate salts: $LiNO_3$, $NaNO_3$, KNO_3 and binary 60:40 wt. ratio of $NaNO_3$-KNO_3 solar salt subjected to thermal analysis and transpiration test was discussed with the aid of apparatus software ‗Calisto‘ [332] and ‗Quadera‘ [347]. The salt sample mounted in high purity 100 µL capacity alumina micro crucible in the case of DSC/TGA transducer and 80 µL alumina micro crucible in the case of protected DTA/TGA transducer thermocouple. Using Calisto [332] software the sample weight loss at various stages, transition HF peaks, melting HF peaks, onset and offset peak temperatures were detected and the subsequent explanation is provided. Using Quadera [347] software, the evolved gasses were detected, and the decomposition temperatures were identified.

For pre-melting and melting events detection such as, solid-solid transition, melting and freezing points the single and binary salts were subjected to DSC/TGA heating and cooling in argon atmosphere (40ml/min) at various ranges of scanning rates: 1, 2, 4, 5, 6, 8, 10 and 15°C/min. All tests were conducted in 100µL alumina crucibles of same batch (Setaram Instruments) and with same starting a salt mass of 35.00 mg (±0.03 mg). All salts were heated just above their respective melting point to avoid any possible vaporization. Before the melting-freezing test, the salts were held at 110°C for an hour to remove moisture.

In the case of thermal degradation temperature detection tests, the salts were heated from 50°C to 800°C in three atmospheres: argon, air, and oxygen using a protected DTA/TGA-MS simultaneous thermal analyzer (STA). All tests were conducted in 80µL alumina crucibles of same batch (Setaram Instruments) and with same starting a salt mass of 35.00 mg (±0.03 mg). In each atmosphere, the salts were heated at identical sweep gas velocity of 40ml/min and 10°C/min heating-cooling rates to observe the effect of blanket gasses on decomposition behavior. The reason to choose the small volume of 35 mg or 35 µL as starting mass is to avoid salt overflow from crucible which commonly known as high temperature volume expansion and subsequent ―creeping” [34] and also to sustain for the full decomposition test. The gas flow rate was chosen 40ml/min (upper limit of the apparatus is 200ml/min) to avoid buoyancy. The upper temperature was chosen an optimal 800°C to minimize thermocouple deterioration in contact of corrosive sample vapor.

7.2 RESULTS

7.2.1 RESULTS: TRANSITION, MELTING, AND FREEZING TEMPERATURES AT VARIOUS HEATING-COOLING RATES

The $LiNO_3$ were subjected to heating and cooling in DSC/TGA from 50 to 265°C for melting and solidification peaks detection in argon atmosphere in following range of heating-cooling rates: 1, 2, 4, 5, 6, 8, 10 and 15°C/min, as shown in Figures 7.1.1 and 7.1.2. At 10°C/min heating and cooling rate, $LiNO_3$ melted (liquidus onset) at 257.7°C and solidified at 241.8°C. The heat of melting and heat of solidification was 355.9J/g and -350.9J/g respectively, as shown in Table 7.2.2.1.

The $NaNO_3$ were subjected to heating and cooling in DSC/TGA from 50 to 315°C for melting and solidification peaks detection in argon atmosphere in following range of heating-cooling rates: 1, 2, 4, 5, 6, 8, 10 and 15°C/min, as shown in Figures 7.1.3 and 7.1.4. At 10°C/min heating and cooling rate, $NaNO_3$ showed solid-solid transition peak temperature at 272.5°C before melting with the heat of transition 30.7J/g and 264°C transition peak temperature before solidification with the heat of transition -19J/g. The salt melted (liquidus onset) at 301.4°C and solidified at 298.8°C. The heat of melting and heat of solidification was 177.9J/g and -167J/g respectively, as shown in Table 7.2.2.1. A smaller peak was appeared just before melting after the solid-solid transition at each scanning rate, as shown in Figure 7.1.3. A similar peak was observed at lower cooling rates just prior to solidification, as shown in Figure 7.1.4.

The KNO_3 were subjected to heating and cooling in DSC/TGA from 50 to 345°C for melting and solidification peaks detection in argon atmosphere in following range of heating-cooling rates: 1, 2, 4, 5, 6, 8, 10 and 15°C/min, as shown in Figures 7.1.5 and 7.1.6. At 10°C/min heating and cooling rate, KNO_3 showed solid-solid transition peak temperature at 142°C prior to melting with heat of transition 38.9J/g and 115.2°C transition peak temperature prior to solidification with heat of transition -19.1J/g. The salt melted (liquidus onset) at 331°C and solidified at 326.8°C. The heat of melting and heat of solidification was 95J/g and -88.8J/g respectively, as shown in Table 7.2.2.1. A smaller peak appeared just prior to melting and solidification at each scanning rate, as shown in Figures 7.1.5 and 7.1.6. Two unusual small peaks were appeared before transition peaks during cooling at 2 and 4°C/min cooling rates, as shown in Figure 7.1.6.

The binary $NaNO_3$-KNO_3 were subjected to heating and cooling in DSC/TGA from 50 to 235°C for melting and solidification peaks detection in argon atmosphere in following range of heating-cooling rates: 1, 2, 4, 5, 6, 8, 10 and 15°C/min, as shown in Figures 7.1.7 and 7.1.8. At 10°C/min heating and cooling rate, binary nitrate showed solid-solid transition peak temperature at 128.3°C prior to melting with heat of transition 16.8J/g. At 10°C/min heating-cooling rate, the salt melted (liquidus onset) at 218.1°C and solidified at 223.6°C. The heat of melting and heat of solidification was 105.9J/g and -106.2J/g respectively, as shown in Table 7.2.2.1. The solid-solid transition was only appeared during first heating step prior to melting and during cooling the transition peak was merged with solidification peak at each cooling rate. The solidification peaks showed a step near solidification onset temperature at each scanning rate.

At 10°C/min heating and cooling rate, there was 15.9°C temperature difference between liquidus and solidus temperature for $LiNO_3$, 2.6°C temperature difference between liquidus and solidus temperature for $NaNO_3$, 3.8°C temperature difference between liquidus and solidus temperature for KNO_3 and 5.6°C temperature difference between liquidus and solidus temperature for binary $NaNO_3$-KNO_3, as shown in Table 7.2.2.1. At 1°C/min heating and cooling rate, there was 10.2°C temperature difference between liquidus and solidus temperature for $LiNO_3$, 1.9°C temperature difference between liquidus and solidus temperature for $NaNO_3$, 0.7°C temperature difference between liquidus and solidus temperature for KNO_3 and 11.8°C temperature difference between liquidus and solidus temperature for binary $NaNO_3$-KNO_3.

The salt samples subjected to different heating rates were showed different heat flow curves, as shown in Figures 7.1.1 to 7.1.8 and summarized in Table 7.2.2.1. Most of the cases the transition peaks, melting, and solidification peaks were increased with increasing heating rates. The heat required for melting and heat released during solidification were also increased with increasing scanning rates. Similarly the onset temperatures of melting, solidification and transition were affected due to heating-cooling rates increment or decrement.

7.2.2 RESULTS: DECOMPOSITION BEHAVIOR

Heating the single and binary nitrate salts from 50 to 800°C, results showed that the decomposition temperature is lower in argon and higher in oxygen. The effect of heating rates for these nitrates was not studied because of test numbers limitation and due to frequent transducer deterioration. The blanket gasses have an effect on rapid weight loss temperatures and heat flow curves as shown in Figures 7.2.1 to 7.2.12. There was no significant trend observed for gaseous evolution temperature while comparing with different atmospheres. The evolution of gaseous species showed sharp increment in intensity at higher temperatures indicated involvement of various decomposition reactions as described in Chapter 3 of this thesis.

The pure $LiNO_3$ showed stability up to 507°C in argon, 540°C in air and 541°C in oxygen. The $NaNO_3$ showed stability up to 568°C in argon, 575°C in air and 590°C in oxygen. The KNO_3 showed stability up to 575°C in argon, 590°C in air and 600°C in oxygen. The binary $NaNO_3$- KNO_3 showed stability up to 570°C in argon, 589°C in air and 603°C in oxygen. The oxygen-rich atmosphere suppressed the decomposition temperature by 34°C compared to the inert atmosphere of argon in the case of $LiNO_3$. The oxygen-rich atmosphere suppressed the decomposition temperature by 22°C compared to the inert atmosphere of argon in the case of $NaNO_3$. The oxygen-rich atmosphere suppressed the decomposition temperature by 25°C compared to the inert atmosphere of argon in the case of KNO_3. The oxygen-rich atmosphere suppressed the decomposition temperature by 33°C compared to the inert atmosphere of argon in the case of binary $NaNO_3$-KNO_3. The NO and

O_2 evolved almost at the same time for all salts as observed in an argon atmosphere, are shown schematically in Figures 7.2.1, 7.2.4, 7.2.7 and 7.2.10. The evolution of other gaseous products at three different atmospheres are summarized in Table 7.2.2.3.

Table 7.2.2.1: Thermal events of single $NaNO_3$, KNO_3, $LiNO_3$ and binary $NaNO_3$-KNO_3 salt (*60-40 weight ratio*) heated at argon atmosphere (flow rate 40ml/min) and at various heating and cooling rates using a Setaram STA DSC/TGA-MS.

Salt type	Thermal events of peak area	Heating and cooling rates (°C/min)							
		1	**2**	**4**	**5**	**6**	**8**	**10**	**15**
$LiNO_3$	Liquidus onset temperature (°C)	252.9	251.7	254.4	255.2	255.8	258.1	257.7	259.9
	Liquidus offset temperature (°C)	254.6	256.8	260.5	260.9	261.8	262.5	263.1	263.1
	Melting peak temperature (°C)	253.9	255	257.7	258.4	258.9	260.4	260.8	261.8
	Solidus onset temperature (°C)	242.7	242.4	242.1	242.4	242.6	242.1	241.8	237.7
	Solidus offset temperature (°C)	241.5	239.6	236.6	235	233.9	231.6	229.5	224
	Freezing peak temperature (°C)	243.2	242.9	240.1	239.2	238.7	236.8	235.5	232.5
	Heat of melting (J/g)	355.5	357.8	358.8	362.5	360.8	353.5	355.9	353.1
	Heat of solidification (J/g)	-383.9	-344.8	-345.5	-343.3	-343.8	-345.4	-350.9	-347.2
	Melting peak height (mW)	-47.2	-71	-99.4	-114.3	-115.2	-124	-122.2	-128.9
	freezing peak height (mW)	80.33	84.9	101.4	111.8	115.3	130	141.4	178.3
$NaNO_3$	Transition peak temperature prior to melting (°C)	270.7	271.1	271.4	271.3	271.4	271.5	272.5	271.9
	Liquidus onset temperature (°C)	300.8	300.8	301	305.5	304.6	306.2	301.4	300.8
	Liquidus offset temperature (°C)	305.3	306.9	309.1	308.9	309.2	310.1	313.2	312.2
	Melting peak temperature (°C)	304.2	305.1	307.3	307.2	307.3	308.4	310.5	309.1
	Solidus onset temperature (°C)	298.9	299.5	299.5	299.5	299.4	299.4	298.8	299.6
	Solidus offset temperature (°C)	295.9	294.1	292.4	291.6	290.7	289	284	285.2
	Freezing peak temperature (°C)	298.1	296.9	296	295.2	295.3	294.2	291.3	292.4
	Transition peak temperature during cooling (°C)	269.3	268.7	267.7	267.3	267.2	266.6	264	264.4
	Heat of transition prior to melting (J/g)	25.5	29.8	32	40.1	41	41.4	30.7	44.4

	Heat of transition during cooling (J/g)	-15.4	-22.6	-36.1	-36.1	-32.3	-30.8	-19	-22.8
	Heat of melting (J/g)	170.6	176.7	175	210	207.1	200.2	177.9	200.3
	Heat of solidification (J/g)	-172.2	-173	-198.7	-201.2	-204.8	-200.1	-167	-196.4
	Melting peak height (mW)	-26.7	-42.1	-61.6	-97.5	-109	-115.4	-75	-130.9
	freezing peak height (mW)	30.3	38.6	65.8	76.6	88.7	97.5	78.2	120.7
KNO_3	Transition peak temperature prior to melting (°C)	128.8	129.6	131	131.5	132	133	142	135.2
	Liquidus onset temperature (°C)	328	327.9	328.2	328.4	328.5	331.1	331	329.2
	Liquidus offset temperature (°C)	332.3	334.3	337	337.7	338.3	338.6	339.8	341.1
	Melting peak temperature (°C)	330.4	331.3	332.6	332.8	333.3	334.7	335.2	335.9
	Solidus onset temperature (°C)	327.3	327.3	327.2	327	326.9	326.9	326.8	326.8
	Solidus offset temperature (°C)	323.7	321.8	319	317.8	316.5	315.1	310.3	309.2
	Freezing peak temperature (°C)	326.1	325.2	323.8	323	322.4	321.4	319.3	319
	Transition peak temperature during cooling (°C)	118.7	117.7, **72.9**[*]	116.8, **84.2**[*]	116	115.7	115.5	115.2	114.4
	Heat of transition prior to melting (J/g)	37.4	37.8	39.2	39.6	38.7	39.5	38.9	42.7
	Heat of transition during cooling (J/g)	-18.9	-19.2	-19.3	-18.1	-18.7	-18.7	-19.1	-19
	Heat of melting (J/g)	84.7	83.8	82.8	85.9	84.8	86.5	95	96.4
	Heat of solidification (J/g)	-84.3	-83.4	-87.8	-84.5	-86	-85.9	-88.8	-84.8
	Melting peak height (mW)	-13.4	-19.2	-26.8	-31.6	-33.6	-47.9	-51.6	-51.6
	freezing peak height (mW)	14.9	20.8	29.4	32.6	35.7	42.7	40.2	49.1
Binary solar salt, 60:40 wt. ratio $NaNO_3$-KNO_3	Transition peak temperature prior to melting (°C)	X	X	X	X	X	X	128.3	X
	Liquidus onset temperature (°C)	217.3	217.4	217.6	217.6	217.7	217.9	218.1	218.5
	Liquidus offset temperature (°C)	232	230.8	232.4	232.3	232.4	232.3	232.2	231.5
	Melting peak temperature (°C)	219.5	221.4	223.5	224.4	224.9	225.7	226.2	226.7
	Solidus onset temperature (°C)	229.1	228.8	228.9	229	224.4	223.9	223.6	223.3
	Solidus offset temperature (°C)	214.4	212.9	210.2	208.8	207.6	205.6	204	201.6
	Freezing peak temperature (°C)	215.8	215	213.8	213.2	212.7	212	211.5	210.6

	Transition peak temperature during cooling (°C)	X	X	X	X	X	X	X	X
	Heat of transition prior to melting (J/g)	X	X	X	X	X	X	16.8	X
	Heat of transition during cooling (J/g)	X	X	X	X	X	X	X	X
	Heat of melting (J/g)	106.2	107.2	108.9	108.4	108.2	107.3	105.9	100.6
	Heat of solidification (J/g)	-110.7	-111	-108.6	-111.8	-109.5	-108.2	-106.2	-99.9
	Melting peak height (mW)	-7.3	-12.3	-20.1	-23.4	-26.3	-30	-31.9	-33.9
	freezing peak height (mW)	7.4	12.7	21.2	25.5	28.1	32.2	34.7	37.5
X indicating no data was acquired. * Indicating different transition peak.									

Table 7.2.2.2: Thermal events comparison of single and binary nitrates heated at 10°C/min heating rate in an argon atmosphere (40ml/min).

Salt type	Thermal events	This study by DSC/TGA -MS	This study by DTA/TGA -MS	Study by others[reference]
$LiNO_3$	$T_{transition}$ (°C)	N/A	N/A	N/A
	T_{fusion} (°C)	257.7	244.8	253[324], 254[208], 254.5[32, 348],
	$T_{crystallization}$ (°C)	241.8	245.1	Nil
	H_{fusion} (J/g)	355.9	360	355.35[32, 348], 363[324],357[349], 370[350],
	$T_{decomposition}$ (°C)	X	507	430[208],
$NaNO_3$	$T_{transition}$ (°C)	272.5, 30.7J/g	259.3	257[351], 267[32], 274[173], 275[352], 275.5[353, 354], 277[349, 355], 273[356], 276[150, 224, 357-360], 263.5[361], 40.1[360], 42.6J/g[358], 11.1J/g[150], 43.3[351], 44.35[354], 45J/g[324], 46.5[359], 52±1.53J/g[349], 8.6J/g[357], 15.3J/g[355],
	T_{fusion} (°C)	301.4	298.5	301[356], 308[208, 350, 362, 363], 305[324, 351], 306[32, 38, 150, 173, 358, 364], 307[357, 360, 363, 365, 366], 310[349, 367], 311[361, 368],
	$T_{crystallization}$ (°C)	298.8	303.7	306[38, 359], 303[356],
	H_{fusion} (J/g)	177.9	180	177[38, 173], 178[369], 172.96[32], 177.66±4.71[349], 174.3[351], 175[364], 176[366], 176.5[360], 176.25[358], 173[324], 172[355, 359], 180[363], 181.65[350, 370], 182[367], 186[368],
	$T_{decomposition}$ (°C)	X	568	510[208], 567±10[34], 520[220],
KNO_3	$T_{transition}$ (°C)	142, 38.9J/g	116.5	130[150, 224, 324], 131[38, 358], 132[365], 132.5[32], 133[349], 128[173, 371-373], 127^{onset}[356], 134^{peak}[356], 129±2[354, 374-377], 120*[374], 105*[374], 48.5[371], 49.95J/g[358], 50.21J/g[150, 173, 377], 50.6J/g[324], 53.5[354, 373, 375], 3.72±1.29J/g[349], 49.65J/g[224, 372, 376],
	T_{fusion} (°C)	331	326.6	331[356], 337[208, 362, 367], 333[350, 358], 334[173, 365], 335[38, 150, 324, 363], 339[32, 349, 361], 334.6[365, 376], 346[368],
	$T_{crystallization}$ (°C)	326.8	333.05	335[38], 335[356],
	H_{fusion} (J/g)	95	90	98.91[32], 103.86±2.97[349, 368], 99.9[367], 99.06[358], 95.2[173], 96.6[324, 376], 98.91±0.8[378], 91[355, 362],106[350], 198[361], 111[363],
	$T_{decomposition}$ (°C)	X	575	530[208], 547±20[34], 628[220],

Binary $NaNO_3$-KNO_3	$T_{transition}$ (°C)	128.3,16.8 J/g	X	120**[33], 109.7***[365], 111***[150], 113**[150], 21.29J/g ***[150], 33.78J/g**[150],
	T_{fusion} (°C)	218.1	211.6	220**[150], 221**[37, 38, 379], 222**[240, 327, 362, 379], 223±3***[365], 227**[153], 225***[150], 230***[150],
	$T_{crystallization}$ (°C)	223.6	221.8	221**[38],
	H_{fusion} (J/g)	105.9	100	100.1**[150], 113.37***[150],
	$T_{decomposition}$ (°C)	X	570	>717**[34], 600***[27]

N/A = indicates not applicable, **Nil** = indicates no data available, X indicating data were unable to acquire.

By DTA= [33, 208, 220, 224, 356, 364, 374], by DSC= [32, 34, 37, 38, 150, 153, 324, 327, 348, 349, 351, 355, 358, 360, 365, 370, 373, 374, 377], by STA= [379], by potentiometer thermocouple= [240, 362], by other calorimetry (e.g: drop calorimetry, adiabatic calorimetry, near adiabatic, dissolution calorimetry)= [173, 350, 354, 355, 357, 359, 366-368, 372, 375, 376, 378], by chemical analysis (e.g: electrochemical measurement, mixing method, volume discontinuity method, XRD, XPS, FEM, Raman Spectroscopy and others)= [27, 224, 352, 353, 361, 363, 371].

* indicating transition upon cooling, ** indicating equimolar (50Na:50K) binary nitrate, *** indicating 64Na:36K molar binary $NaNO_3$-KNO_3 solar salt.

Table 7.2.2.3: Thermal events of single $NaNO_3$, KNO_3, $LiNO_3$ and binary $NaNO_3$-KNO_3 salt (*60-40 weight ratio*) heated from 50 to 800°C at three atmosphere (*sweep gas velocity of 40ml/min*) at 10°C/min heating and cooling rates using a simultaneous STA Setaram setsys DTA/TGA- Pfeiffer MS(off gas analyzer).

Salt type	Sweep gas type	TG rapid weight loss beginning temperature (°C)	Irreversible endothermic heat flow peak starting temperature (°C)	Gaseous products evolution temperature (°C)				
				O_2	**N_2**	**NO**	**NO_2**	**N_2O**
$LiNO_3$	**argon**	507	510	470	515	504	530	525
	air	540	539	545	610	545	575	602
	oxygen	541	538	x	535	535	570	585
$NaNO_3$	**argon**	568	565	532	570	535	520	350
	air	575	572	x	x	555	548	480
	oxygen	590	548	x	630	580	580	390
KNO_3	**argon**	575	590	530	450	530	450	450
	air	590	595	x	x	567	542	490
	oxygen	600	590	x	550	600	560	450
Binary Na-K//NO_3	**argon**	570	564	555	580	555	500	600
	air	589	573	550	x	541	530	480
	oxygen	603	563	x	600	570	570	450

x indicating unable to detect evolve temperature due to similar AMU (Atomic Mass Unit) as a sweep gas. In argon the partial pressure of oxygen, P_{O_2}= 0, in air the P_{O_2}= 0.21 and in oxygen the P_{O_2}= 1.0

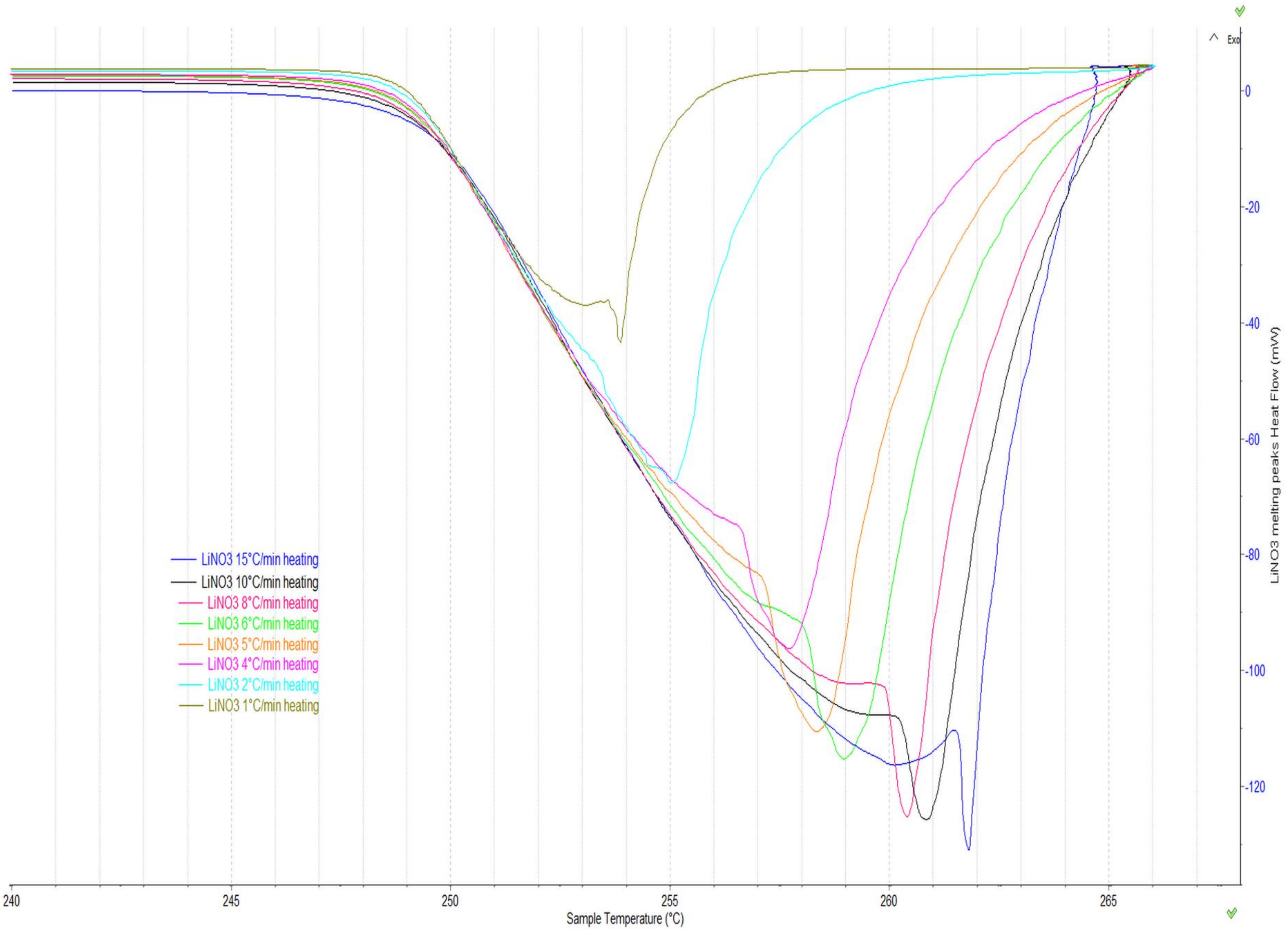

Figure 7.1.1: $LiNO_3$ melting peaks at various heating rates.

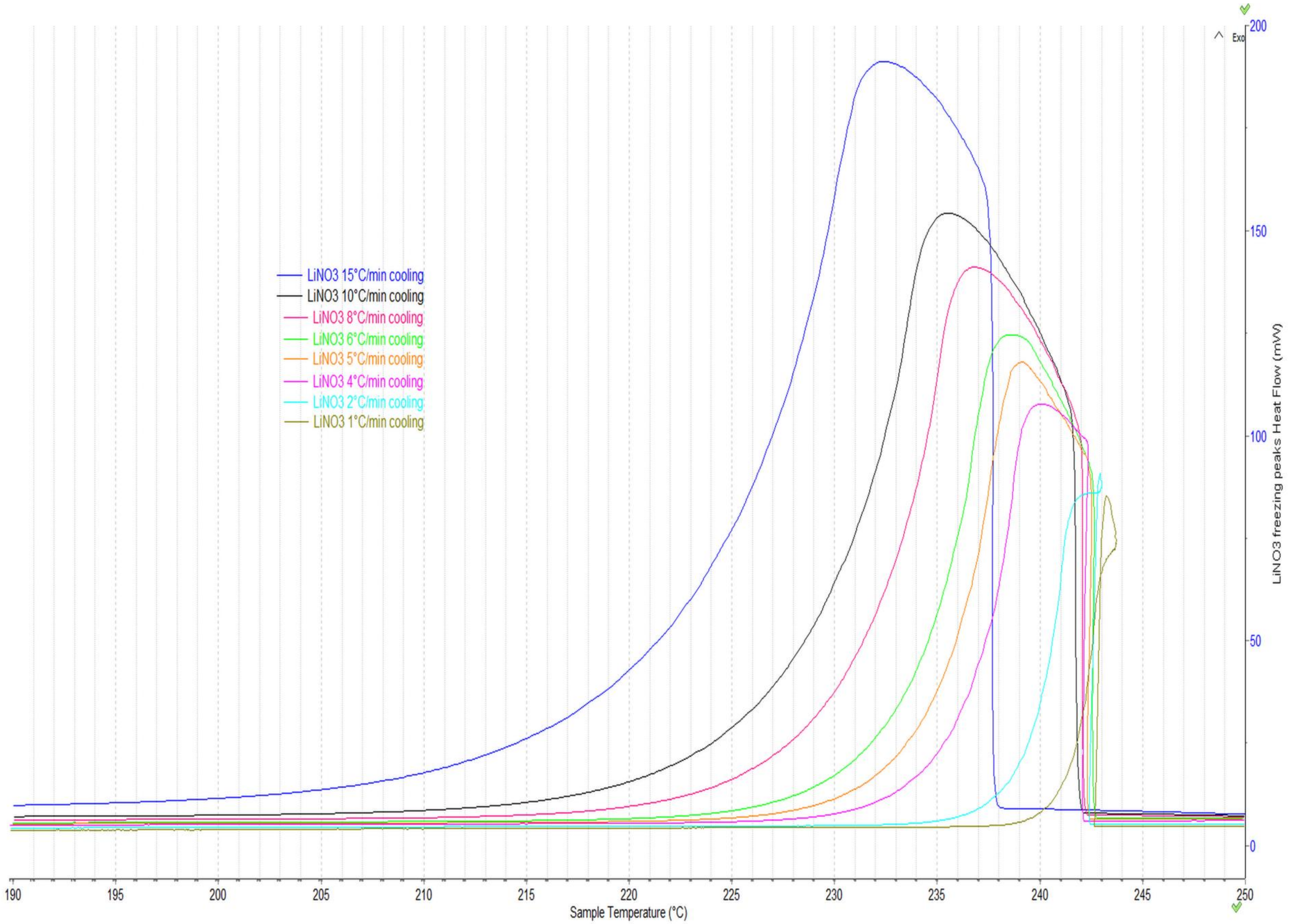

Figure 7.1.2: $LiNO_3$ freezing peaks at various cooling rates.

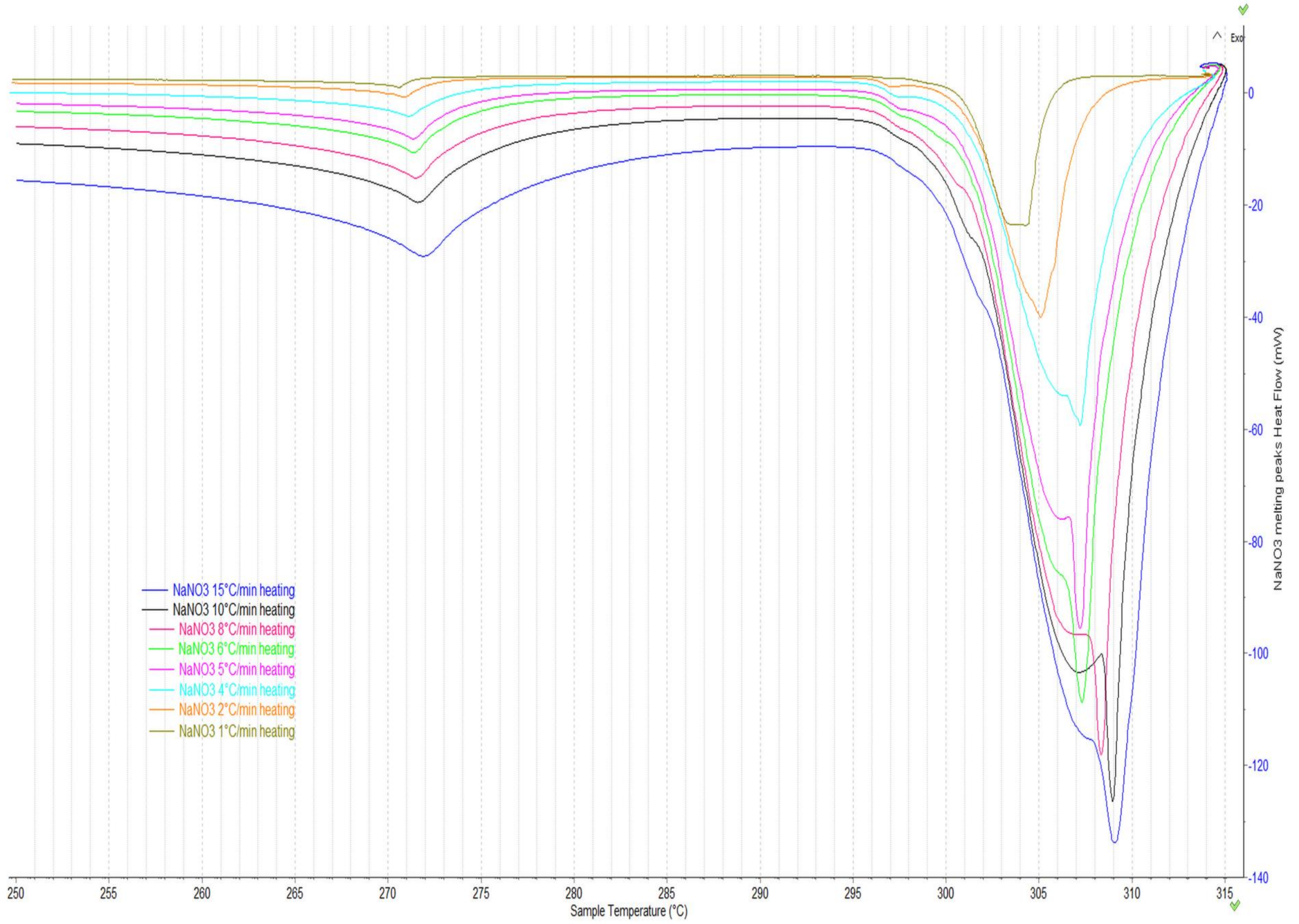

Figure 7.1.3: $NaNO_3$ melting peaks at various heating rates.

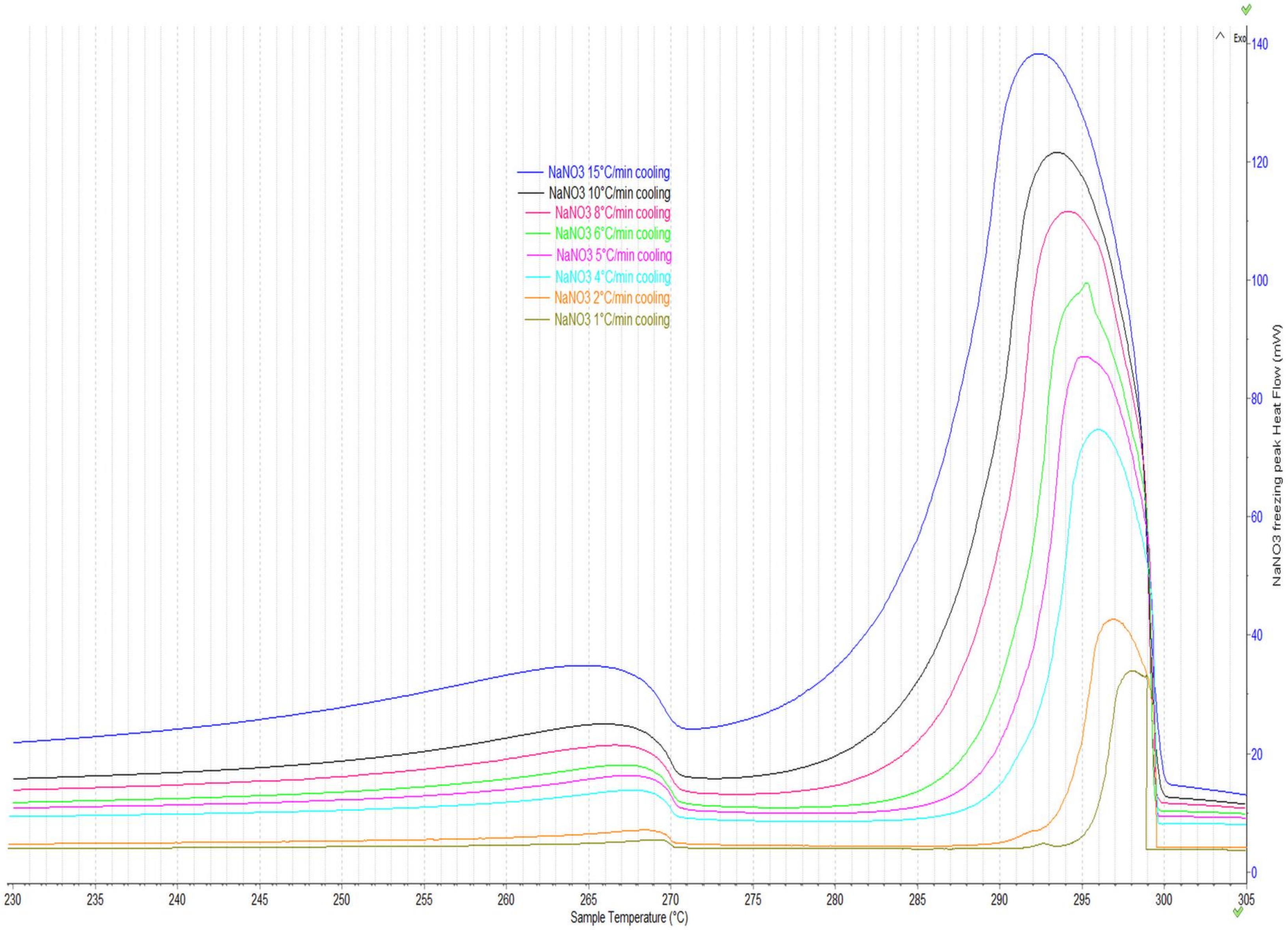

Figure 7.1.4: $NaNO_3$ freezing peaks at various cooling rates.

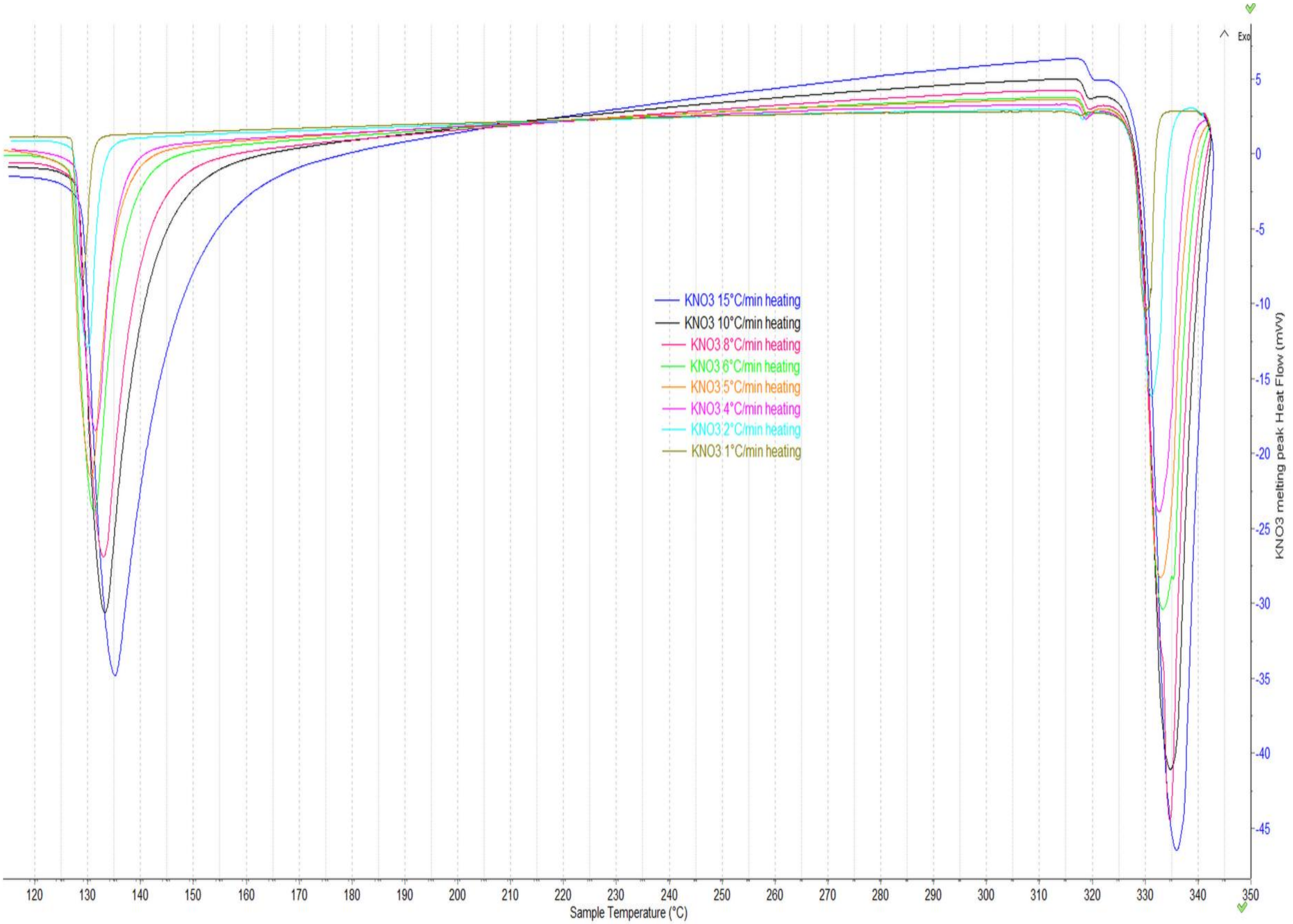

Figure 7.1.5: KNO_3 melting peaks at various heating rates.

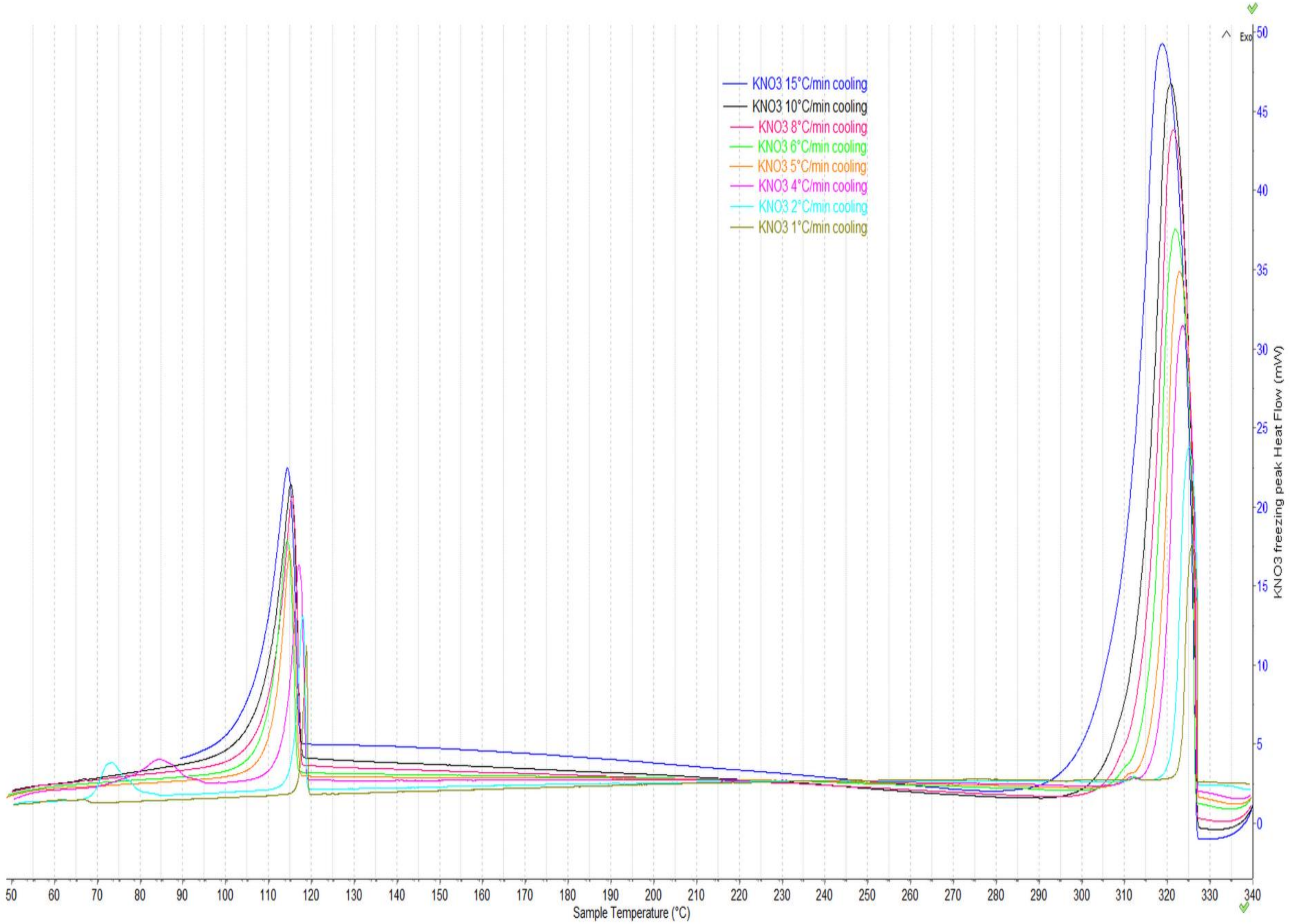

Figure 7.1.6: KNO_3 freezing peaks at various cooling rates.

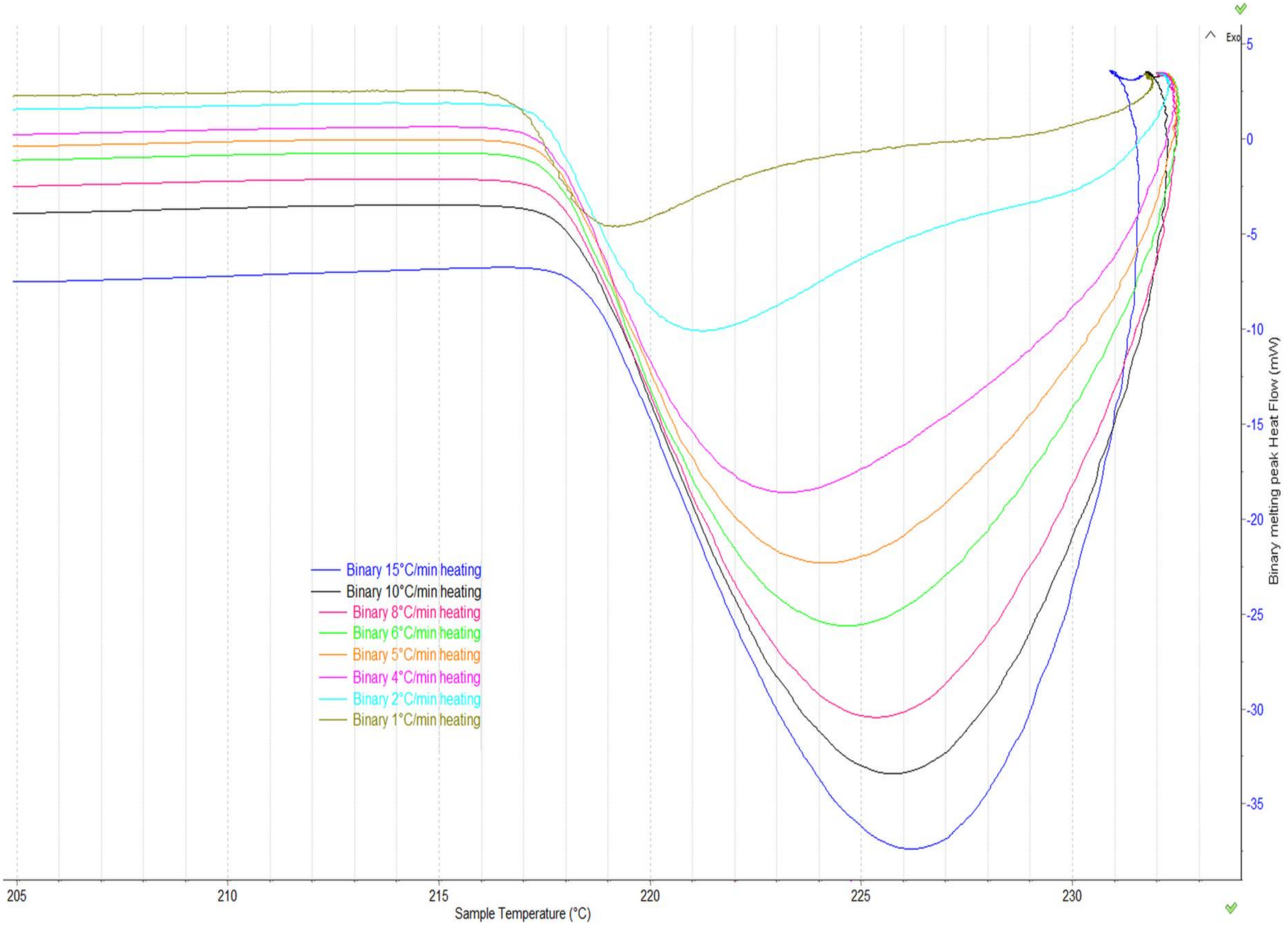

Figure 7.1.7: Binary $NaNO_3$- KNO_3 melting peaks at various heating rates.

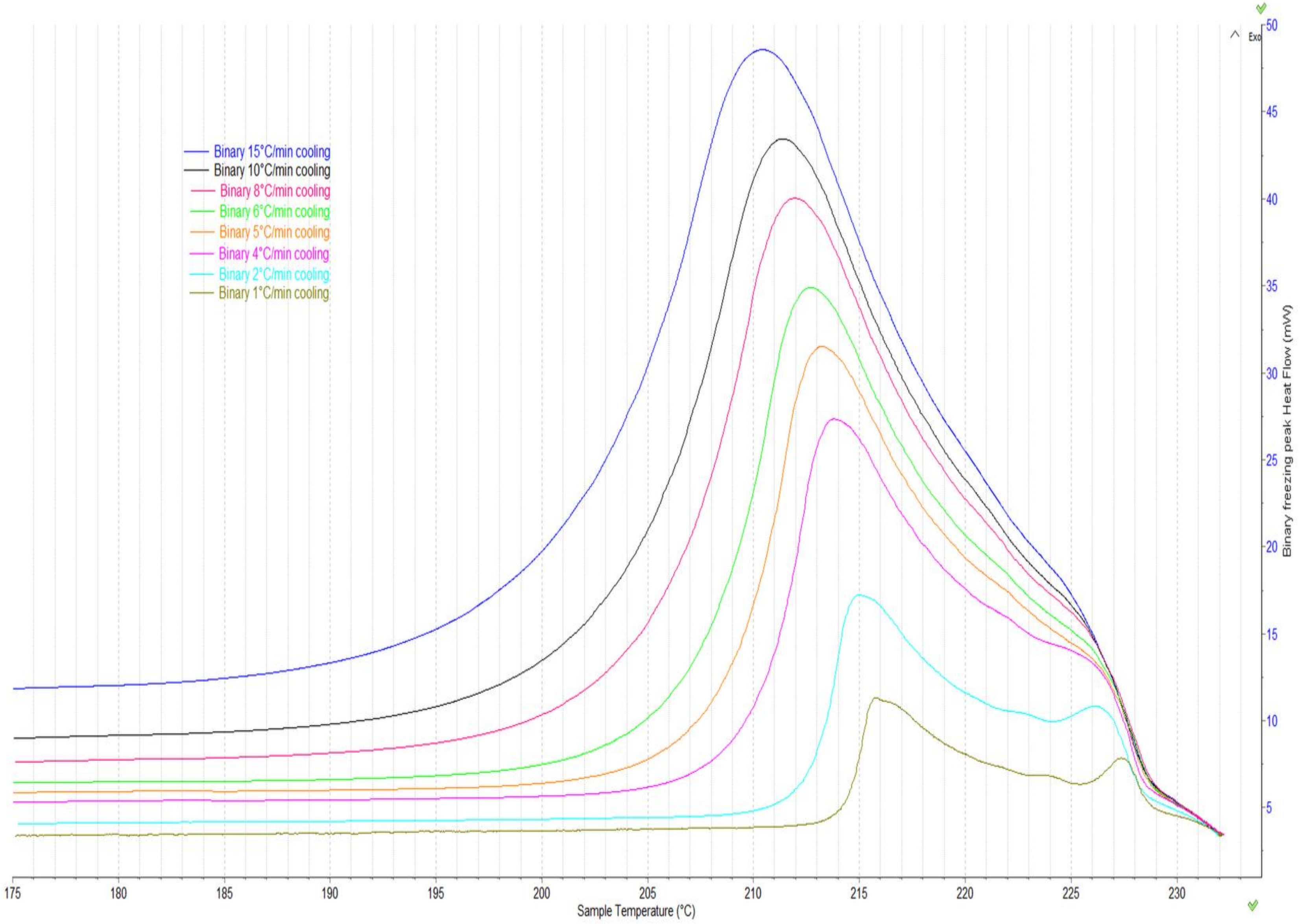

Figure 7.1.8: Binary $NaNO_3$- KNO_3 freezing peaks at various cooling rates.

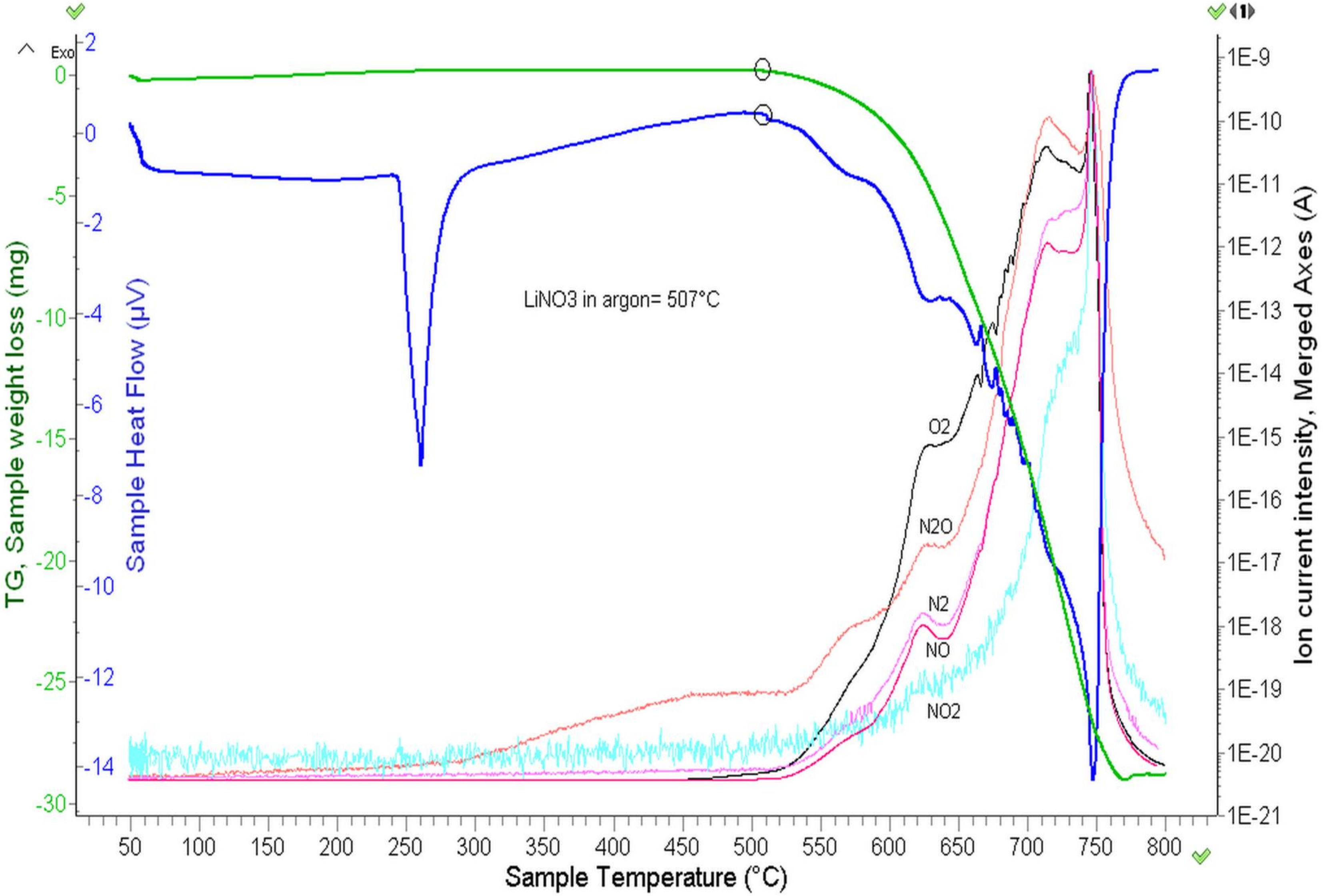

Figure 7.2.1: $LiNO_3$ in an argon atmosphere at 10°C/min heating rate. The black circles are indicating corresponding temperatures.

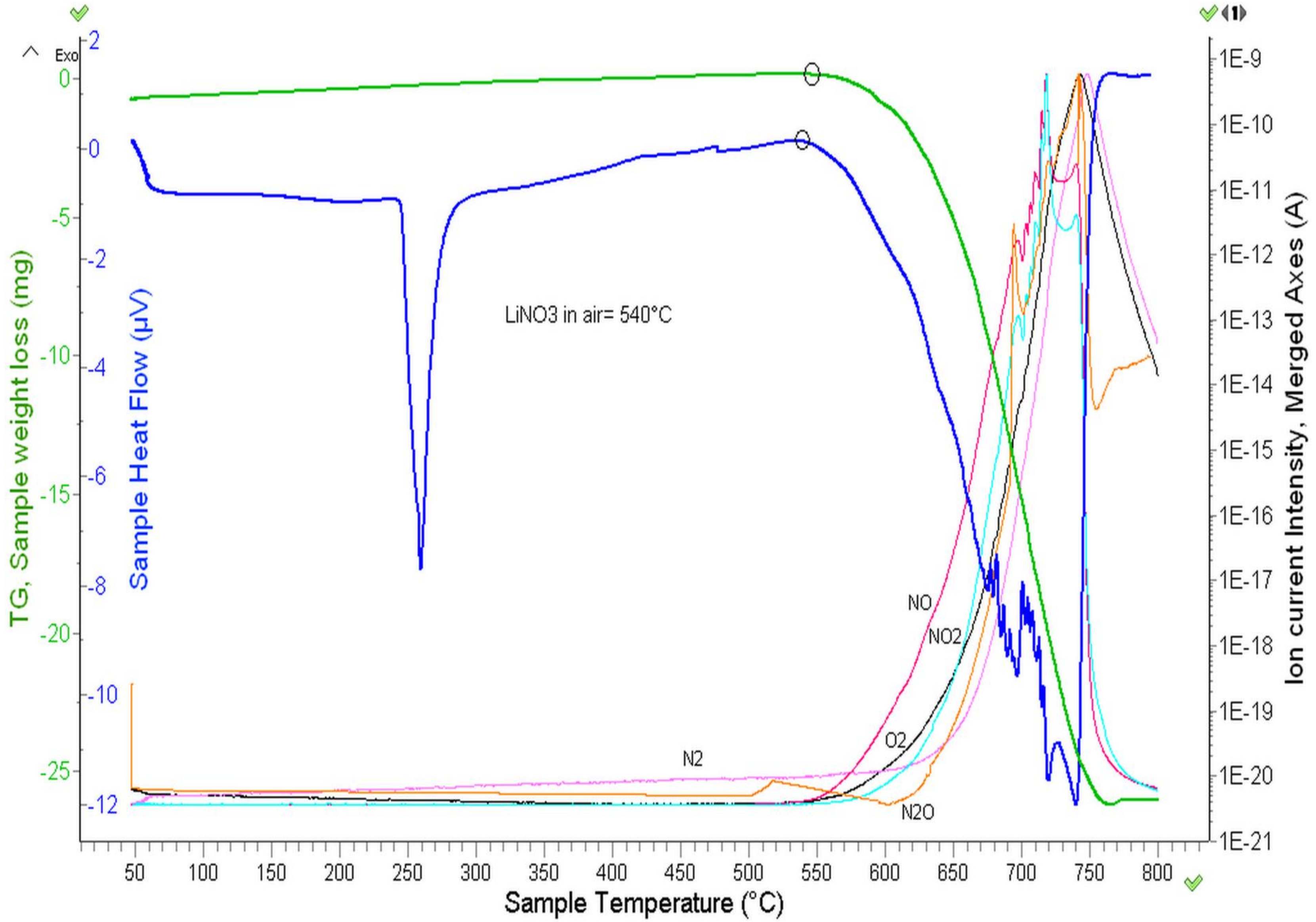

Figure 7.2.2: $LiNO_3$ in an air atmosphere at 10°C/min heating rate. The black circles are indicating corresponding temperatures.

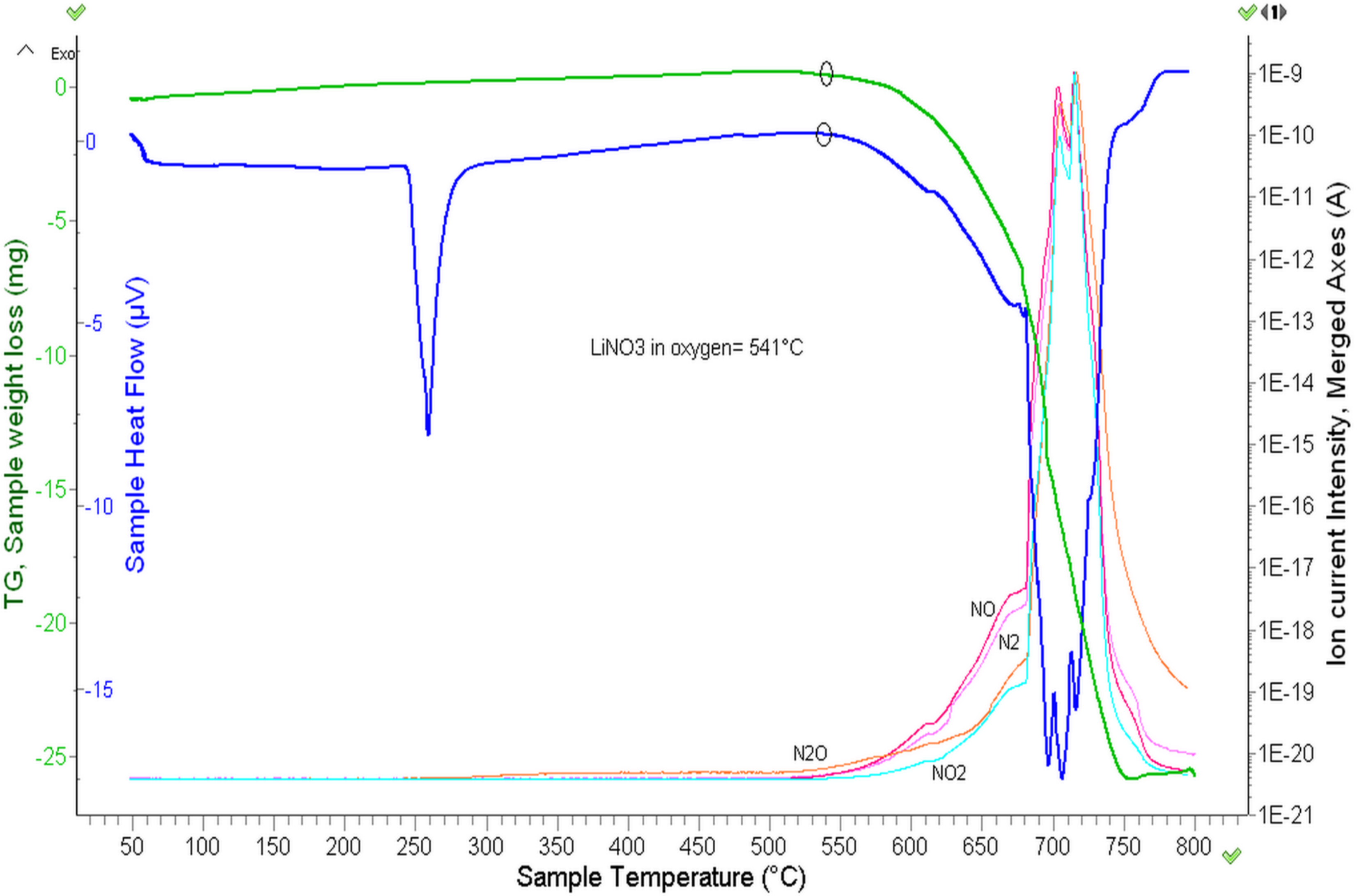

Figure 7.2.3: $LiNO_3$ in an oxygen atmosphere at 10°C/min heating rate. The black circles are indicating corresponding temperatures.

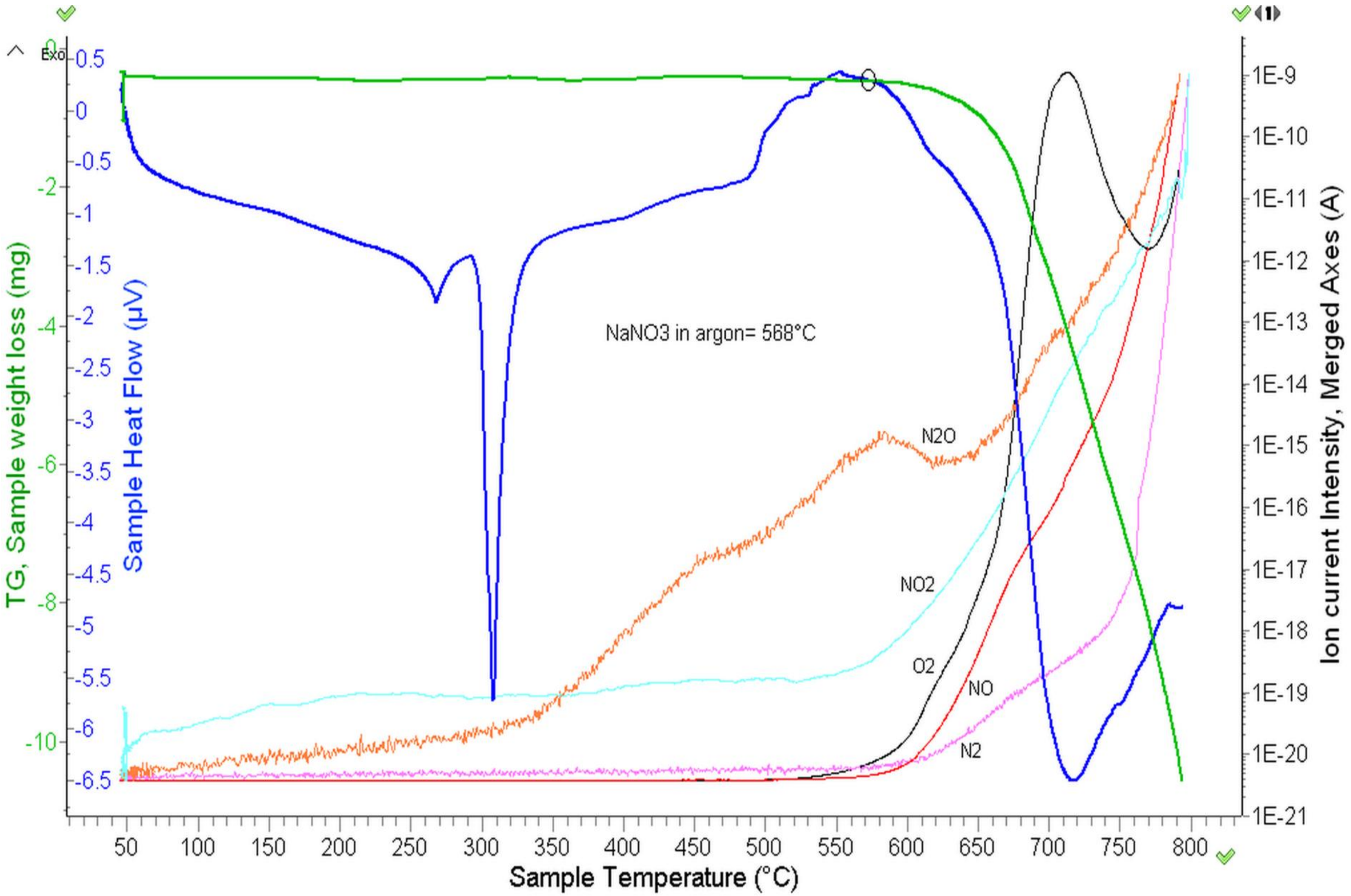

Figure 7.2.4: NaNO$_3$ in an argon atmosphere at 10°C/min heating rate. The black circles are indicating corresponding temperatures.

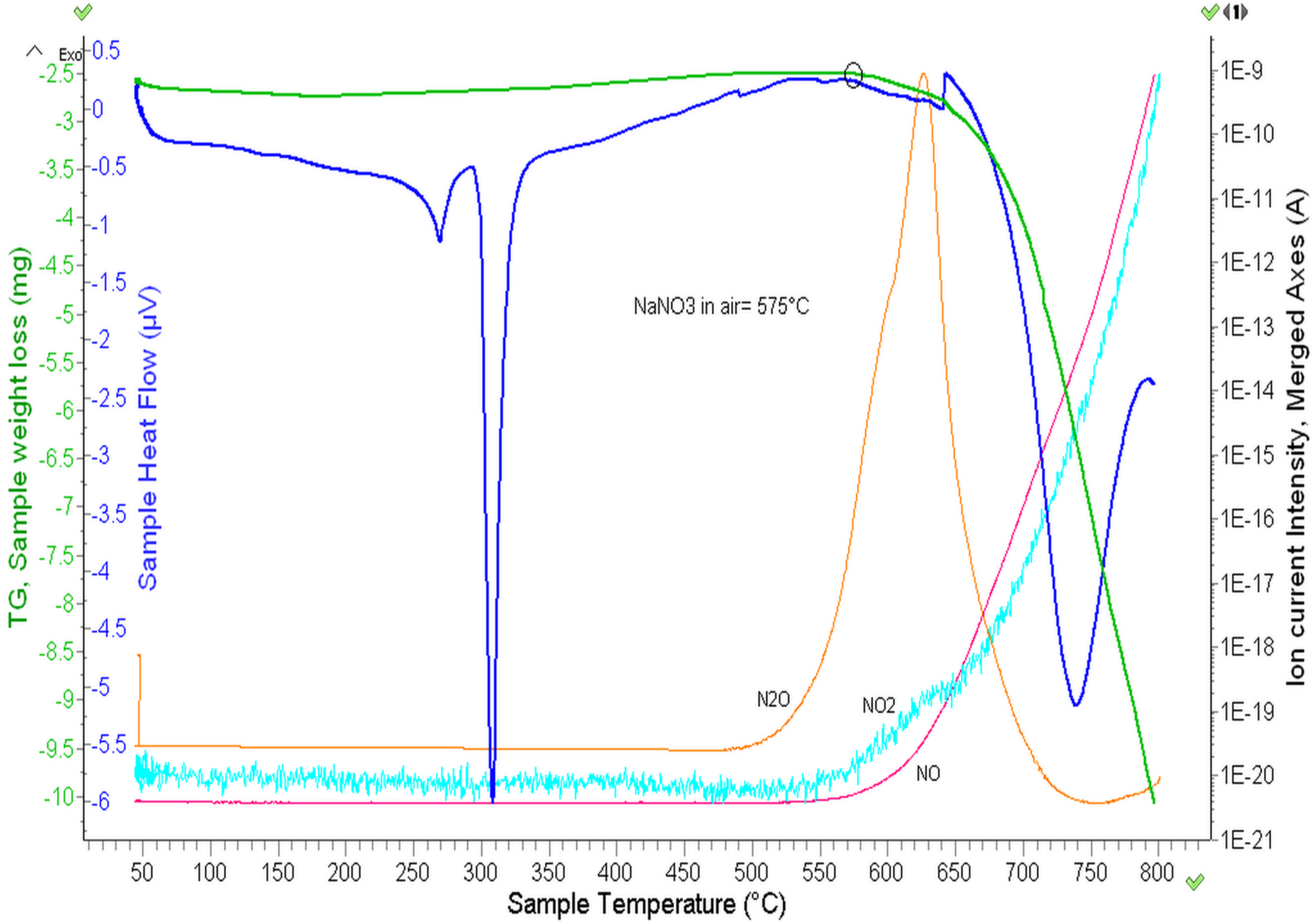

Figure 7.2.5: $NaNO_3$ in an air atmosphere at 10°C/min heating rate. The black circles are indicating corresponding temperatures.

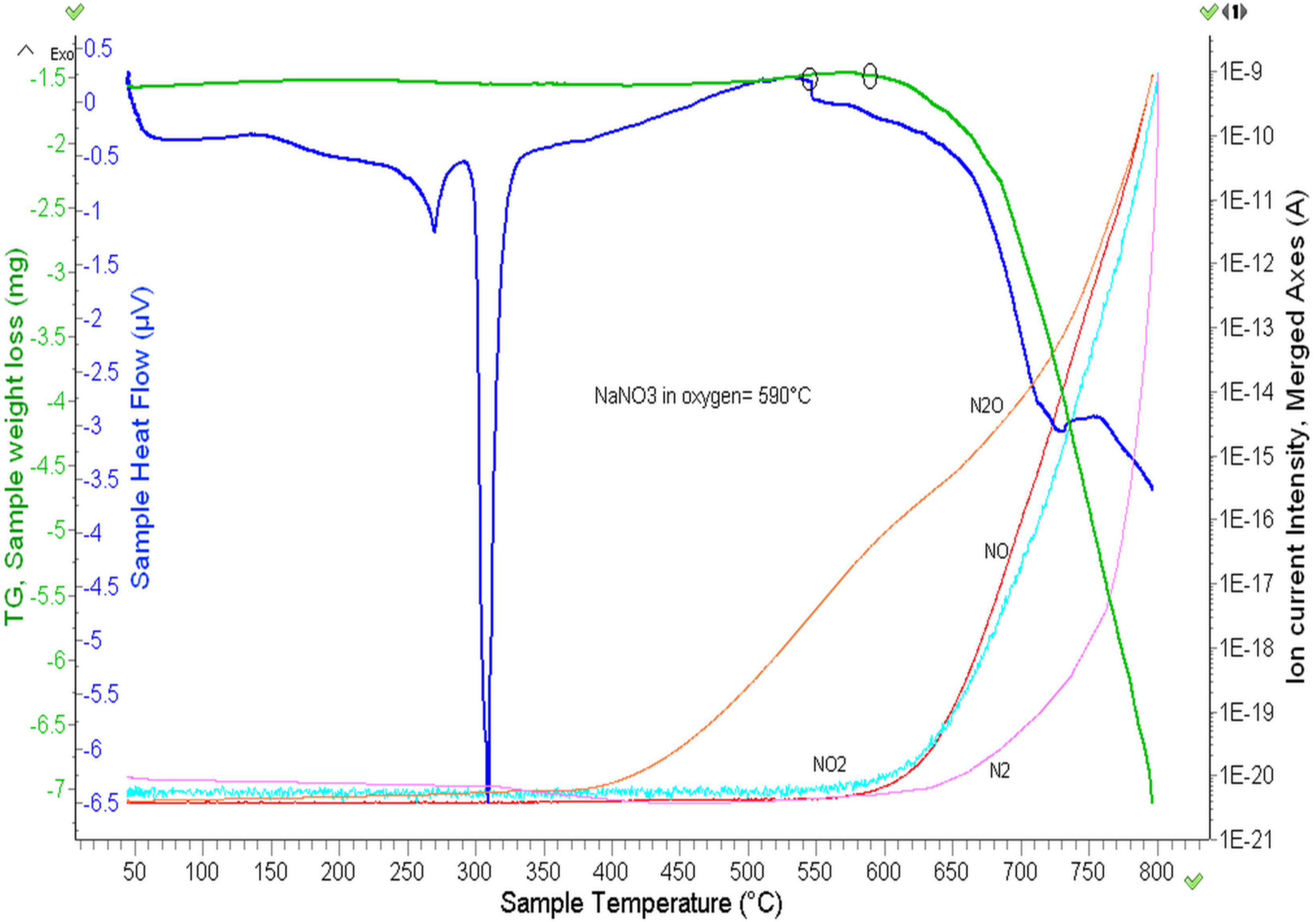

Figure 7.2.6: $NaNO_3$ in O_2 atmosphere at 10°C/min heating rate. The black circles are indicating corresponding temperatures.

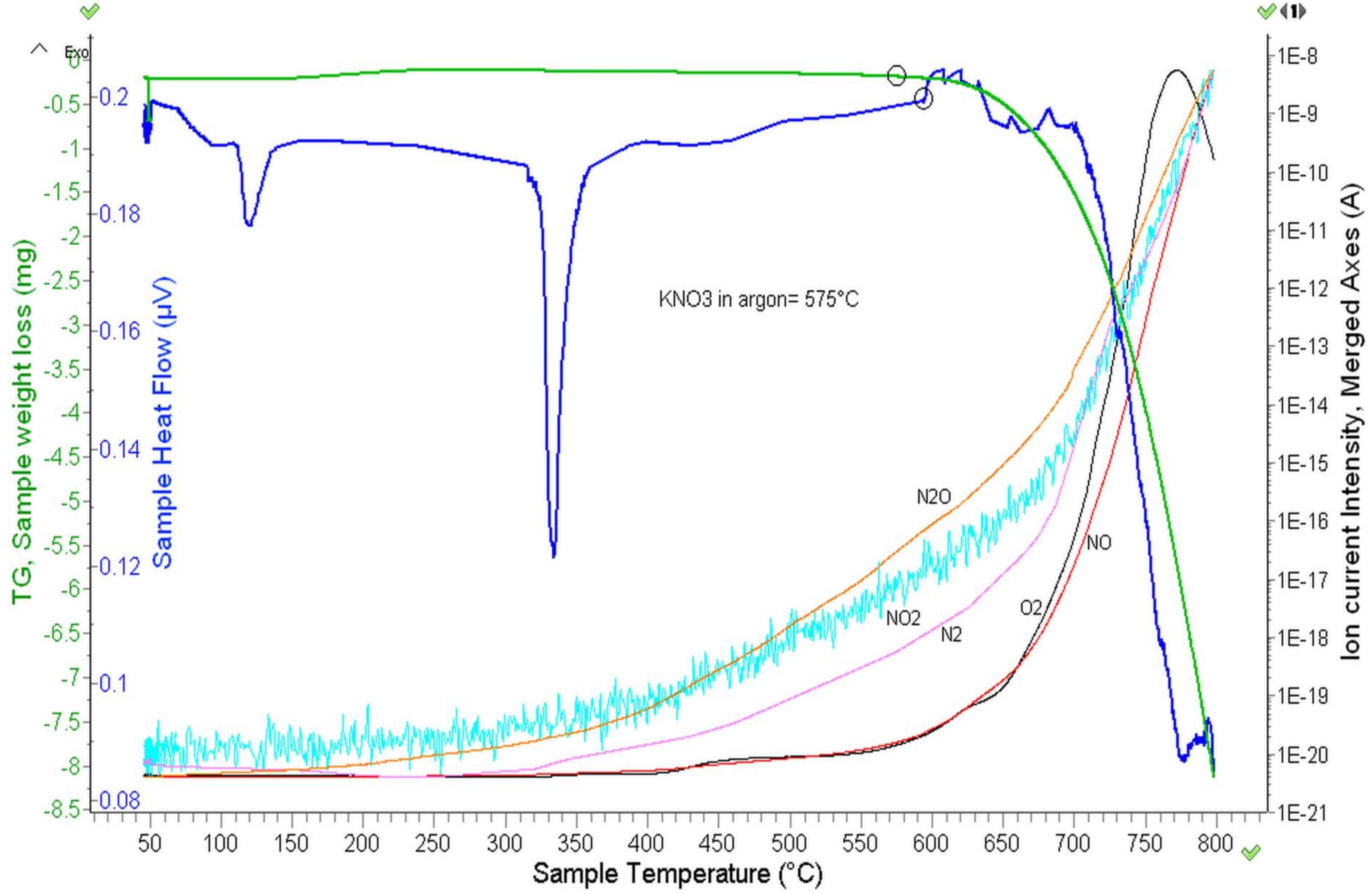

Figure 7.2.7: KNO_3 in an argon atmosphere at 10°C/min heating rate. The black circles are indicating corresponding temperatures.

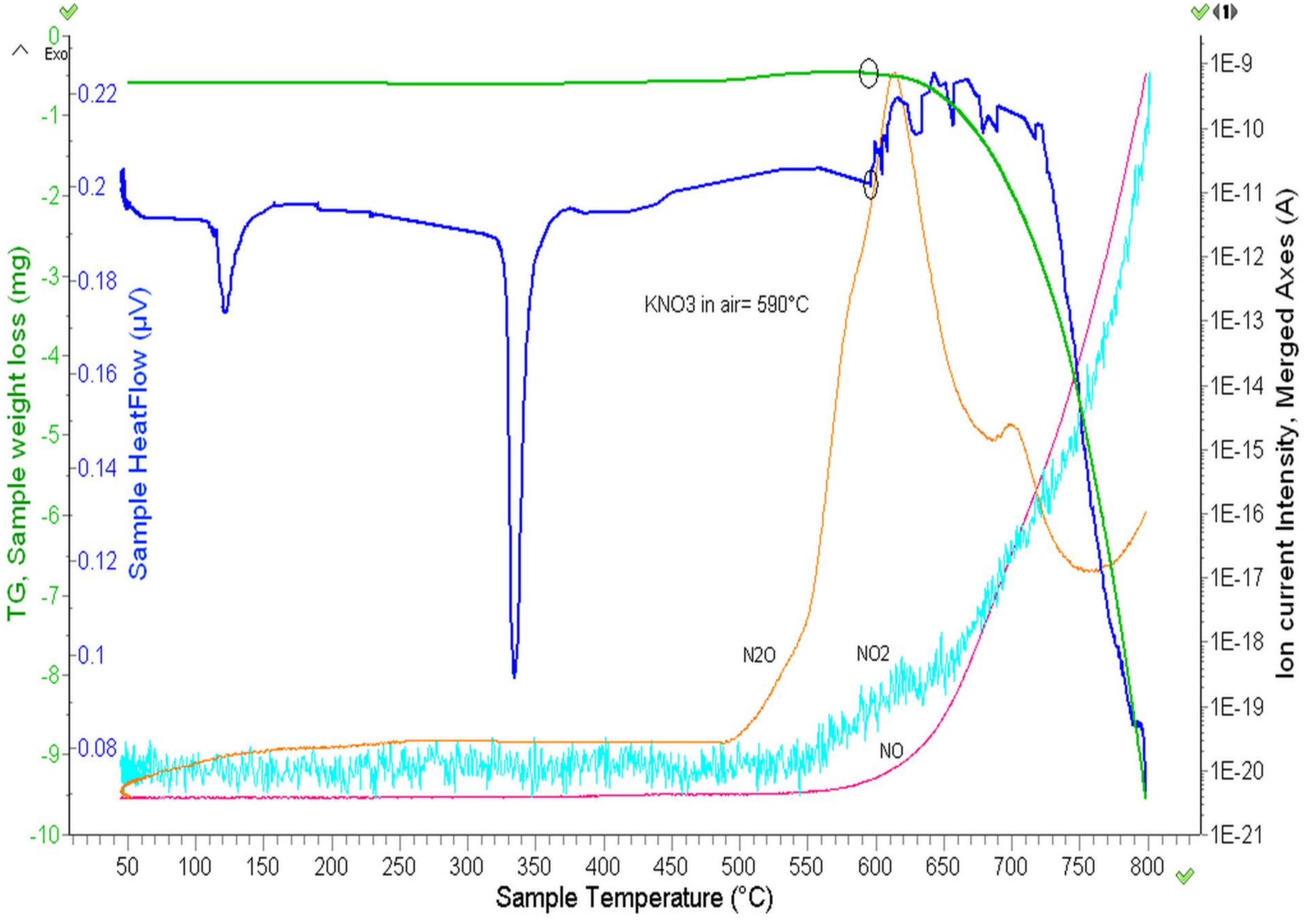

Figure 7.2.8: KNO_3 in an air atmosphere at 10°C/min heating rate. The black circles are indicating corresponding temperatures.

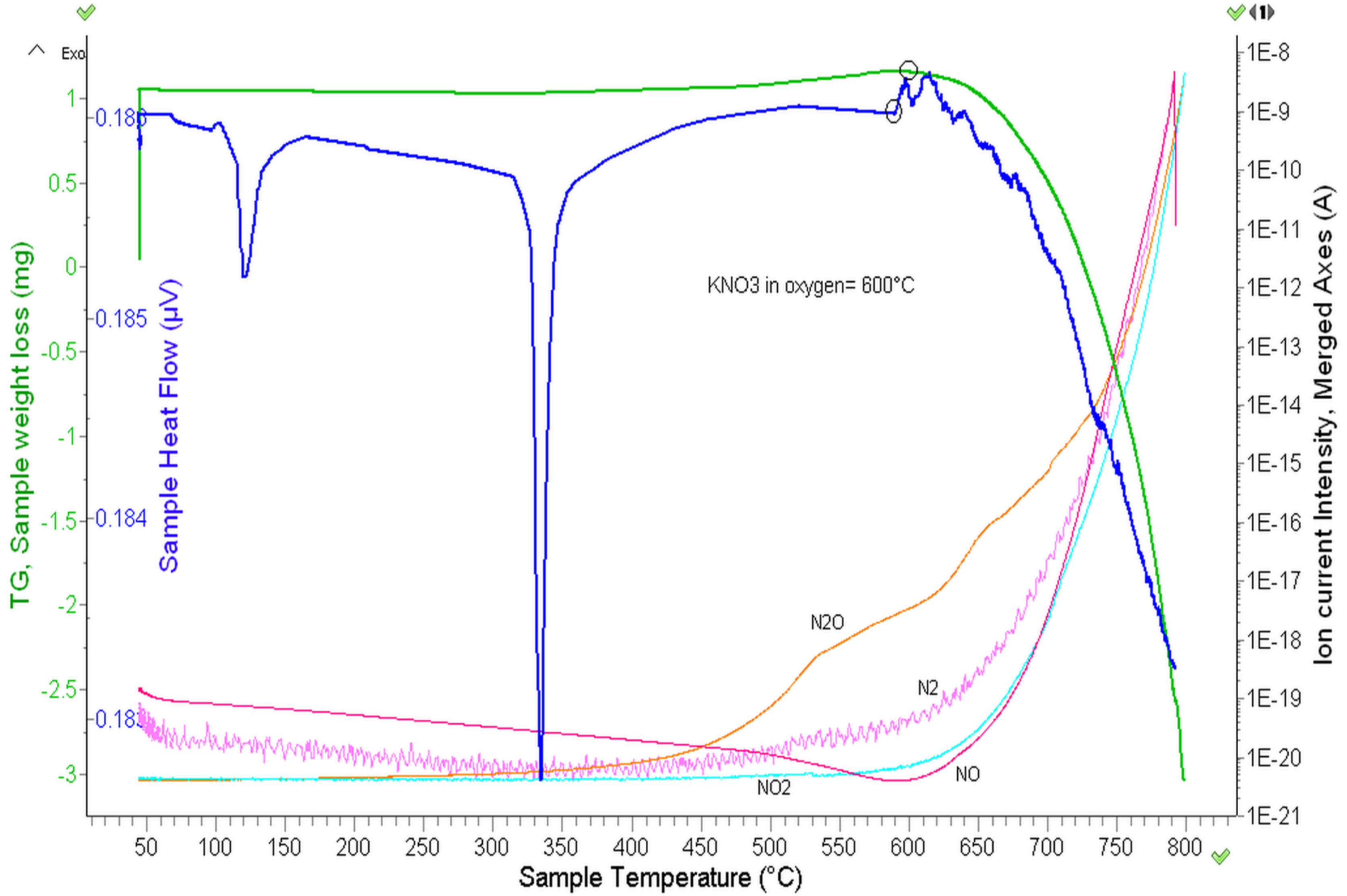

Figure 7.2.9: KNO_3 in an oxygen atmosphere at 10°C/min heating rate. The black circles are indicating corresponding temperatures.

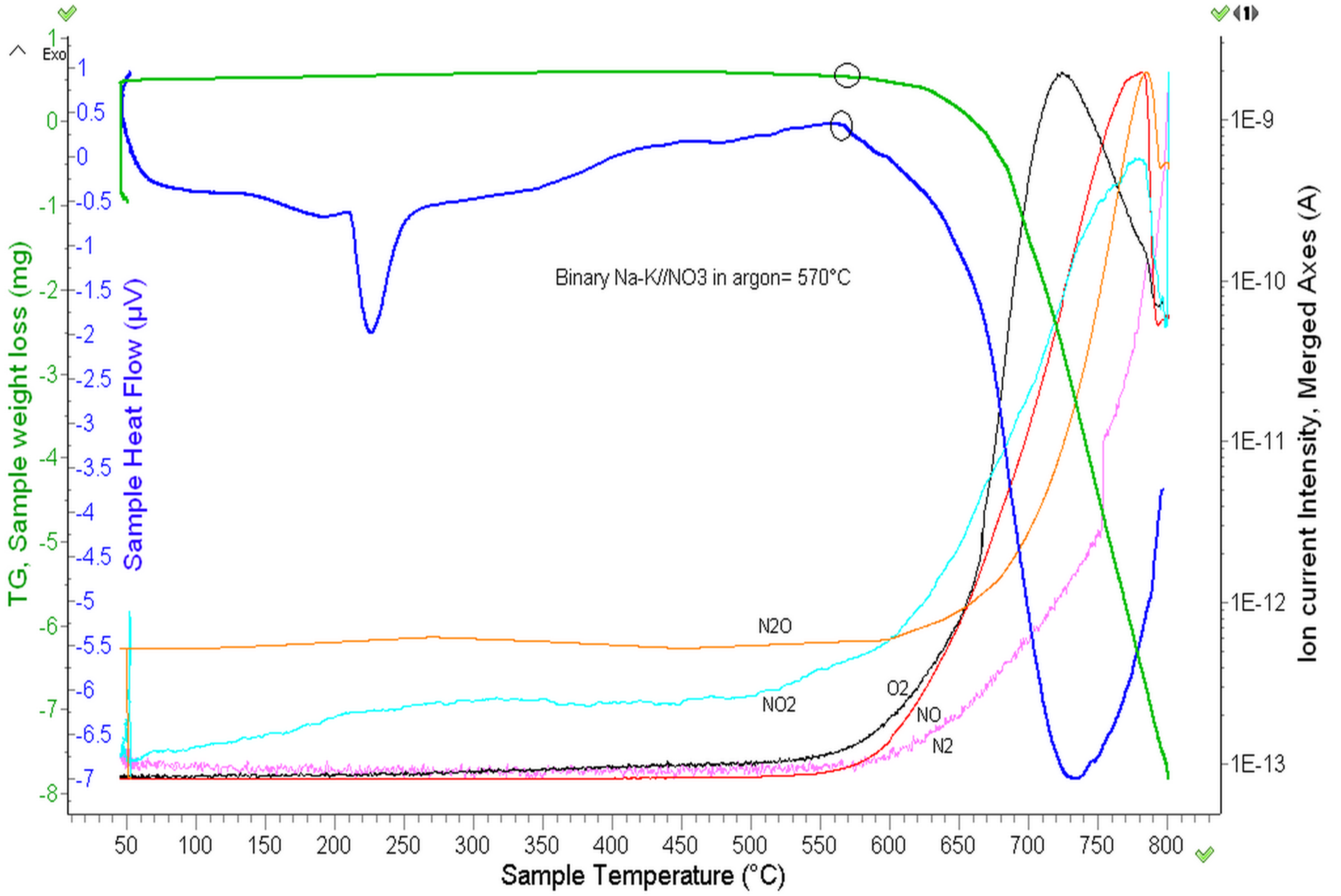

Figure 7.2.10: Binary in an argon atmosphere at 10°C/min heating rate. The black circles are indicating corresponding temperatures.

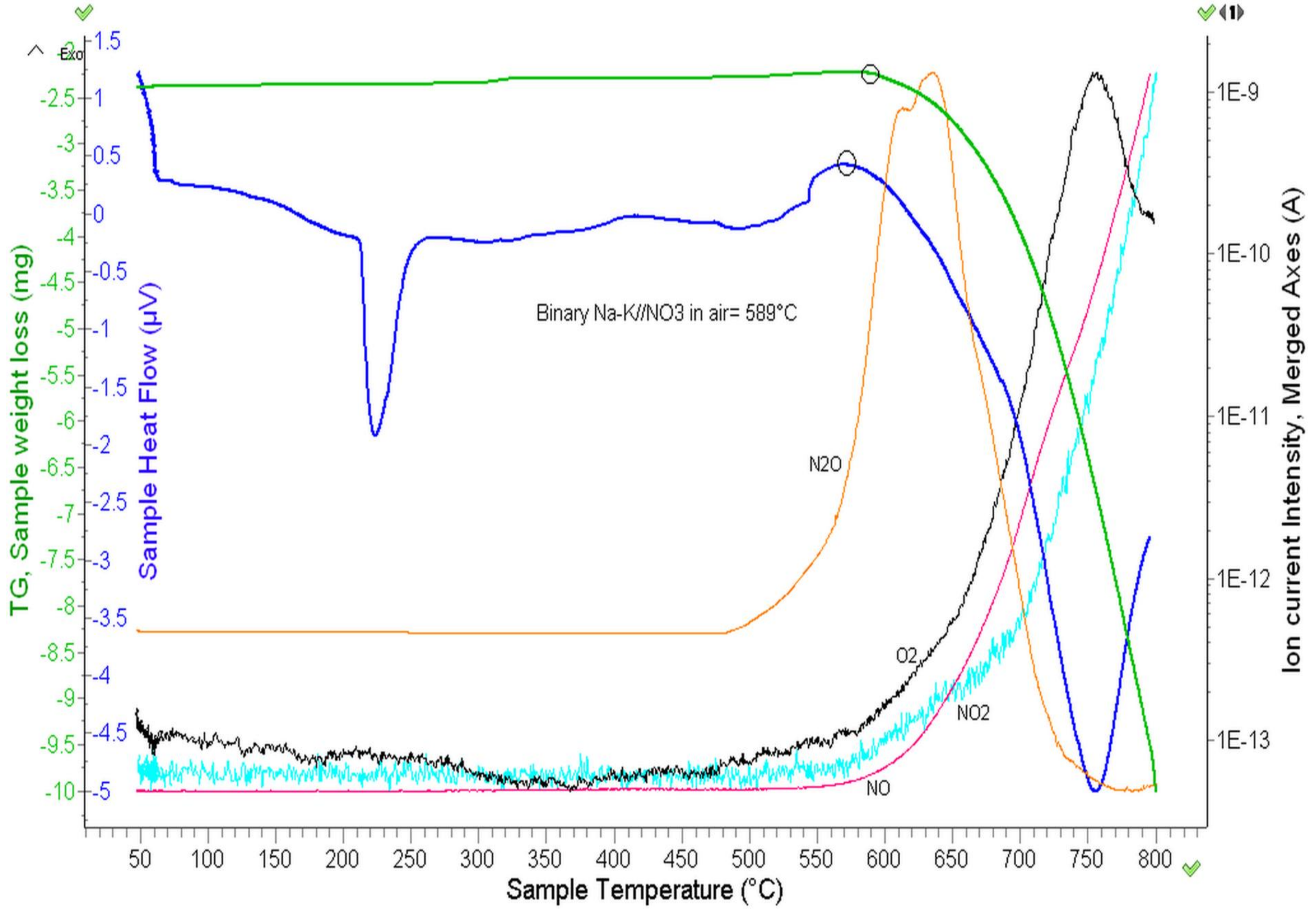

Figure 7.2.11: Binary in an air atmosphere at 10°C/min heating rate. The black circles are indicating corresponding temperatures.

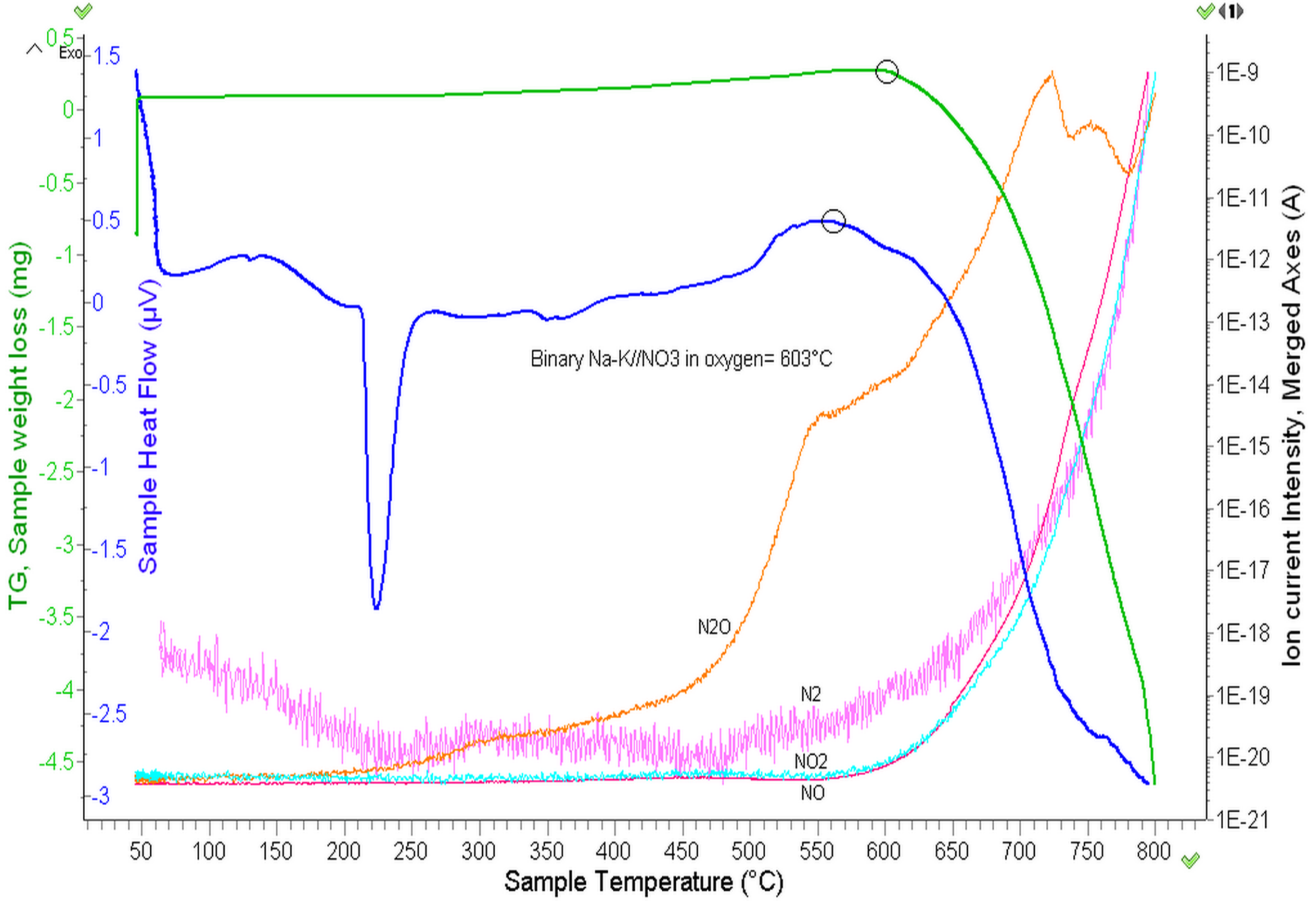

Figure 7.2.12: Binary in O_2 atmosphere at 10°C/min heating rate. The black circles are indicating corresponding temperatures.

7.3 SINGLE AND BINARY SALT THERMAL ANALYSIS: DISCUSSION

Thermal and off-gas analysis was performed on single and binary nitrate salts subjected to 10°C/min heating rate to observe decomposition behavior at inert and oxidative atmospheres. Decomposition temperatures were determined by identifying rapid weight loss beginning temperature in TG curves, endothermic degradation curve starting temperature in HF curves and gaseous products evolution temperature in MS curves.

The Calisto [332] software analysis showed that, before beginning of the actual test while holding the samples at 110°C temperature for one hour for dehydration purpose, the binary samples loss their weight averagely 2 to 3 weight%. Single salt moisture weight loss was around 2% weight%. During the test and before rapid weight loss begin the sample did not exhibit further weight loss (weight change range ±0.05mg). The moisture absorbance in binary salt was mainly due to samples preparation in the air and sample loading in STA.

During melting a small endothermic transformation, the peak was observed followed by a larger endothermic melting peak in all heating HF curves for sodium, potassium, and binary nitrates. For binary nitrate, the melting endothermic peak was broader at the beginning. 1st order solid-solid transition was not appeared during melting and cooling in case of binary salt. Distortion and irreversibility and deviation from linear baseline heat flow curves observed only at or during decomposition and onwards. During or after rapid weight loss begin or rapid degradation process started the heat flow curves showed a decline from the baseline with abrupt distorted endothermic peaks. After high temperature heating at 800°C during cooling the heat flow curves were not identical with the heating HF curves, which indicated an irreversible change in salt composition or altering melt chemistry at a higher temperature.

Lowering the cooling rates minimized the gap between solidus and liquidus temperatures for all three single alkali nitrates. However, for binary nitrate, the gap did not minimize. The lithium nitrate did not show any transition prior to melting. The sodium nitrate, potassium nitrate, and binary salt showed solid-solid transition prior to melting. Solid-solid transition during cooling did not appear for binary nitrate.

The temperatures of starting decomposition were observed in the inert and oxygen rich atmosphere. As consistent with previous studies [26, 109, 121, 380] based on three criteria, the decomposition temperature was determined: temperature at which rapid weight loss start; temperature at which NO, O_2 gases were evolved; and temperature at which rapid, irreversible endothermic heat flow curve was observed [26, 109, 121, 380].

Before the final test, the same mass sample was heated in identical experimental condition with AMU scanning range from 0 to 200 (Faraday MID: for all gas detection) to find evolved gaseous products. At or during decomposition only a few gaseous products showed significant ion current intensity peaks (in Ampere) and were consistent for longer periods. Thus, during final tests, only O_2, N_2, NO, NO_2, N_2O gaseous products were considered for ion current intensity measurement (Faraday Scan stair: for individual gasses detection). Below sections discuss the decomposition behavior of single and binary salt at different sweep gas environments.

7.3.1 LITHIUM NITRATE

In an argon atmosphere, the O_2 and NO evolved at 470°C and 504°C respectively, as shown in Table 7.2.2.3. The rapid weight loss started at 507°C and the endothermic degradation starting peak started temperature at 510°C, as shown in Figure 7.2.1. In an air atmosphere, the rapid weight loss begin at 540°C and the endothermic degradation started at 539°C, as shown in Figure 7.2.2. In an oxygen atmosphere, the rapid weight loss started at 541°C and the endothermic degradation starting peak observed at 538°C, as shown in Figure 7.2.3. The results are summarized in Table 7.2.2.3. Aduru et al. [267] studied the ion simulated decomposition of lithium nitrate by X ray photoelectron spectroscopy (XPS) and found that ion irradiation resulted in N_2 evolution and Li_2O and Li_2O_2 formation mainly. Lithium nitrate did not show any transition prior to melting. The liquidus onset temperature was 257.7°C with the heat of melting 355.9J/g close to literature values as shown in Table

7.2.2.2. The decomposition temperature was not reported vastly in literature. Bordyushkova et al. [208] used DTA and stated 430°C as degradation point for $LiNO_3$. In air and oxygen atmosphere an oxidation weight gain was observed at 500 and 460°C respectively, as shown in Figures 7.2.2 and 7.2.3.

7.3.2 SODIUM NITRATE

In an argon atmosphere, the rapid weight loss begin at 568°C and the endothermic degradation started at 565°C, as shown in Figure 7.2.4. In an air atmosphere, the rapid weight loss begin at 575°C and the endothermic degradation starting peak observed at 572°C, as shown in Figure 7.2.5. In an oxygen atmosphere, the rapid weight loss begins at 590°C and the endothermic degradation starting peak at 548°C, as shown in Figure 7.2.6. Before starting of rapid decomposition weight loss the sample showed slight oxidation weight gain in an air atmosphere at 460°C and in an oxygen atmosphere at 500°C, as shown in Figures 7.2.5 and 7.2.6 respectively. In air temperature after 575°C, the weight loss begins to decline rapidly due to nitrate and nitrite breakdown. Decomposition temperature in argon (568°C) is close to literature value, as shown in Table 7.2.2.2. The literature data indicate that $NaNO_3$ has decomposition temperature in the range of 520 to 567°C studied by Kramer using DTA and DSC respectively [34]. The liquidus and the solidus temperature of sodium nitrate were 301.4 and 299°C, which indicate proximity with literature data 307°C [37, 108] by Zhang and Raade were studied using DSC and TGA respectively. The exothermic peak at the beginning near 272.5°C temperature region is of solid-solid transition as discussed in Chapter 3 of this thesis. Kevin et al. [360] used DTA and observed solid-solid transition temperature 31°C below the melting point. Liquidus onset temperature was higher at high scanning rate. A study from Bauer et al. [35] also showed that higher scanning rate leads to higher liquidus temperature. Hoshino et al. [381] studied the decomposition of sodium nitrate by simultaneous TGA-DTA and GC (gas chromatographer) and found that O_2, N_2 and NO are main evolved gaseous products. Aduru et al. [267] studied the ion simulated decomposition of $NaNO_3$ by XPS and found that ion irradiation resulted in N_2 evolution and Na_2O and Na_2O_2 formation mainly.

7.3.3 POTASSIUM NITRATE

In an air atmosphere, the rapid weight loss begins at 575°C and the endothermic degradation starting peak at 590°C, as shown in Figure 7.2.7. In an air atmosphere, the rapid weight loss begins at 590°C and the endothermic degradation starting peak at 595°C, as shown in Figure 7.2.8. In oxygen, the rapid weight loss begins at 600°C and the endothermic degradation starting peak at 590°C, as shown in Figure 7.2.9. The liquidus temperature and solidus temperature were 331°C and 326.8°C, which is near to literature melting value of 337°C [37, 108] studied by Zhang using DSC and Raade using TGA. The literature data indicate that KNO_3 has decomposition temperature in the range of 520 to 567°C studied by Kramer using DTA and DSC respectively [34]. The exothermic peak at the beginning near 142°C temperature region is of solid-solid transition as discussed in Chapter 3 of this thesis. In air and oxygen atmosphere an oxidation weight gain was observed at 470 and 510°C, as shown in Figures 7.2.8 and 7.2.9 respectively.

7.3.4 BINARY SODIUM-POTASSIUM NITRATE

In an argon atmosphere, the rapid weight loss begins at 570°C and the endothermic degradation starting peak at 564°C, as shown in Figure 7.2.10. In the air, the rapid weight loss begins at 589°C and the endothermic degradation starting peak at 573°C, as shown in Figure 7.2.11. In an oxygen atmosphere, the rapid weight loss begins at 603°C and the endothermic degradation starting peak at 563°C, as shown in Figure 7.2.12. The results are summarized in Table 7.2.2.3. The eutectic melting peak was at 226.2°C, which is close to literature data of 222°C [37, 108]. The onset temperature of liquidus was 218.1°C and solidus were 223.6°C. The solid-solid transition was 128.3°C close to literature value of Abe et al. [33] obtained by DTA. The binary salt showed stability up to 570°C in argon, compared literature value of 700°C [34]. In air and oxygen atmosphere an exothermic oxidation weight gain was observed at 500 and 480°C, as shown in Figures 7.2.11 and 7.2.12 respectively.

For all nitrates, the principle cause of weight loss post-dehydration is due to gaseous product evolution during decomposition process where nitrate partially converts to nitrite (reversible initially), nitrite to oxide and NO_x gaseous products. The difference in results between this study and previous studies for all nitrates may be of different sample configurations, purity level, atmosphere above salt melt, crucible types used in test (whether open type crucible or crucible with lid or crucible with lid and hole in it), apparatus type and transducer type (weather DSC or DTA) [34].

At the lower heating rate, the onset temperature of melting endotherm appeared lower since the DSC furnace will take a longer time to reach the melting temperature of the sample. However, at the higher heating rate, the onset point is appeared at a higher temperature. The one reason according to Speyer [382] is that at faster heating rates the heat transfer lag appeared from the sample interior (inside crucible) [382] to thermocouple junction (beside to the crucible) is responsible for shift of onset point to higher temperature, as shown in Figures 7.1.1 to 7.1.8 and Table 7.2.2.1. The endothermic melting peak temperatures at higher scanning rate showed higher heat values because the sample crucible temperature deviates more quickly (compared to reference crucible) from fast rising temperature set point. Thus, the DSC device compensates this temperature deviation of sample crucible with more heat dissipation per unit time [382]. At faster heating rates, ‗time' required to proceed reaction per degree centigrade increment was less compare to slow heating rates [382]. This is because at the higher heating rate the sample experience greater heat flux rate which accelerate transformation rate, and hence it required less time during this transition period [382].

Bauer [35] and Charsley [383] observed similar phenomena during varying scanning rates. Charsley studied rubidium nitrate and stated that higher heating rates lids to higher transition temperatures, as shown schematically in Figure 7.3.1. Charsley also stated that heating condition (stepwise heating and dynamic or linear heating) also affect the DSC heat flow peaks [384].

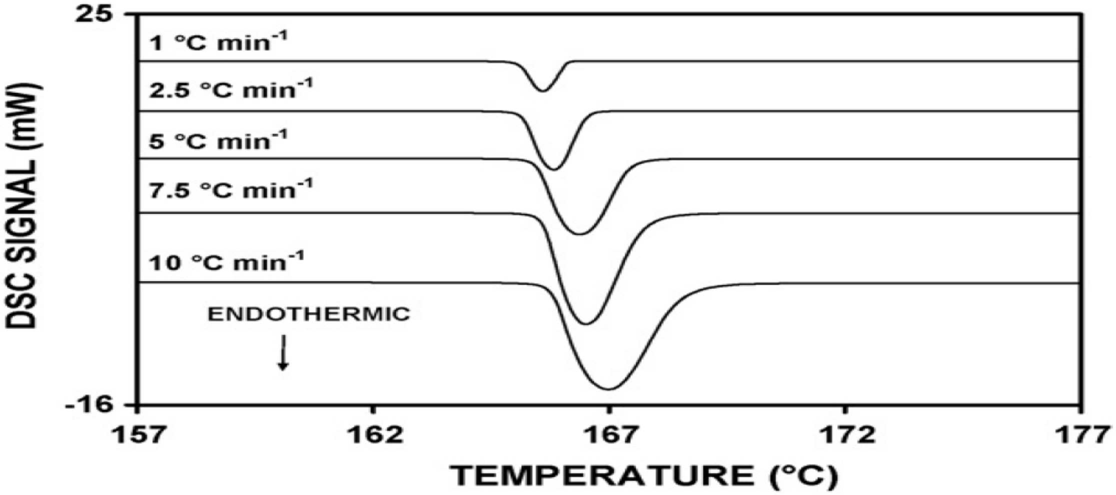

Figure 7.3.1: Influence of heating rates on DSC peaks of rubidium nitrate [383].

There is some effect of heating and cooling rates on transition, melting and freezing temperatures. The eutectic point of binary nitrate should show same liquidus and solidus temperatures. However, in this study they were dissimilar. The reason is for many substances/compounds the exothermic solid-solid transition and freezing events are not always reversible upon cooling compared to the endothermic melting and solid-solid transition events [385]. A possible explanation can be sought. One of the reasons there is no known ASTM CRMs (certified reference materials) for calibration correction (heat flow and temperature correction) of DTA or DSC transducer on cooling to obtain exact cooling behavior of heat flow curves of tested samples. According to Schick and Höhne [386], many CRMs during cooling calibration test showed undefined transition and some degrees of supercooling (mainly during first order transition). Hence, the DSC or DTA thermocouple transducer programmed to measure the cooling heat flow curves (in micro volt or milli Watt) as the mean of negative heating behavior. The negative heating behavior of heat flow curve is predicted/extrapolated from heating behavior (during the heating step of CRMs) of the transducer during calibration [386]. At the slower heating rate of CRMs (*mainly in case of well-defined transition with very little super cooling, such as: CRM with smectic - nematic liquid-crystal transition*) in dynamic condition (non-isothermal), the transformation temperatures change linearly with the change in heating rates. A straight line is then constructed/extrapolated which intersecting zero heating rate point and towards to the desired negative heating rate points to obtain corrected cooling rate behavior [386, 387].

Schawe and Schick [388] indicated that due to sample‘s low heat conductivity a temperature gradient may occur inside crucible, and that might misrepresent some peaks in HF curves. Also due to a different geometry, shape and position of the sample inside crucible have some effect on temperature and transition peaks in HF curves. Hence, samples heat conduction nature, and different loading history may change the HF curves (smearing or distorted peak). According to Boettinger et al. [80] some alloy sample exhibit some degrees of partition (liquidus to solidus gap increasing/decreasing pattern depend on upon heating-cooling rates). Usually, in both DTA and DSC method, the onset temperature of melting of a sample is determined by detecting the extrapolated onset temperature, denoted as T_e; this might tend to provide erroneous HF curves [80, 332]. The extrapolated onset temperature, T_e is the point obtained from the intersection between a tangent at HF peak‘s inflection point towards HF baseline, as shown schematically in Figure B.2.1. The onset of melting of alloy/compounds possesses broader and round slope (endothermic transformation occurs in wider temperature interval) compared to pure metal‘s sharp strip slope (endothermic transformation occurs in narrower temperature interval) [385]. Hence, the actual onset of melting of compounds should be taken where the 1st deviation occurs in HF baseline well before extrapolated tangent of peak slope, denoted as T_i (1st or initial onset temperature), shown schematically in Figures B.2.1 and B.2.4. Hence during melting of compounds, the T_i will be lower compared to T_e [80, 332].

Sometimes because of variation in ‗heat flow response time‘ and ‗heat transfer rate‘ from sample to crucible wall; and crucible wall to furnace thermocouple, may cause thermal lag, which may provide erroneous data on melting and freezing temperatures [80]. Another reason behind dissimilar solidus and liquidus temperature is the DTA transducer‘s heat flow measurement is less sensitive and accurate below 250°C compared to DSC transducer.

As studied and observed by Gordon et al. [220] the nitrous fume (NO) is evolved after melting during bubbling (temperature range 200 to 350°C) of single alkali nitrate salts.

Similar phenomena observed in this study. According to results from MS measurements in this work, NO evolved almost at the same time as O_2 as observed in an argon atmosphere of each scanning rates, as shown schematically in Figures 7.2.1, 7.2.4, 7.2.7 and 7.2.10. The primary decomposition reaction for ternary nitrate may not involve only single reaction but concurrent simultaneous reactions. Thus, the primary thermal reactions include: nitrates converting to nitrites (and liberating O_2); and nitrites to oxide and NO gas. Kramer et al. [189] also described similar results for single nitrates (Na and K) that, the nitrate and nitrite decomposition occurred concurrently with releasing N_2, O_2, and NO.

As described in Chapter 3, at higher temperature nitrate partially decompose to nitrite and liberate oxygen and nitrite partially decompose to oxide and nitrous fume; is tend to show delayed decomposition temperature at oxygen rich atmosphere (P_{O_2}=1). The results of decomposition temperature at three atmosphere and 3 scanning rates are shown in Table 7.2.2.3 and in Figures 7.2.1 to 7.2.12. Bradshaw et al. [137] indicated similar stability of ternary Li/Na/K-NO_3 under oxygen as blanket gas.

DSC transducer thermal lag between set point temperature and sample actual temperature was approximately 15 minutes and 12°C, as shown in Figure 7.3.2. Similar phenomena observed for DTA transducer. The reason for thermal time and temperature lag is mainly delay in time for heat conduction between sample and furnace wall [389]. Usually, at higher temperature the thermal lag is smaller compared to lower heating temperature, as shown in Figure 7.3.3. Thermal lag might affect the heat flow curve during melting-solidification cycles at the end of cooling and start of heating or during the transition in between heating and cooling steps. To minimize the effect of thermal lag, an isothermal holding step of minimum 30 minutes was introduced in between each heating and cooling steps.

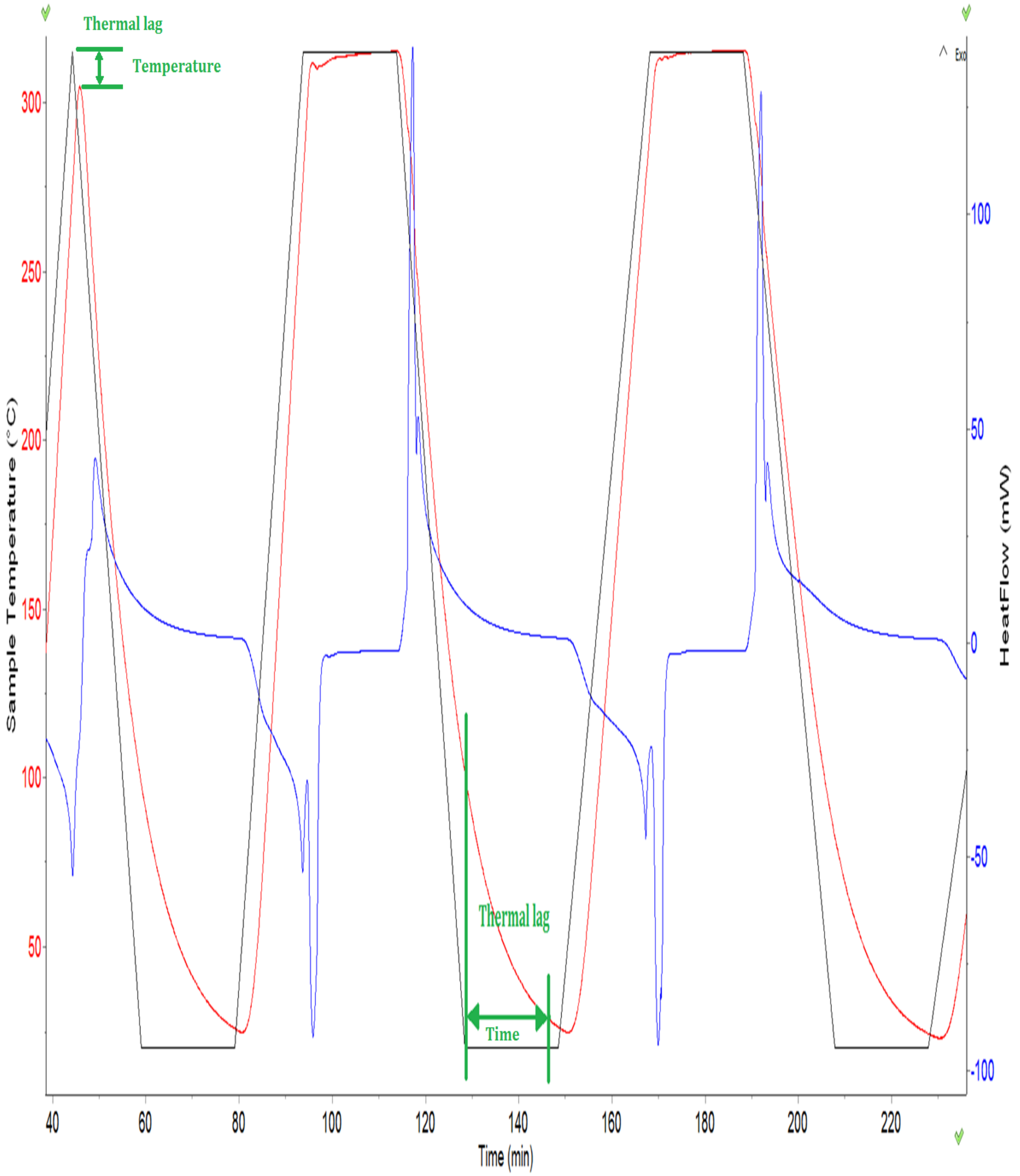

Figure 7.3.2: A typical thermal lag in DSC furnace during sodium nitrate melting-freezing cycles at low set point temperatures. The black line is indicating set temperature, and the red line is indicating actual sample temperature.

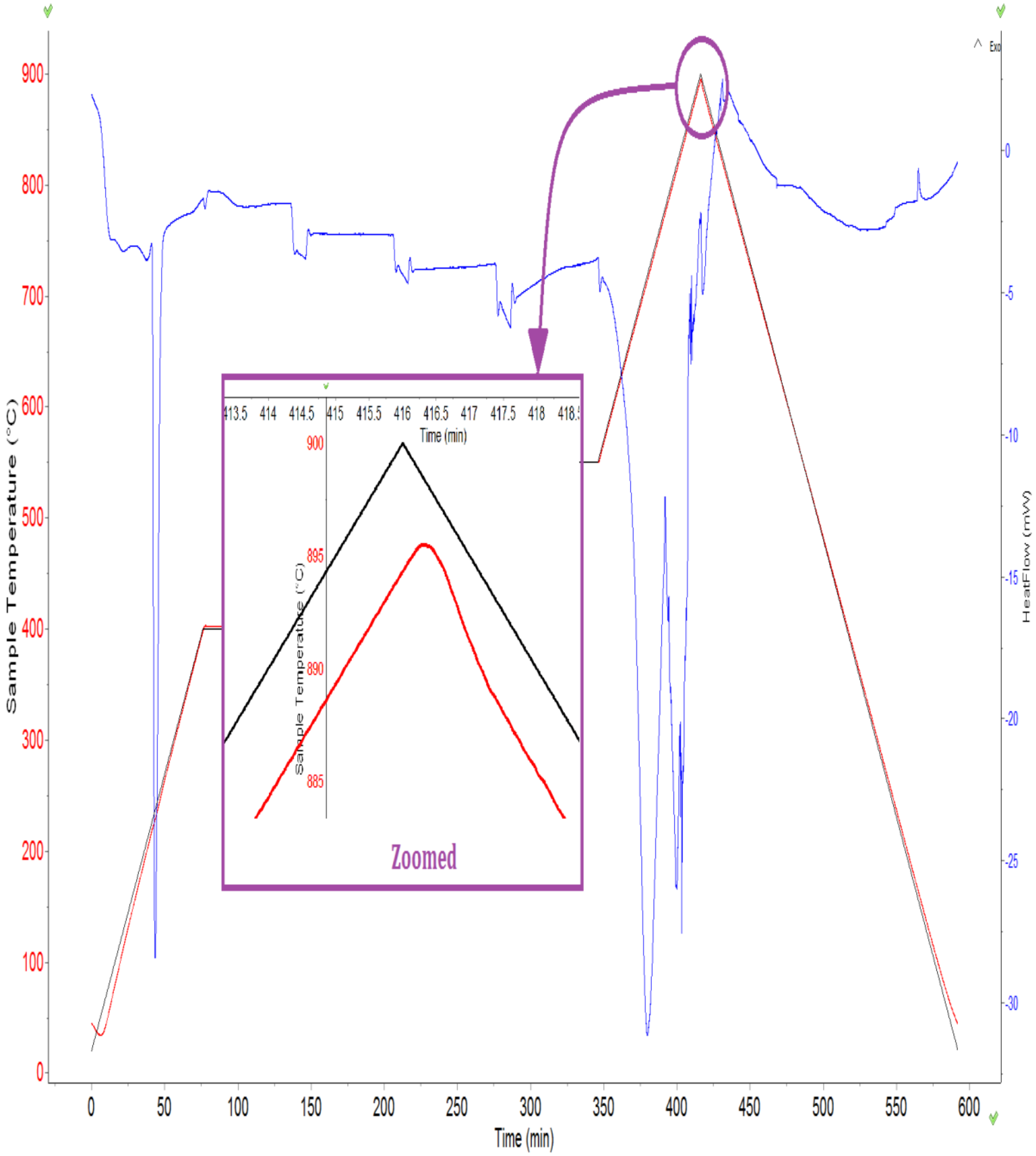

Figure 7.3.3: Thermal lag at the dynamic heating condition at higher set point temperature (900°C) during decomposition of binary salt in single heating-cooling step using DSC/TGA transducer. Sample temperature (red line) is compared with set point temperature (black line) in the inset. Inset picture indicating 5°C temperature lag and approximately 30 second Tau lag.

This thermal lag observed in greater range with both DTA and DSC transducer at the beginning and ending of each test, where sample temperature was not followed linear heating and cooling. The STA controller power regulation did not maintain linear heating/cooling at the beginning and end of the test, as shown in Figure 7.3.3. This phenomenon is known as ‗thermal transient' is a lag observed between furnace thermocouple and sample/reference thermocouple, is described by Boettinger et al. [80].

7.4 SINGLE AND BINARY NITRATES THERMAL ANALYSIS TEST: CONCLUSION

The decomposition temperature results were not accurately reproducible. The results varied within a temperature range of ±10°C. The decomposition temperatures reported by various authors also varied due to sample's sensitivity towards various test parameters as discussed in Chapter 3. The melting points and decomposition temperatures were increased with increasing ionic radius of the cation in order of $LiNO_3 < NaNO_3 < KNO_3$. Stern [25] and Sweeney [275] also observed similar results using thermal analysis. According to Stern [25] the kinetics of decomposition reaction of alkali nitrate is complex as several gaseous products evolved which react with salt melt and with each other. Also the nitrate and nitrite both are unstable, and nitrite partially converts to gaseous phase in concurrent reversible manner. Some decomposed gaseous species react with nitrite to produce nitrate, and again both nitrite and nitrate decompose to oxide and several other gaseous products [25]. The experimental decomposition temperatures of this study are not in agreement in conjunction to some literature value is due to different heating rate, sample size, packing of particles, crucible type used, apparatus type and partial pressure of gaseous environment [102]. Discrepancies among the results at first thought perhaps of salt composition integrity, but the SEM, EDS, ICPOES, and Ion chromatography results of binary salt indicate that sample's integrity was preserved with no formation of nitrite during salt preparation, as presented in subsection 7.5. This also ascertained during melting point detection where no change in melting heat flow peaks observed. Crucible base geometry should match with sample holder base; and sample particles should be finely crashed to ensure good mechanical contact with crucible base, which will improve instrument sensitivity during transformation reactions. A good mechanical contact between sample, crucible base and crucible holder will minimize reaction time recording lag [382]. Also, tightly packed particles usually inhibit free diffusion of gaseous species (sluggish diffusion) from and to reaction zone resulting decomposition point shifting towards higher temperature [382]. Another possibility in case of open-crucible arrangements is the dimension of crucible and gas flow direction may cause stagnation or sluggish removal of evolved vapor species from reaction zone which in turn may suppress transformation during thermal decomposition [382]. Similar comments can be made in the case of manual transpiration rig.

The liquidus and solidus data are considered true value only when the weight loss was net zero, means no vaporization of salt sample occurred, as shown in Figure 7.4.1. The heat flows curve which shows a change in shape for consecutive heat treatment is indicating vapor loss. As a result deviation of liquidus, solidus and transition temperature was observed, such curves are shown in Figure 7.4.2. Figure 7.4.2 showing, due to decomposition at 600°C the salts melting and freezing peaks were changing from cycle to cycle.

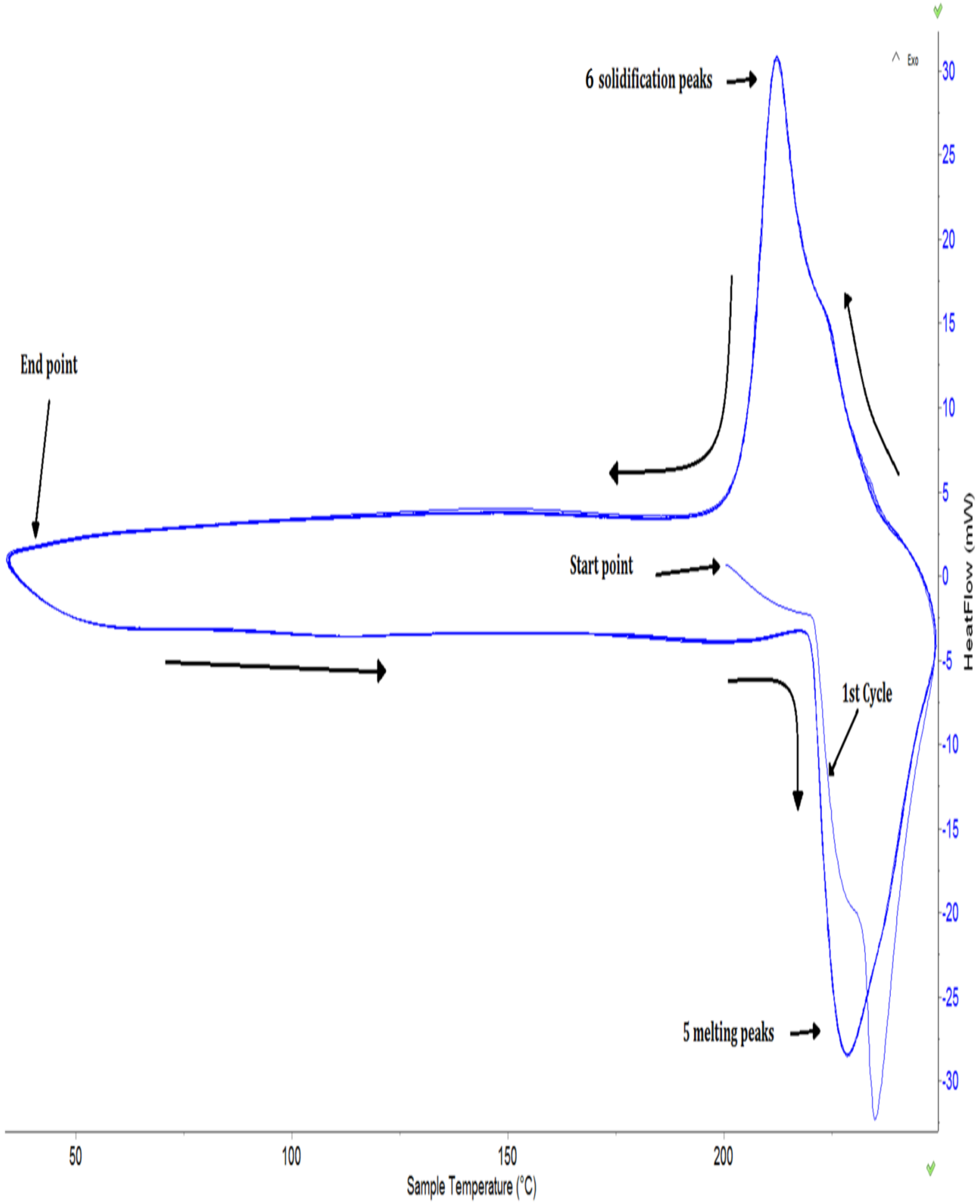

Figure 7.4.1: Identical melting and solidification peaks of binary nitrate salt heated up to 250°C in argon sweep gas.

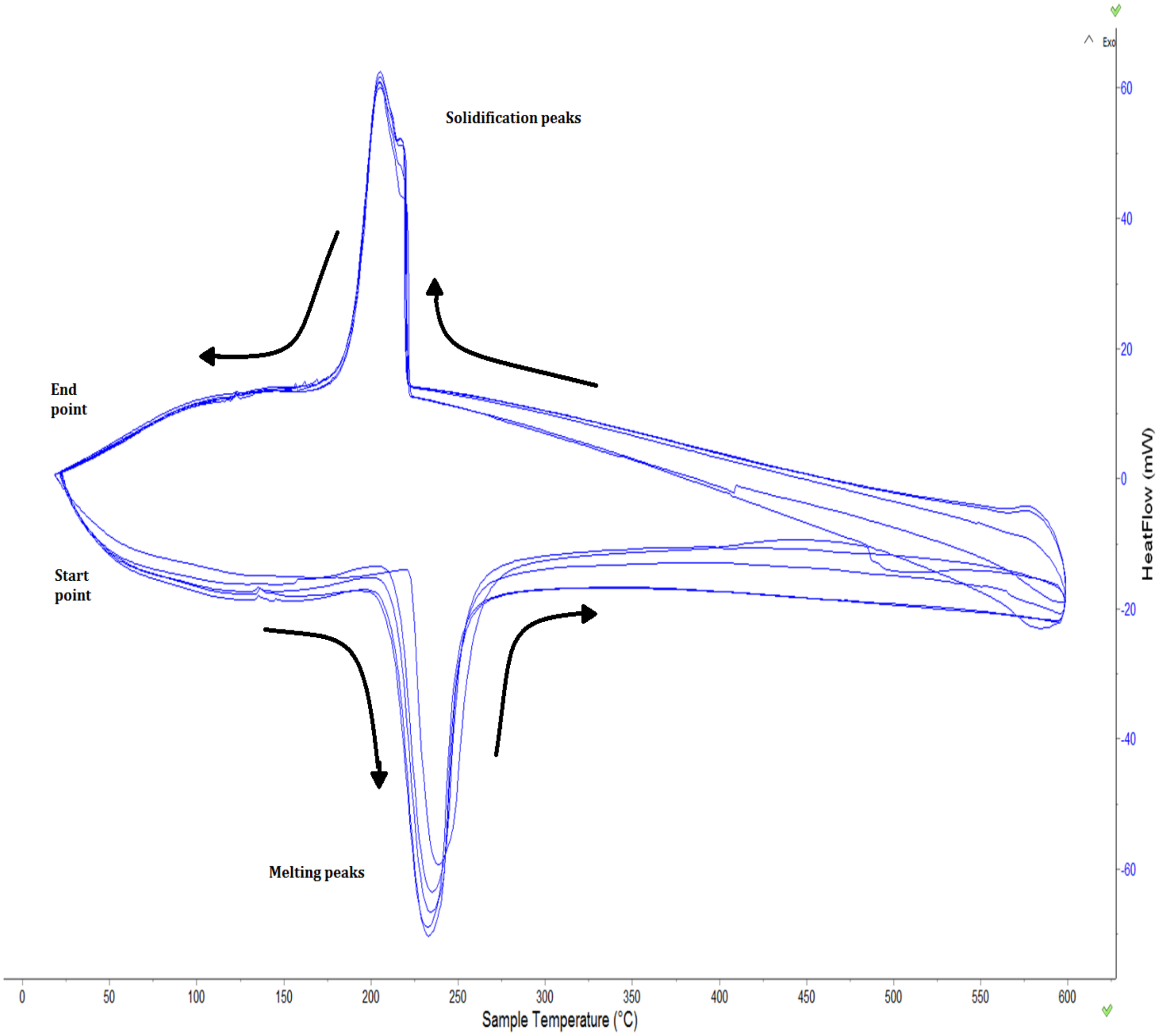

Figure 7.4.2: Cyclic short term DSC heat flow curve (5 heating and cooling) for binary salt heated up to 600°C.

Sample heating and cooling in thermo-balance exhibit buoyancy phenomena usually at a lower temperature where actually no physical and chemical changes occur [390]. Buoyancy is the effect due to hot gas diffusion inside crucible and higher sensitivities of weighing transducer thermocouple. Although the there was no evidence of weight gain/loss during this phenomenon and overall weight change was near zero during this particular period. According to Archimedes principle, the buoyancy of a sample is equal to the mass of the displaced volume of the atmosphere expressed as, m= ρV (ρ=density of the gas in the furnace, V=volume of the crucible, sample, sample holder parts) [391, 392]. Inside the STA apparatus, the furnace gas is heated by conduction at lower temperature and radiation at high temperatures [390]. Usually, at the initial stage, the gas temperature is in advance of sample crucible and sample holder part‘s temperature. This is mainly because the thermal conductivity, density and heat capacity of the gas are different from sample/crucible [390]. When the temperature increases inside the DSC furnace the density of gas decreases results in an upward force equal to the weight of active volume, hence the gas buoyancy reduces. Thus during heating gas buoyancy decreases the resulting weight increase measured [390]. When the heating temperature decreases the gas density increase inside furnace thus buoyancy increases which resulted in weight decrease. The effect of buoyancy is less in more high temperature as radiation heat transfer is dominant compared to lower temperature. Sometimes convection heat currents also cause buoyancy since the furnace wall is hotter than the middle of furnace area where the sample is situated, and gas near furnace wall heated up first and forced down the slightly colder gas in the center of the furnace causing sample crucible weight gain [390]. Other parameters that might exhibit buoyancy are: gas flow drag, high gas velocity, thermal effect on balance mechanism [390]. In this study a blank run with an empty crucible or with the very small sample at high gas flow heated and subtracted from original test run to correct the mass change effect in TG curve [390, 391].

Another issue is noise and smearing in DSC and TGA curve was due to the higher sensitivity of transducer thermocouple where the salt sample bubbling and subsequent overflowing from crucible occurred at higher temperatures. The unsteady baseline of heat flow curve was perhaps due to high noise level happens when the salt vapor deposited in DSC thermocouple rod and chemically attacked the platinum-rhodium thermocouple sensor resulting baseline drifts [34].

DSC/TGA tests showed that the heating and cooling rates have some effect on liquidus and solidus temperature as higher heating rate shift the melting point towards higher temperature and diminishing some intermediate peaks (smaller peaks disappeared or merged to next step prior to melting or solidification). The lower heating rate caused to drift in DSC curves. At higher heating rates (15°C/min) large broad peaks were observed compared to low heating rate (1°C/min). At lower heating rates all the possible DSC peaks were appeared compared to higher scanning rates, but too low heating rates made the peak broader, flatter and closer to the base line, hence might diminish the possibility of seeing sharper peaks such as seen at higher heating rates. Thus during heating test multiple runs were evaluated to observe any unseen events in HF curves.

The heating and cooling rates have some effect on solid-solid transition peaks, melting temperatures and freezing temperature during heating. By decreasing heating and cooling rates, the gaps between liquidus and solidus in single nitrates were minimized, but the gap remains in case of binary salt. The single nitrates and binary salt produce NO fume, and O_2 evolution indicated decomposition reaction involves simultaneous concurrent reversible reactions.

7.4.1 MAJOR CONCLUSIONS ON SINGLE AND BINARY NITRATES

Experimental result of ternary salt can be summarized as follow:

I. The melting temperature increased in the order of $LiNO_3$<$NaNO_3$<KNO_3.
II. The heat of fusion temperature decreased in the order of $LiNO_3$>$NaNO_3$>KNO_3.
III. The thermal stability increased in the order of $LiNO_3$<$NaNO_3$<KNO_3.
IV. The melting point decreased in binary salt compared to KNO_3, but decomposition remains almost same.
V. Dehydration weight loss was higher in binary salt compared to single salts. Lithium nitrate being most hygroscopic and potassium nitrate was less hygroscopic.
VI. Single salts had almost linear melting curves; sharp and striper deviation from the baseline compared to binary salt‘s broad endothermic peak.
VII. The oxygen atmosphere delayed the decomposition temperature. The high partial pressure of oxygen caused some exothermic oxidation of nitrite to delay degradation process.
VIII. In the case of single salts, the lower heating rates increased the heat flow curve resolution.

IX. Lower cooling rates (1°C/min) didn't minimize the gap between liquidus and solidus temperatures of binary salt, possible conclusions are:
   a. The possibility of improper heat flow response time and heat transfer rate of _sample to crucible' and _crucible to thermocouple' (thermal gradients inside different parts of STA).
   b. There are no known ASTM CRMs on the cooling calibration of HF curve for these transducers.

X. Onset temperature of melting and freezing point varied slightly (1 to 5°C) according to holding period. After reaching melting point temperature, When the isothermal holding time was longer (>5min) at or above melting point temperature, the onset melting temperature increased due to proper heat conduction time for phases homogenization and diffusion of tested sample. The isothermal holding at or above salt's melting point did not affect peak temperatures. However, when the mass size increased then the peak height was also increased.

XI. Higher heating rates lead to longer melting peaks as observed in single and binary salts.

XII. N_2, NO, N_2O, NO_2, and O_2 are the main evolved gasses. NO and O_2 are the primarily evolved gasses after melting observed in an argon atmosphere, suggested that the alkali nitrate salt's decomposition pathway involve concurrent simultaneous reversible reactions.

XIII. Salt vapor chemically attacked platinum-rhodium thermocouple wire and caused corrosion in DSC thermocouple wire. Hence, high temperature study was limited to protected DTA transducer only.

7.5 COMPOSITION ANALYSIS OF BINARY SOLAR SALT

XRD, SEM, EDS AND CHEMICAL ANALYSIS RESULTS

In order to identify any change in the composition after binary samples were exposed to ambient air during mixing and homogenization; XRD, EDS/ESM, and chemical analysis were performed. The XRD diffraction patterns were taken at room temperature and analysis indicated two major phases $NaNO_3$, KNO_3 only. The EDS results showed that only $NaNO_3$ and KNO_3 are present, and the elemental percentage indicates only quantitative values of N, O, Na and K. chemical analysis showed that the nitrite ion was not present in the melt.

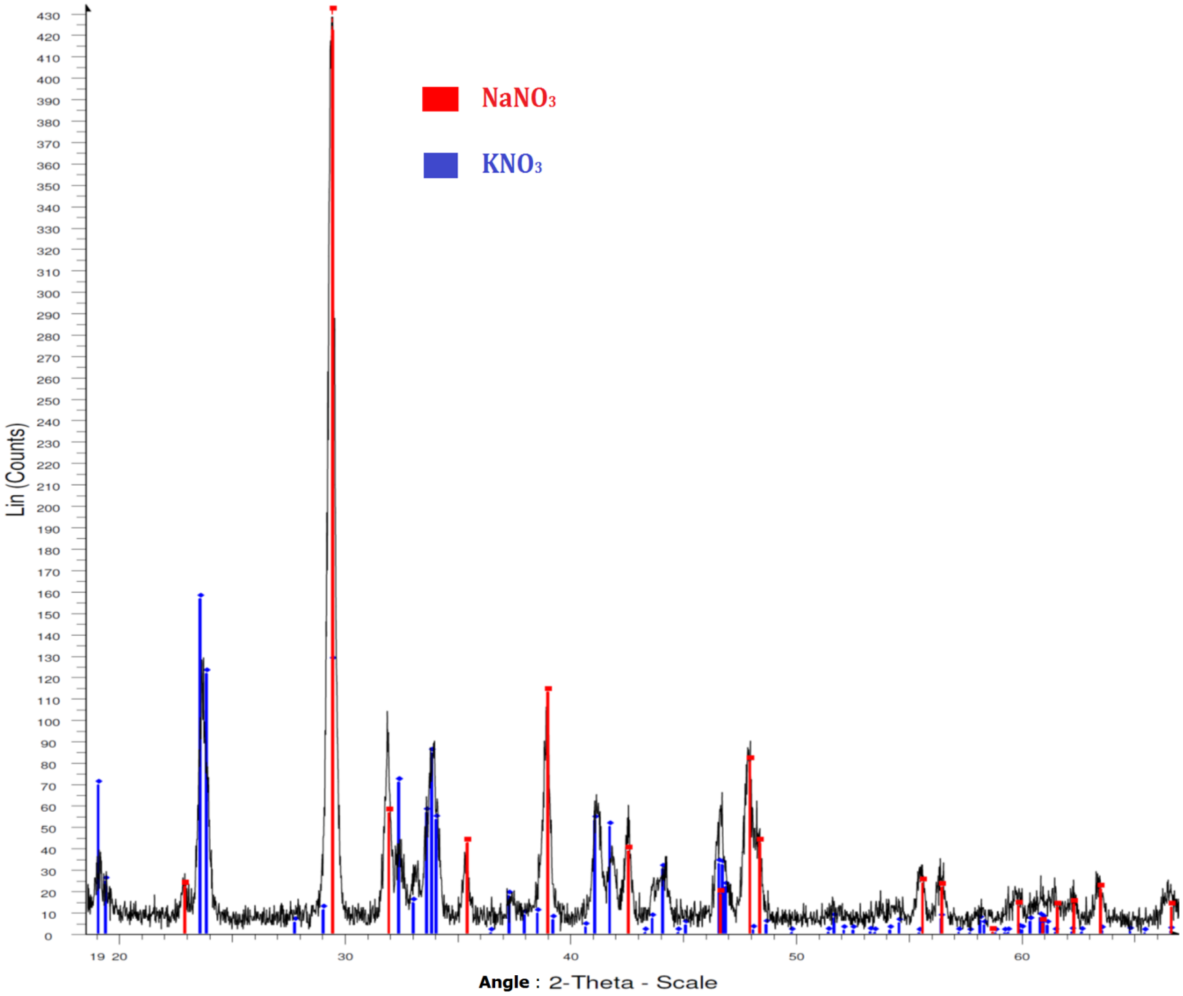

Figure 7.5.1: X-Ray diffraction patterns of 60:40 weight ratio $NaNO_3$-KNO_3 binary salt with Cu K_α emission.

Sodium nitrate occupying almost more than half of the peaks and rest of the peaks represent potassium nitrate, as shown in Figure 7.5.1. The peaks number is higher for sodium nitrate due to higher weight ratio.

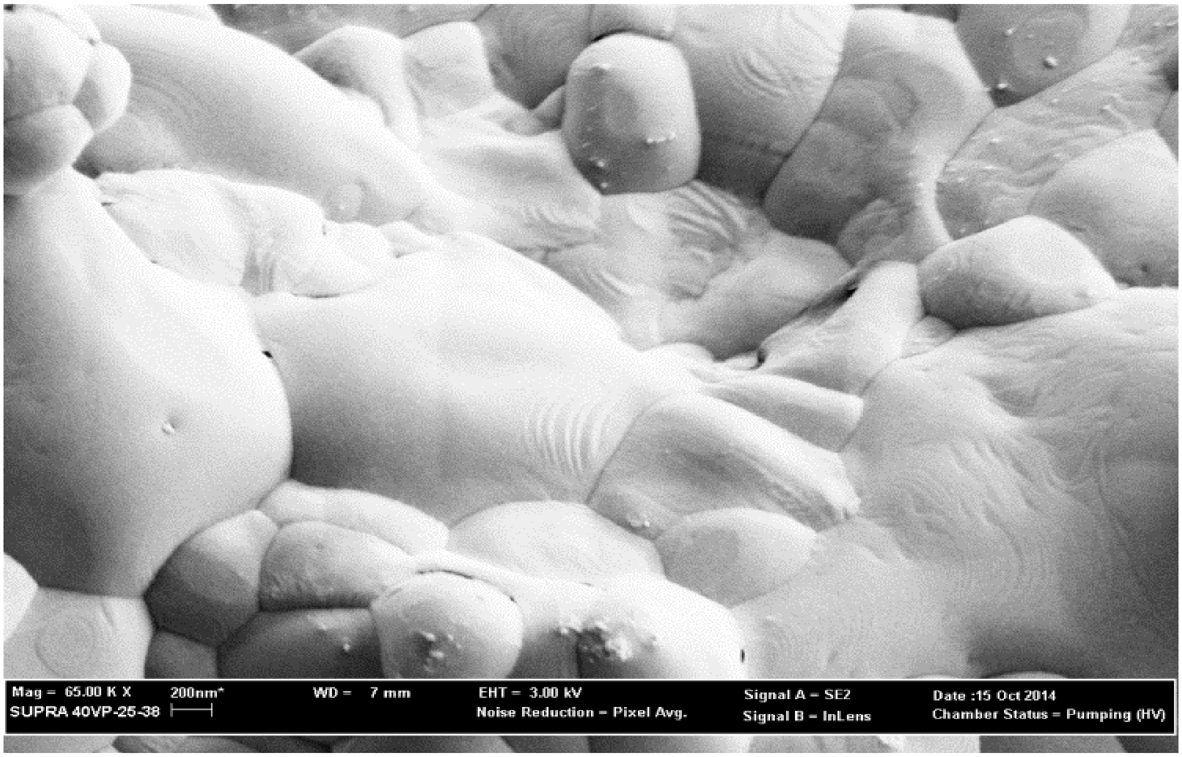

(i)

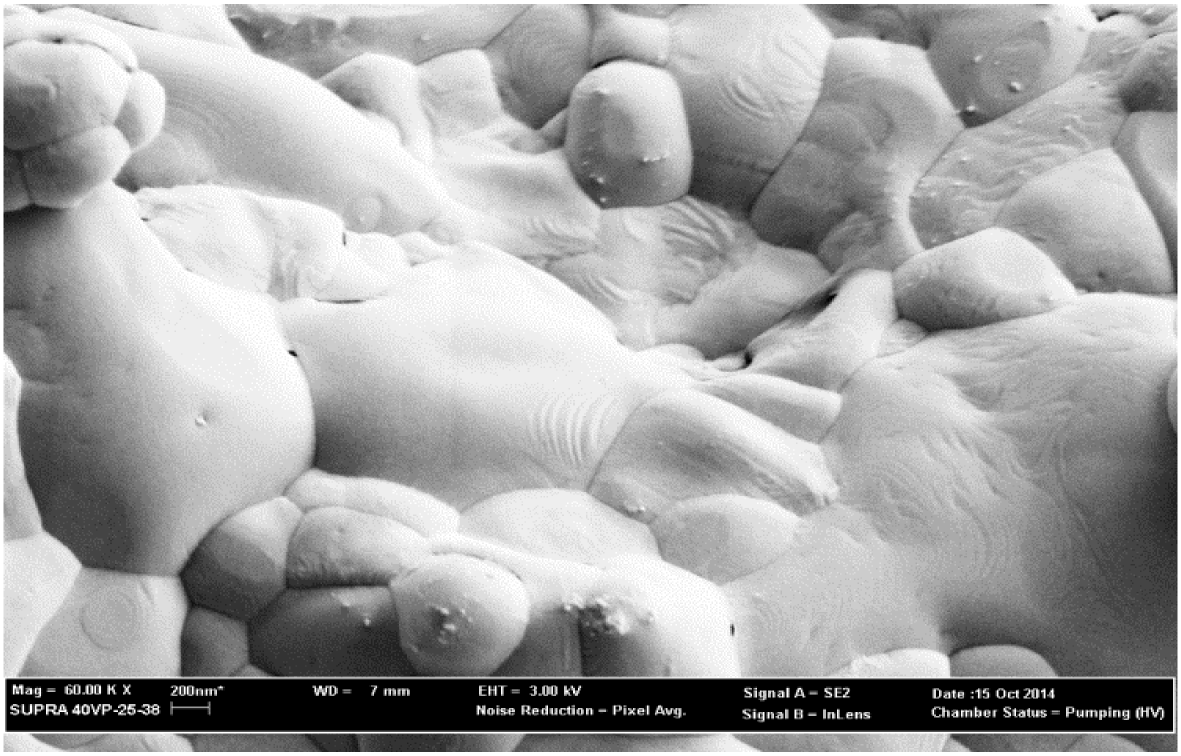

(ii)

(i) Magnification - 65K, EHT=3kV, WD= 7mm. Na/K/NO_3. (ii) Magnification - 60K, EHT=3kV, WD= 7mm.

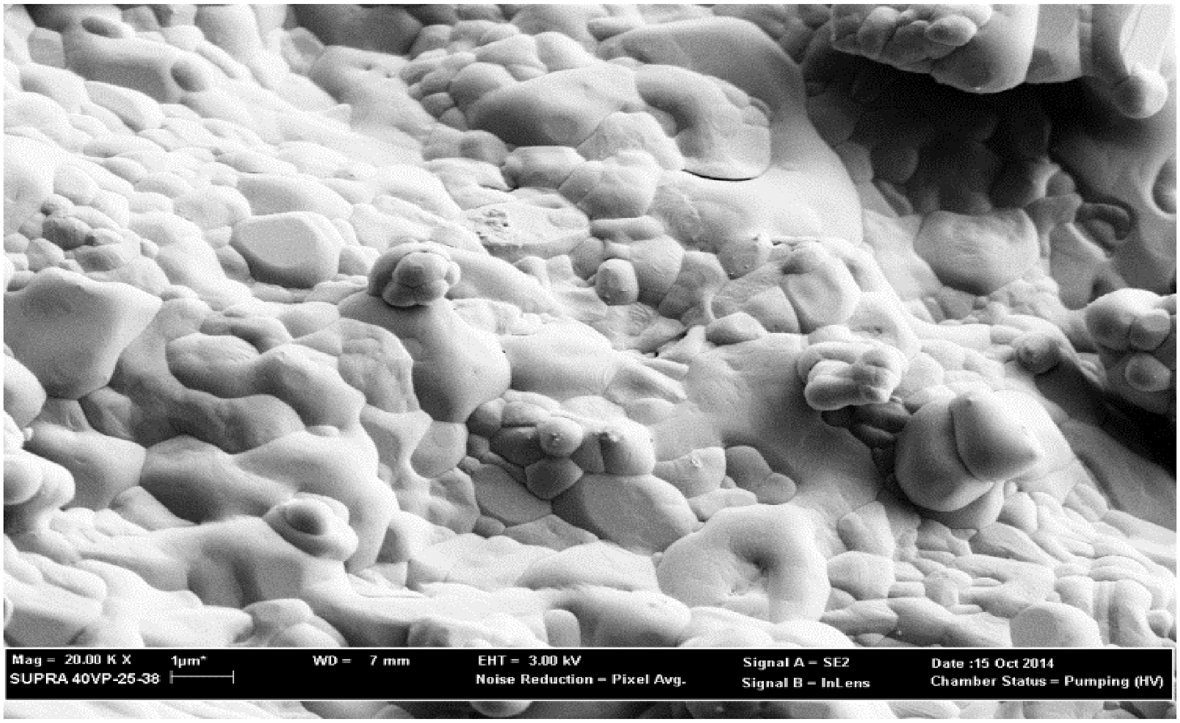

(iii)

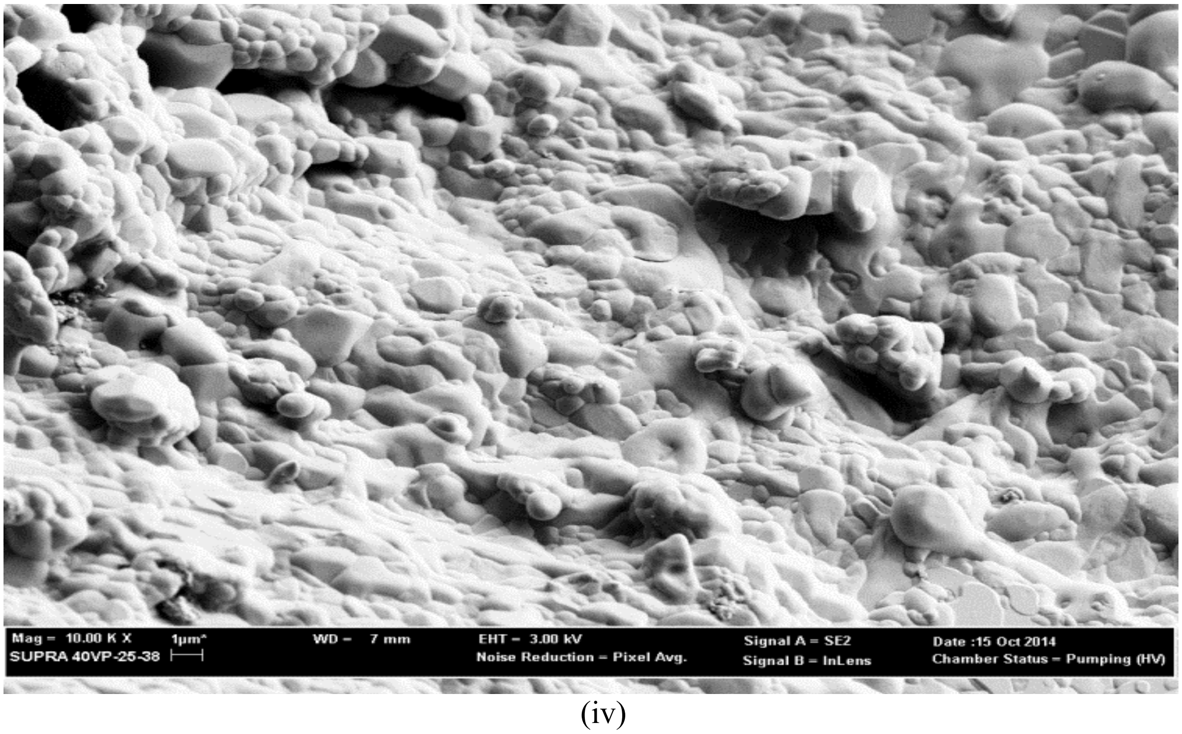

(iv)

(iii) Magnification - 20K, EHT=3kV, WD= 7mm. Na-K/NO_3. (iv) Magnification - 10K, EHT=3kV, WD= 7mm.
Figure 7.5.2: SEM image of 60:40 wt% binary Na-K//NO_3. Salts were mixed, homogenized and equilibrated in air.

Two interesting features at 4 magnifications (x65, x60, x20, x10) are shown in Figure 7.5.2. They showed an agglomerate cluster of various pours regions and non-uniform distribution of solidified mixture with dissimilar morphology. This is indicating a high-density packing. The phases possess deformed pomegranate seeds shape.

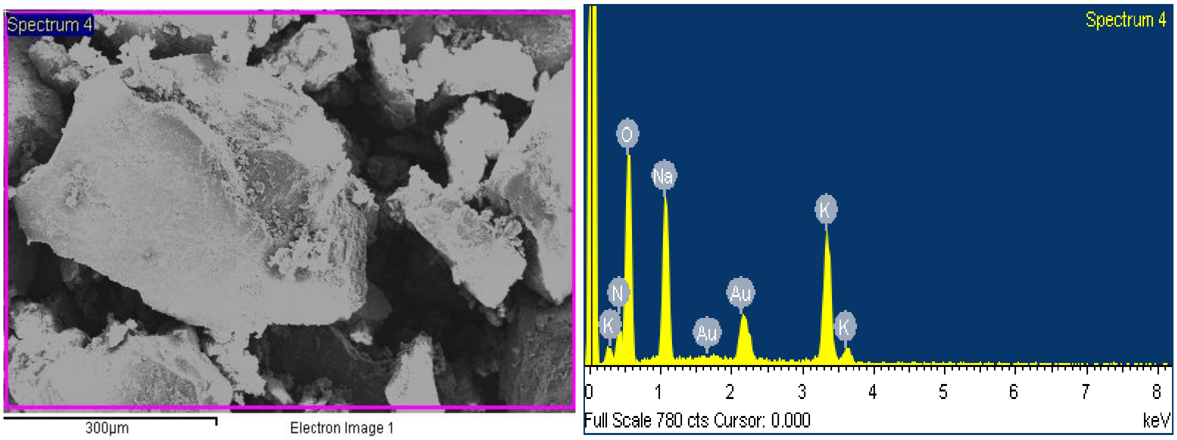

(a) (b)

Element	Weight%	Atomic%
N	14.29	20.43
O	48.14	60.29
Na	12.43	10.84
K	14.33	7.34
Au	10.81	1.10
Totals	100.00	

(c)

Figure 7.5.3: (a) Gold-sputtered sample substrate image of EDS spectrum area; (b) N, O, Na and K showed from surface EDS spectrum; (c) elemental composition percentage of N, O, Na and K.

The elemental results were quite scattered for area to area during sample analysis in EDS, as shown in figure 7.5.3. Oxygen is three times than nitrogen because of polyatomic nitrate ion structure. Due to 60:40 weight ratio of Na-K//NO_3 the sodium percentage is higher than potassium. None of the elements can be distinguished in various separate phase structure regions which suggesting for further testing.

After sending binary sample to UNSW Mark Wainwright Analytical Center, for ICPOES (Inductively coupled plasma optical/atomic emission spectroscopy) and Ion Chromatography test, nitrite (NO_2^-) was not detected in the solution. The salt sample was dissolved in MilliQ water and observed moisture as impurities. The report indicates that the binary sample might contain only Na, K and nitrate (NO_3^-), as shown in Table 7.5.1. The binary solution was diluted 100 times before ICPOES measurement of Na and K and diluted 5000 times before measuring nitrate and nitrite by Ion Chromatography. Also, due to the nature of the test it may assume that the high dilution factors may introduce some uncertainties to the result.

Table 7.5.1: ICPOES and Ion chromatography results of binary nitrate salt.

Binary Na-K//NO_3 salt	Unit	K	Na	NO_3	NO_2
Sample	wt %	15.3	15.8	66.2	0.00
LOR (limit of reporting)	mg/L	0.50	0.20	1.00	0.50
LOR-Limit of Reporting - The lowest concentration of a substance that can be reliably reported, using a specific laboratory method and instrument					

7.6 TRANSPIRATION TEST RESULTS

A horizontal tube (HT) furnace was used for heating the pre-weighed samples in combustion boat to observe weight loss behavior. In all test, the sample size was 1.7±0.005g.

Transpiration test showed that the weight loss curves were not repeatable, as shown in Figures 7.6.1 to 7.6.5. Series of weight loss measurement was carried out for single salts and binary Na-K//NO_3 salt at different isothermal heating and carrier gas flow rates. The salts weight loss was almost independent of flow rate measured at 20 minutes intervals, as shown in Figures 7.6.2 to 7.6.5. Binary 60:40 weight ratio sodium nitrate-potassium nitrate was heated at several temperatures and in argon and air of various flow rates. The curves were not reproducible; weight losses were not linear and were independent of flow rates. Almost all of the salt samples tested showed approximately on an average 3 to 5% mass loss during heat treatment. Higher heating temperature exhibited higher mass loss compared to lower heating temperature, as shown in Figures 7.6.4 and 7.6.5.

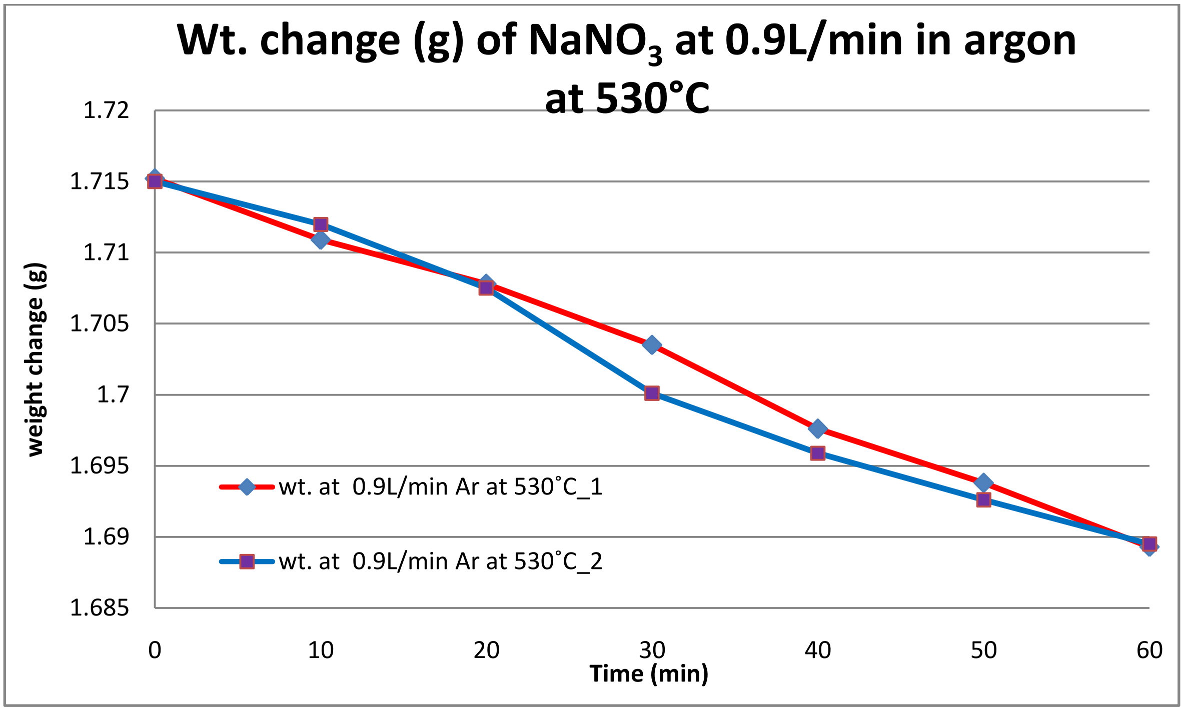

Figure 7.6.1: Weight change curves of $NaNO_3$ at 530°C in argon gas flow rate of 0.9l/min.

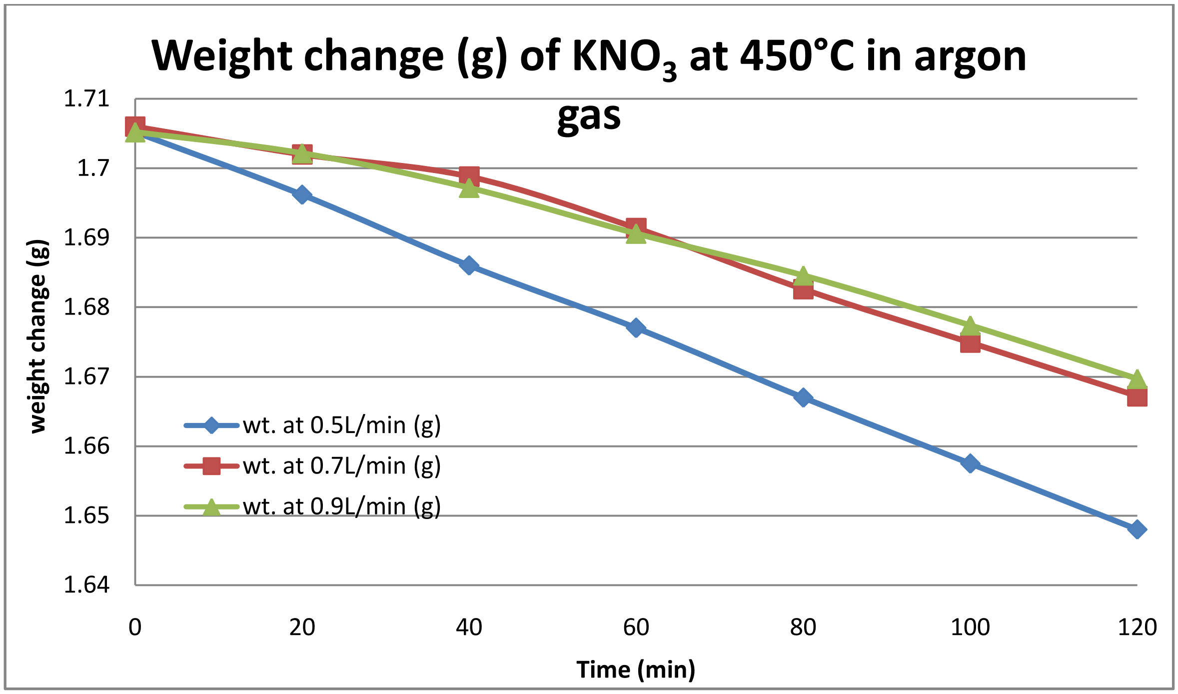

Figure 7.6.2: Weight change curves of KNO_3 at 450°C in various argon gas flow rate.

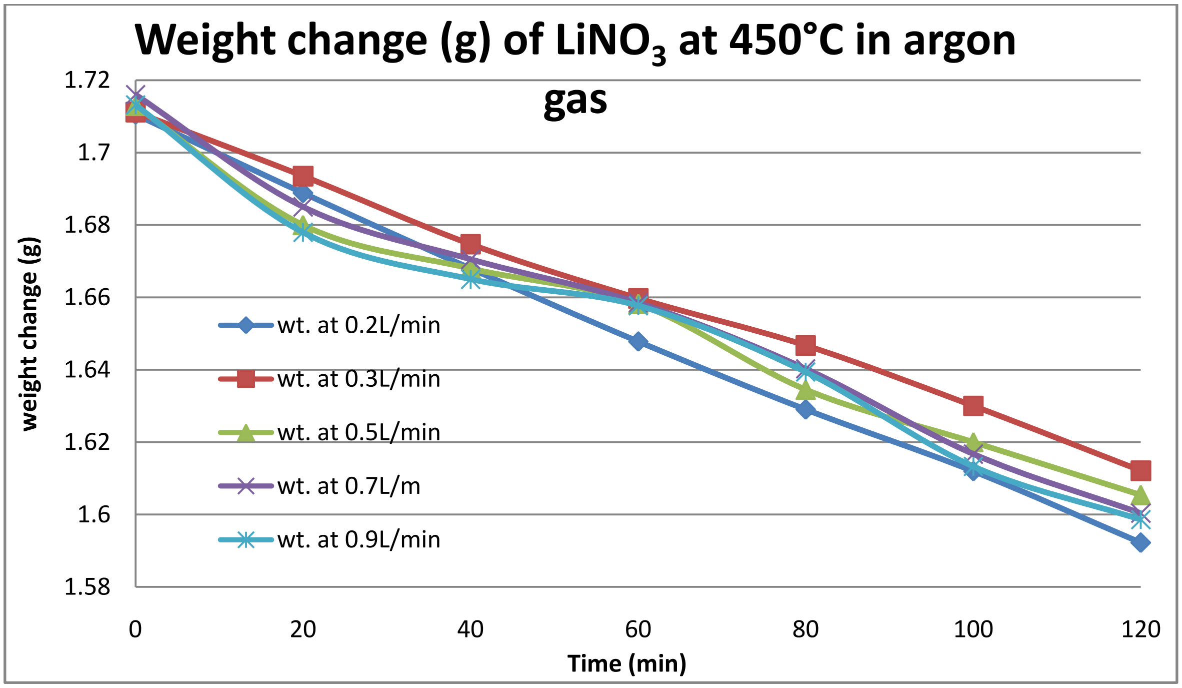

Figure 7.6.3: Weight change curves of $LiNO_3$ at 450°C in various argon gas flow rate.

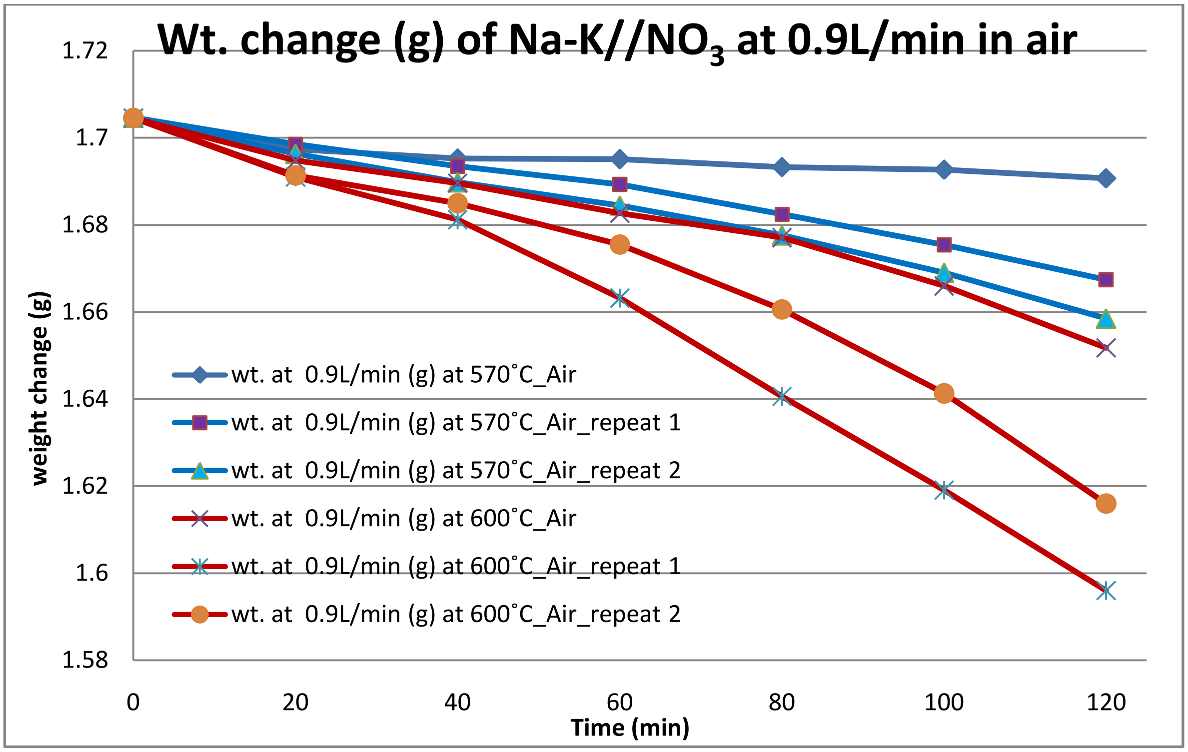

Figure 7.6.4: Weight change curves of Na-K//NO_3 in air flow rate of 0.9l/min.

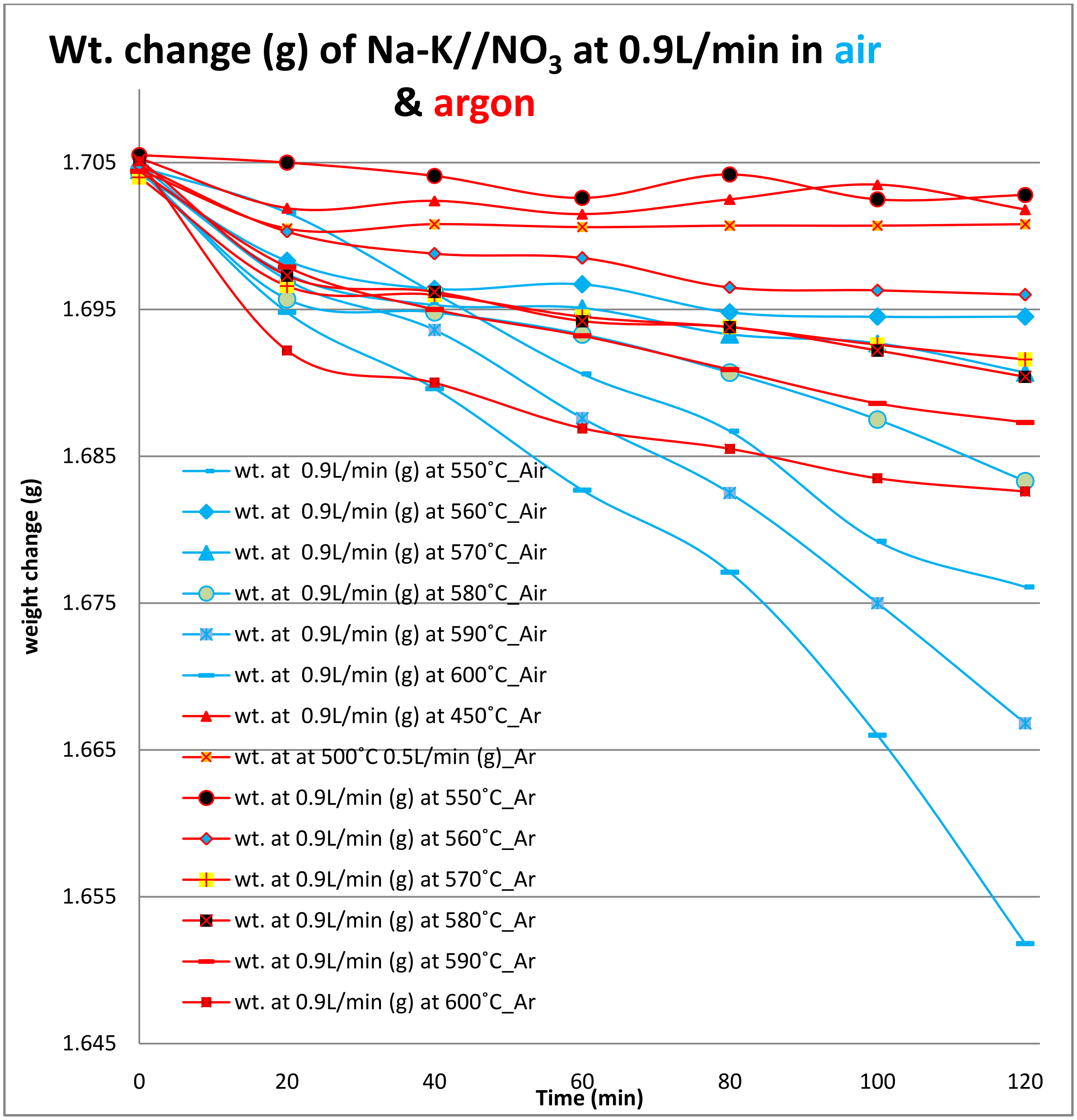

Figure 7.6.5: Weight change curves of Na-K//NO_3 in air and argon flow rate of 0.9l/min.

The moisture was easily caught up during loading and unloading of the sample. In between the run during weighing in microbalance, the weight of the boat sample increased 0.06gm/minute (approximately).

Binary nitrate salt‘s heat treatment in argon should show different behavior compared to air atmosphere (partial pressure of oxygen= 0.21). As previously discussed in Chapter 3, salt melt exposing to ambient air showed reactivity with O_2, and hence nitrite oxidation suppressed the thermal degradation point. Similar behavior was expected in single and binary nitrate melts. Surprisingly quite opposite behavior, more weight loss was observed in the air compared to inert environment, as shown in Figure 7.6.5. The primary reasons are sample‘s exposure to ambient air; sample‘s spillage from combustion boat during boat guiding; and sample‘s sensitivity toward experimental parameters (any fluctuation in temperature and carrier gas flow rates). Several times modifications were performed on transpiration rig to obtain accurate guiding of combustion boat and but the results were not repeatable and inconsistent.

7.6.1 DISCUSSION ON TRANSPIRATION TEST RESULTS

The weight loss curves obtained were not repeatable; the reasons are many, and the possible causes and solutions are:

i) The combustion boat carrying the molten salt did not have uniform lateral movement inside reaction tube and was difficult to control. Hence, tilting of combustion boat occurred, and salt spillage was evident. Several modifications of push rod guide assembly could not improve the control movement of the boat.

ii) While pulling the sample boat out from reaction tube using magnet was not a smooth transition. When the magnet is touched the glass tube, a sudden movement of ferrous bar caused some salt melt spillage.

iii) The salt sample was dried and weighed in microbalance during test intervals. During this weighing period, moisture was absorbed and hence the variation in weight was observed.

iv) Gas flow rates were not steady and had fluctuation might cause irregular vapor species sweeping.

As discussed in Chapter 3, the decomposition temperatures were varied when experimental parameters changed; this was also observed in DTA/TGA test. Also due to the reversible concurrent nature of the reactions and presence of unstable oxides the weight loss pattern affected ambiguously [208]. No compositional change of the binary salt was observed while equilibrated in air atmosphere as discussed in subsection 7.5.

7.6.2 CONCLUSIONS

Transpiration test is not suitable for studying the nitrate systems because of sensitivity towards the experimental condition. Moreover, most importantly due to the nature of the reactions that are concurrent and overlapping as observed in STA in MS graphs of this study.

CHAPTER 8 STA RESULTS FOR TERNARY NITRATE SALT

In this chapter, the ternary nitrate salts subjected to thermal and mass analysis test is discussed with the aid of built-in apparatus software ‗Calisto‘ [332] and ‗Quadera‘ [347]. Using Calisto [332] software the sample weight loss at various stages, transition HF peaks, melting HF peaks, onset and offset peak temperatures were detected and the subsequent explanation is provided. Using Quadera [347] software, the evolved gasses were detected, and the decomposition temperatures were identified.

The ternary $NaNO_3$-KNO_3-$LiNO_3$ (13.23-57.14-29.63 weight ratio) salt was heated from 50°C to 800°C in three atmospheres: argon, air, and oxygen using a DTA/TGA-MS simultaneous thermal analyzer. All tests were conducted in 80µL alumina crucibles of same batch (Setaram Instruments) and with same starting a salt mass of 35.00 mg (±0.03 mg). In the case of DSC/TGA-MS 100µL, alumina crucibles were used. In each atmosphere, the salts were heated at identical sweep velocity of 40ml/min and three scanning rates 2.5, 5 and 10°C/min to observe the effect of heating rates on decomposition behavior. The reason to choose the optimum volume of 35 mg or 35 µL as starting mass is to avoid salt overflow from crucible which commonly known as creeping [34]; to avoid thermal lag from the bulk sample (>40mg) to the thermocouple sensor, and to sustain for the full decomposition test. The gas flow rate was 40ml/min (upper limit of the apparatus is 200ml/min) to avoid buoyancy and excessive salt sample weight loss. The upper temperature was chosen an optimal 800°C to minimize thermocouple deterioration in contact of corrosive sample vapor at a higher temperature than 800°C.

8.1 RESULTS

The ternary salt was subjected to heating and cooling from 50 to 140°C for melting and solidification peaks detection in each atmosphere in following a range of heating-cooling rates: 1, 2, 4, 5, 6, 8, 10 and 15°C/min. The heating rates have some effects on melting and on freezing temperatures. During cooling the solid-solid transition was merged with solidification peak at each cooling rates. There was average 30°C temperature difference between liquidus and solidus temperature both in DTA and DSC transducer. Lower cooling rates did not minimize the gap in-between solidus and liquidus temperatures in greater extent.

In DTA transducer, the α/β solid-solid transition temperature prior to melting was 80°C in argon, 84°C in air and 87°C in the O_2 atmosphere. In argon onset liquidus temperature was 113°C, solidus temperature was 82°C and melting peak temperature was 119°C. These temperatures tend to increase slightly at oxygen rich atmosphere. The transition peak was not appeared in DTA transducer during cooling. In the air the onset liquidus temperature was 114°C, solidus temperature was 83°C and melting peak temperature was 120°C. In O_2 the onset liquidus temperature was found 115°C, solidus temperature was 85°C and melting peak temperature was 121°C. Since DTA transducer is for qualitative measurement less accurate and has lower sensitivity below 250°C heating temperature, thus the results varied compared to DSC transducer.

In DSC transducer, the solid-solid transition onset was 99°C and peak was at 103.4°C in an argon atmosphere (at 10°C/min heating and cooling rate). The transition peak was not appeared in DSC transducer during cooling except at 1°C/min cooling rate. At 10°C/min heating and cooling rate in an argon atmosphere, ternary nitrate showed solid-solid transition peak temperature at 103.4°C before melting with the heat of transition 8.3J/g. The salt melted (liquidus onset) at 122.8°C and solidified at 92.7°C. The heat of melting and heat of solidification was 126J/g and -84.2J/g respectively, as shown in Table 8.1.1.

Heating the ternary salt from 50 to 800°C, results showed that the decomposition temperature is lower in argon and higher in oxygen, as shown in Table 8.1.2. The heating rates have an effect on rapid weight loss temperatures and heat flow curves as shown in Figures 8.2.1 to 8.2.9. With increasing heating rates the decomposition temperature increased. There was no significant trend observed for gaseous evolution temperature while comparing with different heating rates. The ternary salt heated at 10°C/min showed stability up to 545°C in argon, 571°C in air and 600°C in oxygen. At 5°C/min heating rate the salt is stable up to 515°C in argon, 533°C in air and 577°C in oxygen. At 2.5°C/min scanning rate the salt is stable up to 503°C in argon, 518°C in air and 570°C in oxygen. At 10°C/min heating rate the oxygen rich atmosphere suppressed the decomposition temperature by 55°C compared to the inert atmosphere of argon, as shown in Table 8.1.2. With increasing partial pressure of oxygen in the blanket gas, NO evolution was delayed as seen in three atmospheres. In an argon atmosphere NO gas evolved at 500°C whereas in air at 550°C and in oxygen at 540°C.

Table 8.1.1: Thermal events of ternary $LiNO_3$-$NaNO_3$-KNO_3 salt heated at argon atmosphere (flow rate 40ml/min) and at various heating and cooling rates using a simultaneous STA (Setaram setsys DSC/TGA-MS).

Thermal events	Heating and cooling rates (°C/min)							
	1	**2**	**4**	**5**	**6**	**8**	**10**	**15**
Transition peak temperature prior to melting (°C)	95.7	102.5	102.8	102.4	102.6	103.1	103.4	104.1
Liquidus onset temperature (°C)	122.9	123	123.1	123.2	123.2	122.8	122.8	122.9
Liquidus offset temperature (°C)	130.7	132.7	134.3	134.5	134.6	134.6	134.4	133.9
Melting peak temperature (°C)	127.3	128.3	129.5	129.9	130.1	130.2	130.3	130.4
Solidus onset temperature (°C)	100.5	98.1	95.6	94.8	94.1	93.1	92.7	111.7
Solidus offset temperature (°C)	92.2	88.3	83.9	82.1	80.1	77.9	77.1	96.1
Freezing peak temperature (°C)	96.7	93.9	90.7	89.4	88.3	86.3	85.9	105
Transition peak temperature during cooling (°C)	75	X	X	X	X	X	X	X
Heat of transition prior to melting (J/g)	18.1	10.3	9.4	9.9	10	9.3	8.3	11.4
Heat of transition during cooling (J/g)	-6.9	X	X	X	X	X	X	X
Heat of melting (J/g)	117	128.1	123.3	123	122	130.1	126.9	123.9
Heat of solidification (J/g)	-89.9	-88.8	-86	-84.6	-84.7	-85.9	-84.2	-115.8
Melting peak height (mW)	-11.7	-19.6	-29	-31.6	-33	-35.7	-36.2	-37.3
freezing peak height (mW)	8.9	14.6	22.5	24.8	25.5	29.8	29.9	43.2
X indicating no data appeared.								

Table 8.1.2: Thermal events of ternary $NaNO_3$-KNO_3-$LiNO_3$ salt (*13.23-57.14-29.63 weight or 13.53-49.12-37.35 mole ratio*) heated from 50 to 800°C at three atmospheres (*sweep gas velocity of 40ml/min*) and scanning rates using a simultaneous Setaram setsys DTA-TGA-Pfeiffer MS thermal and off-gas analyzer.

Sweep gas type	Scanning rate (°C/min)	TG rapid weight loss beginning temperature (°C)	Irreversible endothermic heat flow peak starting temperature (°C)	Gaseous products evolution temperature (°C)				
				O_2	**N_2**	**NO**	**NO_2**	**N_2O**
argon P_{O_2}=0	**10**	545	517	550	580	500	525	575
	5	515	480	490	600	450	518	490
	2.5	503	470	520	625	500	500	550
air P_{O_2}=0.21	**10**	571	550	x	x	550	540	500
	5	533	485	x	x	515	514	540
	2.5	518	440	x	x	512	575	590
oxygen P_{O_2}=1	**10**	600	490	x	550	540	542	530
	5	577	540	x	535	575	578	620
	2.5	570	450	x	535	525	580	640
x indicating unable to detect evolve temperature due to similar AMU (Atomic Mass Unit) as a sweep gas.								

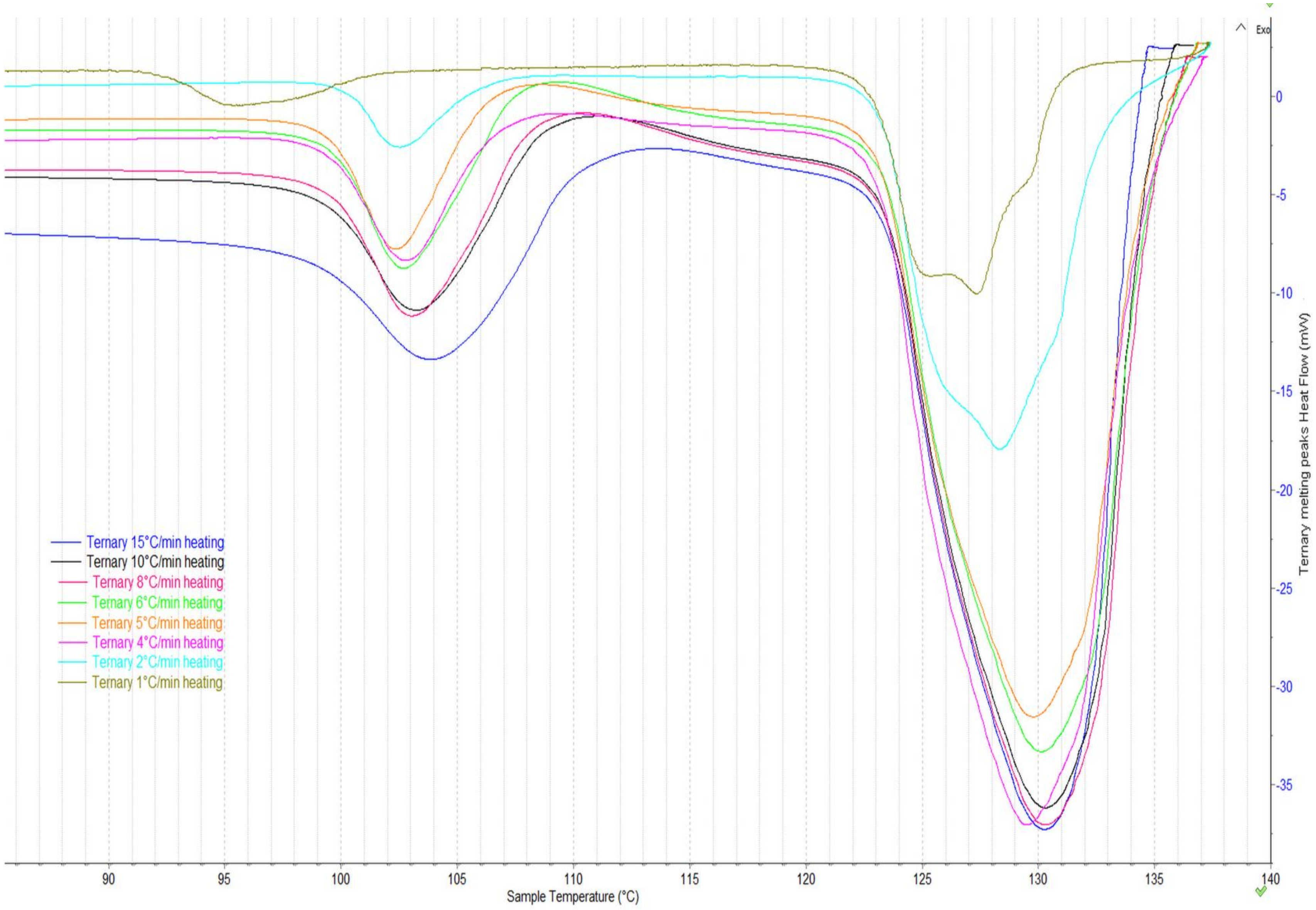

Figure 8.1.1: Ternary melting peaks at various heating rates.

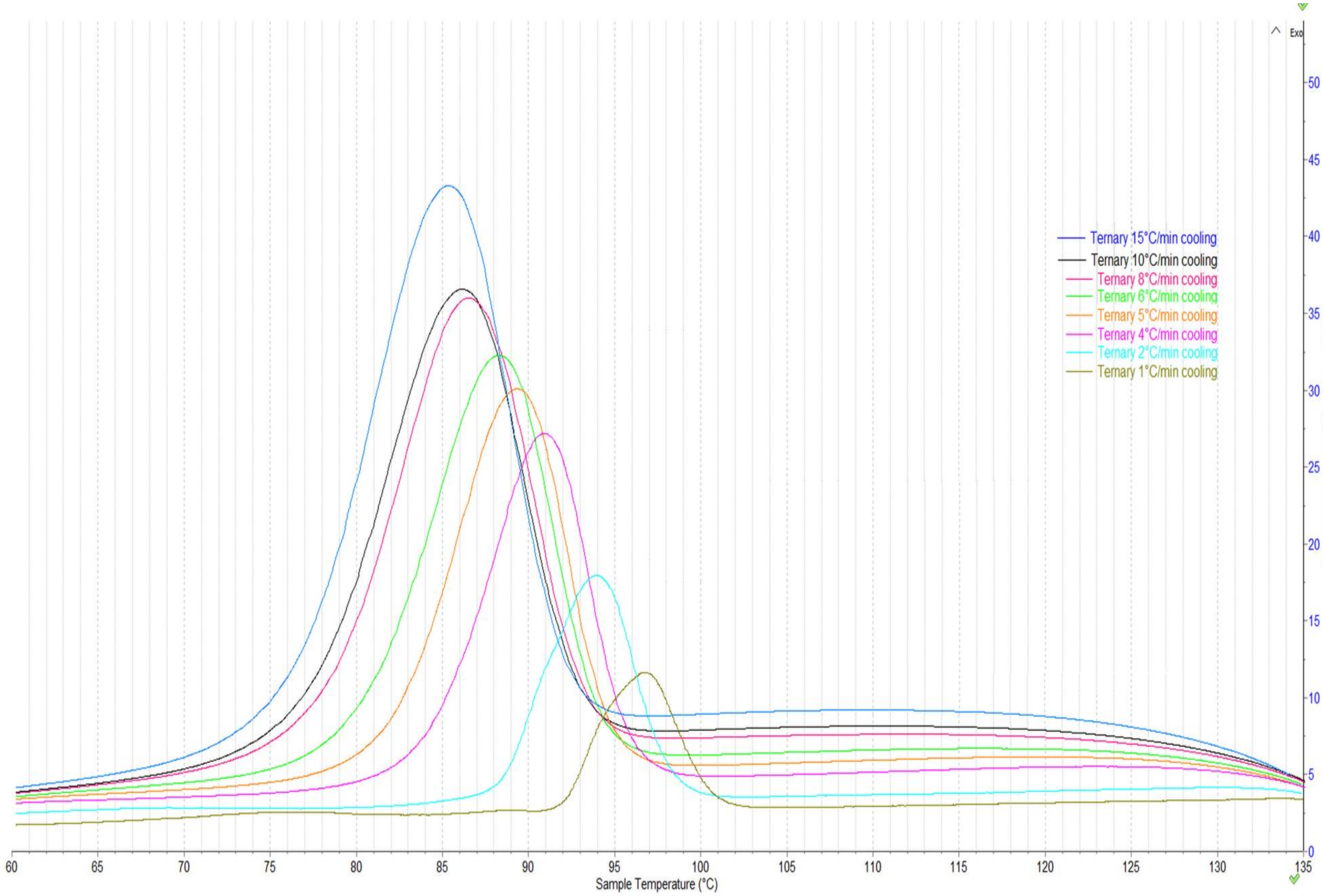

Figure 8.1.2: Ternary freezing peaks at various cooling rates.

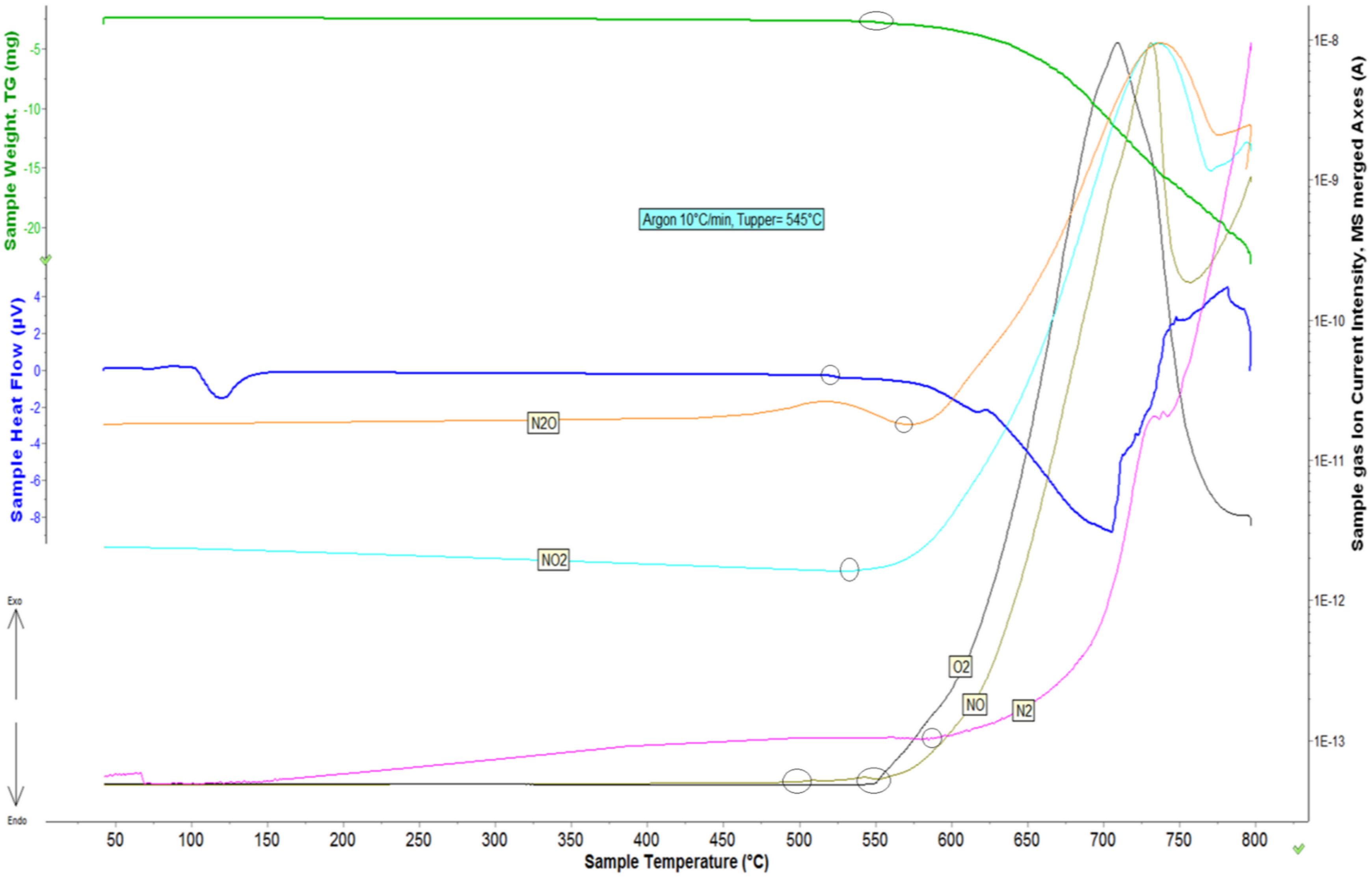

Figure 8.2.1: Ternary salt in an argon atmosphere at 10°C/min heating rate. The black circles are indicating corresponding temperatures.

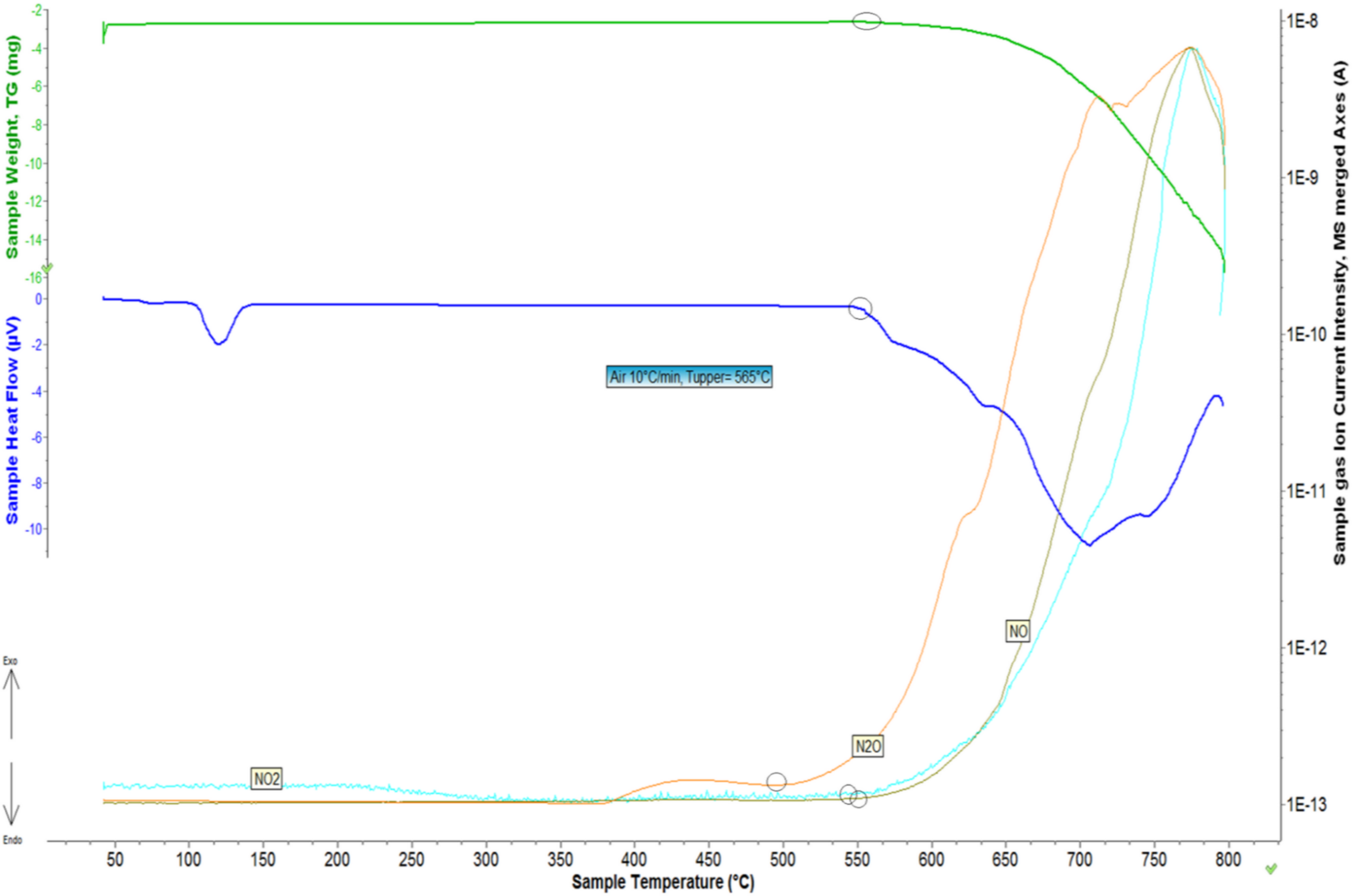

Figure 8.2.2: Ternary salt in an air atmosphere at 10°C/min heating rate. The black circles are indicating corresponding temperatures.

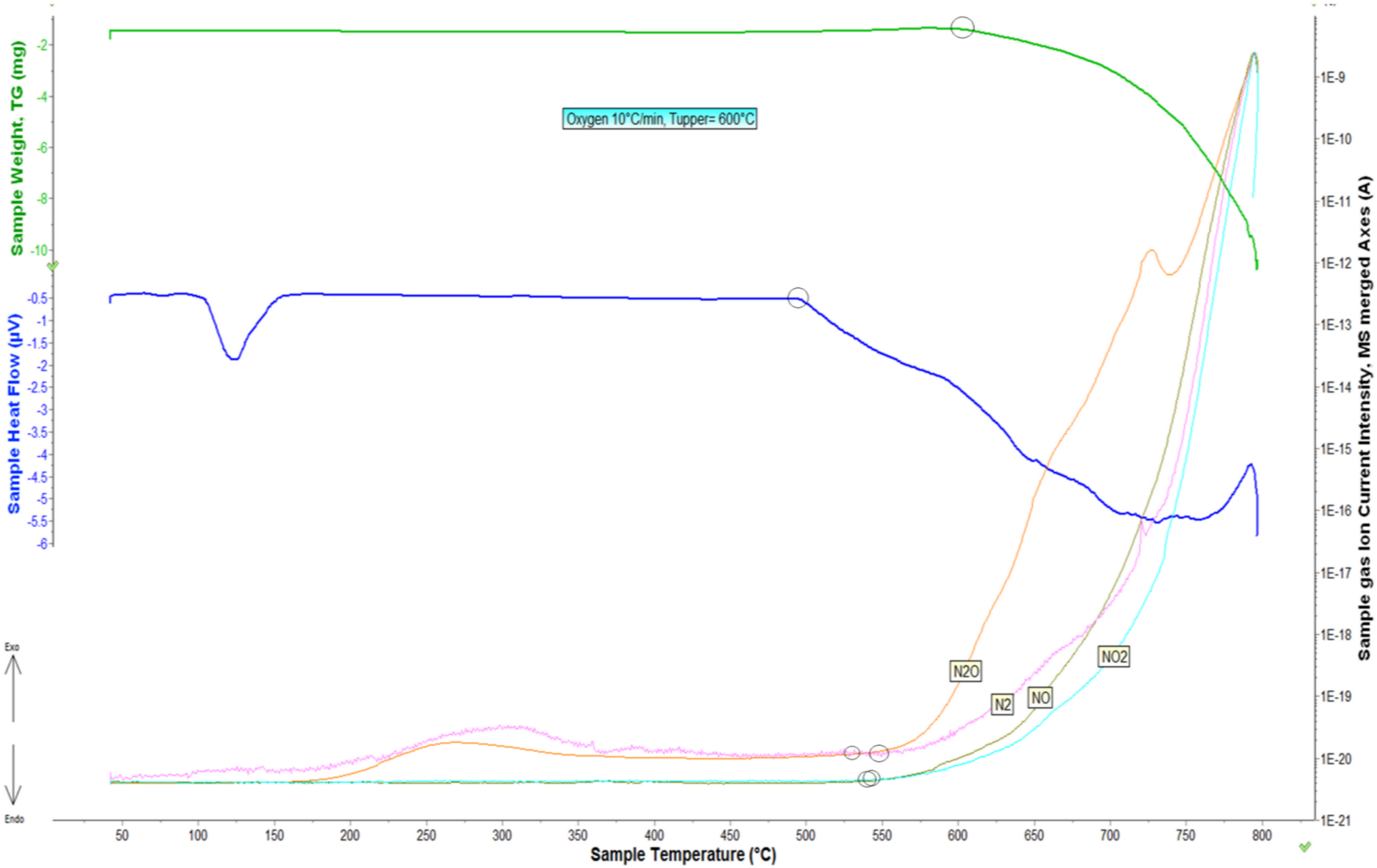

Figure 8.2.3: Ternary salt in an oxygen atmosphere at 10°C/min heating rate. The black circles are indicating corresponding temperatures.

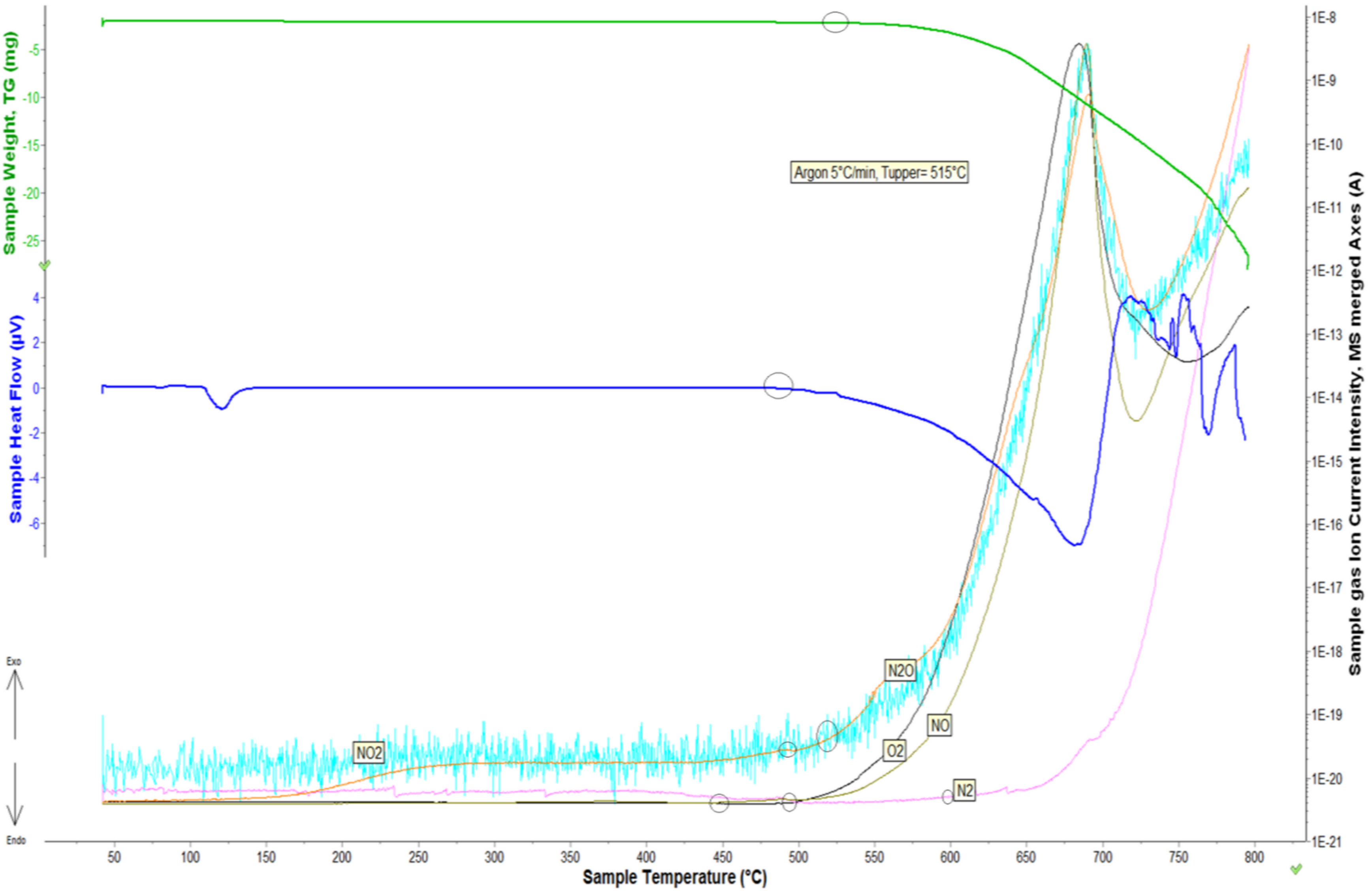

Figure 8.2.4: Ternary salt in an argon atmosphere at 5°C/min heating rate. The black circles are indicating corresponding temperatures.

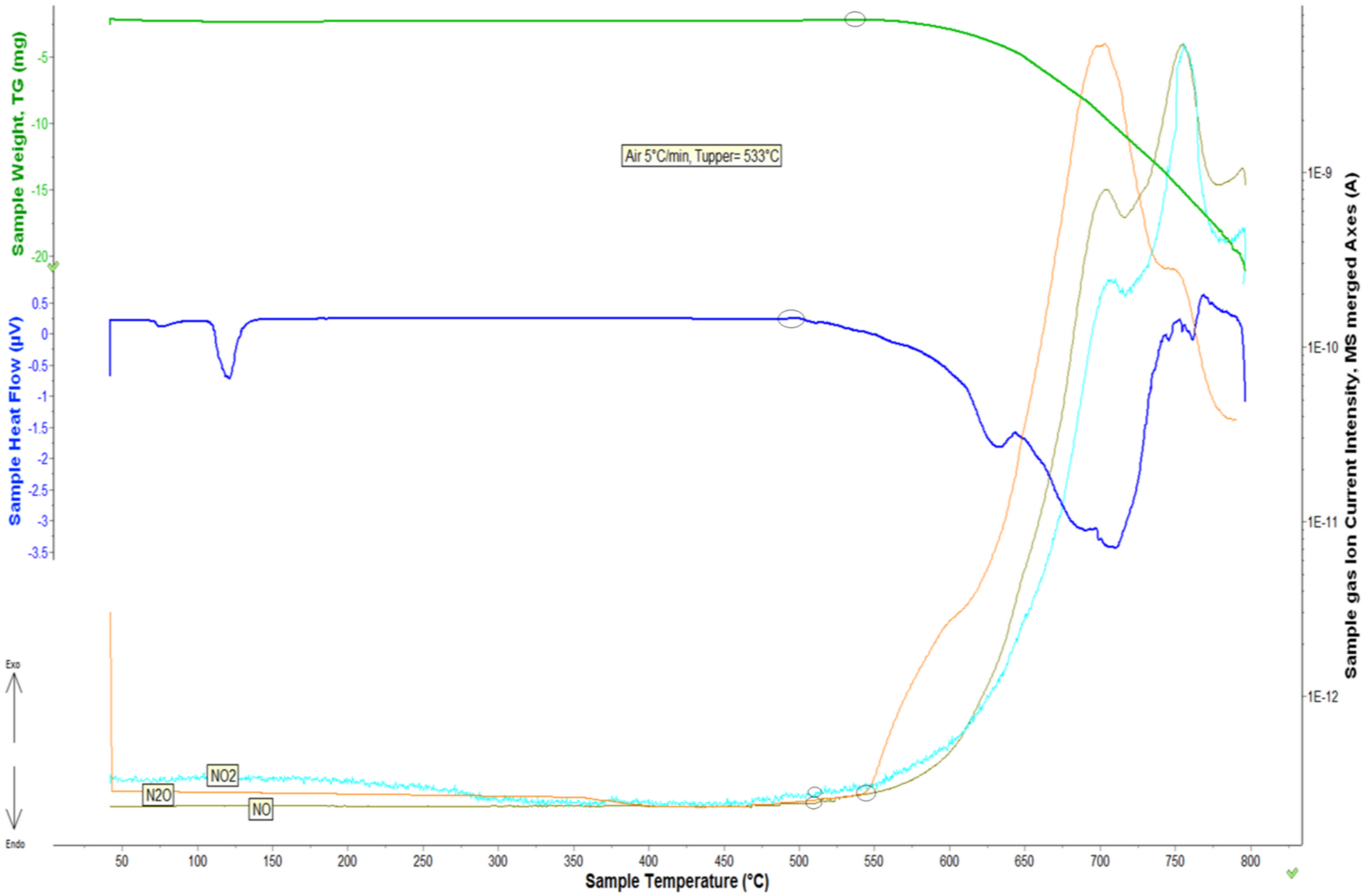

Figure 8.2.5: Ternary salt in an air atmosphere at 5°C/min heating rate. The black circles are indicating corresponding temperatures.

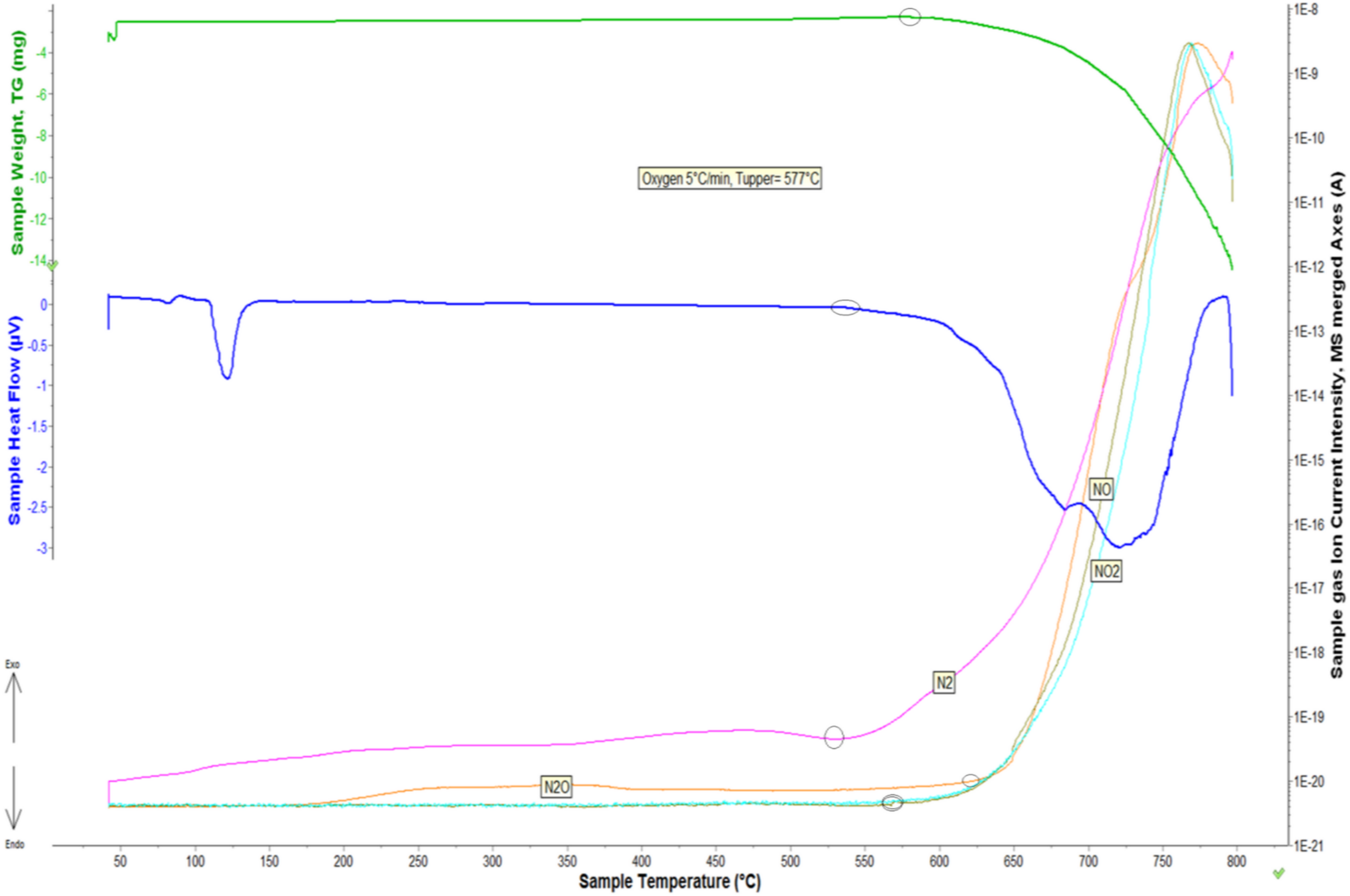

Figure 8.2.6: Ternary salt in an oxygen atmosphere at 5°C/min heating rate. The black circles are indicating corresponding temperatures.

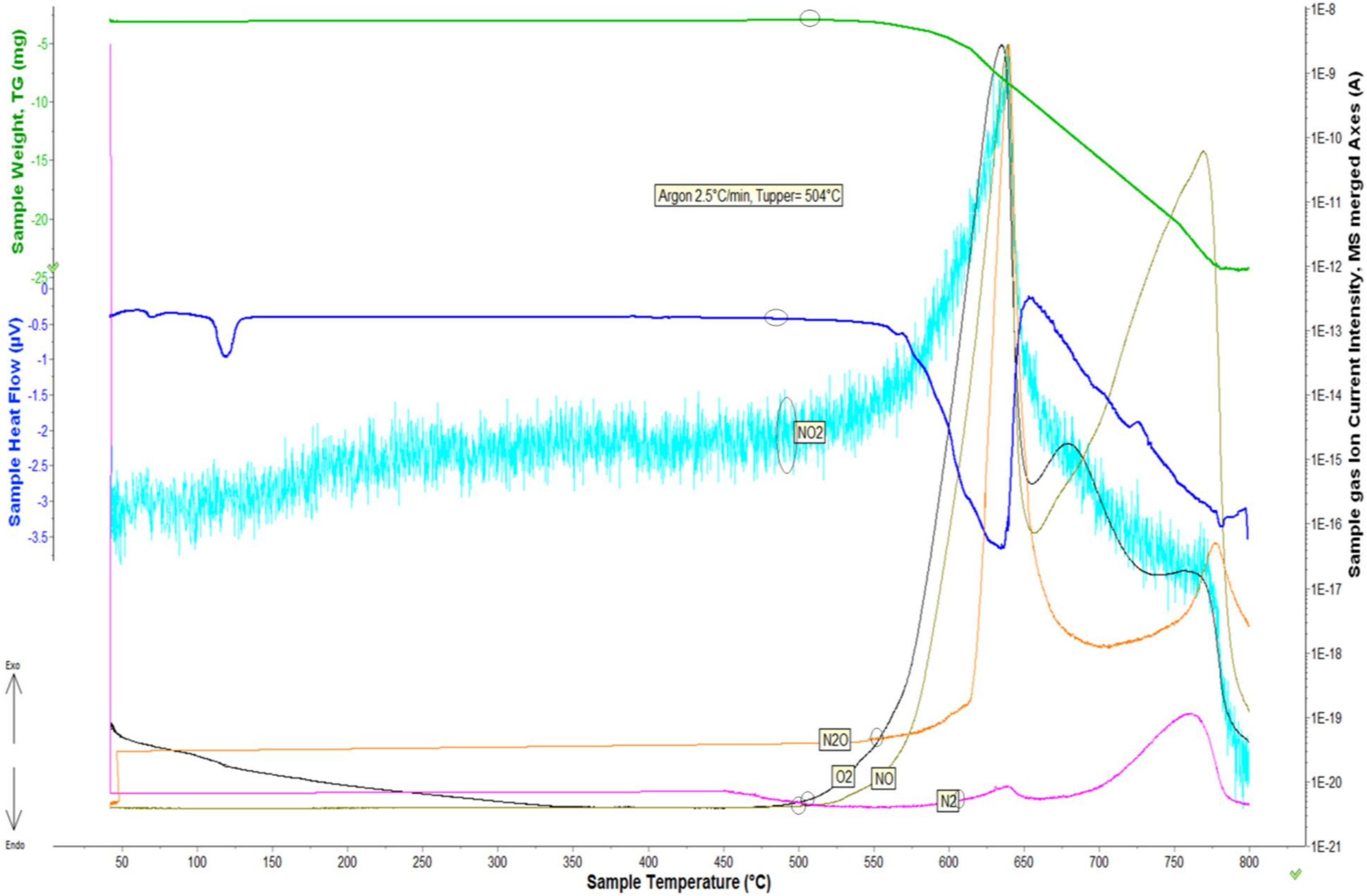

Figure 8.2.7: Ternary salt in an argon atmosphere at 2.5°C/min heating rate. The black circles are indicating corresponding temperatures.

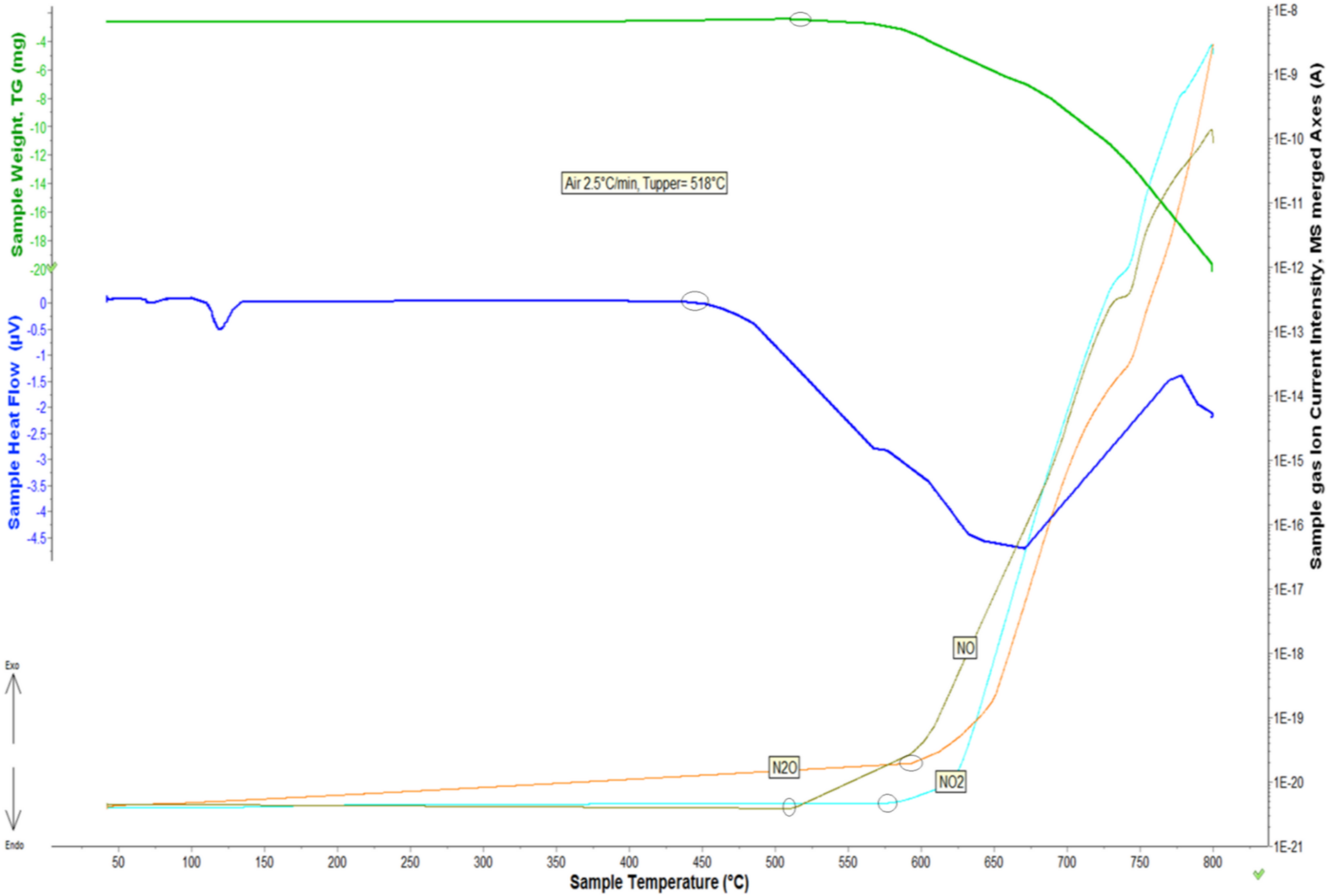

Figure 8.2.8: Ternary salt in an air atmosphere at 2.5°C/min heating rate. The black circles are indicating corresponding temperatures.

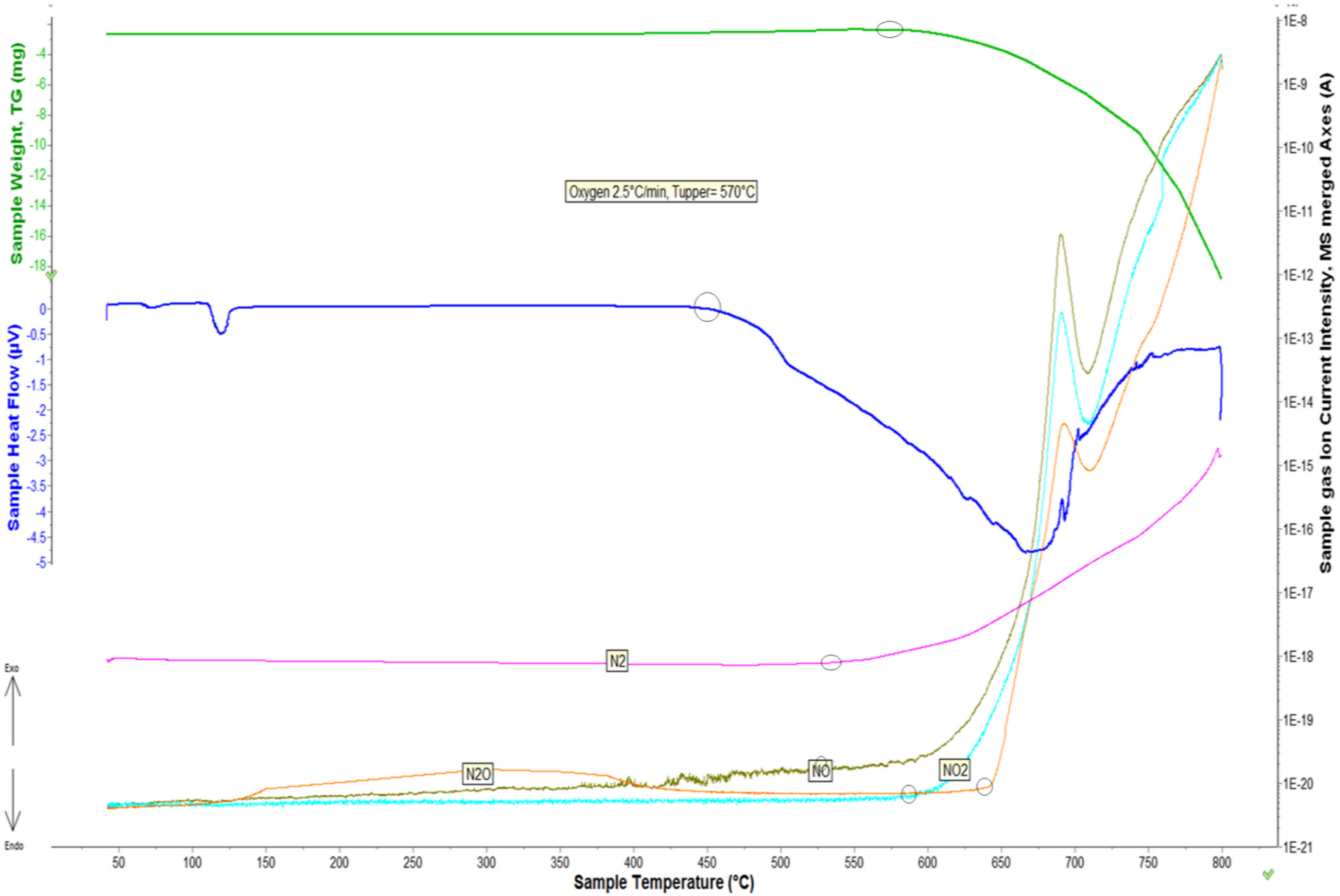

Figure 8.2.9: Ternary salt in an oxygen atmosphere at 2.5°C/min heating rate. The black circles are indicating corresponding temperatures.

8.2 TERNARY SALT THERMAL ANALYSIS: DISCUSSION

Thermal and off-gas analysis was performed on ternary Na-K-Li///NO_3 salt subjected to different heating rates and atmosphere to observe decomposition behavior at inert and oxidative atmosphere. Decomposition temperatures were determined by identifying rapid weight loss beginning temperature in TG curves, endothermic degradation curve starting temperatures in HF curves and gaseous products evolution in MS curves.

The Calisto [332] software analysis showed that, before beginning of the actual test while holding the samples at 105°C temperature for one hour for dehydration purpose, the samples loss their weight averagely 3%, as shown in Table 8.1.3. During the actual test and before rapid weight loss begin the sample did not exhibit further weight loss (weight change range ±0.05mg). The moisture absorbance was mainly due to samples preparation in the air and sample loading in STA. Moisture loss was higher in ternary salt compared to binary salt. Single salt exhibited lowest moisture weight loss compared to binary and ternary salts because single salts were drawn directly from the original container and were less exposed to ambient moisture. Lithium nitrate showed higher moisture weight loss compared to potassium nitrate and sodium nitrate. Reaction mass loss was higher at lower scanning rate and also in an inert atmosphere, as shown in Table 8.1.3.

During melting a small endothermic transformation, peak was observed followed by a larger endothermic melting peak in all heating HF curves for ternary salts. 1st order solid-solid transition was not appeared during cooling, where it merged with freezing HF peak. Distortion and irreversibility and deviation from linear baseline heat flow curves observed only at or during decomposition and onwards. During or after rapid weight loss begin or rapid degradation process started the heat flow curves showed a decline from the baseline with abrupt distorted endothermic peaks. Upon cooling the heat flow curves were not identical with the heating HF curves, which indicated an irreversible change in salt composition or altering melt chemistry at a higher temperature.

Table 8.1.3: Ternary nitrate salt samples (heated from 50 to 800°C) average weight change at three atmospheres (gas velocity: 40ml/min) and scanning rates.

Heating rate and gas type	Initial mass (mg) ±0.03	Average Dehydration weight loss %	Average Total weight loss %
10°C/min Argon	35.0	2.941	76.023
10°C/min Air		2.278	63.378
10°C/min O_2		2.510	52.882
5°C/min Argon		2.705	82.046
5°C/min Air		2.019	70.791
5°C/min O_2		2.923	62.107
2.5°C/min Argon		2.050	86.421
2.5°C/min Air		2.139	75.326
2.5°C/min O_2		2.364	67.015

The melting point of the ternary system was found 121°C in DTA and 122.8°C in DSC, which was in excellent agreement with FactSage formulation value (120.8°C) and close to the regular solution modeling of the ternary eutectic point of 116°C obtained by Mantha et al. [304]. Carveth [393] studied freezing point of a ternary $LiNO_3$-$NaNO_3$-KNO_3 system of 27.3Li-18.2Na-54.5K///NO_3 weight% using iron furnace cylinder and mercury thermometer and found the eutectic temperature of 120°C and presented the triangle phase diagram. Mantha et al. [304] found 118.4°C melting point of 25.9Li-20.06Na-54.1K///NO_3 weight% ternary nitrate by DSC analysis. Bergman and Nogoev [394] used the visual polythermal method on a 30Li-17.8Na-52.2K///NO_3 weight% and found ternary eutectic as 120°C. Bradshaw [36] found melting point of ternary nitrate of 30Li-18Na-52K///NO_3 weight% as 120°C using electrically heated alumina container. Olivares et al. [121] used STA on a 30Li-18Na-52K///NO_3 weight% ternary nitrate and observed eutectic at 121°C. Coscia et al. [305] used DSC on a ternary 30.3Li-14.7Na-55K///NO_3 weight% and found the melting point at 127°C.

There is a minor effect of heating and cooling rates on transition, melting and freezing temperatures as studied using DTA transducer. However, the heating rates did have an effect on decomposition process. The eutectic points should have same liquidus and solidus temperatures but in this study they were dissimilar. Olivares et al. [121] have studied ternary salt of different composition in DSC/TGA-MS. At 10°C/min heating and cooling rate they also observed the gap between liquidus and solidus. They concluded that the difference between liquidus and solidus onset temperature is due to salts exhibit undercooling perhaps due to faster-cooling rates (10°C/min) also described by Verhoeven [81]. In this study, the salt was subjected to various heating and cooling rates ranging from 1°C/min to 15°C/min, but the gaps remain between liquidus and solidus points. The reason is for many substances/compounds the exothermic solid-solid transition and freezing events are not always reversible upon cooling compared to the endothermic melting and solid-solid transition events [385]. A possible explanation is provided in Chapter 7 of this thesis.

Decomposition beginning temperatures were observed in the inert and oxygen rich atmosphere. As consistent with previous studies [26, 109, 121, 380] based on three criteria the decomposition temperature was determined: temperature at which rapid weight loss start; temperature at which NO, O_2 gas were evolved; and temperature at which rapid, irreversible endothermic heat flow curve was observed [26, 109, 121, 380].

Before the final test, a ternary salt of same mass was heated in identical experimental condition with AMU scanning range from 0 to 200 (Faraday MID: for all gas detection) to find evolved gasses. At or during decomposition only a few gaseous product showed significant ion current intensity peaks (in Ampere) and were consistent for longer periods, thus during final tests only O_2, N_2, NO, NO_2, N_2O gaseous products were considered for ion current intensity measurement (Faraday Scan stair: for individual gasses detection). Below sections discuss the decomposition behavior of ternary salt at different sweep gas environment and heating rates.

8.2.1 IN ARGON (PARTIAL PRESSURE OF O_2= 0)

In argon atmosphere, O_2 and N_2 were detected alongside NO, NO_2, and N_2O. In three scanning rates the NO evolved earlier than O_2 as shown in Table 8.1.2. At 10°C/min heating rate the rapid weight loss begin at 545°C and the endothermic degradation starting peak at 517°C, as shown in Figure 8.2.1. At 5°C/min heating rate the rapid weight loss begin at 515°C and the endothermic degradation starting peak at 480°C, as shown in Figure 8.2.4. At 2.5°C/min heating rate the rapid weight loss begin at 503°C and the endothermic degradation starting peak at 470°C, as shown in Figure 8.2.7. The results are summarized in Table 8.1.2.

8.2.2 IN AIR (PARTIAL PRESSURE OF O_2= 0.21)

In air atmosphere, O_2 and N_2 were not detected because the AMU coincides with blanket gas AMU. In air both O_2 and N_2 are present hence, only NO, NO_2 and N_2O were detected. In three scanning rates the NO, NO_2 and N_2O were evolved as shown in Table 8.1.2. At 10°C/min heating rate the rapid weight loss begin at 571°C and the endothermic degradation started at 550°C, as shown in Figure 8.2.2. At 5°C/min heating rate the rapid weight loss begin at 533°C and the endothermic degradation starting peak observed at 485°C, as shown in Figure 8.2.5. At 2.5°C/min heating rate the rapid weight loss begin at 518°C and the endothermic degradation starting peak at 440°C, as shown in Figure 8.2.8. The results are summarized in Table 8.1.2. Before starting of rapid decomposition weight loss, the sample showed slight oxidation weight gain in an air atmosphere.

8.2.3 IN OXYGEN (PARTIAL PRESSURE OF O_2=1.0)

In oxygen atmosphere, O_2 was not detected because the AMU coincides with blanket gas AMU. Hence, N_2, NO, NO_2, and N_2O were detected, as shown in Table 8.1.2. At 10°C/min heating rate the rapid weight loss begin at 600°C and the endothermic degradation starting peak at 490°C, as shown in Figure 8.2.3. At 5°C/min heating rate the rapid weight loss begin at 577°C and the endothermic degradation starting peak at 540°C, as shown in Figure 8.2.6. At 2.5°C/min heating rate the rapid weight loss begin at 570°C and the endothermic degradation starting peak at 450°C, as shown in Figure 8.2.9. The results are summarized in Table 8.1.2. Before starting of rapid decomposition weight loss, the sample showed oxidation weight gain in an oxygen atmosphere. According to Olivares et al. [26] in Hitec salt of ternary nitrate-nitrite salt mixer, the degradation process delayed in presence of oxygen (rapid weight loss occurred later compared to inert atmosphere) as nitrite and oxide interacted with O_2 from the blanket atmosphere to convert back some nitrites to nitrates by exothermic oxidation weight gain. In this study, the exothermic oxidation weight gain was observed in oxygen and air atmosphere just before rapid weight loss begin.

At higher heating rate (10°C/min), the evolution of gasses and rapid weight loss occurred later compared to lower heating rate (2.5°C/min). Lower heating rates exhibit higher mass loss, as shown in Table 8.1.3. During higher heating rates the samples subjected to greater heat flux inside DTA furnace but shorter time for completing thermal reactions compared to lower heating rates. The sample at lower heating rate exposed to longer reaction time with blanket gas which results in higher mass loss compared to higher heating rate. The effect of sweep gas velocity has not studied. The decomposition temperature of same ternary nitrate but of a different composition was found 550°C by Bradshaw and Meeker [36] using electrically heated alumina container in an air atmosphere. Olivares et al. [121] reported decomposition point ternary nitrate of different composition at 602°C in air using DSC/TGA. Wang et al. [106] studied different composition ternary nitrate using DTA/TGA and found the decomposition limit as 500°C in an argon atmosphere. The results varied because of different sample composition and grade; different apparatus technique and sensitivity; and different experimental conditions (sweep gas type and velocity, heating rates, sample mass size).

As studied and observed by Gordon et al. [220] and others (mainly Bond et al. [395], Freeman [253] and Olivares et al. [26, 121]) the nitrous fume (NO) is evolved after melting during bubbling (temperature range 200 to 350°C) of single alkali nitrate salts. Gordon et al. [220] observed that single alkali nitrates undergo thermal reactions at temperatures 100 to 300°C. Gordon et al. [220] observed that the nitrate to nitrite and nitrite to oxide occurs up to 900°C (upper limit of the apparatus) for single alkali nitrate salts. Similar phenomena observed for this study for ternary nitrate salt. According to results from MS measurements in this work, NO evolved earlier or at the same time as O_2 as observed in an argon atmosphere of each scanning rates, as shown schematically in Figures 8.2.1, 8.2.4 and 8.2.7. The primary decomposition reaction for ternary nitrate may not involve only single reaction but concurrent simultaneous reactions. Thus, the primary thermal reactions include: nitrates converting to nitrites (and liberating O_2); and nitrites to oxide and NO gas. Kramer et al. [189] also described similar results for single nitrates (Na and K) that, the nitrate and nitrite decomposition occurred concurrently with releasing N_2, O_2, and NO. The primary and secondary simultaneous, concurrent and reversible thermal reactions are shown in Equations 3.3.3.1, 3.3.3.3 and 3.3.3.4 in Chapter 3 of this thesis.

$$NO_3^- \rightleftharpoons NO_2^- + \frac{1}{2}\, O_2 \qquad \text{eqn 3.3.3.1}$$

$$NO_2^- \rightleftharpoons O_2^- + NO_2 + NO \qquad \text{eqn 3.3.3.3}$$

$$NO_2^- \rightleftharpoons O_2^- + \frac{3}{2}O_2 + N_2 \qquad \text{eqn 3.3.3.4}$$

As described in Chapter 3, at higher temperature nitrate partially decompose to nitrite and liberate oxygen and nitrite partially decompose to oxide and nitrous fume; is tend to show delayed decomposition temperature at oxygen rich atmosphere (P_{O_2}=1). The results of decomposition temperature at three atmosphere and 3 scanning rates are shown in Table 8.1.2 and in Figures 8.1 to 8.9. The heating rates delayed the evolution of gaseous products and eventually rapid weight loss. Bradshaw et al. [137] indicated similar stability of ternary Li/Na/K-NO_3 under oxygen as ullage gas. The results obtained by Olivares et al. [121] using same salt composition heated in DSC/TGA furnace showed less effect of partial pressure of oxygen. The difference between results of this study and by Olivares et al. [121] may be of different sample preparation, sample purity level, crucible types used in test (weather open type crucible or crucible with lid or crucible with lid and hole in it), apparatus type and transducer type (DSC/TGA or DTA/TGA) [34]. Since DSC/TGA transducer is quantitative and DTA/TGA transducer is qualitative hence, the former will provide accurate heat flow curves. Also the TGA and MS curves will vary from experiment to experiment and apparatus to apparatus due to different sample preparation and test conditions. According to Stern [249] another possibility of different result might be, in some instance lithium nitrate might partially decompose to nitrite just after its melting temperature of 252°C (exact temperature of degradation is not specified). The long term thermal stability has not studied due to apparatus limitation. The ternary salt of different composition has been subjected to isothermal stability test by Olivares et al. [121] and found the limit as 400°C.

8.3 TERNARY NITRATE THERMAL ANALYSIS TEST: CONCLUSION

Simultaneous thermal analysis of ternary nitrate salt showed that the decomposition temperature is delayed in the presence of oxygen by 55°C compared to inert environment. The solid-solid α/β phase transformation process was observed at 80°C for the ternary system in DTA and 99°C in DSC. The oxygen-rich atmosphere (O_2 and air) tends to increase melting points slightly (by 1 to 2°C) compared to the inert atmosphere. Lower heating rates lowered the decomposition temperature as seen compared to 10°C/min and 2.5°C/min. As observed in both DTA and DSC the heating and cooling rates have some minor effect on solid-solid transition peaks, melting temperatures and freezing temperature during heating. However, irrespective of decreasing heating and cooling rates the gap between liquidus and solidus did not minimize in both transducer. The ternary nitrate salt produces NO fume after melting followed by O_2 evolution indicated primary decomposition reaction of ternary nitrate involves simultaneous concurrent reversible reaction as follow:

- Nitrates convert to nitrites and oxygen (reversible and slow initially).
- Nitrites convert to oxides and nitrous (reversible and slow initially).

Since the DTA is qualitative and less sensitive below 250°C and HF curves varied from DSC transducer. DSC transducer is quantitative and has higher sensitivity for energy and temperature measurement offered high accuracy compared to DTA. Since both DTA/TGA and DSC/TGA transducer are use same mass balance mechanism in setsys STA. Thus irrespective of transducer type (whether DSC/TGA or DTA/TGA) the TGA curves will be almost identical and might be replicable in both transducers if the sample, crucible, test parameters and experimental condition are identical.

8.4 MAJOR CONCLUSIONS ON TERNARY NITRATE

Experimental result of ternary salt can be summarized as follow:

I. 121°C eutectic melting point from STA was in excellent agreement with FactSage melting point of 120.84°C.

II. Dehydration weight loss was higher in ternary salt compared to single salts and binary salts. Dehydration weight loss was in the order of ternary salt>binary salt>single salt. Lithium nitrate being most hygroscopic and potassium nitrate was less hygroscopic.

III. Higher heating rate (10°C/min) showed higher decomposition temperatures compared to lower heating rate (2.5°C/min) at each three atmospheres.

IV. The oxygen atmosphere delayed the decomposition temperature by 55°C compared to argon atmosphere at a same heating rate (10°C/min). The high partial pressure of oxygen caused some exothermic oxidation of nitrite and delayed degradation process.

XIV. Lower cooling rates (1°C/min) didn't minimize the gap between liquidus and solidus temperatures and the solid-solid phase transformation peaks were not visible during cooling. The possible conclusions are:

    a. The possibility of improper heat flow response time and heat transfer rate of ‗sample to Crucible‘ and ‗crucible to thermocouple‘ (thermal gradients inside different parts of STA).
    b. There are no known ASTM CRMs on the cooling calibration of HF curve for these transducers.

V. The onset temperature of melting and freezing point varied slightly (1 to 5°C) according to holding period. After reaching melting point temperature, When the isothermal holding time was longer (>5min) at or above melting point temperature, the onset melting temperature increased due to proper heat conduction time for phases homogenization and diffusion of tested sample. Although the isothermal holding at or above salt‘s melting point did not affect peak temperatures but peak height increased with mass increase.

VI. Higher heating rates lead to longer melting peaks as observed in the ternary salt system.

VII. O_2, N_2, NO, N_2O, and NO_2 are the main evolved gasses of decomposition. NO, and O_2 are the primary evolved gasses after melting observed in an argon atmosphere, suggested that the ternary nitrate salt decomposition pathway involves concurrent simultaneous reversible reactions (primary and secondary reactions are concurrent and overlapping).

VIII. Decomposition temperatures depend on upon various factors described in Chapter 3 in sections 3.3.3 and 3.3.4. Any change in experimental parameters will change the results of same given samples.

IX. Salt vapor chemically attacked platinum-rhodium thermocouple wire and caused corrosion in DSC thermocouple wire. Hence, thermal stability study was limited to protected DTA transducer only.

CHAPTER 9 DISCUSSION

Knowing the effect of oxygen rich atmosphere on the molten salt top surface is an important aspect of delaying the thermal degradation temperature. The delay mechanism of the thermal degradation temperature is linked with the partial pressure of oxygen and heating temperature. The rate of oxidation or the alteration of nitrite to nitrate ratio is directly proportional to the partial pressure of oxygen of the melt. The decomposition limits of alkali nitrate systems reported by many researchers were based on TGA weight loss curves or DTA/DSC and TGA curves only as shown in Table A.1 in Appendix A. Very few used both DTA/DSC-TGA and off-gas analysis simultaneously. Most researchers did not state the decomposition definition and ignored other parameters such as: decomposition heat flow peaks and the corresponding evolution of gaseous products. Also, nobody reported reproducibility of their results. This is one of the reasons for tentative results and disperses values among the researchers. Another issue is, the alkali nitrates are very sensitive to experimental conditions was a key factor for scattered results. This ternary nitrate system is novel in CSP market, still in R&D stage and only five works of different salt compositions found till date. Olivares et al. [121] did use mass spectrometry alongside DSC and TGA. However, they did not observe any effect of exothermic oxidation prior to degradation in oxygen rich atmosphere which was intriguing. Olivares et al. [121] did not explain in their work. However, in this study, the experiments were designed to observe decomposition parameters simultaneously using STA (TGA, DTA/DSC, and MS curves). Low to high three scanning rates was chosen in dynamic heating condition to observe the degradation behavior of the salt melt. Doing so, it showed that, the pure oxygen gas suppressed the degradation point of nitrates by exothermic oxidation at each scanning rate compared to the inert atmosphere of argon. Also, these careful investigations lead to a postulation that, the decomposition reactions (both primary and secondary) are concurrent overlapping as the evolution of O_2 and NO was observed at the same time (approximately) in MS graph of this study. The evolution of O_2 and NO fume detected above the melting point and the intensities increased with increasing temperature. This study learned and established an effective protocol for thermal stability measurement of nitrate salts using STA to identify true decomposition temperature, they are:

1) Dynamic scanning at a suitable heating rate to observe rapid weight loss starting temperature with simultaneous information of gaseous product evolution and heat flow peak variations.
2) Conduct experiments by same batch crucibles; purge gas type and velocity; and experimental conditions (such as: calibration and transducers) to observe repeatability.
3) Several heating and cooling cycles should be performed from room temperature to the temperature where the rapid weight loss begins and observe the TGA and heat flow curves pattern variation.
4) The isothermal holding of a given period to observe any variation in TGA and heat flow curves.

Due to apparatus limitation the stability limit was not performed according to point 3 and 4 in this study. Oxyanion salts such as alkali nitrates are corrosive according to Ellingham diagrams [345]. The NO_x products viciously attack platinum, rhodium, aluminium and gold [311]. This Setaram STA has one major limitation, which is the direct exposure of transducer thermocouple wire (placed near to sample and reference crucibles) to the corrosive atmosphere inside the furnace. The simultaneous transducer thermobalance (both DTA/TGA and DSC/TGA) hanged vertically inside STA. The salts emit various NO_x (N_2, NO, NO_2, N_2O mainly) gasses which chemically attacked the platinum-platinum/rhodium thermocouple wire and caused high temperature stressed corrosion fracture. Using protected DTA transducer (thermocouple wire hide bottom side of the crucible) was not enough to prevent Pt/Rh wire tip corrosion and subsequent transducer damage. The DTA and DSC both transducers sustained only 20 experiments and are expensive hence the study was limited only to thermal decomposition point detection. One composition was chosen (from FactSage formulation) due to the limitation of experiment numbers. Due to very small size of the sample (35 ml), the phase and morphology study were unable to perform.

The melting peaks of single nitrates (purity 99.99%+) were sharper than binary and ternary nitrates. Usually, fusion point depression and broader liquidus peaks are observed in higher order compounds contrast to pure crystalline substances [396]. The small peak appeared before melting endothermic peak during heating indicated solid-solid phase transformation process is present in the ternary system. Sodium and potassium nitrate both possess solid-solid transition prior to melting which was the reason for small endothermic peak appearance before melting of ternary system. Jriri et al. [358] used DSC and observed that the $NaNO_3$ showed second order transition and KNO_3 showed first order transition. Similar observation was stated by Janz et al. [357] using calorimetry, and Harris et al. [397] using X-ray spectroscopy and infrared. Newns and Staveley [398] studied nitrates using XRD and stated that at higher temperature $NaNO_3$ transform from α-phase calcite type rhombohedral to β-phase rhombohedral; and KNO_3 transform from α-phase aragonite type rhombohedral to β-phase rhombohedral.

The eutectic melting of the ternary system was 120°C, which is 100°C lower than the binary nitrate salt (binary liquidus 220°C). Also, the decomposition temperature of ternary nitrate is lower than binary nitrate because of the presence of lithium nitrate in the former. Based on the regular solution assumption according to Kleppa [302] and Abe et al. [33] the decomposition of each compound in ternary alkali nitrate usually proceed independently. Because alkali nitrate is free energy of mixing depends on upon the entropy term. Also among the alkali nitrates the lithium nitrate is least stable at higher temperatures. Because Li^+ cation is more polarizable compared to potassium and sodium cation, which leads to distortion of polyatomic nitrate anions [249]. The influence of high polarized cation Li^+ is responsible for interaction with nitrites and oxide ion formation leads to lower stability limit in ternary nitrate compared to binary nitrate solar salt [137]. The melting points and decomposition temperatures were increased with increasing ionic radius of the cation in order of $LiNO_3<NaNO_3<KNO_3$ as observed from STA results of this study. Stern [25] and Sweeney [275] also observed similar results using thermal analysis. Higher order compounds showed lower melting and decomposition points as observed from STA results, are shown in Table 9.1.

The possible working temperature range of ternary nitrate salts is 415°C in argon, 451°C in air and 480°C in oxygen. The binary salt‘s possible working temperature limit is 348°C in argon, 366°C in air and 379°C in oxygen. Ternary salt offers 77°C more than the solar binary salt which will likely contribute to increasing the Ranking cycle efficiency, as shown in Table 9.1.

Table 9.1: Comparative thermal events of single, binary and ternary nitrates at 10°C/min heating rate and 40ml/min sweep gas velocity (argon, air, and O_2), using a simultaneous thermal analyzer (DTA/DSC-TGA and MS).

Salt system	Sweep gas type (40ml/min)	Melting point (°C), T_1	Possible decomposition temperature (°C), T_3	Possible working temperature range (°C) T_3-T_1	Calculated Carnot cycle efficiency (η)=$1-\frac{T_1}{T_3}$
$LiNO_3$	argon	257.7	507	249.3	0.492
	air	257.7	540	282.3	0.523
	oxygen	257.7	541	283.3	0.524
$NaNO_3$	argon	301.4	568	266.6	0.470
	air	301.4	575	273.6	0.476
	oxygen	301.4	590	288.6	0.490
KNO_3	argon	331	575	244	0.425
	air	331	590	259	0.439
	oxygen	331	600	269	0.448
Binary solar salt	argon	218.1	570	351.9	0.617
	air	218.1	589	370.9	0.630
	oxygen	218.1	603	384.9	0.639
Ternary nitrate	argon	122.8	545	422.2	0.775
	air	122.8	571	448.2	0.785
	oxygen	122.8	600	477.2	0.795

Melting points are obtained in argon atmosphere only.

The samples were heated in an open crucible (without lid) to observe the evolved gasses (detected by MS unit attached downstream side of STA apparatus) swept by the carrier gas (argon, air or oxygen). Hence, the effect of constant pressure was observed at fixed sweep gas velocity (40ml/min). The effect of high sweep gas velocity was not studied due to restriction in a number of experiments and also to avoid buoyancy in TGA curves. Also, the effect of the constant volume was not studied using closed/crimped crucible (or at least by crucible with a lid with a small hole on top). The gaseous products of the reaction were swept away by a carrier gas. Hence, the reaction between salt melt surfaces with contact atmosphere will vary in open and closed crucible arrangement. The reaction rate in open or constant pressure system might be higher compared to closed or constant volume system.

This study showed that large size samples (>40mg) provide larger peaks compared to smaller mass samples (<35mg). The study of effect of sample size was not performed and mass size was limited to at least half of the crucible volume in order to avoid sample bubbling and consequent sample overflow. Sample overflow was avoided to prevent sample spreading and contacting with the thermocouple plate and wire, and consequent corrosion-induced damage.

The transpiration test is not recommended for vapor pressure measurement of alkali nitrates because of the nature of the salts (readily absorb moisture during loading-unloading). The salt‘s high sensitivity towards experimental conditions (salt sample size, sweep gas type and velocity) and nature of the decomposition reactions (overlapping concurrent reversible reactions) played a role in scattered mass loss results of these nitrates. There is another possibility that the reaction mass loss results were not consistent perhaps due to non-homogeneous sample mixtures in binary nitrate. Similarly, pure salt's mass loss results were also inconsistent.

The regular solution model predicted the experimental and FactSage phase diagrams well suggesting a useful method for describing other alkali nitrate systems. Newton-Raphson iteration method used in built-in solver ‗*fsolve*‘ (trust region dogleg algorithm) was not converging well in the eutectic region of binary systems. Also having difficulties optimizing the roots where the liquidus lines are not continuous (in the case of Li-K and Li-Na nitrates). Hence, a different approach a contour plot technique was used to solve the coupled nonlinear equations numerically. Variation in heat capacities changed the liquidus and solidus curves and but has less effect on eutectic points for each binary nitrate systems. The contour plot technique has not produced any results for the ternary system because of weakly written algorithms.

To verify the practical use of ternary nitrate salt, some future works are proposed:

a. Lithium nitrate is expensive (due to increase use in lithium ion batteries) and sodium nitrate is cheaper among the three constituent nitrates, as discussed in Chapter 3 of this thesis. Hence, formulation of lower lithium content and higher sodium content ternary nitrate salt will minimize production cost.

b. According to literature, the impurities tend to change (elevation/depression) melting and decomposition temperatures. Low purity salt is cheaper compared to high purity grade (99%+). Hence studying the effect of impurities addition (alkali halides/alkali carbonates) into the ternary salt in the range of 1 to 5 weight % (added to original ternary salt) is important to minimize salt production cost. As an example, Na_2CO_3 and NaCl are cheap and naturally available.

c. In actual practice, the HTFs are periodically checked for composition integrity and required substitution if salt fouled by soluble and insoluble oxides. A state of art salt recycling process practice is an important issue.

d. Container materials compatibility study is a crucial criterion for long-term use of HTF. High temperature corrosion between molten salt and container or pipe alloys (various ferrous/carbon-Cr, Mo, Mn alloys) might cause oxide formation. Attention needed on lithium nitrate which has lowest decomposition temperature amongst the three constituent nitrates in the ternary system, and recent studies showed $LiNO_3$ produced lithium oxide at or above degradation temperature.

e. According to previous studies (e.g. alkali nitrates and carbonates), the nanoparticles tend to increase the specific heat capacity and thermal conductivity in the base fluid, could be a useful study regarding storage media (HTF) cost reduction. Although agglomeration, sedimentation of nanoparticles in base fluid might be an issue.

f. According to previous studies unary alkali nitrates have higher decomposition temperature compared to unary alkaline earth nitrates. Moreover, unary alkali halides (e.g. chlorides) and carbonates have higher decomposition temperature compared to alkali nitrates. These alkali halides/carbonates HTF can be used in a cascade TES system or solar multiplier system with binary/ternary nitrates. For an example, alkali carbonates can be used during peak load while alkali nitrates can be used during off-peak hours. A feasibility study required in such issue.

g. Since STA transducer‘s exposure to furnace atmosphere are one major limitation in nitrate salt stability study, as the thermocouple wire was heavily strained and damaged by sample vapor (NO_x gasses mainly). A hermetically sealed or crimped crucible will be the best option regarding constant volume weight loss thermal stability study. Although closed crucible arrangement will restrict off-gas analysis. Hence, a protected separately purged furnace chamber can be used for STA purpose.

h. From transpiration mass loss study, it has been observed that degradation mass loss was higher in the larger surface area (2g) in combustion boat compared to STA cylindrical crucible (sample size: 35mg). Thus, a question arises whether these nitrate salt‘s high temperature alteration chemistry is surface dependent (surface to area ratio) need attention.

i. Crystal and liquid densities, fluid velocities, heat capacities and thermal conductivities of complex oxyanion alkali nitrates/nitrites at full operating temperature ranges are important parameters for HTFs characterization. Due to the high cost of analytical grade sample and apparatus limitation measuring these properties up to maximum operating temperature is difficult. Hence, molecular dynamics simulation (e.g. force field computation models) could be performed to predict these thermophysical properties (e.g. at 500°C).

j. The regular solution predicted the binary alkali nitrate phase diagrams well to indicate which can also work for higher order compounds and other alkali compounds. Thus, a well-written algorithm is required for solving the multidimensional coupled nonlinear equations.

CHAPTER 10 CONCLUSIONS AND RECOMMENDATIONS

Molten nitrate and nitrite salt mixtures have high melting points compared to other HTFs, which require the high energy of melting in TES system and continuous freeze protection in the solar field of STP plants. Also, the molten nitrate salts have low decomposition point compared to carbonates and chlorides which limit the steam Rankine cycle efficiency. To increase the efficiency of STP plant, this study proposed a novel HTF a ternary Li-Na-K nitrate mixture which had a lower melting point compared to binary solar salt, with an aim to enhance the degradation limit in an oxygen atmosphere. Most researchers have studied the stability limit mainly by TGA and/or TGA-DTA/DSC ignoring the evolution of gaseous species and corresponding endothermic decomposition peaks. Thus, this study used STA technique to observe decomposition parameters concurrently. O_2 and NO evolved approximately at the same temperature for various salts suggesting that the primary and secondary reactions are concurrent and overlapping. Oxygen as blanket gas increased the decomposition temperature of alkali nitrates compared to inert argon atmosphere. Lower heating rates lowered the decomposition temperatures of ternary nitrates. Using O_2 as ullage gas can increase the Rankine cycle efficiency as stated in equation 2.2.1. To study the mass loss reaction at higher temperatures the transpiration technique was used. However, complex concurrent-reversible reactions and samples sensitivity towards experimental parameters suggested that transpiration test not suitable for reaction kinetics studies of alkali nitrates. FactSage quasi-chemical modeling was performed to obtain eutectic composition and verified by STA apparatus. Small peak just before melting peak indicated the solid-solid transformation of ternary nitrate which inherited from $NaNO_3$ and KNO_3 polymorphic transition process. Mathematical modelings of three binary nitrates were performed using Gibbs free energy minimization method similar to Elliott and Kramer and by the regular solution assumption by Kleppa. Coupled nonlinear equations were solved numerically using contour plot technique in Matlab to obtain liquidus and solidus curves. Temperature dependent heat capacities were compared with FactSage and literature values. Regular solution assumption predicted binary alkali nitrates well and can be used for ternary nitrates, higher order nitrates, and alkali halides.

The major conclusions are as follow:

1. The lower heating rate did not minimize the solidus and liquidus temperatures of the binary and ternary nitrates.
2. An oxygen cover gas increased decomposition limit of nitrates compared to argon atmosphere. The ternary nitrate is stable in up to 545°C in argon, 571°C in air and 600°C in oxygen. At 10°C/min heating rate extending degradation temperature was 55°C in pure oxygen. The binary nitrate is showed stability at 570°C in argon, 589°C in air, and 603°C in oxygen. Similarly, in an argon atmosphere, the $LiNO_3$ is stable up to 507°C, the $NaNO_3$ is stable up to 568°C, and the KNO_3 is stable up to 575°C. In an air atmosphere, the $LiNO_3$ is stable up to 540°C, the $NaNO_3$ is stable up to 575°C, and KNO_3 is stable up to 590°C. In oxygen blanket gas the $LiNO_3$ is stable up to 541°C, the $NaNO_3$ is stable up to 590°C, and the KNO_3 is stable up to 600°C. The ternary nitrate has a melting point at 120°C and decomposition point at 545°C compared to the binary nitrate of 220°C melting and 570°C decomposition temperature in an argon atmosphere. The ternary salt has 65°C more operating temperature range compared to binary salt will likely to increase the Rankine cycle efficiency by 15%.
3. Higher heating rate (10°C/min) increased the ternary nitrate‘s decomposition limit compared to lower heating rate (2.5°C/min).
4. O_2, NO, N_2, N_2O and NO_2 gasses were the main evolved products of alkali nitrate decomposition. NO and O_2 started to evolve after melting before decomposition indicating primary and secondary reactions are concurrent overlapping.
5. The regular solution model of the three binary nitrate systems predicted the FactSage and experimental literature phase diagrams well and can describe the ternary alkali nitrates too. Newton-Raphson method used in ‗*fsolve*‘ trust region dogleg algorithm was sensitive to initial guess hence contour plot technique was used to find the roots of the couple nonlinear equations. When taken varying heat capacities, the predicted liquidus and solidus curves were reasonably closer to the calculated, experimental literature and FactSage values.

The following recommendations are made to improve this study:

I. Long-term thermal stability of the ternary nitrate was not performed because of the costly experimentation. Ternary nitrate salt should be subjected to thermal cycling and isothermal holding test (at least 50 heating-cooling cycles and 100 hours isothermal holding) at proposed higher temperature (T_3=temperature just before decomposition) to observe TGA, gaseous product evolution, and DSC/DTA HF curves consistency and variability.

II. The study conducted in STA has differences compared to actual TES system. In all CSP plants, the ullage gas is trapped inside the TES tank. As discussed in Chapter 3 of this thesis that product gasses have an effect on salt melt (gas-liquid equilibria). Hence, salt melt at constant volume (closed vessel or crucible) system will show different mass loss reaction compared to salt melt at constant pressure (open vessel or crucible) or non-equilibrium conditions (no reaction between product gas and liquid). There is a need for large-scale testing to simulate the TES scenario.

III. The reaction mass loss and alteration of melt chemistry in transpiration rig were hindered because of salt sensitivity toward experimental parameters. There is a need for modified transpiration rig (e.g. automated horizontal STA) to avoid ambient exposure of samples.

APPENDIX A: SELECTIVE STUDIES TABLE

Studies related to molten nitrate/nitrite salt systems are summarized in Table A.1 showing key results.

Table A.1: Selected studies on various molten nitrate/nitrite salt systems:

	Author/(s)	**Work/ Paper titles**	**Salt system tested, $T_{melt/liquidus}$, $T_{max/upper}$,**	**Apparatus used, crucible used, thermocouple used,**	**Gas/gasses, heating-cooling rate, sample size, heating temperature**	**Key results and conclusion**
1	C.M. Kramer, Z.A. Munir and J.V. Volponi [34]	Differential scanning calorimetry of sodium and potassium nitrates and nitrites	$NaNO_3$, KNO_3, $NaNO_3$–KNO_3, $NaNO_2$, KNO_2, Composition not mentioned.	Perkin- Elmer DSC-2 apparatus, high pressure stainless steel, gold platted stainless steel sealed DSC pans,	Sealed environment, 10K/min, less than 30mg, Temperature range 350 to 990K	Oxidative environment and materials raise the melting point and decomposition temperature (compare to pure salts). For the 5 salts, the endothermic decomposition reactions occurred above the melting points around 850K. 2 to 10 experiments were performed with each salt. $NaNO_3$ began to decompose at 840±10K, and KNO_3 began to decompose 820±10K

2	Rene I. Olivares [26]	The thermal stability of molten nitrite/nitrates salt for solar thermal energy storage in different atmospheres	$NaNO_3$–KNO_3–$NaNO_2$, (in the proportions of 7–53–40 wt.%, NO_2/NO_3 weight ratio of 0.7), T_{melt}=151°C, T_{max}=610°Cto 700°C in four atmospheres.	Simultaneous SETARAM DSC/TG-SETSYS Evolution analyzer apparatus coupled with Pfeiffer QUADSTAR-422 mass spectrometer, 100µL Al_2O_3 crucible,	Ar, N_2,Air,O_2. 10°C/min, 35 to 40mg, 1000°C	Oxidative environment (O_2, air) alter NO_2/NO_3 ratio, converting some nitrite to nitrate and the oxidation rate is $\infty\left(P_{O_2}\right)^{1/2}$. Oxidized atmosphere enhance the thermal stability to 610°C to 700°C, and also enhance melting point to 151°C compared to inert environment.
3	Rene I. Olivares, William Edwards [121]	$LiNO_3$-$NaNO_3$-KNO_3 salt for thermal energy storage: Thermal stability evaluation in different atmospheres	$LiNO_3$–$NaNO_3$–KNO_3, (in the proportions of 30–18–52 wt.%,), T_{melt}=121°C, T_{max}=600°C in Air	simultaneous SETARAM DSC/TG-SETSYS Evolution analyzer apparatus coupled with Pfeiffer QUADSTAR-422 mass spectrometer, 100µL Al_2O_3 crucible,	Ar,N_2,O_2,Air (5 X 10^{-7} m^3/sec), 10°C/min, 15 to 25mg, 1000°C	Oxidative environment (O_2, air) alter NO_2/NO_3 ratio. In Air atmosphere, the salt has thermal stability up to 600°C. Before melting, the ternary system showed α/β solid-solid transition at 87°C.
4	A. G. Fernández, S Ushak, H. Galleguillos, F. J. Pérez [124]	Development of new molten salts with $LiNO_3$ and $Ca(NO_3)_2$ for energy storage in CSP plants	$Ca(NO_3)_2$ – $NaNO_3$–KNO_3, (in the proportions of 48–7–45 wt.%), T_{melt}=130.61°C, T_{max}=554.39°C $LiNO_3$–$NaNO_3$–	Simultaneous DSC-DTA-TGA Q600, DSC Q-20, platinum crucibles for SDT-Q600, hermetically sealed	N_2 (50 ml/min) the heating rate of 10°C/min	Heat capacity for ternary Ca/Na/K-NO_3 is 1.272J/g°C and viscosity 14cP at 300°C. Viscosity decreased with increasing temperature. Heat capacity for ternary Li/Na/K-NO_3 is 1.091J/g°C and viscosity 30cP at 300°C. Heat capacity for ternary Li/Ca/K-

			KNO_3, (in the proportions of 20–28–52 wt.%), T_{melt}=130.15°C, T_{max}=600.05°C $LiNO_3$-KNO_3-$Ca(NO_3)_2$, (in the proportions of 30–60–10 wt.%), T_{melt}=132.5°C, T_{max}=567.18 °C	aluminium for Q-20, Peltier plate rheometer		NO_3 is 1.395J/g°C and viscosity 2cP at 300°C.
5	Osami Abe, Taizo Utsunomiya, and Yoshio Hoshino [33]	The thermal stability of binary alkali metal nitrates	$LiNO_3$, $NaNO_3$-KNO_3, $CsNO_3$, Composition not mentioned.	Rigaku Denki TG-DSC/DTA/EGA, platinum vessel,	Dry Ar/Air ($50cm^3$/min), 1.25 to 10°C/min,2 to 20mg,	Regular solution theory was used to study the thermal stability of solid solution and thermal stability of the liquid solution. Result concluded that decomposition of each nitrate in given mixture proceed independently.
6	Osami Abe, Taizo Utsunomiya, and Yoshio Hoshino [335]	The thermal stability of alkali and alkaline-earth metal hydroxide—nitrate systems	$NaNO_3$, KNO_3, $Sr(NO_3)_2$, $Ba(NO_3)_2$, $Mg(OH)_2$, $Ca(OH)_2$ Composition not mentioned.	Rigaku Denki TG-DSC/DTA/EGA, Rika Denki Kogoyo differentiator, Simadzu Seisakusyo gas Chromatograph, Gaschro Kogyo gas sampler. Alumina cricuble.	Ar ($50cm^3$/min),, 5°C/min, 10gm,	Phase diagram of NaOH-$NaNO_3$ and KOH-KNO_3 were studied, the thermal stability of solid and liquid solution was studied and found out that, anion-anion interaction controls the stabilization of liquid solution and cation-cation and cation-anion interaction act against stabilization of liquid solution. NaOH-NaNO3 has the strong oxidizing ability.
7	Robert W. Bradshaw	MOLTEN NITRATE	$Ca(NO_3)_2$, $NaNO_3$, $LiNO_3$,	Hach Co. DR2010UV-VIS	Not described	For nitrate/nitrite system to prevent oxidation an inert gas needed to be

	and Nathan P. Siegel [17]	SALT DEVELOPMENT FOR THERMAL ENERGY STORAGE IN PARABOLIC TROUGH SOLAR POWER SYSTEMS	KNO_3 (unknown composition) T_{melt}=below 100°C, T_{max}=500°C	spectrometer, Hach Co. analyzer, pyrex test tube, Brookfield DV-II+ viscometer		used. Liquidus temperature can be minimum with 1:1 nitrate/nitrite anion ratio and optimum 20% Li^+. Viscosity increases at a higher temperature with Ca^+ presence. Density decreases with increasing temperature.
8	R.W. Bradshaw, D.E. Meeker [36]	High-temperature stability of ternary nitrate molten salts for solar thermal energy systems	$LiNO_3$- $NaNO_3$-KNO_3, $Ca(NO_3)_2$-$NaNO_3$-KNO_3, Composition not mentioned.	Electrically heated alumina containers, x-ray diffraction,	Air, O_2, Not described	The thermal stability results of the two ternary salts indicate that the stability increases as cation parameter increase.
9	Xuejun Zhang, Jun Tian, Kangcheng Xu, and Yici Gao [399]	Thermodynamic Evaluation of Phase Equilibria in $NaNO_3$-KNO_3 System	$NaNO_3$, T_{melt}=580K, KNO_3, T_{melt}=608K,	DSC-7 Perkin –elmer, X'pert MPD X- ray diffractometer, open aluminium pan, Pt/Pt-13% Rh thermocouple,	N_2, 20cm^3/min, 1.5 to 20K/min, 5 to 20 mg,	Sodium and potassium nitrate is regarded as limited solid solution rather than continuous solid solutions, obtained from x-ray diffractometry at 473K.
10	Tao Wang, Divakar Mantha, Ramana G.Reddy [106]	Thermal stability of the eutectic composition in $LiNO_3$–$NaNO_3$–KNO_3 ternary	$LiNO_3$- $NaNO_3$-KNO_3, (25.9wt%-20.06wt%-54.1wt%,) T_{melt}=118°C,	Perkin elmer Pyris Diamond TG/DTA, Perkin elmer Diamond DSC, XRD, SEM, EDS	Ar, N_2, 3.334 X 10^{-7} m^3/sec to 3.334 X 10^{-6} m^3/sec, 15 to 25mg, 5 to 10°C/min, 500°C,	SEM, XRD, EDS has been done and found out that, Lithium nitrate is an unstable phase at a higher temperature, where it decomposes to its oxide. In the short term cyclic thermal stability experiment, the weight loss in the

		system used for thermal energy storage	T_{max}=435°C,			first heating cycle was due to absorbed moisture removal. In long term stability test the weight loss was 8.57 wt%.
11	Justin W. Raade and David Padowitz [108]	Development of molten salt heat transfers fluid with low melting point and high thermal stability	$LiNO_3$- $NaNO_3$-KNO_3-$CsNO_3$-$Ca(NO_3)_2$, (8-6-23-44-19 wt. %) T_{melt}=65°C, T_{max}=561°C,	Symyx Parallel melting point work station (PMP), Q500 TGA from TA, platinum pan,	Air, N_2,20 mg, 10°C/min,	The minimum melting point is achieved by 30 mol % Cs and 15 mol % Ca. Thermal stability limit in air is 561°C, and thermal stability limit in N_2 is 563°C. $CsNO_3$, and $LiNO_3$ is more expensive compared to Ca/K/Na //NO_3.
12	O. Greis, K.M. Bahamdan and B.M. Uwais [38]	The phase diagram of the system $NaNO_3$ KNO_3 studied by differential scanning calorimetry	$NaNO_3$–KNO_3, $NaNO_3$, T_{melt}=579K, KNO_3, T_{melt}=608K,	DuPont 990 thermal analyser DSC, open/hermetically sealed aluminium and gold pans,	Air or sealed environment, 20 mg, 10K/min,	In Na-K//NO_3 phase diagram. Sodium nitrate has melting and freezing point 579K; potassium nitrate has melting and freezing point 608K. The transition of α,β, and γ phase can shift ±10K depending upon the kinetics.
13	Tao Wang, Divakar Mantha, Ramana G. Reddy [314]	Novel low melting point quaternary eutectic system for solar thermal energy storage	$LiNO_3$-$NaNO_3$-KNO_3-$NaNO_2$, (17.5-14.2-50.5-17.8 wt.%) T_{melt}=372.17K, T_{max}=703.15K,	Perkin–Elmer Diamond DSC/TG/DTA, aluminium pan with lid, K-type thermocouple,	Air, N_2,20cc/min, 5K/min,	The melting point of the quaternary system is 372.17K, heat capacity 1.56J/gK at 623.15K, during long term stability test, 7.4 wt% weight loss occur. Thermal storage capacity is 1143 MJ/m^3 for short term and for long term 950 MJ/m^3. At 673.15K, the vapor pressure was 84.32 mPa in 4.5 l/h Ar gas flow rate, and weight loss was 11.85 μg. With 15 l/h Ar gas flow rate, the vapor pressure was 40.26 mPa and weight loss was 18.86 μg.
14	Ramana G. Reddy, Tao	Thermodynamic properties	$2KNO_3\cdot Mg(NO_3)_2$,	Perkin–Elmer Diamond	Air, N_2,20cc/min,	Two endothermic peaks observed, the first one is at 404.8K regarded to

	Wang, Divakar Mantha [109]	of potassium nitrate–magnesium nitrate compound [$2KNO_3 \cdot Mg(NO_3)_2$]	(66.67mol%K-33.33mol%Mg,) T_{melt}=468.83K	DSC/TG/DTA, aluminium pan with lid,	5K/min, 298.15 to 523.15K, 298.15 to 623.15K	solid state transition and the second one is 468.83 K regarded to the melting of the compound.
15	Tao Wang, Divakar Mantha, Ramana G. Reddy [400]	Thermodynamic properties of $LiNO_3$–$NaNO_3$–KNO_3–$2KNO_3 \cdot Mg(NO3)_2$ system	$LiNO_3$–$NaNO_3$–KNO_3–$2KNO_3 \cdot Mg(NO_3)_2$, (17.77-15.28-35.97-30.98 wt%,) T_{melt}=374.90K	Perkin–Elmer Diamond DSC/TG/DTA, aluminium pan with lid,	Air, N_2,20cc/min, 5K/min, 298.15 to 523.15K, 298.15 to 623.15K	The melting point of the quaternary system is 374.90K, heat capacity 184.88J/molK at 623.15K.
16	Qiang Peng, Jing Ding, Xiaolan Wei, Jianping Yang, Xiaoxi Yang [105]	The preparation and properties of multi-component molten salts	KNO_3-$NaNO_2$-$NaNO_3$ + 5% inorganic compound (Cl additives), the percentage composition, is not described due to patent issue. T_{max}=550°C, T_{melt}=137.62°C,	Q600 SDT thermogravimetric analysis, LFA 447 Nanoflash thermal conductivity apparatus, RSD-06 synthetic test density measurement apparatus, DIL402PC thermal expansion instrument, K type thermocouple,	Not described	By using 5% additive, A (unknown chloride additive) increased the high temperature thermal stability to 550 degree Celsius and lowered the melting point to 137 degree Celsius.
17	C.Y. Zhao, Z.G.Wu	Thermal property characterizati	KNO_3-$Ca(NO_3)_2$-$LiNO_3$, Sample	STA-1500 Simultaneous thermal analyzer,	Not described	The eutectic is cheaper than HitecXL. the melting temperature is below 100°C, and high temperature

	[111]	on of a low melting temperature ternary nitrate salt mixture of thermal energy storage system	A= 67.2-19.3-13.5 wt%, sample B=64.8-24.8-10.4 wt%, Sample C= 63.7-27.3-9.0 wt %, $T_{melt/A}$=78°C,$T_{melt/B}$=80°C,$T_{melt/C}$=76°C,T_{max}=450°C	Kinexus Ultra Rheometer,		thermal stability is 450°C, the viscosity is less than 10cP,
18	Joseph G. Cordaro, Nicholas C. Rubin, Robert W. Bradshaw [24]	Multicomponent Molten Salt Mixtures Based on Nitrate/Nitrite Anions	$LiNO_3$- $NaNO_3$- KNO_3- $NaNO_2$- KNO_2, (30 mol%Li^+,50 mol%K^+, 20mol% Na^+, 0.56 ratio nitrate to nitrite) T_{max}=not mentioned, T_{melt}=72°C,	Atomic absorption SW 8467430, ion chromatography EPA 300.0, Alumina crucible,	10 to 20 g, Not described	Poses low melting point with certain cation ratio and anion ratio. 30 mol%Li^+,50 mol%K^+, 20mol% Na^+, and 0.56 nitrate to nitrite ratio provides a lower melting point at 72°C.
19	V. V. Deshpande, M. D. Karkhanavala, U. R. K. Rao [374]	Phase transitions in potassium nitrate	KNO_3, Potassium nitrate without pre heat treatment, potassium nitrate heated at 120°C and quenched rapidly	Perkin Elmer 1B DSC, Rika denki recorder, Red croft temperature programmer	O_2, N_2,0.5° to 32°C/min, 15 gm, 150°C	Crystallographic phase transition occurs at 129°C, 120°C, and at 105°C. The phase II (orthorhombic) transform to Trigonal I ferroelectric phase occurs at 129°C, phase I to phase III at 120°C, phase III to normal phase II at 105°C. Moreover, these results were independent of sample preheating.
20	Kevin G. Zeeb, Malcolm G. Lowings, Keith G. McCurdy,	Heats of transition and melting of sodium nitrate by differential scanning	$NaNO_3$,	Perkin Elmer DSC-2, Hurden Planimeter, Cahn model 4700 automatic electro balance	3 to 9 mg, 1.25° to 160°C/min,	The results of DSC show that the decomposition of sodium nitrate has two peaks. One peak is for the solid -solid transition and other is for the melting. The heat of melting is 3586 cal/mole.

	Loren G. Hepler [360]	calorimetry: use of indium and sodium nitrate as calibration substances		apparatus,		
21	R N Kust, J D Burke [209]	Thermal decomposition in alkali metal nitrate melts	1:1 mole $NaNO_3$-KNO_3, T_{max}= 650°C,	Apparatus not described.	100gm, Not described	The nitrite ion concentration increases with temperature. Decomposition of nitrite ion takes place at 300°C. The equimolar sodium nitrate and potassium nitrate undergoes thermal decomposition into their corresponding nitrites and oxygen at 300°C. $NaNO_3$ has the enthalpy change at decomposition is around 20.0 kcal and KNO_3 has the enthalpy change at decomposition is around 24.6 kcal.
22	Maeso M. J., Largo J., [32]	The phase diagrams of $LiNO_3$-$NaNO_3$ and $LiNO_3$-KNO_3: the behavior of liquid mixtures	LiNO3, - NaNO3, and LiNO3, - KNO3	Perkin Elmer DSC-2, In and K_2CrO_4, sapphire, hermetically sealed aluminum pans	15 mg, Not described	Activity coefficient is decreased by the increase of molal composition for both binary systems.
23	Kramer, C.M., Munir, Z.A., Stern, K.H. [189]	EVAPORATION OF $NaNO_3$, KNO_3, AND $NaNO_2$	$NaNO_3$-KNO_3-$NaNO_2$	TG and MS, High Temperature Mass Spectrometry, Stainless steel	Vacuum, 627 to 784K	Decomposition of $NaNO_2$ produces N_2, and NO. And other two salts produced N_2, NO, and O_2. Evaporation kinetics is first order rate equation. The activation energies were obtained for individual salt.
24	F. Roget, C. Favotto, J.	Study of the KNO_3–$LiNO_3$	KNO_3–$LiNO_3$, 66-34 wt%.	DSC131 setaram, XL-	2 to 5 K/min, 120 µL	The thermal stability of binary nitrate in the range of 40°C to

	Rogez [280]	and KNO_3–$NaNO_3$–$LiNO_3$ eutectics as phase change materials for thermal storage in a low-temperature solar power plant	KNO_3–$NaNO_3$–$LiNO_3$ 52-18-30 wt%.	DSC calorimeter, K-type thermocouple, captec heat flow meter,	aluminum crucibles, aluminum cylindrical containers,	180°C was quite reproducible but in the case of ternary nitrate the cyclic thermal stability in the temperature range of 40°C to 180°C was fairly reproducible. The density of ternary nitrate was 1975kg/m^3 at 140°C, melting enthalpy 155kJ/kg with melting point 123°C and volumetric storage capacity of 86 kWh/m^3.

APPENDIX B: THERMAL ANALYSIS TECHNIQUES AND DTA/DSC CURVES EVALUATION

B.1 THERMAL ANALYSIS TECHNIQUES

This subchapter describes the thermal analysis methods for the high temperature properties study of molten nitrate salt systems. The alkali nitrate salts were subjected to control heating-cooling inside automated furnace to certain set point temperatures to observe various thermal events simultaneously. The thermal test methods are described in Chapter 6 of this Thesis. The common thermal analysis techniques and curves interpretation are described here.

B.1.1 THERMAL ANALYSIS TECHNIQUES BACKGROUND

To understand the physical and chemical properties of materials, thermal analysis techniques (TA) are commonly used by applying heat to the sample in controlled atmosphere. TA instrument comprised of three components namely: measuring unit, temperature control and recording unit [401]. In TA instrument a variety range of samples (e.g: 0.1µg to 10mg) with any physical form (e.g: solid and liquid) and in any type of sample vessels (e.g: close or open type) in various atmosphere (e.g: inert or oxidative) can be investigated in any experiment conditions (e.g: 1minute to several hours; up to 2000ºC) [402]. TA equipment investigate behavior of tested sample as a function of temperature and time can give accurate data on temperature change, mass change, energy change, phase information, eutectic point, reaction type, decomposition stages, and stability in high temperature, of the sample material [17, 72, 105-109, 111, 402, 403]. In the thermal analysis, the test sample is subjected to heating. Due to heating, the sample undergoes properties change. Thus, some events can be observed; they are: melting, phase transition, sublimation, and decomposition [404, 405]. These thermal events give the qualitative and quantitative thermal analysis curve or thermo gram as an output [406]. These details will be reviewed in this subchapter.

B.1.2 VARIOUS THERMAL ANALYSIS TECHNIQUES

Thermal analysis is done on a sample by observing the heating effect and giving the qualitative or quantitative analytical information [406]. There are many types of thermal analysis technique available, they are: DTA (Differential Thermal Analysis), TGA (Thermo Gravimetric Analysis), DSC (Differential Scanning Calorimetry), EGA (Evolved Gas Analysis), EGD (Evolved Gas Detection), TMA (Thermo Mechanical Analysis), DMA (Dynamic Mechanical Analysis), GC (Gas Chromatography), MS (Mass Spectrometry), FTIR (Fourier Transform Infrared) TEA (Thermo-Electrical Analysis) [385]. In this chapter, the most relevant four thermoanalytical techniques to this study are described; TGA, DTA, DSC, Mass spectrometer and Simultaneous DTA, DSC, and TGA. These systems will be described in this chapter to evaluate the use of these techniques for studying the thermal properties of molten salts.

B.1.2.1 THERMOGRAVIMETRIC ANALYSIS

Thermogravimetry analysis is commonly referred to as “TGA” [406]. In TGA analysis, the change of weight of a test substance or test sample is monitored and measured (in the form of voltage or Watt [407]) as a function of temperature or time [408]. The weight change is recorded and displayed as a thermogravimetric (TG) curve or Derivative thermogravimetric curve (DTG). TGA system has a thermobalance, electronic microbalance, a programmable temperature furnace, and a controller [404, 409]. At first, the sample is weighed into a sample holder. Then, the sample is placed inside the furnace on a suspended balance. Then, the sample and empty crucible are heated at given scanning rate inside the TGA furnace. Finally, the data logging system generated the thermal curves as output.

A TG analyzer and outline of thermobalance working procedure are shown schematically in Figures B.1.2.1.1 (a) and (b) respectively [404]. The carrier gas flows through inside the furnace. The balance and the furnace are packed in a closed system, as shown schematically in Figure B.1.2.1.1 (a).

An enclosed system is used because to control the surrounding atmosphere within the measurement system. The carrier gas can be inert or reactive medium [404]. Usually argon, and nitrogen used as an inert carrier gas. Oxygen, carbon monoxide, and carbon dioxide are commonly used as an oxidative carrier gasses. The whole process is monitored by the DSC/TGA software (such as Calisto [332]) which produces the TG and DTG curves [404].

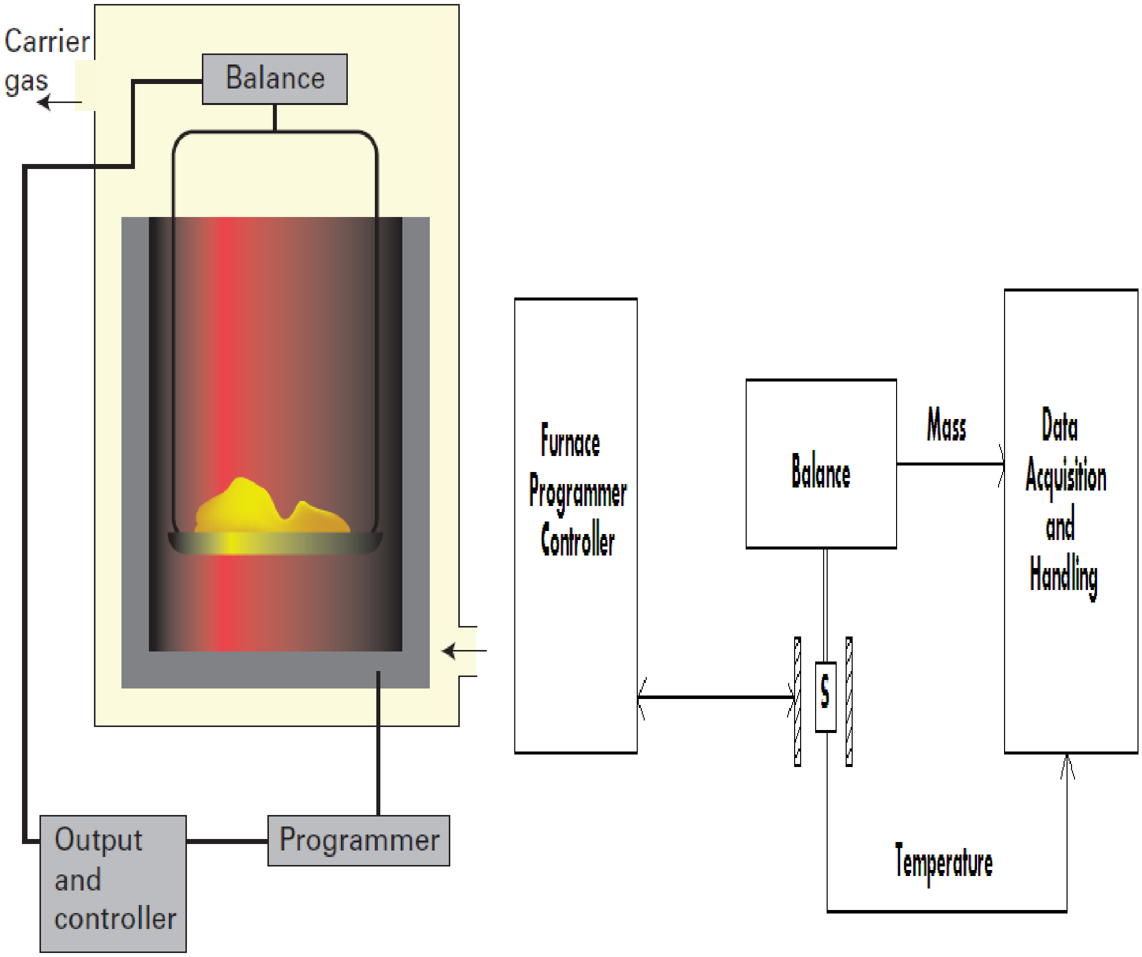

(a) (b)

Figure B.1.2.1.1: (a) Schematic diagram of thermogravimetric analyzer [404] and (b) simple work flow diagram of a thermobalance [410].

Thermogravimetry instruments: A TGA instrument has mainly three parts. The balance, the furnace, the instrument control/data handling system [410], as shown schematically in Figure B.1.2.1.1 (b).

The balance: Analytical balance can be several types, they are: beam spring, cantilever, torsion balances, and null point weighing mechanism [410]. The null balance is the more modern version of the analytical balance and commonly used in various apparatus [411]. The furnace: There are three ways to place the sample in the enclosed balance and furnace system. They are: horizontal placing, top loading, and suspended placing [410]. Instrument control and data handling: The software system can generate both heating and cooling cycle's temperature profile and store the data for thermal analysis. The data can be calculated as a TG curve or DTG curve depends on the complexity or the necessity of the test.

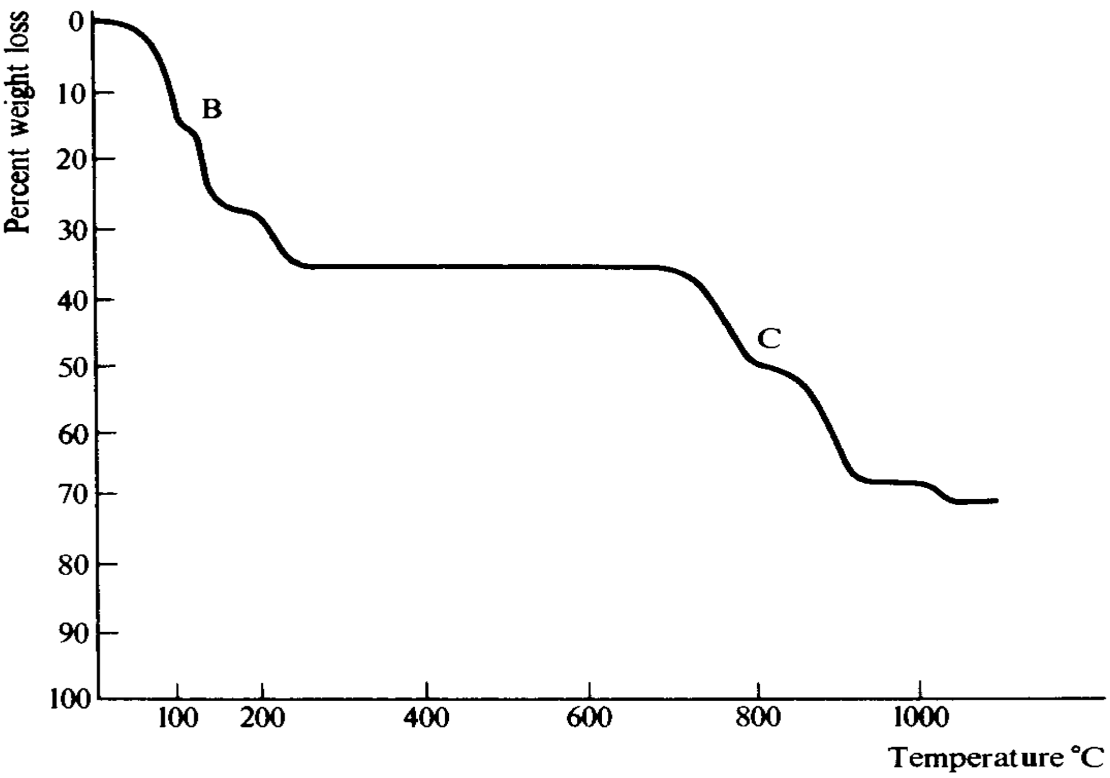

Figure B.1.2.1.2: A TG weight change curve for $CuSO_4 \cdot 5H_2O$ [408].

For a better understanding of TGA curves, an example a normal TG curves with different decomposition stages of $CuSO_4 \cdot 5H_2O$ (copper sulphate pentahydrate) is shown schematically in Figure B.1.2.1.2. The weight loss percentage vs. Temperature curve can be normal TG curve or DTG curve. The slope of the curve at point B and point C indicates the decomposition region (reaction mass loss) of the test substance of $CuSO_4 \cdot 5H_2O$ [408]. The TG curve is quantitative in nature, so by observing the size of the curve, the compound stoichiometry can be calculated at any given temperature [406]. If the TG curve is complex and the changes are slight, the DTG curve can be used for the elaboration of the curve. The DTG curves can also be used to interpret overlapping thermal reactions region [410]. The factors that affect TG test results are: heating rate, furnace atmosphere, crucible geometry and sample characteristics[408].

B.1.2.2 DIFFERENTIAL THERMAL ANALYSIS

Differential thermal analysis is a widely used thermal analysis technique [404]. This analysis technique is commonly known as ‗DTA' [406]. Where the temperature difference (ΔT) between the tested material (recorded by sample thermocouple) and the reference material (recorded by reference thermocouple) are measured as a function of temperature [407, 408, 412]. The sample and reference materials subjected to the same heating source inside the furnace [413]. The ΔT is measured by a differential thermocouple. The thermocouple's one junction has contact with sample crucible, and another junction is connected to the reference crucible [413]. In a DTA test, the controlled heating or cooling program is linear with respect to time. The reference material usually chose according to the sample material. However, commonly Al_2O_3 (Alumina), SiC (Carborundum) are used as reference materials [404, 410] for inorganic samples, and for organic sample silicon oil is used [410]. The reference material should have the same thermal mass, thermal conductivity, and heat capacity as the sample [413].

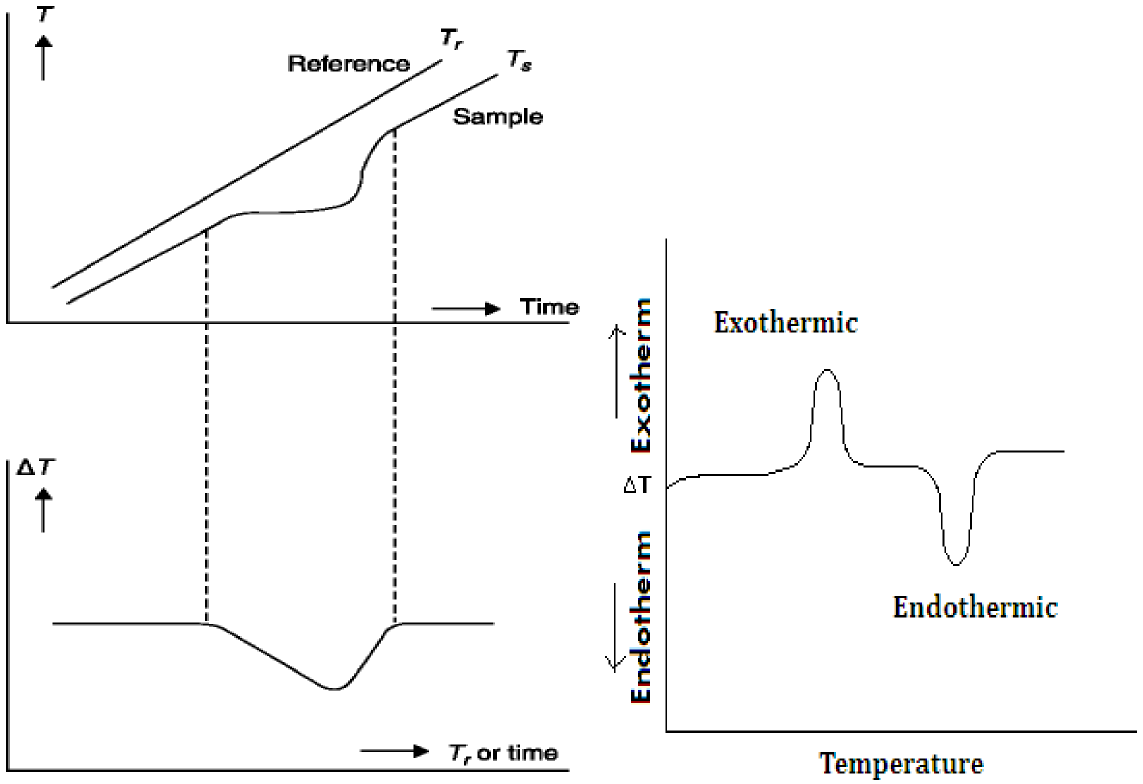

(a) (b)

Figure B.1.2.2.1: (a) the sample and reference temperature as a function of time showing endothermic effect during melting [414]. (b) An ideal ΔT vs. T, DTA curve showing an exothermic peak upward and an endothermic peak downward [406, 408]. Reprinted with kind permission from Wiley copyrights.

An idealized DTA graph is shown schematically in Figure B.1.2.2.1. The sample which absorbed heat shows endothermic events, and heat release shows exothermic event. The curve ideally shows exothermic peak upward vertically and endothermic peak downward vertically, is shown schematically in Figure B.1.2.2.1. The shape and the size of the peak give the information about test nature of the tested material [408]. A sharp change in endothermic peak indicates a fusion process. Broader endothermic peaks generally indicate reactions that take place over a range of temperature. Compounds melting peaks are broader compared to their individual pure material‘s melting peak. During melting heat energy is used for phase transformation of the sample material. The instrument will show in the DTA curve that, the transformation nature is endothermic and indicate that the sample is cooler than the reference. Usually, physical changes give an endothermic curve which generally indicates fusion process or crystalline changes. Chemical reactions usually give exothermic and endothermic curves. During an endothermic event, the sample temperature will lag behind from reference material. Similarly during an exothermic event, the sample temperature will exceed the reference temperature [404]. For instance, If the sample temperature is T_S and reference temperature is T_R, in the case of an endothermic event, the T_S will be lag behind from T_R. Then, the temperature difference $\Delta T = T_S - T_R$. In the case of an exothermic event, the T_R will be lag behind from T_S, in this case, $\Delta T = T_S - T_R$ [410].

B.1.2.3 DIFFERENTIAL SCANNING CALORIMETRY

Unlike DTA the differential scanning calorimetry is also popular analysis technique and is commonly known as DSC [406]. The energy (heat flow) that is required to maintain zero temperature difference ΔT (identical temperature of sample and reference) between the tested material (recorded by sample thermocouple) and the reference material (recorded by reference thermocouple) is measured as a function of temperature or time [407, 408]. The ΔT of the sample and the reference are maintained to zero by adjusting the energy input during the test procedure. The calorimetric measurement of energy transfer to or from the sample system gives the DSC test result. The sample and the reference material maintained at the same temperature in a holder inside the furnace by the separate power supply to each sample and reference [404]. The supplied power difference of the sample and the reference are recorded with respect to the furnace temperature. The whole process is shown as a function of time or temperature[408]. In a DSC curve, the endothermic and exothermic event is seen as a deviation from the baseline. The peak from the baseline gives the idea of supplied power used by the sample material respect to the reference material. For an example, for the endothermic peak, the curve is shown as a positive deviation from the baseline and indicates increased power supply to the sample. In an exothermic peak, the curve is shown as a negative deviation from the baseline and indicates decrease power supply to the sample. Two measurements methods are used in DSC, power compensation DSC and heat flux DSC [408]. As an example, In power compensation DSC, the temperature difference is always kept zero. Thus, ΔT = T_S - T_R= 0 is achieved by independent heaters of power compensating DSC [410]. Another method the Heat flux DSC is also called calorimetric or Boersma DTA [410]. In heat flux, DSC, the sample, and reference are placed in heat flux plate, where ΔT is proportional to heat flux difference between the sample and the reference [410].

During endothermic transition reaction, the energy absorbed by the sample is compensated by increased energy input to the sample for keeping the temperature difference ΔT zero. The calorimetric measurement is used to obtain this balancing energy. The DSC plot is generated as transition temperature (in X- axis) versus total energy transfer to the sample (in Y- axis). The peak of DSC chart indicates the transition temperature. It also indicates total energy transfer from the sample or into the sample.

B.1.2.4 SIMULTANEOUS DSC/DTA, TGA, AND EGA

One particular thermal analysis technique is not sufficient to explore all the problems of a given test sample. Moreover, it is also difficult to compare the test result data of one analyzer with another analyzer. As the test result of material may vary from apparatus to apparatus, due to the differences in calibration, thermocouple and sample history [415]. Besides, performing the test in the separate analyzer is a time-consuming process. To avoid such difficulties, simultaneous multiple analysis of a single sample can be done with one analyzer [410, 416]. This type of analyzer is commonly named as the simultaneous thermal analyzer (denoted as STA) which might consist of DTA, TGA, and DSC system. Sometimes simultaneous thermal analyzer is coupled with evolved gas analyzer (EGA). EGA or off-gas analyzer can be: mass spectrometry (MS), or Fourier transform infrared spectroscopy (FTIR), or gas chromatography [417]. The evolved products from STA outlet is analyzed inside EGA units.

In DTA the ΔT of the sample is observed with respect to the reference sample. In DSC the ΔT of the sample and reference material is always kept same for the entire experimental procedure [404]. In other words, in DTA, the temperature difference between the sample and the reference is measured, and in DSC, the temperatures of both sample and reference are kept same to monitor the difference in heating power needed for the test purpose. These all options of DTA/DSC and TGA can be observed in a single system of Simultaneous DTA/DSC and TGA test machines. In simultaneous TGA, DTA/DSC techniques, the same furnace, program and recording system are used, which were used in DTA and TGA test machines individually. Due to simultaneous measurements and acquisition, now it is possible to obtain TG, DTG/DSC, and EGA curves from a single sample subjected to unary testing [408].

B.1.3 EVOLVED GAS ANALYSIS, MASS SPECTROMETRY

Mass spectrometry (MS) is an instrument that measures the molecular masses of atoms and compounds and provides mass analysis of evolved gas of a tested sample [418, 419]. Usually, EGA is coupled with STA for evolved gaseous products analysis. Where in the vacuum chamber of MS analyzer the individual atoms or molecules acquire charge form ion source or ionizer with the help of heated tungsten or filament which emits an electron. Then the fragmented ions are sorted separately in magnetic mass analyzer according to their mass to charge ratio spectrum and later they are detected separately in ion trap detector (ITD) by the electron multiplier [408], as shown schematically in Figure B.1.3.1.

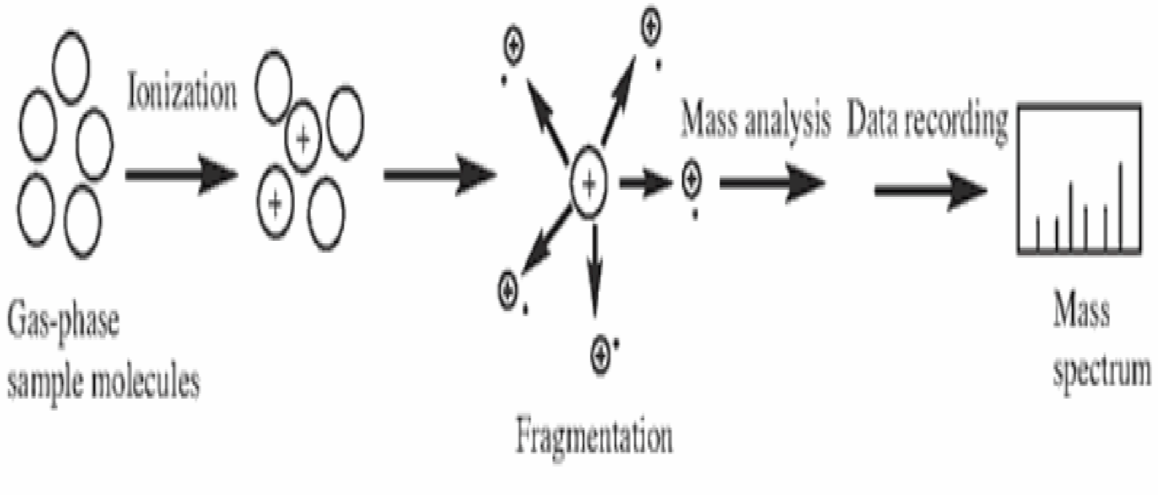

Figure B.1.3.1: Mass spectrometry working basics [418].

Mass spectrometry is performed on liquid, gas, or solid phase samples. The MS provides atomic and molecular weights information and thus it is possible to acquire information on structure, mechanism, kinetics of the reaction, and mixture analysis [408]. Commonly, mass or charge versus intensity is shown as output in MS. In recent times, many MS apparatus are coupled with STA apparatus [332]. In most of the MS experiment, a high vacuum environment is used for measurement and analysis purpose. Vacuum required converting almost all the molecules into gas phase ions. The gas phase ions in vacuum have long lifetime compared to molecules [408]. Most gas phase ions gain a single charge and have identifiable mass, by which the original particle can be identified and measured.

The main components of MS apparatus are: the vacuum system controlled by data acquisition and processing computer software, evolve gaseous products inlet system, ion source producer, a mass analyzer, detector, are shown schematically in a block diagram, in Figure B.1.3.2. There are different types of pumps used for vacuum operation in MS apparatus; they are: two stage rotary pump, oil diffusion pump, turbomolecular pump, differential pumping, automated series pump [408]. Among them, turbomolecular pump, differential pump, and automated series pump are most popular.

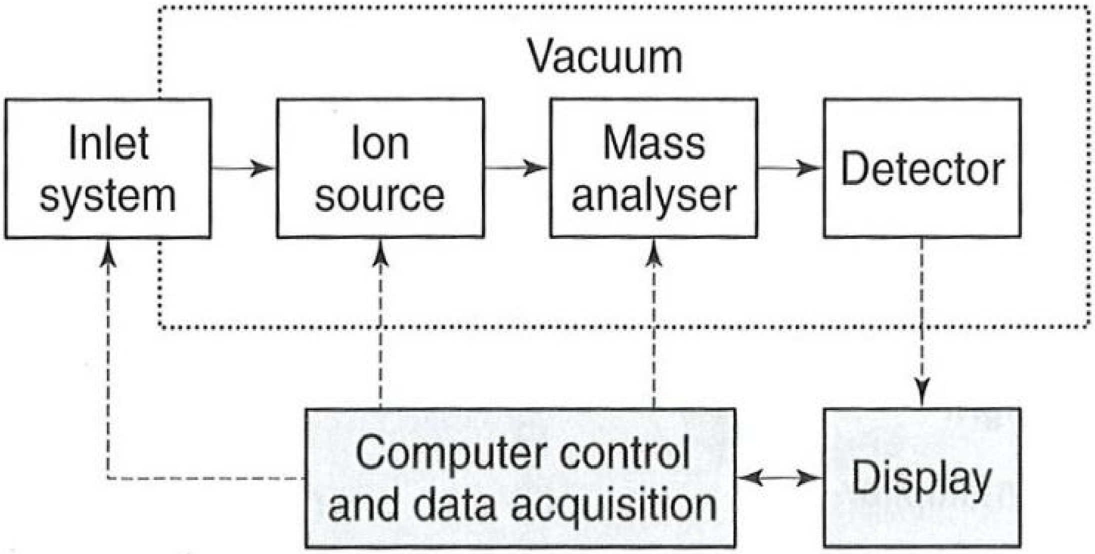

Figure B.1.3.2: Mass Spectrometer block diagram [408].

At higher temperatures the molten nitrate salt, sample produces gaseous products. These high temperature gasses can be detected by MS apparatus from the outlet of STA. At particular temperature range and time, which gasses evolved from the sample is very important to study the thermal decomposition behavior of a given sample.

B.2 THERMAL CURVES ANALYSIS

DSC is used to study purity, phase changes, thermal stability, and heat capacity of sample materials [407]. By interpretation of the curves, thermal properties of the material can be understood. To interpret the DSC or DTA heat flow curves; the baseline, zero line, peak, and peak area need to be known. These are described in this subsection.

Zero line: The zero line in a DSC curve is measured with an empty instrument. A typical zero line is shown schematically in Figure B.2.1. The zero line curve can be constructed without samples and without sample containers or crucibles, or, with sample container empty [385]. It indicates the thermal behavior of the system. For precise measurements, the zero line must be determined before and after every sample test.

Temperature, thermal conductivity of sample, structure of the sample, location of the sample in the crucible, purge gas, sample history, sample purity and heat calibration material need to be checked on a regular basis in order to identify drift, scattering, thermal lag (smearing) and other measuring asymmetries in the zero line and in the baseline [407]. The zero line heat flow rate Φ_o should be subtracted from the measured curve heat flow rate Φ_m, to get the true sample heat flow rate Φ_s,

$$\Phi_s = \Phi_m - \Phi_o \qquad \text{eqn B.2.1}$$

Baseline: The baseline is the part of recorded DSC curve, without any reactions and transitions in the sample in steady state conditions within a peak [407]. The baseline is the sum of zero line and heat flow rate of the reference and sample during scanning mode. The baseline is the dotted line as shown schematically in Figure B.2.1. The baseline can be an isothermal or dynamic baseline. An isothermal baseline temperature is constantly maintained, whereas in a dynamic baseline the temperatures change. The interpolated baseline is a continuous line drawn as if no peak had developed [385]. In the case of different emissivity between sample and reference holder, a slope in the baseline is measured [385]. A baseline can be derived by three methods: instrumental baseline (measured with two empty pans), extrapolated or interpolated baseline, and pre and post-melting baseline [420]. A pre and post-melting baseline also called a sigmoidal baseline, is a linear continuous baseline [420]. Baseline construction is qualitative in nature estimated from known DSC curves [385]. There are different procedures for baseline construction suggested by Brown [385], as shown schematically in Figure B.2.2.

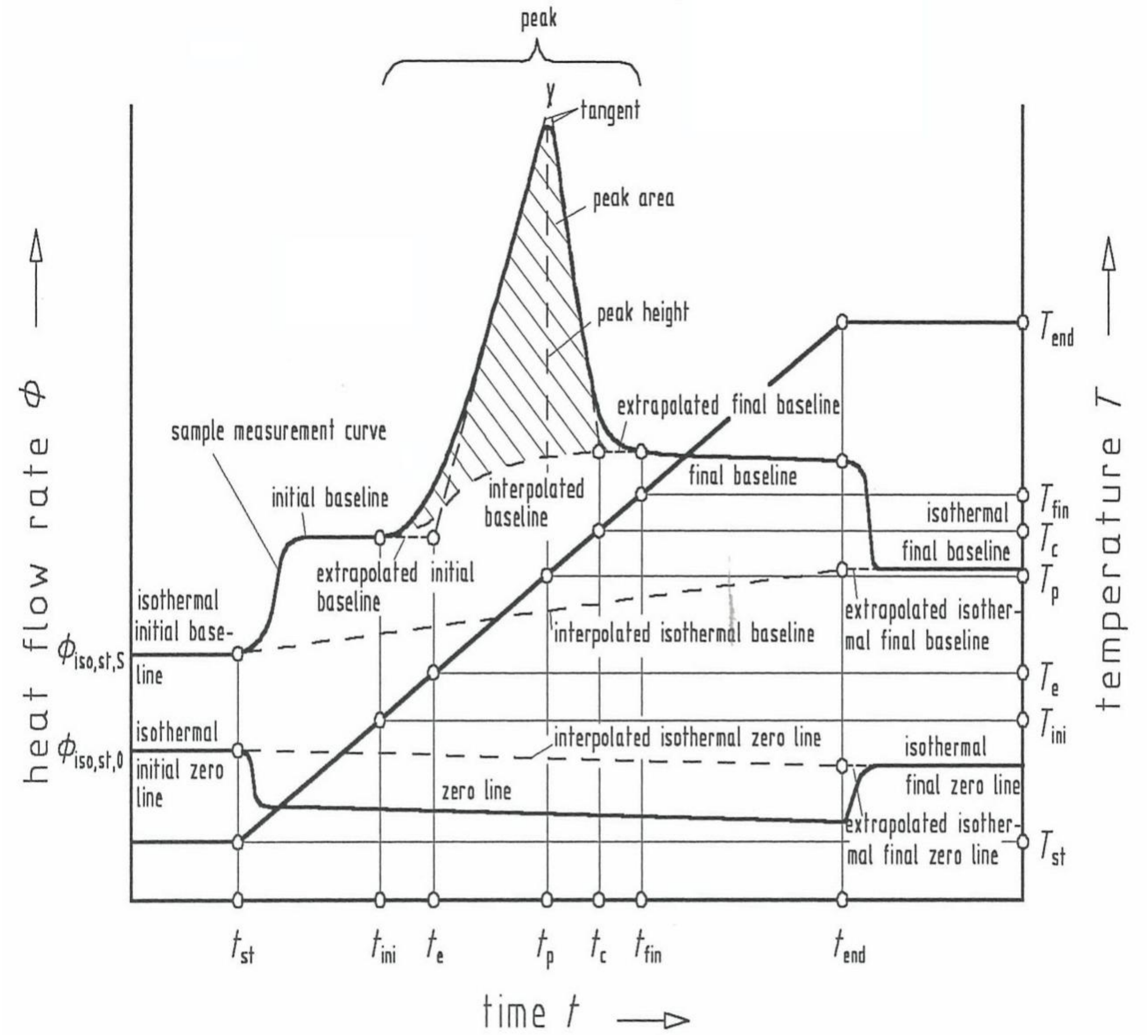

Figure B.2.1: DSC curves indicating baseline, peak, zero line, and their corresponding temperatures [338, 385, 407, 421].

A DSC curve has five temperatures region associate with the peak area, is shown schematically in Figure B.2.1. They are:

Here,

Φ_m = is the measured heat flow.

T_i = initial peak temperature.

T_e = extrapolated peak onset temperature.

T_p = peak maximum temperature.

T_c = extrapolated peak completion temperature.

T_f = final peak temperature [385].

At the initial peak temperature T_i, the peak begins, and the curve starts to deviate from the baseline. T_e and T_c are measured from the intersection of the ascending slope and from the intersection of the descending slope of the baseline. In other words, the auxiliary lines intersection with the base line gave the extrapolated peak onset temperature T_e and extrapolated peak completion temperature T_c. These auxiliary lines are drawn almost linear with the ascending or descending peak slope. Auxiliary lines can be drawn as an inflectional tangent or as a fitted line [407]. At the peak maximum temperature region T_p, the difference between the DSC curve peak point and its vertical intersection to the baseline has the maximum value. At final peak temperature T_f, the peak ends, and the curve returns to the baseline [385].

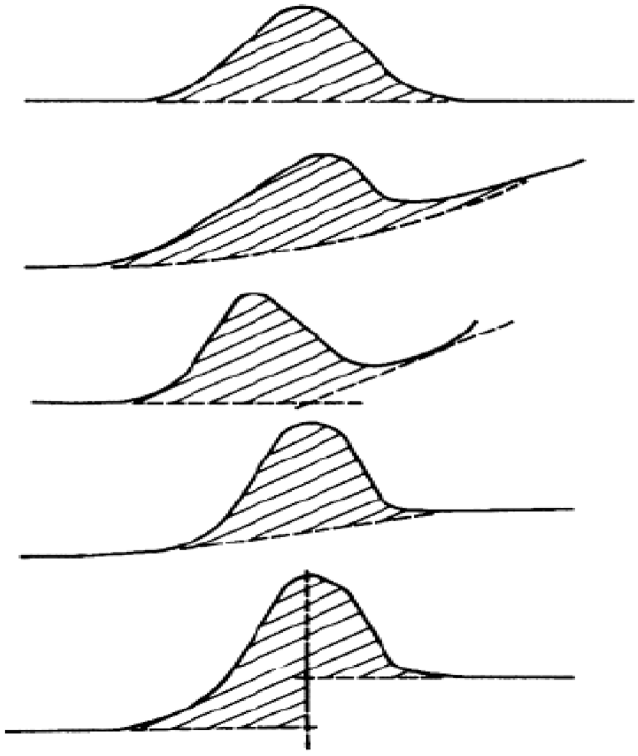

Figure B.2.2: Different procedures for baseline construction suggested by Brown [385].

Peak: The peak is the portion of the DSC curve which deviates from steady state and subsequently returns to the baseline [422]. When the steady states are disturbed by absorption of heat or production of heat by the test sample, then the peak appears as endothermic and exothermic. Such events are, melting, reaction, transition, crystallization. An endothermic peak is shown schematically in Figure B.2.1. The section between initial peak temperature T_i, and final peak temperature T_f, is called _peak‘ [407]. Other than the peak, in a DSC curve, a transition, discontinuity can be seen [385]. The endothermic processes are plotted upwards in a positive direction as heat is added to the system and for exothermic processes, the peaks are downwards as heat is released from the system. Heat processes such as: melting, crystallization are showed as peaks, other transitions give shape changes [407].

Peak area: The peak area is the enclosed portion between the DSC curves and the baseline, as it is shown schematically in Figure B.2.1. The peak area can be calculated by numerical integration of the area inside the baseline and the peak. This integration is done by either Simpson‘s rule or the trapezoidal rule [385]. The peak area is proportional to enthalpy change,

$A \infty \Delta H$,

Thus, the enthalpy change is, $\Delta H = AK/m$ [422, 423] eqn B.2.2

$K = \Delta H m / A$ eqn B.2.3

Here,
m= sample mass
K= calibration factor, determined from the known change of pure metal, such as Indium [385].

For calibration materials, the enthalpy change is, $\Delta H_c = A_c K/m_c$
Thus, $K = \Delta H_c\, m_c/A_c$ eqn B.2.4
Now the enthalpy change of the sample is, $\Delta H_s = A_s K/m_s$ eqn B.2.5

Here,
m_s = sample mass
A_s= area of the sample

Thus, from eqn B.2.4, the value of K can be set into eqn B.2.5 to obtain the sample‘s enthalpy change. The heat capacity can also be measured from DSC curve.

$\Delta H = \int_{T_i}^{T_f} C_p\, dT$ [385] eqn B.2.6

$\Delta S = \int_{T_i}^{T_f} (\frac{C_p}{T})\, dT$ [385] eqn B.2.7

$\Delta G = \Delta H - T\Delta S$ [385] eqn B.2.8

Here, C_p is the heat capacity at constant pressure [385].

Interpretation of DSC curves:

The baseline discontinuities should be examined by paying attention to endothermic and exothermic peaks of the thermal events [385]. The decomposition, dehydration, transition, crystallization, melting should be observed during the DSC measurement then the test event should be checked whether the process is reversible or non-reversible by heating or cooling. Usually, the exothermic events such as solid-solid transitions are not reversible. However, sometimes dehydration is reversible in the moist atmosphere during cooling [385]. Also, carbonate decomposition in CO_2 atmosphere is reversible [385]. In these cases, the comparison of the material under inert and oxidizing atmosphere is required to interpret the thermal events.

The slope of the peak can be read depending upon whether the peak is associated with pure or impure substances. As an example, for pure materials like Indium, the melting peak is very sharp, and the ascending and descending slopes intersections to the baseline are almost linear, and thus, it is used to calculate the area and the enthalpy of fusion. The materials with impurities have a tendency to lower the melting point and broaden the endothermic peak and melting range. This makes it difficult to predict the baseline and extrapolating slopes detection. In this case, the impurity contents are needed to estimate from analysis - the endothermic peak of the impure compounds and from known journals and ASTM books [385].

Baseline construction:

The baseline is the virtual line accepting that, no heat of transition had been released within peak region [407]. The baseline is required to determine and calculate the peak area.

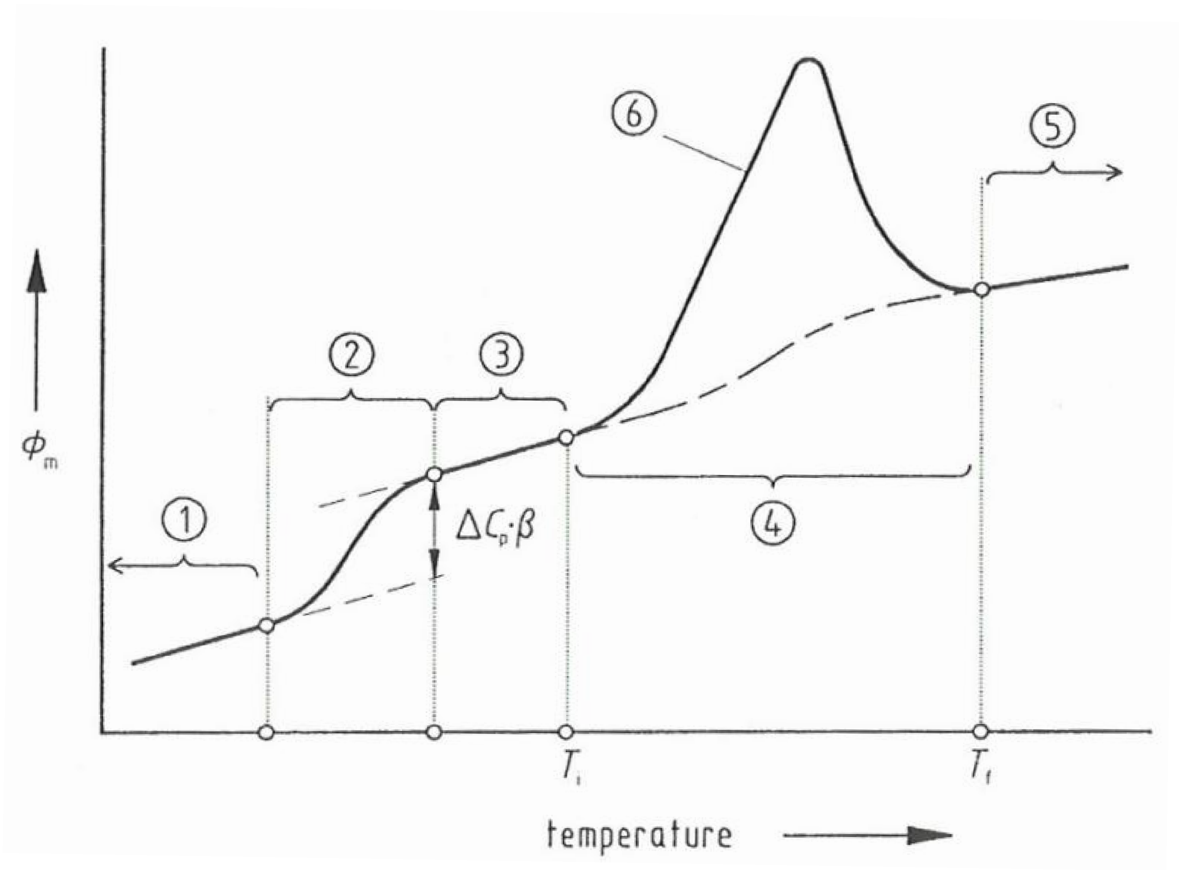

Figure B.2.3: DSC curve showing different parts or region [407].

A curve is measured by DSC showing the base line change or C_p change and an endothermic peak of 1st order transition, as shown schematically in Figure B.2.3. The number 4 region is described in Figure B.2.1.

Here,
ΔC_p = change of specific heat,
T_i = initial peak temperature,
T_f = final peak temperature,
β = heating rate,
Number 1 region in Figure B.2.3, is the initial segment of the measured curve,
Region 2 is indicating ΔC_p,
Region 3 is linear portion of the curve,

Region 4 is indicating interpolated baseline in between T_i and T_f, and also an endothermic peak,
Region 5 is the final segment of the measured curve,
Region 6 is indicating the endothermic peak of the measured curve.

The baseline construction methods are as follow:

The baseline of the irreversible transformation process, with negligible heat capacity change, can be determined by repeating the test with the same sample. In this case, the sample‘s reaction process must be completed, such as, annealing of a plastically deformed metal [407]. An interpolated baseline is obtained for the repeated or second run of the same sample. If the heat capacity of the second run is different form the first or original run, then this baseline construction method cannot be used.

For the non-horizontal curve, the outside of the peak area is shown schematically in Figure B.2.4. The degree of reaction $\alpha(t)$ needs to be determined by approximation in order to construct the baseline [407]. In this case, the baseline slope change between T_i and T_f is approximated and the baseline construction according to van der Plaats equation [407] is as follows:

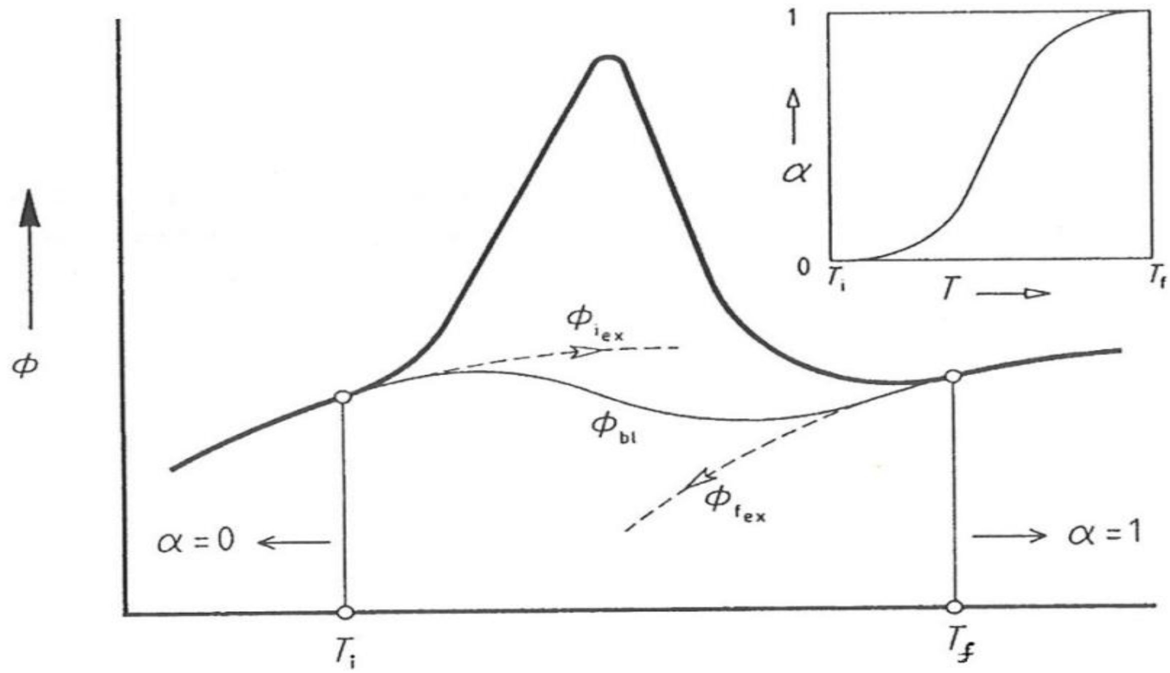

Figure B.2.4: The construction of the baseline with the degree of reaction α(t) [407].

The approximation equation, $\left(\frac{d\Phi}{dT}\right)_{bl} = (1\text{-}\alpha)\left(\frac{d\Phi}{dT}\right)_{T_i} + \alpha\left(\frac{d\Phi}{dT}\right)_{T_f}$ [407] eqn B.2.9

The degree of reaction α(t) describes, the time response (how slow or fast) of the baseline slope change rate [407], as shown schematically in Figure B.2.4.

Here,
At the left hand side of the T_i, α=0; (for the condition of $T<T_i$), [407]
And at the right hand side of the T_f, α=1; (for the condition of $T>T_f$) [407].
In between T_i and T_f, α= α(t); (for the condition of $T_i \leq T \leq T_f$), [407]
$\Phi_{i_{ex}}$ = extrapolated measured curve from T_i within the peak region.
$\Phi_{f_{ex}}$ = extrapolated measured curve from T_f within the peak region.

The approximation in between T_i and T_f, The functional value of baseline slope change Φ_{bl} is given by the equation B.2.10 :

$\Phi_{bl} = (1\text{-}\alpha)\,\Phi_{i,ex} + \alpha\,\Phi_{f,ex}$ (approximation) [407] eqn B.2.10

Both $\Phi_{i_{ex}}$, and $\Phi_{f_{ex}}$ can be calculated as polynomial and they are extrapolate in to peak range, and thus the base line within peak region can be calculated using eqn B.2.10.

Besides this, the sudden or spontaneous change in heat capacity at the transition temperature shows a jump off the baseline. In this case, there is no theoretically proved correct baseline construction method [407]. Although the peak area totally depends on upon the baseline construction. So estimation and several possibilities of baseline construction should be performed. The Figure B.2.5 shows a possible baseline construction.

The possible baseline construction in the case of unknown heat change situated somewhere in between T_i and T_f, as shown schematically in Figure B.2.5. Using apparent transformation function the baseline took a jump inside T_i and T_f. the apparent transformation function is an exponential function of time [407].

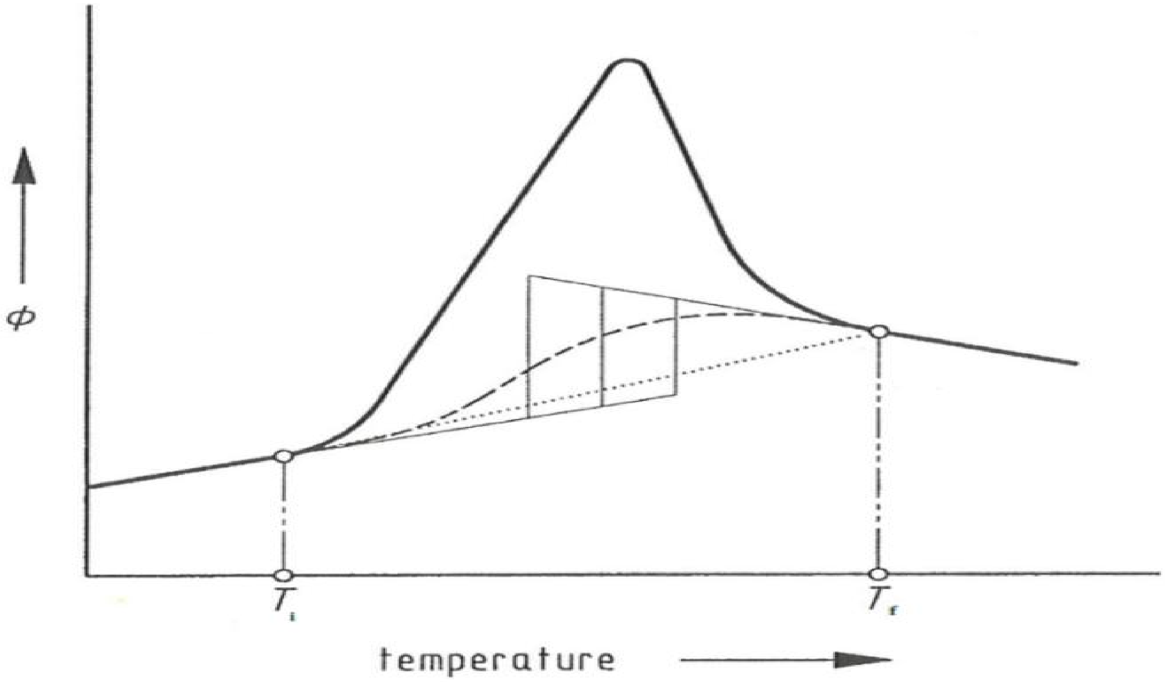

Figure B.2.5: The Possible baseline construction in case of unknown T_i (initial) and T_f (final) temperatures [407].

In a conclusion, there is no single method for true baseline construction [407]. However to avoid the error in measurement, the zero line must be corrected. The zero line should be a straight line or near to absolute straight line, if not, then the zero line must be subtracted from the measured curve before every measurement. Then baseline mentioned above construction methods should be practiced as recommended by Höhne [407]. An instrument baseline should be measured several times consecutively with a given experimental condition to check the curvature and noise level [402]. If all the runs do not give identical instrument baselines, then there is a possibility of moisture residue on the sample holder, improper purge gas flow rate, unexpected voltage spikes, improper level of coolant in the reservoir, and sudden chemical or physical change during sample load up. In these cases, high rate of constant dried purge gas will eliminate the moisture, an electrical malfunction should be avoided with expertise, and frequent cleaning process is necessary [402]. The baseline subtraction should regularly be performed using corresponding DSC software [402].

APPENDIX C: VAPORIZATION CHEMISTRY

C.1 BACKGROUND

Kellogg [424] described different methods of studying the vapor state transport process chemistry of metals and metal compounds extraction. The major techniques were identified by Kellogg; they were: the boiling point method, the vapor density method, the transpiration method, the mass spectrometer, and the Knudsen effusion method. These apparatus are useful in vapor species studies and thermodynamic aspect of partial pressure studies of each species [424].

There are several methods of measuring the vapor pressure. The transpiration method is one of them [425]. Other methods of measuring the pressure of saturated vapor are: static method, flow method (vapor transfer by the current of inert gas), Langmuir method, isotopic exchange method [426], and transportation method [427]. This chapter aims to describe transpiration test method and reaction kinetics.

C.2 TRANSPIRATION METHOD

The Transpiration method is used to measure the vapor pressure of materials in the controlled reactive environment or inert gaseous atmosphere up to 2500K [428]. The transpiration method usually used a steady stream of inert gas and passed or flowed it over the investigating material at a constant temperature inside the experiment rig. The rig has the hotter portion called furnace or reactor, and cooler part of the apparatus sometimes called condenser. The transport gas should be heavier and in pure form. Usually, pure argon gas is used as carrier gas. The total gas flow is measured in volume for a given period. The main experiment tube that holds the sample is inserted into the furnace after the temperature of the furnace is fixed in desired value. The transpiration mechanism is to remove the vapor by evaporation with the help of lower flow rate of an inert gas and collect it at the condenser. The vapor removal is measured at different gas flow rates [427]. The evaporating surface or the reaction tubes cross section has an effect on vapor pressure saturation. The larger the ratio of sample to reaction tube diameter, the saturation occurs at a wider range of flow rates. In contrast, the larger the evaporation surface to fill up the cross section of the reaction tube, the saturation of vapor occurs over a wider range of flow rates [425].

The transpiration test method provides the vapor density information, the species identities, the molecular weight, the equilibrium constant value, and associated partial pressure using the mass action law [425]. In transpiration technique, it is possible to control the chemical potential externally, the temperature, the identification of redox and decomposition reactions, and vapor pressure stability diagram can be obtained by calculating equilibrium constant and contribution of each vapor species.

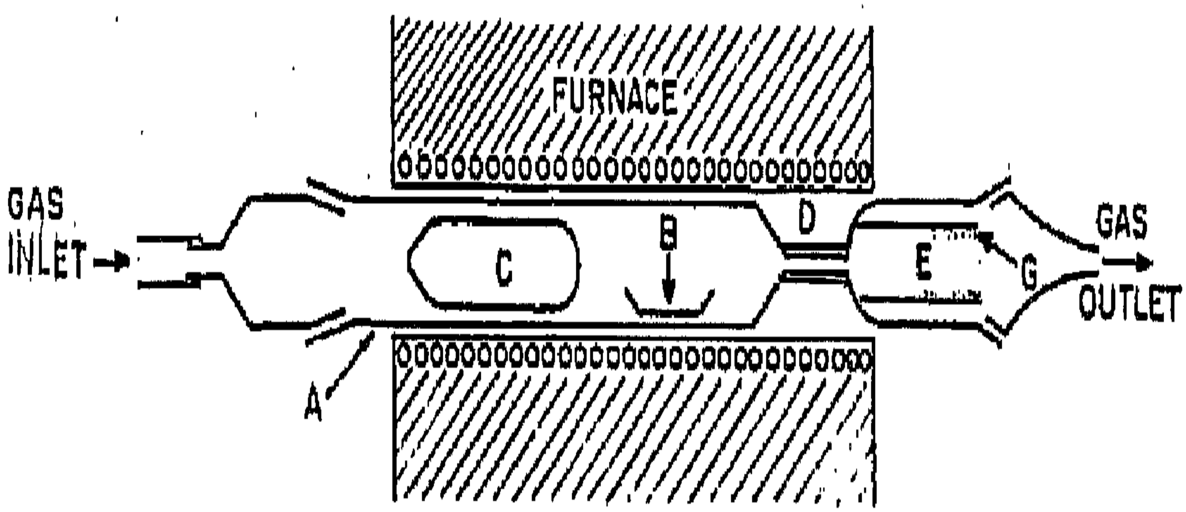

Figure C.2.1 (a): Schematic of transpiration apparatus used by Dharwadkar et al. and Merten [429, 430].

Dharwadkar et al.‘s [429] transpiration rig had ceramic tube denoted as ‗A‘ in Figure C.2.1 (a). The sample boat ‗B‘ was placed inside isothermal zone in the tube inside the furnace. The other portion of the rig is ceramic block ‗C‘, Capillary ‗D‘, detachable condenser tube ‗E‘, Condenser vapor collection arrangement ‗G‘ as shown schematically in Figure C.2.1 (a).

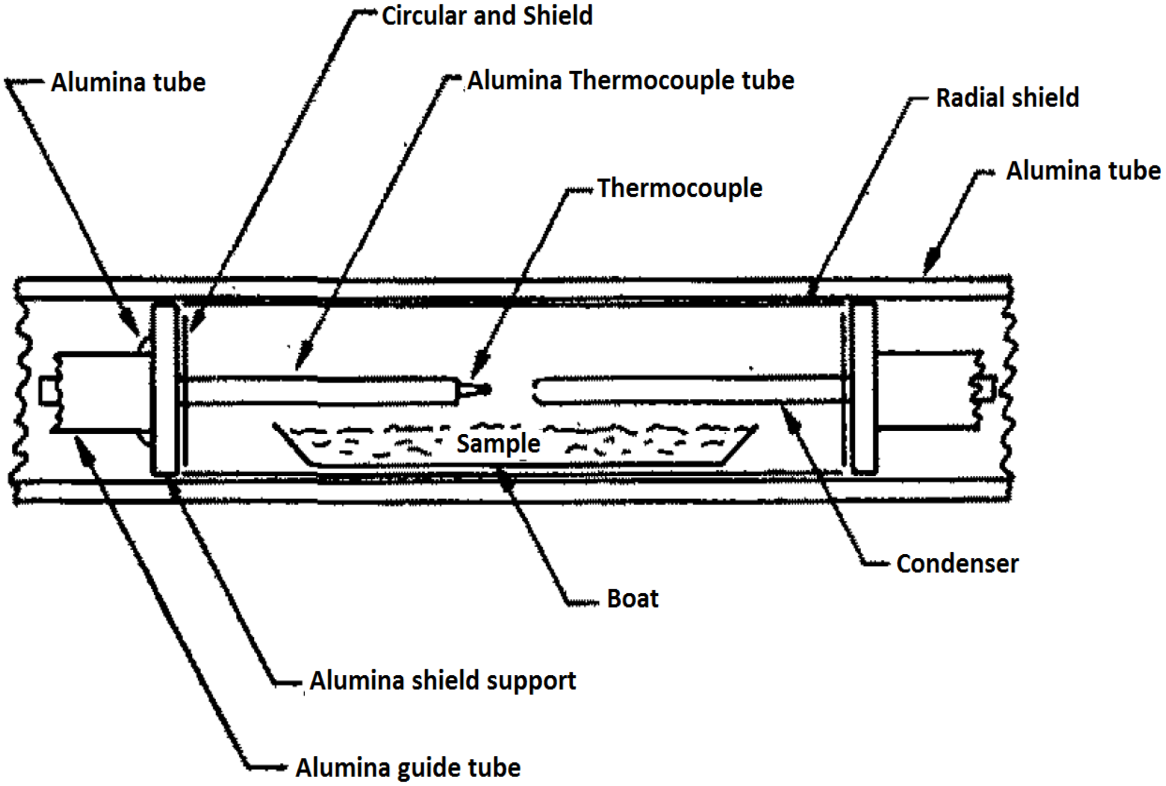

Figure C.2.1 (b): A schematic portion of transpiration apparatus (reaction zone) used by Alexander [431].

The transpiration apparatus described by Alexander [431], the reaction zone is equipped with alumina tube, radial and circular shield, hollow platinum-rhodium cylinder with end plates arrangement and equipped with a thermocouple and condenser is shown schematically in Figure C.2.1 (b). More typical setup of transpiration rig is presented by Son et al. [432] is shown schematically in Figure C.2.1 (c). The argon carrier gas inlet and the outlet are placed at each side of the mullite tube with silicon rubber fittings and copper pipes. The sample boat‘s temperature is measured by a thermocouple, as shown schematically in Figure C.2.1 (c).

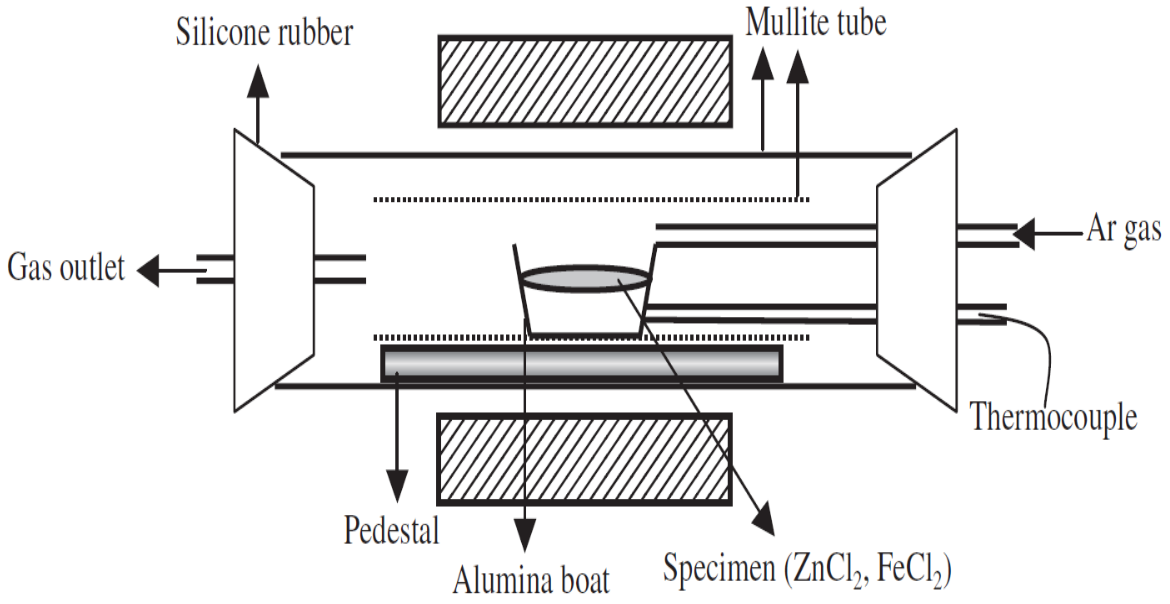

Figure C.2.1 (c): Schematic of transpiration apparatus used by Son et al. [432]. Reprinted with kind permission from copyright© the Mining and Materials Processing Institute of Japan www.mmij.or.jp.

The inert gas flow method is similar to the transpiration method of Nesmeianov et al. [426] and the transportation method of Kubaschewski et al. [427]. Nesmeianov et al. and Kubaschewski et al. both used a current of inert gas to transfer the vapor of the sample material. Here the carrier gas is used as the inert gas, flows over the sample and subjected to any given isothermal temperature [427]. The inert carrier gas is saturated with sample's vapor and carries the vapor into a condenser at almost zero gas flow rate [426, 427]. The inert carrier gas saturated with the vapor implies a relation, that is:

$\frac{p}{n} = \frac{RT}{V} = \frac{p_1}{N}$ [426]

Or, $p = \frac{nRT}{V} = \frac{W_v nRT}{M_v V}$ (n = $\frac{W_v}{M_v}$) [428] eqn C.2.1

Or, $p_1 = \frac{Np}{n} = \frac{RT}{V}$ [426] eqn C.2.2

Here,

p= vapor pressure of the sample

p_1= pressure of the inert gas

V= volume (liter) of the inert carrier gas swept over the sample, which equals to the volume of vapor in the absence of the inert gas flow

n= number of moles of the transported vapor of the tested sample

N= number of moles of inert carrier gas

R= gas constant

W_v= mass loss of the sample or materials

M_v= molecular weight of the vapor species or materials

From equation C.2.1, we can now calculate the vapor pressure of the materials under investigation.

Now, According to Henry‘s Law,

$$P = p + p_1 \qquad [426, 427]$$

So from equation C.2.2, we can rewrite,

$$P = p + p_1 = p + \frac{Np}{n} = p\left(1 + \frac{N}{n}\right) \qquad [426] \qquad \text{eqn C.2.3}$$

$$\text{Or,} \quad p = P\,\frac{n}{n+N} \qquad [426] \qquad \text{eqn C.2.4}$$

The relation in equation C.2.4 is true for, when the inert gas is saturated with vapor and gas flow rate is very low close to zero. Equation C.2.4 applies to low vapor pressure measurement (below 0.1334 kPa) and gives minimal error free results. When the gas flow rate change the result also change [426]. At low flow rates, usually higher evaporation rates achieved compared to the equilibrium rate of a given material. Thus, the low flow rates may give incorrect results. At high flow rates, the transport gas or the inert carrier gas usually don‘t get enough residence time to get in touch with the sample material to reach saturation. Thus at high flow rate, turbulence may occur and long plateau usually achieved [427]. Usually, a constant temperature and constant lower flow rate of carrier gas are maintained in the uniform section of the reaction tube to ensure the undisturbed thermodynamic equilibrium of vaporized materials and the vapor [428].

In an isothermal system for measuring the vapor pressure at various gas flow rates, the results are extrapolated to zero rates and assuming that the saturation of vapor and the inert gas, have occurred at all gas flow rates [426, 427]. Boyle's law can measure the partial pressure,

Partial pressure,

$$p_s = \frac{101.325\ V_s}{V_g + V_s}\ \text{kPa} \qquad [427] \qquad \text{equation C.2.5}$$

Here,

V_s= volume of the transported materials/ substances
V_g= volume of the transported gas

From Dalton‘s law of partial pressure for ideal gas mixtures [314], the vapor pressure of salt mixture or sample is given by:

$$P = \frac{WRT}{MV} \qquad [314] \qquad \text{equation C.2.6}$$

Here,
P= vapor pressure of sample vapor species (Pa).
W= weight loss of sample or mass of vapor species due to vapor transported by carrier gas (g).
R= universal gas constant 8.314 (J/mol. K).
T= absolute temperature of measurement commonly an isothermal temperature inside reaction zone (K).

M= molecular weight of the sample, assuming the vapor species or the vaporization phase has an identical composition as the sample itself.

V= volume of saturated carrier gas obtained from multiplication of flow rate and total time over which the gas flows over the sample (m^3).

Once the melting-boiling temperatures, possible thermal reactions and vapor species of a tested material are known then in selected isothermal temperature (T), the samples are heated in each possible carrier gas flow rates and thus the weight loss data (W) are obtained. Then using weight change data apparent vapor pressures (P) are plotted against flow rates to observe plateau region. The flow rates in plateau regions usually indicate that any flow rates of carrier gas within plateau region are saturated with sample vaporization [433] as shown schematically in Figure C.2.2. At flow rates higher than the plateau region the sample is subjected to slow vaporization which is known as under saturation and at lower flow rates before plateau region the higher vaporization observed known as back diffusion. To avoid unsaturation and back diffusion a mean flow rates value is selected from plateau region, where the vapor pressure is independent of flow rates [428]. Once the equilibrium vapor pressure is obtained from various heating temperatures the mean enthalpy of vaporization can be derived [433]. The equilibrium vapor pressure dependence with temperature can be obtained by plotting log(p) vs. 1/T linear curve is shown in Figure C.2.3. The accuracy of data depends on upon three parameters during the experiment: W, T, and V. Usually the weight change W can be measured direct by weighing of the sample crucible or weighing the condenser after the experiment or testing the vapor condensate chemically by using analytical technique [433]. The flow rates are measured by a rotameter manually, or mass controller digitally, and temperature calibration is performed commonly by use of a thermocouple.

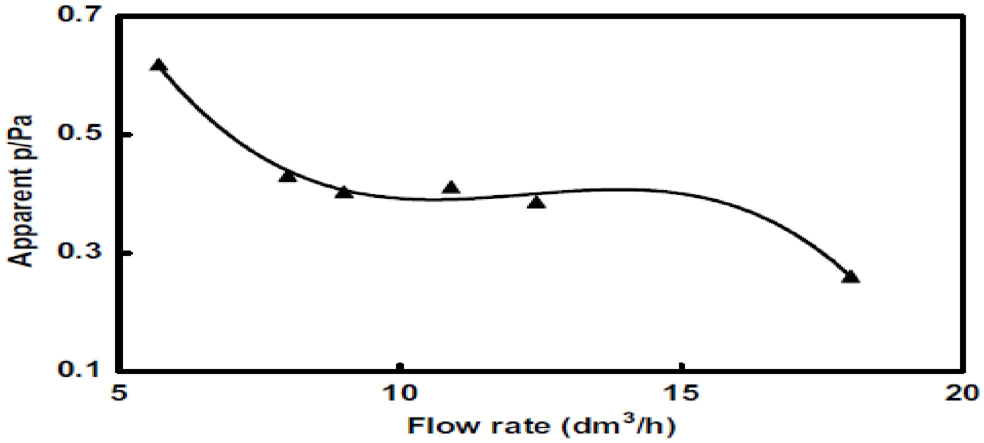

Figure C.2.2: Vapor pressure dependency of a given sample as a function of the flow rate at fixed temperature (404K) [433].

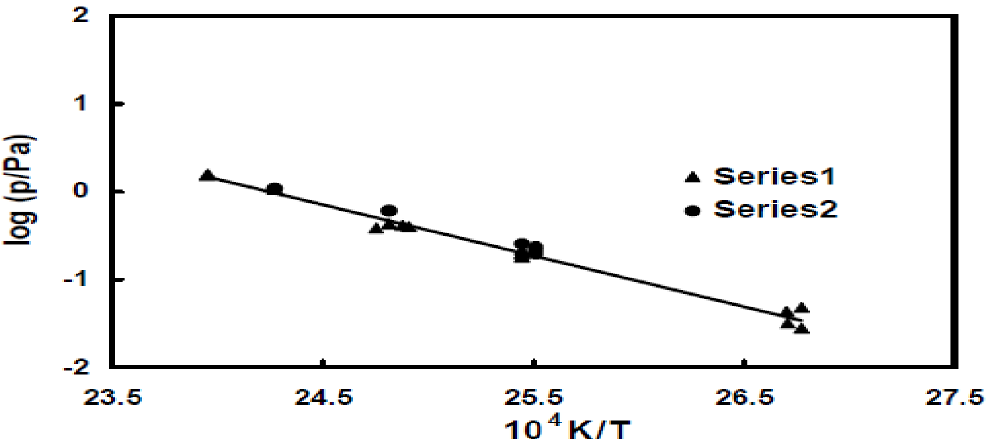

Figure C.2.3: Equilibrium vapor pressure variation as a function of the temperature of $CdCl_2$ [433].

The main difference between thermogravimetric based transpiration apparatus and normal transpiration apparatus is automation, accuracy, and reliability [428]. The TG based transpiration or horizontal apparatus can provide highly accurate temperatures and mass change readings due to its digital thermobalance sensor option equipped with control reaction chamber [428, 434-436]. Moreover, some modified TG based transpiration apparatus (equipped with another analyzer) can provide DSC, TGA, DTA signals with mass spectrometric data (evolved gas analysis) at a time [433, 434, 437-439]. A typical simultaneous horizontal DSC/TGA is shown in Figure C.2.4 (a), and its temperature and heat flow sensors are shown in Figure C.2.4 (b).

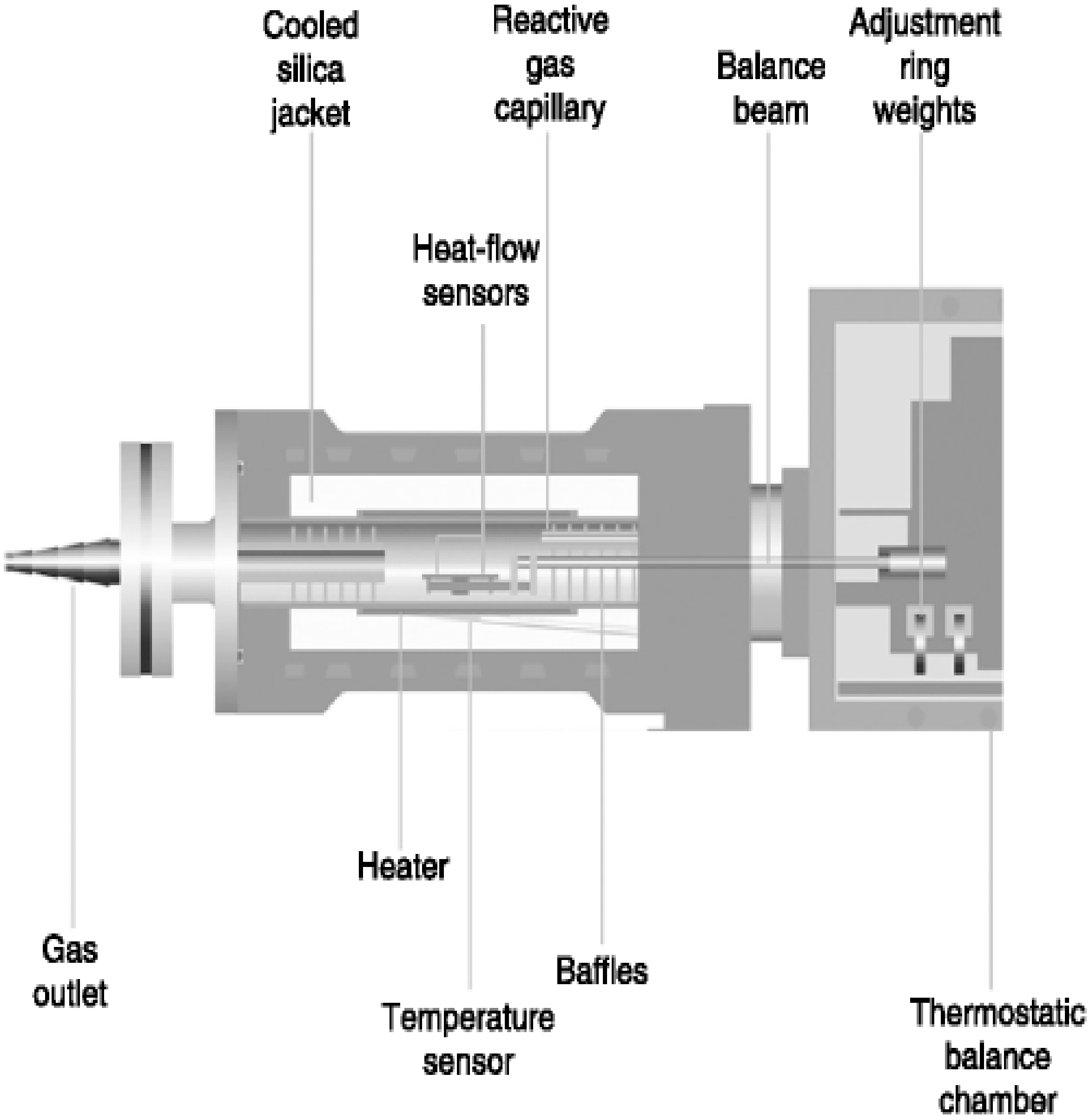

Figure C.2.4 (a): A cross-sectional view of horizontal beam balance simultaneous DSC/TGA with off-gas analyzer coupling option [414].

Figure C.2.4 (b): Horizontal DSC/TGA ceramic transducer for sample temperature and heat flow measurement [414].

APPENDIX D: BINARY PHASE DIAGRAMS THERMODYNAMIC CALCULATION

D.1 INTRODUCTION

Thermodynamics is a science dealing with the transformation of heat into other forms of energy and vice versa of a system and within a system [440]. Chemical thermodynamics provides some information on a given materials, which includes: determination of operating conditions in a reaction or reaction mixture; energy balance calculation at certain temperature and pressure; and maximum possible advancement of reaction at high temperatures, known as thermodynamic modeling [441]. These thermodynamic quantities and operating conditions can be obtained from thermodynamic functions and phase diagrams [286]. The thermodynamic functions include Gibbs free energy or free enthalpy, the affinity of reaction, the activity of a component of phases, the law of mass action, and equilibrium constant of a reaction. The phase diagram shows which phases are present in a given system and what are the relation with thermodynamic functions. The equilibrium diagrams or phase diagrams (Gibbs free energy at minimum state) are used to represent graphically the states and domains of various phases of a given system which is in at equilibrium [441, 442]. A –phase” is a portion of the system. A system consists of components. One phase properties and composition are different from other parts of the system. Within phases, the properties and compositions are homogeneous and distinctive than other phases in the system [443]. The lines on the diagram are called phase boundaries. These boundary lines are the limitation of stability of each phase forms in a given system [442]. Usually, the phase diagrams are illustrated in temperature, pressure, entropy, volume and composition space coordinates.

The most used method of calculating phase diagrams experimentally is the equilibrated alloy method; and commonly used theoretical model is CALPHAD (Calculation of Phase Diagrams) method [444, 445]. Phase diagrams are constructed experimentally during alloy equilibration and/or couple diffusion. Generally, DSC (cooling and heating thermal arrest studies) [119, 446], dilatometry [119], X-ray diffraction (XRD) and electron probe microanalysis (EPMA) are used to measure properties to obtain phase diagrams. In modern days, the phase diagrams are calculated using model assumption in computer simulation programs, such as FactSage, MTDATA, HSC, Thermo-Calc, Lukas, Calphad, and MatLab [119, 447-452].

Usually, Gibbs phase rule is used to construct phase diagrams [117, 119, 442, 453, 454]. To develop a graphical illustration of equilibrium maps the chemical potential and molar Gibbs free energy needed to be understood [442]. Gibbs free energy is a thermodynamic potential of a thermodynamically closed system that describes maximum useful work capacity to perform non-mechanical work in reversible process at constant temperature and pressure. The following equation describes Gibbs free energy of a given system,

$$G = E + PV - TS = H - TS \qquad [119] \qquad \text{eqn D.1.1}$$

Here, Enthalpy $= H$ is the heat content related to the specific heat of a given phase of a system. $H = E + PV$ [E= total bonding internal energy, P =pressure, V =volume]. T = Absolute Temperature, and S= Entropy.

From the first law and second law of thermodynamics (conservation of energy), the reversible or equilibrium Gibbs free energy can be expressed as

$$dE = TdS - pdV + \sum_{i=1}^{r} \mu_i dn_i \qquad [119] \qquad \text{eqn D.1.2}$$

Here, T= temperature, p= pressure, n_i= number of moles of component i, μ_i = chemical potential of component i. By combining equation D.1.1 and D.1.2 and deformation give below equation of Gibbs- Duhem

$$\sum_{i=1}^{r} X_i d\mu_i = vdp - sdT \qquad [119] \qquad \text{eqn D.1.3}$$

To illustrate Gibbs-Duhem equation described in equation D.1.3, let‘s consider a general chemical reaction of $aA + bB + \cdots \quad \leftrightarrow \quad cC + dD + \cdots$. Here lower case characters represent stoichiometric coefficients and upper case character represents species. The Gibbs free energy of reaction can be expressed as:

$$\Delta G = cg_C^0 + dg_D^0 + \cdots - Ag_A^0 - Bg_B^0 + \ldots + cRTln\, a_C + dRTln\, a_D + \cdots - aRTln\, a_A - bRTln\, a_B \ldots.$$

At equilibrium $\Delta G = 0$, thus standard change in Gibbs free energy,

$$\Delta G^0(T) = -RTln\frac{a_C^c a_D^d \ldots..}{a_A^a a_B^a \ldots...} = -RTlnK(T)$$

Here, $K(T)$ is equilibrium constant with relation to each concentration and temperature of the phase diagram, also equivalent to Gibbs-Duhem equation.

A system could be in three equilibrium condition or state: mainly stable, metastable and unstable state [119]. From equilibrium state of a system, an actual conditions can be estimated. When a system is in stable equilibrium condition means at lowest energy condition, $dG = 0$, which indicates no change in the system in it solid and liquid solutions. In metastable equilibrium condition (usually accounted for limited periods of time) an additional dG required to reach true stability in a given system. In unstable equilibrium condition in a system is generally $dG \neq 0$ [119]. Below section introduces Gibbs free energy modeling of three binary and ternary molten nitrate salt systems using regular solution hypothesis.

D.2 FORMULATION OF BINARY NITRATE SYSTEMS: BACKGROUND

Phase diagram calculations were proposed by J. Willard Gibbs in 1876. Gibbs proposed minimum energy criterion stating that the free energies of phases of a given system will be at minimum (ΔG=0) values. This statement is usually used to calculate phase boundaries by mathematical expression with minimum Gibbs free energies of phases for a given system

[119]. Van Laar (1910) expressed a mathematical formulation to calculate a binary phase diagram. Considering a system consist of two component x_i and x_j which exist as phase α and β respectively. α and β commonly represented as lattice stabilities of two different crystallographic arrangement for component x_i and x_j which are denoted as $\Delta G_i^{\alpha\rightarrow\beta}$ and $\Delta G_j^{\beta\rightarrow\alpha}$ [119]. Let's assume component x_i and x_j have interaction energies G_α^E and G_β^E of spices i and j for each phase. Gibbs free energies for two phases for two component binary system can be expressed as following equations [119]:

$$G_\alpha(x,T) = x_i x_j G_\alpha^E + x_i G_i^{\alpha\rightarrow\beta} + RT(x_i ln x_i + x_j ln x_j)$$

$$G_\beta(x,T) = x_i x_j G_\beta^E + x_j G_j^{\beta\rightarrow\alpha} + RT(x_i ln x_i + x_j ln x_j) \qquad \text{eqn D.2.1}$$

Putting numerical values in equations D.2.1 (e.g: temperature, mole) will produce a binary phase diagram. Similarly for ternary system with another component x_k can be calculated using constituent binary system in addition with ternary interaction terms. Thus equation D.2.1 can be rewritten for ternary system for α phase as follow [119]:

$$G_\alpha\left(x_i x_j x_k, T\right) = x_i x_j G_\alpha^E + x_j x_k G_\alpha^E + x_j x_i G_\alpha^E + RT \sum_{x=x_i}^{x=x_k} x ln x + x_i x_j x_k G_\alpha^E \qquad \text{eqn D.2.2}$$

Regular solution theory was introduced by Van Laar [119] and Hildebrand [455-460] in the early twentieth century. The regular solution can be described as a non-ideal solution or the deviation from ideal solution behavior (ideal entropy of mixing) [32, 278]. It showed nonzero heat of mixing (non-zero interchange energy) where it shows some regularities in experimental behavior [456, 459]. According to Vallet [284], the regular solution's excess entropy is zero, and the excess enthalpy is independent of temperature and activity coefficient are proportional to the reciprocal temperature [284]. The regularity hypothesis implies when the excess Gibbs energy and isothermal enthalpy of mixing quantities are identical. According to Guggenheim [459] and Sundman and Ågren [456] various species/ atoms/ molecules that are sufficiently similar in size, shape and electronegativity assumed as random mixing and will go to same sublattices. However, species/molecules that are sufficiently dissimilar will not mix randomly hence occupying different sublattices, as a result the solution will not exhibit an ideal entropy of mixing. In such cases species/molecules within each sublattice are assumed to be ‗random mixing‘ as per the regular solution model.

For a two components A and B (with composition x_A+ x_B=1), the binary formulation of regular solution can be described for each phase as:

$$G(T, x_i) = G_A(T)x_A + G_B(T)x_B + \Omega x_A x_B + RT\ [x_A \ln(x_A) + x_B \ln(x_B)] \quad [119]$$

eqn D.2.3

$G_A(T)$, $G_B(T)$ are pure components Gibbs free energies for A and B. x_A, x_B are mole fraction of component A and B. Ω is the enthalpy of mixing for the phase of interest (either liquid Ω_L or solid Ω_S). The value of Ω depend on A-A, B-B, and A-B neighbors consideration, where first two phases give positive values and A-B gives negative values. Now the regular solution of equation 3.6.2.3 for the binary system can be described as an ideal solution when enthalpies of mixing Ω=0, means enthalpy of mixing at liquid, Ω_L =enthalpy of mixing at liquid, Ω_S. The equation D.2.3 is similar to equation D.2.1, where former can be written for each crystal structure for (liquid or solid) component A and B. The regular solution expression for binary system can be written as a form of chemical potential for each phase as follow:

$$\mu_A(T, x_A) = G_A(T) + \Omega(1 - x_A)^2 + RT \ln x_A \quad [119]$$

$$\mu_B(T, x_B) = G_B(T) + \Omega(1 - x_B)^2 + RT \ln x_B$$

eqn D.2.4

Kramer [153] used regular solution prediction by Kleppa [300-303] and Nissen [299] regarding the behavior of binary common anion molten nitrate salt solution and derived mathematical equations for the binary Na-K//NO_3 system. Kramer [153] used Gibbs free energy minimization method to calculate the binary Na-K//NO_3 phase diagram. Gibbs free energy minimization states that for a binary solution the Gibbs free energies of each component‘s each phase are zero at thermodynamic equilibrium. Also, Abe et. al [33] predicted the thermal stability of solid solutions and liquid solutions of binary alkali nitrates using Kleppa‘s [300-303] regular solution assumption. Kleppa [300-303] and Nissen [299] both have approximated from their respective experimental results that, the behavior of molten nitrate salt with common anions follows regular solution hypothesis. Kleppa using high temperature reaction twin calorimetry [300, 303] investigated the binary alkali nitrates that, the heat of mixing enthalpies, ΔH^M change in a regular fashion with changing difference in size between two participating cations. ΔH^M varies positively for $LiNO_3$ and $NaNO_3$, and ΔH^M varies to negative values for KNO_3 and $RbNO_3$ in a regular manner [302]. He used the least square method to find the empirical coefficients for molar enthalpy of mixing for the liquid phase. He established a semi-empirical relation by following equations (neglecting 2nd order or quadratic term):

$\Delta H^M \cong -X\,(1-X)\,U\,\delta^2$ kcal/mole. [302] eqn D.2.5

OR, $\Delta H^M \cong -X\,(1-X)\,[140\,\delta^2 - 24(\delta - 0.001)]$ kcal/mole. [301] eqn D.2.6

OR, $\Delta H^M \cong X\,(1-X)\,[a + b\,X + c\,X\,(1-X)]$ kcal/mole. [302] eqn D.2.7

Here,

ΔH^M = molar enthalpy of mixing, the enthalpy of mixing is the indication of the thermal stability of solutions. If the values of ΔH^M are large and negative, then it indicating that the system will form stable solution [335].

X = mole fraction of one component with smaller cation.

(1-X) = mole fraction of other component.

U = lattice energy of the mixture.

140 = a numerical factor representing the order of the lattice energy of the salts.

δ^2 = binary salt ionic parameter, commonly known as ‗Tobolsky parameter‘ [302].

δ = $(d_1-d_2)/(d_1+d_2)$; d_1 and d_2 are the interionic distances characteristics of two pure salts. Which d indicates the sum of ionic radii of component 1 and 2 (d_1 and d_2) [335].

d= distances d, were obtained from the approximation, $d_{MeNO_3} = r_{Me^+} + r_{NO_3^-}$. for Li/Na/K/Rb-NO_3 Kleppa used Pauling‘s crystal ionic radii in r_{Me^+}; for d_{MeNO_3} and $r_{NO_3^-}$ were assumed from lattice parameter and hence the Tobolsky parameter were calculated.

a (magnitude of interaction), **b** (energetic asymmetry) and **c** (cation short range order) = were all negative and derived from the least square method. From modified lattice theory Kleppa approximated the relation between a, b and c as: $c \cong 2\,(a+b/2)^2/ZRT$ [Z= number of next nearest neighbors in the fused salt mixture].

Nissen observed the isothermal surface tension curves of equimolar KNO_3-$NaNO_3$ from the heat of mixing data and the results well fitted for the regular solution theory. According to Nissen [299] for binary mixture of the regular solution properties, the enthalpy of mixing is given by the following equation:

$\Delta H = w x_1 x_2$ [299] eqn D.2.8

Here,

w= pairwise interaction parameter or interchange energy is a measure of deviation from ideal solution behavior [for the ideal solution w= 0].
x_1 and x_2 = mole fraction of component 1 and 2.

D 3: BINARY NITRATE THERMODYNAMIC MODELING

This section will re-describe the calculation of Elliott and Kramer in elaboration. Kleppa took the smaller sized cation as the first component in his binary salt solutions formulation. The cation size in alkali metal is increased periodically from Lithium to Francium.

For A-B salt system (A=$NaNO_3$, B=KNO_3):

Kramer [153] described the entropy and enthalpy of the regular solution by following equations. The enthalpy of mixing assumed non-zero and expressed as polynomial form.

$\Delta Smix = x_A \ln x_A + x_B \ln x_B$ [153] eqn D.3.1

$\Delta Hmix = x_A x_B \ (a + bx_A + cx_A x_B)$ [153] (Kelppa‘s assumption) eqn D.3.2

Here,

x_A = mole fraction of component A less than x_B .
x_B = mole fraction of component B,
a, b and c are empirical constants were taken from Kleppa‘s calorimetric work. From binary Na:K//NO$_3$ liquid solution between 618 to 723K the values of a, b and c were -408 cal/mole, -68 cal/mole and 0 cal/mole respectively. Empirical coefficients represent the partial enthalpies of mixing for both phases (liquid and solid).

According to Kramer [153] based on Kelppa‘s [301] regular solution assumption of binary alkali nitrates, at equilibrium the Gibbs free energy ΔG of liquid and solid solution are zero. Consider component A with mole fraction x_A has solid solution $x^A_{Solid\ solution}$ and liquid solution $x^A_{Liquid\ solution}$. Kleppa described component A as salt with smaller cation size (NaNO$_3$). At equilibrium condition at temperature T, $x^A_{Solid\ solution} = x^A_{Liquid\ solution}$ with free energy of the reaction of zero value. Below equations describe the free energy of component A:

$$\Delta G \equiv A_{SS} = A_{LS} = 0 = (\Delta H_A - T\Delta S_A) + (\overline{\Delta H^{A_L}_{mix}} - \overline{T\Delta S^{A_{LS}}_{mix}}) - (\overline{\Delta H^{A_{SS}}_{mix}} - \overline{T\Delta S^{A_S}_{mix}})$$

Term 1 Term 2 Term 3

[153, 305] eqn D.3.3

Here,
1st term $(\Delta H_A - T\Delta S_A)$ represent free energy of fusion of component A,
2nd term $(\overline{\Delta H^{A_L}_{mix}} - \overline{T\Delta S^{A_{LS}}_{mix}})$ represent partial molar energy of mixing of component A liquid solution,
3rd term $(\overline{\Delta H^{A_{SS}}_{mix}} - \overline{T\Delta S^{A_S}_{mix}})$ represent the partial molar energy of mixing of a solid solution of component A [305].

- ***Term 1 of equation D.3.3:***

Free energy of fusion of component A involves phase transition heat of fusion; entropy of fusion and change between solid-liquid isobaric heat capacity. Thus free energy of fusion of component A at temperature other than melting [at melting temperature free energy of fusion is zero]: $A_{Solid} \rightarrow A_{liquid}$ reaction can be described as

$\Delta G = \Delta H_A - T\Delta S_A$ [153]

ΔH_A is enthalpy of melting of component A and ΔS_A is entropy of melting of component A. For temperature variation the first term of eqn 6.6.3 can be rewritten as

$\Delta H_A = \Delta H^0 - \int_T^{T_{MP}} (C_{PL} - C_{PS})dT$ [153]

and $\Delta S_A = \Delta S^0 - \int_T^{T_{MP}} \frac{(C_{PL} - C_{PS})}{T} dT$ [153] eqn D.3.4

Here,

T_{MP}= melting point of component A,
T = temperature at which the equation is being solved,
ΔH^0= Enthalpy of fusion at melting point for component A,
ΔS^0= Entropy of fusion at melting point for component A,
C_{PL}= heat capacity of the liquid phase of component A,
C_{PS}= heat capacity of the solid phase of component A.

To use correction term between melting temperature and the accounted temperature (for which temperature the equation is being solved) eqn D.3.4 is integrated and expressed as follow:

$\Delta H_A = \Delta H_{fus}^A - \Delta C_{PA} (T_{mp}^A - T)$ [153]

$$\Delta S_A = \Delta S^A_{fus} - \Delta C_{PA}\,(\ln\frac{T^A_{mp}}{T}) = \frac{\Delta H^A_{fus}}{T^A_{mp}} - \Delta C_{PA}\,(\ln\frac{T^A_{mp}}{T}) \quad [153] \qquad \text{eqn D.3.4.a}$$

Now the first term of equation D.3.3 becomes

$$(\Delta H_A - T\Delta S_A) = \Delta H^A_{fus} - \Delta C_{PA}\left(T^A_{mp} - T\right) - T\,[\frac{\Delta H^A_{fus}}{T^A_{mp}} - \Delta C_{PA}\,(\ln\frac{T^A_{mp}}{T})]$$

$$= \left(1 - \frac{T}{T^A_{mp}}\right)\Delta H^A_{fus} + \Delta C_{PA}\,[T - T^A_{mp} - T\,\ln\frac{T}{T^A_{mp}}] \quad [153, 313] \quad \text{eqn D.3.4.b}$$

Here,

T^A_{mp} = melting temperature of component A,

ΔH^A_{fus} = heat of fusion of component A,

$\Delta S^A_{fus} = \frac{\Delta H^A_{fus}}{T^A_{mp}}$, entropy of fusion of component A,

ΔC_{PA}= difference between C_{PL} and C_{PS}, heat capacity of component A,

C_{PL}= heat capacity of liquid phase of component A

C_{PS}= heat capacity of solid phase of component A.

- ***1st part of term 2 and 3 of equation D.3.3:***

$A_{Liquid} \rightarrow A_{liquid\ Solution}$ reaction can be described as

$\Delta G = \overline{\Delta H^{A_L}_{mix}} - \overline{T\Delta S^{A_{LS}}_{mix}}$;

partial molar enthalpy of mixing is $\overline{\Delta H^{A_L}_{mix}}$ and partial molar entropy of mixing is $\overline{T\Delta S^{A_{LS}}_{mix}}$ of component A.

$A_{Solid\ solution} \rightarrow A_{Solid}$ reaction can be described as $\Delta G = \overline{\Delta H^{A_{SS}}_{mix}} - \overline{T\Delta S^{A_S}_{mix}}$; partial molar enthalpy of mixing is $\overline{\Delta H^{A_{SS}}_{mix}}$ and partial molar entropy of mixing is $\overline{T\Delta S^{A_S}_{mix}}$; of component A.

$A_{Solid\ solution} = A_{Liquid\ solution}$ reaction have $\Delta G = 0$ at equilibrium.

To obtain partial enthalpy of mixing of component A, can be determined from Gibbs – Duhem equation,

$$\Delta H_{mix}^{A} = \Delta Hmix + (1 - x_A)\frac{d\Delta Hmix}{dx_A} \qquad \text{[Gibbs-Duhem for component A]}$$

Now in Gibbs-Duhem equation ΔH_{mix}^{A} can be obtained taking derivative of $\Delta Hmix$ from Equation 6.6.2. $\Delta Hmix$ is expressed by Kleppa as a polynomial form as follow:

$$\Delta Hmix = x_A\,x_B\,(a + bx_A + cx_A\,x_B) = ax_A\,x_B + bx_A^2x_B + cx_A^2x_B^2 \quad \text{eqn D.3.5.A}$$

Derivation of equation D.3.5.A with respect dx_A and substituting the value for deriving $x_B = 1 - x_A$ gives following equation:

$$\frac{d\Delta Hmix}{dx_A} = ax_A\,\frac{dx_B}{dx_A} + ax_B + bx_A^2\frac{dx_B}{dx_A} + 2bx_A\,x_B + cx_A^2\frac{dx_B^2}{dx_A} + 2cx_A\,x_B^2$$

$$= ax_A\,\frac{d(1-x_A)}{dx_A} + ax_B + bx_A^2\frac{d(1-x_A)}{dx_A} + 2bx_A\,x_B + cx_A^2\frac{d(1-x_A)^2}{dx_A} + 2cx_A\,x_B^2$$

$$= ax_A\,(0 - 1) + ax_B + bx_A^2(0 - 1) + 2bx_A\,x_B + cx_A^2\frac{d}{dx_A}(1 - 2x_A + x_A^2) + 2cx_A\,x_B^2$$

$$= -ax_A + ax_B - bx_A^2 + 2bx_A\,x_B + cx_A^2(0 - 2 + 2x_A) + 2cx_A\,x_B^2$$

$$= -ax_A + ax_B - bx_A^2 + 2bx_A\,x_B + cx_A^2(-2)(1 - x_A) + 2cx_A\,x_B^2$$

$$= -ax_A + ax_B - bx_A^2 + 2bx_A\,x_B + -2cx_A^2(x_B) + 2cx_A\,x_B^2$$

$$= -ax_A + ax_B - bx_A^2 + 2bx_Ax_B - 2cx_A^2x_B + 2cx_Ax_B^2 \qquad \text{[313]} \quad \text{eqn D.3.5.A‘}$$

Now, putting the value of eqn D.3.5.A and eqn D.3.5.A‘ in Gibbs-Duhem relation for component A and simplify gives following equation,

$$\Delta H_{mix}^{A} = \Delta Hmix + (1 - x_A)\frac{d\Delta Hmix}{dx_A}$$

$$\Delta H_{mix}^{A} = ax_A\,x_B + bx_A^2x_B + cx_A^2x_B^2 + (1 - x_A) \quad [\quad -ax_A + ax_B - bx_A^2 + 2bx_Ax_B - 2cx_A^2x_B + 2cx_Ax_B^2\ ]$$

$$\Delta H_{mix}^{A} = ax_A\,x_B + bx_A^2x_B + cx_A^2x_B^2 + (x_B)\,[\,-ax_A + ax_B - bx_A^2 + 2bx_Ax_B - 2cx_A^2x_B + 2cx_Ax_B^2\ ]$$

$$\Delta H_{mix}^{A} = ax_A\, x_B + bx_A^2 x_B + cx_A^2 x_B^2 - ax_A\, x_B + ax_B^2 - bx_A^2 x_B + 2bx_A x_B^2 - 2cx_A^2 x_B^2 + 2cx_A x_B^3\ ]$$

$$\Delta H_{mix}^{A} = ax_B^2 + 2bx_A x_B^2 + 2cx_A x_B^3 - cx_A^2 x_B^2$$

Thus for solid and liquid phase for component A,

$$\Delta H_{mix}^{A_s} = a_s x_B^2 + 2b_s\, x_A x_B^2 + 2c_s x_A x_B^3 - c_s x_A^2 x_B^2$$

$$\Delta H_{mix}^{A_L} = a_l x_B^2 + 2b_l\, x_A x_B^2 + 2c_l x_A x_B^3 - c_l x_A^2 x_B^2$$ [313] eqn D.3.5.B

- ***2nd part of term 2 and 3 of equation D.3.3:***

The partial molar entropy of mixing in liquid and solid phases of component A can be expressed by assuming the mixture a regular solution:

$\Delta S_{mix}^{A_L} = -Rln\, x_A^l$ and $\Delta S_{mix}^{A_S} = -Rln\, x_A^s$ [313] eqn D.3.6

Here,

x_A^l = mole fraction of component A on the liquidus curve for liquid phase,

x_A^s= mole fraction of component A on the solidus curve for solid phase,

R= universal gas constant.

Putting the values from equations D.3.4.b, D.3.5.B and D.3.6 in equation D.3.3 in to 3 terms gives following expression:

$$\Delta G^A = \left(1 - \frac{T}{T_{mp}^A}\right) \Delta H_{fus}^A + \Delta C_{PA} \left[T - T_{mp}^A - T\, \ln \frac{T}{T_{mp}^A}\right] + RT\left(\ln x_A^l - \ln x_A^s\right) + (a_l x_B^2 + 2b_l\, x_A x_B^2 + 2c_l x_A x_B^3 - c_l x_A^2 x_B^2) - (a_s x_B^2 + 2b_s\, x_A x_B^2 + 2c_s x_A x_B^3 - c_s x_A^2 x_B^2)$$ [313]

eqn D.3.7

Similarly for component B Gibbs free energy can be calculated as follow:

$$\Delta G \equiv B_{SS} = B_{LS} = 0 = (\Delta H_B - T\Delta S_B) + (\overline{\Delta H^{B_L}_{mix}} - \overline{T\Delta S^{B_{LS}}_{mix}}) - (\overline{\Delta H^{B_{SS}}_{mix}} - \overline{T\Delta S^{B_S}_{mix}})$$

Term 1 Term 2 Term 3

[153] equation D.3.8

Now term 1 can be derived similarly for component B according to equation 6.6.4.b :

$$(\Delta H_B - T\Delta S_B) = \Delta H^B_{fus} - \Delta C_{PB}\left(T^B_{mp} - T\right) - T\left[\frac{\Delta H^B_{fus}}{T^B_{mp}} - \Delta C_{PB}\left(\ln\frac{T^B_{mp}}{T}\right)\right]$$

$$= \left(1 - \frac{T}{T^B_{mp}}\right)\Delta H^B_{fus} + \Delta C_{PB}\left[T - T^B_{mp} - T\ln\frac{T}{T^B_{mp}}\right] \quad [153, 313] \quad \text{eqn D.3.9. a}$$

Here,

T^B_{mp} = melting temperature of component B,

ΔH^B_{fus} = heat of fusion of component B,

$\Delta S^B_{fus} = \frac{\Delta H^B_{fus}}{T^B_{mp}}$, entropy of fusion of component B,

ΔC_{PB} = difference between C_{PL} and C_{PS}, heat capacity of component B.

T^B_{mp} = melting point of component B,

T = temperature at which the equation is being solved.

Now for partial molar enthalpy of mixing for component B,

$$\Delta H^B_{mix} = \Delta Hmix + (1 - x_B)\frac{d\Delta Hmix}{dx_B} \qquad \text{[Gibbs-Duhem for B]}$$

$$\Delta Hmix = x_A x_B\ (a + bx_A + cx_A x_B) = ax_A x_B + bx_A^2 x_B + cx_A^2 x_B^2 \quad \text{eqn D.3.9. b}$$

Derivation of eqn D.3.9.b with respect to dX_B and putting the value $x_A = 1 - x_B$ gives following equation:

$$\frac{d\Delta Hmix}{dx_B} = ax_B\frac{dx_A}{dx_B} + ax_A + bx_B\frac{dx_A^2}{dx_B} + bx_A^2 + cx_B^2\frac{dx_A^2}{dx_B} + 2cx_A^2 x_B$$

$$= ax_B\frac{d(1-x_B)}{dx_B} + ax_A + bx_B\frac{d(1-x_B)^2}{dx_B} + bx_A^2 + cx_B^2\frac{d(1-x_B)^2}{dx_B} + 2cx_A^2 x_B$$

$$= ax_B\,(0-1) + ax_A + bx_B\,\frac{d}{dx_B}(1-2x_B+x_B^2) + bx_A^2 + cx_B^2\,\frac{d}{dx_B}(1-2x_B+x_B^2) + 2cx_A^2x_B$$

$$= -ax_B + ax_A + bx_B\,(0-2+2x_B) + bx_A^2 + cx_B^2(0-2+2x_B) + 2cx_A^2x_B$$

$$= -ax_B + ax_A - 2bx_B\,(1-x_B) + bx_A^2 - 2cx_B^2(1-x_B) + 2cx_A^2x_B$$

$$= -ax_B + ax_A - 2bx_B\,(x_A) + bx_A^2 - 2cx_B^2(x_A) + 2cx_A^2x_B$$

$$= -ax_B + ax_A - 2bx_B\,x_A + bx_A^2 - 2cx_B^2x_A + 2cx_A^2x_B \qquad [313] \qquad \text{eqn D.3.9.c}$$

Now, putting the value of eqn D.3.9.b and eqn D.3.9.c in Gibbs-Duhem relation for component B and simplify gives the following equation,

$$\Delta H_{mix}^{B} = \Delta Hmix + (1-x_B)\frac{d\Delta Hmix}{dx_B}$$

$$= ax_A\,x_B + bx_A^2x_B + cx_A^2x_B^2 + (1-x_B)\;[\;-ax_B + ax_A - 2bx_B\,x_A + bx_A^2 - 2cx_B^2x_A + 2cx_A^2x_B\,]$$

$$= ax_A\,x_B + bx_A^2x_B + cx_A^2x_B^2 + (x_A)[-ax_B + ax_A - 2bx_B\,x_A + bx_A^2 - 2cx_B^2x_A + 2cx_A^2x_B\,]$$

$$= ax_A\,x_B + bx_A^2x_B + cx_A^2x_B^2 - ax_B\,x_A + ax_A^2 - 2bx_B\,x_A^2 + bx_A^3 - 2cx_B^2x_A^2 + 2cx_A^3x_B$$

$$\Delta H_{mix}^{B} = ax_A^2 + bx_A^3 - bx_A^2x_B - cx_A^2x_B^2 + 2cx_A^3x_B$$

Thus for solid and liquid phase,

$$\Delta H_{mix}^{B_s} = a_sx_A^2 + b_sx_A^3 - b_sx_A^2x_B - c_sx_A^2x_B^2 + 2c_sx_A^3x_B$$

$$\Delta H_{mix}^{B_L} = a_lx_A^2 + b_lx_A^3 - b_lx_A^2x_B - c_lx_A^2x_B^2 + 2c_lx_A^3x_B \qquad [313] \qquad \text{eqn D.3.9.d}$$

The partial molar entropy of mixing of B in liquid and solid phase are:

$$\Delta S_{mix}^{B_L} = -Rln\;x_B^l \quad \text{and} \quad \Delta S_{mix}^{B_S} = -Rln\;x_B^s \qquad [313] \qquad \text{eqn D.3.9.e}$$

Now putting the value from equations D.3.9.a, D.3.9.d and D.3.9.e in equation D.3.8 gives following expression:

$$\Delta G^{B} = \left(1-\frac{T}{T^{B}_{mp}}\right)\Delta H^{B}_{fus} + \Delta C_{PB}\left[T - T^{B}_{mp} - T\ \ln\frac{T}{T^{B}_{mp}}\right] + RT\left(\ln x^{l}_{B} - \ln x^{s}_{B}\right) + (a_l x_A^2 + b_l x_A^3 - b_l x_A^2 x_B - c_l x_A^2 x_B^2 + 2c_l x_A^3 x_B) - (a_s x_A^2 + b_s x_A^3 - b_s x_A^2 x_B - c_s x_A^2 x_B^2 + 2c_s x_A^3 x_B)$$

[313] eqn D.3.10

Two other equations in relation to the concentration of component A($NaNO_3$) and B(KNO_3) for each phase described in equations D.3.11 and D.3.12.

Components composition at liquid phase: $x^{l}_{A} + x^{l}_{B} = 1$ [313] eqn D.3.11

Components composition at solid phase: $x^{S}_{A} + x^{S}_{B} = 1$ [313] eqn D.3.12

$$\Delta G^{\frac{A}{NaNO\ 3}} = \left(1-\frac{T}{T^{A}_{mp}}\right)\Delta H^{A}_{fus} + \Delta C_{PA}\left[T - T^{A}_{mp} - T\ \ln\frac{T}{T^{A}_{mp}}\right] + RT\left(\ln x^{l}_{A} - \ln x^{s}_{A}\right) + (a_l x_B^2 + 2b_l\, x_A x_B^2 + 2c_l x_A x_B^3 - c_l x_A^2 x_B^2) - (a_s x_B^2 + 2b_s\, x_A x_B^2 + 2c_s x_A x_B^3 - c_s x_A^2 x_B^2)$$

eqn D.3.7

$$\Delta G^{\frac{B}{KNO\ 3}} = \left(1-\frac{T}{T^{B}_{mp}}\right)\Delta H^{B}_{fus} + \Delta C_{PB}\left[T - T^{B}_{mp} - T\ \ln\frac{T}{T^{B}_{mp}}\right] + RT\left(\ln x^{l}_{B} - \ln x^{s}_{B}\right) + (a_l x_A^2 + b_l x_A^3 - b_l x_A^2 X_B - c_l x_A^2 x_B^2 + 2c_l x_A^3 x_B) - (a_s x_A^2 + b_s x_A^3 - b_s x_A^2 x_B - c_s x_A^2 x_B^2 + 2c_s x_A^3 x_B)$$

eqn D.3.10

Once the unknown parameter x^{l}_{A}, x^{S}_{A}, X^{l}_{B}, x^{S}_{B} and T are known, then the four equations D.3.7, D.3.10, D.3.11, and D.3.12 can be solved simultaneously at each composition or each temperature then a binary phase diagram can be produced using mathematical packages such as Mat lab [313].

<u>For C-B salt system (C=$LiNO_3$, B=KNO_3):</u>

For Li-K//NO_3 salt, the derivation has been shown with similar calculation as previously obtained for A-B or Na-K//NO_3 system.

$$\Delta G^{C/LiNO_3} = \left(1 - \frac{T}{T_{mp}^{C}}\right) \Delta H_{fus}^{C} + \Delta C_{PC} \left[T - T_{mp}^{C} - T \ \ln \frac{T}{T_{mp}^{C}}\right] + RT \left(\ln x_C^l - \ln x_C^s\right) +$$
$$(a_l x_B^2 + 2b_l \, x_C x_B^2 + 2c_l x_C x_B^3 - c_l x_C^2 x_B^2) - (a_s x_B^2 + 2b_s \, x_C x_B^2 + 2c_s x_C x_B^3 - c_s x_C^2 x_B^2)$$
eqn D.3.13

$$\Delta G^{B/KNO_3} = \left(1 - \frac{T}{T_{mp}^{B}}\right) \Delta H_{fus}^{B} + \Delta C_{PB} \left[T - T_{mp}^{B} - T \ \ln \frac{T}{T_{mp}^{B}}\right] + RT \left(\ln x_B^l - \ln x_B^s\right) +$$
$$(a_l x_C^2 + b_l x_C^3 - b_l x_C^2 x_B - c_l x_C^2 x_B^2 + 2c_l x_C^3 x_B) - (a_s x_C^2 + b_s x_C^3 - b_s x_C^2 x_B - c_s x_C^2 x_B^2 +$$
$$2c_s x_C^3 x_B)$$
eqn D.3.14

Liquid phase: $x_C^l + x_B^l = 1$ eqn D.3.15

Solid phase: $x_C^S + x_B^S = 1$ eqn D.3.16

For C-A salt system (C=LiNO$_3$, A=NaNO$_3$):

For Li-Na//NO$_3$ salt, the derivation has been shown with similar calculation as previously obtained for A-B or Na-K//NO$_3$ system except the expression of enthalpy of mixing is shown in Equation 6.6.17a.

$$\Delta Hmix = x_A \, x_B \ (a + b x_A) = a x_A \, x_B + b x_A^2 x_B$$ eqn D.3.17. a

$$\Delta G^{C/LiNO_3} = \left(1 - \frac{T}{T_{mp}^{C}}\right) \Delta H_{fus}^{C} + \Delta C_{PC} \left[T - T_{mp}^{C} - T \ \ln \frac{T}{T_{mp}^{C}}\right] + RT \left(\ln x_C^l - \ln x_C^s\right) +$$
$$(a_l x_A^2 + 2b_l \, x_C x_A^2) - (a_s x_A^2 + 2b_s \, x_C x_A^2)$$ eqn D.3.17.b

$$\Delta G^{A/NaNO_3} = \left(1 - \frac{T}{T_{mp}^{A}}\right) \Delta H_{fus}^{A} + \Delta C_{PA} \left[T - T_{mp}^{A} - T \ \ln \frac{T}{T_{mp}^{A}}\right] + RT \left(\ln x_A^l - \ln x_A^s\right) +$$
$$(a_l x_C^2 + b_l x_C^3 - b_l x_C^2 x_A) - (a_s x_C^2 + b_s x_C^3 - b_s x_C^2 x_A)$$ eqn D.3.18

Liquid phase: $x_C^l + x_A^l = 1$ eqn D.3.19

Solid phase: $x_C^S + x_A^S = 1$ eqn D.3.20

D 3: TERNARY NITRATE SALT THERMODYNAMIC MODELING

The similar approach of Kramer [153] was used to formulate a ternary salt system. The Gibbs free energy of component A, B and C is assumed zero considering that both phases (liquid and solid) for each compound are in thermodynamic equilibrium [305] with each other. Kevin et. al [305] and Elliott [313] neglected the ternary interaction during formulation [305]. The detail calculation can be found in Elliott‘s work.

APPENDIX E: MATLAB ALGORITHMS AND HEAT CAPACITY VALUES

This section presents algorithms used in Binary phase modeling.

Contour plot

```
clear all
x=0.01:0.01:1;
y=0.01:0.01:1;
M_a = 84.9947;
M_b = 101.103;
Tmp_a=577.5;
Tmp_b=607.4;
Hfus_a=173*M_a;
Hfus_b=96.6*M_b;
Cp_a=-0.11*M_a;
Cp_b=-0.03*M_b;
al=-1707;
bl=-284.5;
cl=0;
as=6276;
bs=0;
cs=0;
R=8.314;
figure(1);
clf;
%hold on
for T=[450:5:610]
   clf;
[x_AS,x_AL] = meshgrid(x,y);
x_BL=1-x_AL;
x_BS=1-x_AS;
f1=((1-(T/Tmp_a))*Hfus_a) + (Cp_a*(T-Tmp_a-(T*log(T/Tmp_a))))...
    + (R*T*(log(x_AL)-log(x_AS)))+((al*((x_BL).^2))+(2*bl*x_AL.*((x_BL).^2))...
    + (2*cl*x_AL.*((x_BL).^3))-(cl*(x_AL.^2)*((x_BL).^2)))-
((as*((x_BS).^2))+(2*bs*x_AS.*((x_BS).^2))...
 + (2*cs*x_AS.*((x_BS).^3))-(cs*(x_AS.^2).*((x_BS).^2)));
  [c,h]=contour(x_AS,x_AL,f1,[0,0],'r');
  %clabel(c,h)
 hold on % one at a time
 f2=((1-(T/Tmp_b))*Hfus_b)+(Cp_b*(T-Tmp_b-(T*log(T/Tmp_b))))...
      + (R*T*(log((x_BL))-log((x_BS))))+((al*(x_AL.^2))+(bl*(x_AL.^3))-
(bl*(x_AL.^2).*(x_BL))...
       - (cl*(x_AL.^2).*((x_BL).^2))+(2*cl*(x_AL.^3).*(x_BL)))-
((as*(x_AS.^2))+(bs*(x_AS.^3))...
       - (bs*(x_AS.^2).*(x_BS))-(cs*(x_AS.^2).*((x_BS).^2))+(2*cs*(x_AS.^3).*(x_BS)));
```

```
  [c,h]=contour(x_AS,x_AL,f2,[0,0],'b');
  %clabel(c,h)
   % one at a time
      hold off;
      grid on;
      xlabel('x_A_s');
      ylabel('x_A_L');
      str = sprintf('T = %g K (%g ^oC)',T,T-273);
      text(0.01,0.99,str);
      pause;
end
hold off
%
clear all
x=0.01:0.01:1;
y=0.01:0.01:1;
M_a = 84.9947;
M_b = 101.103;
Tmp_a=577.5;
Tmp_b=607.4;
Hfus_a=173*M_a;
Hfus_b=96.6*M_b;
al=-1707;
bl=-284.5;
cl=0;
as=6276;
bs=0;
cs=0;
R=8.314;
Cp_Na=xlsread('Cp_values.xlsx',2,'B:B');
T_Na=xlsread('Cp_values.xlsx',2,'A:A');
Cp_K=xlsread('Cp_values.xlsx',2,'B:B');
T_K=xlsread('Cp_values.xlsx',2,'A:A');
figure(1);
clf;

T=335:5:650;
Cp_Na_T=interp1(T_Na,Cp_Na,T,'linear','extrap');
Cp_K_T=interp1(T_K,Cp_K,T,'linear','extrap');
ii=1;
for T=335:5:650
    clf;
[x_AS,x_AL] = meshgrid(x,y);
x_BL=1-x_AL;
x_BS=1-x_AS;
Cp_a=Cp_Na(ii);
```

```
Cp_b=Cp_K(ii);
f1=((1-(T/Tmp_a))*Hfus_a) + (Cp_a.*(T-Tmp_a-(T*log(T/Tmp_a))))...
    + (R*T*(log(x_AL)-log(x_AS)))+((al*((x_BL).^2))+(2*bl*x_AL.*((x_BL).^2))...
    + (2*cl*x_AL.*((x_BL).^3))-(cl*(x_AL.^2)*((x_BL).^2)))-
((as*((x_BS).^2))+(2*bs*x_AS.*((x_BS).^2))...
 + (2*cs*x_AS.*((x_BS).^3))-(cs*(x_AS.^2).*((x_BS).^2)));
  [c,h]=contour(x_AS,x_AL,f1,[0,0],'r');
  %clabel(c,h)
 hold on % one at a time
 f2=((1-(T/Tmp_b))*Hfus_b)+(Cp_b*(T-Tmp_b-(T*log(T/Tmp_b))))...
      + (R*T*(log((x_BL))-log((x_BS))))+((al*(x_AL.^2))+(bl*(x_AL.^3))-
(bl*(x_AL.^2).*(x_BL))...
       - (cl*(x_AL.^2).*((x_BL).^2))+(2*cl*(x_AL.^3).*(x_BL)))-
((as*(x_AS.^2))+(bs*(x_AS.^3))...
       - (bs*(x_AS.^2).*(x_BS))-(cs*(x_AS.^2).*((x_BS).^2))+(2*cs*(x_AS.^3).*(x_BS)));
  [c,h]=contour(x_AS,x_AL,f2,[0,0],'b');
  %clabel(c,h)
   % one at a time
       hold off;
       grid minor;
       set(gca,'Xtick',0.1:0.001:1.0);
       set(gca,'Ytick',0.1:0.001:1.0);
       xlabel('x_A_s (mol fraction of compoent A/NaNO_3 in the solid phase)');
       ylabel('x_A_L (mol fraction of component A/NaNO_3 in the liquid phase)');
          title(['Binary A:B system (Cp function of T) of' '\color NaNO_3
          (A)','\color:','\colorKNO_3 (B)']);
       legend('\Delta G_A=0','\Delta G_B=0','Location','southeast');
       str = sprintf('T = %g K (%g ^oC)',T,T-273);
       text(0.1,0.9,str);
       pause;
       ii=ii+1;
end
hold off
```

Phase plot

```
XAL = linspace(0.01,0.99,201);
ver = 0;
prm = NaKNO3();
figure(4),clf;
[xc1,Tc1,dG1] = BinSltContoursLrev(XAL,ver,prm);
PlotBinSlt3A(XAL,xc1,Tc1,1,'NaKNO_3');
figure(4),clf;
prm = LiKNO3();
[xc2,Tc2,dG2] = BinSltContoursLrev(XAL,ver,prm);
PlotBinSlt3A(XAL,xc2,Tc2,2,'LiKNO_3');
figure(4),clf;
```

```
prm = LiNaNO3();
[xc3,Tc3,dG3] = BinSltContoursLrev(XAL,ver,prm);
PlotBinSlt3A(XAL,xc3,Tc3,3,'LiNaNO_3');
```

Binary salt

```
function [xc,Tc,dG] = BinSltContoursLrev(XAL,ver,prm)
%
if nargin < 3;
    prm = NaKNO3();
end
if nargin < 2;
    ver = 0;
end
if (nargin< 1)||isempty(XAL);
    XAL = linspace(0.01,0.99,21);
end
N = length(XAL);
XAS = linspace(0,1,501);
T = linspace(300,700,501);
[x,y] = meshgrid(XAS,T);
xc = cell(1,N);
Tc = cell(1,N);
dG = cell(1,N);
for n = [1:N];
    F = DeltaG(x,XAL(n),y,prm,ver);
    DGA = F(:,(1:length(F)/2));
    CA = contourc(XAS,T,DGA,[0 0]);
    KA = length(CA);
    k = 1;
    txc = [];
    tTc = [];
    tdG = [];
    while (k < KA);
        dim1 = CA(2,k);
        xA = CA(1,k+1:k+dim1);
        yA = CA(2,k+1:k+dim1);
        k = k+dim1+1;
        if dim1 > 1;
            F1 = DeltaG(xA(1),XAL(n),yA(1),prm,ver);
            for m = (1:dim1-1);
                F2 = DeltaG(xA(m+1),XAL(n),yA(m+1),prm,ver);
                if ((F1(2) <= 0)&&(F2(2) > 0))||((F1(2) >= 0)&&(F2(2) < 0));
                    txc = [txc xA(m)];
                    tTc = [tTc yA(m)];
                    tdG = [tdG F1'];
                end
                F1 = F2;
```

```
            end
        end
    end
    xcn = txc;
    Tcn = tTc;
    dGn = tdG;
end

clf;
h = 0;
for n = (1:N);
    if ~isempty(xcn);
        plot(xcn,Tcn,'xb',XAL(n)*ones(size(Tcn)),Tcn,'or');
        if h == 0;
            hold on;
            h = 1;
        end
    end
end
axis([0 1 300 700]);
xlabel('x_A');
ylabel('T (K)');
hold off;
```

Delta G

```
function F = DeltaG(XAS,XAL,T,prm,ver)
if nargin < 5;
    ver = 1;
end
if nargin < 4;
    prm = NaKNO3();
end

XBS = 1 - XAS;
XBL = 1 - XAL;

if ver == 0;
    DGA = (1 - T/prm.T_mpa)*prm.H_fusa +prm.C_pa*(T - prm.T_mpa -
T.*log(T/prm.T_mpa)) + prm.R*T.*(log(XAL) - log(XAS)) + (prm.a_l*XBL.^2 +
2*prm.b_l*XAL.*XBL.^2 + prm.c_l*XAL.*XBL.^3 - prm.c_l*XAL.^2.*XBL.^2) -
(prm.a_s*XBS.^2 + 2*prm.b_s*XAS.*XBS.^2 + prm.c_s*XAS.*XBS.^3 -
prm.c_s*XAS.^2.*XBS.^2);
    DGB = (1 - T/prm.T_mpb)*prm.H_fusb +prm.C_pb*(T - prm.T_mpb -
T.*log(T/prm.T_mpb)) + prm.R*T.*(log(XBL) - log(XBS)) + (prm.a_l*XAL.^2 +
2*prm.b_l*XBL.*XAL.^2 + prm.c_l*XBL.*XAL.^3 - prm.c_l*XBL.^2.*XAL.^2) -
```

```
(prm.a_s*XAS.^2 + 2*prm.b_s*XBS.*XAS.^2 + prm.c_s*XBS.*XAS.^3 -
prm.c_s*XBS.^2.*XAS.^2);
else
   DGA = (1 - T/prm.T_mpa)*prm.H_fusa +prm.C_pa*(T - prm.T_mpa -
T.*log(T/prm.T_mpa)) + prm.R*T.*(log(XAL) - log(XAS)) + (prm.a_l*XBL.^2 +
2*prm.b_l*XAL.*XBL.^2 + prm.c_l*XAL.*XBL.^3 - prm.c_l*XAL.^2.*XBL.^2) -
(prm.a_s*XBS.^2 + 2*prm.b_s*XAS.*XBS.^2 + prm.c_s*XAS.*XBS.^3 -
prm.c_s*XAS.^2.*XBS.^2);
   DGB = (1 - T/prm.T_mpb)*prm.H_fusb +prm.C_pb*(T - prm.T_mpb -
T.*log(T/prm.T_mpb)) + prm.R*T.*(log(XBL) - log(XBS)) + (prm.a_l*XAL.^2 +
prm.b_l*(XAL.^3-XAL.^2.*XBL) + prm.c_l*XBL.*XAL.^3 - prm.c_l*XBL.^2.*XAL.^2)
- (prm.a_s*XAS.^2 + prm.b_s*(XAS.^3 - XBS.*XAS.^2) + prm.c_s*XBS.*XAS.^3 -
prm.c_s*XBS.^2.*XAS.^2);
end
F = [DGA DGB];
```

LiKNO3

```
function prm = LiKNO3()
prm.R=8.314;
prm.T_mpa=525.9;
prm.T_mpb=607.4;
prm.M_a = 68.946;
prm.M_b = 101.103;
prm.H_fusa=363*prm.M_a;
prm.H_fusb=96.6*prm.M_b;
prm.C_pa=0.25*prm.M_a;
prm.C_pb=-0.03*prm.M_b;
prm.a_l=-9183.9;
prm.b_l=-364;
prm.c_l=-1937.2;
prm.a_s=10460;
prm.b_s=4184;
prm.c_s=0;
```

LiNaNO3

```
function prm = LiNaNO3()
prm.R=8.314;
prm.T_mpa=525.9;
prm.T_mpb=577.5;
prm.M_a = 68.946;
prm.M_b = 84.9947;
prm.H_fusa=363*prm.M_a;
prm.H_fusb=173*prm.M_b;
prm.C_pa=0.25*prm.M_a;
```

```
prm.C_pb=-0.11*prm.M_b;
prm.a_l=-1941.4;
prm.b_l=-2928.8;
prm.c_l=0;
prm.a_s=9204.8;
prm.b_s=3347.2;
prm.c_s=0;
```

NaKNO3

```
function prm = NaKNO3()
prm.R=8.314;
prm.T_mpa=577.5;
prm.T_mpb=607.4;
prm.M_a = 84.9947;
prm.M_b = 101.103;
prm.H_fusa=173*prm.M_a;
prm.H_fusb=96.6*prm.M_b;
prm.C_pa=-0.11*prm.M_a;
prm.C_pb=-0.03*prm.M_b;
prm.a_l=-1707;
prm.b_l=-284.5;
prm.c_l=0;
prm.a_s=6276;
prm.b_s=0;
prm.c_s=0;
```

Plot binary salt

```
function [xl,xs,t] = PlotBinSlt3A(XAL,xc,Tc,fig,ttl)
if nargin < 5;
   ttl = [];
end
if nargin < 4;
   fig = 1;
end
xl = [];
xs = [];
t = [];
N = length(xc);
for n = (1:N);
   xs = [xs xcn];
   t = [t Tcn];
   xl = [xl XAL(n)*ones(size(xc{n}))];
end
[~,indx] = sort(xs);
figure(fig);
```

```
subplot(1,2,1);
plot3(xl(indx),xs(indx),t(indx),'r');
hold on;
plot3(xl(indx),xs(indx),300*ones(size(xl)),'b');
plot3(xl(indx),ones(size(xl)),t(indx),'b');
plot3(ones(size(xl)),xs(indx),t(indx),'b');
hold off
xlabel('X_A^l')
ylabel('X_A^s');
zlabel('T');
if ~isempty(ttl);
   title(ttl);
end
grid on
subplot(1,2,2);
plot(xl(indx),t(indx),'r',xs(indx),t(indx),'b');
legend('Liquidus','Solidus');
xlabel('X_A');
ylabel('T (K)');
axis([0 1 300 650]);
%%%%%% %%%%%% %%%%%%%% %%%%%%% %%%%%% %%%%%%% %%%%% %%%%%
```

Table E1: Heat capacities (C_p) from work of Takahashi et al. [324].

Temperature (K)	C_p of Na (J/mol.K)	Temperature (K)	C_p of K (J/mol.K)	Temperature (K)	C_p of Li (J/mol.K)
335	98.59385	335	98.06991	335	91.69818
340	99.4438	340	99.08094	340	92.38764
345	100.2937	345	100.092	345	93.76656
350	101.9936	350	101.103	350	94.45602
355	102.8436	355	102.114	355	95.14548
360	103.6935	360	102.114	360	95.83494
365	104.5435	365	104.1361	365	96.5244
370	105.3934	370	105.1471	370	97.21386
375	105.3934	375	104.1361	375	96.5244
380	107.9433	380	105.1471	380	97.21386
385	107.9433	385	107.1692	385	97.90332
390	108.7932	390	108.1802	390	97.90332
395	110.4931	395	109.1912	395	98.59278
400	111.3431	400	111.2133	400	99.9717
405	112.193	402.9	125.3	405	99.28224
410	113.8929	410	125.3677	410	100.6612
415	114.7428	415	124.3567	415	102.0401

420	116.4427	420	124.3567	420	103.419
425	115.5928	425	123.3457	425	104.7979
430	117.2927	430	123.3457	430	105.4874
435	118.9926	435	123.3457	435	106.1768
440	120.6925	440	124.3567	440	108.2452
445	121.5424	445	123.3457	445	107.5558
450	124.0923	450	124.3567	450	109.6241
455	125.7922	455	123.3457	455	108.9347
460	128.342	460	124.3567	460	109.6241
465	130.0419	465	125.3677	465	109.6241
470	132.5917	470	125.3677	470	111.0031
475	134.2916	475	125.3677	475	110.3136
480	137.6914	480	125.3677	480	112.382
485	141.0912	485	126.3788	485	113.0714
490	145.3409	490	126.3788	490	115.1398
495	147.0408	495	127.3898	495	113.7609
500	151.2906	500	127.3898	500	115.1398
505	155.5403	505	128.4008	505	116.5187
510	160.64	510	128.4008	510	117.8977
515	166.5896	515	128.4008	515	122.7239
520	174.2391	520	129.4118	525.9	139.9
525	181.8887	525	130.4229	535	139.9604
530	193.7879	530	130.4229	540	140.6498
535	208.237	535	131.4339	545	139.2709
540	238.8351	540	131.4339	550	140.6498
545	284.7322	545	132.4449	555	139.2709
550	164.0398	550	133.456	560	139.9604
555	145.3409	555	134.467	565	140.6498
560	141.0912	560	134.467	570	142.0288
565	139.3913	565	136.4891	575	142.0288
570	151.2906	570	136.4891	580	141.3393
577.5	141.9	575	137.5001	585	141.3393
585	141.9411	580	138.5111	590	142.0288
590	141.0912	585	140.5332	595	141.3393
595	141.9411	590	141.5442	600	143.4077
600	142.7911	595	142.5552	605	142.0288
605	141.9411	600	144.5773	610	142.0288
610	141.9411	607.4	141.5	615	141.3393
615	141.0912	615	141.5442	620	142.7182
620	142.7911	620	141.5442	625	146.1655
625	142.7911	625	140.5332	630	145.4761
630	141.9411	630	140.5332	635	144.7866

635	141.0912	635	139.5221	640	144.7866
640	141.0912	640	139.5221	645	144.7866
645	141.9411	645	140.5332	650	144.0971
650	141.9411	650	140.5332		
		655	140.5332		
		660	140.5332		
		665	139.5221		
		670	140.5332		
		675	139.5221		
		680	139.5221		
		685	140.5332		
		690	139.5221		
		695	139.5221		
		700	139.5221		
		705	139.5221		
		710	140.5332		
		715	140.5332		
		720	140.5332		
		725	140.5332		
		730	140.5332		

APPENDIX F: FACT SAGE6.4 CALCULATIONS

The three binary and the ternary nitrates were obtained using ―Phase diagram” module in calculation section of FactSage, as shown in Figures F1 and F2. Optimized pure thermodynamic database of inorganic systems was used for phase equilibrium calculation, as shown in Figure F3. ―Phase diagram” module used, the compound and solution databases and after optimization, the phase equilibrium diagrams are presented by ―Figure” module. After opening component sub window the compound names were provided as a chemical formula, and then, the compound-solution databases _FTsalt-SALTE‘, _FTsalt-NKNA‘ were selected from databases sub window (containing 20 cations and 8 anions). Then products type were selected. Then in dropdown menu, the immiscibility option were chosen. Next, in the variable box window, type of graph (binary and Gibbs triangle), pressure-composition-temperature has been chosen. After pressing calculate icon, the _Figure‘ module generated the optimized equilibrium diagrams, as shown in Chapter 5 of this thesis. The equilibrium calculation of ternary eutectic is provided in Table F1.

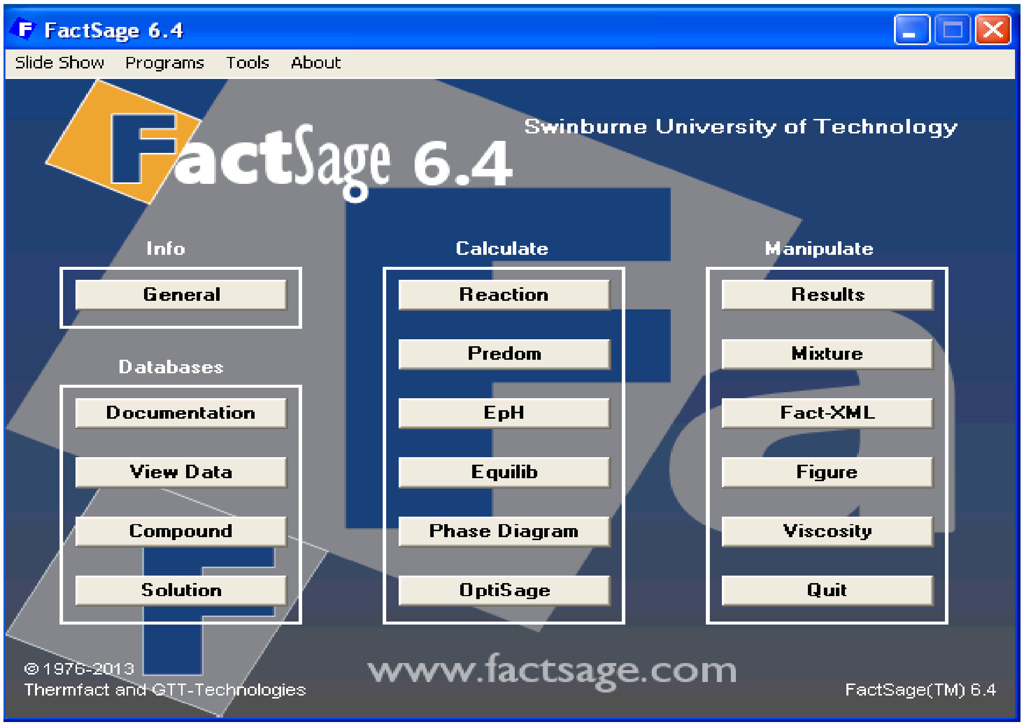

Figure F1: A snapshot of FactSage 6.4 various modules operation window.

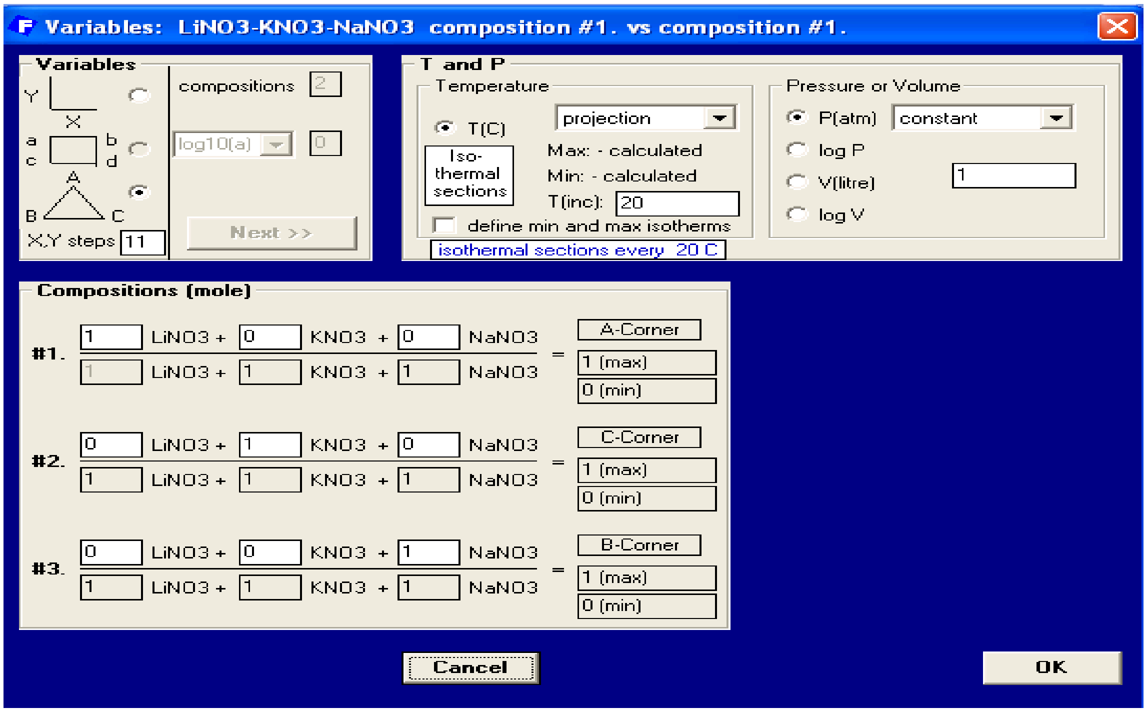

Variables: LiNO3-KNO3-NaNO3 composition #1. vs composition #1.

Variables
○ Y X
○ a b c d
● A B C
compositions 2
log10(a) 0
X,Y steps 11

T and P
Temperature
● T(C) projection
Iso-thermal sections
Max: - calculated
Min: - calculated
T(inc): 20
☐ define min and max isotherms
isothermal sections every 20 C

Pressure or Volume
● P(atm) constant
○ log P
○ V(litre) 1
○ log V

Compositions (mole)

#1.	1 LiNO3 + 0 KNO3 + 0 NaNO3	=	A-Corner	
	1 LiNO3 + 1 KNO3 + 1 NaNO3		1 (max)	0 (min)
#2.	0 LiNO3 + 1 KNO3 + 0 NaNO3	=	C-Corner	
	1 LiNO3 + 1 KNO3 + 1 NaNO3		1 (max)	0 (min)
#3.	0 LiNO3 + 0 KNO3 + 1 NaNO3	=	B-Corner	
	1 LiNO3 + 1 KNO3 + 1 NaNO3		1 (max)	0 (min)

Figure F2: A snapshot of variable sub window.

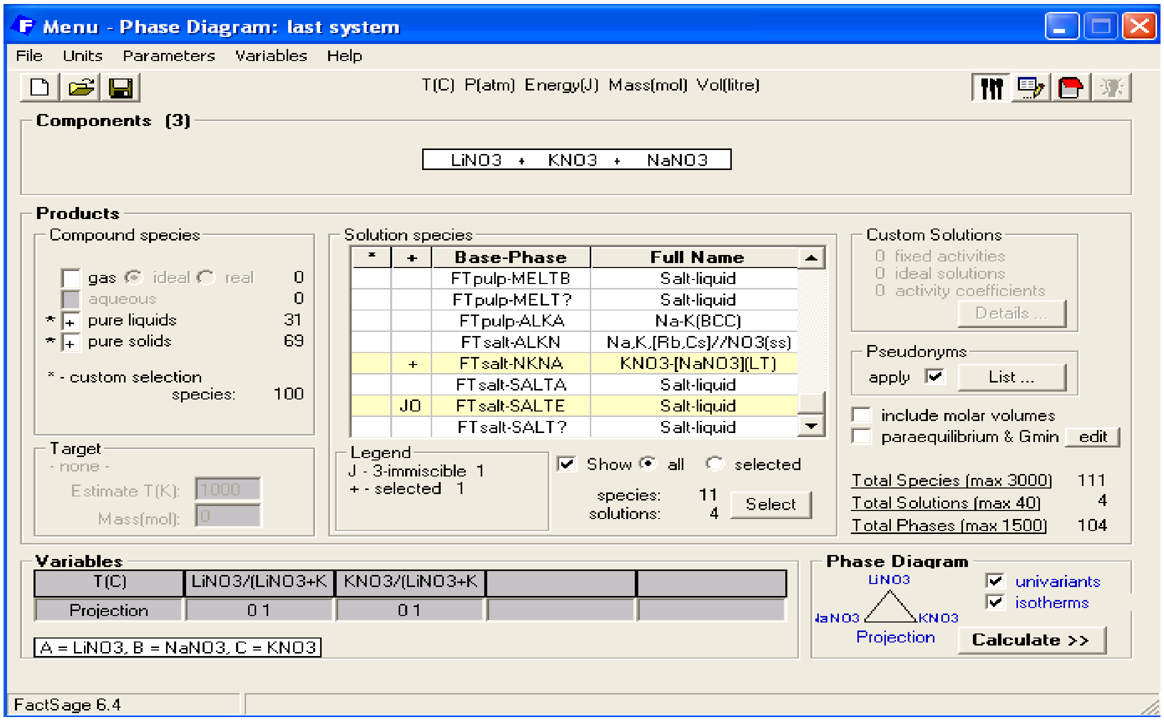

Menu - Phase Diagram: last system

T(C) P(atm) Energy(J) Mass(mol) Vol(litre)

Components (3)

LiNO3 + KNO3 + NaNO3

Products

Compound species
☐ gas ● ideal ○ real 0
☐ aqueous 0
* ☐+ pure liquids 31
* ☐+ pure solids 69
* - custom selection
species: 100

Target
- none -
Estimate T(K): 1000
Mass(mol): 0

Solution species

*	+	Base-Phase	Full Name
		FTpulp-MELTB	Salt-liquid
		FTpulp-MELT?	Salt-liquid
		FTpulp-ALKA	Na-K(BCC)
		FTsalt-ALKN	Na,K,[Rb,Cs]//NO3(ss)
	+	FTsalt-NKNA	KNO3-[NaNO3](LT)
		FTsalt-SALTA	Salt-liquid
	J0	FTsalt-SALTE	Salt-liquid
		FTsalt-SALT?	Salt-liquid

Legend
J - 3-immiscible 1
+ - selected 1

☑ Show ● all ○ selected
species: 11
solutions: 4

Custom Solutions
0 fixed activities
0 ideal solutions
0 activity coefficients

Pseudonyms
apply ☑

☐ include molar volumes
☐ paraequilibrium & Gmin

Total Species (max 3000) 111
Total Solutions (max 40) 4
Total Phases (max 1500) 104

Variables

T(C)	LiNO3/(LiNO3+K	KNO3/(LiNO3+K		
Projection	0 1	0 1		

A = LiNO3, B = NaNO3, C = KNO3

Phase Diagram
LiNO3
NaNO3 KNO3
Projection
☑ univariants
☑ isotherms

FactSage 6.4

Figure F3: A snapshot of ―phase module” ready for calculation.

Table F1: Ternary eutectic point calculation.

From FactSage 6.4

```
LiNO3/(LiNO3+NaNO3+KNO3) (mol/mol)  = 0.3732,  NaNO3/(LiNO3+NaNO3+KNO3)
(mol/mol)  = 0.1352
=================================================================
TL(K) =  773.15,  PL(bar) =   1.0132500
  LiNO3 +  NaNO3 +  KNO3 =
        (120.98 C, 1 atm,     a=1.0000)
        ( 0.37320        LiNO3
        + 0.13518        NaNO3
        + 0.49162        KNO3)
        Site fraction of sublattice constituents:
        Li                  0.37320
        Na                  0.13518
        K                   0.49162
        ----------------------------------
        NO3                   1.0000
        System component       Mole fraction  Mass fraction
        LiNO3_liquid(liq)      0.37320       0.29602
        NaNO3_liquid(liq)      0.13518       0.13218
        KNO3_liquid(liq)       0.49162       0.57181
 Cut-off limit for phase activities = 1.00E-70
 Data on 1 product species identified with "T" have been extrapolated
 ****************************************************************
     H          G           V          S          Cp
    (J)        (J)       (litre)     (J/K)       (J/K)
 ****************************************************************
 -4.58282E+05 -5.32203E+05  0.00000E+00  1.87558E+02  9.98381E+01
 Total mass/gram = 86.924
*T = 120.98 C, P = 1 atm, V = 0 dm3
 ********************************************************************
    Cp                  H                  S                  G                  V
   J.K-1                J                J.K-1                J                 dm3
 ********************************************************************
  9.98381E+01  -4.58282E+05   1.87558E+02  -5.32203E+05   0.00000E+00
 Site fraction of sublattice constituents in Salt-liquid#1:
 Li                  0.37320    Stoichiometry calculated
 Na                  0.13518
 K                   0.49162
 -----------------------------------------------------------
 NO3                   1.0000     Stoichiometry calculated

Cut-off limit for phase activities = 1.00E-70
Data Search options: exclude gas ions; organic CxHy.. X(max) = 2; min soln cpts = 2
```

The calculation procedure of FactSage module is similar to CalPhad method [315]. Where chemical thermodynamic of systems stored in compound and solution databases are coupled with known experimental data to generate equilibrium phase diagrams. The "Phase diagram" module is used for phases calculation (using a set of Gibbs energy parameters) and "Figures" module is used for plotting the phases [315]. An iterative algorithm is used for, continuously compare the generated results between 'known experimental data' and 'optimized thermodynamic data' for a given system (such as: $NaNO_3$-KNO_3 binary system). The calculation and optimization of the phase diagram are performed by 'phase diagram mapping' suggested by Hillert [461, 462]. Phase diagram mapping is performed by using the zero phase fraction (ZPF) line principle [463-465]. After units, constants, components and axes are defined (Gibbs-Duhem equation is used to interrelate variables), then the calculated phase appears on one side of ZPF lines. Depending upon the direction the phase either appears or disappears when crossing the ZPF lines. ZPF lines allow phase mapping without the need for a 'starting points' for phase calculation (no need to define initial estimates).

APPENDIX G: SAMPLE MIXING CALCULATION

Calculation for salt mixing: the required amount of binary and ternary from single $NaNO_3$ (g), KNO_3 (g) and $LiNO_3$ (g) are as follow:

Molecular / mole weight of $NaNO_3$,

M_{NaNO_3}: 22.989770 + 14.0067 + 15.9994 X 3 = 84.99467 g/mol

Molecular weight calculation for KNO_3,

M_{KNO_3}: 39.0983+ 14.0067 + 15.9994 X 3 = 101.1032 g/mol

Molecular weight calculation for $LiNO_3$,

M_{LiNO_3}: 6.9411+ 14.0067 + 15.9994 X 3 = 68.946 g/mol

Here,

Atomic mass of Sodium, Na = 22.989770

Atomic mass of Nitrogen, N = 14.0067

Atomic mass of Oxygen, O = 15.9994

Atomic mass of Potassium, K = 39.0983

Atomic mass of Nitrogen, Li = 6.9411

Molecular weight of Sodium, M_{Na^+} = 22.989769 g/mol

Molecular weight of Potassium, M_{K^+} = 39.0983 g/mol

Molecular weight of Potassium, M_{Li^+} = 6.9411 g/mol

Now mole fraction of Sodium nitrate in 60:40 weight composition, $x_{NaNO_3} = \frac{w_{NaNO_3}/M_{NaNO_3}}{w_{NaNO_3}/M_{NaNO_3}+w_{KNO_3}/M_{KNO_3}}$

$$= \frac{0.6 / 84.9947}{0.6 / 84.9947+0.4 / 101.1032}$$

$$= \frac{0.007059263695}{0.007059263695 + 0.003956353508}$$

$$= \frac{0.007059263695}{0.011015617}$$

= 0.640841425

Now mole fraction of potassium nitrate in 60:40 composition, x_{KNO_3} = $\frac{w_{KNO\ 3}/\ M_{KNO\ 3}}{w_{NaNO\ 3}/M_{NaNO\ 3}+w_{KNO\ 3}/M_{KNO\ 3}}$

$= \frac{0.4\ /\ 101.1032}{0.6\ /\ 84.9947+0.4\ /\ 101.1032}$

$= \frac{0.003956353508}{0.007059263695\ +0.003956353508}$

$= \frac{0.003956353508}{0.011015617}$

= 0.359158593

Here,

$w_{NaNO\ 3}$ = weight precent of $NaNO_3$ = 60%= 0.60

$w_{KNO\ 3}$ = weight precent of KNO_3 = 40%= 0.40

M_{NaNO_3}= molecular weight of $NaNO_3$ = 84.99467 g/mol, previously calculated

M_{KNO_3} = molecular weight of KNO_3 = 101.1032 g/mol, previously calculated

M_{LiNO_3} = molecular weight of $LiNO_3$ = 68.946 g/mol, previously calculated

M_{Na^+} = Molecular weight of Sodium = 22.989769 g/mol

M_{K^+} = Molecular weight of Potassium = 39.0983 g/mol

To obtain 5 g of Sodium nitrate and Potassium nitrate binary mixture,

We need (5 x 0.60) g or 3 gm of Sodium nitrate and (5 x 0.40) g or 2.0 g of Potassium nitrate,

Here,

3 g of $NaNO_3$ contains (3 X $\frac{1\ X\ 22.98977}{84.99467}$) g of Sodium or 0.8114545 g of Sodium

2 g of KNO_3 contains (2 X $\frac{1\ X\ 39.0983}{101.1032}$) g of Potassium or 0.7666734 g of Potassium

Now mass fraction of Sodium nitrate in Na:K:Li= 0.13529: 0.49119: 0.37352 mole ratio (obtain from FACTSAGE [39]),

w_{NaNO_3}

$= \frac{x_{NaNO\ 3}\mathrm{X}\ M_{NaNO\ 3}}{x_{NaNO\ 3}\mathrm{X}\ M_{NaNO\ 3}+x_{KNO\ 3}\mathrm{X}\ M_{KNO\ 3}+x_{LiNO\ 3}\mathrm{X}\ M_{LiNO\ 3}}$

$= \frac{0.13529\ \ X\ \ 84.9947}{0.13529\ \ X\ 84.9947+0.49119\ X\ 101.1032\ +0.37352\ X\ 68.946}$

$$= \frac{11.49893296}{11.49893296 + 49.66088081 + 25.75270992}$$

$$= \frac{11.49893296}{86.912523691}$$

= 0.13230467227 or 13.2304 wt%

Now mass fraction of Potassium nitrate in Na:K:Li= 0.13529: 0.49119: 0.37352 mole ratio,

w_{KNO_3}

$$= \frac{x_{KNO\ 3} \text{X}\ M_{KNO\ 3}}{x_{NaNO\ 3} \text{X}\ M_{NaNO\ 3} + x_{KNO\ 3} \text{X}\ M_{KNO\ 3} + x_{LiNO\ 3} \text{X}\ M_{LiNO\ 3}}$$

$$= \frac{0.49119 \text{ X } 101.1032}{0.13529 \text{ X } 84.9947 + 0.49119 \text{ X } 101.1032 + 0.37352 \text{ X } 68.946}$$

$$= \frac{49.66088081}{11.49893296 + 49.66088081 + 25.75270992}$$

$$= \frac{49.66088081}{86.912523691}$$

= 0.57138923942 or 57.1389 wt%

Now mass fraction of Lithium nitrate in Na:K:Li= 0.13529: 0.49119: 0.37352 mole ratio,

w_{LiNO_3}

$$= \frac{x_{LiNO\ 3} \text{X}\ M_{LiNO\ 3}}{x_{NaNO\ 3} \text{X}\ M_{NaNO\ 3} + x_{KNO\ 3} \text{X}\ M_{KNO\ 3} + x_{LiNO\ 3} \text{X}\ M_{LiNO\ 3}}$$

$$= \frac{0.37352 \text{ X } 68.946}{0.13529 \text{ X } 84.9947 + 0.49119 \text{ X } 101.1032 + 0.37352 \text{ X } 68.946}$$

$$= \frac{25.75270992}{11.49893296 + 49.66088081 + 25.75270992}$$

$$= \frac{25.75270992}{86.912523691}$$

= 0.29630608831 or 29.6306 wt%

To obtain 100 gm of Sodium nitrate, Potassium nitrate and Lithium nitrate ternary mixture in 13.2304: 57.1389: 29.6306 weight ratio,

The stoichiometric amounts of 100 g Ternary reactants are,

(100 x 13.2304) g or 13.2304g of Sodium nitrate,

(100 x 57.1389) g or 57.139 g of Potassium nitrate,

(100 x 29.6306) g or 29.6306 g of Lithium nitrate,

Now mole fraction of Sodium nitrate in Na:K:Li= 13.2304: 57.1389: 29.6306 weight ratio, x_{NaNO_3}

$$= \frac{w_{NaNO_3}/M_{NaNO_3}}{w_{NaNO_3}/M_{NaNO_3}+w_{KNO_3}/M_{KNO_3}+w_{LiNO_3}/M_{LiNO_3}}$$

$$= \frac{0.13529/84.9947}{0.13529/84.9947+0.49119/101.1032+0.37352/68.946}$$

$$= \frac{0.002354264442}{0.002354264442+0.00534800085+0.003759463928}$$

$$= \frac{0.002354264442}{0.011461729}$$

= 0.13529

Now mole fraction of Potassium nitrate in Na:K:Li= 20.01: 54.07: 25.92 weight ratio, x_{KNO_3}

$$= \frac{w_{KNO_3}/M_{KNO_3}}{w_{NaNO_3}/M_{NaNO_3}+w_{KNO_3}/M_{KNO_3}+w_{LiNO_3}/M_{LiNO_3}}$$

$$= \frac{0.49119/101.1032}{0.13529/84.9947+0.49119/101.1032+0.37352/68.946}$$

$$= \frac{0.00534800085}{0.002354264442+0.00534800085+0.003759463928}$$

$$= \frac{0.00534800085}{0.011461729}$$

= 0.49119

Now mole fraction of Lithium nitrate in Na:K:Li= 20.01: 54.07: 25.92 weight ratio, x_{LiNO_3}

$$= \frac{w_{LiNO_3}/M_{LiNO_3}}{w_{NaNO_3}/M_{NaNO_3}+w_{KNO_3}/M_{KNO_3}+w_{LiNO_3}/M_{LiNO_3}}$$

$$= \frac{0.37352/68.946}{0.13529/84.9947+0.49119/101.1032+0.37352/68.946}$$

$$= \frac{0.003759463928}{0.002354264442+0.00534800085+0.003759463928}$$

$$= \frac{0.003759463928}{0.011461729}$$

= 0.37352

APPENDIX H: STA CALIBRATION PROCEDURE

This section describes calibration procedure of STA. Setaram supplied an ASTM (American Society of the International Association for Testing and Materials) kit contained minimum 4N purity (99.99%) of four CRMs (certified reference materials): Indium, Lead, Aluminium and Gold. These pure crystalline CRMs have known standard enthalpies, non-hygroscopic, and didn‘t react with crucible (alumina) materials. They were calibrated to obtain temperature correction and heat sensitivity correction coefficients of STA to cover the temperature range from 150 to 1100°C. In, Pb and Al were supplied for low temperature range calibration (ranging from 157 to 660°C), and Au was provided for high temperature range calibration (660 to 1100°C). For indium and lead particular attention (weighing before and after the test) was given to observe any possible oxide formation during/after melting.

Calibration correction test were performed with same batch crucibles of same type (Setaram alumina); at inert sweep gas and velocity (argon 23ml/min); at three scanning rates (5,10 and 15°C/min) and heating temperatures (165°C for In, 335°C for Pb, 670°C for Al and 1075°C for Au). Lower sweep gas velocity was maintained throughout the experiment in order to avoid buoyancy and smearing in HF curves. The temperature was ramped until 30°C before CRMs melting points, and then the heating was resumed at desired scanning rates to obtain endothermic transformation HF peaks.

At the beginning of the calibration test, three sets of Indium sample were heated at three scanning rates to observe any change in fusion temperatures to understand STA furnace block and sample thermocouple‘s thermal behavior. There was minor change in melting temperature (standard melting point= 156.6°C and measured Avg. 157.4°C), and the results were fairly reproducible (±0.5°C). Then using the same approach and experimental conditions all 4 CRMs were calibrated using fresh samples at three scanning rates and coefficients were obtained against STD ASTM values. Table H1 is showing calculated results for STA transducer calibration. Calisto data processing software calculated the coefficients after manual inputs of CRMs properties.

Table H1: Certified reference materials used for Temperature and energy calibration [337-343].

CRM sample	ASTM standard melting points (°C)	ASTM latent heat of fusions (J/g)	Uncertainty calculation			
			Temperature (°C/ K)	Energy (J/g)	Calculated Temperature (°C)	Calculated energy (J/g)
Indium (In)	156.5985	28.51	±0.046	±0.19	±4.9	±3.02*
Lead (Pb)	327.47	23.00	±0.020	±0.06		
Aluminium (Al)	660.33	401.30	±0.050	±1.6		
Gold (Au)	1064.18	64.50	-	-		
- indicating no. *calculated noise level was ±6.7 mK						

H 2: TEMPERATURE COEFFICIENT CORRECTION AT 3 SCANNING RATES

The sample thermocouple was placed close to the sample crucible to measure temperature change compared to reference crucible. In actual practice the measured temperature of the sample is different (lag behind due to improper thermal response and unpredicted thermal gradient) than the actual temperature of the sample. Hence temperature correction calibration was performed using _temperature correction‘ module in Calisto data acquisition software to adjust and compensate temperature variation. A temperature correction module is shown in Figure H.2.1.

To observe correction on measured temperature, the coefficients of corrected polynomial were calculated according to ISO (International Organization for Standardization) and ASTM guideline. The temperature correction polynomial is expressed as thermocouple time constant and heating rate,

$$\Delta T = B_o + B_1 * T + B_2 * R \qquad [332] \qquad \text{eqn H.2.1}$$

Here,

ΔT =Temperature correction term in °C.

B =Coefficients determined in calibration test.

T =Temperature in °C.

R =Programmed heating rate in K/min.

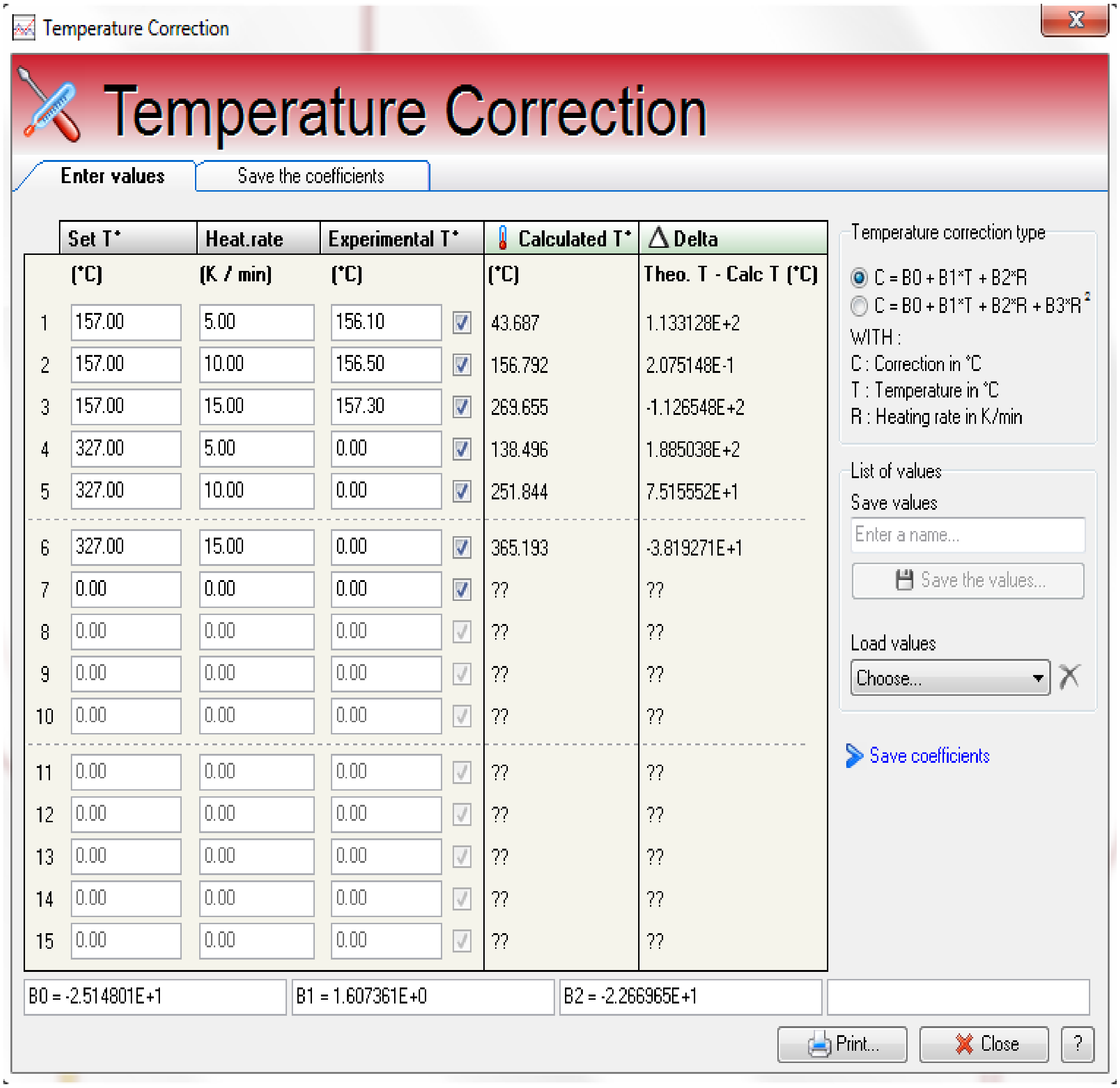

	Set T° (°C)	Heat.rate (K / min)	Experimental T° (°C)		Calculated T° (°C)	Delta Theo. T - Calc T (°C)
1	157.00	5.00	156.10	☑	43.687	1.133128E+2
2	157.00	10.00	156.50	☑	156.792	2.075148E-1
3	157.00	15.00	157.30	☑	269.655	-1.126548E+2
4	327.00	5.00	0.00	☑	138.496	1.885038E+2
5	327.00	10.00	0.00	☑	251.844	7.515552E+1
6	327.00	15.00	0.00	☑	365.193	-3.819271E+1
7	0.00	0.00	0.00	☑	??	??
8	0.00	0.00	0.00	☑	??	??
9	0.00	0.00	0.00	☑	??	??
10	0.00	0.00	0.00	☑	??	??
11	0.00	0.00	0.00	☑	??	??
12	0.00	0.00	0.00	☑	??	??
13	0.00	0.00	0.00	☑	??	??
14	0.00	0.00	0.00	☑	??	??
15	0.00	0.00	0.00	☑	??	??

Temperature correction type

● $C = B0 + B1*T + B2*R$

○ $C = B0 + B1*T + B2*R + B3*R^2$

WITH :

C : Correction in °C

T : Temperature in °C

R : Heating rate in K/min

B0 = -2.514801E+1

B1 = 1.607361E+0

B2 = -2.266965E+1

Figure H.2.1: Temperature correction module in Calisto data processing software.

Built-in least square regression of Calisto program calculated the B_o, B_1 and B_2 values as per following equations:

$$B_o = \frac{\sum dT_i\{(\sum T_{eim}{}^{2})(\sum V_i^2)-(\sum(T_{eim} \cdot V_i)^2\}-\big\{(\sum T_{eim} \cdot dT_i)\big((\sum T_{eim})(\sum V_i^2)-(\sum T_{eim} \cdot V_i)(\sum V_i)\big)\big\}+\{(\sum V_i \cdot dT_i)\big((\sum T_{eim})(\sum T_{eim} \cdot V_i)-(\sum T_{eim}{}^{2})(\sum V_i)\big)\}}{N\{\big((\sum T_{eim}{}^{2})(\sum V_i^2)-(\sum(T_{eim} \cdot V_i)^2\big)\}-\{(\sum T_{eim})^2(\sum V_i^2)\}+2\{(\sum T_{eim})(\sum V_i)(\sum T_{eim} \cdot V_i)\}-\{(\sum T_{eim}{}^{2})(\sum V_i)^2\}}$$

$$B_1 = \frac{N\{((\sum T_{eim} \cdot dT_i)(\sum V_i{}^{2})-(\sum V_i \cdot dT_i)(\sum T_{eim} \cdot V_i))\}-\{(\sum T_{eim})((\sum dT_i)(\sum V_i{}^{2})-(\sum V_i)(\sum V_i \cdot dT_i))\}+\{(\sum V_i)((\sum dT_i)(\sum T_{eim} \cdot V_i)-(\sum T_{eim} \cdot dT_i)(\sum V_i))\}}{N\{\big((\sum T_{eim}{}^{2})(\sum V_i^2)-(\sum(T_{eim} \cdot V_i)^2\big)\}-\{(\sum T_{eim})^2(\sum V_i^2)\}+2\{(\sum T_{eim})(\sum V_i)(\sum T_{eim} \cdot V_i)\}-\{(\sum T_{eim}{}^{2})(\sum V_i)^2\}}$$

$$B_2 = \frac{N\{((\sum T_{eim}{}^{2})(\sum V_i \cdot dT_i)-(\sum T_{eim} \cdot dT_i)(\sum T_{eim} \cdot V_i))\}-\{(\sum T_{eim})((\sum T_{eim})(\sum V_i \cdot dT_i)-(\sum T_{eim} \cdot V_i)(\sum dT_i))\}+\{(\sum V_i)((\sum T_{eim})(\sum V_i \cdot dT_i)-(\sum T_{eim}{}^{2})(\sum dT_i))\}}{N\{\big((\sum T_{eim}{}^{2})(\sum V_i^2)-(\sum(T_{eim} \cdot V_i)^2\big)\}-\{(\sum T_{eim})^2(\sum V_i^2)\}+2\{(\sum T_{eim})(\sum V_i)(\sum T_{eim} \cdot V_i)\}-\{(\sum T_{eim}{}^{2})(\sum V_i)^2\}}$$

[332] eqn H.2.2

Here,

N =Number of calibration tests for sample i

V_i =Scanning temperature rates [for sample i= 5, 10 and 15 (unit: °C/min)]

T_{eim} =CRM‘s extrapolated initial onset melting temperatures (measured from endothermic transformation of fusion peak).

T_{fi} =CRM‘s real melting temperatures.

dT_i =Temperature correction= $T_{eim} - T_{fi}$

Once the values of T_{eim} and T_{fi} were obtained from CRM‘s calibration at three scanning rates ($V_i = 5$, 10 and 15°C/min), then the straight line variation or correcting relation dT_i was determined using coefficients $B_o(= 4.603564E - 1)$, $B_1(= -1.913443E - 3)$ and $B_2(= -1.3247799E - 1)$, is shown as follow:

$dT_i = B_o + B_1 T_{eim} + B_2 V_i$ [332] eqn H.2.3

The obtained temperature correction was used for any given heating temperature and ramping rates in this study.

H 3: HEAT FLOW SENSITIVITY COEFFICIENT CORRECTION AT 3 SCANNING RATES

In STA furnace electrical signals in microvolts are converted to thermal power in milliwatts using transducer calibration method, given by the following equation:

S=K.P [332]

Here,
S=electrical signal (μV),
K=calibration coefficient. K values vary when parameters vary, such as: sample mass and shape; test temperature; crucible type; sweep gas type and velocity; and transducer type,
P=thermal power (μ).

Once the heat of melting peak obtained, then the peak area was integrated into Calisto software. Then the built-in function, integrated the peak area (straight or trapezoidal baseline method) from initial melting onset to final melting onset temperatures and expressed as microvolts time second per milligram ($\mu V.s/mg$). Using the ‗regression‘ module of Calisto software, the sensitivity coefficients were calculated, as shown in Figure H.3.1. Sensitivity is the ratio of peak area by melting enthalpy of CRMs obtained from equation H.3.1.

$$Sensitivity, K = \frac{Area\ of\ fusion\ peak}{Enthalpy\ of\ fusion}$$

$$= \frac{\frac{\mu V\ .\ s}{mg}}{\frac{J}{g}} = \frac{mV.\ s}{J} = \frac{mV.\ s}{W.\ s} = \frac{\mu V}{mW} \qquad [332] \qquad \text{eqn H.3.1}$$

For any given area A ($\mu V.s$) with transformation heat Q (J) is expressed as:

$$Q = \frac{A}{K} \qquad [332] \qquad \text{eqn H.3.2}$$

After calibration test, the K value is plotted against temperature as per equation H.3.3.

$$\frac{y}{\mu V\,.mW^{-1}} = \sum_{i=0}^{4} i \quad A \left(\frac{x}{°C}\right)^{i} \qquad [332] \qquad \text{eqn H.3.3}$$

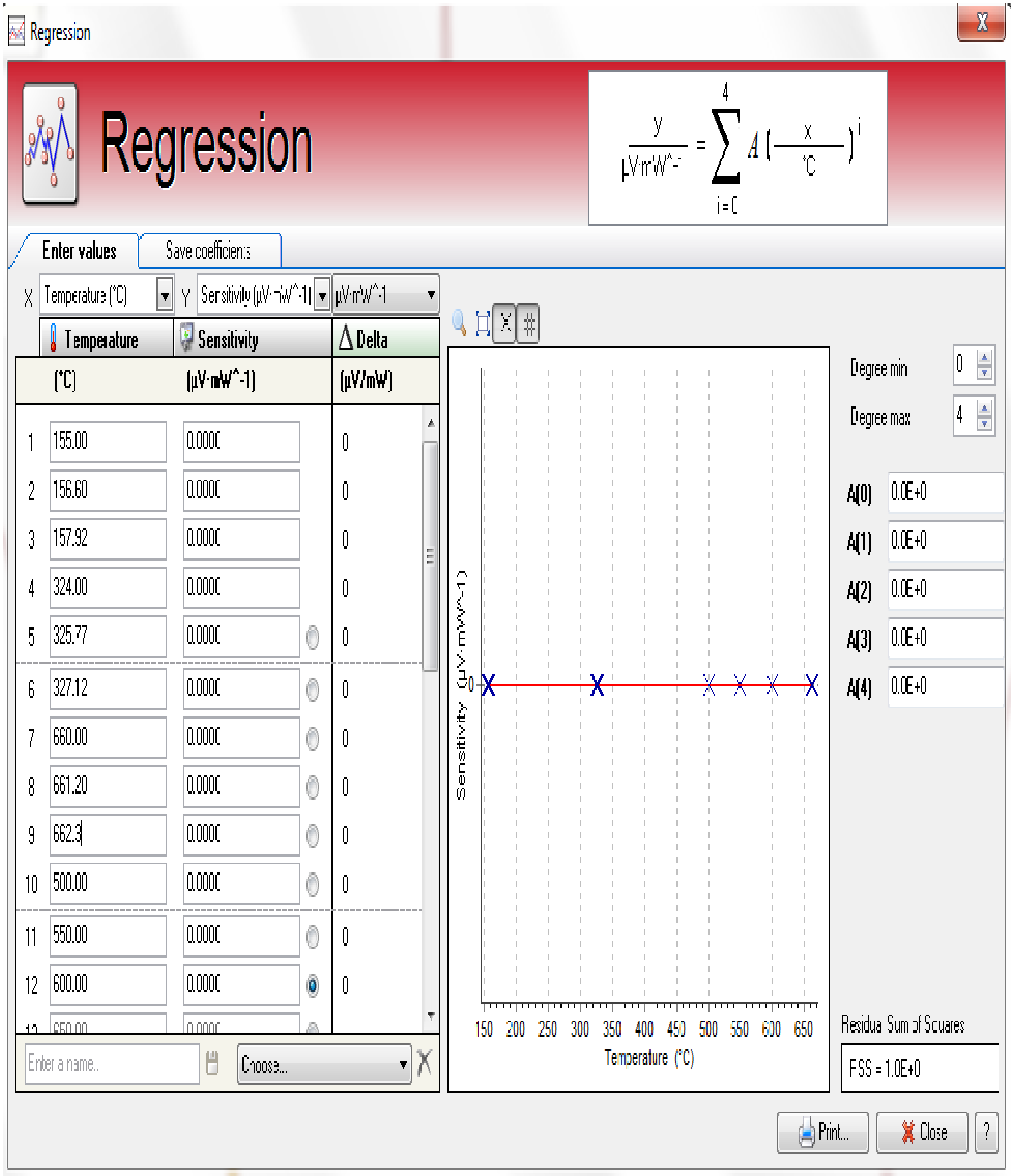

X: Temperature (°C)
Y: Sensitivity (μV·mW^-1)
μV·mW^-1

	Temperature (°C)	Sensitivity (μV·mW^-1)	Delta (μV/mW)
1	155.00	0.0000	0
2	156.60	0.0000	0
3	157.92	0.0000	0
4	324.00	0.0000	0
5	325.77	0.0000	0
6	327.12	0.0000	0
7	660.00	0.0000	0
8	661.20	0.0000	0
9	662.3	0.0000	0
10	500.00	0.0000	0
11	550.00	0.0000	0
12	600.00	0.0000	0

Degree min: 0
Degree max: 4

A(0) 0.0E+0
A(1) 0.0E+0
A(2) 0.0E+0
A(3) 0.0E+0
A(4) 0.0E+0

Residual Sum of Squares
RSS = 1.0E+0

Figure H.3.1: Heat flow sensitivity correction module in Calisto data processing software.

The set of sensitivity coefficients were generated using the built-in polynomial function, as shown in equation H.3.4.

$$K = A_0 + A_1 . T_{eim} + A_2 . {T_{eim}}^2 + A_3 . {T_{eim}}^3 + A_4 . {T_{eim}}^4 \quad [332] \qquad \text{eqn H.3.4}$$

The sensitivity ($\frac{\mu V}{mW}$) of equation H.3.4 converts the original heat flow signal (μV) to power signal (mW) at any given temperature. The coefficients $A_0(= 3.03087E - 1)$, $A_1(= -1.73924E - 4)$, $A_2(= 3.16788E - 8)$, $A_3(= 5.67052E - 11)$ and $A_4(= -1.73924E - 2)$ were calculated automatically by Calisto software.

APPENDIX I: MS CURVES

Spectral intensities of some gasses are shown in Figures I1 to I6. Atomic mass unit (AMU) bar of 100 percent for each gas was indicating its main intensity peak alongside its corresponding smaller peaks. For an example, water‘s main AMU peak (100% intensity) is 18, but a small 17AMU also appeared during the dehydration process. Another issue was of different gasses which have same AMU intensity. Such as nitric oxide and nitrogen dioxide (both have 30AMU). In such cases, the smaller other peaks were noticed carefully for distinguishing purpose. The 3rd issue was identifying impurities among the main intensity peak. Such as argon has 40AMU as the main peak and sometimes 20 or 80 AMU also appeared as secondary peaks. In such case, 20AMU was assumed to be an isotope of argon; and 80AMU indicated argon gas impurities such as krypton.

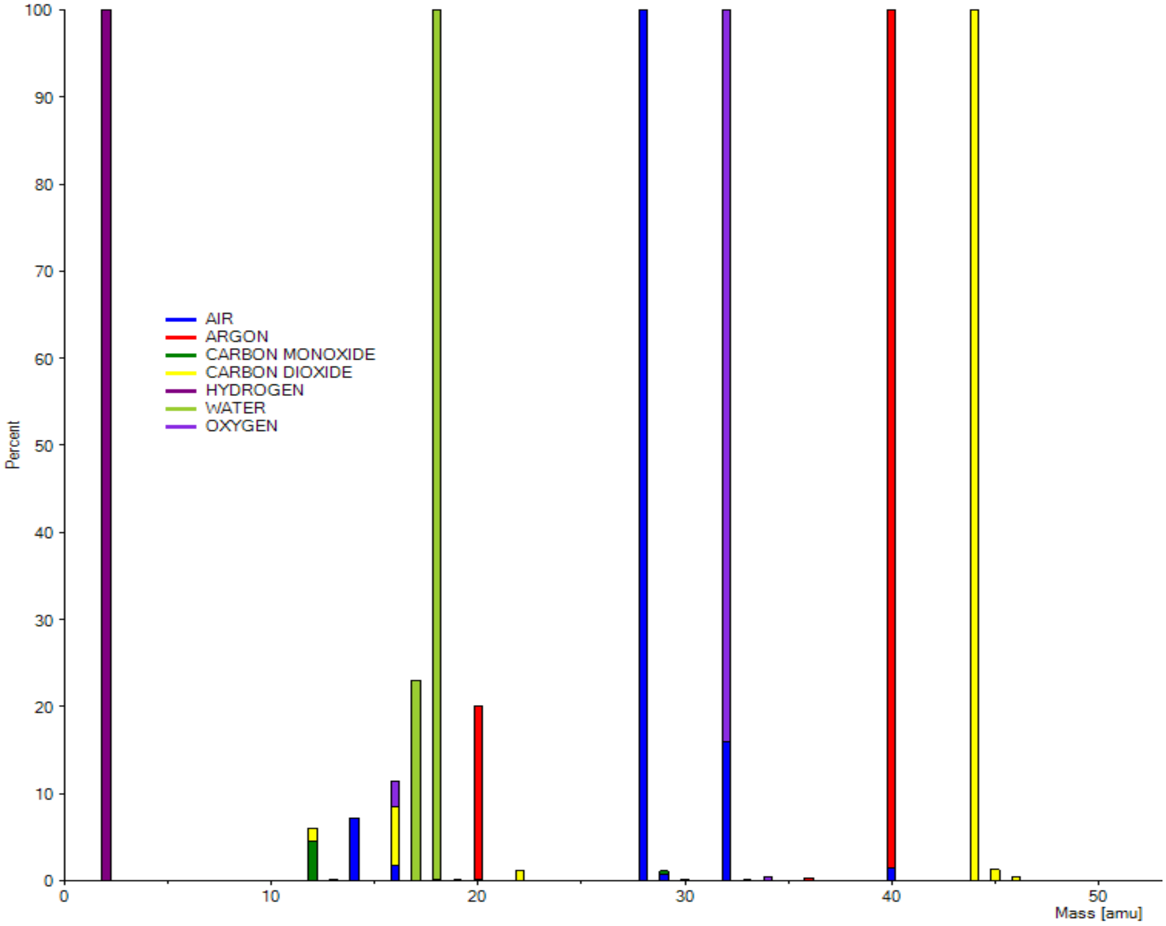

Figure I1: Spectra AMU bar of air and common air impurities.

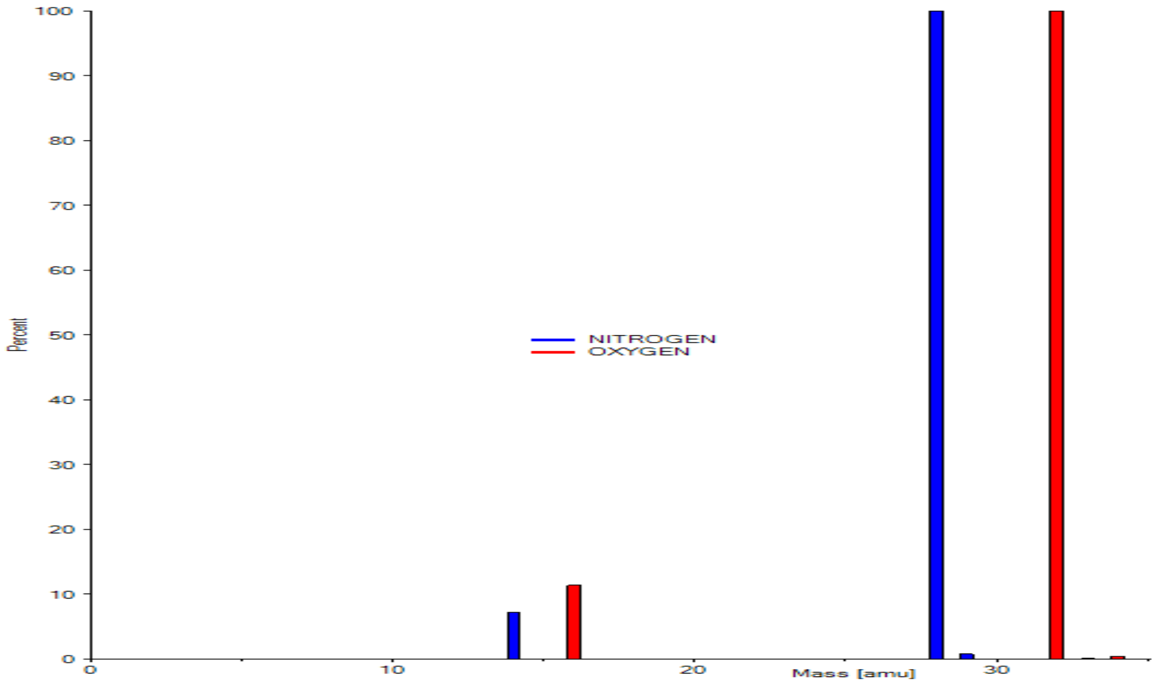

Figure I2: Spectra AMU bar of N_2 and O_2.

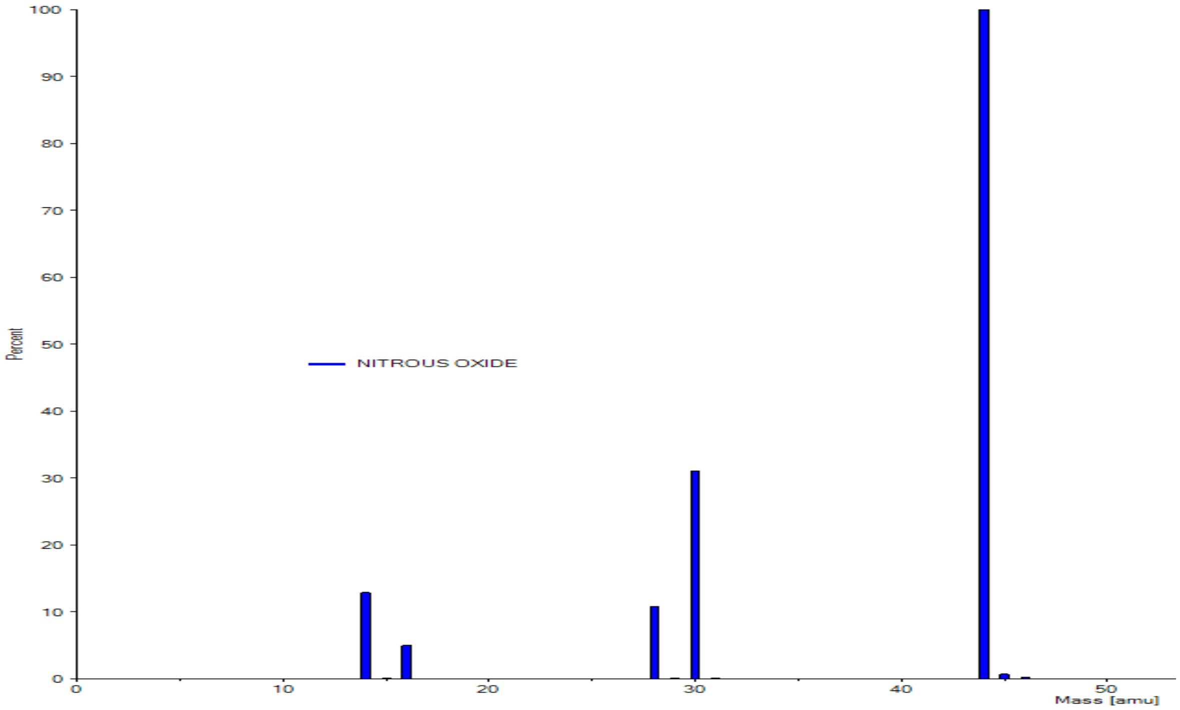

Figure I3: Spectra AMU bar of nitrous oxide.

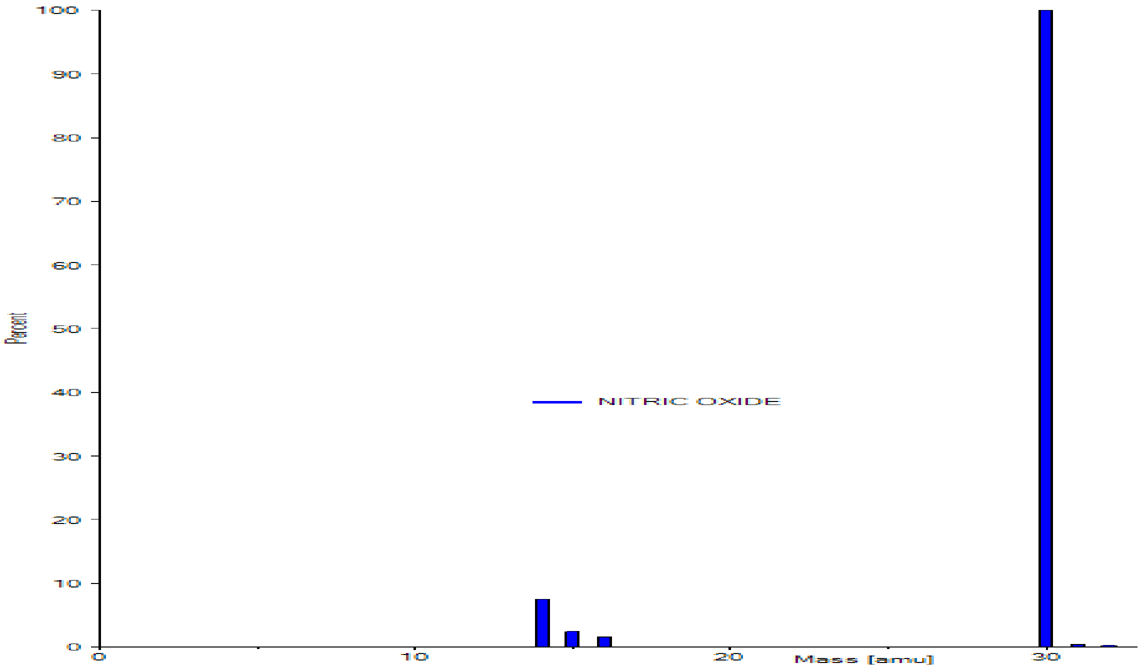

Figure I4: Spectra AMU bar of nitric oxide.

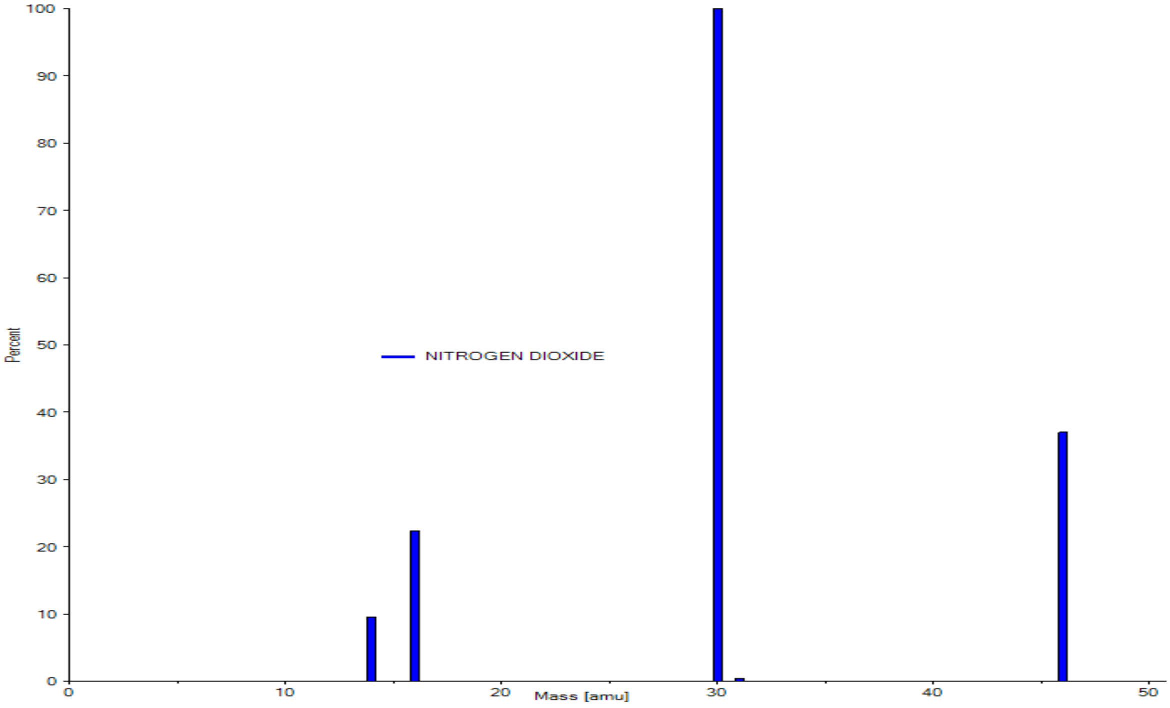

Figure I5: Spectra AMU bar of nitrogen dioxide.

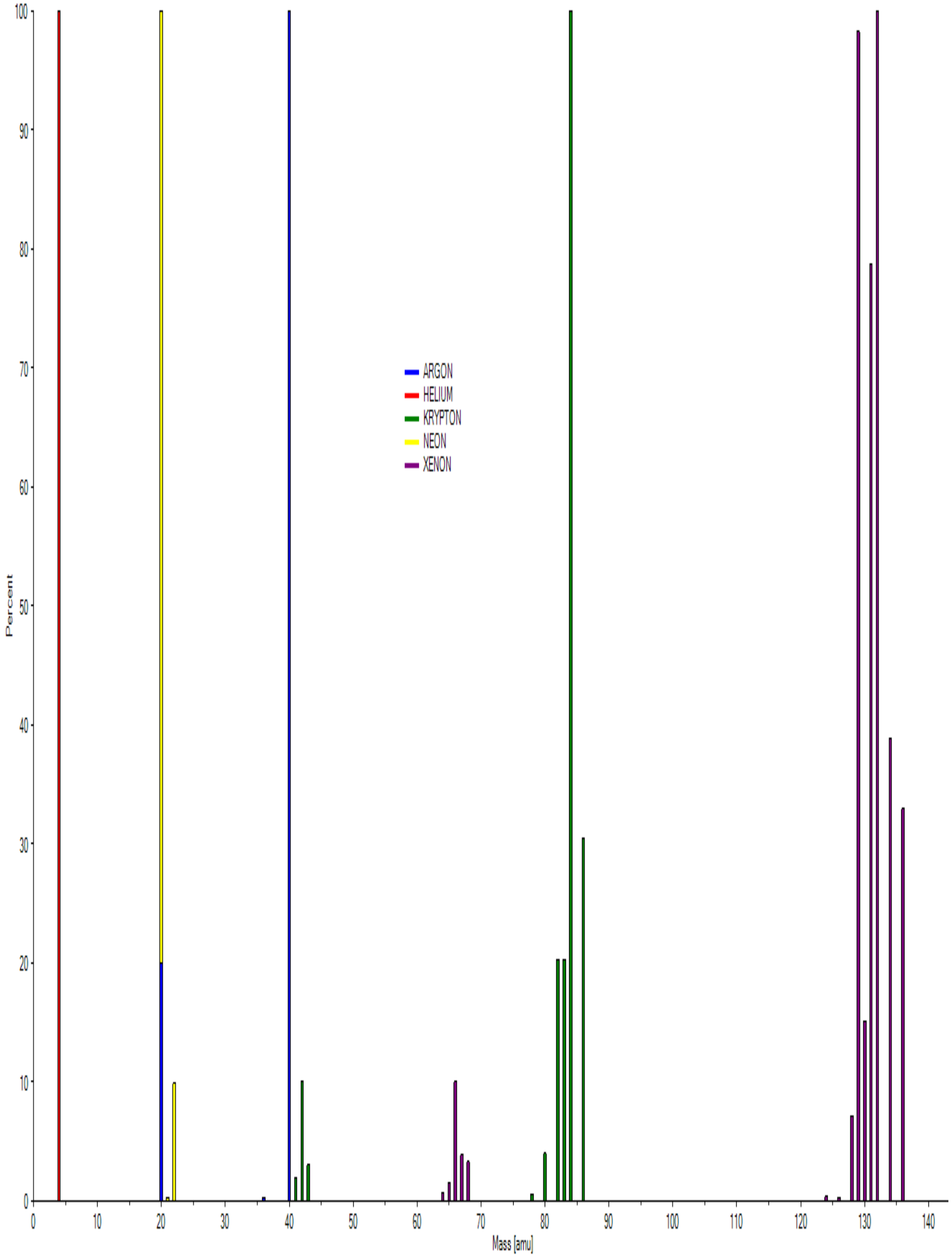

Figure I6: Spectra AMU bar of argon and other noble gasses.

APPENDIX J: ERROR ANALYSIS IN DSC/DTA-TGA-MS

Error analyses of STA apparatus are presented in this section.

Crucible geometry:

High purity alumina crucible from Setaram France might have chemical composition: SiO_2, B_2O_3, Na_2O and others [466]. The crucibles dimensions and weight of the same batch were not identical and varied ±1 to 2%.

Weighing error:

The Mettler Toledo digital balance had ±0.01mg weighing accuracy. The weighing error was mainly associated with sample‘s ambient exposure time and placement inside micro-crucible. Due to hygroscopic nature, the nitrates absorbed moisture quickly and causing erroneous readings. Another issue was sample‘s tendency to adhere to weighing paper. After placing the sample inside micro-crucible, change in weight was approximately ±0.03mg. STA‘s hanging TGA digital microbalance which had a measuring range of ±200mg with 0.002µg resolution and RMS noise of 0.03µg. The accuracy of TGA transducer was 0.005µg.

Temperature and heat flow sensitivity error:

DSC heat-flow sensor had a resolution of 1µW and DTA heat-flow sensor had resolution 0.4µW with root mean square (RMS) noise of 20µW.

Flow rate error:

The digital mass flow controller had a uncertainty approximately ±0.01 mL/min (full range 0 to 200ml/min).

Ion detection error:

Sometimes lighter gasses tend to show smearing and abrupt jump in MS curve due to lower AMU compared to the heavier carrier gas (argon with 40AMU). Hence, multi runs of the same sample with identical test conditions were performed to observe evolved gas evolution process.

APPENDIX K: ERROR ANALYSIS IN TRANSPIRATION RIG

Error analyses of measuring apparatus related to transpiration rig are presented in this section.

Weighing error:

The Mettler Toledo Balance had ±0.0001g weighing accuracy. The weighing error was mainly associated with sample‘s ambient exposure time. Due to hygroscopic nature, the nitrates absorbed moisture easily and causing erroneous readings. Approximately 0.01g moisture was absorbed for 10 minutes exposure time.

Errors in temperature measurement and sample placing:

A K-type (chromel - alumel) thermocouple was used for temperature profile reading. A thermocouple was equipped with ceramic probe and multimeter which had error ±0.1°C below 800°C. The temperature at each centimeter increment progression from the left end to right end, inside HT furnace (reaction tube), was measured at various temperatures, as shown in Figure K1.

The sample was guided via push rod and an ‗o‘ ring magnet assembly manually, might cause improper combustion boat placement in the isothermal zone inside reaction tube. The error associated with combustion boat placement (carrying sample) is approximated to be ±1mm.

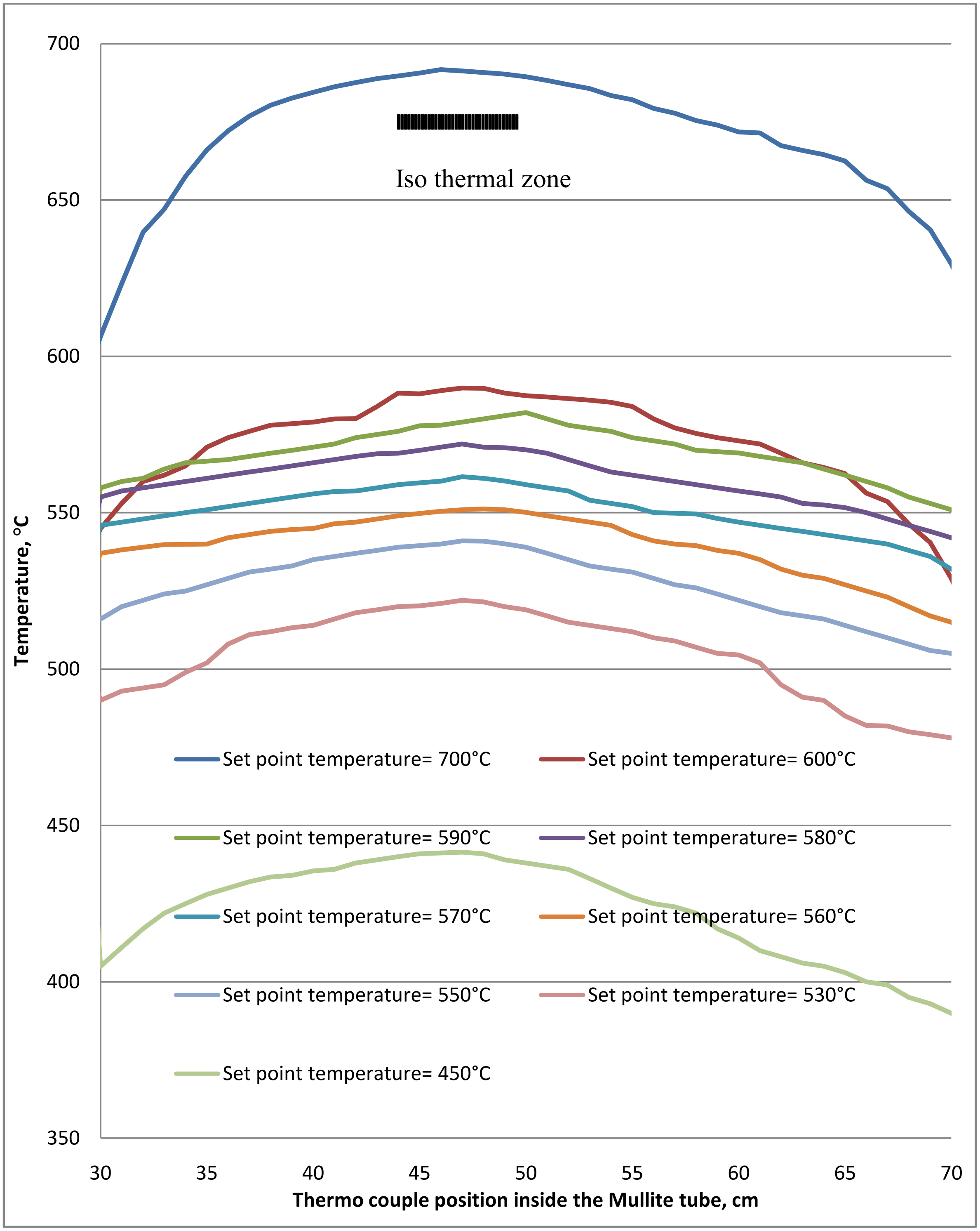

Figure K1: Temperature profile measurements of Labec horizontal tube furnace using K-type (chromel - alumel) thermocouple ceramic sheath/probe and multimeter.

Errors in flow rate:

An MPB 1200 variable area flow meter of 295mm long metering tube ranging from 100 to 1000 mL/min was used for argon, air, and oxygen. As per full-scale deflection, the measurement accuracy was approximated to be ±5% of actual flow.

Errors in XRD and EDS/SEM:

EDS had relative error ±5% without standards, and the order of detection was 0.4wt% according to Klug et al. [467]. XRD has an error associated with distortion of peaks, absorption of monochromator and sample misalignment according to Warren et al. [468].

BIBLIOGRAPHY

[1] S.J. Wagner, E.S. Rubin, Economic implications of thermal energy storage for concentrated solar thermal power, Renewable Energy, (2012) 1-15.

[2] K.H. Solangi, M.R. Islam, R. Saidur, N.A. Rahim, H. Fayaz, A review on global solar energy policy, Renewable and Sustainable Energy Reviews, 15 (2011) 2149-2163.

[3] A. Gil, M. Medrano, I. Martorell, A. Lázaro, P. Dolado, B. Zalba, L.F. Cabeza, State of the art on high temperature thermal energy storage for power generation. Part 1—Concepts, materials and modellization, Renewable and Sustainable Energy Reviews, 14 (2010) 31-55.

[4] P. Schwarzbözl, R. Buck, C. Sugarmen, A. Ring, M.J. Marcos Crespo, P. Altwegg, J. Enrile, Solar gas turbine systems: Design, cost and perspectives, Solar Energy, 80 (2006) 1231-1240.

[5] W. Han, J. Hongguang, S. Jianfeng, L. Rumou, W. Zhifeng, Design of the first chinese 1 MW solar-power tower demonstration plant, International Journal of Green Energy, 6 (2009) 414-425.

[6] P.D. Rufe, Fundamentals of Manufacturing (3rd Edition), in, Society of Manufacturing Engineers (SME), 2013.

[7] M.H. Rashid, Power Electronics Handbook - Devices, Circuits, and Applications (3rd Edition), in, Elsevier, 2011.

[8] V. Quaschning, Technical and economical system comparison of photovoltaic and concentrating solar thermal power systems depending on annual global irradiation, Solar Energy, 77 (2004) 171-178.

[9] F. Trieb, O. Langniβ, H. Klaiβ, Solar electricity generation—A comparative view of technologies, costs and environmental impact, Solar Energy, 59 (1997) 89-99.

[10] J. Clifton, B.J. Boruff, Assessing the potential for concentrated solar power development in rural Australia, Energ Policy, 38 (2010) 5272-5280.

[11] G. Sloan, Z.-G. Feng, K. Bhaganagar, D. Banerjee, Coupled Direct Numerical Simulation and Experimental Approach to Develop Framework for Nano Fluids, in: ASME 2012 International Mechanical Engineering Congress and Exposition, American Society of Mechanical Engineers, 2012, pp. 2877-2882.

[12] U. Herrmann, B. Kelly, H. Price, Two-tank molten salt storage for parabolic trough solar power plants, Energy, 29 (2004) 883-893.

[13] NREL, Report to Congress on Assessment Potential Impact of Concentrating Solar Power for Electricity Generation, in, U.S. Department of Energy, U.S.A., 2007, pp. 33.

[14] J.H. Peterseim, S. White, A. Tadros, U. Hellwig, Concentrated solar power hybrid plants, which technologies are best suited for hybridisation?, Renewable Energy, 57 (2013) 520-532.

[15] S. Kuravi, J. Trahan, D.Y. Goswami, M.M. Rahman, E.K. Stefanakos, Thermal energy storage technologies and systems for concentrating solar power plants, Progress in Energy and Combustion Science, (2013).

[16] A. Skumanich, CSP: Developments in heat transfer and storage materials, Renewable Energy Focus, 11 (2010) 40-43.

[17] R.W. Bradshaw, J.G. Cordaro, N.P. Siegel, Molten nitrate salt development for thermal energy storage in parabolic trough solar power systems, in, 2009, pp. 615-624.

[18] H.J. Hou, Y.P. Yang, Y.H. Cui, S. Gao, Y.X. Pan, Assessment of concentrating solar power prospect in China, in: Sustainable Power Generation and Supply, 2009. SUPERGEN '09. International Conference on, 2009, pp. 1-5.

[19] L. Moens, D.M. Blake, D.L. Rudnicki, M.J. Hale, Advanced thermal storage fluids for solar parabolic trough systems, in, 2002, pp. 277-283.

[20] D. Kearney, B. Kelly, U. Herrmann, R. Cable, J. Pacheco, R. Mahoney, H. Price, D. Blake, P. Nava, N. Potrovitza, Engineering aspects of a molten salt heat transfer fluid in a trough solar field, Energy, 29 (2004) 861-870.

[21] R.W. Bradshaw, C. Tyner, Chemical and Engineering Factors Affecting Solar Central Receiver Applications of Ternary Molten Salts, in: 1988 Summer National Meeting, American Institute of Chemical Engineering (AIChE), Denver, Colorado, USA, 1988.

[22] F.S. Barnes, J.G. Levine, Large Energy Storage Systems Handbook, Taylor & Francis Group, CRC Press, 6000 Broken Sound Parkway NW, Suite 300 Boca Raton, FL 33487-2742, U.S.A, 2011.

[23] R.I. Dunn, P.J. Hearps, M.N. Wright, Molten-Salt Power Towers: Newly Commercial Concentrating Solar Storage, Proceedings of the IEEE, 100 (2012) 504-515.

[24] J.G. Cordaro, RUBIN Nicholas C., BRADSHAW Robert W., Multicomponent molten salt mixtures based on nitrate/nitrite anions, Journal of solar energy engineering, 133 (2011).

[25] K.H. Stern, High temperature properties and thermal decomposition of inorganic salts with oxyanions, CRC press, 2001.

[26] R.I. Olivares, The thermal stability of molten nitrite/nitrates salt for solar thermal energy storage in different atmospheres, Solar Energy, Volume 86 (2012) Pages 2576–2583.

[27] D. Nissen, D. Meeker, Nitrate/nitrite chemistry in sodium nitrate-potassium nitrate melts, Inorganic Chemistry, 22 (1983) 716-721.

[28] G. Sirotkin, Equilibrium in melts of the nitrates and nitrites of sodium potassium, Russian Journal of Inorganic Chemistry, 4 (1959) 1180-1184.

[29] R. MAR, R. BRADSHAW, R. CARLING, A. NAGELBERG, The use of molten nitrate salts in high temperature energy conversion systems, in: International symposium on molten salt chemistry and technology. 1, 1983, pp. 285-288.

[30] R.W. Carling, R.W. Mar, Industrial use of molten nitrate/nitrite salts, in, 1981, pp. Medium: X; Size: Pages: 24.

[31] A.J. Bard, J.A. Plambeck, Encyclopedia of Electrochemistry of the Elements: Fused salt systems, Marcel Dekker, INC., 270 Madison Avenue, New york, New york 10016, 1976.

[32] M.J. Maeso, J. Largo, The phase diagrams of LiNO3-NaNO3 and LiNO3-KNO3: the behaviour of liquid mixtures, Thermochimica Acta, 223 (1993) 145-156.

[33] O. Abe, T. Utsunomiya, Y. Hoshino, The thermal stability of binary alkali metal nitrates, Thermochimica Acta, 78 (1984) 251-260.

[34] C.M. Kramer, Z.A. Munir, J.V. Volponi, Differential scanning calorimetry of sodium and potassium nitrates and nitrites, Thermochimica Acta, 55 (1982) 11-17.

[35] T. Bauer, D. Laing, R. Tamme, Recent Progress in Alkali Nitrate/Nitrite Developments for Solar Thermal Power Applications, Molten Salts Chemistry and Technology, MS9, Trondheim, Norway, June, (2011) 5-9.

[36] R.W. Bradshaw, D.E. Meeker, High-temperature stability of ternary nitrate molten salts for solar thermal energy systems, Solar Energy Materials, 21 (1990) 51-60.

[37] X. Zhang, J. Tian, K. Xu, Y. Gao, Thermodynamic evaluation of phase equilibria in NaNO3-KNO3 system, Journal of Phase Equilibria, 24 (2003) 441-446.

[38] O. Greis, K.M. Bahamdan, B.M. Uwais, The phase diagram of the system NaNO3 • KNO3 studied by differential scanning calorimetry, Thermochimica Acta, 86 (1985) 343-350.

[39] FACTSAGE©, CRCT- ThermFact Inc. & GTT-Technologies, viewed 6 August 2014, <http://www.factsage.com/> . (2014).

[40] H. Zhang, J. Baeyens, J. Degrève, G. Cacères, Concentrated solar power plants: Review and design methodology, Renewable and Sustainable Energy Reviews, 22 (2013) 466-481.

[41] E. Pihl, Concentrating solar power, Energy Committee Report, April, (2009).

[42] S. Kalogirou, Solar energy engineering : processes and systems, Elsevier/Academic Press, Burlington, MA, 2009.

[43] C. Philibert, Technology roadmap: concentrating solar power, OECD/IEA, 2010.

[44] M. Yang, X. Yang, X. Yang, J. Ding, Heat transfer enhancement and performance of the molten salt receiver of a solar power tower, Applied Energy, 87 (2010) 2808-2811.

[45] T.G.S. Society, Planning and Installing Solar Thermal Systems - A Guide for Installers, Architects and Engineers, in, Earthscan, 2010.

[46] W. Vogel, H. Kalb, Large-scale solar thermal power: technologies, costs and development, Wiley-VCH Verlag GmbH & Co. KGaA, Weinheim, 2010.

[47] Y. Tian, C.-Y. Zhao, A review of solar collectors and thermal energy storage in solar thermal applications, Applied Energy, 104 (2013) 538-553.

[48] D.Y. Goswami, Advances in Solar Energy: An Annual Review of Research And Development, Earthscan, 2007.

[49] D.A. Baharoon, H.A. Rahman, W.Z.W. Omar, S.O. Fadhl, Historical development of concentrating solar power technologies to generate clean electricity efficiently – A review, Renewable and Sustainable Energy Reviews, 41 (2015) 996-1027.

[50] G. Chen, Q. Yang, Y. Zhao, Z. Wang, Nonrenewable energy cost and greenhouse gas emissions of a 1.5 MW solar power tower plant in China, Renewable and Sustainable Energy Reviews, 15 (2011) 1961-1967.

[51] O. Behar, A. Khellaf, K. Mohammedi, A review of studies on central receiver solar thermal power plants, Renewable and Sustainable Energy Reviews, 23 (2013) 12-39.

[52] J.T. Hinkley, J.A. Hayward, B. Curtin, A. Wonhas, R. Boyd, C. Grima, A. Tadros, R. Hall, K. Naicker, An analysis of the costs and opportunities for concentrating solar power in Australia, Renewable Energy, 57 (2013) 653-661.

[53] A. Hoshi, D.R. Mills, A. Bittar, T.S. Saitoh, Screening of high melting point phase change materials (PCM) in solar thermal concentrating technology based on CLFR, Solar Energy, 79 (2005) 332-339.

[54] A.L. Avila-Marin, Volumetric receivers in solar thermal power plants with central receiver system technology: a review, Solar energy, 85 (2011) 891-910.

[55] J.E. Pacheco, R. Bradshaw, D. Dawson, W. De la Rosa, R. Gilbert, S. Goods, M. Hale, P. Jacobs, S. Jones, G. Kolb, Final test and evaluation results from the Solar Two project, Report No. SAND2002-0120, Sandia National Laboratories, Albuquerque, NM, (2002).

[56] H.E. Reilly, G.J. Kolb, An evaluation of molten-salt power towers including results of the solar two project, in, Sandia National Labs., Albuquerque, NM (US); Sandia National Labs., Livermore, CA (US), 2001.

[57] K. Lovegrove, M. Dennis, Solar thermal energy systems in Australia, International Journal of Environmental Studies, 63 (2006) 791-802.

[58] B. Hoffschmidt, S. Alexopoulos, C. Rau, J. Sattler, A. Anthrakidis, C. Boura, B. O'Connor, P. Hilger, 3.18 - Concentrating Solar Power, in: A. Sayigh (Ed.) Comprehensive Renewable Energy, Elsevier, Oxford, 2012, pp. 595-636.

[59] P. Breeze, Power Generation Technologies, 1st ed., Newnes, 2005.

[60] H. Price, E. Lupfert, D. Kearney, E. Zarza, G. Cohen, R. Gee, R. Mahoney, Advances in Parabolic Trough Solar Power Technology, Journal of solar energy engineering, 124 (2002) 109-125.

[61] G. Zhu, T. Wendelin, M.J. Wagner, C. Kutscher, History, current state, and future of linear Fresnel concentrating solar collectors, Solar Energy, 103 (2014) 639-652.

[62] A.K. Raja, A.P. Srivastava, Power Plant Engineering, New Age International, 4835/24, Ansari Road, Daryaganj, New Delhi - 110002, India, 2006.

[63] Z. Eduardo, R.-A. Manuel, Concentrating Solar Thermal Power, in: Handbook of Energy Efficiency and Renewable Energy, CRC Press, 2007, pp. 21-21-21-98.

[64] S.A. Rice, Advances in Chemical Physics, John Wiley & Sons, 2007.

[65] G.J. Kolb, Evaluation of annual performance of 2-tank and thermocline thermal storage systems for trough plants, Journal of solar energy engineering, 133 (2011) 031023.

[66] S. Millennium, The parabolic trough power plants Andasol 1 to 3, Tech. Solar Millennium AG, (2008).

[67] R. Foster, M. Ghassemi, A. Cota, Solar Energy: Renewable Energy and the Environment, CRC Press, 2009.

[68] M.-M. Rodríguez-García, M. Herrador-Moreno, E. Zarza Moya, Lessons learnt during the design, construction and start-up phase of a molten salt testing facility, Applied Thermal Engineering, 62 (2014) 520-528.

[69] R. Serrano-López, J. Fradera, S. Cuesta-López, Molten salts database for energy applications, Chemical Engineering and Processing: Process Intensification, 73 (2013) 87-102.

[70] C.K. Ho, B.D. Iverson, Review of high-temperature central receiver designs for concentrating solar power, Renewable and Sustainable Energy Reviews, 29 (2014) 835-846.

[71] I. Dincer, M. Rosen, Thermal energy storage: systems and applications, John Wiley & Sons, 2002.

[72] N.B. Thomas Bauer, Nicole Pfleger, Doerte Laing, Markus Eck, Overview of molten salt storage systems and material development for solar thermal power plants, (2012).

[73] L.F. Cabeza, Advances in thermal energy storage systems: Methods and applications, Elsevier, 2014.

[74] H. Garg, S. Mullick, A. Bhargava, Solar thermal energy storage, D Reidel Publishing Company, 1985.

[75] S.M. Hasnain, Review on sustainable thermal energy storage technologies, Part I: heat storage materials and techniques, Energy Conversion and Management, 39 (1998) 1127-1138.

[76] A. Sharma, V. Tyagi, C. Chen, D. Buddhi, Review on thermal energy storage with phase change materials and applications, Renewable and Sustainable Energy Reviews, 13 (2009) 318-345.

[77] F. Roget, C. Favotto, J. Rogez, Study of the KNO_3–$LiNO_3$ and KNO_3–$NaNO_3$–$LiNO_3$ eutectics as phase change materials for thermal storage in a low-temperature solar power plant, Solar Energy, 95 (2013) 155-169.

[78] M.M. Farid, A.M. Khudhair, S.A.K. Razack, S. Al-Hallaj, A review on phase change energy storage: materials and applications, Energy Conversion and Management, 45 (2004) 1597-1615.

[79] M. Kenisarin, K. Mahkamov, Solar energy storage using phase change materials, Renewable and Sustainable Energy Reviews, 11 (2007) 1913-1965.

[80] W.J. Boettinger, U. Kattner, K. Moon, J. Perepezko, DTA and heat-flux DSC measurements of alloy melting and freezing, US Department of Commerce, Technology Administration, National Institute of Standards and Technology, 2006.

[81] J.D. Verhoeven, Fundamentals of physical metallurgy, Wiley New York, 1975.

[82] A.A. El-Sebaii, S. Al-Amir, F.M. Al-Marzouki, A.S. Faidah, A.A. Al-Ghamdi, S. Al-Heniti, Fast thermal cycling of acetanilide and magnesium chloride hexahydrate for indoor solar cooking, Energy Conversion and Management, 50 (2009) 3104-3111.

[83] H. Michels, R. Pitz-Paal, Cascaded latent heat storage for parabolic trough solar power plants, Solar Energy, 81 (2007) 829-837.

[84] L.F. Cabeza, I. Martorell, L. Miró, A.I. Fernández, C. Barreneche, 1 - Introduction to thermal energy storage (TES) systems, in: L.F. Cabeza (Ed.) Advances in Thermal Energy Storage Systems, Woodhead Publishing, 2015, pp. 1-28.

[85] L.F. Cabeza, 3.07 - Thermal Energy Storage, in: A. Sayigh (Ed.) Comprehensive Renewable Energy, Elsevier, Oxford, 2012, pp. 211-253.

[86] F. Agyenim, N. Hewitt, P. Eames, M. Smyth, A review of materials, heat transfer and phase change problem formulation for latent heat thermal energy storage systems (LHTESS), Renewable and Sustainable Energy Reviews, 14 (2010) 615-628.

[87] F. Trausel, A.-J. de Jong, R. Cuypers, A Review on the Properties of Salt Hydrates for Thermochemical Storage, Energy Procedia, 48 (2014) 447-452.

[88] D. Shin, D. Banerjee, Enhanced specific heat of silica nanofluid, Journal of heat transfer, 133 (2011) 024501.

[89] O. Mahian, A. Kianifar, S.A. Kalogirou, I. Pop, S. Wongwises, A review of the applications of nanofluids in solar energy, International Journal of Heat and Mass Transfer, 57 (2013) 582-594.

[90] D. Shin, D. Banerjee, Specific heat of nanofluids synthesized by dispersing alumina nanoparticles in alkali salt eutectic, International Journal of Heat and Mass Transfer, 74 (2014) 210-214.

[91] D. Wen, G. Lin, S. Vafaei, K. Zhang, Review of nanofluids for heat transfer applications, Particuology, 7 (2009) 141-150.

[92] R. Saidur, K. Leong, H. Mohammad, A review on applications and challenges of nanofluids, Renewable and Sustainable Energy Reviews, 15 (2011) 1646-1668.

[93] X.-Q. Wang, A.S. Mujumdar, A review on nanofluids-part II: experiments and applications, Brazilian Journal of Chemical Engineering, 25 (2008) 631-648.

[94] W. Yu, H. Xie, A Review on nanofluids: Preparation, stability mechanisms, and applications, Journal of Nanomaterials, 2012 (2012) 1.

[95] W. Yu, D.M. France, J.L. Routbort, S.U. Choi, Review and comparison of nanofluid thermal conductivity and heat transfer enhancements, Heat Transfer Engineering, 29 (2008) 432-460.

[96] P. Pardo, A. Deydier, Z. Anxionnaz-Minvielle, S. Rougé, M. Cabassud, P. Cognet, A review on high temperature thermochemical heat energy storage, Renewable and Sustainable Energy Reviews, 32 (2014) 591-610.

[97] L. Heller, Literature Review on Heat Transfer Fluids and Thermal Energy Storage Systems in CSP Plants, STERG Report, May, 31 (2013).

[98] J. Pacio, T. Wetzel, Assessment of liquid metal technology status and research paths for their use as efficient heat transfer fluids in solar central receiver systems, Solar Energy, 93 (2013) 11-22.

[99] S. Furbo, 2 - Using water for heat storage in thermal energy storage (TES) systems, in: L.F. Cabeza (Ed.) Advances in Thermal Energy Storage Systems, Woodhead Publishing, 2015, pp. 31-47.

[100] S. Ushak, A.G. Fernández, M. Grageda, 3 - Using molten salts and other liquid sensible storage media in thermal energy storage (TES) systems, in: L.F. Cabeza (Ed.) Advances in Thermal Energy Storage Systems, Woodhead Publishing, 2015, pp. 49-63.

[101] T. Kousksou, P. Bruel, A. Jamil, T. El Rhafiki, Y. Zeraouli, Energy storage: Applications and challenges, Solar Energy Materials and Solar Cells, 120, Part A (2014) 59-80.

[102] T. Bauer, N. Pfleger, D. Laing, W.-D. Steinmann, M. Eck, S. Kaesche, 20 - High-Temperature Molten Salts for Solar Power Application, in: F. Lantelme, H. Groult (Eds.) Molten Salts Chemistry, Elsevier, Oxford, 2013, pp. 415-438.

[103] B. Hoffschmidt, S. Alexopoulos, J. Göttsche, M. Sauerborn, O. Kaufhold, 3.06 - High Concentration Solar Collectors, in: A. Sayigh (Ed.) Comprehensive Renewable Energy, Elsevier, Oxford, 2012, pp. 165-209.

[104] H. Tiznobaik, D. Shin, Enhanced specific heat capacity of high-temperature molten salt-based nanofluids, International Journal of Heat and Mass Transfer, 57 (2013) 542-548.

[105] Q. Peng, J. Ding, X. Wei, J. Yang, X. Yang, The preparation and properties of multi-component molten salts, Applied Energy, 87 (2010) 2812-2817.

[106] T. Wang, D. Mantha, R.G. Reddy, Thermal stability of the eutectic composition in LiNO 3NaNO 3KNO 3 ternary system used for thermal energy storage, Solar Energy Materials and Solar Cells, 100 (2012) 162-168.

[107] L.M.T. D. F. Williams, K. T. Clarno, Assessment of Candidate Molten Salt Coolants for the Advanced High-Temperature Reactor (AHTR), in, Oak Ridge National Laboratory, Oak Ridge, TN 37831 2006.

[108] J.W. Raade, D. Padowitz, Development of molten salt heat transfer fluid with low melting point and high thermal stability, Journal of Solar Energy Engineering, Transactions of the ASME, 133 (2011).

[109] R.G. Reddy, T. Wang, D. Mantha, Thermodynamic properties of potassium nitrate–magnesium nitrate compound [2KNO3·Mg(NO3)2], Thermochimica Acta, 531 (2012) 6-11.

[110] B. Wu, R. Reddy, R. Rogers, Novel ionic liquid thermal storage for solar thermal electric power systems, Solar Engineering, (2001) 445-452.

[111] C.Y. Zhao, Z.G. Wu, Thermal property characterization of a low melting-temperature ternary nitrate salt mixture for thermal energy storage systems, Solar Energy Materials and Solar Cells, 95 (2011) 3341-3346.

[112] D. Williams, Assessment of candidate molten salt coolants for the NGNP/NHI heat-transfer loop, ORNL/TM-2006/69, Oak Ridge National Laboratory, Oak Ridge, Tennessee, (2006).

[113] K. Coscia, S. Neti, A. Oztekin, S. Nelle, S. Mohapatra, T. Elliott, The Thermophysical Properties of the NaNO3-KNO3, LiNO3-NaNO3, and LiNO3-KNO3 Systems, in: ASME 2011 International Mechanical Engineering Congress and Exposition, American Society of Mechanical Engineers, 2011, pp. 889-894.

[114] Molten salts vs Oil, Archimede solar energy, viewed 25 May 2015, <http://www.archimedesolarenergy.it/molten_salt_vs_oil.htm>. .

[115] D. Kearney, U. Herrmann, P. Nava, B. Kelly, R. Mahoney, J. Pacheco, R. Cable, N. Potrovitza, D. Blake, H. Price, Evaluation of a molten salt heat transfer fluid in a parabolic trough solar field, in: ASME Solar 2002: International Solar Energy Conference, American Society of Mechanical Engineers, 2002, pp. 293-299.

[116] W. Michel, Heat transfer fluid of potassium nitrate lithium nitrate and 0–38% calcium nitrate, in, 1993.

[117] I. Prigogine, R. Defay, Chemical Thermodynamics, Longmans, Green 1954.

[118] M.L. McGlashan, Chemical Thermodynamics, Chemical Society, London, 1978.

[119] K.H.J. Buschow, R.W. Cahn, M.C. Flemings, B. Ilschner, E.J. Kramer, S. Mahajan, Encyclopedia of Materials - Science and Technology, Volumes 1-11, in, Elsevier, 2001.

[120] J.W. Raade, D. Padowitz, Development of Molten Salt Heat Transfer Fluid With Low Melting Point and High Thermal Stability, Journal of Solar Energy Engineering, 133 (2011) 031013.

[121] R.I. Olivares, W. Edwards, LiNO3-NaNO3-KNO3 salt for thermal energy storage: Thermal stability evaluation in different atmospheres, Thermochimica Acta, (2013).

[122] U. Herrmann, D.W. Kearney, Survey of Thermal Energy Storage for Parabolic Trough Power Plants, Journal of Solar Energy Engineering, 124 (2002) 145-152.

[123] J.G. Cordaro, Chemical Perspectives on Alkali and Earth Alkaline Nitrate and Nitrite Salts for Concentrated Solar Power Applications, Green, 3 (2013) 9-18.

[124] A.G. Fernández, S. Ushak, H. Galleguillos, F.J. Pérez, Development of new molten salts with LiNO3 and Ca(NO3)2 for energy storage in CSP plants, Applied Energy, 119 (2014) 131-140.

[125] M. Geyer, Thermal storage for solar power plants, in: Solar Power Plants, Springer, 1991, pp. 199-214.

[126] D. Kearney, Overview on use of a Molten Salt HTF in a Trough Solar Field, National Renewable Energy Laboratory, 2003.

[127] D. Kearney, U. Herrmann, P. Nava, B. Kelly, R. Mahoney, J. Pacheco, R. Cable, N. Potrovitza, D. Blake, H. Price, Assessment of a molten salt heat transfer fluid in a parabolic trough solar field, Journal of solar energy engineering, 125 (2003) 170-176.

[128] M.D. Silverman, J.R. Engel, Survey of technology for storage of thermal energy in heat transfer salt, in, 1977, pp. Medium: ED; Size: Pages: 26.

[129] D. Fernandes, F. Pitié, G. Cáceres, J. Baeyens, Thermal energy storage: ―How previous findings determine current research priorities", Energy, 39 (2012) 246-257.

[130] Dow, DOWTHERM A Heat Transfer Fluid, DOW, viewed 27 May 2015, <http://www.dow.com/heattrans/products/synthetic/dowtherm.htm>. (1997).

[131] Solutia, THERMINOL VP-1 vapour phase liquid phase heat transfer fluid, Solutia, viewed 27 May 2015, <http://www.therminol.com/products/Therminol-VP1>. (1998).

[132] B. Zalba, J.M. Marín, L.F. Cabeza, H. Mehling, Review on thermal energy storage with phase change: materials, heat transfer analysis and applications, Applied Thermal Engineering, 23 (2003) 251-283.

[133] M.M. Kenisarin, High-temperature phase change materials for thermal energy storage, Renewable and Sustainable Energy Reviews, 14 (2010) 955-970.

[134] W. Kelly, Perry‛s chemical engineers‛ handbook, (1973).

[135] R. Mar, C. Kramer, Pressure-temperature-composition relationships for heated drawsalt systems, Solar Energy Materials, 5 (1981) 71-79.

[136] L.L.C. HITEC® Heat Transfer Salt. Coastal Chemical Co., viewed 18 September 2014, <http://www.coastalchem.com/>. , (2014).

[137] R.W. Bradshaw, D. Meeker, Chemical Equilibria of Molten Ternary Nitrate Salt Mixtures, SAND88-8845, Sandia National Laboratories, Albuquerque, New Mexico, May, (1989).

[138] W. Delameter, N. Bergan, Review of the Molten Salt Electric Experiment: A solar central receiver project, in, Sandia National Labs., Livermore, CA (USA), 1986.

[139] J.E. Pacheco, S.K. Showalter, W.J. Kolb, Development of a molten-salt thermocline thermal storage system for parabolic trough plants, Journal of Solar Energy Engineering, 124 (2002) 153-159.

[140] R. Carling, R. Bradshaw, Review of the characterization of molten nitrate salt for solar central receiver applications, in: Intersociety energy conversion engineering conference. 21, 1986, pp. 834-838.

[141] D. Laing, C. Bahl, T. Bauer, D. Lehmann, W.-D. Steinmann, Thermal energy storage for direct steam generation, Solar Energy, 85 (2011) 627-633.

[142] Q. Peng, X. Yang, J. Ding, X. Wei, J. Yang, Design of new molten salt thermal energy storage material for solar thermal power plant, Applied Energy, 112 (2013) 682-689.

[143] P. Speidel, B. Kelly, M. Prairie, J. Pacheco, R. Gilbert, H. Reilly, Performance of the solar two central receiver power plant, Le Journal de Physique IV, 9 (1999) Pr3-181-Pr183-187.

[144] U.H. M. Geyer, A. Sevilla, et al., Dispatchable Solar Electricity for Summerly Peak Loads from the Solar Thermal Projects Andasol-1 and Andasol-2 (sic) (2006).

[145] Archimede, NREL, viewed 20 May 2015, <http://www.nrel.gov/csp/solarpaces/project_detail.cfm/projectID=19>. .

[146] F. Donatini, C. Zamparelli, A. Maccari, M. Vignolini, High efficency integration of thermodynamic solar plant with natural gas combined cycle, in: Clean Electrical Power, 2007. ICCEP'07. International Conference on, IEEE, 2007, pp. 770-776.

[147] Gemasolar Thermosolar Plant, NREL, viewed 20 May 2015, <http://www.nrel.gov/csp/solarpaces/project_detail.cfm/projectID=40>. .

[148] J.s.M. Lata, M. RodrÃguez, M.n.Ã. lvarez de Lara, High flux central receivers of molten salts for the new generation of commercial stand-alone solar power plants, Journal of Solar Energy Engineering, 130 (2008) 021002.

[149] N. Boerema, G. Morrison, R. Taylor, G. Rosengarten, Liquid sodium versus Hitec as a heat transfer fluid in solar thermal central receiver systems, Solar Energy, 86 (2012) 2293-2305.

[150] D. Rogers, G. Janz, Melting-crystallization and pre-melting properties of NaNO/sub 3/-KNO/sub 3, (1984).

[151] R.W. Berg, D.H. Kerridge, The NaNO 3/KNO 3 system: the position of the solidus and sub-solidus, Dalton Transactions, (2004) 2224-2229.

[152] T. Bauer, D. Laing, R. Tamme, Overview of PCMs for concentrated solar power in the temperature range 200 to 350 C, Advances in Science and Technology, 74 (2011) 272-277.

[153] C.M. Kramer, C.J. Wilson, The phase diagram of NaNO3—KNO3, Thermochimica Acta, 42 (1980) 253-264.

[154] A. Kofler, Mikrothermoanalyse des Systems NaNO3-KNO3, Monatshefte für Chemie und verwandte Teile anderer Wissenschaften, 86 (1955) 643-652.

[155] N. Voskresenskaia, Handbook of solid-liquid equilibria in systems of anhydrous inorganic salts, (1970).

[156] W. Benaissa, D. Carson, Oxidation properties of "solar Salt", in: 45th Annual Loss Preventive Symposium 2011 (LPS), AIChE, Chicago,Illinois, USA, 2011.

[157] Q. Peng, X. Wei, J. Ding, J. Yang, X. Yang, High-temperature thermal stability of molten salt materials, International Journal of Energy Research, 32 (2008) 1164-1174.

[158] R. Santini, L. Tadrist, J. Pantaloni, P. Cerisier, Measurement of thermal conductivity of molten salts in the range 100–500°C, International Journal of Heat and Mass Transfer, 27 (1984) 623-626.

[159] G.J. Janz, G.N. Truong, Melting and premelting properties of the potassium nitrate-sodium nitrite-sodium nitrate eutectic system, Journal of chemical and engineering Data, 28 (1983) 201-202.

[160] L. Drouot, M. Hillairet, The Themis program and the 2500-KW Themis solar power station at Targasonne, Journal of solar energy engineering, 106 (1984) 83-89.

[161] M.C. Sneed, R.C. Brasted, C. King, Comprehensive inorganic chemistry, Journal of The Electrochemical Society, 103 (1956) 83C-83C.

[162] W. Kirst, W. Nagle, J. Castner, A new heat transfer medium for high temperatures, Trans. Am. Inst. Chem. Eng, 36 (1940) 371.

[163] J. Alexander, S.G. Hindin, Phase Relations in Heat Transfer Salt systems, Industrial & Engineering Chemistry, 39 (1947) 1044-1049.

[164] S. Berul, A. Bergman, Triple Mutual System of Sodium and Potassium Nitrates and Nitrites, Izv. Sekt. Fiz-Khim. Anal. Inst. Obshch. Neorg. Khim. Akad. Nauk SSSR, 25 (1954) 218-235.

[165] G.J. Janz, R. Tomkins, Physical Properties Data Compilations Relevant to Energy Storage. Pt. 4. Molten Salts: Data on Additional Single and Multicomponent Salt Systems.(Pamphlet), National Bureau of Standards, 861, (1981) 1981.

[166] K. Sakai, A Microphotographic Research on Salt System: NaNO 2–KNO 3, Bulletin of the Chemical Society of Japan, 27 (1954) 463-465.

[167] M.J. Kelly, P.F. Hlava, D.A. Brosseau, Testing Thermocline Filler Materials and Molten-Salt Heat Transfer Fluid for Thermal Energy Storage Systems Used in Parabolic Trough Solar Power Plants, Sandia Report SAND2004-3207, Sandia National Laboratories, Albuquerque NM, USA, (2004).

[168] R.W. Bradshaw, D.A. Brosseau, Low-melting point inorganic nitrate salt heat transfer fluid, in, Google Patents, 2009.

[169] E. Levin, C. Robbins, H. McMordie, Phase Diagrams for Chemists, The American Ceramic Society, (1964) 430.

[170] J.C. Gomez, N. Calvet, A.K. Starace, G.C. Glatzmaier, Ca (NO3) 2—NaNO3—KNO3 Molten Salt Mixtures for Direct Thermal Energy Storage Systems in Parabolic Trough Plants, Journal of Solar Energy Engineering, 135 (2013) 021016.

[171] A.W. Menzies, N. Dutt, THE LIQUIDUS SURFACE OF THE TERNARY SYSTEM COMPOSED OF THE NITRATES OF POTASSIUM, SODIUM AND CALCIUM, Journal of the American Chemical Society, 33 (1911) 1366-1375.

[172] E.M. Levin, H.F. McMurdie, C.R. Robbins, Phase diagrams for ceramists.[Vol. 1], American ceramic society, 1979.

[173] A. Bergman, I. Rassonskaya, N. Shmidt, удельные веса вязкость тройной системы из нитратов натрия калия и кальция (densities and viscosity of the ternary nitrate system of sodium, potassium and calcium), Sektora Fiz. Khim Anal. Akad. Nauk SSSR, 26 (1955) 156-163.

[174] A. Bondar, F.Y. Galakhov, E. Levin, C. Robbins, H. McMurdie, Phase diagram for Ceramists, Phase diagram for Ceramists, (1969).

[175] Palma del Río I, NREL, viewed 20 May 2015, <http://www.nrel.gov/csp/solarpaces/project_detail.cfm/projectID=16>. .

[176] Palma del Río II, NREL, viewed 20 May 2015, <http://www.nrel.gov/csp/solarpaces/project_detail.cfm/projectID=6>. .

[177] Manchasol-1, NREL, viewed 20 May 2015, <http://www.nrel.gov/csp/solarpaces/project_detail.cfm/projectID=7>. .

[178] Manchasol-2, NREL, viewed 20 May 2015, <http://www.nrel.gov/csp/solarpaces/project_detail.cfm/projectID=8>. .

[179] Andasol-1, NREL, viewed 20 May 2015, <http://www.nrel.gov/csp/solarpaces/project_detail.cfm/projectID=3>. .

[180] Andasol-2, NREL, viewed 20 May 2015, <http://www.nrel.gov/csp/solarpaces/project_detail.cfm/projectID=4>. .

[181] Andasol-3, NREL, viewed 20 May 2015, <http://www.nrel.gov/csp/solarpaces/project_detail.cfm/projectID=117>. .

[182] Nevada Solar One, NREL, viewed 20 May 2015, <http://www.nrel.gov/csp/solarpaces/project_detail.cfm/projectID=20>. .

[183] Genesis Solar Energy Project, NREL, viewed 20 May 2015, <http://www.nrel.gov/csp/solarpaces/project_detail.cfm/projectID=54>. .

[184] O. Arthur, M.A. Karim, An investigation into the thermophysical and rheological properties of nanofluids for solar thermal applications, Renewable and Sustainable Energy Reviews, 55 (2016) 739-755.

[185] G.Y. Lai, High-Temperature Corrosion and Materials Applications, ASM International, 2007.

[186] K.-O. Honikel, The use and control of nitrate and nitrite for the processing of meat products, Meat Science, 78 (2008) 68-76.

[187] A.J. Gutiérrez, C. Rubio, J.M. Caballero, A. Hardisson, Nitrites, in: P. Wexler (Ed.) Encyclopedia of Toxicology (Third Edition), Academic Press, Oxford, 2014, pp. 532-535.

[188] I. Wolff, A. Wasserman, Nitrates, nitrites, and nitrosamines, Science, 177 (1972) 15.

[189] C.M. Kramer, Z.A. Munir, K.H. Stern, EVAPORATION OF NaNO3, KNO3, AND NaNO2, High temperature science, 16 (1983) 257-267.

[190] A.L. Mehring, W.H. Ross, A.R. Merz, Preparation of Potassium Nitrate, Industrial & Engineering Chemistry, 21 (1929) 379-382.

[191] C.W. VOLLEY, Explosive Compound, in, Google Patents, New york, USA, 1881.

[192] C.M. Kramer, Z.A. Munir, J.V. Volponi, Screening tests of sodium nitrate and potassium nitrate decomposition, Solar Energy, 29 (1982) 437-439.

[193] S.H. Goods, R.W. Bradshaw, Corrosion of Stainless Steels and Carbon Steel by Molten Mixtures of Commercial Nitrate Salts, J Mater Eng Perform, 13 (2004) 78-87.

[194] S. Guillot, A. Faik, A. Rakhmatullin, J. Lambert, E. Veron, P. Echegut, C. Bessada, N. Calvet, X. Py, Corrosion effects between molten salts and thermal storage material for concentrated solar power plants, Applied Energy, 94 (2012) 174-181.

[195] K. Vignarooban, X. Xu, A. Arvay, K. Hsu, A.M. Kannan, Heat transfer fluids for concentrating solar power systems – A review, Applied Energy, 146 (2015) 383-396.

[196] X. Wei, Q. Peng, J. Ding, X. Yang, J. Yang, B. Long, Theoretical Study on Thermal Stability of Molten Salt for Solar Thermal Power, Applied Thermal Engineering, (2013).

[197] C.B. Colburn, Developments in Inorganic Nitrogen Chemistry, Edited by Charles B. Colburn, 1973.

[198] K. Jones, The Chemistry of Nitrogen, Pergamon, 1975.

[199] J.D. Lee, Concise Inorganic Chemistry, 5th ed., Wiley, 1999.

[200] G. Rayner-Canham, T. Overton, Descriptive Inorganic Chemistry, 5th ed., W. H. Freeman, 2009.

[201] E.A.K. James E. Huheey, Richard L. Keiter, Inorganic Chemistry: Principles Of Structure And Reactivity, 4th ed ed., HarperCollins College Publishers, 1993.

[202] H.J. Emele´us, A.G. Sharpe, Advances in Inorganic Chemistry and Radiochemistry, Academic Press, New York, 1964.

[203] K. Furukawa, Structure of molten salts near the melting point, Discussions of the Faraday Society, 32 (1961) 53-62.

[204] R.B. King, Encyclopedia of inorganic chemistry, Wiley & Sons Ltd., 1994.

[205] W.A. Hart, O.F. Beumel, The Chemistry of Lithium, Sodium, Potassium, Rubidium, Cesium and Francium, Pergamon Press, 1973.

[206] H. Remy, Treatise on Inorganic Chemistry: Sub-groups of the periodic table and general topics, Elsevier Publishing Company, 1963.

[207] W.L. Jolly, The chemistry of the non-metals, Prentice-Hall, 1966.

[208] E. Bordyushkova, P. Prostsenko, L. Venerovskaya, Kinetics of thermal dissociation and stability of melts and alkali-metal nitrates, Russ J Appl Chem, 40 (1967) 1386-1390.

[209] R.N. Kust, J.D. Burke, Thermal decomposition in alkali metal nitrate melts, Inorganic and Nuclear Chemistry Letters, 6 (1970) 333-335.

[210] B.J. Brough, D.H. Kerridge, S.A. Tariq, Molten lithium-potassium nitrate eutectic: The reactions of some compounds of chromium, Inorganica Chimica Acta, 1 (1967) 267-270.

[211] X. Wei, Y. Wang, Q. Peng, J. Yang, X. Yang, J. Ding, NOx emissions and NO2-formation in thermal energy storage process of binary molten nitrate salts, Energy, 74 (2014) 215-221.

[212] E. Divers, Preparation of Pure Alkali Nitrites, (1898).

[213] A. Holderness, Inorganic and physical chemistry, 2nd ed., Heinemann, 1962.

[214] H. Bloom, Recent progress in the high temperature chemistry of inorganic salt systems, Pure and Applied Chemistry, 7 (1963) 389-406.

[215] D.W. Barnum, Some History of Nitrates, Journal of Chemical Education, 80 (2003) 1393.

[216] F.L. Haigh, CERTAIN PHYSICAL PROPERTIES OF THE ALKALI NITRATES AND CHLORIDES, Journal of the American Chemical Society, 34 (1912) 1137-1159.

[217] R.A.F.P. Jr, The Nitrate Deposits of Chile, The Journal of Geology, 18 (1910) 1-32.

[218] G. Diaz, The Nitrate Deposits of Chile, in: K.-J. Reutter, E. Scheuber, P. Wigger (Eds.) Tectonics of the Southern Central Andes, Springer Berlin Heidelberg, 1994, pp. 303-316.

[219] A.I. Vogel, A text-book of macro and semimicro qualitative inorganic analysis, (1724).

[220] S. Gordon, C. Campbell, Differential thermal analysis of inorganic compounds, Analytical chemistry, 27 (1955) 1102-1109.

[221] U. Müller, Polymorphism and Phase Transitions, in: Inorganic Structural Chemistry, John Wiley & Sons, Ltd, 2007, pp. 30-38.

[222] H. Jendoubi, D. Hellali, H. Zamali, M. Jemal, The phase diagram of KNO3–RbNO3, Journal of Thermal Analysis and Calorimetry, 111 (2013) 877-883.

[223] S.W. Kennedy, W.M. Kriven, Surface effects before and after the aragonite-type to calcite-like transformation in potassium nitrate in relation to mechanism, J Mater Sci, 7 (1972) 1092-1095.

[224] C.N.R. Rao, B. Prakash, M. Natarajan, Crystal structure transformations in inorganic nitrites, nitrates, and carbonates, Nat. Stand. Ref. Data Ser. Nat. Bur. Stand., (1975) 1-48.

[225] S. Kennedy, M. Odlyha, Polymorphic transformation II→ I in potassium nitrate: multiple orientations, Australian Journal of Chemistry, 27 (1974) 1121-1124.

[226] R. Benages-Vilau, T. Calvet, M. Cuevas-Diarte, Polymorphism, crystal growth, crystal morphology and solid-state miscibility of alkali nitrates, Crystallography Reviews, 20 (2014) 25-55.

[227] J.R. Ferraro, The nitrate symmetry in metallic nitrates, Journal of Molecular Spectroscopy, 4 (1960) 99-105.

[228] P.S. Diamond, R.F. Denman, Laboratory techniques in chemistry and biochemistry, Butterworths, 1973.

[229] B. Brough, D. Kerridge, Reactions of Metals in Fused Nitrate Eutectic, Inorganic Chemistry, 4 (1965) 1353-1356.

[230] R.W. Bradshaw, Effect of composition on the density of multi-component molten nitrate salts, Sandia National Laboratories Technical Report No. SAND2009-8221, (2009).

[231] L.R. White, H.T. Davis, Thermal conductivity of molten alkali nitrates, The Journal of Chemical Physics, 47 (1967) 5433-5439.

[232] J. McDonald, H.T. Davis, Thermal conductivity of binary mixtures of alkali nitrates, The Journal of Physical Chemistry, 74 (1970) 725-730.

[233] K.H. Stern, High temperature properties and thermal decomposition of inorganic salts with oxyanions, CRC press, 2000.

[234] G.J. Janz, Molten salts handbook, Academic Press, 111 Fifth avenue, New york, New York 10003, USA, 1967.

[235] M. Liu, W. Saman, F. Bruno, Review on storage materials and thermal performance enhancement techniques for high temperature phase change thermal storage systems, Renewable and Sustainable Energy Reviews, 16 (2012) 2118-2132.

[236] M. Yamada, M. Tago, S. Fukusako, A. Horibe, Melting point and supercooling characteristics of molten salt, Thermochimica Acta, 218 (1993) 401-411.

[237] A.D.P. C.W. Bale, W.T. Thompson -- G. Eriksson, K. Hack P. Chartrand, S. Decterov, I-H. Jung, J. Melancon -- S. Petersen, FactSage ™, www.factsage.com, Copyright (c) 1976-2013, in, Thermfact and GTT- Technologies, 2013.

[238] D.D. Wagman, W.H. Evans, V.B. Parker, R.H. Schumm, I. Halow, The NBS tables of chemical thermodynamic properties. Selected values for inorganic and C1 and C2 organic substances in SI units, in, DTIC Document, 1982.

[239] D.R. Lide, CRC handbook of chemistry and physics, CRC press, 2004.

[240] Y. Dessureault, J. Sangster, A. Pelton, Evaluation critique des données thermodynamiques et des diagrammes de phases des systèmes AOH-AX, ANO3-AX, ANO3, AOH-BOH où A, B, Journal de chimie physique, 87 (1990) 407-453.

[241] J. Sangster, Thermodynamics and phase diagrams of 32 binary common-ion systems of the group Li, Na, K, Rb, Cs//F, Cl, Br, I, OH, NO3, Journal of phase equilibria, 21 (2000) 241-268.

[242] Y. Dessureault, J. Sangster, A.D. Pelton, Coupled Phase Diagram-Thermodynamic Analysis of the 24 Binary Systems, A2CO3-AX and A2SO4-AX Where A= Li, Na, K and X= Cl, F, NO3, OH, Journal of physical and chemical reference data, 19 (1990) 1149-1178.

[243] I. Barin, O. Knacke, O. Kubaschewski, Thermochemical properties of inorganic substances: supplement, Springer-Verlag Berlin, 1977.

[244] H.E. Barner, R.V. Scheuerman, Handbook of thermochemical data for compounds and aqueous species, Wiley New York, 1978.

[245] T. Bauer, D. Laing, U. Kröner, R. Tamme, Sodium nitrate for high temperature latent heat storage, in: 11th International Conference on Thermal Energy Storage–Effstock, 2009, pp. 14-17.

[246] K.C. Patil, R.K. Gosavi, C.N.R. Rao, Infrared spectra and thermal decomposition of metal nitrites and nitrates, Inorganica Chimica Acta, 1 (1967) 155-160.

[247] C. Hardy, B. Field, 982. The volatility of nitrates and nitrites of the alkali metals, J. Chem. Soc., 11 (1963) 5130-5134.

[248] A. Lee, E. Johnson, Stoichiometry and kinetics of the thermal decomposition of molten anhydrous lithium nitrite, Inorganic Chemistry, 11 (1972) 782-787.

[249] K.H. Stern, High Temperature Properties and Decomposition of Inorganic Salts Part 3, Nitrates and Nitrites, Journal of Physical and Chemical Reference Data, 1 (1972) 747-772.

[250] E.S. Freeman, The Kinetics of the Thermal Decomposition of Potassium Nitrate and of the Reaction between Potassium Nitrite and Oxygen1a, Journal of the American Chemical Society, 79 (1957) 838-842.

[251] P. Gimenez, S. Fereres, Effect of Heating Rates and Composition on the Thermal Decomposition of Nitrate Based Molten Salts, Energy Procedia, 69 (2015) 654-662.

[252] R. Bradshaw, S. Goods, Corrosion of alloys and metals by molten nitrates, Not Available, (2003) 117-134.

[253] E.S. Freeman, The kinetics of the thermal decomposition of sodium nitrate and of the reaction between sodium nitrite and oxygen, The Journal of Physical Chemistry, 60 (1956) 1487-1493.

[254] A. Büchler, J.L. Stauffer, Gaseous Alkali—Nitrogen—Oxygen and Alkali—Phosphorus—Oxygen Compounds1, The Journal of Physical Chemistry, 70 (1966) 4092-4094.

[255] F. Paniccia, P. Zambonin, Redox mechanisms in an ionic matrix. III. Kinetics of the reaction nitrite ion+ molecular oxygen= nitrate ion in molten alkali nitrates, The Journal of Physical Chemistry, 77 (1973) 1810-1813.

[256] G. McConohy, A. Kruizenga, Molten nitrate salts at 600 and 680°C: Thermophysical property changes and corrosion of high-temperature nickel alloys, Solar Energy, 103 (2014) 242-252.

[257] R.F. Bartholomew, A Study of the Equilibrium KNO3 (l) ↔ KNO2 (l)+ 1/2O2 (g) over the Temperature Range 550-750°, The Journal of Physical Chemistry, 70 (1966) 3442-3446.

[258] T. Oza, Thermal decomposition of sodium and potassium nitrites, J Indian Chem Soc, 22 (1945) 173-180.

[259] T. Oza, S. Patel, Thermal decomposition of strontium nitrite, J Ind Chem Soc, 31 (1954) 519.

[260] D.D. Gill, N.P. Siegel, R.W. Bradshaw, C.K. Ho, Design, fabrication and testing of an apparatus for material compatibility testing in nitrate salts at temperatures up to 700 C,

in: ASME 2011 5th International Conference on Energy Sustainability, American Society of Mechanical Engineers, 2011, pp. 605-610.

[261] A. Kruizenga, D. Gill, Corrosion of Iron Stainless Steels in Molten Nitrate Salt, Energy Procedia, 49 (2014) 878-887.

[262] A.G. Fernández, H. Galleguillos, F.J. Pérez, Thermal influence in corrosion properties of Chilean solar nitrates, Solar Energy, 109 (2014) 125-134.

[263] A.G. Fernández, M. Grágeda, H. Galleguillos, Impurity Influence in Physico-chemical and Corrosion Properties of Chilean Solar Nitrates, Energy Procedia, 49 (2014) 607-616.

[264] R.I. Olivares, C. Chen, S. Wright, The Thermal Stability of Molten Lithium--Sodium--Potassium Carbonate and the Influence of Additives on the Melting Point, Journal of solar energy engineering, 134 (2012) 041002-041008.

[265] C.M. Kramer, Z.A. Munir, J.V. Volponi, Screening tests of sodium nitrate decomposition, Solar Energy Materials, 6 (1981) 85-95.

[266] J.H. Espenson, Chemical kinetics and reaction mechanisms, McGraw-Hill, 1981.

[267] S. Aduru, S. Contarini, J.W. Rabalais, Electron-, X-ray-, and ion-stimulated decomposition of nitrate salts, The Journal of Physical Chemistry, 90 (1986) 1683-1688.

[268] G.J. Janz, D.W. James, Raman spectra and ionic interactions in molten nitrates, The Journal of Chemical Physics, 35 (1961) 739-745.

[269] J. Greenberg, L.J. Hallgren, Infrared absorption spectra of alkali metal nitrates and nitrites above and below the melting point, The Journal of Chemical Physics, 33 (1960) 900-902.

[270] A.R. Ubbelohde, Melting and Crystal Structures, Pergamon Press, Oxford university press, 1965.

[271] L. Maxwell, S. Hendricks, V. Mosley, Interatomic Distances of the Alkali Halide Molecules by Electron Diffraction, Physical Review, 52 (1937) 968.

[272] C. Hardy, B. Field, VOLATILITY OF NITRATES AND NITRITES OF ALKALI METALS, JOURNAL OF THE CHEMICAL SOCIETY, (1963) 5130-&.

[273] L. Pauling, Atomic radii and interatomic distances in metals, Journal of the American Chemical Society, 69 (1947) 542-553.

[274] K.H. Stern, The effect of cations on the thermal decomposition of salts with oxyanions: A semi-empirical correlation, Journal of Chemical Education, 46 (1969) 645.

[275] M. Sweeney, Thermal stabilities of isoelectronic, isostructural nitrates, carbonates and borates, Thermochimica Acta, 11 (1975) 409-424.

[276] C.C. Addison, N. Logan, Anhydrous Metal Nitrates, in: H.J. Emeléus, A.G. Sharpe (Eds.) Advances in Inorganic Chemistry and Radiochemistry, Academic Press, 1964, pp. 71-142.

[277] S. Yuvaraj, L. Fan-Yuan, C. Tsong-Huei, Y. Chuin-Tih, Thermal decomposition of metal nitrates in air and hydrogen environments, The Journal of Physical Chemistry B, 107 (2003) 1044-1047.

[278] S. Stølen, T. Grande, Chemical thermodynamics of materials: macroscopic and microscopic aspects, John Wiley & Sons, 2004.

[279] N. Pfleger, M. Braun, M. Eck, T. Bauer, Assessment of Novel Inorganic Storage Medium with Low Melting Point, Energy Procedia, 69 (2015) 988-996.

[280] F. Roget, C. Favotto, J. Rogez, Study of the KNO 3–LiNO 3 and KNO 3–NaNO 3–LiNO 3 eutectics as phase change materials for thermal storage in a low-temperature solar power plant, Solar Energy, 95 (2013) 155-169.

[281] O. Levenspiel, Chemical reaction engineering, in, John Wiley & Sons, USA, 1999.

[282] K.J. Laidler, Chemical Kinetics, 3rd ed., Harper & Row Publishers, Inc., 10 East 53d Street, New york, NY 10022-5299, 1987.

[283] J.J. Carberry, Chemical and catalytic reaction engineering, Courier Dover Publications, 2001.

[284] C. Vallet, Phase diagrams and thermodynamic properties of some molten nitrate mixtures, The Journal of Chemical Thermodynamics, 4 (1972) 105-114.

[285] H. Okamoto, T. Massalski, Guidelines for binary phase diagram assessment, Journal of phase equilibria, 14 (1993) 316-335.

[286] U.R. Kattner, The thermodynamic modeling of multicomponent phase equilibria, JOM, 49 (1997) 14-19.

[287] M. Hillert, Empirical methods of predicting and representing thermodynamic properties of ternary solution phases, Calphad, 4 (1980) 1-12.

[288] K.-C. Chou, Y. Austin Chang, A Study of Ternary Geometrical Models, Berichte der Bunsengesellschaft für physikalische Chemie, 93 (1989) 735-741.

[289] Y.A. Chang, S. Chen, F. Zhang, X. Yan, F. Xie, R. Schmid-Fetzer, W.A. Oates, Phase diagram calculation: past, present and future, Progress in Materials Science, 49 (2004) 313-345.

[290] J.M. Prausnitz, R.N. Lichtenthaler, E.G. de Azevedo, Molecular thermodynamics of fluid-phase equilibria, Pearson Education, 1998.

[291] J.V. Sengers, Applied Thermodynamics of Fluids, Royal Society of Chemistry, 2010.

[292] Z. Nickmand, S.F. Aghamiri, A new modified van Laar model for associating mixtures, Journal of Dispersion Science and Technology, 31 (2010) 1638-1647.

[293] E. Neau, J. Escandell, C. Nicolas, Modeling of highly nonideal systems: 1. A generalized version of the NRTL equation for the description of low-pressure equilibria, Industrial & Engineering Chemistry Research, 49 (2010) 7580-7588.

[294] W. Yu, S. Guoquan, L. Shaobo, S. Yimin, Q. Zhiyu, Phase equilibria calculation of LaI 3-MI (M= Na, K, Cs) binary systems, Journal of Rare Earths, 27 (2009) 300-303.

[295] G.M. Wilson, Vapor-liquid equilibrium. XI. A new expression for the excess free energy of mixing, Journal of the American Chemical Society, 86 (1964) 127-130.

[296] K. Nakanishi, Thermodynamic Studies of Phase Equilibria in Molten Salt Systems. Prediction of Liquidus and Eutectic Behavior in Mixtures Having a Common Ion, Industrial & Engineering Chemistry Fundamentals, 9 (1970) 449-453.

[297] M. Blander, S. Yosim, Conformal ionic mixtures, The Journal of Chemical Physics, 39 (1963) 2610-2616.

[298] M. Saboungi, H. Schnyders, M. Foster, M. Blander, Phase diagrams of reciprocal molten salt systems. Calculations of liquid-liquid miscibility gaps, The Journal of Physical Chemistry, 78 (1974) 1091-1096.

[299] D.A. Nissen, B.H. Van Domelen, Regular solution theory and the surface tension of molten salt mixtures, The Journal of Physical Chemistry, 79 (1975) 2003-2007.

[300] L.S. Hersh, O.J. Kleppa, Enthalpies of Mixing in Some Binary Liquid Halide Mixtures, The Journal of Chemical Physics, 42 (1965) 1309-1322.

[301] O.J. Kleppa, R.B. Clarke, L.S. Hersh, Studies of Fused Salts. III. Heats of Mixing in Silver Nitrate-Alkali Nitrate Mixtures, The Journal of Chemical Physics, 35 (1961) 175-180.

[302] O.J. Kleppa, L.S. Hersh, Heats of Mixing in Liquid Alkali Nitrate Systems, The Journal of Chemical Physics, 34 (1961) 351-358.

[303] O.J. Kleppa, A NEW TWIN HIGH-TEMPERATURE REACTION CALORIMETER. THE HEATS OF MIXING IN LIQUID SODIUM-POTASSIUM NITRATES, The Journal of Physical Chemistry, 64 (1960) 1937-1940.

[304] D. Mantha, T. Wang, R. Reddy, Thermodynamic modeling of eutectic point in the LiNO3-NaNO3-KNO3 ternary system, Journal of phase equilibria and diffusion, 33 (2012) 110-114.

[305] K. Coscia, T. Elliott, S. Mohapatra, A. Oztekin, S. Neti, Binary and ternary nitrate solar heat transfer fluids, Journal of Solar Energy Engineering, 135 (2013) 021011.

[306] A. Bergman, S. Berul, Interrelation Between Sodium and Potassium Nitrates in Fusions, Izv. Sekt. Fiz-Khim. Anal. Inst. Obshch. Neorg. Khim. Akad. Nauk SSSR, 21 (1952) 178-183.

[307] W.M. Madgin, H.V.A. Briscoe, R.S. Hughesdon, H.G. Smith, J. Read, S. Glasstone, S. Biggs, F.G. Pope, CCCXLIV.—The melting-point (solidus) curve for mixtures of potassium nitrate and sodium nitrate, Journal of the Chemical Society, Transactions, 123 (1923) 2914-2916.

[308] A. Kirgintsev, V. Kosyakov, Use of Progressive Crystallization for Definition of the Sollidus in the Sodium Nitrate-Potassium Nitrate System, Izv. Akad. Nauk. SSSR, Ser. Khim, 10 (1968) 2208-2213.

[309] W. Klement, Variation of λ transition temperature in $NaNO_3$-base binary alloys with $AgNO_3$, KNO_3 and $NaNO_2$, Journal of Inorganic and Nuclear Chemistry, 36 (1974) 1916-1918.

[310] D. Rogers, G. Janz, Melting-crystallization and pre-melting properties of $NaNO_3$-KNO_3, (1984).

[311] R. Benages-Vilau, T. Calvet, M. Cuevas-Diarte, H. Oonk, The NaNO3–KNO3 phase diagram, Phase Transitions, (2015) 1-20.

[312] H. Oonk, Solid-state solubility and its limits. The alkali halide case, Pure and Applied Chemistry, 73 (2001) 807-823.

[313] T. Elliott, Gibbs Energy Modeling of Binary and Ternary Molten Nitrate Salt Systems, (2012).

[314] T. Wang, D. Mantha, R.G. Reddy, Novel low melting point quaternary eutectic system for solar thermal energy storage, Applied Energy, Volume 102 (2012) Pages 1422–1429.

[315] C. Bale, E. Bélisle, P. Chartrand, S. Decterov, G. Eriksson, K. Hack, I.-H. Jung, Y.-B. Kang, J. Melançon, A. Pelton, FactSage thermochemical software and databases—recent developments, Calphad, 33 (2009) 295-311.

[316] MATLAB-Simulink, Mathworks®, viewed 6 August 2014, <http://www.mathworks.com.au/products/matlab/> . (2014).

[317] K.E. Atkinson, An introduction to numerical analysis, John Wiley & Sons, 2008.

[318] W.H. Press, S.A. Teukolsky, W.T. Vetterling, B.P. Flannery, Numerical recipes in C, Cambridge university press Cambridge, 1996.

[319] J.E. Dennis Jr, R.B. Schnabel, Numerical methods for unconstrained optimization and nonlinear equations, Siam, 1996.

[320] A.R. Conn, N.I. Gould, P.L. Toint, Trust region methods, Siam, 2000.

[321] W. Sun, Y.-X. Yuan, Optimization theory and methods: nonlinear programming, Springer Science & Business Media, 2006.

[322] J.W. Harris, H. Stöcker, Handbook of mathematics and computational science, Springer Science & Business Media, 1998.

[323] W.H. Press, Numerical recipes 3rd edition: The art of scientific computing, Cambridge university press ©, 2007.

[324] Y. Takahashi, R. Sakamoto, M. Kamimoto, Heat capacities and latent heats of LiNO3, NaNO3, and KNO3, International journal of thermophysics, 9 (1988) 1081-1090.

[325] H.A. Oonk, M.T. Calvet, Equilibrium between phases of matter: phenomenology and thermodynamics, Springer Science & Business Media, 2007.

[326] R.D. Weir, T.W. de Loos, Measurement of the thermodynamic properties of multiple phases, Gulf Professional Publishing, 2005.

[327] W. Klement, Variation of λ transition temperature in NaNO 3-base binary alloys with AgNO 3, KNO 3 and NaNO 2, Journal of Inorganic and Nuclear Chemistry, 36 (1974) 1916-1918.

[328] D. Hussink, The Solidus Curve for Mixtures of Potassium and Sodium Nitrates, Z. Phys. Chem, 32 (1900) 536-540.

[329] X. Zhang, K. Xu, Y. Gao, The phase diagram of LiNO3–KNO3, Thermochimica Acta, 385 (2002) 81-84.

[330] K. Xu, Raman evidence for the congruently melting compound KLi (NO 3) 2 in the LiNO 3–KNO 3 system, Journal of Physics and Chemistry of Solids, 60 (1999) 5-11.

[331] R.J. Angelici, Synthesis and technique in inorganic chemistry, 2nd ed., Saunders Philadelphia, 1977.

[332] C.-S.S. Evolution, Thermal Analysis Software - CALISTO, KEP Technologies, viewed 4 March 2013, <http://www.setaram.com/CALISTO.htm>. , in, 2013.

[333] M.F. Henry, Hazardous materials response handbook National Fire Protection Association, 1989.

[334] E. Meyer, Chemistry of Hazardous Materials, 4th ed., Pearson Prentice Hall, 2004.

[335] O. Abe, T. Utsunomiya, Y. Hoshino, The thermal stability of alkali and alkaline-earth metal hydroxide—nitrate systems, Thermochimica Acta, 87 (1985) 99-108.

[336] D.A. Skoog, D.M. West, H.F. J., C.S. R., Fundamentals of analytical chemistry, 8th ed., Brooks/Cole, Cengage 2004.

[337] H.K. Cammenga, W. Eysel, E. Gmelin, W. Hemminger, G.W. Höhne, S.M. Sarge, The temperature calibration of scanning calorimeters: part 2. Calibration substances, Thermochimica Acta, 219 (1993) 333-342.

[338] G.W.H. Höhne, H.K. Cammenga, W. Eysel, E. Gmelin, W. Hemminger, The temperature calibration of scanning calorimeters, Thermochimica Acta, 160 (1990) 1-12.

[339] P.K. Gallagher, M.E. Brown, R.B. Kemp, Handbook of thermal analysis and calorimetry, Elsevier, 1998.

[340] F.D. Rossini, Thermogravimetry (TG) or Thermogravimetric Analysis (TGA), viewed on 10 October 2015, <http://www.astm.org/Standards/E967.htm>. Pure applied chemistry, 22 (1970) 577.

[341] S.M. Sarge, E. Gmelin, G.W. Höhne, H.K. Cammenga, W. Hemminger, W. Eysel, The caloric calibration of scanning calorimeters, Thermochimica Acta, 247 (1994) 129-168.

[342] I.W. Group, R. Sabbah, A. Xu-wu, J.C. USA, M.P. Leitão, M. Roux, L. Torres, Reference materials for calorimetry and differential thermal analysis, Thermochimica Acta, 331 (1999) 93-204.

[343] J. Emsley, The elements, 3rd ed, Oxford press,, Clarendon press, 1989.

[344] C.H. Spink, Differential scanning calorimetry, Methods in cell biology, 84 (2008) 115-141.

[345] H. Bartlett, K. Johnson, Electrolytic reduction and Ellingham diagrams for oxy-anion systems, CANADIAN JOURNAL OF CHEMISTRY, 44 (1966) 2119-&.

[346] A.S. Nagelberg, R.W. Mar, Thermochemistry of Nitrate Salts, in: Proceedings of the Symposium on High Temperature Materials Chemistry, Electrochemical Society, 1982, pp. 89.

[347] Q.-P.V. 2014, viewed 6 August 2014, <http://www.pfeiffer-vacuum.com/know-how/mass-spectrometers-and-residual-gas-analysis/introduction-operating-principle/portfolio/data-analysis-systems/technology.action?chapter=tec4.1.4.2>. (2014).

[348] M.J. Maeso, J. Largo, The Heat-Capacities of Lino3 and Csno3 from 350 to 700-K, Thermochimica Acta, 222 (1993) 195-201.

[349] R.W. Carling, Heat capacities of NaNO3 and KNO3 from 350 to 800 K, Thermochimica Acta, 60 (1983) 265-275.

[350] H.M. Goodwin, H.T. Kalmus, On the latent heat of fusion and the specific heat of salts in the solid and liquid state, Physical Review (Series I), 28 (1909) 1.

[351] E.A. Dancy, Molar enthalpy of the solid-solid transition in NaNO3, Thermochimica Acta, 59 (1982) 251-252.

[352] J. Ketelaar, B. Strijk, The atomic arrangement in solid sodium nitrate at high temperatures, Recueil des Travaux Chimiques des Pays-Bas, 64 (1945) 174-182.

[353] F.C. Kracek, Gradual transition in sodium nitrate. I. Physico-chemical criteria of the transition, Journal of the American Chemical Society, 53 (1931) 2609-2624.

[354] H. Miekk-oja, Kalorimetrische Untersuchungen über Umwandlungen in NaNO3 und KNO3, in, Suomalainen tiedeakatemia, 1941.

[355] E.A. Dancy, P. Nguyen-Duy, Comments on —heats of melting of sodium nitrate and indium by differential scanning calorimetry: a suggestion for a new calibration substance", Thermochimica Acta, 31 (1979) 395.

[356] D. Sergeev, E. Yazhenskikh, D. Kobertz, K. Hack, M. Müller, Phase equilibria in the reciprocal NaCl–KCl–NaNO3–KNO3 system, Calphad, 51 (2015) 111-124.

[357] G.J. Janz, F.J. Kelly, J.L. Pérano, Melting and pre-melting phenomena in alkali metal nitrates, Journal of Chemical and Engineering Data, 9 (1964) 133-136.

[358] T. Jriri, J. Rogez, C. Bergman, J.C. Mathieu, Thermodynamic study of the condensed phases of NaNO3, KNO3 and CsNO3 and their transitions, Thermochimica Acta, 266 (1995) 147-161.

[359] A. Mustajoki, The specific heat of cesium nitrate in the temperature interval 50–450 C as well as the heat of transition and heat of fusion, Ann Acad Sci Fenn A, 6 (1957) 1-12.

[360] K.G. Zeeb, M.G. Lowings, K.G. McCurdy, L.G. Hepler, Heats of transition and melting of sodium nitrate by differential scanning calorimetry: use of indium and sodium nitrate as calibration substances, Thermochimica Acta, 40 (1980) 245-249.

[361] C. Person, Untersuchung über die latente Wärme, Annalen der Physik, 146 (1847) 300-301.

[362] P. Nguyen-Duy, E.A. Dancy, Calorimetric determination of the thermodynamic properties of the alkali metal salts NaNO3, KNO3, Na2Cr2O7, K2Cr2O7 and their binary eutectic solutions, Thermochimica Acta, 39 (1980) 95-102.

[363] M. Bakes, J. Dupuy, J. Guion, ELECTROCHIMIE-ETUDE DANOMALIES ELECTROCHIMIQUES DORIGINE STRUCTURALE EN SELS FONDUS, COMPTES RENDUS HEBDOMADAIRES DES SEANCES DE L ACADEMIE DES SCIENCES, 256 (1963) 2376-&.

[364] D. Speros, R. Woodhouse, REALIZATION OF QUANTITATIVE DIFFERENTIAL THERMAL ANALYSIS. I HEATS AND RATES OF SOLID—LIQUID TRANSITIONS, The Journal of Physical Chemistry, 67 (1963) 2164-2168.

[365] O. Beneš, R.J.M. Konings, S. Wurzer, M. Sierig, A. Dockendorf, A DSC study of the NaNO3–KNO3 system using an innovative encapsulation technique, Thermochimica Acta, 509 (2010) 62-66.

[366] T. Hu, Calorimetric investigations of molten salts, Journal of Physical Chemistry, 68 (1964) 387-390.

[367] O.J. Kleppa, Heats of fusion of the monovalent nitrates by high-temperature reaction calorimetry, Journal of Chemical and Engineering Data, 8 (1963) 331-332.

[368] H. Kutsuna, T. Morita, K. Fukuda, Natural circulation including boiling in a rectangular loop, (1990).

[369] M.G. Lowings, K.G. McCurdy, L.G. Hepler, Heats of melting of sodium nitrate and indium by differential scanning calorimetry: a suggestion for a new calibration substance, Thermochimica Acta, 23 (1978) 365-370.

[370] D.J. Rogers, G.J. Janz, MELTING-CRYSTALLIZATION AND PREMELTING PROPERTIES OF NANO//3-KNO//3. ENTHALPIES AND HEAT CAPACITIES, J CHEM ENG DATA, V 27 (1982) 424-428.

[371] P.W. Bridgman, Polymorphic changes under pressure of the univalent nitrates, in: Proceedings of the American Academy of Arts and Sciences, JSTOR, 1916, pp. 581-625.

[372] A. Arell, M. Varteva, Transition Energy and Temperature of TiNO 3 at the Transition I II, Suomalainen Tiedeakatemia, 1962.

[373] E. Wang, Latent heat measurement of phase transformations in potassium nitrate, Journal of The Electrochemical Society, 123 (1976) 435-437.

[374] V.V. Deshpande, M.D. Karkhanavala, U.R.K. Rao, Phase transitions in potassium nitrate, Journal of Thermal Analysis and Calorimetry, 6 (1974) 613-621.

[375] A. Mustajoki, Calorimetric measurements with respect to the polymorphic transformations of potassium nitrate, Ann Acad Sci Fenn. A, 6 (1962) 1-11.

[376] N. Shmidt, D. Maksimov, ADIABATIC CALORIMETER, WORKING IN 300-800-K RANGE-HEAT-CAPACITY OF CORUNDUM, QUARTZ GLASS AND POTASSIUM-NITRATE, ZHURNAL FIZICHESKOI KHIMII, 53 (1979) 1895-1899.

[377] M. Westphal, J. Wood, R. Redin, T. Ashworth, Calorimetric and photoacoustic investigation of KNO3 phase transitions, Journal of applied physics, 73 (1993) 7302-7310.

[378] R.P. Clark, Heats of fusion and heat capacities of Lithium Chloride-Potassium Chloride eutectic and potassium nitrate, Journal of Chemical and Engineering Data, 18 (1973) 67-70.

[379] H. Zamali, M. JEMAL, PHASE-DIAGRAMS OF THE BINARY-SYSTEMS KNO3-CSNO3 AND KNO3-NANO3, JOURNAL OF THERMAL ANALYSIS, 41 (1994) 1091-1099.

[380] Georg Widmann, 2001, Interpreting TGA curves, Mettler-Toledo International Inc, viewed 1 July 2015,< http://us.mt.com/us/en/home/supportive_content/usercom/TA_UserCom13.html>. .

[381] Y. Hoshino, T. Utsunomiya, O. Abe, The thermal decomposition of sodium nitrate and the effects of several oxides on the decomposition, Bulletin of the Chemical Society of Japan, 54 (1981) 1385-1391.

[382] R. Speyer, Thermal analysis of materials, CRC Press, 1993.

[383] E.L. Charsley, P.G. Laye, H.M. Markham, J.O. Hill, B. Berger, T.T. Griffiths, Determination of the equilibrium temperatures and enthalpies of the solid–solid transitions of rubidium nitrate by differential scanning calorimetry, Thermochimica Acta, 469 (2008) 65-70.

[384] E. Charrier, E.L. Charsley, P.G. Laye, H.M. Markham, B. Berger, T.T. Griffiths, Determination of the temperature and enthalpy of the solid–solid phase transition of caesium nitrate by differential scanning calorimetry, Thermochimica Acta, 445 (2006) 36-39.

[385] E.M. Brown, Introduction to Thermal Analysis: Techniques and Applications, 2nd Edition, Kluwer Academic Publishers, Netherlands, 2001.

[386] C. Schick, G. Höhne, On temperature calibration of power compensation DSC in cooling mode, Thermochimica acta, 187 (1991) 351-356.

[387] I. Egry, Chapter 2.1 - Structure and Properties of Molten Metals, in: S. Seetharaman (Ed.) Treatise on Process Metallurgy, Elsevier, Boston, 2014, pp. 61-148.

[388] J. Schawe, C. Schick, Influence of the heat conductivity of the sample on DSC curves and its correction, Thermochimica acta, 187 (1991) 335-349.

[389] G. Wang, I.R. Harrison, Polymer melting: thermal resistance effects in a DSC, Thermochimica acta, 230 (1993) 309-317.

[390] THASS-GmbH, Buoyancy Phenomenon in TGA Systems,Thermal Analysis and Surface Solutions GmbH. viewed 19 OCtober 2014, <http://www.thass.org>. (2014).

[391] MettlerToledo©, Physical Influences METTLER TOLEDO, viewed 19 October 2014, <http://au.mt.com/au/en/home/supportive_content/specials/Proper_Wei_4.html>. (2014).

[392] T.C. Vaimakis, Thermogravimetry (TG) or Thermogravimetric Analysis (TGA), viewed on 19 October 2014, <http://thanma.web.auth.gr/files/Thermogravimetry_TG.pdf>.

[393] H.R. Carveth, Study of a Three-Component System, The Journal of Physical Chemistry, 2 (1898) 209-228.

[394] A. Bergman, K. Nogoev, The CO (NH2) 2-LiNO3; K, Li, Na|| NO3; and K, NH4, Na|| NO3 Systems, Russ. J. Inorg. Chem, 9 (1964) 771-773.

[395] B. Bond, P. Jacobs, The thermal decomposition of sodium nitrate, Journal of the Chemical Society A: Inorganic, Physical, Theoretical, (1966) 1265-1268.

[396] I. Péter, 2.11. Purity check by differential scanning calorimetry, Identification and Determination of Impurities in Drugs, (2000) 396.

[397] M.J. Harris, E.K.H. Salje, B.K. Guttler, An infrared spectroscopic study of the internal modes of sodium nitrate: implications for the structural phase transition, Journal of Physics: Condensed Matter, 2 (1990) 5517.

[398] D. Newns, L. Staveley, The significance of entropies of transition in salts, with special reference to nitrates, Chemical Reviews, 66 (1966) 267-278.

[399] X. Zhang, J. Tian, K. Xu, Y. Gao, Thermodynamic evaluation of phase equilibria in NaNO 3-KNO 3 system, Journal of phase equilibria, 24 (2003) 441-446.

[400] T. Wang, D. Mantha, R.G. Reddy, Thermodynamic properties of LiNO3–NaNO3–KNO3–2KNO3.Mg(NO3)2 system, Thermochimica Acta, Volume 551 (2012) Pages 92–98.

[401] T. Daniels, Thermal Analysis, (1973) 272.

[402] T. Hatakeyama, F.X. Quinn, Thermal analysis: fundamentals and applications to polymer science, 2nd ed., Wiley, 1999.

[403] W. Hemminger, S.M. Sarge, Chapter 1 - Definitions, Nomenclature, Terms and Literature, in: E.B. Michael (Ed.) Handbook of Thermal Analysis and Calorimetry, Elsevier Science B.V., 1998, pp. 1-73.

[404] P.W. Atkins, D.F. Shriver, Shriver & Atkins Inorganic chemistry, 4th Edition, Oxford University Press, Oxford, 2006.

[405] P.J. van Ekeren, Chapter 2 - Thermodynamic Background to Thermal Analysis and Calorimetry, in: E.B. Michael (Ed.) Handbook of Thermal Analysis and Calorimetry, Elsevier Science B.V., 1998, pp. 75-145.

[406] F.W. Fifield, D. Kealey, Principles and Practice of Analytical Chemistry, 4th Edition, Taylor & Francis, 1995.

[407] G. Höhne, W.F. Hemminger, H.J. Flammersheim, Differential Scanning Calorimetry, 2nd ed., Springer, 2003.

[408] A.I. Vogel, J. Mendham, Vogel's textbook of quantitative chemical analysis, Prentice Hall, 2000.

[409] P.K. Gallagher, Chapter 4 - Thermogravimetry and Thermomagnetometry, in: E.B. Michael (Ed.) Handbook of Thermal Analysis and Calorimetry, Elsevier Science B.V., 1998, pp. 225-278.

[410] U. Karst, Analytical Chemistry. A Modern Approach to Analytical Science. 2nd Edition. Edited by Robert Kellner, Jean-Michel Mermet, Matthias Otto, Miguel Valcarcel, Michael Widmer, ChemPhysChem, 6 (2005) 2435-2436.

[411] P.J. Haines, R.S.o. Chemistry, Principles of Thermal Analysis and Calorimetry, Royal Soc. of Chemistry, 2002.

[412] P.J. Haines, M. Reading, F.W. Wilburn, Chapter 5 - Differential Thermal Analysis and Differential Scanning Calorimetry, in: E.B. Michael (Ed.) Handbook of Thermal Analysis and Calorimetry, Elsevier Science B.V., 1998, pp. 279-361.

[413] R.F. Speyer, Thermal analysis of materials, Marcel Dekker, New York :, 1994.

[414] R. Pignatello, Drug-biomembrane interaction studies: The application of calorimetric techniques, Elsevier, 2013.

[415] M.J. Richardson, E.L. Charsley, Chapter 13 - Calibration and Standardisation in DSC, in: E.B. Michael (Ed.) Handbook of Thermal Analysis and Calorimetry, Elsevier Science B.V., 1998, pp. 547-575.

[416] J. Van Humbeeck, Chapter 11 - Simultaneous Thermal Analysis, in: E.B. Michael (Ed.) Handbook of Thermal Analysis and Calorimetry, Elsevier Science B.V., 1998, pp. 497-508.

[417] J. Mullens, Chapter 12 - EGA - Evolved Gas Analysis, in: E.B. Michael (Ed.) Handbook of Thermal Analysis and Calorimetry, Elsevier Science B.V., 1998, pp. 509-546.

[418] C. Dass, Fundamentals of contemporary mass spectrometry, John Wiley & Sons, 2007.

[419] A.W. Czanderna, S.P. Wolsky, Microweighing in vacuum and controlled environments, Elsevier Science, 2012.

[420] J.D. Menczel, R.B. Prime, Thermal Analysis of Polymers : Fundamentals and Applications, in, Wiley, Chicester, 2009.

[421] M.E. Brown, Handbook of Thermal Analysis and Calorimetry: Principles and Practice. Volume 1. 1998. second impression 2003, 1st ed., Elsevier, Netherlands, 1998.

[422] W.W. Wendlandt, Thermal methods of analysis, 2nd ed., Wiley, 1974.

[423] J.W. Dodd, K.H. Tonge, B.R. Currell, ACOL, Thermal methods, Published on behalf of ACOL, London, by Wiley, 1987.

[424] H.H. Kellogg, VAPORIZATION CHEMISTRY IN EXTRACTIVE METALLURGY, Transactions of the Metallurgical Society of Aime, 236 (1966) 602-&.

[425] J.W. Hastie, J.P. Hager, Vapor transport in materials and process chemistry, In Proc. The Elliot Symposium on Chemical Process Metallurgy, pp. 263-286, Iron and Steel Soc., Warrendale, PA., (1990).

[426] A.N. Nesmeianov, R. Gary, A.N. Nesmei͡anov, Vapor pressure of the chemical elements, Elsevier Amsterdam, 1963.

[427] O. Kubaschewski, E.L. Evans, C. Alcock, Metallurgical thermochemistry, 5th Revised and Enlarged ed., Pergamon press Oxford, 1979.

[428] S.R. Dharwadkar, A.S. Kerkar, M.S. Samant, A microthermogravimetric system for the measurement of vapour pressure by a transpiration method, Thermochimica Acta, 217 (1993) 175-186.

[429] S. Dharwadkar, A. Kerkar, M. Samant, A microthermogravimetric system for the measurement of vapour pressure by a transpiration method, Thermochimica Acta, 217 (1993) 175-186.

[430] U. Merten, Diffusion effects in the transpiration method of vapor pressure measurement, The Journal of Physical Chemistry, 63 (1959) 443-445.

[431] C. Alexander, J. Ogden, A. Levy, Transpiration study of magnesium oxide, The Journal of Chemical Physics, 39 (1963) 3057.

[432] S.H. Son, F. Tsukihashi, Vapor Pressure Measurements for the FeCl2-ZnCl2 System by the Transpiration Method, Materials Transactions, 44 (2003) 1116-1119.

[433] R. Pankajavalli, C. Mallika, O. Sreedharan, V. Raghunathan, P. Antony Premkumar, K. Nagaraja, Thermal stability of organo-chromium or chromium organic complexes and vapor pressure measurements on tris (2, 4-pentanedionato) chromium (III) and hexacarbonyl chromium (0) by TG-based transpiration method, Chemical engineering science, 57 (2002) 3603-3610.

[434] R. Pankajavalli, K. Ananthasivan, S. Anthonysamy, P. Vasudeva Rao, Vapour pressure and standard enthalpy of sublimation of KBF< sub> 4</sub> by a TG based transpiration technique, Journal of nuclear materials, 345 (2005) 96-100.

[435] R. Pankajavalli, C. Mallika, O. Sreedharan, M. Premila, P. Gopalan, Vapour pressure of C< sub> 60</sub> by a transpiration method using a horizontal thermobalance, Thermochimica acta, 316 (1998) 101-108.

[436] T. Lakshmi Narasimhan, R. Viswanathan, S. Nalini, Study of Vaporization of Sodium Metaborate by Transpiration Thermogravimetry and Knudsen Effusion Mass Spectrometry, The Journal of Physical Chemistry B, 115 (2011) 13261-13270.

[437] J.P. Hager, R.B. Hill, Thermodynamic properties of the vapor transport reactions in the Au− Cl system by a transpiration-mass spectrometric technique, Metallurgical Transactions, 1 (1970) 2723-2731.

[438] R. Viswanathan, T.L. Narasimhan, S. Nalini, Vapor pressure measurements by mass loss transpiration method with a thermogravimetric apparatus, The Journal of Physical Chemistry B, 113 (2009) 8362-8368.

[439] R. Balasubramanian, T. Lakshmi Narasimhan, R. Viswanathan, S. Nalini, Investigation of the vaporization of boric acid by transpiration thermogravimetry and Knudsen effusion mass spectrometry, The Journal of Physical Chemistry B, 112 (2008) 13873-13884.

[440] K.K. Prasad, Chemical and Metallurgical Thermodynamics, New Age International, 2007.

[441] A. Vignes, Extractive Metallurgy 1: Basic Thermodynamics and Kinetics, John Wiley & Sons, NJ, USA, 2013.

[442] R. DeHoff, Thermodynamics in Materials Science, Second Edition, Taylor & Francis, 2006.

[443] K.E.E. David A. Porter, Mohamed Y. Sherif, Phase transformations in metals and alloys, 3rd ed., CRC press Taylor and Francis Group, FL, USA, 2009.

[444] J.C. Zhao, Methods for Phase Diagram Determination, Elsevier Science, 2011.

[445] H.L. Lukas, S.G. Fries, B. Sundman, Computational thermodynamics: the Calphad method, Cambridge university press Cambridge, 2007.

[446] H. Wiedemann, G. Bayer, Application of simultaneous thermomicroscopy/DSC to the study of phase diagrams, Journal of Thermal Analysis and Calorimetry, 30 (1985) 1273-1281.

[447] A. Miodownik, N. Saunders, Applications of Thermodynamics in the Synthesis and Processing of Materials, Nash and B. Sundman, Ed., TMS, (1995).

[448] B. Sundman, B. Jansson, J.-O. Andersson, The Thermo-Calc databank system, Calphad, 9 (1985) 153-190.

[449] H.L. Lukas, E.T. Henig, B. Zimmermann, Optimization of phase diagrams by a least squares method using simultaneously different types of data, Calphad, 1 (1977) 225-236.

[450] H.L. Lukas, J. Weiss, E.T. Henig, Straegies for the calculation of phase diagrams, Calphad, 6 (1982) 229-251.

[451] M. Hillert, B. Sundman, Predicting miscibility gaps in reciprocal liquids, Calphad, 25 (2001) 599-605.

[452] E.M. Levin, H.F. McMurdie, Phase diagrams for ceramists, 1975 supplement, (1975).

[453] V. Danek, Physico-chemical analysis of molten electrolytes, 1st ed., Elsevier Science, Amsterdam, Nehterlands, 2006.

[454] W.D. Callister, D.G. Rethwisch, Fundamentals of Materials Science and Engineering: An Integrated Approach, Wiley, 2012.

[455] J.H. Hildebrand, Solubility. XII. Regular solutions, The Journal of the American Chemical Society, 51 (1929) 66-80.

[456] B. Sundman, J. Ågren, A regular solution model for phases with several components and sublattices, suitable for computer applications, Journal of Physics and Chemistry of Solids, 42 (1981) 297-301.

[457] J.H. Hildebrand, Solubility, Journal of the American Chemical Society, 38 (1916) 1452-1473.

[458] J. Vidal, Thermodynamics - Applications in Chemical Engineering and the Petroleum Industry, in, Editions Technip, 2003.

[459] E.A. Guggenheim, The Statistical Mechanics of Regular Solutions, Proceedings of the Royal Society of London. Series A - Mathematical and Physical Sciences, 148 (1935) 304-312.

[460] E. Salstrom, J. Hildebrand, The thermodynamic properties of molten solutions of lead chloride in lead bromide, Journal of the American Chemical Society, 52 (1930) 4641-4650.

[461] A.D. Pelton, Thermodynamics and phase diagrams of materials, Materials science and technology, (1991).

[462] M. Hillert, How to select axes for a phase diagram, Journal of phase equilibria, 18 (1997) 249-263.

[463] H. Gupta, J. Morral, H. Nowotny, Constructing multicomponent phase diagrams by overlapping ZPF lines, Scripta metallurgica, 20 (1986) 889-894.

[464] J. Morral, Two-dimensional phase fraction charts, Scripta metallurgica, 18 (1984) 407-410.

[465] T. Bramblett, J. Morral, Construction of two-dimensional phase fraction charts from ternary phase diagrams, Bulletin of Alloy Phase Diagrams, 5 (1984) 433-436.

[466] F. Feher, Handbook of Preparative Inorganic Chemistry, Vol. I, 2nd ed, Georg Brauer, Ed., Academic Press Inc., New York, N. Y, (1963) 447-454.

[467] H.P. Klug, L.E. Alexander, X-ray diffraction procedures, (1954).

[468] B.E. Warren, X-ray Diffraction, Courier Corporation, 1969.